PROCEEDINGS

7TH INTERNATIONAL WORKSHOP ON RELIABLE ENGINEERING COMPUTING

COMPUTING WITH POLYMORPHIC UNCERTAIN DATA

June 15 – 17, 2016 | Ruhr University Bochum, Germany

EDITORS

Steffen Freitag, Rafi L. Muhanna, Robert L. Mullen

RUHR UNIVERSITÄT BOCHUM RUB

WORKSHOP ORGANIZATION

FOUNDERS AND GENERAL CHAIRS

Rafi L. Muhanna, Georgia Institute of Technology, USA
Robert L. Mullen, University of South Carolina, USA

CHAIR

Steffen Freitag, Ruhr University Bochum, Germany

TECHNICAL SUPPORT

Svenja Schützner, Ruhr University Bochum, Germany
Stefan Kunter, Ruhr University Bochum, Germany
Melanie Breyer, Ruhr University Bochum, Germany
Sebastian Mauso, Ruhr University Bochum, Germany
Sangeetha Sivagnanasothy, Ruhr University Bochum, Germany
Janis Reinold, Ruhr University Bochum, Germany
Philipp Edler, Ruhr University Bochum, Germany

WORKSHOP SPONSORS AND SUPPORTING INSTITUTIONS

North Rhine-Westphalian Academy of Sciences, Humanities and Arts
Science Ministry of the federal state of North Rhine-Westphalia

Ruhr University Bochum
Institute for Structural Mechanics, Ruhr University Bochum
Collaborative Research Center SFB 837, Ruhr University Bochum

INTERNATIONAL SCIENTIFIC COMMITTEE

TABLE OF CONTENTS

PREFACE

Reliable Engineering Computing has emerged as a multi-disciplinary quality brand with this conference series, which was hosted at Georgia Tech Savannah in 2004, 2006, and 2008, at the National University of Singapore in 2010, at Brno University of Technology in Brno, Czech Republic in 2012, and at Illinois Institute of Technology in Chicago in 2014. The REC-meetings provide a unique symbiosis of various engineering and associated disciplines with the kernel areas of Civil and Mechanical Engineering, Computer Science, and Mathematics. The central issue of the discussions is the reliability of engineering computations. Cross-disciplinary advisements generate synergy and impulses of a new quality for research and development, as well as for innovative applications.

The 7th International Workshop on Reliable Engineering Computing (REC2016) is hosted by the Institute for Structural Mechanics at Ruhr University Bochum, Germany. The topic of REC2016 “Computing with Polymorphic Uncertain Data” aims to bring together different uncertainty quantification strategies. Polymorphic uncertainty modelling combines stochastic and non-stochastic approaches to quantify aleatory and epistemic uncertainties. Several simulation techniques are discussed to compute and predict the reliability of engineering structures and systems.

As in the previous conferences, different fields of engineering, sciences, and mathematics within the context of risk and uncertainty are addressed. While providing solutions for real life problems is the ultimate goal of the engineering profession, it is crucial to retain the rigor of mathematical formulations and their computational implementations to ensure safety, reliability, and more accurate predictions. For that purpose, reliable approaches are required, starting with uncertainty quantification of input parameters with respect to available information, computing with uncertain data, and ending with the assessment and communication of responses due to uncertainty. The potential for research ranges over all scientific and societal issues related to reliability and computations of engineering structures and processes.

REC2016, with its unique multi-disciplinary character, provides an ideal platform that brings the various aforementioned aspects together to achieve advancements in the field of Reliable Engineering Computing. Additionally, solution strategies are discussed and examined within the framework of polymorphic uncertain data. The results of this conference will provide support for the translation of Reliable Engineering Computing into general engineering practice.

The editors would like to thank all authors and reviewers for their contributions. The conference is financially supported by the Science Ministry of the federal state of North Rhine-Westphalia, Germany by means of a scholarship awarded to Steffen Freitag as a Junior Member of the North Rhine-Westphalian Academy of Sciences, Humanities and Arts, the Collaborative Research Center SFB 837, and by Ruhr University Bochum. We appreciate the support of the sponsors and the supporting institutions. Additionally, the efforts of the technical support team of the Institute for Structural Mechanics at Ruhr University Bochum are highly appreciated.

Steffen Freitag
Rafi L. Muhanna
Robert L. Mullen

Emerging Concepts and Approaches for Efficient and Realistic Uncertainty Quantification *

Michael Beer[1),2)], Ioannis A. Kougioumtzoglou[3)], Edoardo Patelli[2)]
[1)] *Institute for Risk and Reliability, Leibniz Universität Hannover, Hannover, Germany / University of Liverpool, Liverpool, UK / Tongji University, Shanghai, China*
beer@irz.uni-hannover.de
[2)] *Institute for Risk and Uncertainty, University of Liverpool, Liverpool, UK*
[3)] *Department of Civil Engineering & Engineering Mechanics, Columbia University, USA*

Abstract: Our built environment is increasingly dominated by structures and infrastructure from previous decades, partly even with a century of experienced lifetime. These structures and infrastructure are, to a significant extent, critical for the functionality of our economic and societal life, and thus, require proper approaches and measures to verify and ensure their safety. Safety analysis and maintenance scheduling, however, become increasingly complicated due to uncertainties and complexity, which result significantly from ageing and from interactive phenomena. The realistic quantification of uncertainties and their numerically efficient processing in complex analyses are the two key challenges in this context. In this Chapter we discuss emerging concepts and approaches which address these challenges in three directions.

* From: M. Beer, I.A. Kougioumtzoglou and E. Patelli. Emerging Concepts and Approaches for Efficient and Realistic Uncertainty Quantification. In: Maintenance and Safety of Aging Infrastructure: Structures and Infrastructures Book Series, Vol. 10, D. Frangopol, Y. Tsompanakis (eds.), pp. 121–161, 2014, CRC Press/Balkema. For full text please check DOI: 10.1201/b17073-6, Reproduced in the printed Proceedings by permission of Taylor & Francis Books UK.

Analyzing Uncertainty in Civil Engineering

Michael Oberguggenberger
Institute of Basic Sciences in Engineering Science, University of Innsbruck, 6020 Innsbruck, Austria; michael.oberguggenberger@uibk.ac.at

Abstract: This paper is meant as a survey of uncertainty analysis in civil engineering with an emphasis on one of the unifying models: random sets. After a brief historical note about probability in civil engineering, various fundamental questions are addressed: sources of uncertainty in engineering; measuring uncertainty: models and axioms; semantics: from the real world to the model and back; aggregation and propagation of uncertainty; classification of models. In this general discussion, a wide range of models will be incorporated: interval analysis, set-valued models, fuzzy sets, probability, imprecise probability, random sets, sets of probability measures, and more. Further, the theory of random sets will be featured in an engineering example. This theory is of intermediate generality, but it allows one to treat intervals, bounding sets, probability distributions and imprecise probability distributions on the same footing.

Keywords: uncertainty modeling, probability, intervals, random sets, unifying concepts

1. Introduction

Uncertainty analysis in engineering is a vast domain. *Uncertainty* has come a long way from being ignored (or buried in safety factors) to the idea that it should be actively controlled—as exemplified by the fashionable catch words *risk management* and *uncertainty quantification*. Historically, the civil engineering community formed the avantgarde in the 1950s by introducing probability as a framework for modeling and quantifying uncertainty (Freudenthal, 1956; Bolotin, 1969). By now, the probabilistic framework is the prevalent paradigm in civil engineering, as is expressed by the European codes (Eurocode, 2002). For reasons discussed below, however, a certain uneasiness about the sole use of probability emerged in parts of the community in the 1990s. Alternative models found their entrance in the engineering literature, among them interval arithmetic, fuzzy sets, convex models, info-gap analysis, worst case scenarios, random sets, belief functions, interval probability, upper and lower previsions—just to mention a few of the proposals.

Most of the methods can be classified as one or the other combination of the poles *intervals* and *probability*. In fact, the theory of *random sets* can provide a unifying framework in which most (but not all) of the mentioned approaches can be accommodated.

This article starts with various general considerations about uncertainty in civil engineering. Next, a list of models is presented, followed by a discussion of their axioms, semantics, and numerical aspects. The last part of the paper presents an application of random sets in a geotechnical example. This brief article cannot cover the whole picture, nor provide an extended list of references. For that we refer to the review articles (Beer, Ferson and Kreinovich, 2013; Oberguggenberger, 2011)

and, especially on random sets, (Oberguggenberger, 2014). The present paper is a condensed and updated version of the latter two articles.

2. Modeling Uncertainty in Engineering

Three important ingredients have to be observed in uncertainty analysis in engineering. First, there is reality (with materials, soils etc.). Second, there is the model of reality (formulated in mathematical terms and containing physical laws and constitutive equations). Third, correspondence rules (prescribing how to translate one into the other) are needed. The physical model establishes what are the state variables and what are the material constants, the *parameters* to be observed. Once this has been decided, the values of the parameters have to be determined from information extracted from the real world and will serve as input in the physical model. This plus the design of the structure enters in numerical computations in the form of an input-output model $Y = \varphi(X)$ where X are the input parameters, φ is the model function, and Y is the output. Both X and φ are uncertain, and the issue is the propagation of this uncertainty to the output Y. Apart from providing insight into the behavior of the structure, the model output should provide a design that works, reliable guidelines for action, and aids for decision making.

Models of the data uncertainty should reflect and incorporate the level of information available on the data and, second, must be able to propagate it through numerical computations and deliver an output whose uncertainty is formulated in the same terms. In addition, the uncertainty models need correspondence rules themselves, that is, well-defined semantics. A further aspect that has to be taken into account is how the information on the uncertainty of different parameters is combined—this refers to modeling the dependence of variables as well as the combination of information from different sources. For example, in a sum $A+B$ of two parameters A and B, will the joint uncertainty be the smallest interval containing all realizations $a+b$, or do we believe that extreme combinations of realizations $a+b$ are less *probable* than those near the *standard values*? The first choice implies adherence to the axiomatics of interval arithmetic, the second to the axiomatics of probability theory. Thus three aspects of the modeling of uncertainty are isolated:

- *Definition and axiomatics:* How is uncertainty described and what are the combination rules?
- *Numerics:* How is uncertainty propagated through the computational model?
- *Semantics:* What is the meaning of the results—what do they say about our conception of reality?

There are two major categories of uncertainty: model uncertainties and parameter uncertainties, the latter encompassing the uncertainty of the data used to determine the parameter values.

Model uncertainties. The choice of the structural model is one of the central engineering decisions to be made. For example, for the description of the soil, there are continuum models and granular models, there are two- and three-dimensional models, there are multi-phase models (solids, liquids, gases), and so on. The next point is the adequate selection of state variables and parameters

(constant or not). In engineering, failure of a structure is described by the so-called *limit state function* that separates the safe states from the unsafe states. The choice of the limit state function is again an engineering decision. For example in geotechnics, is failure due to bounds exceeded by average values of the total loads or due to localized disturbances?

Parameter uncertainties. Parameter variability can be attributed to a large number of causes. There are random fluctuations, lack of information, random measurement errors, but also systematic measurement errors (deriving, e.g., from uncontrollable changes of the properties of the soil material caused by its extraction in bore holes before being analyzed in the laboratory). There are fluctuations due to spatial inhomogeneity, and errors made by assigning parameter status to state variables. This is one of the essential and often unavoidable errors in engineering, because models typically are valid in certain ranges only. If the state of the structure exits the intended range, constants may turn into variables depending on external forces (for example, the friction coefficient of most materials is approximately constant for small loads, but starts becoming a function of the internal stresses for larger loads). Finally, there is variability arising from the fact that parameters have to carry the burden of model insufficiency. The available information on data uncertainty may range from frequency distributions obtained from large samples, values from small samples or single measurements, interval bounds, to experts' point estimates and educated guesses from experience.

Failure probability. Traditionally, engineers have dealt with uncertainty by employing *safety factors*. That is, the traditional codes would require that the load carrying capacity of the structure exceeds the design loads by a certain factor > 1, typically 1.35 for permanent loads (such as dead weight) and $1.5 - 2.0$ for temporary loads. These factors have been negotiated in the committees of standards. This state of affairs has been considered as unsatisfactory: no information about the *actual* distance to failure can be extracted from such a procedure. Based on the desire for a more analytical description of the uncertainties, engineering codes have been put on a probabilistic foundation, starting with the pioneering work of (Freudenthal, 1956), (Bolotin, 1969) and others in the 1950s. Under this point of view, every relevant parameter of the engineering model is a random variable. There is no absolute safety, but rather a probability of failure.

To make it more precise, let the vector R comprise all random variables describing the resistance of a structure, S the loads and denote by $g(R, S)$ the limit state function (that is, $g(R, S) < 0$ means failure, $g(R, S) > 0$ signifies a safe state). Then $p_f = P(g(R, S) < 0)$ is the *failure probability*; $R = 1 - p_f$ is the *reliability* of the structure. To determine the probability p_f, the types and parameters of the probability distributions of R and S are needed. This multiplies the number of parameter values that have to be provided by the designing engineer: each model parameter comes with a distribution type and a set of (uncertain) distribution parameters. Actually, the current codes employ critical values R_k and S_k (certain percentiles of R and S) and partial safety factors γ_R and γ_S, so that the designing engineer has to verify a relation of the type $R_k/\gamma_R \geq \gamma_S S_k$. In theory, the critical values and the partial safety factors are computed in such a way that this inequality holds if and only if p_f attains a certain required value p_{fr}. In practice, γ_R and γ_S are not computed but rather prescribed in the codes. Starting with the 1980s and 1990s, the European codes have been changed into probability based codes. By now, this is the standard in civil engineering (see e.g. EN 1990:2002 (Eurocode, 2002)). In addition, risk analysis and risk management have become

a major ingredient in construction and project management. Especially calls for tender by public organizations ask the contractor to supply a risk analysis together with the proposed design.

The civil engineering codes require that the designed structure obtains an instantaneous probability of failure of $p_f = 10^{-6}$ and a long-term failure probability of $p_f = 10^{-5}$. To credibly estimate tail probabilities of such a small magnitude, *a lot* of information is needed. Problems with the notion of failure probability, its meaning and practicability have been discussed at many places, e.g., (Elishakoff, 1999; Fellin, Lessmann, Oberguggenberger and Vieider, 2005).

Imprecise probability models. As described above, there are many types of uncertainties in an engineering model. It has been questioned whether a purely probabilistic approach is capable of catching all aspects, for example, ignorance or fluctuations due to systematic model errors. In addition, large samples allowing a frequentist assessment of data are rarely available. (Due to high costs, sample sizes in laboratory experiments or soundings in soil investigations are usually small.) However, what is generally known about a model parameter is a central value and a coefficient or range of fluctuation. In geotechnics, geologists can provide interval estimates of soil parameters; a geological report in tunneling may deliver rock classes and interval probabilities for their occurrence.

The uneasiness about the probabilistic safety concept and the desire for models of the data uncertainty that reflect and incorporate the level of available information led to the search for alternative concepts in the engineering community. On the one hand, probabilistic models and probabilistic reasoning were considered as too tight a concept. On the other hand, engineering practice shows that interval estimates should be incorporated in the framework of uncertainty analysis. Here is a short list of concepts under consideration: fuzzy sets, evidence theory, interval analysis, interval probability, random sets (random sets can bee seen as a framework bridging the gap between probability and interval analysis and admitting easily accessible visualization tools such as probability boxes), upper and lower previsions, clouds, info-gap analysis, ellipsoidal modeling, anti-optimization, and more. A long list of references has been compiled in (Oberguggenberger, 2011). To subsume all these different approaches, the term *Imprecise Probability* has been introduced (Walley, 2000; Augustin, Coolen, de Cooman and Troffaes, 2014).

3. Models of the Uncertainty

3.1. Definitions

In this section we shall focus on describing the main theories of uncertainty in the univariate case of a single parameter. The following convention will be in use throughout the paper: parameters will be denoted by upper case letters, e.g. A, while corresponding lower case letters, such as a, will be reserved for their realizations. The description of the semantics is deferred to the next subsection, except for the straightforward first two cases.

Deterministic values. The simplest approach is what in engineering terminology usually is called *deterministic description*, that is, the parameter A is described by a single value a. The semantics is simply that a is an expert estimate (or educated guess). Clearly, possible variations are not modeled

in this approach, though their influence can be assessed to some extent by a classical sensitivity analysis.

Intervals. The next level in modeling uncertainty is interval analysis. The uncertainty of the input A is described by an interval $[a_L, a_R]$, signifying bounds in terms of a worst/best case assumption. In this way the total variability is captured, but no detailed information on the distribution of the uncertainty is provided.

Probability. The most informative, but also most stringent description of the uncertainty of a parameter A is by means of *probability*. If the probability distribution is given by a density $p_\lambda(a)$, the probability that the realizations of the parameter A lie in a set S is

$$P(A \in S) = \int_S p_\lambda(a)\, \mathrm{d}a.$$

The notation p_λ indicates that, usually, the probability distributions arise as members of a class of distributions which in turn are parametrized by parameters λ. For example, the class of Gaussian normal distributions $\mathcal{N}(\mu, \sigma^2)$ is given by the Gaussian densities $p_\lambda(a)$ with parameters $\lambda = (\mu, \sigma)$,

$$p_\lambda(a) = \frac{1}{\sqrt{2\pi}\sigma} \mathrm{e}^{-\frac{(a-\mu)^2}{2\sigma^2}}.$$

Thus the complete specification of a probability distribution requires determination of the type it belongs to as well as the values of its parameters.

Sets of probability measures. A central idea in relaxing the precision inherent in a probabilistic model is to replace the single measure by a set of probability measures, a family $\mathcal{M} = \{p_\lambda : \lambda \in \Lambda\}$ where the parameter $\lambda \in \Lambda$ specifies each participating single measure. A set of probability measures defines lower and upper probabilities according to the rules

$$\begin{aligned} \underline{P}(A \in S) &= \inf\{P(A \in S) : P \in \mathcal{M}\}, \\ \overline{P}(A \in S) &= \sup\{P(A \in S) : P \in \mathcal{M}\}. \end{aligned}$$

The lower probability is the greatest lower bound of all probabilities that are assigned to the event $A \in S$ by choosing one of the probability measures from the set $\mathcal{M}$ (if attained, it is the minimum of those values). Similarly, the upper probability is the least upper bound of such probabilities (if attained, it is the maximum of those values). A frequently encountered instance of a set of probability measures arises from parametrized probability distributions whose statistical parameters are not singletons, but vary in intervals. For example, one might think of a family of Gaussian variables with means μ from an interval $[\underline{\mu}, \overline{\mu}]$.

As most of the models of uncertainty, the two subsequent theories—random and fuzzy sets—can be seen as special prescriptions for obtaining *sets of probability measures*.

Random sets. A *finite random set*, also referred to as a *Dempster-Shafer structure*, is given by finitely many subsets $A_i, i = 1, \ldots, n$ of a given set $\mathcal{A}$, called the *focal elements*, each of which

comes with a *probability weight* $m_i = m(A_i), \sum m(A_i) = 1$. The general case of an infinite number of focal elements can be treated as well; the concept of a set-valued random variable being the defining notion (see Subsection 3.2).

In the Dempster-Shafer approach (Shafer, 1976), the random set allows one to define a degree of belief $\gamma(S)$ and a degree of plausibility $\eta(S)$, respectively, that the realizations of the parameter A lie in S by

$$\gamma(S) = \sum_{A_i \subset S} m(A_i)\,, \quad \eta(S) = \sum_{A_i \cap S \neq \emptyset} m(A_i). \tag{1}$$

A random set can also be interpreted as a prescription for a set of probability distributions. Denote by $\mathcal{M}(A_i)$ the totality of all probability measures supported by A_i, that is, a probability measure P on the underlying set $\mathcal{A}$ belongs to $\mathcal{M}(A_i)$ if $P(A_i) = 1$. The set of probability measures induced by the given random set is

$$\mathcal{M} = \{P : P = \sum m(A_i)P_i, P_i \in \mathcal{M}(A_i)\}. \tag{2}$$

One can show that the corresponding lower and upper probabilities coincide with the degrees of belief and plausibility, respectively. That is, for any (measurable) subset S of $\mathcal{A}$, it holds that

$$\underline{P}(S) = \gamma(S)\,, \quad \overline{P}(S) = \eta(S). \tag{3}$$

Fuzzy sets. Fuzzy sets can be viewed as ordered families of sets or as membership functions. It is simplest to describe the ideas by means of the special case of a fuzzy real number A. From the first point of view, A is a family of parametrized intervals. The parametrization is done in terms of levels α, $0 \leq \alpha \leq 1$. Each level α has a corresponding interval A^α so that $A^\beta \subset A^\alpha$ if $\alpha \leq \beta$. Thus the intervals are stacked and can be depicted by their left/right contour functions. More generally, one could allow the A^α to be arbitrary, stacked subsets of a given set of objects under investigation (complex numbers, vectors, matrices, functions or the like).

In the second approach, the contour function is taken as the primary object, and a fuzzy set A (over the real numbers) is just a map from the real line to the interval $[0, 1]$, assigning to each real number a a value $\pi_A(a) \in [0, 1]$. This value may be interpreted as the membership degree to which a belongs to the fuzzy set A, or in the language of parameters, as the degree of possibility that the parameter A takes the value a. In classical set theory, the membership degree is either 0 or 1; fuzzy set theory permits gradual membership as well. The intervals from the first interpretation are now the *α-level sets* $A^\alpha = \{a : \pi_A(a) \geq \alpha\}$. In analogy to the situation in probability theory, one can introduce a *possibility measure* on the underlying set, defining a degree of possibility for each subset by $\pi_A(S) = \sup\{\pi_A(a) : a \in S\}$, giving the degree of possibility that the parameter A takes a value in S. The possibility measure is monotone, i.e., $\pi_A(S) \leq \pi_A(T)$ if $S \subset T$. Possibility measures are actually in one-to-one correspondence with fuzzy sets; given a possibility measure π, its evaluation on singletons defines the membership function of a fuzzy set: $\pi_A(a) = \pi(\{a\})$.

Lower and upper previsions. In the probabilistic setups discussed so far, probability P is the fundamental quantity. The outcomes of a random variable X can be described by their probabilities

$P(X \in S)$. The expectation $\mathrm{E}(X)$ and the moments $\mathrm{E}(X^m)$ are derived quantities, e.g., in terms of a probability density $p(x)$:

$$\mathrm{E}(X) = \int xp(x)\,\mathrm{d}x, \qquad \mathrm{E}(X^m) = \int x^m p(x)\,\mathrm{d}x.$$

Conversely, the probability of an event S can be viewed as the expectation of its indicator function $X(x) = \mathbf{1}_S(x)$, which equals one if x belongs to S and zero otherwise: $P(S) = \mathrm{E}(\mathbf{1}_S)$. This opens the way to setting up a theory based on expectations of random variables as fundamental quantities. Actually, the approach is more general, as one may admit smaller or larger sets of random variables, now called *gambles*. A *linear prevision*, as introduced by (de Finetti, 1970) is a linear functional E, assigning to each gamble a value between 0 and 1. The extension to interval-valued previsions, see e.g. (Walley, 1991), can be done as follows. The basic gambles are given by a random variable X and a number of functions $f_1(X), ..., f_m(X)$ of it. *Lower and upper previsions* are functionals on the set of gambles with $\underline{\mathrm{E}}(f_i) \leq \overline{\mathrm{E}}(f_i)$. Various types of information can be modeled by means of lower and upper previsions. For example, if $\mathbf{1}_S$ is the indicator function of an event S, then the previsions $\underline{\mathrm{E}}(\mathbf{1}_S)$ and $\overline{\mathrm{E}}(\mathbf{1}_S)$ can be regarded as lower and upper probabilities of the event S. If $f_i(X) = X$, then $\underline{\mathrm{E}}(f_i)$ and $\overline{\mathrm{E}}(f_i)$ are bounds on the mean value of the corresponding random variable.

For computing new previsions $\underline{\mathrm{E}}(g)$ and $\overline{\mathrm{E}}(g)$ of a gamble $g(X)$ from the available information, *natural extension* is used which can be written as the optimization problem

$$\underline{\mathrm{E}}(g) = \min_p \int g(x)p(x)\,\mathrm{d}x, \qquad \overline{\mathrm{E}}(g) = \max_p \int g(x)p(x)\,\mathrm{d}x$$

subject to

$$p(x) \geq 0, \quad \int p(x)\,\mathrm{d}x = 1, \quad \underline{\mathrm{E}}(f_i) \leq \int f_i(x)p(x)\,\mathrm{d}x \leq \overline{\mathrm{E}}(f_i),\ 1 \leq i \leq m. \tag{4}$$

Here the minimum and maximum are taken over the set of all possible probability density functions $p(x)$ satisfying conditions (4).

3.2. Semantics

As outlined in the introduction, the interpretation of a theory is an essential ingredient for achieving an adequate translation from model into reality and back. Needless to say that the assertions made by a model become meaningful only in the context of the underlying semantics. Different semantics imply different meanings. One has to be aware of the interpretations used when comparing assertions made by different authors, all the more so as often the same vocabulary is employed for notions that differ in the various interpretations.

Probability. The interpretation of probability has been the subject of scientific dispute for centuries; see (Fine, 1973) as an encompassing reference. The most prevalent and important semantics in engineering practice are:

1. *Classical probability*, based on principles like the *principle of non-sufficient reason* would, in colloquial terms, determine the probability of an event S as the fraction of favorable cases among the possible cases.

2. *Frequentist probability*, based on the idea of random occurrence of an event in a sequence of independent trials, would approximate the probability of an event S by its relative frequency.

3. *Subjective probability* is meant to be a measure of personal confidence. It can be assessed by introspection and/or elicitation through experts.

Example: As an illustration, let us assess the probability p of throwing a six with a dice. If nothing is known about the dice, there is no sufficient reason to assume that it is biased. Thus the classical probabilist would assess the probability as 1 (favorable outcome) over 6 (possible outcomes), hence $p = 1/6$. A frequentist person would repeatedly roll the dice a large number of times and use the fraction of sixes among all results as an estimate for the probability. (If the dice is indeed unbiased and N is large, say $N = 10000$, the fraction will be close to $1/6$.) The subjectivist would guess the probability as $p = 1/6$, if he/she has enough trust into the unbiasedness of the dice. If the subjectivist is willing to bet 1 monetary unit for a gamble that rewards him/her with 6 units when a six is thrown, an observer could infer that the subjectivist believes the probability p to be at least $1/6$.

In its applications, classical probability often takes the form of *combinatorial* probability. Aside from the obvious application in computing the chances in a lottery, it is often the means by which the standard probability distributions are derived, like the binomial or geometric distributions. Another example would be the exponential distribution for the survival time of a radioactive particle which is an immediate combinatorial consequence of the law of radioactive decay.

The central idea of frequentist probability is the sample with its statistical parameters. It is viewed or designed as a sequence of independent realizations of the random variable whose distribution parameters have to be determined—keeping the boundary conditions constant. The relative frequencies of the realizations of an event are taken as estimates for the probability of the event. The sample parameters like sample mean or sample variance correspond to moments of the random variable—expectation value and variance in this case. From there, the parameters of the distribution of the random variable can be estimated. This is one of the wide-spread procedures for fitting models based on the frequentist interpretation.

From the viewpoint of the philosophy of science, the frequentist interpretation carries a number of problems, among them the question *whose* probability is realized in the sample (of the random variable, or of the experiment which was designed to measure it—a possible answer to this question has been given by Popper with his notion of *propensity* (Popper, 1957)). A pragmatic approach with a cautious and critical attitude has proven to provide a successful basis for probabilistic models in science and engineering.

A further issue of debate has been the fact that the decision aids mentioned above provide meaningful evaluations only if the sample size is *sufficiently large*, a condition which remains vague, and in civil engineering—with often very small sample sizes—is frequently lacking. This is the point where subjective probability enters engineering. When such a switch of interpretation is undertaken, we believe that it is the responsibility of the engineer to put it in the open. Otherwise the meaning of probability in the final result is lost or at least obscured.

Turning to subjective probability, we first mention that schemes have been developed that allow one to deduce it from decision theoretic principles, assuming *rational behavior* of the agent. This has been done to obtain operational ways of extracting the personal probability assessment of an

agent/decision maker quantitatively. One way promoted by (Savage, 1954) has been the notion of *indifference price*. To determine a probability of an event S, the decision maker is required to imagine a gamble which pays one monetary unit if event S occurs and zero otherwise. The decision maker surely would buy the gamble at the price of zero units, but surely not for more than one unit. Raising the lower bound for the price and lowering the upper bound should eventually lead to a price at which the decision maker is indifferent to buying the gamble or not. This indifference price is the probability $P(S)$ of the event. It is argued that the indifference price also equals the minimal price $\underline{P}(S)$ at which the decision maker is willing to sell the gamble, as well as the maximal buying price $\overline{P}(S)$.

This has been a point of critique, because real world persons do not behave strictly rational in this sense and often lack the information to decide about the minimal selling and maximal buying price. Thus an interval $[\underline{P}(S), \overline{P}(S)]$ appears to be a more accurate description of a decision maker's information. This line of argument directly leads to *imprecise probability*, probability intervals, and lower and upper probabilities. In practical engineering applications, *elicitation* of probabilities from *experts* is the paradigm for obtaining subjective probabilities quantitatively. We refer e.g. to (Meyer and Booker, 2001; Ross, Booker and Parkinson, 2002).

Finally, we should not fail to mention the *Bayesian* approach to assessing probability distributions. From the Bayesian viewpoint, everything is a random variable, including the parameters, say Θ, of the distributions of the original variables, say X, to be assessed. The Bayesian approach has interpretations both in the frequentist as well as the subjective setting. In the civil engineering literature, it has been found useful for combining expert knowledge with sample data (Martz and Waller, 1982; Rackwitz, 2000). The expert knowledge may be based on known frequencies or on subjective estimates and is encoded in the *prior distribution* of the parameter θ. Sample data x (or again expert estimates obtained in situ) are then used to produce a *posterior distribution* of the distribution parameter θ according to Bayes' rule, loosely stated as

$$p(\theta|x) = \frac{p(x|\theta)p(\theta)}{p(x)}.$$

The data vector x may have length 1, or may consist in a large sample of size n, so that the Bayesian procedure may accommodate single estimates up to sample sizes satisfying frequentist requirements. The assessment of the distribution of the original variable X is completed by the *Bayes estimate* of its distribution parameter $\hat{\theta} = \int_{-\infty}^{\infty} \theta\, p(\theta|x)\, \mathrm{d}\theta$.

Sets of probability measures. Sets of probability measures can arise both in a frequentist as well as in a subjectivist approach. In a frequentist setting, sets of probability measures arise as sets of fitted distributions: in fact, confidence regions for the distribution parameters imply that parametrized *families* of distributions are employed. Further, *robust statistics* is based on distributions neighboring a given distribution, see e.g. (Huber, 1981).

As we have just seen above, sets of probability distributions are inherent in Bayesian statistics (each parameter value θ defines a distribution of the original variable). In order to avoid implausible determinations due to the choice of a prior distribution, families of prior distributions have been employed (robust Bayesian methods), as well as fuzzy prior distributions.

Further, referring to the decision theoretic foundation of probability, replacing the indifference price by an interval $[\underline{P}(S), \overline{P}(S)]$ leads to interval-valued probabilities, which again imply that a set of probabilities is considered.

Random sets. In a frequentist interpretation, this might correspond to a sample of size n of interval data for a parameter A, the probability weight being approximated by the relative frequency. The difference to a histogram then is that the focal elements A_i may overlap. In geotechnical engineering, for example, interval data arise as ranges of rock parameters associated with certain rock classes. These rock classes in turn may be the outcomes, obtained with a certain frequency from in situ measurements. In a subjectivist interpretation, the focal elements A_i may be (possibly conflicting) estimates given by different experts and the weights might correspond to each expert's relative credibility.

Random sets have turned out to be useful for bracketing probability estimates given by different sources as well as for combining information of different type, due to the observation that every histogram, every interval and every fuzzy set can be viewed as a random set, without a need for artificial transformations (Goodman and Nguyen, 2002; Kreinovich, 1997).

A good visualization of a random set can be given through its *contour function* on the basic space $\mathcal{A}$, assigning each singleton a its plausibility: $a \to \overline{P}(\{a\})$. It is simply obtained by adding the probability weights p_i of those focal elements A_i to which a belongs.

When $\mathcal{A}$ is the set of real numbers, the random set defines a so-called *probability box* which is bounded by the upper and lower distribution functions

$$\overline{F}(x) = \overline{P}(-\infty, x], \quad \underline{F}(x) = \underline{P}(-\infty, x], \tag{5}$$

see (Ferson, Kreinovich, Ginzburg and Myers, 2003). Any distribution function $F(x)$ that arises from one of the probability measures from the set $\mathcal{M}$ (cf. Equation (2)) is necessarily bounded by the probability box: $\underline{F}(x) \le F(x) \le \overline{F}(x)$. Thus the probability box is a good representation of the variability of a quantity described by a random set.

We now turn to the more general case of infinite random sets. For most applications in reliability theory it suffices to consider *closed random sets* defined on the probability space $\Omega = [0, 1]$ with the uniform probability distribution. Recall that the uniform probability P on the interval $[0, 1]$ assigns to each subinterval of $[0, 1]$ its length, that is, $P[\alpha, \beta] = \beta - \alpha$ for $0 \le \alpha \le \beta \le 1$.

Thus—in our narrower sense—a random set is a function $[0, 1] \to \mathcal{A} : \alpha \to A_\alpha$ where each A_α is a closed subset of the real line $\mathcal{A}$ as basic space. Often, the *focal elements* A_α are just closed intervals. In the multivariate case, we would take the d-dimensional unit hypercube $\Omega = [0, 1]^d$ as probability space and the focal elements as closed subsets of d-dimensional coordinate space.

In generalization of formulas (1) and (3) we define the *plausibility* of an event S as

$$\overline{P}(S) = P(\alpha \in [0, 1] : A_\alpha \cap S \neq \emptyset) = \int_{\{\alpha \in [0,1] : A_\alpha \cap S \neq \emptyset\}} \mathrm{d}\alpha \tag{6}$$

and the *belief*

$$\underline{P}(S) = P(\alpha \in [0, 1] : A_\alpha \subset S) = \int_{\{\alpha \in [0,1] : A_\alpha \subset S\}} \mathrm{d}\alpha, \tag{7}$$

and the upper and lower distribution functions are given by formula (5). They form a probability box which may be viewed as the envelope of all cumulative distribution functions encoded in the random set.

Examples: (a) Every Dempster-Shafer structure can be viewed as an infinite random set, in which the focal elements S_i arise as certain A_α with repetition. For this purpose, we subdivide the interval $[0,1]$ into n subintervals of length p_i and put

$$A_\alpha = A_1,\ 0 \le \alpha \le p_1, \quad A_\alpha = A_2,\ p_1 < \alpha \le p_1 + p_2,$$

and so on until $A_\alpha = A_n$, $p_1 + p_2 + \ldots + p_{n-1} < \alpha \le 1$.
(b) Fuzzy sets. every normalized fuzzy number can be seen as a random set; the sets A_α are just the α-level sets. It is not difficult to prove that the possibility measure of a subset S of the real line coincides with its plausibility: $\overline{P}(S) = \sup\{\pi(x) : x \in S\}$.
(c) Random variables. A random variable X can be reconstructed as a random set on $[0,1]$ by putting $A_\alpha = F^{-1}(\alpha)$ where $F(x)$ is the distribution function of the random variable and F^{-1} its inverse or, more generally, pseudo-inverse. The plausibility and belief of an event B coincide with the probability of the outcome $P(X \in B)$.
(d) Random sets constructed from Tchebycheff's inequality. A major application of the tools outlined above is the construction of random sets from minimal information on a random variable X. Let $\mu = \mathrm{E}(X)$ be its expectation and $\sigma^2 = \mathrm{V}(X)$ its variance. Tchebycheff's inequality asserts that

$$P(|X - \mu| > d_\alpha) \le \alpha \quad \text{with} \quad d_\alpha = \sigma/\sqrt{\alpha} \tag{8}$$

for $\alpha \in (0,1]$. Let $A_\alpha = [\mu - d_\alpha, \mu + d_\alpha]$. By Tchebycheff's inequality, the probability of A_α is greater or equal to $1-\alpha$, while the probability of its complement A_α^{c} is less or equal to α. Thus A_α will contain approximately a fraction of $1-\alpha$ of the realizations of the random variable X, e.g., $A_{0.05}$ contains about 95%, $A_{0.10}$ contains about 90%, etc. This is a conservative, non-parametric estimate valid for whatever distribution of the random variable X. It encodes the minimal information that can be extracted from the expectation and the variance of a random variable without further parametric assumptions. We formalize this information as an infinite random set (actually a random interval) $\alpha \to A_\alpha$ on the space $\Omega = (0,1]$, equipped with the uniform probability distribution. Of course, Tchebycheff's inequality can be replaced by narrower estimates if more is known about the distribution of the given random variable, for example, symmetry or unimodularity.

Fuzzy sets. In engineering and in risk analysis applications, probabilistic models have been criticized as requiring more input from the designing engineer or the decision maker than could be plausibly provided—or that would be reasonably required for a rough estimate. In particular, the requirement that probabilities have to add up to 1 causes the problem that probabilities of events change when additional events are taken into consideration. Further, probabilities have to be set up in a consistent way, e.g. satisfying the rule $p(S \cup T) = p(S) + p(T) - p(S \cap T)$ and thus do not admit incorporating conflicting information (in the sense that the intersection of an event S with its complement can never have positive probability). Fuzzy set theory appears to provide a resolution of these difficulties in as much as it admits much more freedom in modeling. Further, fuzzy sets may be used to model vagueness and ambiguity.

The notion of *possibility* provides an interpretation for a fuzzy set and an operational method of constructing it, as we wish to argue here. We imagine that a fuzzy set describing the uncertainty of a real-valued parameter has to be designed. The procedure proposed here is based on a scale $0 \leq \alpha \leq 1$. The linguistic meaning of the α-values is specified verbally by the designing engineer or the decision maker in advance, but then remains fixed during the whole modeling process (for example, $\alpha = 1$ signifies the standard value of the parameter, $\alpha = 2/3, 1/3, 0$ might indicate high, medium, and low *degree of possibility*).

One would start by specifying the standard value a_S of the parameter, in engineering terminology often referred to as the *deterministic approximation* and assign degree of possibility $\alpha = 1$ to it. Next, possible deviations of the parameter from the standard value are taken into account, corresponding to decreasing degree of possibility, until the minimal and maximal values, which are assumed with very small degree of possibility, are reached at level $\alpha = 0$.

The notion of *possibility* can be given an operational meaning, using the language of subjective risk assessments. Thereby, it is envisaged that the risks leading to parameter fluctuations at the corresponding possibility level are established in an analysis of scenarios. The level sets correspond to the bounds a parameter attains under a certain risk level.

There is also a normative approach which uses pre-shaped, parametrized membership functions as well as the suggestion to use elicitation procedures; see (Dubois and Prade, 1988; Ross, Booker and Parkinson, 2002) for further details.

An alternative way of establishing the semantics of *possibility* is to start from the notion of *potential surprise* and to define possibility as its complementary notion or as a transformed quantity thereof (Neumaier, 2003). For a decision-theoretic foundation, see (Dubois, Prade and Sabbadin, 2001), for possibility as a transformation of probability, see (Dubois, Prade and Sandri, 1993).

Lower and upper previsions. A behavioral interpretation of lower and upper previsions has been elaborated by Walley (Walley, 1991), who also set up an axiomatic system of lower and upper previsions, derived from certain principles, such as *avoiding sure loss*. Previsions are functionals defined on gambles, thus the betting analogy (already used in the operational definition of subjective probability) comes in naturally. The lower prevision $\underline{\mathrm{E}}(g)$ of a gamble $g(X)$ is the supremum buying price (the largest sum the decision maker is willing to pay for the gamble), while the upper prevision $\overline{\mathrm{E}}(g)$ is the infimum selling price. Lower and upper probabilities of events are obtained as lower and upper previsions of their indicator functions. In contrast to subjective probability (which would translate into linear previsions), the decision maker is not obliged to end up with a single number (the indifference price), but has the freedom to remain undecided about the probability of an event, within the bounds given by its lower and upper probability.

3.3. Axiomatics

Referring to probability theory, it has been emphasized by (Popper, 1994, Section 71) that a formal mathematical system of axioms and postulates is required in order to approach the problem of relations between the different interpretations of probability. All the more so, this applies to the problem of comparing the different theories of uncertainty. By now, all these theories can be based

on appropriate axioms, the most well known being the Kolmogorov axioms of probability and the Choquet axioms of capacities.

We do not give a detailed exposition of the axioms here, but just highlight a few of them, showing that they lead to different combination rules in the various models of uncertainty. This may serve as a means of distinguishing the models as well as a guiding criterion to decide which model should be selected for what purpose.

The axioms fix the algebraic properties of the corresponding set functions. For example, probability measures p define additive set functions, that is,

$$p(S \cup T) = p(S) + p(T) - p(S \cap T)$$

for sets S, T. This is not true of possibility measures π, which in turn satisfy

$$\pi(S \cup T) = \max\{\pi(S), \pi(T)\}.$$

Both probability measures and possibility measures are special cases of plausibility measures η which enjoy the more general property

$$\eta(S \cup T) \leq \eta(S) + \eta(T) - \eta(S \cap T).$$

All these set functions are contained in the largest class of monotone set functions μ, also called fuzzy measures, characterized by the property

$$\mu(S \cup T) \geq \max\{\mu(S), \mu(T)\}.$$

Suitably completing these algebraic properties to full systems of axioms, it is actually possible to *characterize* all these type of measures (and many more). The following hierarchical relations obtain:

$$\begin{array}{rcl} \text{probability} & \rightarrow & \text{plausibility} \\ \text{possibility} & \rightarrow & \text{plausibility} \\ \text{plausibility} & \rightarrow & \text{monotonicity}. \end{array}$$

This means that every probability measure is a plausibility measure, and so on (thus plausibility theory is more general than probability theory, in the sense that it admits a larger class of measures). Probability measures and possibility measures are in no implication relation in either direction.

Alternatively, if one starts from the notion of random sets, probability would correspond to singletons as focal elements, possibility to nested focal elements, and plausibility to arbitrary focal elements.

3.4. Numerics

Practically all engineering models are input-output systems. Given certain input values (model parameters, initial conditions, dimensions, etc.) the model produces output values (displacements, stresses, costs, etc.). In other words, the model is a function φ that assigns to the input data A certain output values $\varphi(A)$. Both A and $\varphi(A)$ may be multidimensional (for simplicity, we shall consider $\varphi(A)$ as one-dimensional in the sequel—corresponding to a single component of a

multidimensional output). Often, the function φ is a computer code, in which case the output is obtained as a numerical approximation. If the input data consist of a single, *deterministic* data value, then the model produces a uniquely determined output. If the input data fluctuate, so does the output. If the fluctuation of the input is described by one or the other theories of uncertainty discussed so far, the fluctuation of the output should be captured on the same terms. This is the issue of this section: how is data uncertainty propagated through an input-output system?

Deterministic values. If a is an expert estimate of some input parameter A, the output is just the value $\varphi(a)$ of the function φ at a. In this framework, the effects of the uncertainty of the input parameters can still be assessed by performing a *sensitivity analysis*. In its classical form, sensitivity analysis means the study of the derivatives of the function φ at the fixed value a of interest, that is, the linear approximation to the change in output when the input parameter a is changed to a nearby value b:

$$\varphi(b) \approx \varphi(a) + \frac{\mathrm{d}\varphi}{\mathrm{d}a}(a)(b-a), \qquad \varphi(b) \approx \varphi(a) + \sum_{i=1}^{n} \frac{\partial \varphi}{\partial a_i}(a)(b_i - a_i)$$

(left: univariate case; right: n-dimensional parameter $a = (a_1, \ldots, a_n)$), where the approximation error is of order $|b-a|^2$. The sign and size of the partial derivative $\frac{\partial \varphi}{\partial a_i}(a)$ is an indicator of the influence of the i-th component of the parameter a on the output (provided all components a_i are of the same scale).

Intervals. If A is an interval, the functional evaluation $\varphi(A)$ results in a set of values (an interval, if φ is continuous and one-dimensional). In general, both A and $\varphi(A)$ could be sets of arbitrary geometry. In interval arithmetic, one would bound these sets by the smallest multidimensional intervals (boxes) that contain them (see (Neumaier, 1990)). In any case this approach represents the full range of the possible output values without further fine structure.

Probability measures and random sets. Given a single probability measure and a (measurable) map φ, the output probabilities are determined through the induced image measure, that is, $P(\varphi(A) \in S) = P(A \in \varphi^{-1}(S))$. Though the distribution of the random variable $\varphi(A)$ can be computed by this prescription in principle, this is practically impossible as soon as φ attains a rather moderate complexity. *The* numerical method for approximating the output distribution by means of an artificially created sample is *Monte Carlo simulation*.

In case the uncertainty of the input is modeled by a set $\mathcal{M}$ of probability measures, the map φ induces a set of probability measures as well, namely the collection of all image measures, obtained from $\mathcal{M}$ under this map. The computation of lower and upper probabilities turns into an optimization problem.

If the input is described by a random set with focal elements $A_i, i = 1, \ldots, n$ and probability weights $m(A_i)$, the output is again a random set which consists of the focal elements $\varphi(A_i), i = 1, \ldots, n$, supplied with the original weights $m(A_i)$ (or sums of weights in case some of the image sets $\varphi(A_i)$ coincide). In case the sets $\varphi(A_i)$ are intervals, their boundaries can be found by optimization (minimizing/maximizing the function φ on A_i). The determination of lower and upper probabilities is then a combinatorial task involving the formulas for belief and plausibility.

Fuzzy sets. The question of propagating the uncertainty of a fuzzy input A through a function φ needs some more explication. If the input is a fuzzy set with membership function $\pi_A(a)$, say, the output will also be a fuzzy set, described by a membership function $\pi_{\varphi(A)}(b)$. According to the *Zadeh extension principle* (Zadeh, 1975), it is given by

$$\pi_{\varphi(A)}(b) = \sup\{\pi_A(a) : \varphi(a) = b\}.$$

In case the input consists of a vector of parameters $A = (A_1, \ldots, A_m)$, the extension principle takes the form

$$\pi_{\varphi(A)}(b) = \sup\{\min(\pi_{A_1}(a_1), \ldots, \pi_{A_m}(a_m)) : \varphi(a_1, \ldots, a_m) = b\}.$$

Note that this comes naturally from the possibility-theoretic interpretation: to compute the degree of possibility that $\varphi(A)$ takes the value b, one has to look for all combinations $a_1, \ldots, a_m$ producing the value b; each single combination gets the smallest possibility among its participants, while b gets the supremum of all possibility degrees that can be obtained in this way. In case φ is continuous and the α-level sets of $A_1, \ldots, A_m$ are compact ($0 < \alpha \leq 1$), this corresponds exactly to computing the range of the function φ on each α-level set,

$$\varphi(A)^\alpha = \varphi(A^\alpha), \quad \text{respectively,} \quad \varphi(A_1, \ldots, A_m)^\alpha = \varphi(A_1^\alpha, \ldots, A_m^\alpha).$$

When the A_j^α are intervals, in addition, the set $\varphi(A_1, \ldots, A_m)^\alpha$ is an interval as well. The computation of its boundaries is then a task of global optimization: finding the minimum and maximum value of φ on the set A^α. In any case, the procedure is consistent: if the input data are structured as stacked intervals, so is the output.

3.5. The multivariate case

In principle, the multivariate case, that is, the case when the input A has several components $A_1, \ldots, A_n$, has been covered by what has been said above—all applies to multidimensional intervals, random sets, fuzzy sets and multivariate distribution functions. However, the issue is how to model mutual dependence, correlation, interaction, influence of the different components. In addition, the task remains to model infinitely many components, as arising in spatial fields or temporal processes, when the parameters are functions of space and/or time.

There is a rather well established notion of independence in probability theory: two random variables are *independent* when their joint distribution function is the product of the individual (marginal) distribution functions. The situation is also clear in interval analysis: two parameters taking interval values are *non-interactive* when their joint behavior is described by the product of the two intervals (a rectangle), and *interactive* when their joint range is a proper subset of the product interval. This idea extends to fuzzy sets: Two fuzzy sets are non-interactive, when all their α-level sets are rectangles.

More precisely, given d univariate fuzzy sets $A^1, \ldots, A^d$, the non-interactive joint fuzzy set has the α-level sets

$$A_\alpha = A_\alpha^1 \times \cdots \times A_\alpha^d, \quad \alpha \in (0, 1].$$

Interactivity can be modeled by certain parametric restrictions on the α-level sets. To avoid combinatorial complications, consider interactivity of at most two out of the d variables. Since an α-level

set of the form $A^i_\alpha \times A^j_\alpha$ is a homothetic image of the unit square, it suffices to give the definitions for $A^1_\alpha = A^2_\alpha = [0,1]$. Interactivity can be modeled by replacing the unit square by a diamond-shaped region, symmetric around one of the diagonals. Let $0 \le \rho \le 1$ and define the points $P_1, \dots, P_4$ by

$$\begin{aligned} P_1 &= (\rho/2, \rho/2), & P_2 &= (1-\rho/2, \rho/2), \\ P_3 &= (1-\rho/2, 1-\rho/2), & P_4 &= (\rho/2, 1-\rho/2). \end{aligned}$$

Interactivity of *positive degree* ρ is modeled by taking the rhombus with corners $(0,0)$, P_2, $(1,1)$, P_4 as joint level set, while interactivity of *negative degree* $-\rho$ is modeled by the rhombus with corners $(0,1)$, P_1, $(1,0)$, P_3 as joint level set. This is a straightforward way of introducing parametric interactivity in fuzzy sets. Of course, one can imagine replacing the diamond shapes by other geometric shapes.

Switching to random sets, the situation becomes more complicated. The concept of independence splits into a number of different concepts, all coinciding when the focal elements are singletons (i.e., when the random set is actually a scalar random variable). *Random set independence* is characterized by two properties: the joint focal elements are products of intervals, and the joint weights are the products of the corresponding individual (marginal) weights. *Strong independence* is obtained when the underlying set of joint probability measures is required to consist of product measures only. Going deeper into the structure of the underlying set of probability measures, many more notions of independence can be considered, one of the more prominent being *epistemic independence*. For further details on this, see e.g. (Fetz and Oberguggenberger, 2004).

To model *dependence*, the notion of *copulas* has gained increased attention in the past decade. An n-dimensional copula is a multivariate probability distribution function on the n-dimensional unit hypercube whose marginals are uniform distributions. Thus in the two-dimensional case, it is a function $C(u,v)$ of two variables $u, v \in [0,1]$ which satisfies

$$C(u,0) = 0, \quad C(u,1) = u, \quad C(0,v) = 0, \quad C(1,v) = v$$

and which is two-monotone, i.e.,

$$C(u+h, v+k) + C(u,v) - C(u+h,v) - C(u,v+k) \ge 0.$$

The joint distribution $F_{XY}(x,y)$ of two random variables X, Y can be reconstructed from the marginal distributions $F_X(x)$, $F_Y(y)$ by means of a copula:

$$F_{XY}(x,y) = C(F_X(x), F_Y(y)).$$

The point is that given the marginals $F_X(x)$, $F_Y(y)$, parametric copulas can be found that produce a joint distribution with a prescribed correlation structure. In the situation of random sets, copulas can be used to introduce correlations on the basic probability weights.

4. Application to an Example From Geotechnics

In this section, some of the methods will be shown at work in an example from geotechnics: an infinite beam on a linear elastic bedding. We begin by discussing the setup and a straightforward probabilistic model, which will be refined subsequently.

4.1. Deterministic/probabilistic dimensioning

The simplest, one-dimensional model is the so-called Winkler beam, extending along the real line with coordinate $x \in \mathbb{R}$. The displacement $u(x)$ is described by the bending equation

$$EI\, u^{IV}(x) + bc\, u(x) = q(x),\ -\infty < x < \infty,$$

see e. g. (Bolotin, 1969, Section 61). Here EI is the flexural rigidity of the beam, b its effective width, c the bearing coefficient of the foundation and $q(x)$ the loading. One may imagine that the beam describes a buried pipeline, the loading $q(x)$ resulting from the covering soil. The parameters EI and b of the beam may be considered as precisely known, whereas the soil properties c and q vary in an imprecisely known fashion. We will study the singular boundary value problem for the standardized equation

$$u^{IV}(x) + 4k^4 u(x) = p(x),\ -\infty < x < \infty \tag{9}$$

with $bc/EI = 4k^4$, $p(x) = q(x)/EI$, requiring that the solution should remain bounded at $\pm\infty$. In case k is a constant and $p(x)$ is an integrable function, both deterministic, its unique deterministic solution is given by

$$u(x) = \int_{-\infty}^{\infty} G(x,y)\, p(y)\, dy$$

in terms of its Green function

$$G(x,y) = \frac{1}{8k^3} e^{-k|x-y|}(\sin k|x-y| + \cos k|x-y|).$$

In case the load $q(x) \equiv q$ (and hence $p(x) \equiv p$) is constant, the displacement is constant as well and simply given by

$$u(x) \equiv \frac{p}{4k^4} = \frac{q}{bc}.$$

For the computational examples to follow we let the parameters vary around central moduli of $k = 10^{-2},\ p = 10^{-8}$. Approximately, this corresponds to the case of a buried cast-iron pipeline with an effective diameter of 6 [cm], covered by about 100 [cm] of top soil ($q = 10$ [N/cm]) and bedded in loosely packed sand ($c \approx 6.7$ [N/cm^3]). The resulting overall displacement would amount to $u(x) \equiv 0.25$ [cm] in the deterministic case.

In a probabilistic design, one would assume that the input parameters are random variables. In a standard engineering approach, one would argue that their mean values are given by the deterministic design values; further, a coefficient of variation is assumed (for material properties, usually around 5%, for soil parameters up to 15%, cf. (Rackwitz, 2000)). In the simple example, the most uncertain parameters are q (mean $\mu_q = 10$) and bc (mean $\mu_{bc} = 40$); we take a coefficient of

variation of 10%. Next, a type of distribution for the parameters has to be assumed. Both q and c are soil- and bedding related parameters, whose values strongly depend on what actually happens at construction site. Thus little evidence about the type of distribution is available. For the sake of presentation, we make the assumption that both parameters are normally distributed, that is, $q \sim \mathcal{N}(10, 1)$, $bc \sim \mathcal{N}(40, 16)$. Under this assumption, we can compute the probability density of the displacement $u = q/bc$, see Figure 1, and read off the quantiles. For example, the probability that the displacement is larger than 0.5 [cm] is $\approx 3.9 \cdot 10^{-6}$.

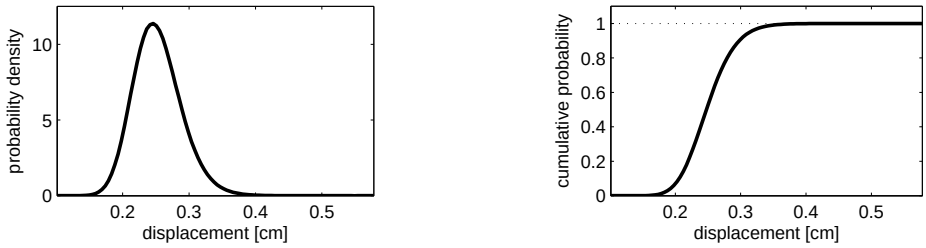

Figure 1. Probability density (left) and distribution function (right) of displacement under constant, but random load.

It is quite clear that the model is too simple to be credible. In particular, the load will certainly not be given by a single, albeit random, value along the whole beam, but will rather vary from point to point.

This suggests describing the load as a random field $q(x), x \in \mathbb{R}$, and thus brings us to a second important aspect of probabilistic modeling in engineering. At each point x in space, the load $q(x)$ is assumed to be a random variable. To define the field, the joint distributions of the loads at any finite number of points $q(x_1), \dots q(x_n)$ should be specified. The standard assumption in soil engineering is that the random field is homogeneous (i.e. the finite dimensional distributions are translation invariant) and Gaussian. In this case, the field is completely specified by the mean value μ_q and the second moments, i.e., the covariance $\mathrm{COV}(q(x), q(y))$ for any two points x, y. Due to homogeneity, the covariance depends only on the distance $\rho = |x - y|$ of the points and is of the form

$$\mathrm{COV}(q(x), q(y)) = \sigma^2 C(\rho)$$

with the variance σ^2 and the so-called autocorrelation function $C(\rho)$. A typical autocorrelation function is of the form

$$C(\rho) = \exp(-|\rho|/\ell),$$

where ℓ is the so-called correlation length (available in the literature for different types of soil, see e.g. (Rackwitz, 2000)).

Thus for modeling the load as a homogeneous Gaussian field, we need to provide the mean value, the variance and the autocorrelation function. As above, the mean value is assumed to be $\mu_q = 10$; for the field variance we take $\sigma_q^2 = 4$. In the following, we assume a moderate correlation length of $\ell = 100$ [cm] and take bc fixed at its deterministic design value 40 [N/cm^2]. A realization of the load and the corresponding displacement is shown in Figure 2; Figure 3 (left) shows the corresponding realization of the bending moment.

A critical quantity for assessing the safety against failure is the maximal bending moment $M_{\max}$ in the beam, which is given by $M_{\max} = \max(EIu''(x))$. A typical failure criterion would require that the maximal stress $M_{\max}/W$ (with the section modulus W) does not exceed the admissible stress (corresponding to the 0.1% yield strength, that is, the stress after which 0.1% plastic deformations remain). We drop the lengthy details and just show how $M_{\max}$ would be assessed probabilistically. To this end, a Monte Carlo simulation of $N = 500$ trajectories has been undertaken, yielding an estimate for the distribution of $M_{\max}$. Figure 3 (right) shows the result; the histogram has been extrapolated with the aid of a kernel smoother. In this way, we get the estimate $P(M_{\max} > 6000) \approx 6.52 \cdot 10^{-5}$, for example. We record this value for reasons of comparison with Section 4.4.

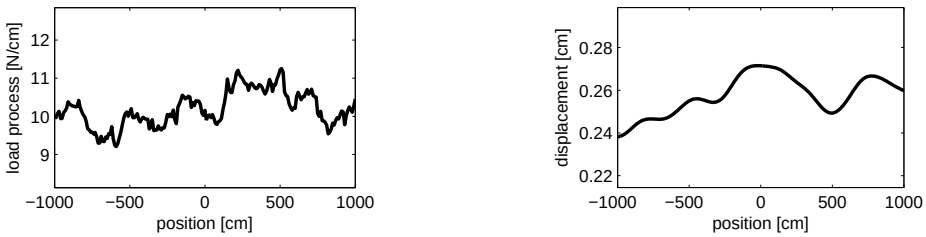

Figure 2. Random field model: trajectories of load process (left) and corresponding displacement (right).

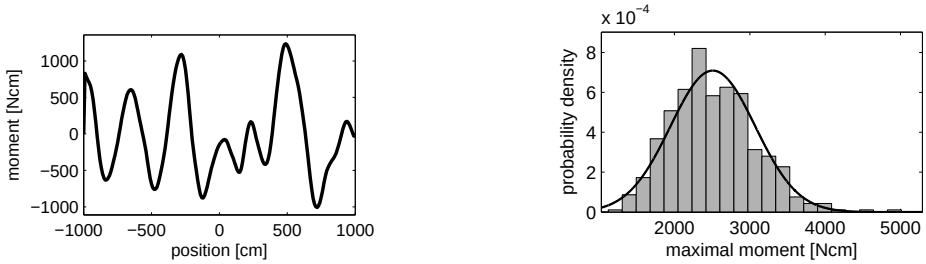

Figure 3. Random field model: trajectory of bending moment (left) and simulation of maximal bending moment (right).

The possibilities of more refined statistical methods, like confidence intervals for quantiles or robust estimates, are left aside here, and we close our brief survey of classical probability in this example.

4.2. Fuzzy set modeling

In order to present a fuzzy model of the elastically bedded beam, we assume that the parameters k and p are described by fuzzy numbers K and P. More generally, one could admit, e.g., loads of the form $p(x) = \sum_{i=1}^{n} a_i p_i(x)$ as a combination of fixed shape functions $p_i(x)$ with parameters a_i, which in turn can be taken as fuzzy numbers $A_i, i = 1, \ldots, n$. We adopt here the simple case that both parameters are fuzzy constants and model the data as a non-interactive fuzzy vector with two components (K, P). This signifies that the joint membership function is given by the formula $\pi_{(K,P)}(k, p) = \min\{\pi_K(k), \pi_P(p)\}$, hence the level sets are two-dimensional intervals. We shall compute the fuzzy point values of the fuzzy response $u(x)$ by applying the Zadeh extension

principle to the solution operator

$$(k,p) \to u(x) = L_x(k,p) = \frac{p}{4k^4},$$

see Subsection 4.1. By the discussion above, an α-level set of $L_x(K,P)$ is computed as the collection of the values of the solutions attained when the parameters vary in the respective level sets K^α, P^α.

For the sake of exposition in the example to follow, we take both K and P as triangular fuzzy numbers, centered around the values indicated in Subsection 4.1, namely

$$K = \langle \tfrac{1}{2}, 1, 2\rangle \cdot 10^{-2}, \qquad P = \langle 0, 1, 2\rangle \cdot 10^{-8},$$

Then the (constant) fuzzy solution is simply given by the fuzzy number $L_x(K,P) = P/4K^4$. It is depicted in Figure 4.

We observe that the fuzzy model consistently describes the fluctuations of the response in dependence on the data variability. In addition, the α-level structure provides a good picture of the sensitivity of the result.

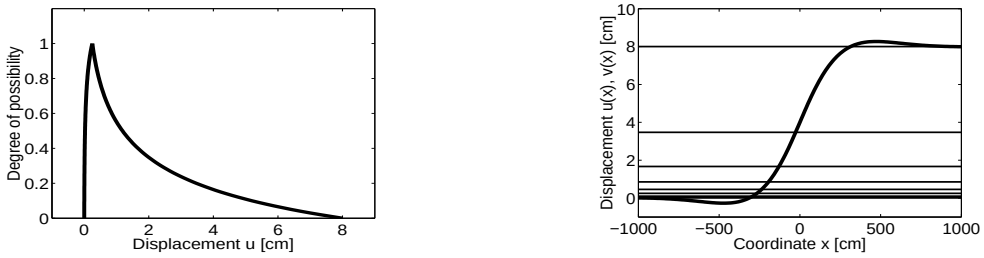

Figure 4. Fuzzy displacement u (left) and fuzzy solution (right, horizontal lines depicting α-levels) versus effect of localization.

We now discuss a certain limitation of the (simple) fuzzy model. The semantics of fuzzy sets allows the parameter p to vary in the range given by its fuzzy description, in the example its support $[0, 2 \cdot 10^{-8}]$. If one permits non-constant realizations of the parameter p, the bounds predicted by the fuzzy output may be exceeded. Indeed, assume that p jumps from 0 to $2 \cdot 10^{-8}$ at the point $x = 0$. This means that we have to solve Equation (9) with a load

$$p(x) = \begin{cases} 0, & x < 0, \\ p = 2 \cdot 10^{-8}, & x > 0. \end{cases}$$

The corresponding displacement is

$$v(x) = \begin{cases} \frac{p}{8k^4}\, e^{kx} \cos kx, & x < 0, \\ \frac{p}{8k^4}(2 - e^{-kx} \cos kx), & x > 0. \end{cases}$$

Taking the admissible value $k = \frac{1}{2} \cdot 10^{-2}$, it is seen that the graph of v exceeds the band described by the fuzzy displacement with constant parameters.

This is an example of the effect, observed in other circumstances as well, that a localized parameter fluctuation may produce a response not predicted by a simple fuzzy model. In Figure 4.2,

the 0-level set of the fuzzy displacement is indicated by the horizontals $u = 0$ and $u = 8$, the curve is the graph of v, and the other horizontals indicate level sets of the fuzzy displacement u for $\alpha = 0.2, 0.4, 0.6, 0.8$. Degree of possibility equal to one occurs at $u = 0.25$.

4.3. Random set modeling

As mentioned in Subsection 4.1, assuming that q and bc are normally distributed random variables is rather artificial. The available information consists of a nominal value and a coefficient of variation. One way of organizing this information is by means of a Tchebycheff random set as described in Subsection 3.2. If the loading q, say, is preliminarily viewed as a random variable with unknown probability distribution, but with expectation value μ_q and variance σ_q^2, Tchebycheff's inequality asserts that the probability of the event $\{|q - \mu_q| > \sigma_q/\sqrt{\alpha}\}$ is less or equal to α, where $\alpha \in (0, 1]$. Let

$$Q(\alpha) = [\mu_q - \sigma_q/\sqrt{\alpha}, \mu_q + \sigma_q/\sqrt{\alpha}].$$

As outlined in Subsection 3.2, we may use the $Q(\alpha)$ to define a random set on the space $\Omega = (0, 1]$, equipped with the uniform probability distribution, the Tchebycheff random set arising from μ_q and σ_q^2.

We take up the example of Subsection 4.1 and apply this construction to the loading q with $\mu_q = 10$ and $\sigma_q = 1$ (from a coefficient of variation of 10%). This results in a random set Q, whose contour function is depicted in Figure 5 (left).

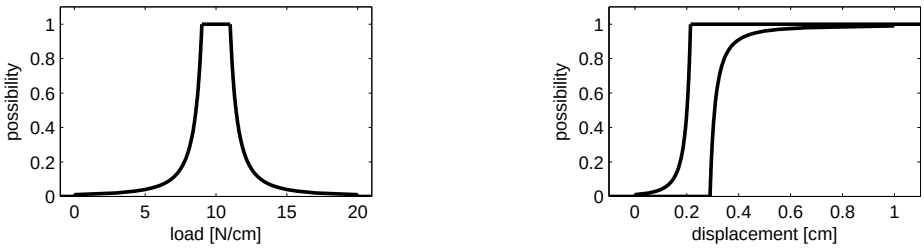

Figure 5. Tchebycheff random set for load (left) and probability box for resulting displacement (right).

In a similar way, we construct a Tchebycheff random set BC for the variable bc, using $\mu_{bc} = 40$ and $\sigma_{bc} = 4$. To form the joint random set (Q, BC), the dependence of Q and BC has to be modeled. To make computations easy, we settle for the so-called *fuzzy set independence*; that is, the joint random set is also defined on $\Omega = (0, 1]$ with focal elements $Q(\alpha) \times BC(\alpha)$, $\alpha \in \Omega$ (and thus only focal elements corresponding to the same index α are combined). The random set data can be propagated through the mapping that gives the displacement $u(q, bc) = q/bc$, resulting in a random set U with focal elements $U(\alpha) = u(Q(\alpha) \times BC(\alpha))$, the set of values attained when (q, bc) range in $Q(\alpha) \times BC(\alpha)$.

The evaluation of the interval bounds for $U(\alpha)$ requires a global optimization. It is useful to describe the output random set as a probability box, which is bounded by the lower and the upper distribution functions

$$\underline{F}(x) = \underline{P}(-\infty, x], \qquad \overline{F}(x) = \overline{P}(-\infty, x].$$

The resulting probability box for the displacement is shown in Figure 5 (right).

The probability box immediately gives information on quantile ranges. For the event $A = \{U \geq 0.5\}$, for example, we get the probability interval $[\underline{P}(A), \overline{P}(A)] = [0, 0.04]$, which is more credible than the point estimate $P(A) \approx 3.9 \cdot 10^{-6}$ from the Subsection 4.1 (obtained under the stringent assumption that q and bc were normally distributed).

An even more realistic combination of the random field model with random set parameters will be described in the following subsection.

4.4. A hybrid model

A combination of stochastic differential equations with random set parameters has been recently worked out in (Schmelzer, 2010). This can be used in the dynamics of structures. Earthquake induced vibrations can be modeled by stochastic processes, like colored noise, whereas uncertain material parameters can be modeled by random intervals. We shall demonstrate a more modest hybrid model for the elastically bedded beam. The load q will be modeled as a random field as in Section 4.1, while the bedding parameter bc will be modeled as a random set. Of course, the model can be generalized to higher levels by also taking the field parameters σ_q and ℓ as random sets, etc. For the sake of simplicity, we shall take bc as an interval and the field parameters as in Section 4.1, i.e., $\mu_q = 10$, $\sigma_q = 2$, $\ell = 100$. For bc we choose the interval $[20, 40]$, which has the previously assumed mean value for bc as its upper boundary.

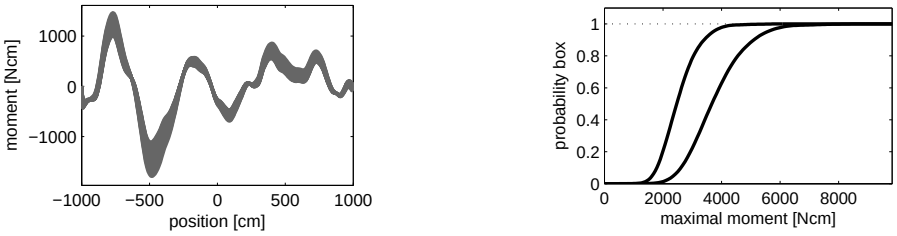

Figure 6. Hybrid model: Single interval trajectory of bending moment (left) and p-box for maximal bending moment (right).

The resulting output will be a set-valued stochastic process; more precisely, each trajectory will be interval-valued. Figure 6 (left) shows a single trajectory of the bending moment. In order to assess the statistical properties of the output, a sample of trajectories has to be generated. From there, one can compute, e.g., the upper and lower distribution functions of the maximal bending moments in the beam. This is a critical quantity on which the failure criterion from Section 4.1 is based. A p-box of the maximal bending moment is shown in Figure 6 (right), based on $N = 500$ trajectories of the field. From the list of computed values (interpolated using a kernel smoother) one may obtain upper and lower probabilities that given limits are being exceeded, e.g.,

$$\underline{P}(M_{\max} > 6000) \approx 6.51 \cdot 10^{-5}, \quad \overline{P}(M_{\max} > 6000) \approx 2.05 \cdot 10^{-2},$$
$$\underline{P}(M_{\max} > 8000) \approx 0, \quad \overline{P}(M_{\max} > 8000) \approx 1.21 \cdot 10^{-3}.$$

5. Conclusion

This brief exposition presented an overview over various important aspects of uncertainty modeling, including axiomatic, semantic, and numerical aspects. Necessarily, a lot of important additional topics had to be left aside. Concerning families of probability measures and random sets, we mention the differing lower/upper probabilities obtained from families of random variables versus the random set corresponding to the family (Fetz and Oberguggenberger, 2015). Further issues are Monte Carlo simulation of random sets and imprecise stochastic processes, as well as sensitivity analysis based on random sets (Oberguggenberger, King and Schmelzer, 2009; Oberguggenberger, 2015). For interval methods and their application in finite elements we refer to (Moens and Vandepitte, 2005; Muhanna, Zhang and Mullen, 2007); for recent results on interval methods related to stochastic processes, see (Sofi, 2015; Muscolino, Santoro and Sofi, 2016).

References

Augustin, T., F. Coolen, G. de Cooman and M. Troffaes (Eds.). *Introduction to Imprecise Probabilities.* John Wiley & Sons Ltd, Chichester, 2014.

Beer, M., S. Ferson and V. Kreinovich. Imprecise probabilities in engineering analyses. *Mechanical Systems and Signal Processing*, 37:4–29, 2013.

Bolotin, V. V. *Statistical Methods in Structural Mechanics.* Holden-Day Inc., San Francisco, 1969.

de Finetti, B. Teoria delle probabilità: sintesi introduttiva con appendice critica. Volumi primo e secondo. Nuova Biblioteca Scientifica Einaudi, 25* et 25**. Giulio Einaudi Editore, Torino, 1970. English translation: Theory of probability: a critical introductory treatment. Vol. 1 and Vol. 2. John Wiley & Sons, London, 1974/1975.

Dubois, D. and H. Prade. *Possibility theory. An approach to computerized processing of uncertainty.* Plenum Press, New York, 1988.

Dubois, D., H. Prade and S. Sandri. On possibility/probability transformations. In: R. Lowen, M. Roubens, editors, *Fuzzy Logic: State of the Art.* Kluwer Academic Publishers, Dordrecht, pages 103–112, 1993.

Dubois, D., H. Prade and R. Sabbadin. Decision-theoretic foundations of qualitative possibility theory. *European Jornal of Operational Research*, 128:459–478, 2001.

Elishakoff, I. *Whys and Hows in Uncertainty Modelling: Probability, Fuzziness and Anti-Optimization*, volume 388 of *CISM Courses and Lectures*. Springer-Verlag, Wien/New York, 1999.

European Committee for Standardization. *EN 1990:2002. Eurocode – Basis of Structural Design.* CEN, Brussels, 2002.

Fellin, W., H. Lessmann, M. Oberguggenberger and R. Vieider. *Analyzing Uncertainty in Civil Engineering.* Springer-Verlag, Berlin, 2005.

Ferson, S., V. Kreinovich, L. Ginzburg, D. S. Myers and K. Sentz. Constructing probability boxes and Dempster-Shafer structures. Technical Report SAND2002–4015, Sandia National Laboratories, 2003.

Fetz, T. and M. Oberguggenberger. Propagation of uncertainty through multivariate functions in the framework of sets of probability measures. *Reliability Engineering and System Safety*, 85:73–87, 2004.

Fetz, T. and M. Oberguggenberger. Imprecise Random Variables, Random Sets, and Monte Carlo Simulation. In: T. Augustin, S. Doria, E. Miranda, E. Quaeghebeur, editors, *ISIPTA 15. Proceedings of the 9th International Symposium on Imprecise Probability: Theories and Applications*, pp. 137–146. Aracne Editrice, Roma, 2015.

Fine, T. L. *Theories of Probability. An Examination of Foundations.* Academic Press, New York, 1973.

Freudenthal, A. N. Safety and the probability of structural failure. *Transactions ASCE*, 121:1337–1397, 1956.

Goodman, I. R. and H. T. Nguyen. Fuzziness and randomness. In C. Bertoluzza, M. Á. Gil, and D. A. Ralescu, editors, *Statistical Modeling Analysis and Management of Fuzzy Data*. Physica-Verlag, Heidelberg, pages 3–21, 2002.

Huber, P. J. *Robust Statistics*. John Wiley & Sons, New York, 1981.

Kreinovich, V. Random sets unify, explain, and aid known uncertainty methods in expert systems. In: J. Goutsias, R. P. S. Mahler and H. T. Nguyen, editors, *Random Sets. Theory and Applications.* Springer-Verlag, New York, pages 321–345, 1997.

Martz, H. F. and R. A. Waller. *Bayesian Reliability Analysis*. John Wiley & Sons Ltd., Chichester, 1982.

Meyer, M. A. and J. M. Booker. *Eliciting and Analyzing Expert Judgement.* Society for Industrial and Applied Mathematics, Philadelphia PA, 2001.

Moens, D. and D. Vandepitte. A survey of non-probabilistic uncertainty treatment in finite element analysis. *Computer Methods in Applied Mechanics and Engineering*, 194:1527–1555, 2005.

Muhanna, R. L., H. Zhang and R. L. Mullen. Interval finite elements as a basis for generalized models of uncertainty in engineering mechanics. *Reliable Computing*, 13(2):173–194, 2007.

Muscolino, G., R. Santoro and A. Sofi. Reliability analysis of structures with interval uncertainties under stationary stochastic excitations. *Computer Methods in Applied Mechanics and Engineering*, 300:47–69, 2016

Neumaier, A. *Interval Methods for Systems of Equations.* Cambridge University Press, Cambridge, 1990.

Neumaier, A. Fuzzy modeling in terms of surprise. *Fuzzy Sets and Systems* 135:21–38, 2003.

Oberguggenberger, M., J. King and B. Schmelzer. Classical and imprecise probability methods for sensitivity analysis in engineering: A case study. *International Journal of Approximate Reasoning*, 50(4):680–693, 2009.

Oberguggenberger, M. Combined methods in nondeterministic mechanics. In I. Elishakoff and C. Soize, editors, *Nondeterministic Mechanics*, pages 263–356. Springer-Verlag, CISM International Centre for Mechanical Sciences, Vol. 539, Wien, 2012.

Oberguggenberger, M. Engineering. In T. Augustin, F. Coolen, G. de Cooman and M. Troffaes, editors, *Introduction to Imprecise Probabilities*, pp. 291–304. John Wiley & Sons Ltd, Chichester, 2014.

Oberguggenberger, M. Analysis and computation with hybrid random set stochastic models. *Structural Safety*, 52:233–243, 2015.

Popper, K. The propensity interpretation of the calculus of probability and the quantum theory. In: S. Körner, editor, *Observation and Interpretation*, London, pages 65–70, 1957. The propensity interpretation of probability. *British Journal for the Philosophy of Science* 10:25–42, 1959.

Popper, K. *Logik der Forschung.* 10. Auflage, J. C. B. Mohr (Paul Siebeck), Tübingen, 1994.

Rackwitz, R. Reviewing probabilistic soils modelling. *Computers and Geotechnics*, 26:199–223, 2000.

Ross, T. J., J. M. Booker and W. J. Parkinson, editors, *Fuzzy Logic and Probability Applications. Bridging the Gap.* Society for Industrial and Applied Mathematics/American Statistical Association, Philadelphia, PA/Alexandria, VA, 2002.

Savage, L. J. *The Foundations of Statistics.* Wiley, New York, 1954.

Schmelzer, B. On solutions to stochastic differential equations with parameters modeled by random sets. *International Journal of Approximate Reasoning*, 51:1159–1171, 2010.

Shafer, G. *A Mathematical Theory of Evidence.* Princeton University Press, Princeton NJ, 1976.

Sofi, A. Structural response variability under spatially dependent uncertainty: Stochastic versus interval model. *Probabilistic Engineering Mechanics*, 42:78–86, 2015.

Walley, P. *Statistical Reasoning with Imprecise Probabilities.* Chapman & Hall, London, 1991.

Walley, P. Towards a unified theory of imprecise probability. *International Journal of Approximate Reasoning*, 24:125–148, 2000.

Zadeh, L. A. The concept of a linguistic variable and its applications to approximate reasoning, Part 1–3. *Information Sci.*, 8:199–250, 8:301–357; 9:43–80, 1975.

Epistemic Uncertainty in Agent-based Modeling

Scott Ferson[1)] and Kari Sentz[2)]
[1)] *Applied Biomathematics, USA, scott@ramas.com*
[2)] *Los Alamos National Laboratory, USA, ksentz@lanl.gov*

Abstract: Traditional approaches to handling uncertainty in agent-based models employ Monte Carlo methods to randomly sample parameters and probabilistically determine whether and how a behavior or interaction rule is realized by an individual agent. A simulation of all agents thereby represents a single realization from among many possible scenarios, and simulations with many replications are used to reveal differential probabilities and the likelihoods of extreme results. Unfortunately, Monte Carlo is a poor way to project epistemic uncertainty through a complex model, and it is an unsatisfying scheme for representing the uncertainty about volitional choices of agents. Adding epistemic uncertainty to agent-based models properly requires the ability to (1) characterize stochastic drivers imprecisely, (2) specify agent attributes and other quantities as intervals, probability distributions, or p-boxes, and (3) execute behavior rules in a way that respects uncertainty in their conditional clauses. When uncertainty makes the truth value of the conditional clause of any rule unclear, the simulation should hold that the rule both fires and does not fire. This may result in subsequent uncertainties elsewhere in the simulation including the status of attributes of agents, even perhaps whether an agent exists or not. These facilities advance agent-based modeling to uncover a more comprehensive picture of the effects of epistemic uncertainty, which can be vastly more important than aleatory uncertainty. We compare this approach with traditional simulation using only Monte Carlo methods to reveal the differences between these two approaches to uncertainty.

Keywords: agent-based models, epistemic uncertainty, Monte Carlo simulation, p-boxes, intervals

1. Introduction

Predictive failures are more common in probabilistic modeling and simulation than they should be. For instance, NASA estimated the risk of catastrophic failure of its Space Shuttle to be 1/10,000 per flight, but its observed failure rate was about 1 per 70 flights (Hamlin et al. 2011; Oberkampf and Roy 2010). The National Weather Service and the Army Corps of Engineers strongly underestimate risks of "100-year floods" and miscommunicate uncertainties about flooding risks (Morss and Wahl 2007; NRC 2006; NWS 1998). Observed failures and near-misses found at the Diablo Canyon Nuclear Power Plant reveal gross understatement of its assessed risks (Lochbaum 2011). Failure cascades in electricity distribution systems are more common than they are forecasted to be (RAWG 2005; USCPSOTF 2006). Probabilistic assessments understating risks in the financial industry precipitated the Great Recession (Savage 2012; Silver 2012). These are not random rare events in a discipline that estimates and controls risks well overall. They are not the unlucky but expected tail events sometimes called "noble failures". They seem instead to be wholesale errors which are the result of pervasive and systemic errors that undermine the credibility of all modeling and simulation efforts. The comment by a prominent engineer that the 2007 bridge collapse in Minneapolis was a "billion to one" event typifies the raw fact that uncertainties are sometimes not well understood in engineering.

What can be done about this situation when such predictive failures are intolerable? We believe that a pervasive cause of these predictive failures is neglecting or mishandling uncertainties. This paper focuses on practical methods for introducing uncertainty into agent-based models because such models are widely used and growing in importance within engineering. The problem of correctly handling uncertainties in this context also seems to be rather subtle.

2. Kinds of Uncertainty

In the past, uncertainty analysis considered the source of uncertainty to be its salient aspect, so modelers talked, for example, about their parametric uncertainty or their model-form uncertainty. A more modern view is that the nature of the uncertainty, rather than its source, is a more important characteristic. We can distinguish between two main forms of uncertainty: epistemic and aleatory. Aleatory uncertainty refers to the variability or stochastic fluctuations in a quantity through time, variation across space, manufacturing or genetic differences among components or individuals, or similar heterogeneity within some ensemble or population. The word aleatory comes from *alea*, the Latin word for dice. This is considered to be a form of uncertainty because the value of the quantity can change each time one looks, and we cannot predict precisely what the next value will be (even though the distribution of values may be known). Epistemic uncertainty, on the other hand, refers to the lack of full knowledge about a quantity that arises from imperfect measurement, limited sampling effort, or incomplete scientific understanding about the underlying processes that govern its value.

These two forms of uncertainty have important differences. Epistemic uncertainty can in principle be reduced by empirical effort; investing more in measurement and study of a system should yield better precision. Aleatory uncertainty, in contrast, can sometimes be better characterized, but cannot generally be reduced by empirical effort. Epistemic uncertainty depends on the observer and the observations made. Aleatory uncertainty does not depend on an observer at all. It exists whether or not anyone witnesses it, like the sound waves emanating from the proverbial tree falling unseen in the forest. Although epistemic and aleatory uncertainty can sometimes be like ice and snow in that their distinction can be difficult to discern through complicating details (and sometimes one can change into the other depending on the scale and perspective of the analyst), the macroscopic differences between these two forms of uncertainty are usually obvious and often significant in practical settings.

3. Agent-based Modeling

Agent-based models (Wooldridge 2009) arose from early research on cellular automata (Gardner 1970) when computing first became widely accessible. These models were generalized to allow individual objects to move about on the plane or in space. Simulations also endowed the objects with goals and the ability to make choices in complex environments, and even emulated how agents might learn from their past interactions and experiences to adapt and evolve within the simulation. As a consequence, agent-based models have the potential to capture emergent behavior that was not conceived *a priori*. Most recently, the models have considered more than a single kind of entity interacting with each other. These include agent-based models, multi-agent simulations, individual-based models, and swarm models. Today, these

heterogeneous agent-based models are considered a new paradigm for design in computer science with self-structuring software systems (Shoham and Leyton-Brown 2009), and models for distributed decision-making and problem solving (Weiss 2001).

The practical applications of agent-based models are many and include fleet and supply-chain management, logistics, portfolio planning, forestry, biological resource management, epidemiological modeling, and analysis of coalitions and joint mission planning. Ilachinski (2004) described the use of agent-based models in modeling military conflicts, which is natural because of the importance in that context of nonlinear interactions among elements organized in command-and-control hierarchies of often fluctuating coherence. Simulations using autonomous agents to model individual behaviors represent a bottom-up approach to synthetic modeling. They can complement or perhaps supersede conventional analytic and reductionist approaches, which may be less useful in the study of emergent patterns of self organization that commonly arise in complex systems of systems. Although much effort has been devoted to developing this approach, and to combining it with uncertainty analysis (e.g., Wu et al. 2003), further work is needed, particularly workable schemes to express and propagate not just aleatory but also epistemic uncertainties about agent status and rule outcomes through simulations.

4. What's Wrong with Sampling

A traditional sampling approach to uncertainty projection in engineered systems routinely and often profoundly underestimates the overall uncertainty that should be associated with outcomes (Atwood 1985; Ferson and Ginzburg 1996; Oberkampf and Roy 2010; Ferson and Siegrist 2012; Savage 2012). Figure 1 illustrates this underestimation, showing Monte Carlo results in a tangle of trajectories whose overall uncertainty grossly underexplores the true range of possibilities arising from the epistemic uncertainty about the outcome circumscribed by outer bounds. The actual uncertainty is often much wider, sometimes much larger than that predicted by ordinary probability methods such as Monte Carlo simulation, Latin hypercube simulation, or second-order Monte Carlo. The outer bounds are not necessarily worst-case outcomes, but they may be envelopes of the plausible scenarios in a proper accounting of uncertainty that, unlike traditional Monte Carlo approaches, does not make unjustified assumptions about independence among variables, and does not use equiprobability or uniform distribution assumptions to represent incertitude (empirical ignorance). We can sometimes observe the difference between the Monte Carlo simulations and the outer bounds in Figure 1 to be several orders of magnitude. Sometimes the Monte Carlo results are in the middle of the true possible range of outcomes on some scale as depicted in the figure, but this is not always the case. While the Monte Carlo results may 'fill up' the possible range for some intervals in time dependent models, this is rare. When it does happen in time-dependent models, it is often an ephemeral occurrence at the start of a simulation or at pinch points or ranges were the direction of trajectories shift. Monte Carlo sees uncertainty through a glass darkly, in general. Variants of Monte Carlo methods are only marginally different. Latin hypercube sampling, for example, is usually worse at identifying extreme events. Second-order Monte Carlo does generally produce slightly wider results, but these trajectories form a halo around the regular Monte Carlo results, and they also come nowhere near to filling up the range of possible outcomes in most cases.

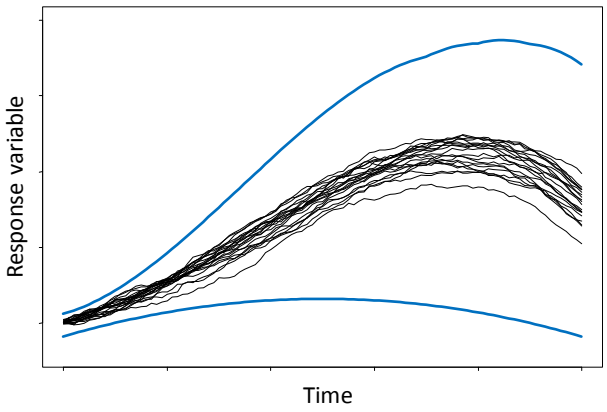

Figure 1. Discrepancy between the true possible range (outer bounds) and Monte Carlo realizations.

Often, what strategists and planners actually need to know is the range of possible outcomes, mostly because they are especially concerned with the extreme cases. There are the outer bounds shown in Figure 1. Unfortunately, Monte Carlo simulation is well known to be a very poor technique for uncovering this range. David Alderson (Alderson et al. 2012) of the Naval Postgraduate School has noted that "Random sampling is terrible at finding worst-case scenarios, although terrorists are pretty good at it." He was talking about estimating the reliability of transport networks and supply chains and their susceptibility to malevolent disruption, but the observation is actually quite general.

The problem is related to what is sometimes called the "curse of dimensionality". It can be illustrated with a very simple example. Suppose we are interested in estimating the possible range of the sum of 30 uncertain values each constrained to the unit interval. It is clear that this range is an interval between zero and 30. Random sampling, in which uniform random deviates independently sampled from each of the 30 unit intervals are added together, reveals a range that is almost always much smaller. If there are 100 such sample summations adding 30 deviates together, the output range of the sum is roughly one third of what it should be. Even with a million replications, the observed range of sums is only half as wide as it should be. Using different distributions other than uniform or even systematic rather than uniform sampling for the addends does not help widen the result appreciably. This underestimation worsens dramatically as the number of inputs grows.

Some analysts argue that the larger bounds are unreasonable characterizations of uncertainty and insist that the narrower tangle of Monte Carlo outputs for the example above is actually correct. They say that it would be silly to suppose that all 30 of the addends could be extreme in the same direction at the same time. Such analysts will often be surprised by the outcomes of real-world systems, because this constellation of extremes can indeed be realized in the outcomes of real-world systems. Disasters and extreme events are often born when multiple things go wrong together. Before the 2007 financial crisis, many analysts asserted—and apparently also really believed—that it would be essentially impossible for a significant fraction of the hundreds of mortgages bundled together in securities to all default. But the financial analysts neglected to account for the dependence relationships in risk among these mortgages that made them far from independent. Contracting home markets affected lots of mortgages at the same time, and there were unfortunate positive feedbacks that made the situation worse. The more mortgages that defaulted, the harder it became for any homeowner to stay above water. These examples are very simple instances of the general problem. When the elements become more complex than mortgages that either default or do not, and the

functions relating them together become more complicated than simple addition, the potential for dependencies to play a dominant role in the overall risk of failure is both more likely and harder to foretell.

Why do regular probabilistic analyses often badly underestimate risks? There are several reasons, but the most common and significant ones are

- Unjustified use of independence assumptions or overly precise dependence assumption,
- Inappropriate use of equiprobability and uniformity assumptions,
- Underestimation of the uncertainties of original measurements,
- Modeling volitional choices with distributions as though they are random,
- Using averaging as an aggregation, and
- Making assumptions for the sake of mathematical convenience (wishful thinking).

For example, standard approaches based on probability theory almost always assume independence among variables, even when there is little evidence or argument to support such an assumption. In fact, when there is no information about a dependency, many consider this to be a reason to assume independence. This is profoundly wrong in any risk-analytic or uncertainty-analytic context, and the consequences of this are underestimated risks and incorrect assessments of uncertainty. The standard probabilistic approaches grossly understate the uncertainty when they fail to account for the correlations, dependencies, and interactions among the components and among stochastic driver variables (Hartung et al. 1985; Hickman et al. 1983; Hokstad and Rausand 2008). These connections that join together the elements of the model are frequently neglected in the modeling exercise. In principle, each such connection should be characterized. There are two reasons that such a task is generally extremely hard: First, there are often many dependencies to worry about. If there are n elements in a system, there may be up to $(n^2 - n)/2$ pairwise interactions between those elements, and this is just the beginning. There may also be triple-wise or even higher-level interactions as well, which are essentially never even considered in most models. The second reason it is difficult to address these interconnections in modeling is that dependence between stochastic variables can be complex. If we're lucky, one inter-variable dependence can be fully characterized by a simple real value like a correlation coefficient, but this is often not really possible because the dependency is nonlinear. We know that such complex interactions can and do exist among many variables, but human intuition is not well adapted to consider them, especially when nonlinearities, trade-offs, feedbacks, problem cascades, and other complexities complicate the story.

Poor models of dependences are not the only important reason that naïve Monte Carlo methods understate uncertainty. Space limits preclude a full discussion of each of the other causes mentioned above. Ferson and Ginzburg (1996) review the problems that arise for risk analyses from using assumptions of equiprobability or uniform distributions to model incertitude. Henrion and Fischhoff (1986) review the apparently pervasive and systemic underestimation of measurement uncertainties for physical constants. The situation is probably even worse for routine test-site and field measurements (Morgan and Henrion 1990; Youden 1972). On account of these issues, exclusively using Monte Carlo or similar traditional probability techniques in risk, reliability, or uncertainty assessments for critical infrastructures is unsound when extreme events are the focus. This crosses over to the ridiculous for modeling behavior when malevolent human actors are involved such as in warfare, terrorism, arson, crime, and competition. Modern approaches (Beer et al. 2013; Ferson and Ginzburg 1996; Walley 1991) to handling epistemic uncertainty that treat it differently from aleatory uncertainty and respect epistemological limits on inferences are designed to remedy these problems and provide reliable characterizations and conclusions that do not depend on making assumptions that analysts cannot justify or do not even believe.

Considerable progress has been made recently in developing algorithms for numerical calculations that respect and distinguish epistemic and aleatory uncertainty (Beer et al. 2013; Ferson and Siegrist 2012; Sentz and Ferson 2011). Figure 2 below shows several examples of 'uncertain numbers', where the abscissas are arbitrary axes of real values. A *probability box* or p-box (depicted at the far right) is the most general form because it has both aleatory and epistemic uncertainty. In Bayesian analyses, this structure is also called a distribution band (Berger 1994; Basu and DasGupta 1995). They are closely related to what frequentists call meta-distributions or second-order distributions (Vose 2008), and to the collections of probability distribution functions known in the theory of imprecise probabilities as credal sets (Walley 1991). P-boxes arise in robust Bayes analyses in which there is doubt about the prior that should not be neglected or condensed into a single distribution, or when there is non-negligible measurement error about input data that induce a family of likelihoods rather than a unique one. P-boxes can also arise from partial constraint information such as might be available from an incomplete or faulty set of sensors. A p-box is defined by left and right bounds, which delimit the class of probability distributions denoted by the p-box as in the rightmost graph in Figure 2. When those edges coincide, the class has only a single member, which is a precise cumulative probability distribution such as the second graph from left in Figure 2. This distribution represents aleatory uncertainty but not epistemic uncertainty. In contrast, the edges of the p-box could be rectangular in which case the p-box degenerates to an interval (third graph in Figure 2), which might consist entirely of epistemic uncertainty. Finally, the leftmost graph in Figure 2 depicts a known, fixed quantity, which we might call a scalar. It is a completely degenerate kind of uncertain number in that it has neither aleatory nor epistemic uncertainty.

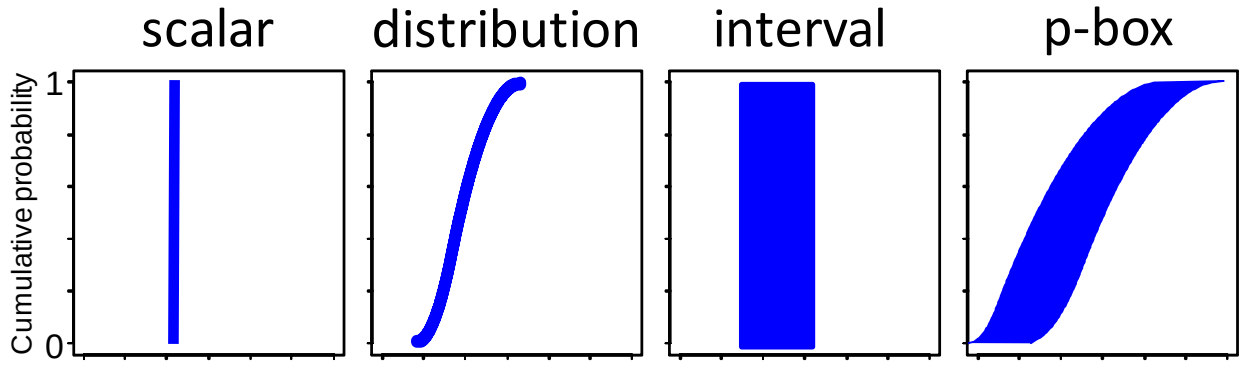

Figure 2. Bestiary of uncertain numbers.

We know how to do math on these uncertain numbers. Mathematical operations such as addition, subtraction, multiplication, division, minimum, maximum, powers, logs, roots, etc. have been worked out and implemented in stable software (Ferson et al. 2003; Ferson 2002). These operations are closed in the set of uncertain numbers, except in obvious cases that involve division by zero or taking the log or root of negative values. The results can be proven to be rigorous in that the bounds are guaranteed to surely contain the actual value or distribution given the uncertainty. Moreover, in many cases defined by well understood conditions, the results can also be proven to be best possible, which is to say that the bounds cannot be made any tighter without reducing the uncertainty about the inputs. P-boxes are a relatively simple way to express both aleatory and epistemic uncertainty about quantities; they are much simpler than credal sets

from the theory of imprecise probabilities (Walley 1991), fuzzy numbers (Kaufmann and Gupta 1985) or more general info-gap structures (Ben-Haim 2001), or even Dempster–Shafer structures (Ferson et al. 2003). This simplicity gives analysts great power to do practical computations at moderately large scales that are simply not achievable under the more delicate theories. The application of p-boxes as models of uncertainty in practical assessment problems is called probability bounds analysis. The Wikipedia article on the topic (http://en.wikipedia.org/wiki/Probability_box) lists dozens of applications published over the last decade. The p-box approach can be used to improve uncertainty analysis and the analysis of risk assessments in general by providing automatic sensitivity analysis for a probabilistic assessment.

5. Generalizd Agent-Based Modeling

There has been considerable research in the interface between uncertainty analysis and agent-based modeling (Faanes and Skogestad 2004; Zellner 2008; Bobashev and Morris 2010; Hancock et al. 2010; Hassan et al. 2010; Harp and Vesselinov 2011; Fonoberova et al. 2013; Magliocca and Ellis 2013), but it has focused exclusively on using agent-based models to analyze aleatory uncertainty, rather than what is proposed here, which is to project both forms of uncertainty through agent-based models.

Agent-based models represent and follow agents or meta-agents, which are composed of multiple, partially independent agents. Every agent consists of a name or identifier and a list of attributes, each of which is a vector of real or categorical values that characterize its status. The models also include rules governing the temporal evolution of agents and interactions among agents within the simulation. There may also be environmental variables such as weather shared by all agents that are determined by exogenous stochastic drivers that introduce randomness into the system. Traditionally, the behaviors and interactions of agents are simulated using randomly sampled parameters that probabilistically determine whether and how a rule is realized by an individual agent. A simulation thus represents a single realization from among many possible. Each simulation is a plausible scenario without information about the likelihood of that scenario. Monte Carlo replications of such simulations are typically employed to show differential probabilities and the likelihoods of extreme results.

As explained above, however, Monte Carlo is a very poor way to project epistemic uncertainty through a complex model, and an even worse way to represent the uncertainty about the volitional choices of friends or especially foes. Adding epistemic uncertainty to agent-based models in a proper way will require the ability to

1) Characterize stochastic drivers imprecisely,
2) Specify agent attributes and other quantities as uncertain numbers,
3) Execute rules in a way that respects uncertainty in their conditional clauses, and
4) Accept user specifications of uncertain numbers.

We address each of these facilities below. Through their development, agent-based modeling based on Monte Carlo methods can be generalized and expanded to uncover a more comprehensive picture of the effects of epistemic uncertainty.

6. Uncertainty about Stochastic Drivers

The traditional way to characterize a modeled variable that is influenced by stochastic drivers is to specify a precise probability distribution for the variable. Such distributions are usually derived in one of three ways: statistical analysis of available sample data collected about the variable, a forecast about it from related information, or informed judgment produced by the modeler or elicited from experts. Yet these distributions are rarely known with the confidence that is implied by employing a precise specification. For instance, there can be substantial epistemic uncertainty about diurnal, seasonal and longer-term patterns of weather and space weather that may affect threat detectability and response speeds of movable assets. We know future environmental conditions will be variable, but planners cannot forecast their precise probability distributions even in the short term (cf. Kharin 2009). The further into the future the prediction must be made, the broader the uncertainty will likely be. Conscientious assessments today characterize the epistemic uncertainty about probabilistic forecasts derived from quantitative models. One of the simplest ways to do this is with a p-box (Ferson et al. 2003). Even when the distribution is thought to be stationary and there are actually random sample data available to estimate its shape and parameters, the sample size may be limited, which means there is inferential uncertainty about any empirically estimated distribution. Balch (2012; Ferson et al. 2013) described ways to derive p-boxes from random sample data that respect and propagate this empirical uncertainty. P-boxes can also be obtained directly in expert elicitations, either from introspection by a single expert, or by forming an envelope of the distributional predictions from several experts (Linkov and Burmistrov 2003; Sentz and Ferson 2002; Ferson et al. 2003).

If we use a p-box rather than a precise probability distribution to characterize a stochastic driver, how would the agent-based model use the p-box in simulations? There are essentially two ways, depending on the nature of the uncertainty projection that is intended. The left graph in Figure 3 below depicts a precise cumulative probability distribution for a random variable that ranges between 3 and 6. Also depicted in the graph is a random deviate being generated from the distribution via inverse transform sampling (a uniform random number between zero and one on the probability axis is transformed into a random deviate from the distribution by mapping it to the abscissa through the cumulative distribution). The middle graph in the figure depicts a p-box over the same range that might express the epistemic uncertainty about the distribution in question. The first way to take into account the epistemic uncertainty of the p-box is to generalize the inverse-transform sampling approach that generates random deviates. Instead of producing a single scalar number for each uniform probability value, the p-box yields an *interval* of possible values for each probability value. The interval deviates can then be used in agent-based modeling software augmented with the ability to compute with intervals just as well as regular scalar numbers.

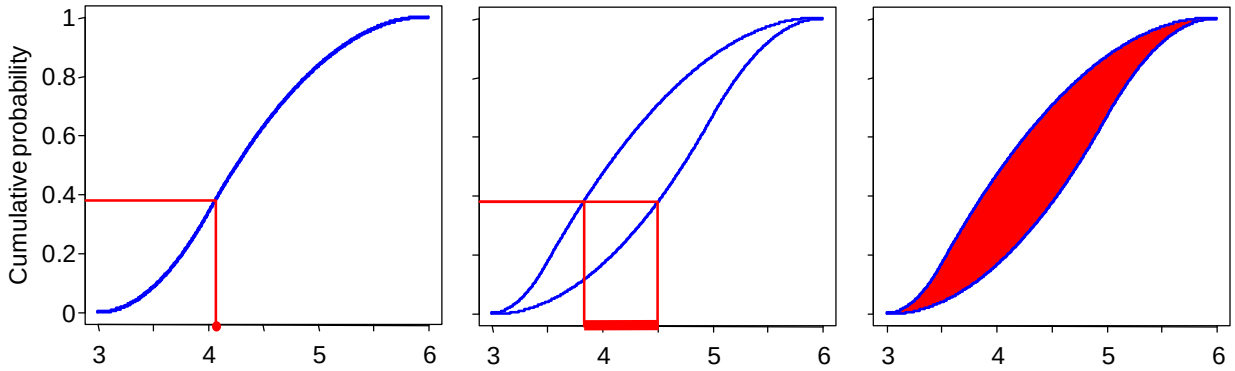

Figure 3. Three depictions of sampling aleatory uncertainty about a stochastic driver.

The second way to account for epistemic uncertainty in the p-box is to project the *entire p-box* through the calculations in the model. This idea is depicted in the rightmost graph in Figure 3 above. Doing this characterizes all possible scenarios at the same time, each weighted by their respective probabilities as well as can be specified under the acknowledged epistemic uncertainty of the p-box. This way of handling the p-box produces no additional complexity. In the exceptional case lacking epistemic uncertainty, where the stochastic driver is characterized by a precise distribution, the first way produces a single scalar number and the second way produces the whole probability distribution. In the other special case lacking aleatory uncertainty, where the driver is characterized by a simple interval, the first and second ways both produce the same deviate, which is the whole interval itself. Whatever is generated, whether it is a point value, an interval, a distribution, or a p-box, the structure can be projected through the calculations that depend on this stochastic driver.

7. Uncertainty in Agent Attributes

Attributes of the various agents are updated during the model simulation. In general, attributes are updated in one of two ways. Either the new value of the attribute is computed and assigned to that attribute replacing any value already there, or a modification term or factor is computed and then combined with the current state of the attribute. The new value can be any uncertain number, i.e., a scalar, probability distribution, interval, or p-box. For instance, the mass of a missile may be one of its attributes which should be modified if the missile releases decoys or chaff. The amount of the modification depends on an estimation of the mass of the released material. Note that, when an attribute's value is to be replaced, the uncertainty in the current value is irrelevant, but if the current value is to be modified, its uncertainty cannot thereby decrease. When an attribute has more than a single dimension, such as the current position of an agent specified by a vector consisting perhaps of its longitude, latitude and elevation, issues of dependency in the uncertainties of those components can arise (Miranda et al. 2013). In many cases, modelers will account for these dependencies in the rules they specify that govern agents' evolution. For instance, when a sea-surface asset is attacked, its sensors may perform differently or go off line. There may be epistemic uncertainty about these dependencies, and in principle these dependencies can be handled in the same way as other uncertainties in dependencies between variables, as modeled in probability bounds analysis (Ferson et al. 2004).

There may be other variables besides the attributes of agents and stochastic drivers that the software must update and which may therefore also have uncertainty. For instance, tallies, traces and synopses used to report the results and predictions of the simulation must be computed. Also, if many rules use the same calculation, the modeler may chose for efficiency's sake to define a parameter within the simulation to the hold the result of the calculation so that it can be used by all the rules without recomputing.

8. Uncertainty in Rule Conditions

Agent-based modeling consists of a system of rules specified by the modeler that govern the behavior and evolution of the agents. A simple rule typically has two parts, the condition and its consequence. The condition is the *if* part that determines whether the consequence is to occur. The consequence is the *then* part that specifies what should happen if it does. Compound rules can have an *else* part that specifies what should happen otherwise. The previous section described how agent attributes and other parameters can be updated with uncertainties when rules are applied that replace or modify their values. This section will review how uncertainty can be propagated through the *if* parts of the rules.

Consider a situation in which there is uncertainty about the inputs used in a binary rule, say, to fire an asset or not to fire the asset. Suppose that the rule is stated as

If $A < \theta$, then fire, else don't fire,

where A is the value of some environmental parameter or an attribute of some agent and θ is a threshold set by the modeler who specified the rule. When the uncertainties about A and θ are both characterized as intervals, there are only three cases for the condition $A < \theta$. The first case is when the uncertainty about A and θ are such that it is perfectly clear that $A < \theta$ is true. This case is depicted in the left graph in Figure 4 below, where the horizontal axis gives the magnitudes of the uncertain numbers. The value of the rule's condition is one, representing true, so we fire. The second case, depicted in the middle graph of Figure 4, is when the value of A is surely larger than the threshold θ despite their respective uncertainties. The value of the condition $A < \theta$ in this case is zero, for false, so we don't fire. The third case is when the two uncertainties overlap so that we cannot be sure whether A is larger or smaller or equal to the threshold θ. In this case, we say the value of the condition is the interval [0,1], which we call the 'dunno interval'. Because of the epistemic uncertainty about the terms, we do not know whether we should fire or not.

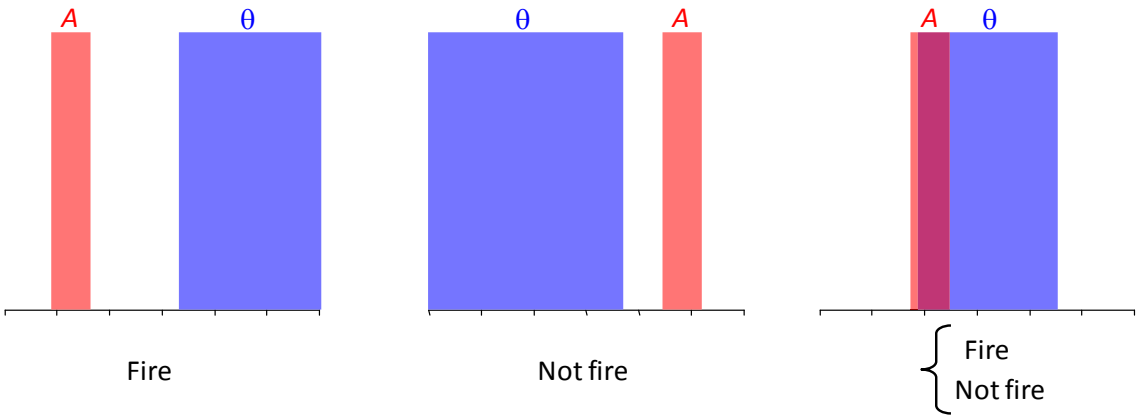

Figure 4. Three possibilities about whether A is less than θ given their respective uncertainties: yes, no and not sure.

This epistemic uncertainty about the rule's condition should be fully propagated through the simulation. Doing so means that we fire and not fire at the same time. This contradiction can be resolved in software by modeling two universes, one where the action of firing the asset occurs and one where it does not. But instead of following two diverging timelines requiring separate instantiations, the software will translate the consequences of the ambiguity of firing/not firing *back into intervals* in the attributes of the agents involved. This might mean, for instance, that the agent which was the target has status of both destroyed and intact. And, unlike the proverbial cake, we both consumed the asset by firing it, and yet still have it to fire later. Any behavior or result that depends on, or could be produced by, an agent is multiplied by its existence attribute so as to project the uncertainty about whether the agent exists to any outcomes that depend on the agent. If the agent surely exists, its existence attribute is 1, and outcomes are unaffected. If the agent surely does not exist, the attribute is 0, and the outcomes are nullified. If the existence attribute is dunno, the outcome is the interval between the full-strength outcome and a nullified outcome.

Whether the resulting ambiguity in attributes of agents matters or not depends on the dynamics of the system and the other uncertainties that may be present. This approach to agent-based modeling requires a new constitutive attribute 'exists', which, like an agent's name or identifier, must always be present in order to handle such cases. Aside from all the agents that surely exist, the software can also keep track of some agents that may or may not exist. We do not expect this approach to epistemic uncertainty in agent-based models to predict the future perfectly. What it should do is capture all possible scenarios given the available information and model structure and compute best-possible bounds on the probabilities associated with those scenarios. This harkens to the film *Men in Black 3* and its character Griffin who is a "fifth-dimensional" alien who sees all possible futures at the same time. He cannot tell what will happen but only what the possibilities and probabilities are, which is still very useful. It seems to us that Griffin's information is much more valuable than predictions from an oracle that are precise but often wrong, as are the results of traditional agent-based models. Predicting the future is dangerous because we sometimes believe our predictions, so the predictions ought to be guaranteed in some sense and not just merely possible.

Of course, the A and θ parameters may not always be intervals. They could also be probability distributions or p-boxes, in which case the resulting value of the rule's condition may not be one of the three simple logical values (zero for false, one for true, or the interval [0,1] for dunno). If aleatory uncertainty is present, issues of dependence between the terms of the comparison arise. Modelers should specify whether and how the parameters are dependent if they have this knowledge. The default behavior of the software is to presume their dependence is unknown and to use the Fréchet (1935; Hailperin 1986) inequalities to compute the logical value of the condition. The requisite mathematical framework for defining the logical values of magnitude comparisons between arbitrary p-boxes has been worked out, and stable software exists to compute them (Ferson 2002).

It turns out that magnitude comparisons among uncertain numbers of any kind produce at worst only intervals. Comparing uncertain numbers with the $<$, $>$, $\leq$, and $\geq$ operators in general yields interval logical values (Hailperin 1986). The exceptions are when (*i*) both operands are scalars, in which case the result is a Boolean value, (*ii*) one operand is a scalar and one is a probability distribution, in which case the result is a frequency, and (*iii*) both operands are probability distributions and they are independent or have another precisely specified dependence function, in which cases the comparison yields a frequency. For example, the comparison $3 <$ uniform(2,6) gives the scalar 0.75, but the comparison [1,3] $<$ uniform(2,6) gives the interval [0.75, 1]. Assuming the operands are independent, the comparison uniform(2,4) $<$ uniform(1,3)

gives the scalar 0.125, but *without* an assumption about their dependence, the comparison instead gives the big interval [0, 0.5]. As we saw above, comparing intervals that overlap at more than a single point always produces the dunno interval [0,1]. No matter what kind of uncertain numbers are compared, the result is always a scalar or an interval and never anything more complex. Rule conditions that produce these scalars and intervals are also translated to existence attributes as appropriate. Existence attributes are uncertain logical values and may take the form of any p-box on the unit interval, including scalars and arbitrary subintervals of [0,1]. The same multiplication convention used to project dunno uncertainty can be used to propagate the epistemic and aleatory uncertainty encoded as interval or scalar frequencies and probabilities. Despite the simplicity of magnitude comparisons always producing interval logical values, the value in the condition of a rule may not be an interval. If the rule is expressed in reference to an event which is described by its probability, the value of the condition is in general an uncertain logical value. These can include probability distributions and p-boxes on the unit interval. Our strategy for handling uncertainty in the rule condition for such cases is the same as was used before for magnitude comparisons. The uncertainty, which can include both epistemic and aleatory features, implies an *ensemble of ensembles* of possible universes expressing a class of different frequencies. We do not have to instantiate or even envision the entire population of possible universes. Indeed, we could not do so. Instead, we translate the uncertainty from those possible universes back into the existence attributes. For magnitude comparisons, these attributes were only intervals, but in the general case with arbitrary conditions, they will be uncertain logical values characterized by p-boxes. The multiplication convention can again be used to project the uncertainty whenever an agent acts or produces something that affects other agents or parameters.

The general issue of dependency in agent-based modeling is addressed in various ways. It is usually the job of the modeler to understand and represent in the model the basic functional dependencies that tether agents together and link stochastic processes, including relevant command-control chains, cooperations and collaborations, agent hierarchies, learning processes, cross-referential decision making, and other nonlinear interactions and mission dependencies. The software will have a sufficiently flexible language for specifying rules to develop these dependencies whenever they are understood by the modeler. However, we believe that modelers often cannot be aware of all the dependencies in a system that may become significant in some context. For this reason, the software will have default features that produce conservative treatments of uncertainties even when the modeler lacks details about the interdependencies among the components of the model. When a modeler is confident that two processes cannot interact, because they are distant in space or time or causation, this fact can be captured to improve (tighten) the propagation of uncertainty by using independence assumptions. But, when the modeler does not make a conscious decision to declare the processes independent, they are treated by the software as potentially interacting. The software does this by employing mathematical operations that generalize the classical Fréchet inequalities which make no assumptions whatsoever about inter-variable dependencies (Frank et al. 1987; Williamson and Downs 1990; Ferson et al. 2003).

Compound conditions consist of functions of logical quantities combined with AND, OR and NOT operations. The mathematical definitions and software implementations needed to handle compound conditions composed from elements with epistemic and aleatory uncertainty are exactly the same as are used in the analysis of fault trees, and present no special problems in the context of agent-based models. Whenever those elements—which are the operands of the logical operations—are uncertain logical values, whether coming as magnitude comparisons (which are always intervals) or arbitrary p-boxes on the unit interval, the logical functions built from conjunctions (AND), disjunctions (OR) and negations (NOT) are always still uncertain logical values. At worst, these are p-boxes on the unit interval which we have already

described how to handle. The issue of stochastic dependence arises whenever multiple logical elements are combined, and the software supports a fairly rich array of possible assumptions about these dependencies, including independence and the Fréchet case making no assumption at all, perfect and opposite dependence, positive- and negative-sign dependence, and dependence parameterized by various indices including Pearson, Kendall and Spearman correlations coefficients (Ferson et al. 2004; Nelsen 1986; 1987).

9. Can Uncertainty Grow Too Wide?

This paper has argued that the uncertainty associated with results from probabilistic modeling and simulation is often underestimated, particularly with agent-based models. Is it possible that, in our zeal to not underestimate uncertainty, we might overestimate it? Can the uncertainty grow wider than in mathematically justified? In fact, there are reasons one might worry about this.

Although it can always be guaranteed to rigorously enclose the actual uncertainty, naïve application of bounding methods of uncertainty propagation can sometimes yield results with unnecessarily inflated uncertainties (Beer et al. 2013). In such cases, the uncertainty is not characterized in a best-possible way and is overly conservative. This inflation usually arises either from repeated variables (Manes 1982), which the interval analysis community knows as the "dependency problem", or from the "wrapping effect" (Moore 1966) which can occur in multivariate problems when there is inter-variable dependence does not fit well into a rectangular multivariate box. Uncertainty inflation problems may be common and dominating in some complex calculations, and, if they are, special methods must be employed to keep the artifactual inflation of uncertainty to a minimum. Practical approaches to handling the problems have been worked out in several fields where the repeated variable problem has been encountered, including finite-element models (Zhang et al. 2012), differential equation models (Enszer et al. 2011), statistical analyses (Ferson et al. 2007; Nguyen et al. 2011).

We have already mentioned that the evaluation of epistemic uncertainty about logical quantities can be improved by reducing the replications of uncertain values in the expressions. The same is true for the bounding calculations used in the generalized agent-based modeling described in this paper. The idea is that, whatever universe the simulation is talking about, an event either happens or doesn't happen in that particular universe and both of these events do not occur together, even when we may not be sure which happens. In a mathematical expression with multiple instances of an uncertain logical quantity, if we do not account for this self-dependency (that the event either happens or doesn't) and instead used naïve interval or other bounding methods to evaluate the logical expression, the uncertainty about the logical value would be entered into the evaluation multiple times and the uncertainty of the result could be larger than necessary. In practice, software will be able, in any case, to detect when such uncertainty inflation is possible, and can report a warning to users if appropriate.

Beyond a possible inflation of uncertainty, some analysts incorrectly believe that bounding methods are not useful in practice because their uncertainties often quickly explode to become vacuous. In order to assess whether there is an intrinsic problem with bounding approaches to uncertainty propagation in complex problems, we conducted numerical experiments with randomly constructed mathematical expressions involving addition, subtraction, multiplication, division, minimum and maximum operations on

randomly constructed interval ranges centered between zero and one hundred with widths defined by significant digits randomly chosen between one and five. Such intervals vary widely in magnitude and width, as illustrated by these examples:

[95, 105]	[60.5, 61.5]	[43.9995, 44.0005]	[46.35, 46.45]	[6.35, 6.45]
[25, 35]	[18.5, 19.5]	[34.135, 34.145]	[99.15, 99.25]	[54.5, 55.5]

We measured the relative uncertainty of the outcomes, from many sequences of mathematical operations, as the widths of the final intervals divided by their midpoints. We found that most such calculations had uncertainties smaller than about 10%, and more than 95% yielded uncertainties smaller than unity. These results were typical for mathematical expressions with lengths ranging from 10 to 250 sequential operations, and, importantly, do not seem to vary with the number of operations. It is possible for relative uncertainties to be very large (perhaps 10 or larger), but these seems to be rather rare in random simulations. And when the output uncertainties are very large, it is fair to say that the uncertainty is authentically large. The outputs are as tight as possible given their respective inputs. Artifactual inflation of uncertainty which is not an authentic reflection of the uncertainty in the inputs can only occur in interval analysis when there are repeated variables in the mathematical expressions. When we broadened the uncertainties of the inputs still further by allowing there to be possibly zero significant digits, then input intervals such as [50,150] and [–50,50] were entered into the calculation streams. Even when about 17% of the inputs were these very broad intervals, still more than 50% of the resulting uncertainties were less than one, and about 80% were less than 5. About 15% of the final results were actually infinite, resulting from a division by zero (that was not later erased by subsequent minimum and maximum operations that return the result to a finite range). These results also seem to be invariant to the number of sequential operations ranging from 10 to 250. These simulations reveal plainly that uncertainty need not, and probably doesn't, grow to become vacuously wide even when there are many broadly uncertainty inputs involved in a calculation. This conclusion extends immediately to probability bounds analysis as well because intervals give outer bounds on the uncertainties that it would yield.

10. Conclusions

There are twin myths in modeling and simulation that prevent our reaping the benefits from broader application of uncertainty quantification and analysis. The first myth is that the results of traditional calculations are reliable and precise merely because they are expressed with 7 or 14 decimal places. It is unlikely that many actually believe this myth, but they *behave* as though they do. Few modelers construct comprehensive uncertainty or sensitivity analyses that might explore the full implications of the limits of knowledge about model structure and parameter values. Without such analyses, we cannot really say whether or to what extent our model outputs should be trusted. The second myth is that a full and proper accounting of the uncertainty inherent in the simulations and models would blow up to a vacuous conclusion that says nothing because any signal would be lost in the noise of uncertainty. Many people actually seem to believe this pernicious myth although simple simulations described above show it to be as misguided as the first myth.

We have developed alpha-version software implementing the features described above in the R programming language (R Core Team 2015). Preliminary applications on hypothetical model systems characterizing population growth patterns in biological species have corroborated several expectations,

including the broad discrepancy between Monte Carlo results and the true range of possible outcomes as illustrated in Figure 1. We expect to encounter computational challenges from circular calculations (one result depends on other results that depend on the first), and repeated variable problems which may arise when the interaction rules in our agent-based models become more complex. Special strategies may be needed to tackle these computational challenges.

Acknowledgements

We thank Nick Friedenberg who does not for a second believe that it is possible to project epistemic uncertainty through agent-based models in the way we have described. We thank him as well as Robert Garrett, Jon Helton, and Lev Ginzburg for helpful discussions. This paper was developed under funding from a Small Business Technology Transfer grant (award number HQ0147323251) from the Missile Defense Agency to Applied Biomathematics, and under a Cooperative Research and Development Agreement (CRADA No. LA13C10694) between Los Alamos National Laboratory and Applied Biomathematics.

References

Alderson, D. L., G. G. Brown, W. M. Carlyle and L. A. Cox, Jr. Sometimes there is no "most vital" arc: assessing and improving the operational resilience of systems. Society for Risk Analysis, San Francisco, CA, 2012.

Atwood, J. A. *A Monte Carlo Study of the Incidence of Probability Underestimation Versus Probability Overestimation Errors With Alternative Safety First Models (Risk)*. ETD collection for University of Nebraska–Lincoln. AAI8602105, 1985. http://digitalcommons.unl.edu/dissertations/AAI8602105

Basu, S., and A. DasGupta. Robust Bayesian analysis with distribution bands. *Statistics and Decisions* 13:333–349, 1995.

Beer, M., S. Ferson, and V. Kreinovich. Imprecise probabilities in engineering analyses. *Mechanical Systems and Signal Processing* 37:4–29, 2013.

Berleant, D. Automaticaly verified reasoning with both intervals and probability density functions. *Interval Computations* 1993 (2):48–70, 1993.

Berleant, D. and C. Goodman-Strauss. Bounding the results of arithmetic operations on random variables of unknown dependency using intervals. *Reliable Computing* 4:147–165, 1998.

Berleant, D., and J. Zhang. Using Pearson correlation to improve envelopes around distributions of functions. *Reliable Computing* 10:139–161, 2004. http://class.ee.iastate.edu/berleant/home/me/cv/papers/correlationpaper.pdf

Berleant, D., G. Anderson and C. Goodman-Strauss. Arithmetic on bounded families of distributions: a DEnv algorithm tutorial. Pages 183–210 in *Knowledge Processing with Interval and Soft Computing*, edited by C. Hu, R.B. Kearfott, A. de Korvin and V. Kreinovich, Springer (ISBN 978-1-84800-325-5), 2008.

Ben-Haim, Y. *Information-gap Theory: Decisions Under Severe Uncertainty*. Academic Press, 2001.

Berger, J. O. An overview of robust Bayesian analysis. *Test* 3:5-124, 1994.

Bobashev, G. V. and R. J. Morris. Uncertainty and Inference in Agent-Based Models. *Second Int. Conference on Advances in System Simulation (SIMUL2010)*, 22–27 August 2010, Nice, France, pages 67–71. IEEE Xplore Digital Library, 2010.

Cossette, H., M. Denuit and É. Marceau. Distributional bounds for functions of dependent risks. Discussion paper 0128, Institut de Statistique, Université Catholique de Louvain, 2001.

Enszer, J. A., Y. Lin, S. Ferson, G. F. Corliss and M. A. Stadtherr. Probability bounds analysis for nonlinear dynamic process models. *AIChE [American Institute of Chemical Engineers] Journal* 57:404–422, 2011.

Faanes, A. and S. Skogestad. Feedforward control under the presence of uncertainty. *European Journal of Control* 10:30–46, 2004.

Ferson, S. *RAMAS Risk Calc 4.0 Software: Risk Assessment with Uncertain Numbers*. Lewis Publishers, Boca Raton, Florida, 2002.

Ferson, S. and L. R. Ginzburg. Different methods are needed to propagate ignorance and variability. *Reliability Engineering and Systems Safety* 54:133–144, 1996.

Ferson, S. and J. Siegrist. Verified computation with probabilities. Pages 95–122 in *Uncertainty Quantification in Scientific Computing*, edited by A. Dienstfrey and R.F. Boisvert, Springer, New York, 2012.

Ferson, S., V. Kreinovich, L. Ginzburg, K. Sentz and D. S. Myers. *Constructing Probability Boxes and Dempster–Shafer Structures*. Sandia National Laboratories, SAND2002-4015, Albuquerque, New Mexico, 2003. http://www.ramas.com/ unabridged.zip

Ferson, S., R. Nelsen, J. Hajagos, D. Berleant, J. Zhang, W. T. Tucker, L. Ginzburg and W. L. Oberkampf. Dependence in Probabilistic Modeling, Dempster–Shafer Theory, and Probability Bounds Analysis. Sandia National Laboratories, SAND2004-3072, Albuquerque, New Mexico, 2004. http://www.ramas.com/depend.pdf

Ferson, S., V. Kreinovich, J. Hajagos, W.L. Oberkampf and L. Ginzburg. *Experimental Uncertainty Estimation and Statistics for Data Having Interval Uncertainty*. SAND2007-0939, Sandia National Laboratories, Albuquerque, New Mexico, 2007. http://www.ramas.com/intstats.pdf

Ferson, S., M. Balch, K. Sentz, and J. Siegrist. Computing with confidence. *Proceedings of the 8th International Symposium on Imprecise Probability: Theories and Applications,* edited by F. Cozman, T. Denœux, S. Destercke and T. Seidenfeld. SIPTA, Compiègne, France, 2013.

Fetz, T. and M. Oberguggenberger. Propagation of uncertainty through multivariate functions in the framework of sets of probability measures. *Reliability Engineering and System Safety* 85:73–88, 2004.

Fonoberova, M., V. A. Fonoberov and I. Mezić. Global sensitivity/uncertainty analysis for agent-based models. *Reliability Engineering and System Safety* 118:8–17, 2013.

Frank, M. J., R. B. Nelsen and B. Schweizer. Best-possible bounds for the distribution of a sum—a problem of Kolmogorov. *Probability Theory and Related Fields* 74:199–211, 1987.

Fréchet, M. Généralisations du théorème des probabilités totales. *Fundamenta Mathematica* 25:379–387, 1935.

Gardner, M. Mathematical games: the fantastic combinations of John Conway's new solitaire game "life". *Scientific American* 223:120–123, 1970.

Goovaerts, M. J., J. Dhaene and A. De Schepper. Stochastic upper bounds for present value functions. *Journal of Risk and Insurance* 67:1–14, 2000.

Hailperin, T. *Boole's Logic and Probability*. North-Holland, Amsterdam, 1986.

Hamlin, T. L., E. Thigpen, J. Kahn and Y. Lo. Shuttle risk progression: use of the shuttle probabilistic risk assessment (PRA) to show reliability growth. American Institute of Aeronautics and Astronautics, 2011. http://ntrs.nasa.gov/archive/nasa/casi.ntrs.nasa. gov/20110004917_2011004008.pdf

Hancock, P., N. Simpson and E. Rhee. Modeling uncertainty through agent-based participatory simulation: implication to businesses in China. *International Journal of China Marketing* 1, 2010.

Harp, D. R. and V. V. Vesselinov. An agent-based approach to global uncertainty and sensitivity analysis. *Computers & Geosciences* doi:10.1016/j.cageo.2011.06.025, 2011.

Hartung, J.A., H. W. Ho, P. D. Rutherford, E. U. Vaughan. The statistical correlation model for common cause failures. Pages 337-352 in *Risk Analysis in the Private Sector, Advances in Risk Analysis* Volume 220, edited by C. Whipple and V.T. Covello. Springer-Verlag, 1985.

Hassan, S., L. Garmendia and J. Pavón. Introducing uncertainty into social simulation: using fuzzy logic for agent-based modeling. *International Journal of Reasoning-based Intelligent Systems* 2:118–124, 2010.

Henrion, M. and B. Fischhoff. Assessing uncertainty in physical constants. *American Journal of Physics* 54:791–798, 1986.

Hickman, J. W., et al. *PRA Procedures Guide: A Guide to the Performance of Probabilistic Risk Assessments for Nuclear Power Plants*, in two volumes. NUREGCR-2300-V1 and -V2, National Technical Information Service, Washington, DC, 1983.

Hokstad, P. and M. Rausand. Common cause failure modeling: status and trends. Pages 621-640 in *Handbook of Performability Engineering*, edited by K.B. Misra. Springer, London, 2008.

Ilachinski, A. *Artificial War: Multiagent-Based Simulation of Combat*. World Scientific, Singapore, 2004.

Kaas, R., J. Dhaene and M. J. Goovaerts. Upper and lower bounds for sums of random variables. *Insurance:Mathematics and Economics* 27:151–168, 2000.

Kaufmann, A., and M. M. Gupta. *Introduction to Fuzzy Arithmetic: Theory and Applications*. Van Nostrand Reinhold, 1985.

Kharin, V. V., Q. Teng, F. W. Zwiers, G. J. Boer, J. Derome and J. S. Fontecilla. Skill assessment of seasonal hindcasts from the Canadian Historical Forecast Project. *Atmosphere-Ocean* 47:204–223, 2009. See also http://weather.gc.ca/saisons/info_pc_e.html

Li, W. and J. M. Hyman. Computer arithmetic for probability distribution variables. *Reliability Engineering and System Safety* 85:191–210, 2004.

Linkov, I. and D. Burmistrov. Model uncertainty and choices made by modelers: lessons learned from the International Atomic Energy Agency model intercomparisons. *Risk Analysis* 23:1297–1308, 2003.

Lochbaum, D. *The NRC and Nuclear Power Plant Safety in 2010: A Brighter Spotlight Needed*. Union of Concerned Scientists, Cambridge, Massachusetts, 2011. http://www.ucsusa.org/assets/documents/nuclear_power/nrc-2010-full-report.pdf

Magliocca, N. R. and E. C. Ellis. Using pattern-oriented modeling (POM) to cope with uncertainty in multi-scale agent-based models of land change. *Transactions in GIS* [DOI: 10.1111/tgis.12012], 2013. http://onlinelibrary.wiley.com/doi/10.1111/tgis. 12012/pdf

Manes, E. G. A class of fuzzy theories. *Journal of Mathematical Analysis and Its Applications* 85:409–451, 1982.

Miranda, E., I. Montes, R. Pelessoni and P. Vicig. Bivariate p-boxes. *Proceedings of the 8th International Symposium on Imprecise Probability: Theories and Applications,* edited by F. Cozman, T. Denœux, S. Destercke and T. Seidenfeld. SIPTA, Compiègne, France, 2013.

Moore R. E. *Interval Analysis*. Prentice-Hall, Englewood Cliffs, New Jersey, 1966.

Morgan, M. G., and M. Henrion. *Uncertainty: A Guide to Dealing with Uncertainty in Quantitative Risk and Policy Analysis*. Cambridge University Press, Cambridge, United Kingdom, 1990.

Morss, R. E. and E. Wahl. An ethical analysis of hydrometeorological prediction and decision making: The case of the 1997 Red River flood. *Environmental Hazards* 7:342–352, 2007.

Nelsen, R. B. Properties of a one-parameter family of bivariate distributions with specified marginals. *Communications in Statistics (Theory and Methods)* A15:3277–3285, 1986.

Nelsen, R. B. Discrete bivariate distributions with given marginals and correlation. *Communications in Statistics (Simulation and Computation)* B16:199–208, 1987.

Nguyen, H. T., V. Kreinovich, B. Wu and G. Xiang. *Computing Statistics under Interval and Fuzzy Uncertainty: Applications to Computer Science and Engineering*. Studies in Computational Intelligence, volume 393. Springer-Verlag, Berlin, 2011.

NRC [National Research Council Committee on Estimating and Communicating Uncertainty in Weather and Climate Forecasts]. *Completing the Forecast: Characterizing and Communicating Uncertainty for Better Decisions Using Weather and Climate Forecasts*, http://www.nap.edu/openbook.php?record_id=11699, The National Academies Press, Washington, DC, 2006.

NWS [National Weather Service]. Service assessment and hydraulic analysis: Red River of the North 1997 floods, 1998. http://www.nws.noaa.gov/oh/Dis_Svy/RedR_Apr97/TOC.htm

Oberkampf, W. L. and C. J. Roy. *Verification and Validation in Scientific Computing*. Cambridge University Press, New York, 2010.

R Core Team. *R: A language and environment for statistical computing*. R Foundation for Statistical Computing, Vienna, Austria, 2015. https://www.R-project.org/

RAWG [Risk-Assessment Working Group]. *Risk-Assessment Methodologies for Use in the Electric Utility Industry*, Critical Infrastructure Protection Committee, North American Electric Reliability Council [North American Electric Reliability Corporation], Atlanta, Georgia, 2005. http://www.ercot.com/content/meetings/cipag/keydocs/2007/0115/Risk_Assessment__Methodologies_9_9_2005.pdf

Savage, S. L. *The Flaw of Averages: Why We Underestimate Risk in the Face of Uncertainty*. Wiley, 2012.

Sentz, K. and S. Ferson. *Combination of Evidence in Dempster–Shafer Theory*. Sandia National Laboratories, SAND 2002-0835, Albuquerque, New Mexico, 2002.

Sentz, K. and S. Ferson. Probabilistic bounding analysis in the quantification of margins and uncertainties. *Reliability and Engineering System Safety* 96:1126–1136, 2011.

Shoham, Y. and K. Leyton-Brown. *Multiagent Systems: Algorithmic, Game-Theoretic, and Logical Foundations*. Cambridge University Press, 2009.

USCPSOTF [U.S.-Canada Power System Outage Task Force]. *Final Report on the Implementation of the Task Force Recommendations*. Natural Resources Canada and U.S. Department of Energy., 2006. http://www.nrcan.gc.ca/energy/sources/__electricity/1378, http://energy.gov/oe/downloads/us-canada-power-system-outage-task-force-final-report-implementation-task-force

Vesely, W. E., F. F. Goldberg, N. H. Roberts and D. F. Haasl. *Fault Tree Handbook*. Nuclear Regulatory Commission, Washington, DC, 1981.

Vose, D. *Risk Analysis: A Quantitative Guide*. John Wiley and Sons, West Sussex, England, 2008.

Walley, P. *Statistical Reasoning with Imprecise Probabilities*. Chapman & Hall, London, 1991.

Weiss, G. *Multiagent Systems: A Modern Approach to Distributed Artificial Intelligence*. MIT Press, 2001.

Williamson, R. C. and T. Downs. Probabilistic arithmetic I: Numerical methods for calculating convolutions and dependency bounds. *International Journal of Approximate Reasoning* 4:89–158, 1990.

Wooldridge, M. *An Introduction to MultiAgent Systems*. John Wiley and Sons, West Sussex, England, 2009.

Wu, W., E. Ekaette and B. H. Far. Uncertainty management framework for multi-agent system. Pages 122–131 in *Proceedings of the ATS*, 2003. http://www.enel.ucalgary.ca/People/far/pub/papers/2003/ ATS2003-06.pdf

Yager, R. R. Arithmetic and other operations on Dempster–Shafer structures. *International Journal of Man-machine Studies,* 25:357–366, 1986.

Youden, W. J. Enduring values. *Technometrics,* 14:1–11, 1972.

Zhang, H., R. L. Mullen and R. L. Muhanna. Safety structural analysis with probability-boxes. *International Journal of Reliability and Safety,* 6:110–129, 2012.

Zellner, M. L. Embracing complexity and uncertainty: the potential of agent-based modeling for environmental planning and policy. *Planning Theory and Practice* , 9:437–457, 2008.

Inverse Analysis of Coupled Hydro-Mechanical Problem in Dynamically Excited Dams

Muyiwa Alalade[1)], Long Nguyen-Tuan[1)], Frank Wuttke[2)] and Tom Lahmer[1)]
[1)] *Institute of structural mechanics, Bauhaus Universität, 99423 Weimar, Germany; muyiwa.alalade@uni-weimar.de*
[2)] *Geomechanics and Geotechnics, Christian-Albrechts-University Kiel, Germany*

Abstract: Dams play a major role in the development and sustenance of communities, economies and civilizations. Apart from being exposed to a variety of dynamic forces (ambient and induced), many dams today have been in operation beyond their design life cycle and thus uncertainty and deterioration in the material properties would be expected. In order to reduce the risk of failure of these structure, a strict and frequent monitoring of the structure is required. However as a result of the physical scale of most dams, this is cumbersome and in many cases expensive. In an attempt to gain insight into the physical properties (such as stiffness and density distribution, permeability, etc) which are crucial to the effective operation of these dams an inverse analysis is carried out on the coupled hydro-mechanical finite element model. The parameter identification is done using experimental data obtained from recorded responses resulting from induced vibrations on the dams' crest. As with most engineering problems, we are faced with an ill-posed problem. Thus we intend to propose an efficient algorithm for the inverse problem and also ascertain the quality of the calculated parameters by making a comparison between the simulated and recorded dam response.

Keywords: inverse problem, optimization, structural health monitoring

1. Introduction

Dams are structures used to retain or control the flow of water in a catchment area, this could be for agricultural purposes (irrigation), flood prevention or for electricity generation. Although the demand for such structures are on the increase to cater for the increasing population and demand for renewable energy, building new dams requires lots of time and money, thus the efficiency and operating capacities of existing dams should be maximized.

Today most dams have been in operation far beyond their designed operation period and as such a decrease in the reliability of such structures is expected. As much as these structures are of great value to communities, a failure in such a structure is in most cases catastrophic, thus great care must be taken in its design, operation and maintenance. In order to assess both the structural integrity and reliability of these structures routine inspections are required. However as a result of the physical sizes and the increasing heterogeneity in the material properties of these structures it is often very difficult and tedious to carry out both a qualitative and quantitative assessment of the dams.

A number of literature proposing models based on a variety of formulation for the analysis of various phenomena during the design and operation of a dam exist. These includes (Lahmer, 2010), (Lahmer et al., 2011), and (Khoei et al., 2014).
Furthermore, in order to ascertain the structural integrity and monitor the performance of these very important structures irrespective of when it was constructed, it is necessary to obtain reliable values of certain parameters which are crucial to the safe operation of these dams. These parameters provide vital information such as material heterogeneity, saturation distribution, crack or void location, stiffness degradation etc. The identification of the parameters is made possible by the inverse analysis of a validated numerical model that adequately describes the dams' behavior during its life cycle.

2. Mathematical Formulation

The finite element methods are employed in the calculations of the displacements, pore pressures, stresses and strains induced on the dynamically excited dam. The mechanical system involves the solution of the second order differential equation, derived from Newtons' equation of motion. Where the time varying excitation force is $\{f_t\}$, the mass, damping and stiffness are denoted by $[M]$, $[C]$ and $[K]$, the displacement, velocity and accelerations are also denoted by $\{u\}$, $\{\dot{u}\}$ and $\{\ddot{u}\}$ in Eq. (1). The mass matrix is formulated for each element as obtained in Eq. (2), the stiffness in Eq. (3) and the resulting damping matrix is obtained in Eq. (4).

$$[M]\{\ddot{u}\} + [C]\{\dot{u}\} + [K]\{u\} = \left\{f_{(t)}\right\} \tag{1}$$

$$m^e = \int_\Omega N^{e^T} \rho^e N^e d\Omega \tag{2}$$

$$k^e = \int_\Omega B^{e^T} D^e B^e d\Omega \tag{3}$$

where:
N^e is the element shape function
ρ^e is the density of the element
B is a matrix containing the derivatives of the shape function
D is a stress/strain matrix which is a function of the materials Youngs' modulus, E and Poisson's ratio, ν

$$[C] = \alpha[M] + \beta[K] \tag{4}$$

The α and β coefficients in Eq. (4) are the Rayleigh damping coefficients. These can be obtained from experiments or through other methods proposed in literature. The method proposed by (Chowdhury and Dasgupta, 2003) was used to calculate α and β.

The Newmark scheme (Chopra, 1995) is applied in solving Eq. (1) such that the values of the nodal displacements, velocities and accelerations are obtained. Depending on the β^* and γ^* values

used to implement the scheme, it is necessary that the time step δt chosen is less than the critical time step T_c to ensure stability. The resulting displacements obtained are used to compute the strains and stresses as done in standard FEM calculations.

In order to get a more realistic idea of the dams' operation state, it is necessary to consider the effects and interaction of other phenomena on the structure. In this case the hydraulic effect of water seepage into the dam material, this induces pore pressures in addition to the mechanical induced deformation thus generating additional stresses which may impair the safe operation of the dam. Fluid flow through a porous medium is assumed to be incompressible with constant material densities along the motion of the fluid through varying pressure points in the domain. Material permeability is assumed to be isotropic, with displacement, u describing the main variable for the mechanical process and pore water pressure, p_w describing the main variable for the hydraulic process.

The mathematical modeling of the fluid flow structure interaction involves the momentum conservation law and fulfilling the mass balance of liquid law (Lahmer, 2010). This is best understood from the effective stress law (Eq. (5)) which describes the contribution of the hydraulic effects of the pore pressures on the normal components of the mechanical stresses. When considering that negative stresses describes the compression state and positive stress the tension state, the effective stress is written as in Eq. (5) .

$$\sigma' = \sigma + \alpha m p_w \tag{5}$$

where:

- σ' is the effective stress tensor $[N/m^2]$
- p_w is the water pore pressure vector $[N/m^2]$
- α is the Biot's constant (usually $\alpha = 1$)
- m is specified unit tensor ($m = [1, 1, 1, 0, 0, 0]^T$)

The total discrete equation for the fluid-structure medium can be expressed in 10.

$$[M]\{\ddot{u}\} + [C]\{\dot{u}\} + \int_\Omega [B]^T \sigma d\Omega = \left\{f_{(t)}\right\} \tag{6}$$

$$\int_\Omega [B]^T \sigma d\Omega = \int_\Omega [B]^T \sigma' d\Omega + \int_\Omega [B]^T \alpha m p_w d\Omega \tag{7}$$

$$[K]\{u\} \approx \int_\Omega [B]^T \sigma' d\Omega \tag{8}$$

$$[Q]\{p\} \approx \int_\Omega [B]^T \alpha m p_w d\Omega \tag{9}$$

$$[M]\{\ddot{u}\} + [C]\{\dot{u}\} + [K]\{u\} - [Q]\{p\} = \left\{f_{(t)}\right\} \tag{10}$$

Whereas from the mass fluid balance the seepage equation of fluid through the solid structure is given in Eq. (11).

$$[Q]^T\{\dot{u}\} + [S]\{\dot{p}\} + [H]\{p\} = \{q\} \tag{11}$$

The linear version of the equations in Eq. (10) and Eq. (11) for the dynamic coupled hydro-mechanical problem is given in Eq. (12).

$$\begin{bmatrix} M & 0 \\ 0 & 0 \end{bmatrix} \begin{Bmatrix} \ddot{u} \\ \ddot{p} \end{Bmatrix} + \begin{bmatrix} C & 0 \\ Q^T & S \end{bmatrix} \begin{Bmatrix} \dot{u} \\ \dot{p} \end{Bmatrix} + \begin{bmatrix} K & -Q \\ 0 & H \end{bmatrix} \begin{Bmatrix} u \\ p \end{Bmatrix} = \begin{Bmatrix} f \\ q \end{Bmatrix} \tag{12}$$

The coupling, permeability and compressibility matrices Q, S and H are defined in Eq. (13 - 15) whereas the mass, damping and stiffness matrices M, C and K have been defined in Eq. (1).

$$Q_e = \int_{\Omega_e} B^T \alpha m N_p \, d\Omega \tag{13}$$

$$H_e = \int_{\Omega_e} (\nabla N_p)^T \, \kappa \, \nabla N_p \, d\Omega \tag{14}$$

$$S_e = \int_{\Omega_e} N_p^T \left(\frac{\alpha - n}{K_s} + \frac{n}{K_w} \right) N_p \, d\Omega \tag{15}$$

3. Forward Modeling

In order to identify the material properties, it is necessary to have a running forward model that simulates the observed phenomena. In this case the formulations in section 2 and Eq. (12) are implemented for a hypothetical dam using the material properties in Table I and II.

Table I. Mechanical dam properties.

Height $H\,[m]$	*Breadth* $B\,[m]$	*Length* $L\,[m]$	*Youngs' modulus* $E\,[MPa]$	*Poissons'ratio* ν	*Density* $\rho\,[kg/m^3]$	*Rayleigh* α	*coeff.* β	*Newmark* β^*	$-\beta$ γ^*
28	19	0.1	2.4×10^3	0.15	24×10^2	-0.354	0.0162	0.5	0.25

For this analysis, a dynamic force is induced on the upstream part of the dam crest and the response is recorded at an observation point as shown in Figure 1. The basic properties of the dynamic force can also be seen in Figure 2. The total excitation time is 4 $[s]$ during which peak amplitudes are reached and then the excitation is stopped, a time-step of 0.1 $[s]$ is used for the

Table II. Hydraulic dam properties.

Water density $\rho_w\,[kg/m^3]$	*Fluid bulk modulus* $K_f\,[N/m^2]$	*Porosity* n	*Viscosity* $\mu\,[N/s^2]$	*Permeability* $\kappa\,[m^2]$	*Fluid flux* $q\,[m^2/s]$
1000	2.2×10^6	1×10^{-6}	1×10^{-3}	1×10^{-18}	1.12×10^{-12}

numerical integration of the mechanical part. For the solution of the hydraulic part of the coupled equation, a time-step of 1 $[s]$ is used.
Ideally, Eq. (11) is first solved and the resulting pore pressures are updated in Eq. (10), the resultant displacements due to the coupled hydro-mechanical action are then computed. However, in this case the effect of mechanical velocity ($\dot{u}$) on Eq. (11) is not considered.

To further investigate the effect of the hydro-mechanical coupling on the dynamic response of the dam, a comparison is made in Figure 3 between the frequency response of the mechanical system and the hydro-mechanical system for both the undamped and damped cases.

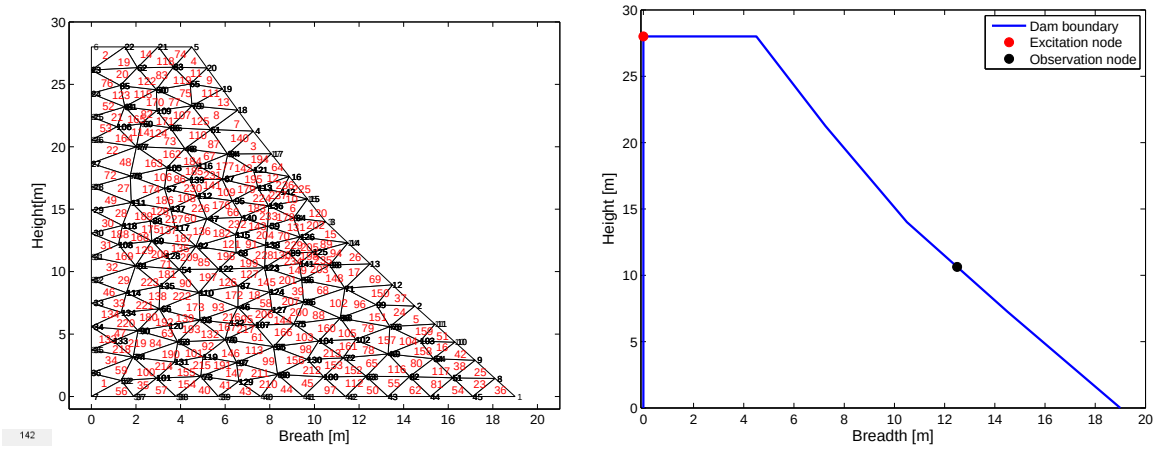

(a) Dam geometry and mesh (b) Dam excitation and observation points

Figure 1. Dam geometry.

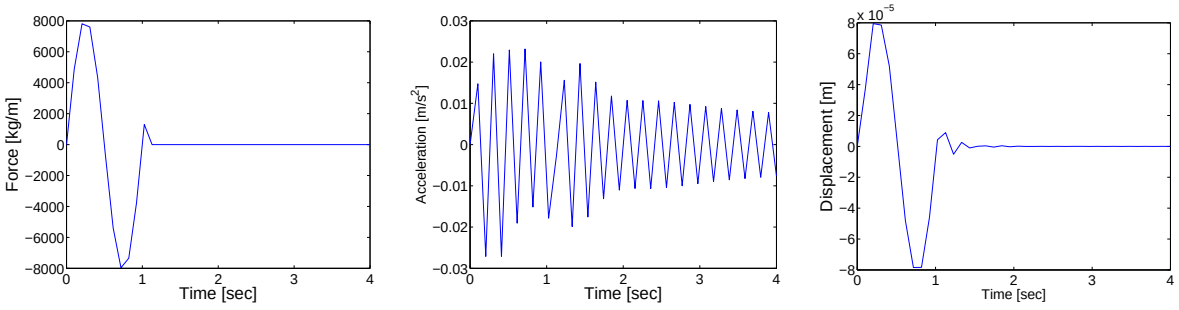

(a) Excitation force (b) Acceleration (c) Excitation displacement

Figure 2. Dynamic load on dam.

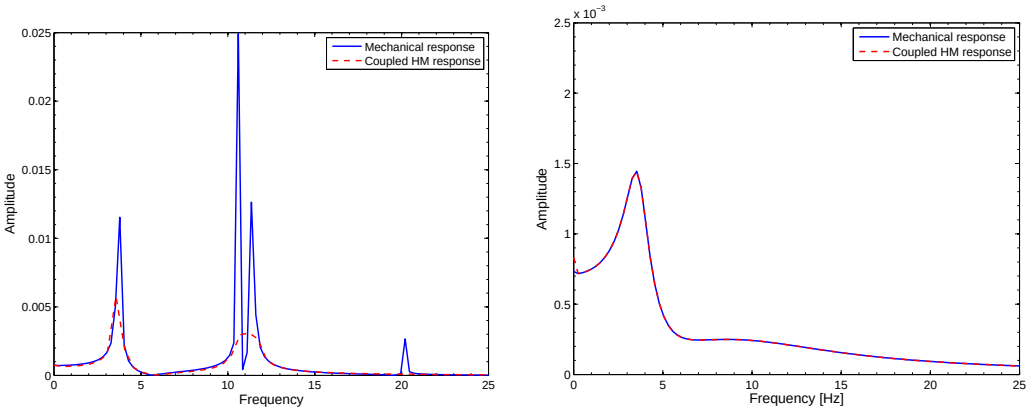

(a) Frequency response for undamped case (b) Frequency response for damped case

Figure 3. Comparison between coupled and uncoupled frequency response at excitation node.

4. Inverse Modeling

The objective of the inverse analysis is to obtain reliable parameter values by minimizing the error between experimental data (describing in most cases a phenomena) and numerical results obtained from a mathematical model developed to simulate (as close as possible) the natural phenomena. Strategies based on different concepts exist for the calibration and optimization of models in engineering. These includes the Newton methods, which are part of the gradient methods with line search strategies used in unconstrained nonlinear optimization that gives very fast results when the initial guess is close to the minimum. The Nelder–Mead method is another of the direct search or gradient free strategies for locating the minima of a function. The algorithm was originally published in 1965 and according to (Singer and Nelder, 2009), it is one of the best known algorithms for multidimensional unconstrained optimization without derivatives. The Particle swarm optimization (PSO) is a population based stochastic optimization technique developed by (Eberhart and Kennedy, 1995), inspired by social behavior of bird flocking or fish schooling. It is a heuristic based global optimizer easily applicable to a number of situations.

In this section an attempt is made on identifying the material parameters: Youngs' modulus E and Permeability κ of the dam from FE model discussed in previous sections. The material parameters are identified by minimizing the error between the experimental data and model results using the Nelder-mead algorithm which can be easily implemented in matlab.
The objective function being minimized (Eq. (16))is the sum of squared error with respect horizontal acceleration calculated at node 13 which located at about $1/3^{rd}$ of the dams' height from the base.

$$C_f(p, nn) = \sum_{i}^{n} (\ddot{U}\ {}^{mod}_{(t_i,p,nn)} - \ddot{U}\ {}^{exp}_{(t_i)})^2 \tag{16}$$

where:

- C_f is the cost function to be minimized

- $\ddot{U}^{\,mod}_{(t_i,p,nn)}$ is the horizontal acceleration calculated at node (in this case 13) by the model
- $\ddot{U}^{\,exp}_{(t_i)}$ is the horizontal acceleration obtained from the experiment
- p is a vector of M, K and C
- t_i is the time step at each point
- n is the total number of data points

After several iterations the values of E and κ were obtained. Although the value of κ is unrealistic, a good fit is observed between the experimental response and simulated response. Figure 4 shows the quality of fit obtained after parameter optimization. The calculated values were $E = 2.4 \times 10^9$ and $\kappa = -2.64 \times 10^{-}17$, with the value of E being same as in Table I.

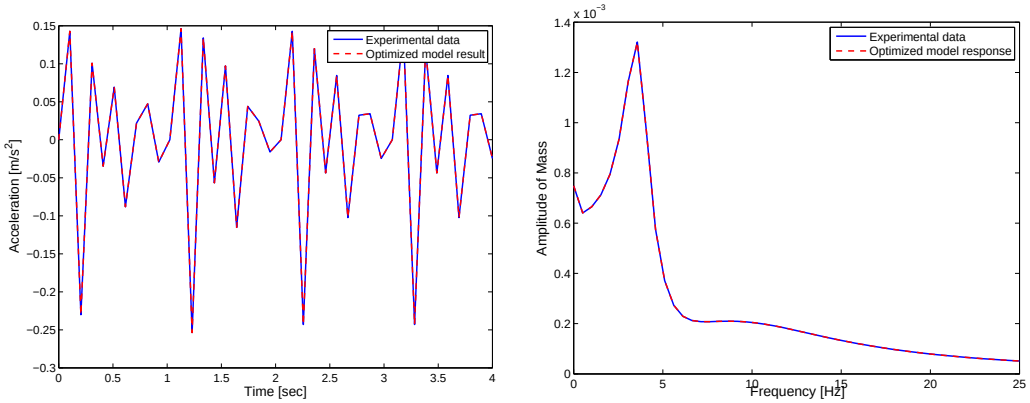

(a) Nodal acceleration (b) Frequency response

Figure 4. Comparison between experimental and model response for HM coupling.

The solutions obtained in this section would serve as "synthetic experimental data" for the inverse analysis to identify the dam material properties. In practice the acquisition of such data is done via acceleration sensors (Geo-phones) or other types of sensors instrumented on the dam to record various types of vibrations. This data after undergoing processing is used for the inverse modeling.

5. Conclusion

The damping effect of water on the dam response considering the hydro-mechanical coupling can be observed in the frequency response plots for the undamped case in Figure 3(a), this effect is minimal when structural damping is considered as obtain in Figure 3(b). To reduce computation cost the acceleration data was used as objective function instead of the frequency response which required more time. However in situations where data from acceleration sensors are available, these

data are usually voluminous and may be difficult to fit, thus a frequency based objective function would be required to give better quality results after minimization.

Furthermore during the optimization, it was observed that no unique value of κ could be obtained although $E = 2.4 \times 10^9$ was obtained. This shows that κ is less sensitive as a result of the very low permeability of concrete. The ill-posed nature of the model is also observed here which would have been more pronounced if the dam material was more porous. In such cases, a regularization parameter Γ introduced to the objective function according to (Tikhonov, 1963) would improve the stability of the results as was obtained in (Alalade et al., 2015).

References

Alalade, M., B. Kafle, F. Wuttke, and T. Lahmer. Calibration of cyclic constitutive models for soils by oscillatory functions. In Gürlebeck, K. and Lahmer, T., editors, *Digital Proceedings, International Conference on the Applications of Computer Science and Mathematics in Architecture and Civil Engineering : July 20 - 22 2015, Bauhaus-University Weimar*, 2015.

Chopra, A. K. *Dynamics of structures*, volume 3. Prentice Hall New Jersey, 1995.

Chowdhury, I. and S. P. Dasgupta. Computation of rayleigh damping coefficients for large systems. *The Electronic Journal of Geotechnical Engineering*, 8(0), 2003.

Eberhart, R. C. and J. Kennedy. A new optimizer using particle swarm theory. In *Proceedings of the sixth international symposium on micro machine and human science*, volume 1, pages 39–43. New York, NY, 1995.

Khoei, A., M. Vahab, E. Haghighat, and S. Moallemi. A mesh-independent finite element formulation for modeling crack growth in saturated porous media based on an enriched-fem technique. *International Journal of Fracture*, 188(1):79–108, 2014.

Lahmer, T. Crack identification in hydro-mechanical systems with applications to gravity water dams. *Inverse Problems in Science and Engineering*, 18(8):1083–1101, 2010.

Lahmer, T., C. Könke, and V. Bettzieche. Optimal monitoring of gravity dams by multifield considerations.

Nelder, J. A. and R. Mead. A simplex method for function minimisation. *The Computer Journal*, 7:308–313, 1965.

Nguyen-Tuan, L., T. Lahmer, M. Datcheva, E. Stoimenova, and T. Schanz. A novel parameter identification approach for buffer elements involving complex coupled thermo-hydro-mechanical analyses. *Computers and Geotechnics*, 76:23 – 32, 2016.

Singer, S. and J. Nelder. Nelder-mead algorithm. *Scholarpedia*, 4(7):2928, 2009. ISSN 1941-6016. doi: 10.4249/scholarpedia.2928.

Shi, Y. and R. C. Eberhart. Parameter selection in particle swarm optimization. In *Evolutionary programming VII*, pages 591–600. Springer, 1998.

Tikhonov, A. N. Regularization of incorrectly posed problems. Soviet Mathematics Doklady, 1963.

Propagating Snow Measurement Uncertainty to Structural Reliability by Statistical and Interval-based Approaches

Á. Rózsás[1)] and M. Sýkora[2)]
[1)]*Department of Structural Engineering, Budapest University of Technology and Economics, Budapest 1111, Hungary, rozsas.arpad@epito.bme.hu*
[2)]*Department of Structural Reliability, Klokner Institute, Czech Technical University in Prague, Prague 16608, Czech Republic, miroslav.sykora@cvut.cz*

Abstract: Observations are inevitably contaminated by measurement uncertainty, which is a predominant source of uncertainty in some cases. In reliability analysis, probabilistic models are typically fitted to measurements without considering this uncertainty. Hence, this paper intends to explore the effect of this simplification on structural reliability and to provide recommendations on its treatment. Statistical and interval-based approaches are used to quantify and propagate measurement uncertainty. They are critically compared by analyzing ground snow measurements that are often affected by large measurement uncertainty. It is propagated through the mechanical model of a generic structure to investigate its effect on reliability. Parametric studies facilitate to analyze the effect of key parameters, such as measurement uncertainty, coefficient of variation of ground snow load, and distribution type. The interval analysis is performed as a hybrid interval-probabilistic analysis. Measurements are represented as intervals and probabilistic model is then fitted to them. Thus, snow parameters and the reliability index are also interval variables; other random variables are described by standard probabilistic distributions. Implementation of the statistical approach is based on the frequentist paradigm where the contamination mechanism is expressed in terms of random variables. This approach allows decoupling measurement uncertainty from a variable of interest. The results indicate that measurement uncertainty may lead to significant (order of magnitude) underestimation of failure probability and should be taken into account in reliability analysis. If more information than interval endpoints is available, a statistical approach is recommended; otherwise the interval representation should be used. Ranges of the key parameters are identified where measurement uncertainty should be considered. For practical applications, the lower interval bound and predictive reliability index are recommended as point estimates using interval and statistical analysis, respectively. The point estimates should be accompanied by uncertainty intervals, which convey valuable information about the credibility of results. Although general recommendations are given, treatment of measurement uncertainty should be handled on a case-specific basis.

Keywords: measurement uncertainty, snow, structural reliability, interval arithmetic, maximum likelihood, deconvolution

1. Introduction

1.1. MOTIVATION

Models accounting for all uncertainties are of a considerable interest in structural reliability since these are the bases of design specifications, hence impacting the building and structure stocks of large regions. Snow

is particularly important for light-weight structures for which it is typically the governing action. To our knowledge, the effect of snow measurement uncertainty on structural reliability has not yet been studied and other probabilistic models are treated similarly in civil engineering. For instance, neither the joint European research on snow actions (Sanpaolesi et al., 1998) or the JCSS Probabilistic Model Code (JCSS, 2002) provides any information on the treatment of measurement uncertainty and its effect. Therefore, the aim of this paper is to explore the effect of this simplification on structural reliability and to provide recommendations on its treatment.

Observations are inevitably contaminated by measurement uncertainty (MU) which is a predominant source of uncertainty in some cases. Uncertainty is understood here as the lack of knowledge (epistemic) and natural variability (aleatory)[1] not including known systematic error that are assumed to be adjusted. In reliability analysis, probabilistic models are typically fitted to measurements without considering their uncertainty. This is the case for snow measurements where often only the snow depth is measured and the applied techniques makes the derived loads highly uncertain, for example, the uncertainty range can reach 50% of the measured depth [based on a personal correspondence with a meteorologist]. The World Meteorological Organization conducted a comprehensive comparative study on the then available solid precipitation measurement techniques and experimentally confirmed that measurements should be adjusted for wetting loss, evaporation loss, and wind induced undercatch (Goodison et al., 1998). They found that the snow catch ratio of the four most widely used gauges range from 20% to 70% at 6 m/s wind speed. Even for automated systems, measurement error in solid precipitation can vary from 20% to 50% due to undercatch in windy conditions (Rasmussen et al., 2011). Although these mainly contribute to systematic error they indicate uncertainties in snow measurements as these errors cannot be exactly corrected. For instance coefficient of determination (R^2) values vary from 0.40 to 0.80 for the fitted wind correction equations at certain sites; these are associated with about 10% standard error in catchment ratio. Additional uncertainty may be introduced if no site specific auxiliary data, e.g. wind speed measurements, are available (Goodison et al., 1998). These issues are not limited to snow measurements but valid for all evidence based models – that is for every model – although their importance may vary.

1.2. ADOPTED APPROACHES

We assume that measurements are corrected for known systematic errors. Additionally, the following model is assumed to describe the connection between observed (Y) and real, true, physical (X) values, that is the variable of interest:

$$\text{(true, real}^2\text{)}\ \ X \xrightarrow{h(X,E)} Y\ \ \text{(observed)} \qquad (1)$$

The *h(X, E)* function represents the mathematical relationship between the true and observed random variables referred hereinafter as reality-observation link. E covers the unknown processes contributing to measurement uncertainty. The recommended probabilistic models – typically distributions – in the literature are almost exclusively given for the true variable and not for the observed, potentially contaminated one. Possible reasons for this are that:

- The contamination is commonly site- and measuring technique-dependent, thus no general recommendations can be given for the distribution of Y.

[1] This division is subjective as conditioned on the selected "model universe".

[2] Herein we tacitly assume the existence of some objective reality independent of the observer.

- The model type is often selected based on theoretical arguments considering the physical phenomena generating X, e.g. normal distribution if X is the result of summation; lognormal if X is the product of random variables; extreme value distribution if X is related to extremes.
- Structural reliability is ultimately dependent on X and not on Y, although we are limited to access only Y.

The last point is especially important since structures are subjected to actions coming from X and not from Y; the latter is affected by our ignorance or inability to make accurate measurements (epistemic uncertainty). In a broader sense this also applies for X, but for now we remain in the commonly accepted model universe of engineering and treat X as a random variable. If the distribution type of X is known or agreed, then the reality-observation link uniquely determines the distribution of Y. Hence, if any measurement uncertainty is present, its distribution type almost certainly differs from the distribution of X. This is prevalently neglected while fitting distributions in civil engineering – Y is assumed to be distributed as X. This simplification is acceptable in some practical cases. This method is termed hereinafter as Approach 1 while it is referred to as Approach 2 when the difference between distributions is appreciated:

Approach 1 Use the probabilistic model of true random variable (X) and treat the observations – contaminated by measurement uncertainty – ($\mathbf{y}$) as the realizations of this model: $\mathbf{y} \sim X$.

Approach 2 Differentiate between the distribution of true and observed random variables. Within this, the following two sub-approaches are considered:

Approach 2a Representation of measurement uncertainty with intervals at the level of observations and propagating them to the derived parameters via interval analysis. As interval representation by nature contains no information about the reality-observation link, the decontamination of observations is not possible.

Approach 2b Representation of measurement uncertainty with a probability distribution. Use a mathematical model ($h(X, E)$) to describe the connection between measurement uncertainty (E), true phenomenon (X), and observed phenomenon (Y). Based on this model and on observations ($\mathbf{y}$), infer the parameters of the true random variable (X). These issues are referred to as *measurement error problems* in the literature (Kondlo, 2010).

Additional assumptions for all considered approaches:

- $\mathbf{y} = \{y_1, y_2,...y_n\}$ and $\mathbf{x} = \{x_1, x_2,...x_n\}$ each are independent, identically distributed realizations; $\mathbf{y}$ is contaminated by measurement uncertainty.
- The realizations of the true phenomenon ($\mathbf{x}$) and the measurement uncertainty ($\boldsymbol{\varepsilon}$) are mutually independent;
- The true phenomenon (X) follows arbitrary, but known distribution type;
- Only for Approach 2b: the measurement uncertainty (E) follows arbitrary, but known distribution type, and the reality-observation link is also known.

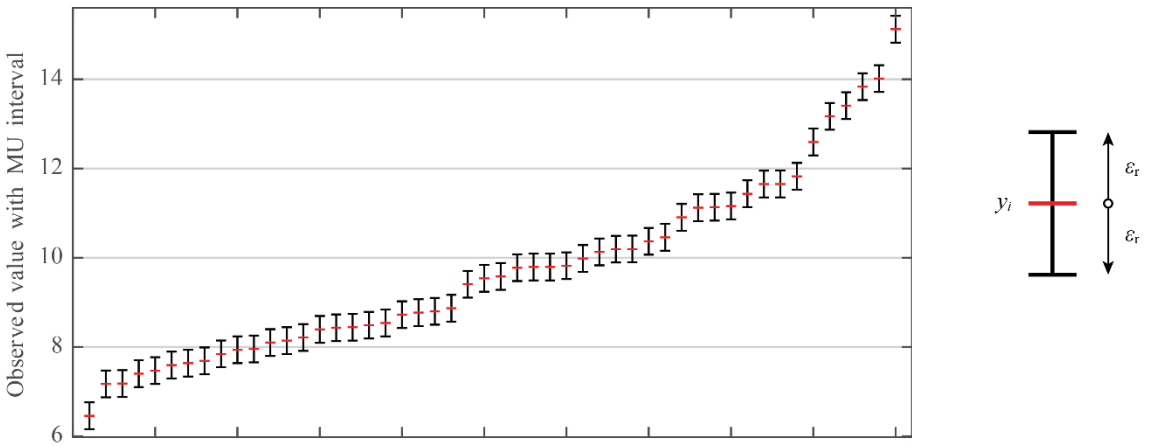

Figure 1. Interval representation of measurement uncertainty (black) on a sorted random sample (red). The sample is generated from Q_1 with properties given in Table 1 and $CoV_{Q1} = 0.2$.

2. Uncertainty Representation and Propagation

2.1. Interval analysis

Interval representation is one possible approach to quantify uncertainty in an observed variable: the width of the interval expresses our uncertainty (Figure 1). In this concept the true value is certainly within the interval but we know nothing about how likely it takes a particular value from that. In other words no probability distribution function is assumed over the interval, thus it expresses greater ignorance than probability distributions can (Huber, 2010).

The basic objective of interval analysis is to propagate the interval uncertainty of input variables to the outputs. Its main challenge is to calculate the interval bounds without overestimating them. This typically occurs if floating point computations are simply replaced by intervals and caused by interval dependency (Moore et al., 2009). Since the operators are typically not known explicitly and are non-monotonic, special algorithms are needed to obtain sufficiently narrow approximate interval bounds.

Interval analysis is traditionally used to model floating point truncation error in numerical computations; however, it is also successfully applied to various civil engineering issues, for instance, reliability of structures (Qiu et al., 2008) and systems (Qiu et al., 2007). Rao et al. (2015) analyzed the effect of incorrect fitting on trusses and frames using mixed interval finite element formulation, using intervals to model fabrication errors. Muhanna et al. (2015) demonstrated the feasibility of non-linear interval finite element analysis for beam-column structures. In their study geometric, material and load uncertainties are modeled with intervals.

In this paper the general definition of interval variables is used and constrained numerical optimization is applied to find the interval endpoints. This is motivated by the readily available optimization algorithms, and its feasibility due to the analyzed simple, computationally cheap examples. For computationally demanding models more efficient algorithms are available (Zhang et al., 2010; Alibrandi and Koch, 2015; Muhanna et al., 2015).

Intervals in this paper are defined by midpoint and radius (ε_r), the midpoint is taken as the observed value, y_i, see Figure 1. In this approach the true value is assumed to be certainly within the interval given the modeling assumptions are valid.

2.2. STATISTICAL ANALYSIS

An alternative approach to represent measurement uncertainty is statistical by means of probability distributions. The likelihood function depends on the reality-observation link (Eq.(1)). This connection is also uncertain, but for simplicity, known relationship is assumed here and a possible treatment of this uncertainty is discussed in Section 4. Algebra of random variables can be used to obtain the likelihood function reflecting the distribution of involved random variables and the reality-observation link:

$$L\left(\boldsymbol{\theta}_X, \boldsymbol{\theta}_E \mid \mathbf{x}, \boldsymbol{\varepsilon}\right) = \prod f\left(h(x_i, \varepsilon_i) \mid \boldsymbol{\theta}_X, \boldsymbol{\theta}_E\right). \tag{2}$$

In Approach 1, this means no additional complication because the observations are assumed to be distributed as the true random variable since the reality-observation link is neglected. However, in Approach 2b the likelihood function should be constructed to remove the effect of measurement uncertainty (E) on the variable of interest (X).

The *measurement error problem* arises in many areas where only the contaminated values are attainable to the observer but the interest lays in the inference of true, uncontaminated values. Among others, these areas include astronomy, econometrics, biometrics, medical statistics, and image reconstruction (Stefanski, 2000; Koen and Kondlo, 2009; Meister, 2009). A straightforward solution is to construct the likelihood function (Eq.(2)) and to infer the parameters of the variable of interest (X) by a selected method. To the authors knowledge this approach has not been applied in civil engineering yet.

Maximum likelihood method is used herein to infer the parameters in the statistical formulation of the measurement uncertainty problem. This method is a widespread technique that favors parameters at which the data are most likely generated by the assumed model. It is a typically asymptotically efficient and consistent method (Casella and Berger, 2001).

Additive and multiplicative reality-observation links are considered. For the additive relationship: $Y = X + E$, the density function of the sum of two independent, continuous random variables is obtained by convolution:

$$f_Y\left(y\right) = \left(f_X * f_E\right)\left(y\right) = \int_{-\infty}^{\infty} f_X\left(y - x\right) \cdot f_E\left(x\right) \cdot \mathrm{d}x\,. \tag{3}$$

The integral can be efficiently solved by utilizing Fourier transformation since afterwards it reduces to a point-wise multiplication. Here, the fast-Fourier transformation is used to accomplish this task. For the multiplicative relationship: $Y = X \cdot E$, the density function of the product of two independent, continuous random variables is obtained by computing the following integral:

$$f_Y\left(y\right) = \int_{-\infty}^{\infty} f_X\left(x\right) \cdot f_E\left(\frac{y}{x}\right) \cdot \frac{1}{|x|} \cdot \mathrm{d}x\,. \tag{4}$$

This can be efficiently solved by Mellin transformation but here the integral is directly calculated due to the small computational burden.

Sampling variability (parameter estimation uncertainty) is accounted for by using the predictive reliability index (Der Kiureghian, 1989):

$$\tilde{\beta} = \frac{\text{mean}_B}{\sqrt{1+\text{std}_B^{\,2}}} \approx \frac{\text{median}_B}{\sqrt{1+\left(1.483\cdot\text{mad}_B\right)^2}} \tag{5}$$

Where B is the posterior reliability index, std and mad are the standard deviation and median absolute deviation of B, respectively. The formulation with median and mad are used in this paper, as that is more robust to outliers. Eq.(5) is an approximation as it is valid only for Normal distributed B. Additionally, the statistics are estimated from repeated analyses, and no Bayesian formulation of the reliability problem is used, however that was used to derive the formula. For this study it is deemed sufficiently accurate to indicate tendencies and to identify critical cases.

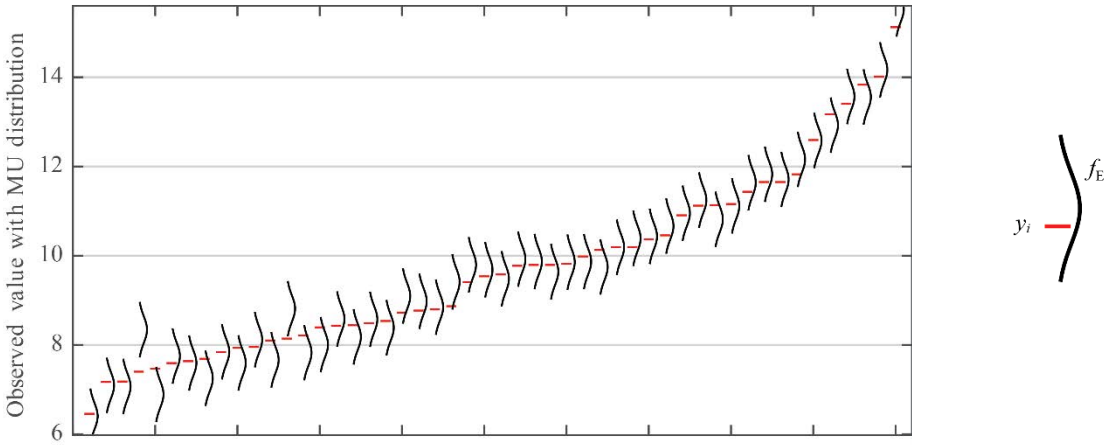

Figure 2. Illustration of probability distribution representation of measurement uncertainty (black) on a sorted random sample (red). The sample is generated from Q1 with properties given in Table 1and $CV_{Q1} = 0.2$.

3. Example: Reliability of a Generic Structure

3.1. MODEL DESCRIPTION

The reliability of a simple structural member is analyzed using a generic limit state function:

$$g(\mathbf{X}) = R - \left(G + Q_{50}\right) \tag{6}$$

It represents a structure subjected to permanent (G) and variable (Q_{50}) actions, where the subscript 50 indicates 50-year reference period (common design working life). The probabilistic model of involved random variables are based on the recommendations of JCSS (2001) and summarized in Table *1*. For simplicity only the variable action is assumed to be affected by measurement uncertainty; it could be easily extended to more variables. Coefficient of variations 0.2, 0.4 for Q_1 represent annual snow maxima of

mountains, highlands, while 0.6 characterizes lowlands in the Carpathian Region. The Lognormal model for snow maxima is typically adopted in the USA (ASCE, 2010), while the Gumbel model is widespread in Europe (Sanpaolesi et al., 1998; JCSS, 2001). The Normal and Gumbel distributions are light-tailed while the Lognormal is heavy-tailed. The adopted distributions and parameter ranges cover also other variable actions such as wind and thermal actions, thus the results can be readily generalized.

Table 1: Probabilistic models.

Variable name (symbol)	Distribution	Mean	Coefficient of variation (*CV*)
Resistance (*R*)	Lognormal	*	0.10
Permanent action (*G*)	Normal	8	0.10
Variable action (Q_1)†	Normal, Lognormal, Gumbel	10	[0.20, 0.40, 0.60]

* set to reach $\beta_t = 3.8$ for each combination of inputs.

† the specified parameters are used to generate 50-element sample and the parameters of the model used in reliability analysis are inferred from it.

The annual maxima are assumed to be independent:

$$F_{50}(q) = F_1(q)^{50} \tag{7}$$

where $F(.)$ is the cumulative distribution function.

3.2. INTERVAL AND RELIABILITY ANALYSIS

To model the effect of measurement uncertainty, 50 random observations are generated from Q_1, these are treated as observed (Y) values as the reality-observation link by definition is unknown in interval representation (Figure 3). Then intervals are centered at observations and various interval radiuses are considered. Using these interval variables, the distribution of Q_1 is fitted by the method of moments that is a widely used approach in civil engineering (Sanpaolesi et al., 1998) and was proved to be robust e.g. for modeling hydrological extremes (Madsen et al., 1997). The hybrid interval-probabilistic reliability problem is solved using optimization and first order reliability method (FORM). An outcome of the analysis is an interval reliability index.

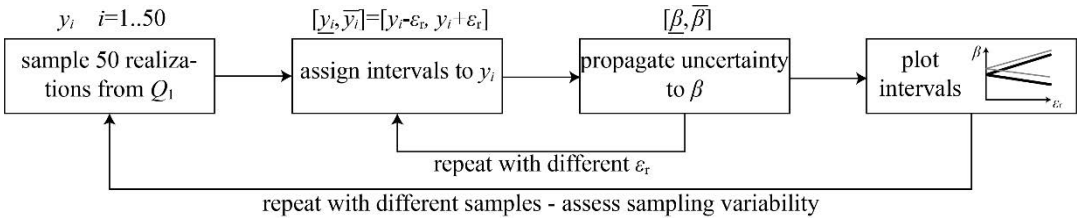

Figure 3. Algorithm of analyzing the effect of interval measurement uncertainty on reliability.

The upper bound of it is irrelevant from safety point of view and the lower bound is recommended for practical applications (Qiu et al., 2007). This is due to the special nature of intervals and how they represent uncertainty: the real value can be anything within the interval but one cannot assume that all points are equally likely (principle of indifference) at least because the consequence of specific values are not equal. Hence we chose the recommended, careful engineering approach and use the lower endpoint of the reliability index interval as representative value.

3.2.1. Full and approximate propagation of interval uncertainty

As measurement uncertainty is expressed at the level of individual observations its full propagation yields to two distinct 50-dimensional constrained optimization problems that can be computationally demanding if each iteration step involves fitting a distribution function and solving a reliability problem. The computational burden can be considerably lessened by a two-step approximate technique where first the distribution parameters are fitted to the interval observations. Then only the interval representation of distribution parameters are used in further reliability analysis. Thus, the optimization with reliability analysis is reduced to a two-dimensional search space. Moreover, our experience show that the optimum is at the bounds so as it can be found by considering only the possible permutations of the parameter bounds.

The accuracy of full and two-step approximate uncertainty propagations are compared using Gumbel distributed Q_1. The results in terms of reliability indices are presented in Figure 4. The interval uncertainty is expressed as the ratio of interval radius and mean of annual maxima (Q_1). 0-10% range is covered and it is assumed that all observations are contaminated by the same radius. For each coefficient of variation the mean of the resistance is set to reach the 3.8 target reliability level. This is performed by considering no measurement uncertainty ($\varepsilon_r = 0$) and using the parameters given in Table *1*, thus sampling variability has no effect. The calculated upper and lower reliability index endpoints are presented in the plots with solid and dashed lines for two-step and full propagations, respectively. Figure 3 shows also the reliability index obtained by Approach 1. This is illustrated with a dotted line and is not affected by the assumed measurement uncertainty interval.

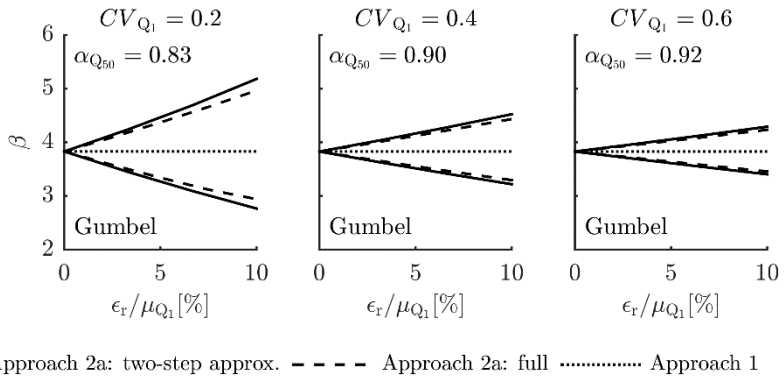

Figure 4. Reliability index intervals as the function of normalized measurement uncertainty radius (ε_r) with full and approximate propagation of interval uncertainty.

The plots show that the approximate technique slightly overestimates the accurate (full) reliability intervals, the largest difference is observed for $CV_{Q1} = 0.2$ with large measurement uncertainty. Since in

general the overestimation of the approximate technique is small, it is used in all further analysis. The sensitivity factor of the 50-year reference period maxima (α_{Q50}) is also displayed on the plots. It corresponds to a model without uncertainty in measurement and parameters. The decreasing interval range of β with increasing CV_{Q1} is explained by the decreasing contribution of interval uncertainty to the full uncertainty of Q_1, i.e. the aleatory uncertainty becomes dominating. Figure 5 illustrates this shrinkage of uncertainty interval by comparing the transformed cumulative distribution functions with different coefficient of variations. The plots correspond to 50 particular random realizations; the same pattern is observed for other sets of random realizations.

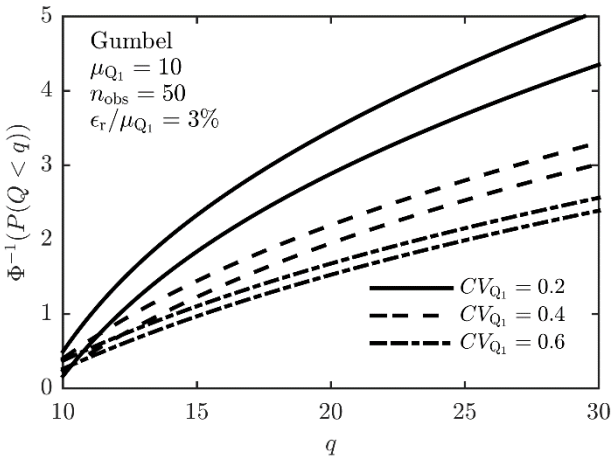

Figure 5. Illustration of the shrinkage of uncertainty interval with increasing coefficient of variation but constant measurement uncertainty interval.

3.2.2. Effect on reliability index and required resistance

Equation (3) is solved for Normal, Lognormal and Gumbel distributed variable action (Q_1) using the two-step approximation technique. The results are summarized in Figure 6; they have the same rationale as is given for Figure 4. The light gray lines show the opening reliability interval with increasing measurement uncertainty for 20 random samples, each with 50 realizations. These are indicative of the effect of sampling variability: in this case this is entirely parameter estimation uncertainty due to the finite sample size. The results show that sampling variability – with 50 realizations that is typical for maxima model of climatic actions – has significant effect on reliability. It is dominating over measurement uncertainty for small interval radiuses and comparable for larger values. The thick black lines are the median of the 20 sample sets. The reliability index without considering measurement uncertainty can be seen at the common starting point of the lower and upper bound lines. The difference of this value and the lower bound is of interest here as it indicates the extent of the non-conservative neglect of measurement uncertainty. The difference is deemed significant if it is larger than 0.5, this level is indicated by a dashed horizontal line while the significant range with a red half line. With the selected target reliability level, this corresponds to more than six-fold increase in failure probability.

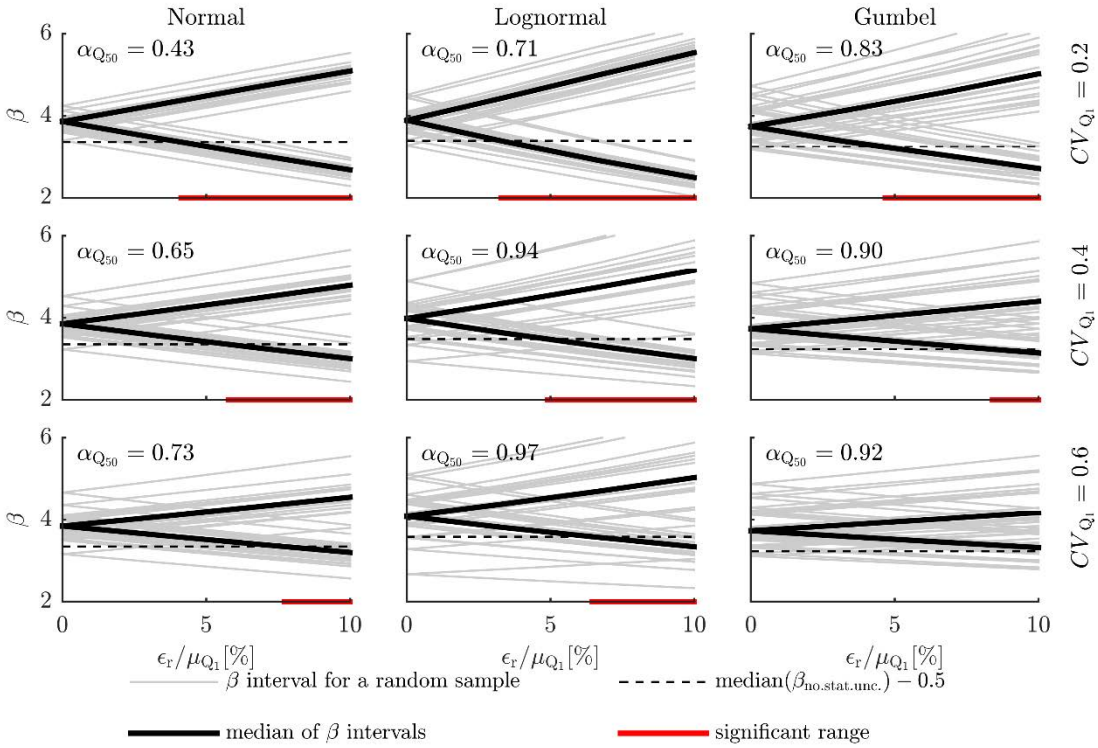

Figure 6. Reliability index intervals as the function of the normalized measurement uncertainty radius (ε_r/μ_{Q1}). The gray lines represent 20 random samples, indicating sampling variability. The black lines are the median lower and upper interval endpoints of the reliability index. The red half line indicates the range where the lower endpoint of the reliability interval is significantly lower (0.5) than the reliability calculated without measurement uncertainty ($\varepsilon_r = 0$).

The results suggest that moderate ±4% measurement uncertainty can lead to significant reduction of reliability level for mountains and highlands represented by $CV_{Q1} = 0.2$-0.4. For the largest considered value of $CV_{Q1} = 0.6$, the Gumbel model does not reach the limiting value. This indicates that for lowlands even a quite large ±10% measurement uncertainty has no practically significant effect. The reliability interval ranges indicate that even a small ±2% measurement uncertainty can lead to an order of magnitude uncertainty in the failure probability, e.g. Lognormal distribution with $CV_{Q1} = 0.2$. For larger measurement uncertainties, the width of the reliability intervals can be larger than 2.0; the widths are quite considerable for large $CV_{Q1} = 0.6$ models too.

Measurement uncertainty thus seems to have a marked effect on structural reliability. The practical question then arises: what are its implications on design and how it should be accounted? To examine this, we calculated the mean resistance required to reach the target reliability with the lower bound of the reliability interval (Approach 2a). Then this value is compared to the mean resistance required to reach the target reliability without explicit consideration of measurement uncertainty (Approach 1). The ratios of the mean values (with interval MU/without explicit MU) are illustrated in Figure 7. These indicate how large adjustment might be needed in representative resistance values to meet target reliability in the presence of measurement uncertainty. The plots are structured and have the same rationale as Figure 6. The ratio is deemed practically significant if it is larger than 1.1. This level is indicated by a dashed horizontal line while

the significant range with a red half line. The small effect of sampling variability for Normal distribution is likely due to the small sensitivity factor of Q_{50}. On the contrary, sampling variability is quite considerable for Lognormal distribution. The selected threshold is reached for all the distributions. The Lognormal model shows opposite trend; this might be attributed to its heavy tail. For this distribution the 1.1 threshold is reached at about 4% radius and the ratio can be over 1.4 for larger radiuses that is a huge potential adjustment. The Gumbel distribution illustrates decreasing ratio with increasing coefficient of variation. For $CV_{Q1} = 0.2$ (mountains), moderate ±4% measurement uncertainty can lead to significant mean resistance ratio. For the lowlands ($CV_{Q1} = 0.6$), the ratio is over the selected threshold only for excessive measurement uncertainty ±9% which suggests that measurement uncertainty can be neglected for large values of CV_{Q1}.

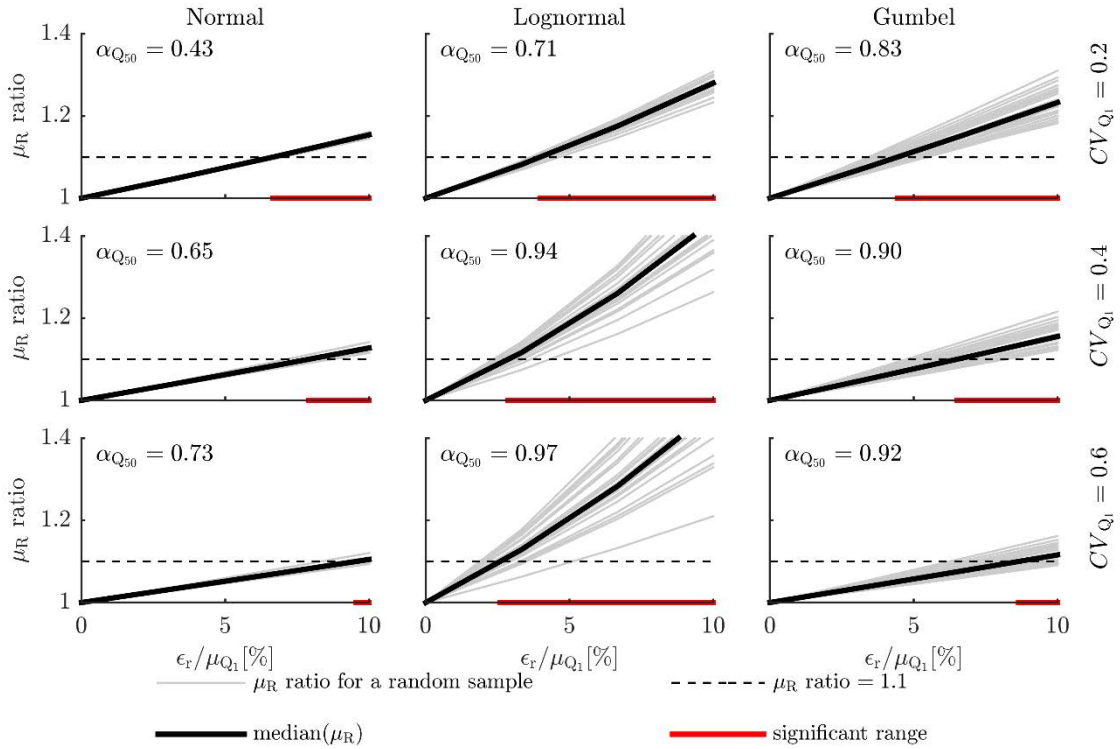

Figure 7. Mean resistance ratio for the variable action with and without measurement uncertainty as the function of the normalized measurement uncertainty radius (ε_r/μ_{Q1}). The red half line indicates the significant range where the ratio is larger than 1.1.

3.3. STATISTICAL AND RELIABILITY ANALYSIS

This section presents the statistical approach to quantify and propagate measurement uncertainty (Approach 2b). To model the effect of measurement uncertainty, 50 random observations are generated from Q_1 and treated as true (X) values. Then by using the assumed reality-observation link, it is contaminated by measurement uncertainty. This is generated from a known, independent distribution (E). The algorithm is outlined in Figure 8. Additive and multiplicative reality-observation links are assumed and the measurement uncertainty is taken as normally distributed with zero mean (unbiased). After the contamination of data, the

information about the parameters of the underlying generating models – with the exception of the zero mean of measurement uncertainty – is disregarded and the maximum likelihood method is applied to decouple true values from measurement uncertainty. Finally, the model of decontaminated observations is used in reliability analysis. The sampling variability is again indicated by 20 samples and taken into account in an approximate manner through the predictive reliability index (Eq.(5)). The median and mean absolute deviation are calculated.

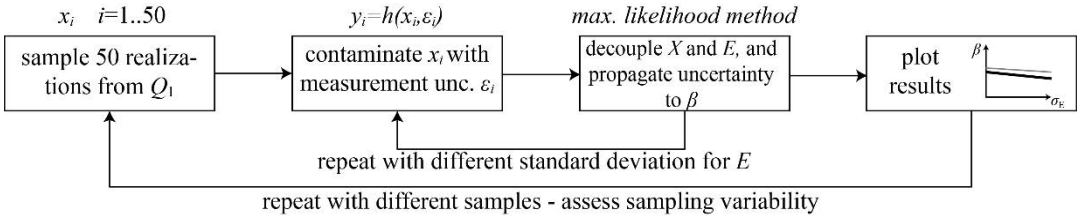

Figure 8. Algorithm of analyzing the effect of measurement uncertainty on reliability using statistical technique.

3.3.1. Decontamination of observations

To illustrate the technique and the effect of decontamination, random realizations are generated from Gumbel distribution – with parameters given in Table *1* – and contaminated by measurement uncertainty (Figure 8). First, additive reality-observation relationship is assumed and Approach 1 and Approach 2b are used to infer the model parameters. The maximum likelihood method is used to obtain point estimates and the delta method is applied to construct 90% confidence intervals to illustrate parameter estimation uncertainty (Coles, 2001). The results for three cases of Gumbel distribution and two cases of measurement uncertainty with varying standard deviation are discussed only. The realizations and the fitted models are shown in Figure 9. It comprises return value–return period plots transformed to Gumbel space where the Gumbel distribution appears as a straight line. Though the plots are corresponding to a particular set of realizations, they convey reliably the trends and expected differences: (*i*) Approach 1 typically overestimates the fractiles thus leading to lower reliability level and being conservative; (*ii*) the difference between models increases with increasing return period. Due to the small sample size, the difference is affected by large sampling variability.

The calculations are repeated with multiplicative measurement uncertainty (Figure 10). The results correspond well with those obtained for the additive format; wider confidence intervals of Approach 2b compared with Approach 1 are observed. This is due to the larger model space where the same sample size allows less certain inference. This effect is less pronounced for the additive model.

For both models, Approach 1 is inherently biased since it is not using the correct likelihood function, while Approach 2b asymptotically converges to the true model. Thus, in the long run – from theoretical point of view – Approach 2b is better, however Approach 1 seems to be generally conservative for the considered reality-observation links. This latter aspect is analyzed in more detail in the following section focusing on reliability index as a quantity of practical interest.

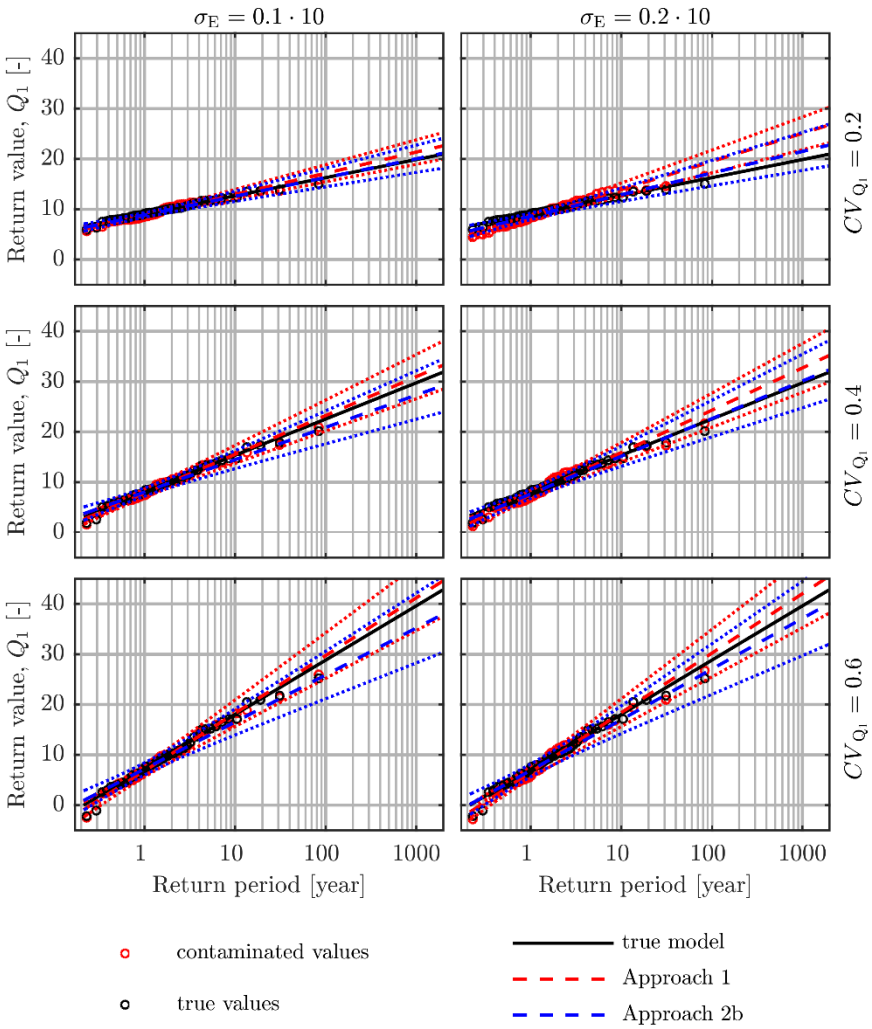

Figure 9. Gumbel distributions fitted to random realizations contaminated by additive measurement uncertainty using Approach 1 and Approach 2b. The point estimates (dashed lines) are accompanied by 90% confidence intervals (dotted lines).

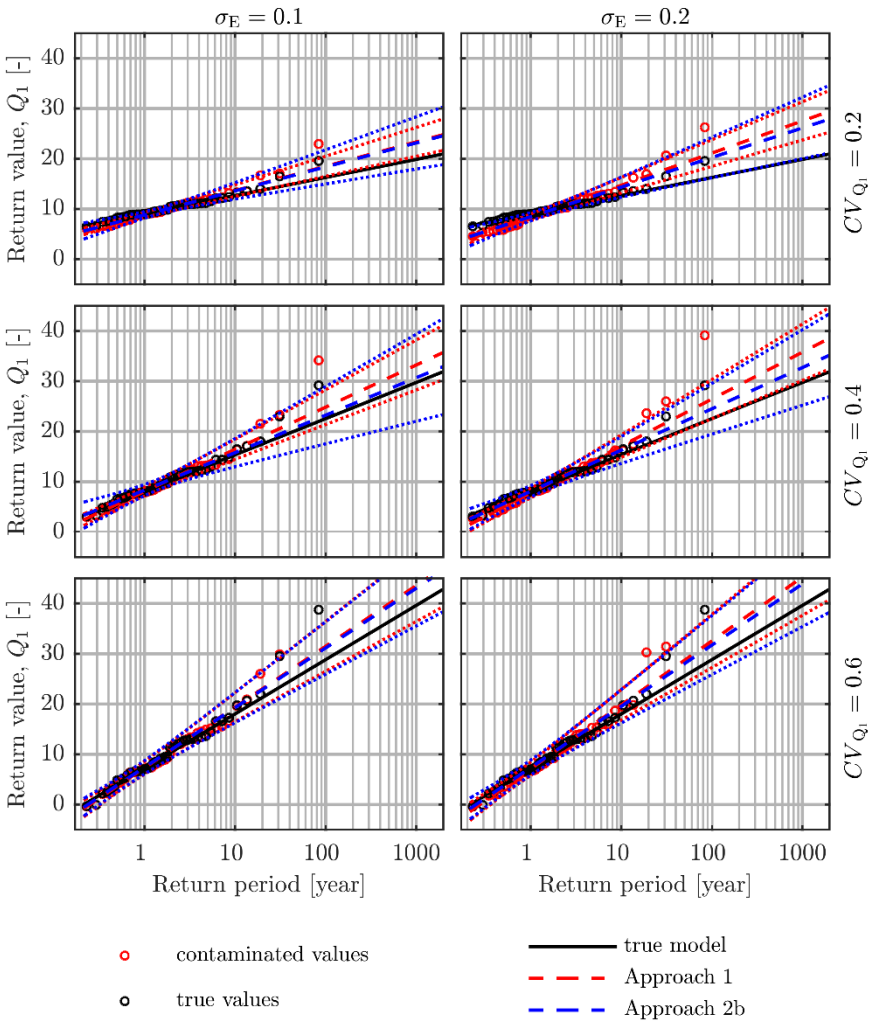

Figure 10. Gumbel distributions fitted to random realizations contaminated by multiplicative measurement uncertainty using Approach 1 and Approach 2b. The point estimates (dashed lines) are accompanied by 90% confidence intervals (dotted lines).

3.3.2. Effect on reliability index

The effect of measurement uncertainty on reliability index is analyzed for the additive relationship considering Normal, Lognormal and Gumbel distributed true values and with coefficient of variation ranging from 0.2 to 0.6. The measurement uncertainty has normal distribution with known zero mean and varying standard deviation. Consistently with the interval analysis in Section 3.2, the mean value of the resistance is determined to reach the target reliability without measurement uncertainty and parameter estimation uncertainty. Then the algorithm presented in Figure 8 is applied to generate contaminated observations, to decontaminate them, and to calculate the reliability index using the inferred parameters. The calculations are repeated for 20 samples with sample size of 50. The results in terms of reliability indices are shown in Figure 11 and in Figure 12. Grey and light blue solid lines are representing the 20 samples, and the corresponding

thick solid and dashed lines are the median and predictive reliability indices, respectively. The difference between these latter two lines expresses the effect of parameter estimation uncertainty. For Normal distribution, this effect is small compared to Lognormal and Gumbel for which it is increasing with increasing standard deviation of measurement uncertainty. For Approach 2b it is typically larger than Approach 1 as the larger model space allows less certain inference with the same sample size. In case of Lognormal and Gumbel models, the ratio of the predictive and median failure probabilities can be as large as an order of magnitude or larger. Additionally, the plots show that the reliability index can considerably be overestimated when parameter estimation uncertainty is neglected. The salient large scatter of Approach 2b might be partially attributed to the unstable maximum likelihood estimators for small samples (Hosking et al., 1985; Martins and Stedinger, 2000).

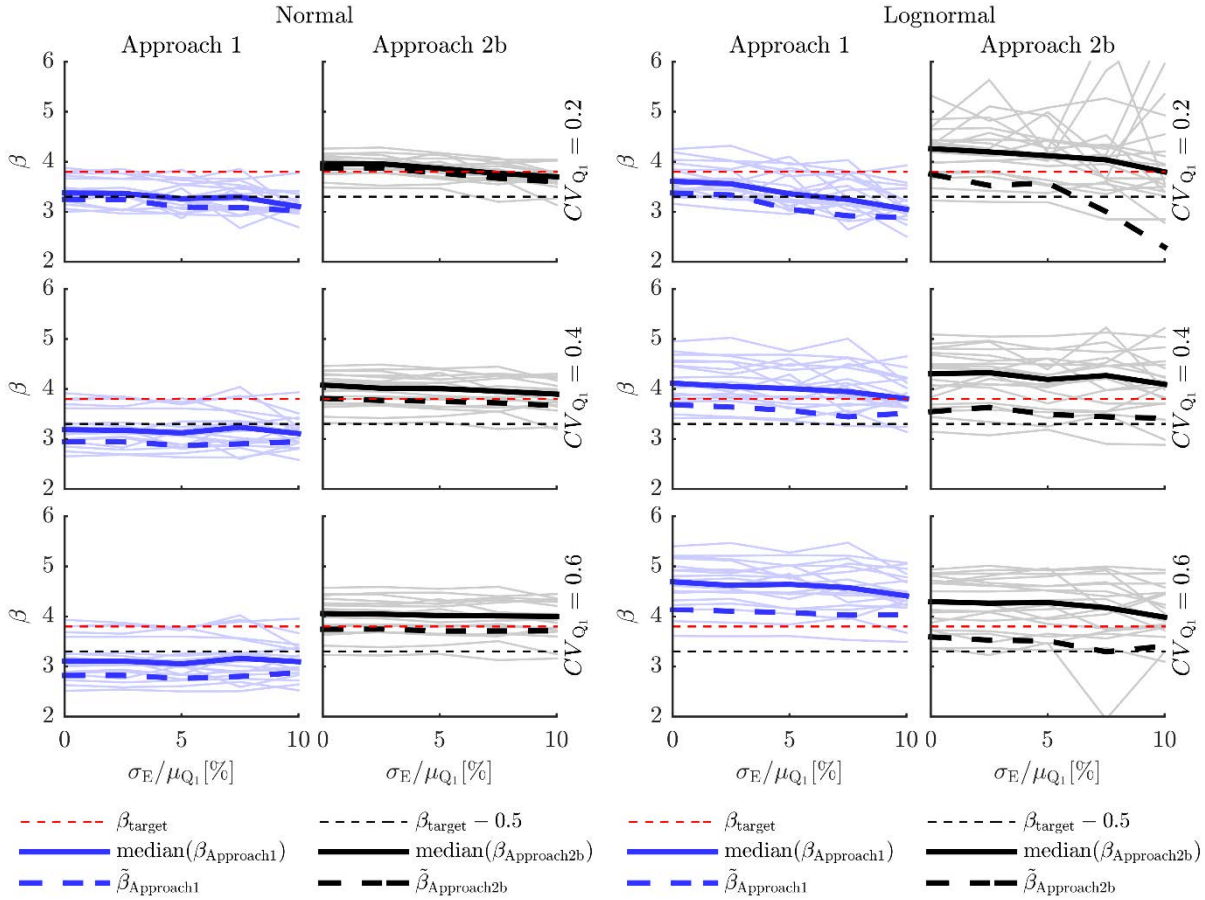

Figure 11. Reliability indices as the function of the normalized standard deviation of measurement uncertainty (σ_E/μ_{Q1}). The thick solid lines are the median of the reliability indices while the thick dashed lines are the approximate predictive reliability indices.

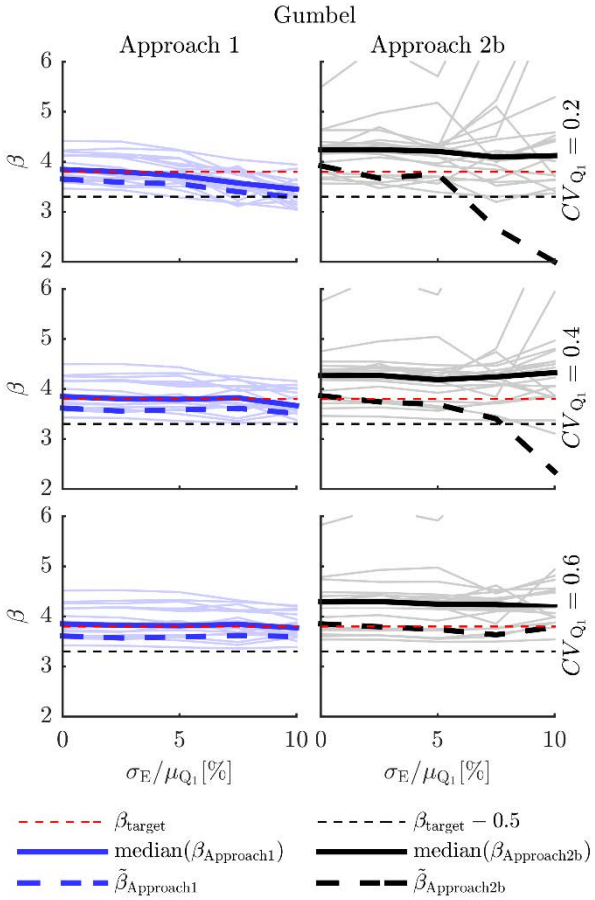

Figure 12. Reliability indices as the function of the normalized standard deviation of measurement uncertainty (σ_E/μ_{Q1}). The thick solid lines are the median of the reliability indices while the thick dashed lines are the approximate predictive reliability indices.

Comparing Approach 1 with Approach 2b for Normal and Gumbel distributions, the former approach yields to systematically lower reliability indices. The opposite trend observed for Lognormal distribution might be attributed to its heavy-tail. For Normal distribution, Approach 1 seems to be overly conservative, the median is well below the target reliability level.

For all distributions, Approach 1 is reasonably conservative with the exception of Lognormal distribution and coefficient of variation of 0.6. However, even in this case the predictive reliability index corrects the overestimation. Though for Normal distribution it is too conservative, the currently prevalent Approach 1 appears to be safely applicable to measurement uncertainty problems in case of additive reality-observation relationship. Approach 2b is sound from theoretical point of view, however its median overestimates reliability level, thus the predictive reliability index is to be used to avoid underestimation of failure probability. Its larger parameter estimation uncertainty can lead large reduction in reliability index for small sample sizes.

4. Discussion

One can distinguish two components of measurement uncertainty: the reality-observation link and the nature of the contamination *E*. The three approaches considered here differ in how they treat these two components. The present prevalent approach (Approach 1) neglects both components, thus entirely ignores the possibility that the real values are greater or smaller than the observed due to measurement uncertainty.

The interval approach (Approach 2a) expresses full ignorance in respect of reality-observation link and represents measurement uncertainty with intervals. Therefore, no decoupling of true values from measurement uncertainty is possible. Intervals should be used with caution because by definition values outside of the interval are impossible. This is an assumption that is rarely met in civil engineering. Measurement uncertainty is often described on the basis of expert judgment and wide intervals are applied to almost surely capture real, unobserved values.

The statistical approach (Approach 2b) requires the knowledge of the reality-observation link and represents measurement uncertainty with distribution function. This is the only approach that can decontaminate the observations and can directly infer the variable of interest, true variable. This is important since structural reliability is dependent on the true variable. The statistical and interval analysis based approaches are conceptually different, thus they are only comparable on that level but not quantitatively. Their uncertainty representation is inherently distinct, thus there is no equivalency between interval and distribution based representations.

Additionally, it must be emphasized that another type of uncertainty – statistical uncertainty in parameter estimation and selection of distribution function – often needs to be taken into account in reliability analysis as it may be even more important as measurement uncertainty investigated here (Rózsás and Sýkora, 2015a; 2015b). Bayesian paradigm is a natural choice to incorporate this uncertainty, consequently that is recommended for practical applications. For example, in real-life situations, the reality-observation link cannot be established with certainty. Yet, this uncertainty can be captured by using multiple models and averaging them with respect their goodness of describing the data, this can be achieved for example by Bayesian model averaging (Hoeting et al., 1999).

Although this study is limited by the considered distribution types, reality-observation functions, and parameter range, it is believed to cover many practically relevant random variables. The presented approach and algorithms can be easily used for other distribution types and measurement error structure. An additional limitation of this study is that measurement uncertainty is considered only for the dominant variable action. However, it is anticipated that for other random variables the effect is smaller due to their typically smaller sensitivity factor. Moreover, measurement uncertainty is much smaller for other than climatic actions such as resistance and permanent actions. Furthermore, the effect of sample size should be analyzed in later works. It is believed that the outcomes would be similar for sample sizes ranging from 20 to couple of hundreds, which cover the majority of cases in civil engineering. More data would allow more certain model identification.

5. Conclusions

The current practice in probabilistic engineering treats observed data contaminated by measurement uncertainty as realizations of the true distribution, thus neglecting the contamination mechanism. Statistical

and interval-based analyses are thus conducted to investigate the effect of this simplification on structural reliability. Extensive parametric analyses – based on 50 realizations, which is a typical length of records for climatic actions – reveal that:

If interval representation of measurement uncertainty is used:

- Sampling variability (parameter estimation uncertainty) has significant effect on reliability: it is dominant over measurement uncertainty for small interval radiuses and comparable for large radiuses.
- For mountains and highlands, moderate ±4% measurement uncertainty – relative to value of an observed variable – can lead to significant reduction of reliability level. For lowlands, even a large ±10% measurement uncertainty has no significant effect. An effect is deemed significant if it yields to greater than six fold increase in failure probability compared with Approach 1 (neglect of measurement uncertainty.
- Reliability interval ranges indicate that a small ±2% measurement uncertainty can lead to reduction of 0.6 in reliability index. For larger measurement uncertainties, the width of the reliability intervals can be larger than 2.0.
- The effect of measurement uncertainty is more pronounced for low variability random variables where its contribution to the total uncertainty increases.
- Parameter ranges where Approach 1 often overestimates the reliability index are identified.

If statistical (distribution function) representation of measurement uncertainty is used:

- It is demonstrated that the statistical approach can be used to decontaminate the observations, thus to access the variable of interest.
- The ratio of the predictive and median failure probabilities can be as large as an order of magnitude or larger (~30 for Lognormal distribution).
- If parameter estimation uncertainty is disregarded, the reliability index can be considerably overestimated.
- For all distributions with additive measurement uncertainty, Approach 1 is reasonably conservative in most cases.

Practical recommendations:

- Figure 6 and Figure 7 can be used to identify cases when Approach 1 significantly overestimates reliability index. In such cases and when no or very limited information on measurement uncertainty is available, then interval analysis could be used, considering the lower bound of the reliability interval.
- If the reality-observation link is known then the statistical approach is recommended. For small and moderate sample sizes (<100), the predictive reliability index is recommended. For additive measurement uncertainty, Approach 1 is conservative.
- Point estimates such as median reliability index should be accompanied by uncertainty intervals to indicate the credibility of results.
- For ground snow extremes at lowlands, Approach 1 provides a reasonable approximation, thus the effect of measurement uncertainty can be neglected. Otherwise more advanced analysis is recommended.

Assessment of measurement uncertainty should be region and case-specific accounting for measuring techniques, and applied correction equations, thus involvement of meteorologists, analysts or other experts is beneficial. Moreover, the selected approach to propagate measurement uncertainty should always be based on the particular issue in question, acknowledging “the degree of precision to which the nature of the subject admits”.

Acknowledgements

This study is an outcome of the research project DG16P02M050 "Optimisation of Observations and Assessment of Heritage Structures", supported by the Ministry of Culture of the Czech Republic. The numerical analyses are completed using Matlab (Matlab, 2015) and FERUM (Der Kiureghian et al., 2006) the work and commitment of the developers of these applications are highly appreciated. All codes/ scripts, processed data, and results can be obtained from the authors.

References

Aitchison J. and I. R Dunsmore. *Statistical Prediction Analysis*. New York, USA: Cambridge University Press, 1980.

Alibrandi, U. and C. Koh. First-order reliability method for structural reliability analysis in the presence of random and interval variables. *ASCE-ASME Journal of Risk and Uncertainty in Engineering Systems, Part B: Mechanical Engineering*, 1(4):041006, 2015.

ASCE. Minimum Design Loads for Buildings and Other Structures. ASCE/SEI 7-10. Reston, Virginia: American Society of Civil Engineers, 2010.

Casella, G. and R. L. Berger. *Statistical inference*. Cengage Learning, 2nd edition, 2001.

Coles, S. *An Introduction to Statistical Modeling of Extreme Values*. Springer-Verlag, London, 2001.

Der Kiureghian, A. Measures of Structural Safety Under Imperfect States of Knowledge. *Journal of Structural Engineering*, 115: (5):1119-1140, 1989.

Der Kiureghian, A., T. Haukaas and K. Fujimura. Structural reliability software at the University of California, Berkeley. *Structural Safety*, 28(1–2):44–67, 2006.

Goodison, B. E., P. Y. T. Louie and D. Yang. WMO solid precipitation measurement intercomparison. WMO Instruments and Observing Methods Rep. 67, WMO/TD-872, 1998.

Hoeting, J. A., D. Madigan, A. E. Raftery and C. T. Volinsky. Bayesian model averaging: A tutorial. *Statistical Science*, 14(4):382–417, 1999.

Hosking, J., J. Wallis and E. Wood. Estimation of the generalized extreme-value distribution by the method of probability-weighted moments. *Technometrics,* 27:251–261, 1985.

Huber, W. A. Ignorance is not probability. *Risk Analysis*, 30(3):371–376, 2010.

JCSS. Probabilistic Model Code. Part I-III. Joint Committee on Structural Safety. ISBN 978-3-909386-79-6, 2002.

Koen, C. and L. Kondlo. Fitting power law distributions to data with measurement errors. *Monthly Notices of the Royal Astronomical Society*, 397, 495-505, 2009.

Kondlo, L. O. Estimation of Pareto Distribution Functions from Samples Contaminated by Measurement Errors. MSc thesis. Department of Statistics, University of the Western Cape, 2010.

Madsen, H., , P. F. Rasmussen and D. Rosbjerg. Comparison of annual maximum series and partial duration series methods for modeling extreme hydrologic events: 1. at-site modeling. *Water Resources Research*, 33(4):747–757, 1997.

Martins, E. S. and J. R. Stedinger. Generalized maximum-likelihood generalized extreme-value quantile estimators for hydrologic data. *Water Resources Research,* 36 (3):737-744, 2000.

Matlab. version 7.10.0 (R2015a). The MathWorks Inc. Natick, Massachusetts, 2015.

Meister, A. *Deconvolution Problems in Nonparametric Statistics*, Springer-Verlag, Berlin, 2009.

Moore, R. E., R. B. Kearfott and M. J. Cloud. *Introduction to Interval Analysis*. Cambridge University Press; 1st edition, 2009.

Muhanna, R. L., R. L. Mullen and M. V. R. Rao. Nonlinear finite element analysis of frames under interval material and load uncertainty. *ASCE-ASME Journal of Risk and Uncertainty in Engineering Systems, Part B: Mechanical Engineering*, 1(4):041003, 2015.

Qiu, Z., D. Yang and I. Elishakoff. Combination of structural reliability and interval analysis. *Acta Mechanica Sinica*, 24(1):61–67, 2007.

Qiu, Z., D. Yang and I. Elishakoff. Probabilistic interval reliability of structural systems. *International Journal of Solids and Structures*, 45(10):2850 – 2860, 2008.

Rao, M. R., R. L. Muhanna and R. L. Mullen. Geometric misfitting in trusses and frames: an interval-based approach. *International Journal of Reliability and Safety*, 9(2-3):132–153, 2015.

Rasmussen, R., B. Baker, J. Kochendorfer, T. Meyers, S. Landolt, A. P. Fischer, J. Black, J. M. Thériault, P. Kucera, D. Gochis, C. Smith, R. Nitu, M. Hall, K. Ikeda and E. Gutmann. How Well Are We Measuring Snow: The NOAA/FAA/NCAR Winter Precipitation Test Bed. *Bulletin of American Meteorological Society*, 93, 811–829. doi: http://dx.doi.org/10.1175/BAMS-D-11-00052.1, 2012.

Rózsás, Á. and M. Sýkora. Effect of statistical uncertainties in ground snow load on structural reliability. In *IABSE Conference: Structural Engineering: Providing Solutions to Global Challenges*, pages 220–227, 2015a.

Rózsás, Á. and M. Sýkora. Model comparison and quantification of statistical uncertainties for annual maxima of ground snow loads. In Podofillini, L., Sudret, B., Stojadinovic, B., Enrico, Z., and Kröger, W., editors, *Safety and Reliability of Complex Engineered Systems: ESREL 2015*, pages 2667–2674. CRC Press, 2015b.

Sanpaolesi, L., D. Currie, P. Sims, C. Sacré, U. Stiefel, S. Lozza, B. Eiselt, R. Peckham, G. Solomos, I. Holand, R. Sandvik, M. Gränzer, G. König, D. Sukhov, R. Del Corso and P. Formichi. Scientific support activity in the field of structural stability of civil engineering works: Snow loads. final report phase i. Report, Commission of the European Communities. DGIII-D3, 1998.

Stefanski, L. Measurement error models. *Journal of the American Statistical Association*, 95, 1353-1358, 2000.

Zhang, H., R. L. Mullen and R. L. Muhanna. Interval estimates of structural reliability. In Beer, M., Muhanna, R. L., and Mullen, R. L., editors, *4th International Workshop on Reliable Engineering Computing. REC 2010*, pages 386–395. Research Publishing Services, 2010.

Interval Finite Element Analysis of Thin Plates

M. V. Rama Rao[1)], R. L. Muhanna[2)] and R. L. Mullen[3)]
[1)]*Vasavi College of Engineering, Hyderabad - 500 031 India, dr.mvrr@gmail.com*
[2)]*School of Civil and Environmental Engineering, Georgia Institute of Technology Atlanta, GA 30332-0355, USA, rafi.muhanna@gtsav.gatech.edu*
[3)]*School of Civil and Environmental Engineering, University of South Carolina, GA 30332-0355, USA, rlm@cec.sc.edu*

Abstract: This paper focuses on the analysis of thin plates with uncertain structural parameters modelled as intervals. The plate is assumed to be orthotropic. Interval uncertainty is associated with the Young's modulus of the plate and also with the applied load. Interval Finite Element Method (IFEM) developed in the earlier work for line elements of the authors for truss and frame structures (Rama Rao et al., 2011) is applied to the case of thin plates in the present work. This method is capable of obtaining bounds for interval forces and moments with the same level of sharpness as displacements and rotations. Example problems pertaining to various edge conditions of the thin plate are solved to demonstrate that the present method is capable of obtaining sharp bounds. Results are compared to the values of displacements and forces obtained using combinatorial and Monte Carlo solutions.

Keywords: interval, interval finite elements, uncertainty, thin plates, structural analysis

1. Introduction

Plates play a major role in several important structures viz. ships, pressure vessels, and other structural components. Thus it is important to understand their structural behaviour and possible conditions of failure especially under conditions of uncertainty. The structural behaviour of thin plates in bending depends on several important factors including load, stiffness characteristics of plate and support conditions. The problem of plate bending is one of the oldest in the theory of elasticity and is discussed in several textbooks (Timoshenko and Krieger, 1959; Szilard, 2004; Reddy, 2007). Lim et.al. (2007) derived exact analytical solutions to bending of rectangular thin plates by employing the Hamiltonian principle with Legendre's transformation. The solution obtained by them for example problems of plates with selected boundary conditions shows excellent agreement with the classical solutions. Batista (2010) used the Fourier series to compute the analytical solutions of uniformly loaded rectangular thin plates with symmetrical boundary conditions.

On the other hand, structural analysis without considering uncertainty in loading or material properties leads to an incomplete understanding of the structural performance. Structural analysis using interval variables has been used by several researchers to incorporate uncertainty into structural analysis (Koyluoglu, Cakmak and Nielson, 1995; Muhanna and Mullen, 1995; Nakagiri and Yoshikawa, 1996; Rao and Sawyer, 1995; Rao and

Berke, 1997; Rao and Chen, 1998; Muhanna and Mullen, 2001; Pownuk, 2004; Neumaier and Pownuk, 2007).

To the authors' knowledge, applications of interval methods for the analysis of plates with uncertainty of load and material properties do not exist anywhere in literature. In view of this, we present an initial investigation into the application of interval finite element methods to problems of bending of thin plates. Usually, derived quantities in Interval Finite Element Method (IFEM) such as stresses and strains have additional overestimation in comparison with primary quantities such as displacements. This issue has plagued displacement-based IFEM for quite some time. The recent development of mixed/hybrid IFEM formulation by the authors (Rama Rao et al., 2011) is capable of simultaneous calculation of interval strains and displacements with the same accuracy.

This work presents the application of interval finite element methods to the analysis of thin plates. Uncertainty is considered in both the applied load and Young's modulus as explained in section 2. Examples are finally presented and discussed. In the present study a rectangular plate is analysed different type of edge conditions of such as clamped and simply supported edge conditions and the deformations are obtained.

2. Linear Interval Finite Element Method

Finite element method is one of the most common numerical methods for solving differential and partial differential equations with enormous applications in different fields of science and engineering. Interval finite element methods have been developed to handle the analysis of systems for which uncertain parameters are described as intervals. A variety of solution techniques have been developed for IFEM. A comprehensive review of these techniques can be found in (Zhang, 2005; Muhanna et al., 2007; Rama Rao et al., 2011). Interval analysis concerns the numerical computations involving interval numbers. All interval quantities will be introduced in non-italic boldface font. The four elementary operations of real arithmetic, namely addition (+), subtraction (-), multiplication (×) and division (÷) can be extended to intervals. Operations $\circ \in \{+,-,\times,\div\}$ over interval numbers x and y are defined by the general rule (Moore, 1966; Moore, 1979; Moore et al., 2009; Neumaier, 1990)

$$\mathbf{x} \circ \mathbf{y} = [\min(x \circ y), \max(x \circ y)] \quad for \ \circ \in \{+,-,\times,\div\}, \tag{1}$$

in which x and y denote generic elements $x \in \mathbf{x}$ and $y \in \mathbf{y}$. Software and hardware support for interval computation are available such as (Sun microsystems, 2002; Knüppel, 1994; INTLAB, 1999). For a real-valued function $f(x_1,...,x_n)$, the interval extension of $f(\,)$ is obtained by replacing each real variable xi by an interval variable xi and each real operation by its corresponding interval arithmetic operation. From the fundamental property of inclusion isotonicity (Moore, 1966), the range of the function $f(x_1,...,x_n)$ can be rigorously bounded by its interval extension function

$$f(\mathbf{x}_1,..,\mathbf{x}_n) \supseteq \{f(x_1,..,x_n) \,|\, x_1 \in \mathbf{x}_1,..,x_n \in \mathbf{x}_n\} \tag{2}$$

Eq. (2) indicates that $f(\boldsymbol{x}_1,\ldots,\boldsymbol{x}_n)$ contains the range of $f(x_1,\ldots,x_n)$ for all $x_i \in \boldsymbol{x}_i$. A natural idea to implement interval FEM is to apply the interval extension to the deterministic FE formulation. Unfortunately, such a naïve use of interval analysis in FEM yields meaningless and overly wide results (Muhanna and Mullen, 2001; Dessombz et al., 2001). The reason is that in interval arithmetic each occurrence of an interval variable is treated as a different, independent variable. It is critical to the formulation of the interval FEM that one identifies the dependence between the interval variables and prevents the overestimation of the interval width of the results. In this paper, an element-by-element (EBE) technique is utilized for element assembly (Muhanna and Mullen, 2001; Zhang, 2005). The elements are detached so that there are no connections between elements, avoiding element coupling. The Lagrange multiplier method is then employed to impose constraints to ensure the compatibility. Then a mixed/hybrid formulation is incorporated to simultaneously calculate the interval strains and displacements (Rama Rao, Mullen and Muhanna, 2011). This linear formulation results in the interval linear system of equations that has the following structure:

$$(K + B\boldsymbol{D}A)\boldsymbol{u} = a + F\boldsymbol{b}, \tag{3}$$

with interval quantities in $\boldsymbol{D}$ and $\boldsymbol{b}$ only. The term $(K + B\boldsymbol{D}A)$ represents the interval structural stiffness matrix and the $a + F\,\mathbf{b}$ term, the structural loading. Any interval solver can be used to solve Eq. (3), however, the following iterative scheme that is developed by Neumaier and Pownuk (Neumaier and Pownuk, 2007) is superior for large uncertainty, defining:

$$C := (K + BD_0A)^{-1} \tag{4}$$

where D_0 is chosen in a manner that ensures its invertability (often D_0 is selected as the midpoint of **D**), the solution **u** can be written as:

$$\mathbf{u} = (Ca) + (CF)\mathbf{b} + (CB)\mathbf{d} \tag{5}$$

To obtain a solution with tight interval enclosure we define two auxiliary interval quantities,

$$\begin{aligned} \mathbf{v} &= A\mathbf{u} \\ \mathbf{d} &= (D_0 - \mathbf{D})\mathbf{v}, \end{aligned} \tag{6}$$

which, given an initial estimate for **u**, we iterate as follows:

$$\mathbf{v}^{k+1} = \{ACa) + (ACF)\mathbf{b} + (ACB)\mathbf{d}^k\} \cap \mathbf{v}^k, \quad \mathbf{d}^{k+1} = \{(D_{c0} - \mathbf{D}_c)\mathbf{v}^{k+1} \cap \mathbf{d}^k, \tag{7}$$

until the enclosures converge, from which the desired solution **u** can be obtained in a straightforward manner.

In this paper the above mentioned iterative enclosure has been used for the solution of the linear interval system of Eq. (3). The solution includes displacements, strains, and forces simultaneously with the same high level of accuracy.

3. Finite Element Model of the Plate

Thin plates are characterized by a structure that is bounded by upper and lower surface planes that are separated by a distance h as shown in Figure 1. The x-y coordinate axes are located on the neutral plane of the plate (the "in-plane" directions) and the z-axis is normal to the x-y plane. In the absence of in-plane

loading, the neutral plane is at the midpoint through the thickness. In the present work, it will be assumed that the thickness of plate h is a constant. Consequently, the location of the x-y axes will lie at the mid-surface plane (z=0).

In most plate applications, the external loading includes distributed load normal to the plate (z direction), concentrated loads normal to the plate, or in-plane tensile, bending or shear loads applied to the edge of the plate. Such loading will produce deformations of the plate in the x, y, z coordinate directions which in general can be characterized by displacements $u(x,y,z)$, $v(x,y,z)$ and $w(x,y,z)$ in the x, y and z directions, respectively.

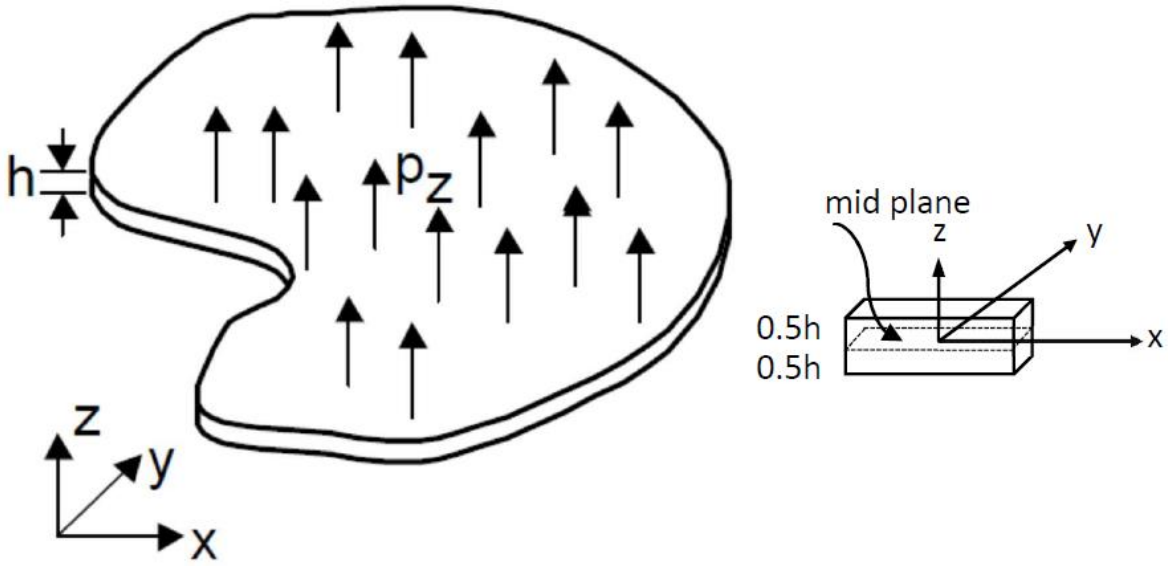

Figure 1. Geometry of thin plate.

The plate is discretized into rectangular ACM (Adini-Clough-Melosh) plate elements. The ACM element is a non-conforming element with 12 degrees of freedom (3 degrees of freedom at each of the four nodes). Degrees of freedom at each node (i) are the transverse displacement and normal rotation about each axis, w_i , $\theta_{xi} = \frac{\partial w_i}{\partial y}$ and $\theta_{yi} = \frac{\partial w_i}{\partial x}$, as illustrated in Figure 2. Note that θ_{yi} is a vector in the *negative* y direction.

Node "1" is selected at the lower left comer of the plate (x=-a, y=-b) and that the nodes are numbered 1,2,3,4 in counterclockwise direction around the plate. We assume that the plate dimensions are given by 2a and 2b as shown in Figure 1 and that the x-y coordinate system is located at the center of plate. The 12 degrees of freedom are arranged in the vector of generalized nodal displacements $\{d\}$ as:

$$\{d\}^T = \{w_1 \quad \theta_{x1} \quad \theta_{y1} \quad w_2 \quad \theta_{x2} \quad \theta_{y2} \quad w_3 \quad \theta_{x3} \quad \theta_{y3} \quad w_4 \quad \theta_{x4} \quad \theta_{y4}\}^T \tag{8}$$

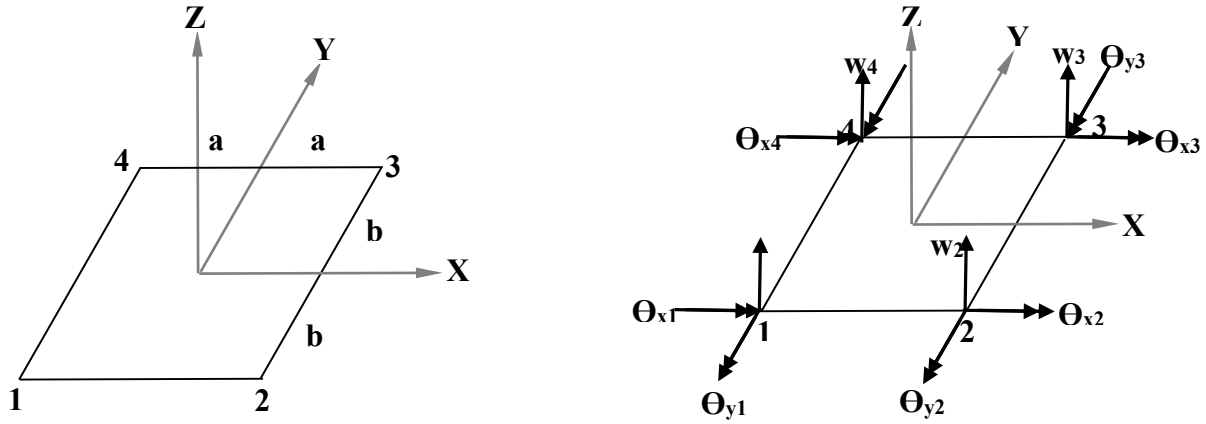

Figure 2. Rectangular element with 12 degrees of freedom.

3.1. STIFFNESS MATRIX AND FORCE VECTOR OF THE ACM PLATE ELEMENT

We assume that $w(x,y)$ is some function over the plate geometry as follows:

$$w(x,y) = a_1 + a_2x + a_3y + a_4x^2 + a_5xy + a_6y^2 + a_7x^3 + a_4x^2y + a_9xy^2 + a_{10}y^3 + a_{11}x^3y + a_{12}xy^3 \quad (9)$$

$$w(x,y) = \begin{bmatrix} 1 & x & y & x^2 & xy & y^2 & x^3 & x^2y & xy^2 & y^3 & x^3y & xy^3 \end{bmatrix} \{\alpha\} \quad (10)$$

which is represented as

$$w(x,y) = \lfloor N(x,y) \rfloor \{\alpha\} \quad (11)$$

$$\begin{Bmatrix} w(x,y) \\ \theta_x \\ \theta_y \end{Bmatrix} = \begin{bmatrix} 1 & x & y & x^2 & xy & y^2 & x^3 & x^2y & xy^2 & y^3 & x^3y & xy^3 \\ 0 & 0 & 1 & 0 & x & 2y & 0 & x^2 & 2xy & 3y^2 & x^3 & 3xy^2 \\ 0 & -1 & 0 & -2x & -y & 0 & -3x^2 & -2xy & -y^2 & 0 & -3x^2y & -y^3 \end{bmatrix} \{\alpha\} \quad (12)$$

Substituting the values of x and y coordinates of nodes 1,2,3,4 of the plate in the Eq. 12 will yield:

$$\{d\} = [\Phi]\{\alpha\} \quad (13)$$

where $\{\alpha\}$ and $\{d\}$ are vector of unknown coefficients and vector of generalized nodal displacements for the element respectively. Substituting $\{\alpha\}$ from Eq. (13) in Eq. (11), we obtain

$$w(x,y) = \lfloor N(x,y) \rfloor [\Phi]^{-1} \{d\} \quad (14)$$

The curvatures of the plate element viz. κ_{xx} , κ_{yy} and κ_{xy} are obtained from the second order partial differentiation of $w(x,y)$ w.r.t x and y as follows:

$$\kappa_{xx} = \frac{\partial^2 w}{\partial x^2} \;\; ; \kappa_{yy} = \frac{\partial^2 w}{\partial x^2} ; \quad \kappa_{xy} = 2\frac{\partial^2 w}{\partial x \partial y} \tag{15}$$

$$\begin{Bmatrix} \kappa_x \\ \kappa_y \\ \kappa_{xy} \end{Bmatrix} = \begin{bmatrix} 0 & 0 & 0 & 2 & 0 & 0 & 6x & 2y & 0 & 0 & 6xy & 0 \\ 0 & 0 & 0 & 0 & 0 & 2 & 0 & 0 & 2x & 6y & 0 & 6xy \\ 0 & 0 & 0 & 0 & 2 & 0 & 0 & 4x & 4y & 0 & 6x^2 & 6y^2 \end{bmatrix} \left[\Phi^{-1}\right]\{d\} \tag{16}$$

Thus the vector of curvatures $\{\kappa^{(e)}\}$ for the plate element can be expressed as

$$\{\kappa^{(e)}\} = \begin{Bmatrix} \kappa_x \\ \kappa_y \\ \kappa_{xy} \end{Bmatrix} = [B][\Phi]^{-1}\{d\} \tag{17}$$

From the moment-curvature relationship $\{M\} = [D]\{\kappa\}$ we obtain

$$\begin{Bmatrix} M_x \\ M_y \\ M_{xy} \end{Bmatrix} = [D]\begin{Bmatrix} \kappa_x \\ \kappa_y \\ \kappa_{xy} \end{Bmatrix} = [D][B][\Phi]^{-1}\{d\} \tag{18}$$

where $[D] = \dfrac{Eh^3}{12(1-\nu^2)} \begin{bmatrix} 1 & \nu & 0 \\ \nu & 1 & 0 \\ 0 & 0 & \dfrac{(1-\nu)}{2} \end{bmatrix}$ (19)

Total potential energy stored in the plate due to bending is given by (Gallagher, 1975; Bathe, 1996)

$$\Pi = \frac{1}{2}\int_{-a}^{a}\int_{-b}^{b} \{\kappa\}^T \{M\} dxdy - \{d\}^T \{P^{(e)}\} = \frac{1}{2}\{d\}^T \left[\Phi^{-1}\right]^T \left(\int_{-a}^{a}\int_{-b}^{b} [B]^T [D][B] dxdy \right) \left[\Phi^{-1}\right]\{d\} - \{d\}^T \{P^{(e)}\} \tag{20}$$

Using the first variation of Π , we obtain,

$$\{P^{(e)}\} = \left[\Phi^{-1}\right]^T \left(\int_{-a}^{a}\int_{-b}^{b} [B]^T [D][B] dxdy \right) \left[\Phi^{-1}\right]\{d\} = \left[K^{(e)}\right]\{d\} \tag{21}$$

where the stiffness matrix $\left[K^{(e)}\right]$ is given as

$$\left[K^{(e)}\right] = \left[\Phi^{-1}\right]^T \left(\int_{-a}^{a}\int_{-b}^{b} [B]^T [D][B] dxdy \right) \left[\Phi^{-1}\right] \tag{22}$$

and the nodal force vector for the plate element $\{P^{(e)}\}$ is given as:

$$\{P^{(e)}\} = [\Phi^{-1}]^T \left(\int_{-a}^{a} \int_{-b}^{b} p_z \lfloor N(x,y) \rfloor^T dxdy \right) \tag{23}$$

4. Interval Finite Element Model of the Plate

An element-by-element (EBE) technique is utilized for element assembly as outlined in section 2. Interval uncertainty is considered in pressure $\boldsymbol{p}_z$ and Young's modulus of the plate $\boldsymbol{E}$. Accordingly, the stiffness matrix and the force vector of the plate element are rewritten, denoting interval quantities in boldface, as follows:

$$[\boldsymbol{K}^{(e)}] = \int_{-a}^{a} \int_{-b}^{b} [B\Phi^{-1}]^T [\boldsymbol{D}] [B\Phi^{-1}] dxdy \tag{24}$$

and

$$\{\boldsymbol{P}^{(e)}\} = [\Phi^{-1}]^T \left(\int_{-a}^{a} \int_{-b}^{b} \boldsymbol{p}_z [N(x,y)]^T dxdy \right) \tag{25}$$

For convenience, $[B\Phi^{-1}]$ is denoted as $[B_1]$. Thus Equation (24) can be rewritten as

$$[\boldsymbol{K}^{(e)}] = \int_{-a}^{a} \int_{-b}^{b} [B_1]^T [\boldsymbol{D}] [B_1] dxdy \tag{26}$$

The $[\boldsymbol{D}]$ matrix appearing in the above equation is an interval matrix owing to the uncertainty of Young's modulus $\boldsymbol{E}$. It can be expressed as follows:

$$[\boldsymbol{D}] = \frac{Eh^3}{12(1-\nu^2)} \begin{bmatrix} 1 & \nu & 0 \\ \nu & 1 & 0 \\ 0 & 0 & \dfrac{(1-\nu)}{2} \end{bmatrix} = \begin{bmatrix} \dfrac{Eh^3}{12(1-\nu^2)} & \dfrac{Eh^3\nu}{12(1-\nu^2)} & 0 \\ \dfrac{Eh^3\nu}{12(1-\nu^2)} & \dfrac{Eh^3}{12(1-\nu^2)} & 0 \\ 0 & 0 & \dfrac{Eh^3}{24(1+\nu)} \end{bmatrix} \tag{27}$$

where $\boldsymbol{E}$ is the interval Young's modulus and ν is the Poisson's ratio.

Following the work of Xiao et.al., (Xiao, Fedele and Muhanna, 2013), the $[\boldsymbol{D}]$ matrix is decomposed as follows:

$$[\boldsymbol{D}] = A_k \, diag(\boldsymbol{\Lambda}_k \boldsymbol{\alpha}_k) A_k^T \tag{28}$$

where $\boldsymbol{\alpha}_k = \boldsymbol{E}$; $\boldsymbol{\Lambda}_k = \left\{ \frac{h^3}{12(1-\nu^2)} \quad \frac{h^3}{12} \quad \frac{h^3}{24(1+\nu)} \right\}^T$; $A_k = \begin{bmatrix} 1 & 0 & 0 \\ \nu & 1 & 0 \\ 0 & 0 & 1 \end{bmatrix}$ (29)

Applying numerical integration to Eq. (26), then

$$\left[\boldsymbol{K}^{(e)}\right] = \sum_{i=1}^{M}\sum_{j=1}^{N} w_i w_j B_1^T(x_i, y_i)\tilde{D}(x_i, y_i)B_1(x_i, y_i) \tag{30}$$

that leads to $$\left[\boldsymbol{K}^{(e)}\right] = \sum_{i=1}^{M}\sum_{j=1}^{N} w_i w_j B_1^T(x_i, y_i) A_k \, diag(\boldsymbol{\Lambda}_k \boldsymbol{\alpha}_k) A_k^T B_1(x_i, y_i) \tag{31}$$

Eq. (31) can be rewritten as

$$\left[\boldsymbol{K}^{(e)}\right] = \left\lfloor B_1^T(x_1, y_1)A_k \quad B_2^T(x_2, y_2)A_k \quad \ldots \right\rfloor \begin{bmatrix} diag(\boldsymbol{\Lambda}_k \boldsymbol{\alpha}_k(x_1, y_1)) & & \\ & diag(\boldsymbol{\Lambda}_k \boldsymbol{\alpha}_k(x_1, y_1)) & \\ & & \ldots \end{bmatrix} \begin{Bmatrix} A_k^T B_1(x_1, y_1) \\ A_k^T B_1(x_2, y_2) \\ \ldots \end{Bmatrix} \tag{32}$$

So the decomposition for the element stiffness matrix $\left[\boldsymbol{K}^{(e)}\right]$ is expressed as

$$\left[\boldsymbol{K}^{(e)}\right] = \left[A^{(e)}\right] diag(\Lambda \boldsymbol{\alpha}) \left[A^{(e)}\right]^T \tag{33}$$

The stiffness matrix of the structure $\boldsymbol{K}$ is obtained from the element stiffness matrices $\boldsymbol{K}^{(e)}$ described in Eq. (33) as follows:

$$[\boldsymbol{K}] = \begin{bmatrix} \boldsymbol{K}_1^{(e)} & & & \\ & \boldsymbol{K}_2^{(e)} & & \\ & & \boldsymbol{K}_3^{(e)} & \\ & & & \ldots \end{bmatrix} = \begin{bmatrix} A_1^{(e)} & A_2^{(e)} & A_3^{(e)} & \ldots \end{bmatrix} \begin{bmatrix} diag(\Lambda_1 \boldsymbol{\alpha}_1) & & & \\ & diag(\Lambda_2 \boldsymbol{\alpha}_2) & & \\ & & diag(\Lambda_3 \boldsymbol{\alpha}_3) & \\ & & & \ldots \end{bmatrix} \begin{Bmatrix} A_1^{T(e)} \\ A_2^{T(e)} \\ A_3^{T(e)} \\ \ldots \end{Bmatrix} \tag{34}$$

This can be denoted as

$$[\boldsymbol{K}] = [A][\boldsymbol{D}][A]^T \tag{35}$$

When each plate element is subjected to an interval pressure $\boldsymbol{p}_z$, the corresponding interval force vector $\{\boldsymbol{P}\}$ described in Eq. (23) for the structure can be defined using the M matrix approach outlined by the authors (Muhanna and Mullen, 1999) as follows:

$$\{\boldsymbol{P}\}_{n\times 1} = \begin{Bmatrix} \boldsymbol{P}_1^{(e)} \\ \boldsymbol{P}_2^{(e)} \\ \boldsymbol{P}_3^{(e)} \\ \ldots \end{Bmatrix} = [M]_{n\times m}[\boldsymbol{\delta}]_{m\times 1} \tag{36}$$

where n is the number of degrees of freedom for the structure and m is the number of elements. Each column of $[M]$ matrix contains the contribution of deterministic pressure p_z on each plate element and the interval vector $\{\boldsymbol{\delta}\}$ contains interval multipliers corresponding to pressures acting on each of the m elements of the structure. In addition, the vector of point loads acting on the nodes of the structure can be represented as $\{\boldsymbol{P}_c\}$.

The current interval formulation is based on the Element-By-Element (EBE) finite element technique (Muhanna and Mullen, 2001; Rama Rao, Mullen and Muhanna, 2011). In the EBE method, each element has its own set of nodes, but the set of elements is disassembled, so that a node belongs to a single element. A set of additional constraints is introduced to force unknowns associated with coincident nodes to have identical values. Thus, the constraint equation $CU = V$ takes the form

$$[C]\{\boldsymbol{U}\} = 0 \tag{37}$$

where the constraint matrix C is a deterministic one (fixed point matrix). Eq. (17) can be rewritten to represent the interval form of strain-curvature relationship as

$$\{\boldsymbol{\kappa}^{(e)}\} = [B][\Phi]^{-1}\{\boldsymbol{d}\} \tag{38}$$

where $\{\boldsymbol{d}\}$ is the vector of nodal displacements for the element. At the global level, this relation can be expressed as

$$[B_1]\{U\} = \{\boldsymbol{\kappa}\} \tag{39}$$

where $[B_1]$ is the strain-curvature matrix and $\{\boldsymbol{\kappa}\}$ is the vector of interval curvatures for the structure. Eq. (39) can be used as an additional constraint in addition to Eq. (37). Thus the modified potential energy Π^* can be expressed as

$$\Pi^* = \frac{1}{2}\{\boldsymbol{U}\}^T[\boldsymbol{K}]\{\boldsymbol{U}\} - \{\boldsymbol{U}\}^T\{\boldsymbol{P}\} + \lambda_1^T([C]\{\boldsymbol{U}\} - \{V\}) + \lambda_2^T([B_1]\{\boldsymbol{U}\} - \{\boldsymbol{\kappa}\}) \tag{40}$$

Invoking the stationarity of Π^*, that is $\delta\Pi^* = 0$, and considering Eq. (40), we obtain

$$\left(\begin{pmatrix} \boldsymbol{0} & C^T & B_1^T & 0 \\ C & 0 & 0 & 0 \\ B_1 & 0 & 0 & -I \\ 0 & 0 & -I & 0 \end{pmatrix} + \begin{bmatrix} A \\ 0 \\ 0 \\ 0 \end{bmatrix}[\boldsymbol{D}][A \quad 0 \quad 0 \quad 0]\right)\begin{pmatrix} \boldsymbol{U} \\ \boldsymbol{\lambda_1} \\ \boldsymbol{\lambda_2} \\ \kappa \end{pmatrix} = \begin{pmatrix} \boldsymbol{P_C} \\ 0 \\ 0 \\ 0 \end{pmatrix} + \begin{Bmatrix} M \\ 0 \\ 0 \\ 0 \end{Bmatrix}\{\boldsymbol{\delta}\} \tag{41}$$

where λ_1 and λ_2 are vectors of Lagrange Multipliers. The solution of Eq. (41) will provide the values of interval displacements $\boldsymbol{U}$ (primary unknowns) as well as interval values of $\{\boldsymbol{\lambda_1}\}$, $\{\boldsymbol{\lambda_2}\}$ and $\{\boldsymbol{\kappa}\}$ (secondary unknowns) with the same level of sharpness (Rama Rao, Mullen and Muhanna ,2011). It is further observed from Eq. (41) that the Lagrange multipliers $\{\boldsymbol{\lambda_2}\}$ have zero value.

$$\left(\begin{pmatrix} \boldsymbol{0} & C^T & B_1^T & 0 \\ C & 0 & 0 & 0 \\ B_1 & 0 & 0 & -I \\ 0 & 0 & -I & 0 \end{pmatrix}\begin{pmatrix} \boldsymbol{K} & 0 & 0 & 0 \\ 0 & 0 & 0 & 0 \\ 0 & 0 & 0 & 0 \\ 0 & 0 & 0 & 0 \end{pmatrix}\right)\begin{pmatrix} \boldsymbol{U} \\ \boldsymbol{\lambda_1} \\ \boldsymbol{\lambda_2} \\ \boldsymbol{\kappa} \end{pmatrix} = \begin{pmatrix} \boldsymbol{P_C} \\ 0 \\ 0 \\ 0 \end{pmatrix} + \begin{Bmatrix} [M] \\ 0 \\ 0 \\ 0 \end{Bmatrix}\{\boldsymbol{\delta}\} \tag{42}$$

Eq. (41) is now similar to Eq. (3) and thus can be solved using the Neumaier's approach outlined in section 2. The vector of interval moments $\{\boldsymbol{M}\}$ can be obtained from the vector of interval curvatures $\{\boldsymbol{\kappa}\}$ as

$$\begin{Bmatrix} \boldsymbol{M}_x \\ \boldsymbol{M}_y \\ \boldsymbol{M}_{xy} \end{Bmatrix} = [\boldsymbol{D}]\begin{Bmatrix} \boldsymbol{\kappa}_x \\ \boldsymbol{\kappa}_y \\ \boldsymbol{\kappa}_{xy} \end{Bmatrix} = \frac{\boldsymbol{E}h^3}{12(1-\nu^2)}\begin{bmatrix} 1 & \nu & 0 \\ \nu & 1 & 0 \\ 0 & 0 & \dfrac{(1-\nu)}{2} \end{bmatrix}\begin{Bmatrix} \boldsymbol{\kappa}_x \\ \boldsymbol{\kappa}_y \\ \boldsymbol{\kappa}_{xy} \end{Bmatrix} \tag{43}$$

The applicability of the procedure outlined above is illustrated by solving numerical examples in the next section.

5. Example Problems

A thin rectangular plate with clamped edges is chosen to illustrate the applicability of the present approach to handle uncertainty in load and material properties in case of thin plate problems. These examples are chosen to demonstrate the ability of the current approach to obtain sharp bounds to the displacements and forces even in the presence of large number of interval variables. The two example problems are solved for various levels of interval widths of the loads centered at their nominal values. All interval variables are assumed to vary independently. Solution procedure outlined in the previous sections is used to perform the linear interval finite element analysis. The material and geometric properties of the plate are given in Table 1 below. The discretization scheme adopted is shown in Figure 3.

Table 1. Properties of rectangular plate and discretization scheme.

Length Lx	2.0 m
Width Ly	3.0 m
Thickness	0.025 m
Young's modulus	210 GPa
Poisson's ratio ν	0.3
Applied Pressure p_z	14.0×10^3 Pa
Number of divisions along x-axis	nx
Number of divisions along y-axis	ny
Notation for discretization scheme	$nx \times ny$

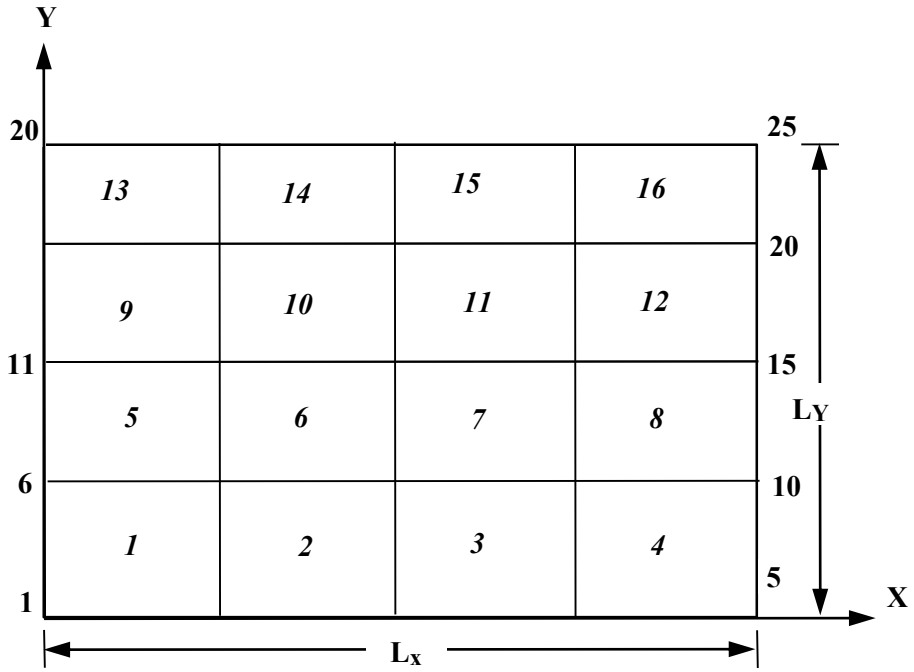

Figure 3. Discretization scheme of rectangular plate.

First the present interval approach is validated by solving the problem of a rectangular plate with a 4x4 discretization scheme. Solution is computed using the present interval approach and combinatorial solution. The computation of results for combinatorial solution required computation of results for 2^{16}=65,536 combinations.

The results obtained for clamped plate for vertical displacement at center of the plate (at node 13), slope θ_y at node 12 and slope θ_x at node 7 at various levels of uncertainty of Young's modulus (E) are shown in Figure 4 , Figure 5 and Figure 6 respectively. Figure 7 and Figure 8 show the variation of M_{xx} and M_{yy} at the center of the plate (at node 13) at various levels of uncertainty of Young's modulus (E). These figures show the lower and upper bounds of the present interval solution and the corresponding results of the combinatorial solution for various levels of uncertainty of Young's modulus from 0 percent to 10 percent. It is observed from these figures that the bounds of the present interval solution sharply enclose the bounds of combinatorial solution at all levels of uncertainty.

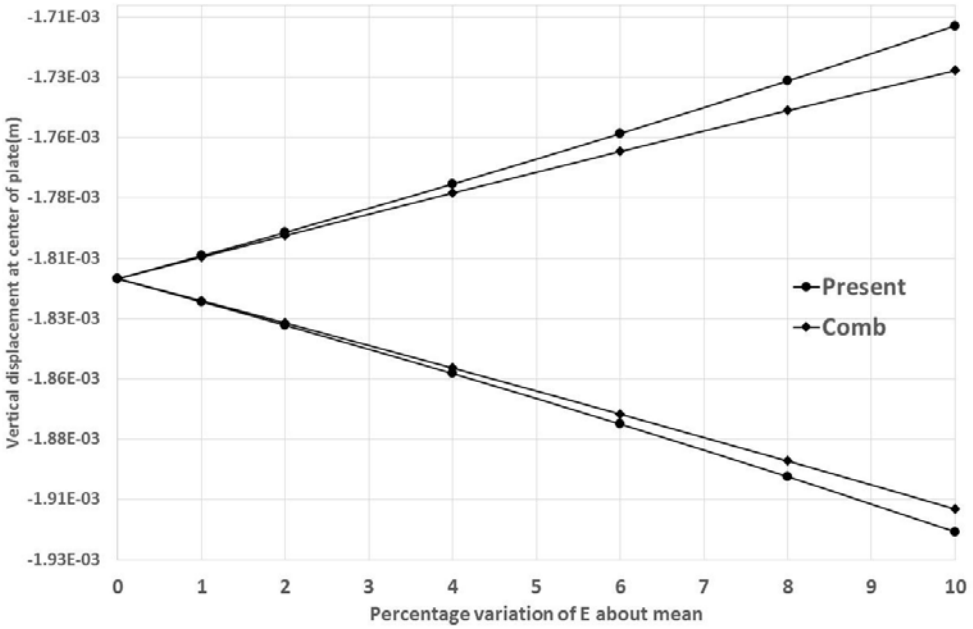

Figure 4. Clamped plate- variation of vertical displacement w_z of center of plate (at node 13) w.r.t. uncertainty of E.

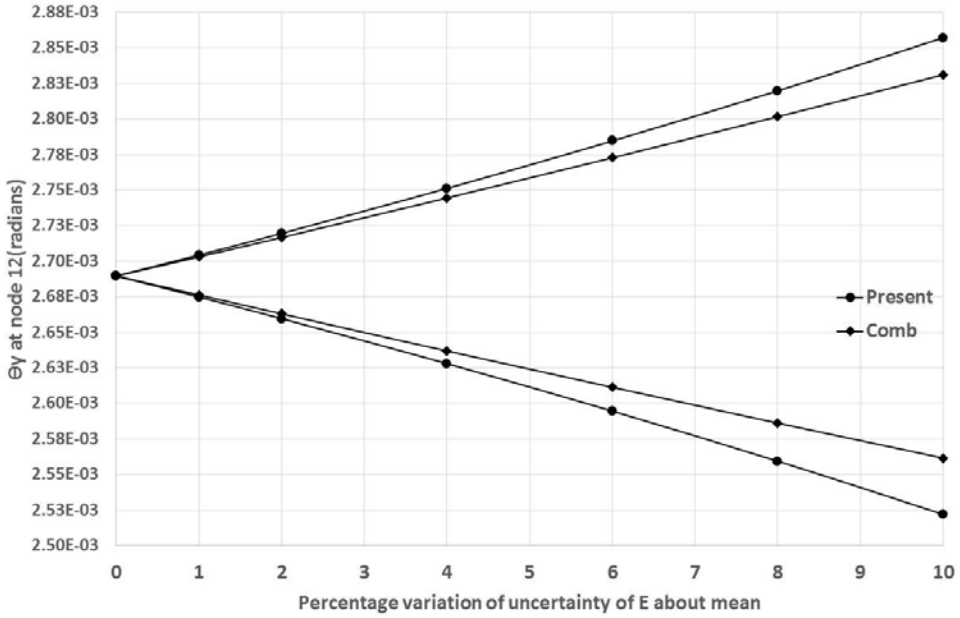

Figure 5. Clamped plate- variation of θ_y at node 12 w.r.t. uncertainty of E.

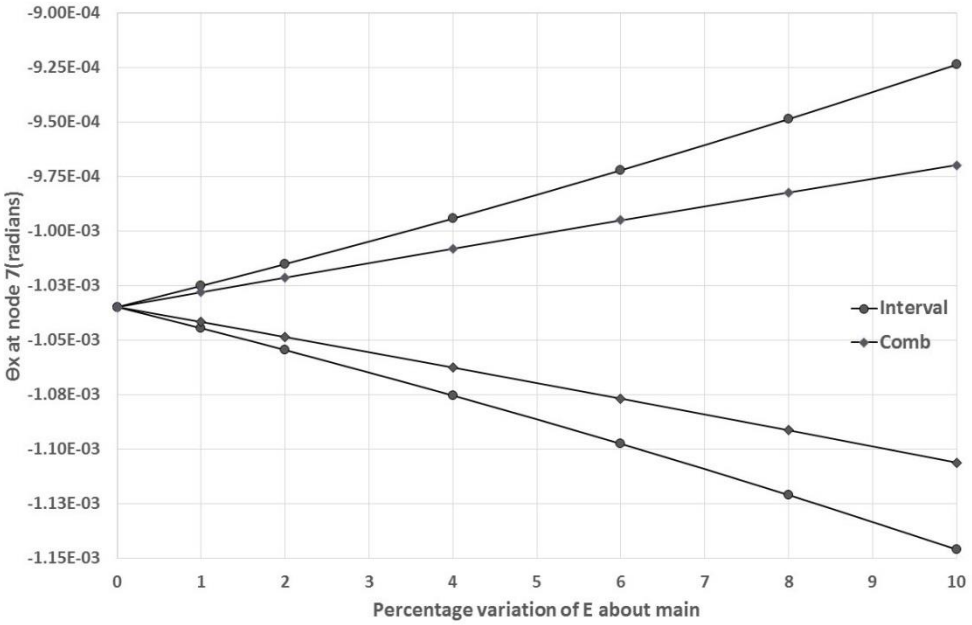

Figure 6. Clamped plate- variation of θ_x at node 7 w.r.t. uncertainty of E.

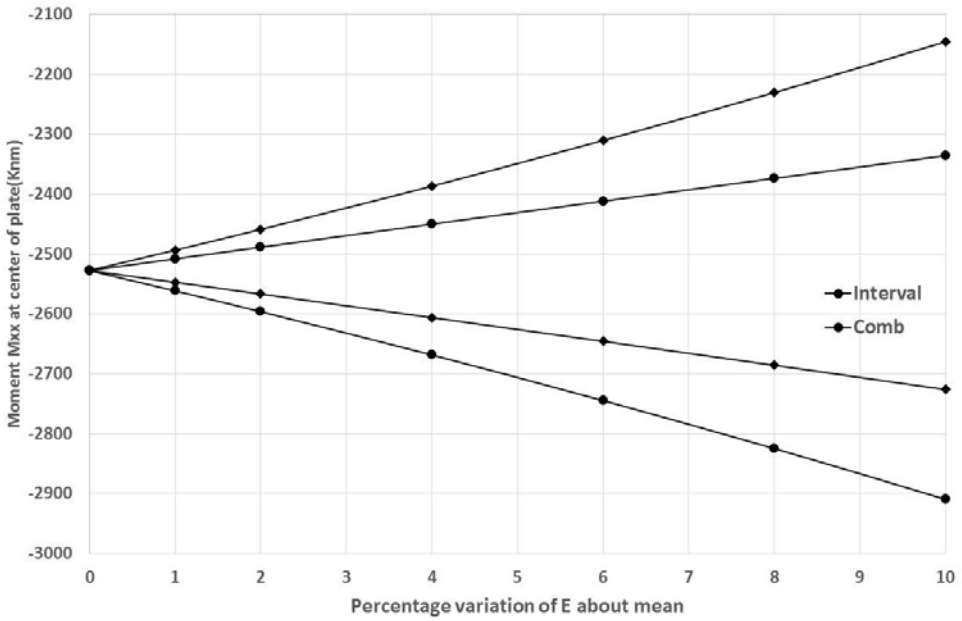

Figure 7. Clamped plate- variation of M_{xx} at center of plate (at node 13) w.r.t. uncertainty of E.

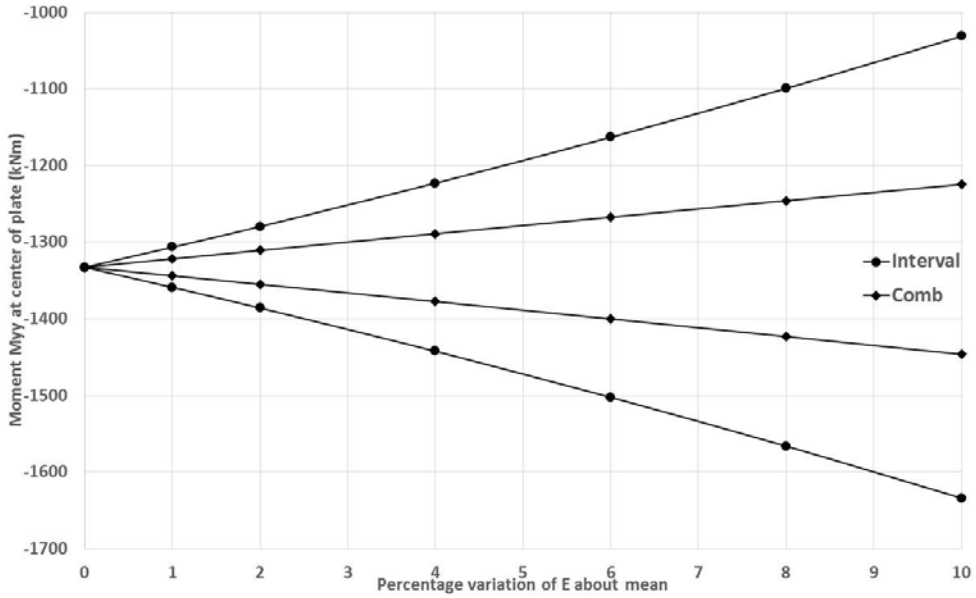

Figure 8. Clamped plate- variation of M_{yy} at center of plate (at node 13) w.r.t. uncertainty of E.

Results are computed for the 4×4 plate for the following cases:

A) Load uncertainty of 10 percent (±5 percent variation of load about its mean value) alone is present
B) 1 percent uncertainty of E(±0.5 percent variation of E about its mean value) alone
C) Load uncertainty of 10 percent along with 1 percent uncertainty of E.

Tables 2, 3 and 4 present the results of selected displacements and rotations corresponding to cases A, B and C respectively. Similarly, Tables 5, 6 and 7 present the results of moments at the center of the plate corresponding to cases A, B and C respectively.

It is observed from the Tables 2 and 5 that the results of the interval solution coincide with those obtained using combinatorial approach and thus provide exact bounds to the combinatorial solution. It is observed from Tables 3 and 6 that the interval solution gives sharp bounds to the values of selected displacements and rotations w.r.t the corresponding values obtained using combinatorial solution. As already mentioned, these solutions required computation of 2^{16} =65536 combinations. Tables 4 and 7 show the results computed for 10 percent load uncertainty along with 1 percent uncertainty of Young's modulus E. It is impractical to compute combinatorial solution in this case, as it would require computation of solution for $2^{16}\times2^{16}$=4,294,967,296 combinations. Instead, the bounds of the solution are computed using MCS (Monte-Carlo Simulations). The results computed in Tables 4 and 7 are for 20,000 simulations. It is to be noted here that the results obtained using MCS provide inner bounds to the combinatorial solution whereas the results obtained using interval solution provide outer bounds to the combinatorial solution.

Table 2. Clamped rectangular plate (4×4)– selected displacements and rotations of the plate for 10% uncertainty of load (Case-A).

Method	$w_{13}\times10^3$(m)		$\theta_x \times10^3$(radians) at node 7		$\theta_y \times10^3$(radians) at node 12	
	Lower	Upper	Lower	Upper	Lower	Upper
Combinatorial	-1.90416	-1.72281	-1.10534	-0.96432	2.55516	2.82412
Interval	-1.90416	-1.72281	-1.10534	-0.96432	2.55516	2.82412
Error%	0.0	0.0	0.0	0.0	0.0	0.0

Table 3. Clamped rectangular plate(4×4)- selected displacements and rotations of the plate for 1% uncertainty of E (Case-B).

Method	$w_{13}\times10^3$(m)		$\theta_x \times10^3$(radians) at node 7		$\theta_y \times10^3$(radians) at node 12	
	Lower	Upper	Lower	Upper	Lower	Upper
Combinatorial	-1.82260	-1.80446	-1.04167	-1.02805	2.67626	2.70315
Interval	-1.82302	-1.80395	-1.04455	-1.02510	2.67482	2.70446
Error%	0.023	0.028	0.276	0.287	0.054	0.048

Table 4. Clamped rectangular plate(4×4)- selected displacements and rotations of the plate for 10% uncertainty of load and 1% uncertainty of E (Case–C).

Method	$w_{13}\times10^3$(m)		$\theta_x \times10^3$(radians) at node 7		$\theta_y \times10^3$(radians) at node 12	
	Lower	Upper	Lower	Upper	Lower	Upper
MCS	-1.87530	-1.74648	-1.07575	-0.97905	2.59554	2.78867
Interval	-1.91180	-1.71030	-1.10937	-0.94955	2.54020	2.84412
Error%	1.946	2.072	3.125	3.013	2.132	1.988

Table 5. Clamped rectangular plate (4×4)- moments at the center of the plate for 10% uncertainty of load (Case-A).

Method	M_{xx} (kN) at node 13		$M_{yy} \times10^3$(kN) at node 13	
	Lower	Upper	Lower	Upper
Comb	-2653.612	-2400.887	-1421.684	-1243.397
Interval	-2653.612	-2400.887	-1421.684	-1243.397
Error%	0.0	0.0	0.0	0.0

Table 6. Clamped rectangular plate (4×4)- moments at the center of the plate for 1% uncertainty of E (Case-B).

Method	M_{xx} (kN) at node 13		$M_{yy} \times10^3$(kN) at node 13	
	Lower	Upper	Lower	Upper
Comb	-2546.794	-2507.773	-1343.636	-1321.502
Interval	-2561.199	-2493.300	-1358.769	-1306.311
Error%	0.566	0.577	1.126	1.150

Table 7. Clamped rectangular plate (4×4)- moments at the center of the plate for 10% uncertainty of load and 1% uncertainty of E (Case-C).

Method	M_{xx} (kN) at node 13		M_{yy} ×10^3(kN) at node 13	
	Lower	Upper	Lower	Upper
MCS	-2612.438	-2425.942	-1383.487	-1259.684
Interval	-2678.945	-2358.225	-1434.310	-1211.391
Error%	2.546	2.791	3.674	3.834

Figure 9 presents the variation of the lower and upper bounds of the interval displacement w_z along the length and width of the plate respectively. Figure 10 presents the variation of the lower and upper bounds of the slope θ_x along the width of the plate. Figure 11 presents the variation of the lower and upper bounds of the slope θ_y along the length of the plate.

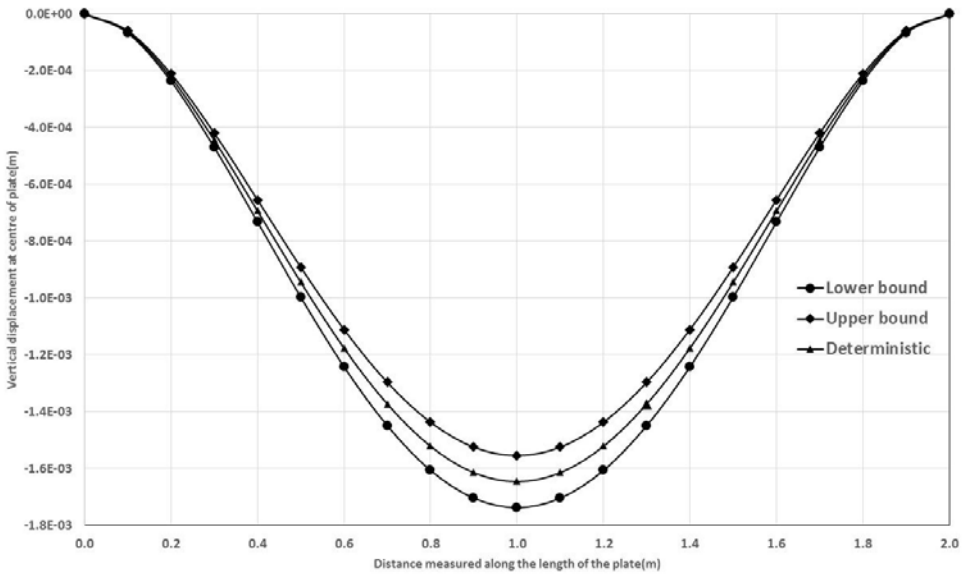

Figure 9. Clamped plate- variation of vertical displacement along the length of the plate with 10% uncertainty of load and 1% uncertainty of E.

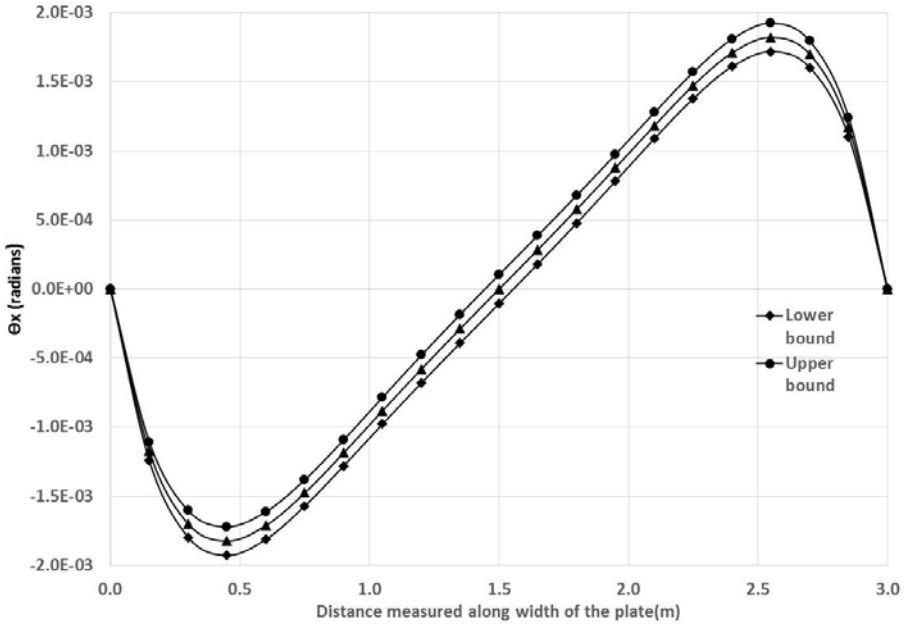

Figure 10. Clamped plate- variation of θ_x along the width of the plate with 10% uncertainty of load and 1% uncertainty of E.

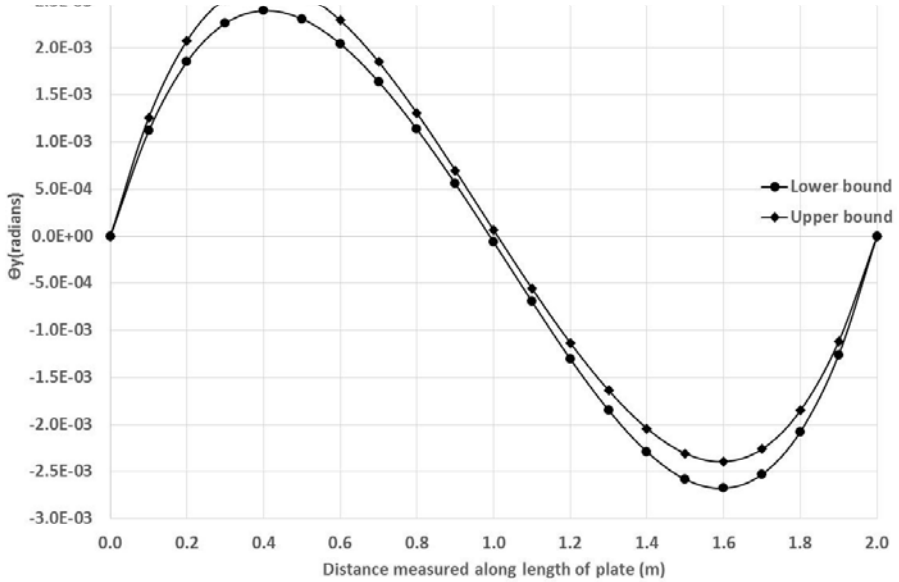

Figure 11. Clamped plate- variation of θ_y along the length of the plate with 10% uncertainty of load and 1% uncertainty of E.

Tables 8, 9 and 10 present the values of selected displacements and rotations for a discretization scheme of 20×20 (400 elements) for cases A, B and C respectively. Similarly, Tables 11, 12 and 13 present the values of moments at the center of the plate for cases A, B and C respectively. It is to be noted here that the computation of combinatorial solution for cases A or B would require 2^{400} combinations while it would require computation of 2^{800} combinations for case C. Thus it is practically impossible for to compute the combinatorial solution. Instead, the results of the bounds obtained using 10000 Monte Carlo simulations are presented. It is here to be noted that the bounds of the interval solution enclose the corresponding bounds of the combinatorial solution from outside. On the other hand, the bounds of the results computed using Monte Carlo solution enclose the corresponding bounds of combinatorial solution from inside. It is to be further noted that the percentage error reported in Tables 5 *through* 13 can be reduced by increasing the number of simulations. However it is observed that it is computationally time consuming.

Table 8. Clamped rectangular plate (20×20)– displacements at the center of the plate for 10% uncertainty of load (Case-A).

Method	$w_{221}\times10^3$(m)		$\theta_x\times10^3$(radians) at node 111		$\theta_y\times10^3$(radians) at node 216	
	Lower	Upper	Lower	Upper	Lower	Upper
MCS	-1.65855	-1.63336	-8.43218	-8.25503	2.42576	2.46399
Interval	-1.72747	-1.56295	-8.85896	-7.81985	2.32204	2.56667
Error%	4.155	4.311	5.061	5.272	4.276	4.167

Table 9. Clamped rectangular plate (20×20)– displacements center of the plate for 1% uncertainty of E (Case-B).

Method	$w_{221}\times10^3$(m)		$\theta_x\times10^4$(radians) at node 111		$\theta_y\times10^3$(radians) at node 216	
	Lower	Upper	Lower	Upper	Lower	Upper
MCS	-1.64694	-1.64384	-8.35812	-8.32283	2.44201	2.44683
Interval	-1.65386	-1.63656	-8.42754	-8.25127	2.43025	2.45845
Error%	0.420	0.443	0.831	0.860	0.482	0.475

Table 10. Clamped rectangular plate (20×20)– displacements at the center of the plate for 10% uncertainty of load and 1% uncertainty of E (Case-C).

Method	$w_{221}\times10^3$(m)		$\theta_x\times10^3$(radians) at node 111		$\theta_y\times10^3$(radians) at node 216	
	Lower	Upper	Lower	Upper	Lower	Upper
MCS	-1.66052	-1.63068	-8.43013	-8.25141	2.42244	2.46768
Interval	-1.73665	-1.55377	-8.95341	-7.72540	2.30699	2.58172
Error%	4.585	4.716	6.207	6.375	4.766	4.621

Table 11. Clamped rectangular plate (20×20)– moments center of the plate for 10% uncertainty of load (Case-A).

Method	M_{xx} (kN) at node 221		$M_{yy}\times10^3$(kN) at node 221	
	Lower	Upper	Lower	Upper
MCS	-2096.211	-2057.435	-1154.767	-1124.961
Interval	-2180.916	-1973.210	-1204.756	-1077.381
Error%	4.041	4.094	4.329	4.229

Table 12. Clamped rectangular plate (20×20)– moments at the center of the plate for 1% uncertainty of E (Case-B).

Method	M_{xx} (kN) at node 221		$M_{yy} \times 10^3$(kN) at node 221	
	Lower	Upper	Lower	Upper
MCS	-2088.860	-2064.535	-1146.630	-1135.780
Interval	-2127.365	-2026.761	-1175.676	-1106.461
Error%	1.843	1.830	2.533	2.581

Table 13. Clamped rectangular plate (20×20)– moments at the center of the plate for 10% uncertainty of load and 1% uncertainty of E (Case-C).

Method	M_{xx} (kN) at node 221		$M_{yy} \times 10^3$(kN) at node 221	
	Lower	Upper	Lower	Upper
MCS	-2108.068	-2051.424	-1161.423	-1121.883
Interval	-2234.305	-1919.821	-1242.057	-1040.080
Error%	5.988	6.415	6.943	7.292

6. Conclusion

A linear Interval Finite Element Method (IFEM) for structural analysis of thin plates is presented. Uncertainty in the applied load and Young's modulus is represented as interval numbers. Results are also computed using combinatorial solution and Monte Carlo simulations as appropriate. Example problems illustrate the applicability of the present approach to the problem of predicting the structural behavior of thin plates in the presence of uncertainties.

Acknowledgements

The first author would like to gratefully acknowledge the help received via international travel funding by the Technical Education Quality Improvement Program (TEQIP- Phase II) of Government of India and its sanction by the administration of Vasavi College of Engineering, Hyderabad, India.

References

Bathe, K. Finite Element Procedures, Prentice Hall, Englewood Cliffs, New Jersey 07632, New Jersey, 1996.

Batista, M. Uniformly Loaded Rectangular Thin Plates with Symmetrical Boundary Conditions. Cornel University Library, USA, http://arxiv.org/abs/1001.3016,2010.

Dessombz, O., F. Thouverez, J.-P. Laîné, and L. Jézéquel. Analysis of mechanical systems using interval computations applied to finite elements methods. *J. Sound. Vib.*, 238(5):949-968, 2001.

Gallagher, R. H. Finite Element Analysis Fundamentals, Prentice Hall, Englewood Cliffs, USA, 1975.

Knüppel,O. PROFIL / BIAS — A Fast Interval Library. Computing, 53:277–287, 1994.

Köylüoglu, U., S. Cakmak, N. Ahmet and R. K. Soren. Interval Algebra to Deal with Pattern Loading and Structural Uncertainty. *Journal of Engineering Mechanics* 121(11): 1149–1157, 1995.

Lim, C.W., S. Cui, W. A. Yao. On new symplectic elasticity approach for exact bending solutions of rectangular thin plates with two opposite sides simply supported, International Journal of Solids and Structures, Volume 44(16):5396-5411, 2007.

Moore, R., E. Interval Analysis, Prentice-Hall, Englewood Cliffs, N.J., 1966.

Moore, R. E. *Methods and applications of interval analysis*, SIAM, Philadelphia, 1979.

Moore, R. E., R. B. Kearfott, M. J. Cloud. Introduction to Interval analysis, SIAM, 2009.

Muhanna, R. L. and R. L. Mullen. Development of Interval Based Methods for Fuzziness in Continuum Mechanics. In Proceedings of *ISUMA-NAFIPS'95*: *17-20 September, IEEE, 1995*.

Muhanna, R. L. and R. L. Mullen. Uncertainty in Mechanics Problems—Interval-Based Approach, *Journal of Engineering Mechanics* 127(6): 557–566, 2001.

Muhanna, R. L., H. Zhang and R. L. Mullen. Interval finite element as a basis for generalized models of uncertainty in engineering mechanics. *Reliable Computing*, 13(2):173–194, 2007.

Nakagiri, S. and N. Yoshikawa. Finite Element Interval Estimation by Convex Model. *In Proceedings of 7th ASCE EMD/STD Joint Specialty Conference on Probabilistic Mechanics and Structural Reliability, WPI, MA, 7.-9. August, 1996.*

Neumaier, A. *Interval methods for systems of equations*, Cambridge University Press, 1990.

Neumaier, A. and A. Pownuk. Linear Systems with Large Uncertainties, with Applications to Truss Structures, *Reliable Computing*, 13(2):149-172, 2007.

Pownuk, A. Efficient method of solution of large scale engineering problems with interval parameters." *Proc. NSF workshop on reliable engineering computing* (REC2004), R. L. Muhanna and R. L. Mullen, eds., Savannah, GA, USA, 2004.

Rama Rao, M. V., R. L. Mullen, R. L. Muhanna. A New Interval Finite Element Formulation with the Same Accuracy in Primary and Derived Variables, International Journal of Reliability and Safety, Vol. 5, Nos. ¾, 2011.

Rao, S. S. and P. Sawyer. Fuzzy finite element approach for analysis of imprecisely defined systems. *AIAA J.*, 33(12):2364–2370, 1995.

Rao, S. S. and L. Berke. Analysis of uncertain structural systems using interval analysis. *AIAA J.,* 35(4):727–735, 1997.

Rao, S. S. and Li Chen. Numerical solution of fuzzy linear equations in engineering analysis. *International Journal of Numerical Methods in Engineering.*,43:391–408, 1998.

Reddy, J.N. *Theory and Analysis of Elastic Plates and Shells*. Second edition. CRC Press. Taylor and Francis group, Boca Raton, London and New York, 2007.

Rump, S.M. INTLAB - INTerval LABoratory. In Tibor Csendes, editor, Developments in Reliable Computing*,* pages 77-104. Kluwer Academic Publishers, Dordrecht, 1999.

Sun microsystems. *Interval arithmetic in high performance technical computing*. Sun microsystems. (A White Paper), 2002.

Szilard, R. *Theories and Applications of Plate Analysis: Classical Numerical and Engineering Methods,* 2004.

Wiley Timoshenko, S. and S. Woinowsky-Krieger. *Theory of Plates and Shells.* Second edition. McGraw Hill, 1959.

Xiao, N., F. Fedele and R. L. Muhanna. *Inverse Problems Under Uncertainties-An Interval Solution for the Beam Finite Element*, in Deodatis, B. R. Ellingwood, D. M. Frangopol, Icossar, ISBN: 978-1-138-00086-5, 2013.

Zhang, H. Nondeterministic Linear Static Finite Element Analysis: An Interval Approach. *Ph.D. Dissertation, Georgia Institute of Technology, School of Civil and Environmental Engineering*, 2005.

A New Interval Finite Element Method: Computational Issues

Alba Sofi[1)] and Eugenia Romeo[2)]
[1)]*Department of Architecture and Territory (dArTe) and Inter-University Centre of Theoretical and Experimental Dynamics, University "Mediterranea" of Reggio Calabria, 89124, Reggio Calabria Italy, alba.sofi@unirc.it*
[2)]*Department of Civil, Energy, Environmental and Materials Engineering, University "Mediterranea" of Reggio Calabria, 89124 Reggio Calabria, Italy, eugenia.romeo@unirc.it*

Abstract: This paper deals with finite element analysis of linear structures with uncertain parameters modeled as interval variables. Uncertainties are handled by means of the *improved interval analysis via extra unitary interval* which enables to keep track of the dependencies between interval variables and thus reduce overestimation affecting both the assembly and solution phases of finite element procedures. Approximate explicit expressions of the bounds of the interval displacements are derived by applying the so-called *Interval Rational Series Expansion*. The computational efficiency of the method is enhanced by performing a preliminary sensitivity analysis to identify the most influential parameters on the selected response quantity. Numerical results are presented to demonstrate the accuracy and efficiency of the proposed procedure.

Keywords: finite element method, interval uncertainties, improved interval analysis, explicit expressions, sensitivity analysis, lower bound and upper bound

1. Introduction

Propagation of uncertainties affecting the design parameters has attracted the attention of several researchers over the last decades (Ayyub and Klir, 2006). Indeed, it is widely recognized that small variations of the input parameters may seriously affect the performance of an engineering system. In this context, the key issue is the selection of an appropriate mathematical model of uncertainty based on available empirical information. As known, the most widely used representation of uncertainties arising in engineering problems is the probabilistic one which is based on the concepts of random variable and random field characterized by appropriate Probability Density Functions (PDFs). In recent years, alternative uncertainty models based on non-probabilistic concepts (Elishakoff and Ohsaki, 2010; Corotis, 2015) have gained increasing importance in engineering applications. Such models turn out to be effective tools to describe and process uncertainties described by incomplete of fragmentary data, as happens in early design stages. Among non-probabilistic approaches, the interval model, originally developed on the basis of the interval analysis (Moore, 1996; Moore et al., 2009), has attracted the attention of many researchers mainly because of its simplicity and the small amount of required information. This model represents uncertainties as interval variables with given lower bound (LB) and upper bound (UB). No information is provided on the frequency of occurrence of values between the LB and UB.

The interval model of uncertainty has been extensively used in the context of finite element structural analysis giving rise to the so-called Interval Finite Element Method (IFEM). For a general overview of the

state-of-art and recent advances in interval finite element analysis, readers are referred to (Moens and Vandepitte, 2005; Moens and Hanss, 2011). The main challenge to be faced in the application of the IFEM to real engineering problems is the so-called *dependency phenomenon* (Moore et al., 2009) which introduces conservatism both in the solution and matrix assembly phases. This phenomenon is mainly due to the inability of the *classical interval analysis* (*CIA*) to keep track of the dependency between interval variables. To limit overestimation of the interval solution, several versions of the IFEM have been developed, such as the element-by-element technique (Muhanna and Mullen, 2001), the sensitivity analysis method (Pownuk, 2004; Kreinovich et al., 2007) or the improvement of interval finite element analysis proposed by Degrauwe et al. (2010) based on *affine arithmetic*. Recently, the so-called *improved interval analysis via extra unitary interval* (*IIA via EUI*) (Muscolino and Sofi, 2012) has been introduced to perform interval structural analysis by taking into account dependencies between interval variables modeling uncertain physical properties. This is achieved by associating to each interval variable a particular unitary interval, the so-called *EUI*, which does not follow the rules of the *CIA*.

In this paper, a novel IFEM for the static analysis of linear-elastic structures with uncertain parameters is presented. Without loss of generality, Young's moduli of the FEs are modeled as independent interval variables, while applied loads are assumed to be deterministic. The key idea of the method is to handle interval variables by applying the *IIA via EUI* (Muscolino and Sofi, 2012) in order to reduce overestimation of the interval solution. Accordingly, an *EUI* is associated to each uncertain parameter and, therefore, to each FE. This allows to keep track of the dependencies between interval variables both in the assembly and solution phases of the finite element procedure. Then, approximate explicit expressions of the bounds of the interval nodal displacements are derived by applying the so-called *Interval Rational Series Expansion* (*IRSE*) (Muscolino and Sofi, 2013), recently proposed to evaluate the explicit inverse of an interval matrix with modifications. Finally, attention is focused on the computational efficiency of the presented IFEM. It is shown that the computational burden associated to the *IRSE* can be drastically reduced by retaining just the contribution of the most influential uncertain parameters. Such parameters are efficiently identified by performing a preliminary sensitivity analysis.

For validation purpose, a 3D cantilever beam with uncertain Young's modulus is analyzed. Both the accuracy and computational efficiency of the presented IFEM are investigated.

2. Interval Finite Element Formulation

2.1. INTERVAL MODEL OF UNCERTAINTY

The interval model of uncertainty describes the generic uncertain parameter as an interval variable (Moore, 1966) with given lower bound (LB) and upper bound (UB). It turns out to be very useful when only range information on the uncertain parameters is available, as happens in early design stages.

Let $\alpha_i^I = [\underline{\alpha}_i, \overline{\alpha}_i] \in \mathbb{IR}$ be an interval variable where $\mathbb{IR}$ is the set of all real interval numbers; the symbols $\underline{\alpha}_i$ and $\overline{\alpha}_i$ denote the LB and UB of the interval, respectively, while the apex I characterizes the interval variables. The i-th real interval variable $\alpha_i^I = [\underline{\alpha}_i, \overline{\alpha}_i]$ is such that $\underline{\alpha}_i \le \alpha_i \le \overline{\alpha}_i$ and it is characterized by the midpoint value (or mean), $\alpha_{0,i}$, and the deviation amplitude (or radius), $\Delta\alpha_i$, given by:

$$\alpha_{0,i} = \text{mid}\{\alpha_i^I\} = \frac{\underline{\alpha}_i + \overline{\alpha}_i}{2}; \qquad \Delta\alpha_i = \frac{\overline{\alpha}_i - \underline{\alpha}_i}{2} \tag{1a,b}$$

where $\text{mid}\{\bullet\}$ is an operator yielding the midpoint of the interval quantity between curly brackets.

In the framework of interval symbolism, a generic interval-valued function f and a generic interval-valued matrix function $\mathbf{A}$ of the interval vector $\boldsymbol{\alpha}^I \in \mathbb{IR}^r$, collecting the variables α_i^I, $(i=1,2,\ldots r)$, will be denoted in equivalent form, respectively, as:

$$\begin{aligned} f^I &\equiv f(\boldsymbol{\alpha}^I) \Leftrightarrow f(\boldsymbol{\alpha}), \quad \boldsymbol{\alpha} \in \boldsymbol{\alpha}^I = \left[\underline{\boldsymbol{\alpha}}, \overline{\boldsymbol{\alpha}}\right]; \\ \mathbf{A}^I &\equiv \mathbf{A}(\boldsymbol{\alpha}^I) \Leftrightarrow \mathbf{A}(\boldsymbol{\alpha}), \quad \boldsymbol{\alpha} \in \boldsymbol{\alpha}^I = \left[\underline{\boldsymbol{\alpha}}, \overline{\boldsymbol{\alpha}}\right]. \end{aligned} \tag{2a,b}$$

2.2. INTERVAL GLOBAL EQUILIBRIUM EQUATIONS

Let us consider a continuous elastic body which occupies the volume V bounded by the surface S in its undeformed state. The body is subjected to volume forces $\mathbf{b}(\mathbf{x})$ in V and surface forces $\mathbf{t}(\mathbf{x})$ on the loaded (or free) portion S_t of the boundary surface S, with $\mathbf{x} = [x_1 \quad x_2 \quad x_3]^{\mathrm{T}}$ denoting the position vector of a generic point referred to a Cartesian coordinate system $O(x_1, x_2, x_3)$; the displacements $\tilde{\mathbf{u}}(\mathbf{x})$ are imposed on the constrained portion S_u of S. The constitutive behavior of the material is linear-elastic isotropic. All input parameters are assumed to be known deterministically, except Young's modulus of the material which is modeled as an uncertain parameter.

Let the volume V of the body be subdivided into N_e finite elements (FEs). Young's modulus of each FE is modeled as an interval variable, i.e.:

$$E^{(i)}(\alpha_i^I) = E_0^{(i)}\left(1+\alpha_i^I\right), \qquad (i=1,2,\ldots,N^{(e)}) \tag{3}$$

where $\alpha_i^I = [\underline{\alpha}, \overline{\alpha}] \in \mathbb{IR}$ is a symmetric interval variable, i.e. characterized by a zero midpoint value $\alpha_{0,i} = 0$, which represents the dimensionless fluctuation around the nominal value $E_0^{(i)}$. Following the *improved interval analysis via extra unitary interval* (*IIA via EUI*) (Muscolino and Sofi, 2012), such fluctuation is herein expressed as (see Appendix):

$$\alpha_i^I = \Delta\alpha_i \hat{e}_i^I \tag{4}$$

where $\hat{e}_i^I = [-1,+1]$ is the *EUI*. In order to guarantee always positive values of the uncertain Young's modulus, the deviation amplitude of α_i^I must satisfy the condition $\Delta\alpha_i < 1$. Notice that an *EUI* is associated to each uncertain Young's modulus and, therefore, to each FE. This allows to link physical properties to the FEs and limit the overestimation due to the *dependency phenomenon* which typically affects both the assembly and solution phases of IFEMs based on the *CIA* (Moore et al., 2009).

Taking into account Eqs. (3) and (4), the elastic matrix of the i-th FE can be expressed as:

$$\mathbf{E}^{(i)}(\alpha_i^I) = \left(1+\Delta\alpha_i\hat{e}_i^I\right)\mathbf{E}_0^{(i)} \tag{5}$$

where $\mathbf{E}_0^{(i)}$ is the elastic matrix of the FE with nominal Young's modulus $E_0^{(i)}$.

Following the standard displacement-based FE formulation, the interval displacement field and the associated strain field within the i-th FE can be approximated as follows:

$$\mathbf{u}^{(i)}(\mathbf{x};\boldsymbol{\alpha}^I) = \mathbf{N}^{(i)}(\mathbf{x})\mathbf{d}^{(i)}(\boldsymbol{\alpha}^I) \tag{6}$$

and

$$\boldsymbol{\varepsilon}^{(i)}(\mathbf{x};\boldsymbol{\alpha}^I) = \mathbf{B}^{(i)}(\mathbf{x})\mathbf{d}^{(i)}(\boldsymbol{\alpha}^I) \tag{7}$$

where $\boldsymbol{\alpha}^I = \left[\underline{\boldsymbol{\alpha}}, \overline{\boldsymbol{\alpha}}\right] \in \mathbb{IR}^{N_e}$ is the interval vector collecting the dimensionless fluctuations α_i^I, $(i=1,2,\ldots,N^{(e)})$, of Young's moduli of the N_e FEs; $\mathbf{N}^{(i)}(\mathbf{x})$ denotes the shape-function matrix; $\mathbf{B}^{(i)}(\mathbf{x})$ is

the strain-displacement matrix; $\mathbf{d}^{(i)}(\boldsymbol{\alpha}^I)$ is the nodal displacement vector of the i-th FE which depends on the interval variables α_i^I.

Taking into account Eqs. (5) and (7), the stress field can be expressed by means of the constitutive equations as follows:

$$\boldsymbol{\sigma}^{(i)}(\mathbf{x};\boldsymbol{\alpha}^I) = \mathbf{E}^{(i)}(\alpha_i^I)\boldsymbol{\varepsilon}^{(i)}(\mathbf{x};\boldsymbol{\alpha}^I) = \left(1+\Delta\alpha_i\hat{e}_i^I\right)\mathbf{E}_0^{(i)}\mathbf{B}^{(i)}(\mathbf{x})\mathbf{d}^{(i)}(\boldsymbol{\alpha}^I). \tag{8}$$

Due to Young's modulus uncertainty, the element stiffness matrix turns out to be an interval matrix, defined as:

$$\mathbf{k}^{(i)}(\alpha_i^I) = \int_{V^{(i)}} \mathbf{B}^{(i)\mathrm{T}}(\mathbf{x})\mathbf{E}^{(i)}(\alpha_i^I)\mathbf{B}^{(i)}(\mathbf{x})\mathrm{d}V^{(i)} = \left(1+\Delta\alpha_i\hat{e}_i^I\right)\mathbf{k}_0^{(i)} \tag{9}$$

where $\mathbf{k}_0^{(i)} = \mathbf{k}^{(i)}(\alpha_i)\big|_{\boldsymbol{\alpha}=\mathbf{0}}$ is the nominal stiffness matrix.

The element force vector is not affected by uncertainties, i.e.:

$$\mathbf{f}^{(i)} = \int_{V^{(i)}} \mathbf{N}^{(i)\mathrm{T}}(\mathbf{x})\mathbf{b}(\mathbf{x})\mathrm{d}V^{(i)} + \int_{S_t^{(i)}} \mathbf{N}^{(i)\mathrm{T}}(\mathbf{x})\mathbf{t}(\mathbf{x})\mathrm{d}S^{(i)}. \tag{10}$$

It is worth emphasizing that, by applying the *IIA via EUI*, an *EUI* is associated to the stiffness matrix of each FE (see Eq.(9)). This allows to keep track of the dependencies between interval Young's moduli of the various FEs and thus perform standard assembly. Specifically, the assembly procedure yields the following set of linear interval equations governing the equilibrium of the FE model:

$$\mathbf{K}(\boldsymbol{\alpha}^I)\mathbf{U}(\boldsymbol{\alpha}^I) = \mathbf{F} \tag{11}$$

where $\mathbf{U}(\boldsymbol{\alpha}^I)$ is the interval vector collecting the n unknown nodal displacements, while

$$\mathbf{K}(\boldsymbol{\alpha}^I) \equiv \mathbf{K}^I = \sum_{i=1}^{N_e} \mathbf{L}^{(i)\mathrm{T}}\mathbf{k}^{(i)}(\alpha_i^I)\mathbf{L}^{(i)} \tag{12}$$

and

$$\mathbf{F} = \sum_{i=1}^{N_e} \mathbf{L}^{(i)\mathrm{T}}\mathbf{f}^{(i)} \tag{13}$$

are the interval global stiffness matrix of order $(n\times n)$ and the nodal force vector, respectively. Finally, in the previous equations, $\mathbf{L}^{(i)}$ denotes the connectivity matrix.

Taking into account Eq.(9), the interval global stiffness matrix can be rewritten as sum of the nominal value plus an interval deviation, i.e.:

$$\mathbf{K}^I = \mathbf{K}_0 + \sum_{i=1}^{N_e} \mathbf{L}^{(i)\mathrm{T}}\mathbf{k}_0^{(i)}\mathbf{L}^{(i)}\Delta\alpha_i\hat{e}_i^I \tag{14}$$

where $\mathbf{K}_0 = \mathbf{K}(\boldsymbol{\alpha})\big|_{\boldsymbol{\alpha}=\mathbf{0}}$ is the global nominal stiffness matrix

3. Bounds of the Solution

Within the interval framework, the solution of the set of interval equilibrium equations (11) involves the evaluation of the LB and UB vectors $\underline{\mathbf{U}}(\boldsymbol{\alpha})$ and $\overline{\mathbf{U}}(\boldsymbol{\alpha})$. To this aim, the knowledge of the explicit inverse of the interval stiffness matrix is crucial. Recently, the so-called *Interval Rational Series Expansion* (*IRSE*) (Muscolino and Sofi, 2013) has been derived as a modified explicit form of the Neumann series for

evaluating the approximate inverse of an interval matrix with modifications. In the sequel, first the *IRSE* is summarized, then it is applied to derive approximate explicit bounds of the interval displacements.

3.1. APPROXIMATE EXPLICIT SOLUTION: INTERVAL RATIONAL SERIES EXPANSION

The first step to apply the *IRSE* is the decomposition of the interval stiffness matrix as sum of the nominal value plus an interval deviation given by a superposition of rank-one matrices, i.e.:

$$\mathbf{K}(\boldsymbol{\alpha}^I) = \mathbf{K}_0 + \sum_{i=1}^{N_e} \alpha_i^I \, \mathbf{K}_i = \mathbf{K}_0 + \sum_{i=1}^{N_e} \sum_{\ell=1}^{p_i} \mathbf{s}_i^{(\ell)} \mathbf{v}_i^{(\ell)\mathrm{T}} \Delta\alpha_i \, \hat{e}_i^I \tag{15}$$

where $\mathbf{s}_i^{(\ell)}$ and $\mathbf{v}_i^{(\ell)}$ are column vectors and p_i is an integer number. The definition of these quantities depends on the kind of decomposition adopted for the matrices $\mathbf{K}_i$ (see e.g., Impollonia, 2006; Muscolino and Sofi, 2013; Muscolino et al., 2014).

By applying the *IRSE* truncated to first-order terms, the inverse of the interval stiffness matrix can be expressed in approximate explicit form as follows:

$$\left(\mathbf{K}^I\right)^{-1} \approx \mathbf{K}_0^{-1} - \sum_{i=1}^{N_e} \sum_{\ell=1}^{p_i} \frac{\Delta\alpha_i \, \hat{e}_i^I}{1 + d_{i\ell} \, \Delta\alpha_i \, \hat{e}_i^I} \mathbf{D}_{i\ell} \tag{16}$$

where

$$d_{i\ell} = \mathbf{v}_i^{(\ell)\mathrm{T}} \mathbf{K}_0^{-1} \mathbf{s}_i^{(\ell)}; \quad \mathbf{D}_{i\ell} = \mathbf{K}_0^{-1} \mathbf{s}_i^{(\ell)} \mathbf{v}_i^{(\ell)\mathrm{T}} \mathbf{K}_0^{-1}. \tag{17a,b}$$

Equation (16) provides the following approximate closed-form expression of the interval displacement vector:

$$\mathbf{U}^I = \left(\mathbf{K}^I\right)^{-1} \mathbf{F} \approx \mathbf{U}_0 - \sum_{i=1}^{N_e} \sum_{\ell=1}^{p_i} \frac{\Delta\alpha_i \, \hat{e}_i^I}{1 + d_{i\ell} \, \Delta\alpha_i \, \hat{e}_i^I} \mathbf{D}_{i\ell} \mathbf{F} \tag{18}$$

where $\mathbf{U}_0 = \mathbf{K}_0^{-1} \mathbf{F}$ is the solution pertaining to the nominal system.

3.2. BOUNDS OF THE INTERVAL DISPLACEMENTS

In order to evaluate the lower bound and upper bound of the interval displacement vector, Eq. (18) can be conveniently rewritten in the following *affine form*:

$$\mathbf{U}^I = \mathbf{U}_0 + \sum_{i=1}^{N_e} \sum_{\ell=1}^{p_i} \left(a_{0,i\ell} - \Delta a_{i\ell} \hat{e}_i^I \right) \mathbf{D}_{i\ell} \mathbf{F} \tag{19}$$

where $a_{0,i\ell}$ and $\Delta a_{i\ell}$ are the midpoint and deviation amplitude of the generic term of the double summation in Eq. (18), given by:

$$a_{0,i\ell} = \frac{\Delta\alpha_i^2 d_{i\ell}}{1 - \left(\Delta\alpha_i d_{i\ell}\right)^2}; \qquad \Delta a_{i\ell} = \frac{\Delta\alpha_i}{1 - \left(\Delta\alpha_i d_{i\ell}\right)^2}. \tag{20a,b}$$

The argument $\Delta\alpha_i$ of the functions $a_{0,i\ell}$ and $\Delta a_{i\ell}$ is omitted for conciseness.

Based on Eq. (19) and applying the *IIA via EUI*, the following approximate explicit expressions of the LB and UB of the interval displacement vector $\mathbf{U}^I$ are obtained:

$$\underline{\mathbf{U}}(\boldsymbol{\alpha}) = \mathrm{mid}\left\{\mathbf{U}^I\right\} - \Delta\mathbf{U}(\boldsymbol{\alpha}); \quad \overline{\mathbf{U}}(\boldsymbol{\alpha}) = \mathrm{mid}\left\{\mathbf{U}^I\right\} + \Delta\mathbf{U}(\boldsymbol{\alpha}) \tag{21a,b}$$

where

$$\Delta\mathbf{U}(\boldsymbol{\alpha}) = \sum_{i=1}^{N_e} |\mathbf{R}_i| = \sum_{i=1}^{N_e} \left| \sum_{\ell=1}^{p_i} \Delta a_{i\ell}\, \mathbf{D}_{i\ell}\mathbf{F} \right| \tag{22}$$

is the deviation amplitude of $\mathbf{U}^I$ and the symbol $|\bullet|$ denotes absolute value component wise.

4. Sensitivity Analysis

The *IRSE* allows the evaluation of the interval displacement vector and the associated bounds in approximate closed-form. As known, the knowledge of the explicit dependence of the structural response on the design parameters is very useful for several purposes, such as reanalysis, optimization, sensitivity analysis, reliability analysis, etc. In this section, attention is focused on the evaluation of the sensitivities of the response with respect to the uncertain parameters. To this aim, let us recast Eq. (18) in the following form:

$$\mathbf{U}(\boldsymbol{\alpha}) = \mathbf{U}_0 - \sum_{i=1}^{N_e} \sum_{\ell=1}^{p_i} \frac{\alpha_i}{1 + d_{i\ell}\,\alpha_i} \mathbf{D}_{i\ell}\mathbf{F} \tag{23}$$

where $\alpha_i \in \alpha_i^I = \Delta\alpha_i\, \hat{e}_i^I$. Direct differentiation of Eq.(23) yields the following approximate explicit expression of the vector collecting the sensitivities of the interval displacements with respect to the i-th uncertain parameter:

$$\mathbf{s}_{\mathbf{U},i} = \left. \frac{\partial \mathbf{U}(\boldsymbol{\alpha})}{\partial \alpha_i} \right|_{\boldsymbol{\alpha}=\mathbf{0}} = -\sum_{\ell=1}^{p_i} \mathbf{D}_{i\ell}\mathbf{F}, \quad (i = 1, 2, \ldots, N_e). \tag{24}$$

Sensitivities enable to predict how structural response is affected by a small change of the uncertain parameters. In the context of the presented IFEM, the knowledge of explicit response sensitivities can be exploited to enhance the computational efficiency of the *IRSE*. Indeed, the main drawback of the *IRSE* is that it involves a double summation (see Eq. (23)) which may be time consuming for real-sized structures. However, it can be readily inferred that not all the terms appearing in the *IRSE* approximation of the response (23) are equally important since each uncertain parameter has a different effect on the various DOFs of a structure. Based on this observation, we may perform a sensitivity analysis in order to detect those parameters which actually have a negligible influence on the response of a given DOF and then omit the corresponding contribution in the *IRSE*. This approach enables a drastic reduction of the computational time required by the *IRSE* which therefore can be efficiently used to analyze the response of structures with a large number of uncertain parameters.

The most influential parameters for each DOF can be identified by evaluating the so-called *coefficient of sensitivity* which provides a percentage measure of the global variability of the response with respect to its nominal value due to the generic uncertain parameter. Specifically, the *coefficient of sensitivity* of the nodal displacement $U_j(\boldsymbol{\alpha})$ with respect to the i-th parameter α_i can be defined as follows (Muscolino et al., 2014):

$$\beta_{i,U_j}(\%) = \left| \frac{1}{U_{0,j}} \left(\left. \frac{\partial U_j(\boldsymbol{\alpha})}{\partial \alpha_i} \right|_{\boldsymbol{\alpha}=\mathbf{0}} \right) \right| \Delta\alpha_i \times 100 \tag{25}$$

where $\Delta\alpha_i$ denotes the deviation amplitude of the dimensionless interval parameter $\alpha_i \in [-\Delta\alpha_i, \Delta\alpha_i]$; $U_{0,j} = U_j(\boldsymbol{\alpha})\big|_{\boldsymbol{\alpha}=\mathbf{0}}$ is the nominal value of the j-th displacement component.

For each DOF, the most crucial uncertain parameters are those characterized by higher values of the *coefficient of sensitivity*. Retaining only the terms of the *IRSE* corresponding to these parameters, say $r < N_e$, allows one to obtain simpler and more efficient analytical approximations of the response.

5. Numerical Application

For validation purpose, the response of a 3D cantilever beam with uncertain Young's modulus of the material (Figure 1) is analyzed. The beam is subjected on the top edge to a deterministic transversally distributed load $p_z = 10$ kN/m^2. The following geometrical properties are assumed: length $L = 5$m and rectangular cross section with width $b = 0.25$ m and thickness $h = 0.5$ m. The nominal Young's modulus and Poisson ratio of the material are selected as $E_0 = 230$ GPa and $\nu = 0.3$, respectively. A uniform FE mesh consisting of $N_e = 320$ eight-node brick elements is adopted. Young's modulus of each FE is modelled as an interval variable $E^{(i)}(\alpha_i^I) = E_0(1 + \Delta\alpha_i \hat{e}_i^I)$ with $\Delta\alpha_i = \Delta\alpha = 0.1$, $(i = 1,2,\ldots,N_e)$.

The spectral decomposition of the nominal element stiffness matrix, $\mathbf{k}_0^{(i)} = \mathbf{k}^{(i)}(\alpha_i)\big|_{\boldsymbol{\alpha}=\mathbf{0}}$, is adopted in order to decompose the global stiffness matrix according to Eq. (15) and then apply the *IRSE*. In this case, $p_i = 18$ represents the number of deformation modes of the eight-node brick FE. The proposed IFEM is applied to evaluate the bounds of the interval displacement components, U_{zj}^I, $(j = 1,2,\ldots,20)$, along the z-axis of twenty selected nodes shown in Figure 1.

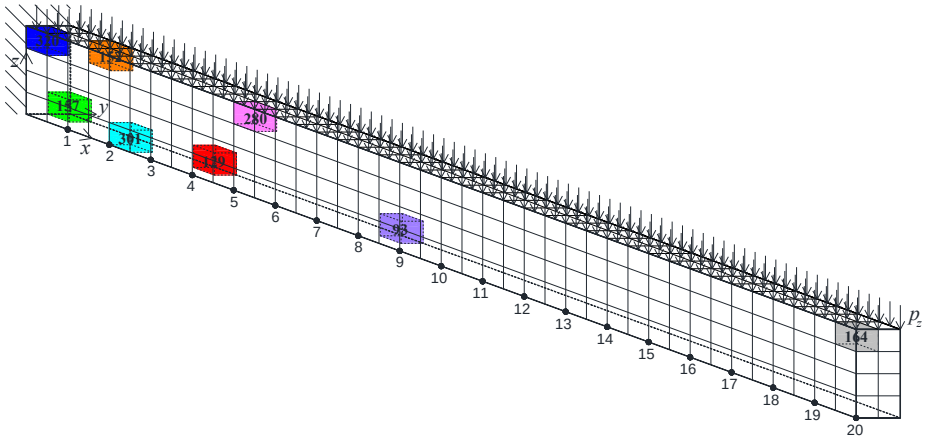

Figure 1. 3D cantilever beam with uncertain Young's modulus.

The accuracy of the estimates of displacement bounds could be assessed by comparisons with the exact bounds evaluated by applying a combinatorial procedure, known as *vertex method* (Dong and Shah, 1987). However, for the selected application, the *vertex method* is unfeasible since it requires 2^{320} deterministic analyses, as many as are the possible combinations of the endpoints of the uncertain parameters. For this reason, a comparison with the results obtained by applying a procedure based on sensitivity analysis (Pownuk, 2004; Kreinovich et al., 2007), herein referred to as *Sensitivity Method* (*SM*), is carried out.

First, the sensitivity of beam's response to the variability of Young's moduli of the $N_e = 320$ FEs is investigated by exploiting the closed-form expressions of displacement sensitivities derived from the *IRSE* (see Eqs. (24)). Figure 2 displays the sensitivities of the 20 nodal displacements $U_{zj}(\boldsymbol{\alpha})$, ($j = 1,2,\ldots,20$), of interest with respect to the fluctuations of the uncertain Young's moduli of eight selected FEs highlighted in Figure 1.

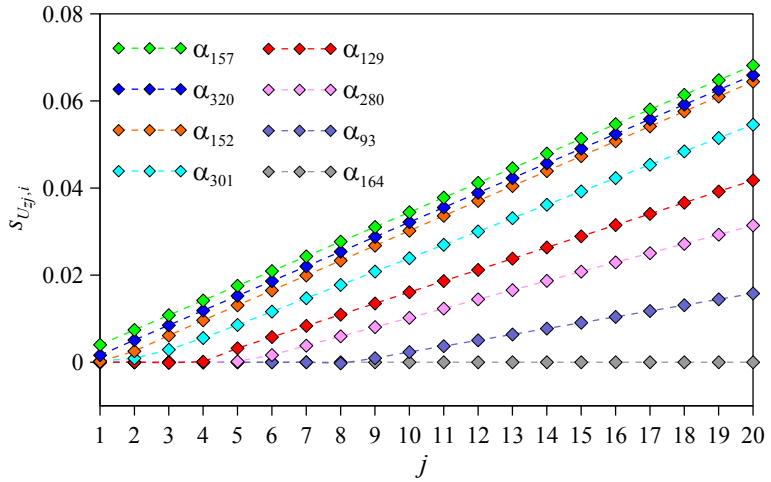

Figure 2. Sensitivities of the 20 selected nodal displacements of the cantilever beam with respect to the fluctuations of eight uncertain Young's moduli $E^{(i)}(\alpha_i^I) = E_0^{(i)}\left(1+\alpha_i^I\right)$, (see Figure 1).

In order to identify for each DOF the most crucial parameters, sensitivities can be ranked based on the corresponding *coefficients of sensitivity* reported in Figure 3. For instance, it can be observed that for all displacements the largest *coefficients of sensitivity* are those pertaining to the parameters α_{157} and α_{320} which, therefore, turn out to be the most influential among the eight selected parameters. Conversely, α_{93} and α_{164} are characterized by the smallest *coefficients of sensitivity* which means a less significant influence on the response. It is also observed that the displacement $U_{z1}(\boldsymbol{\alpha})$ is more sensitive to variations of the parameters α_{157} and α_{320} than the other displacements.

Based on the results of sensitivity analysis, a reduced form of the *IRSE* can be deduced by retaining for each DOF just the terms associated to the most influential uncertain parameters. Figure 4 shows a possible selection of the number r_j of significant terms of the *IRSE* for the 20 nodal displacements $U_{zj}(\boldsymbol{\alpha})$, $(j = 1,2,\ldots,20)$. Notice that the largest number of terms is needed to approximate $U_{z20}(\boldsymbol{\alpha})$ and it is still much smaller than the total number of uncertain parameters. This allows a substantial reduction of the computational effort.

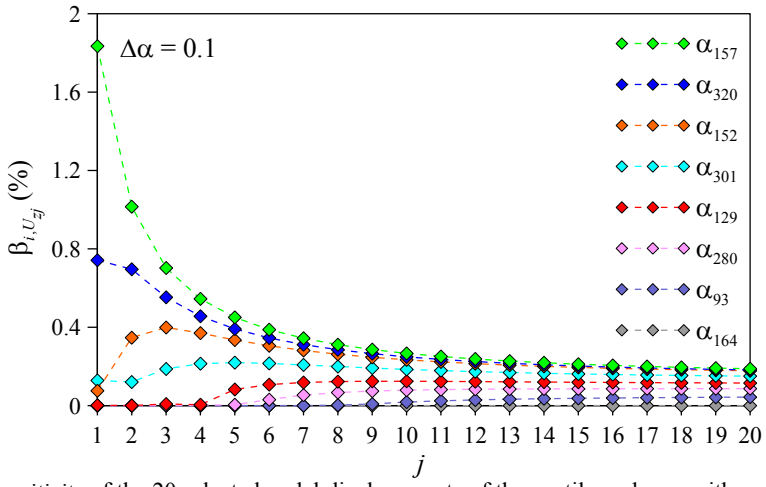

Figure 3. Coefficients of sensitivity of the 20 selected nodal displacements of the cantilever beam with respect to the fluctuations of eight uncertain Young's moduli $E^{(i)}(\alpha_i^I) = E_0^{(i)}\left(1+\alpha_i^I\right)$, $\alpha_i^I = \Delta\alpha\,\hat{e}_i^I$ with $\Delta\alpha = 0.1$ (see Figure 1).

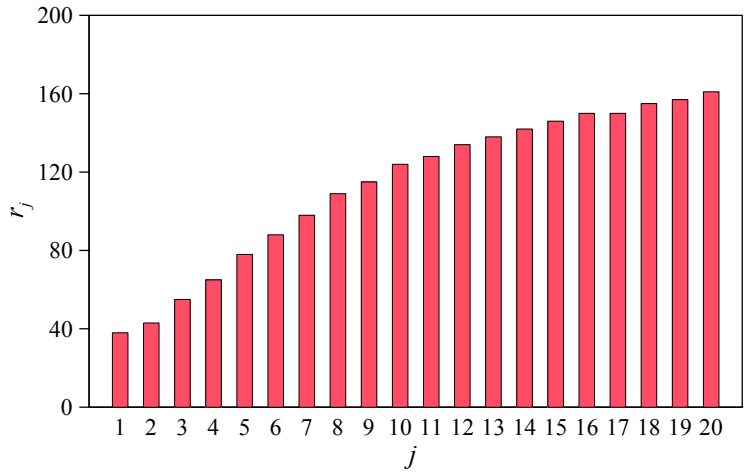

Figure 4. Number of terms r_j retained in the reduced *IRSE* for the 20 selected nodal displacements of the cantilever beam based on sensitivity analysis ($\Delta\alpha_i = 0.1$).

Figure 5 shows the comparison between the proposed bounds of the 20 selected nodal displacements obtained by applying the complete *IRSE* (with all terms retained) and a reduced *IRSE* involving just the number of terms reported in Figure 4. For validation purpose, the LB and UB of displacements provided by the *SM* are also reported. It can be seen that both the complete and reduced *IRSE*s yield approximate bounds in good agreement with those obtained by applying the *SM*. Furthermore, it is observed that the estimates pertaining to the reduced *IRSE* are very close to those provided by the complete *IRSE*. In particular the absolute percentage errors between the two approximations, reported in Figure 6, are always less than 0.5%. This demonstrates that terms omitted from the *IRSE* are actually negligible and the computational efficiency of the proposed IFEM can be greatly enhanced without affecting the accuracy of the results.

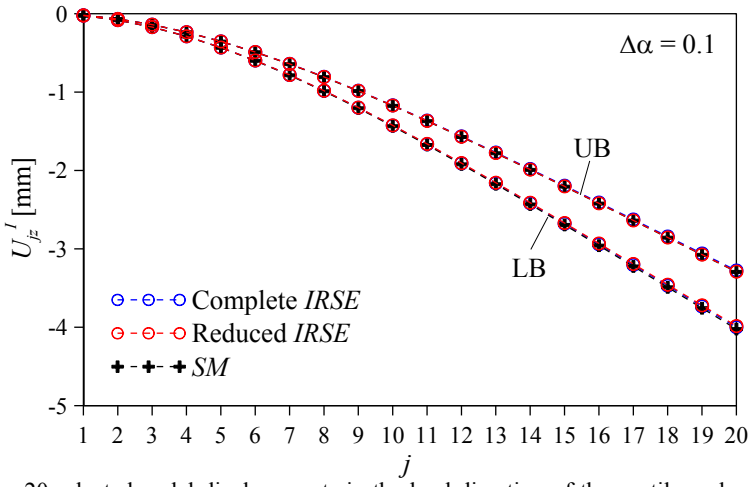

Figure 5. LB and UB of the 20 selected nodal displacements in the load direction of the cantilever beam with uncertain Young's moduli: comparison between the proposed bounds obtained by applying the reduced *IRSE* resulting from sensitivity analysis, the complete *IRSE* and the solution provided by the *SM* ($\Delta\alpha_i = 0.1$).

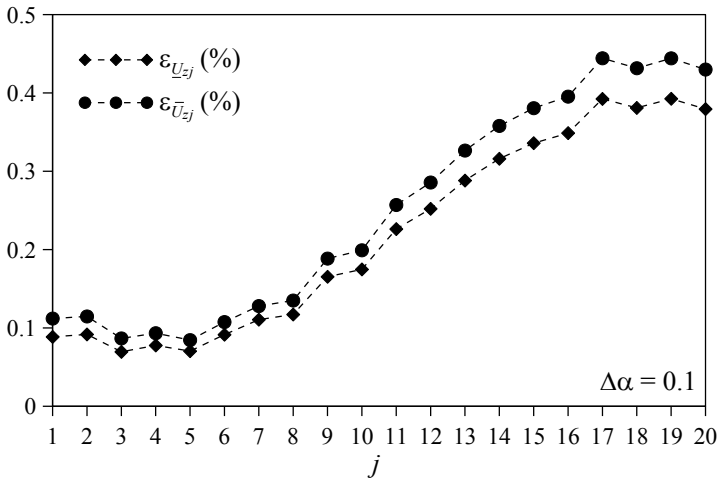

Figure 6. Absolute percentage errors affecting the LB and UB of the 20 selected nodal displacements of the cantilever beam provided by the reduced *IRSE* resulting from sensitivity analysis compared to the bounds yielded by the complete *IRSE* ($\Delta\alpha_i = 0.1$).

6. Conclusions

A novel Interval Finite Element Method (IFEM) for the static analysis of linear structures with uncertain parameters modeled as interval variables has been presented. The formulation relies on the use of the so-called *improved interval analysis*, recently introduced to limit the overestimation affecting the *classical interval analysis*. Accordingly, a particular unitary interval, called *extra unitary interval*, is associated to each uncertain parameter thus enabling to keep track of the dependencies between interval uncertainties in

both the assembly and solution stages of the finite element procedure. The bounds of the interval displacements have been derived in approximate explicit form by applying the so-called *Interval Rational Series Expansion* (*IRSE*). Then, it has been shown that a preliminary sensitivity analysis of the response allows a drastic reduction of the computational effort required by the *IRSE* thus making the IFEM applicable to structures with a large number of uncertain parameters. To demonstrate the accuracy and efficiency of the proposed IFEM, a 3D cantilever beam with uncertain Young's modulus has been analyzed.

References

Ayyub, B.M. and G.J. Klir. Uncertainty Modeling and Analysis in Engineering and the Sciences. Chapman & Hall/CRC, Taylor & Francis Group, Boca Raton, 2006.

Corotis, R.B. An Overview of Uncertainty Concepts Related to Mechanical and Civil Engineering. *ASCE-ASME Journal of Risk and Uncertainty in Engineering Systems, Part B: Mechanical Engineering* 1(4) 040801, 2015.

Degrauwe, D., G. Lombaert and G. De Roeck. Improving Interval Analysis in Finite Element Calculations by Means of Affine Arithmetic. *Computers and Structures* 88: 247–254, 2010.

Dong, W. and H.C. Shah. Vertex Method for Computing Functions of Fuzzy Variables. *Fuzzy Sets and Systems* 24: 65 – 78, 1987.

Elishakoff, I. and M. Ohsaki. *Optimization and Anti-optimization of Structures under Uncertainty*. Imperial College Press, London, 2010.

Impollonia, N. A Method to Derive Approximate Explicit Solutions for Structural Mechanics Problems. *International Journal of Solids and Structures* 43: 7082–7098, 2006.

Kreinovich, V., J. Beck, C. Ferregut, A. Sanchez, G.R. Keller, M. Averill and S.A. Starks, Monte-Carlo-Type Techniques for Processing Interval Uncertainty, and their Potential Engineering Applications. *Reliable Computing* 13: 25–69, 2007.

Moens, D. and D. Vandepitte. A Survey of Non-Probabilistic Uncertainty Treatment in Finite Element Analysis. *Computer Methods in Applied Mechanics and Engineering* 194: 1527–1555, 2005.

Moens, D. and M. Hanss. Non-Probabilistic Finite Element Analysis for Parametric Uncertainty Treatment in Applied Mechanics: Recent Advances. *Finite Element and Analysis Design* 47: 4-16, 2011.

Moore, R. E. *Interval Analysis*. Prentice-Hall, Englewood Cliffs, 1966.

Moore, R. E., R. B. Kearfott and M. J. Cloud. *Introduction to Interval Analysis*. SIAM, Philadelphia, USA, 2009.

Muhanna, R. L. and R. L. Mullen. Uncertainty in Mechanics: Problems-Interval-Based Approach. *Journal Engineering Mechanics ASCE* 127: 557-566, 2001.

Muscolino, G. and A. Sofi. Stochastic Analysis of Structures with Uncertain-but-Bounded Parameters via Improved Interval Analysis. *Probabilistic Engineering Mechanics* 28: 152-163, 2012.

Muscolino, G., R. Santoro and A. Sofi. Explicit Sensitivities of the Response of Discretized Structures under Stationary Random Processes. *Probabilistic Engineering Mechanics* 35: 82-95, 2014.

Muscolino, G. and A. Sofi. Bounds for the Stationary Stochastic Response of Truss Structures with Uncertain-but-Bounded Parameters. *Mechanical Systems and Signal Processing* 37: 163-181, 2013.

Pownuk, A. Efficient Method of Solution of Large Scale Engineering Problems with Interval Parameters. In R.L. Muhanna and R.L. Mullen, editors, *Proceedings NSF Workshop on Reliable Engineering Computing*, 305–316, 2004.

Appendix-Improved Interval Analysis via Extra Unitary Interval

Interval computations based on the *classical interval analysis* (*CIA*) suffer from the overestimation due to the so-called *dependency phenomenon* which occurs when an expression contains multiple instances of one or more interval variables (Moore et al., 2009). In order to limit the conservatism due to this phenomenon and thus allow the applicability of the interval model of uncertainty to engineering problems, recently the

improved interval analysis via extra unitary interval (*IIA via EUI*) has been proposed (Muscolino and Sofi, 2012). The key idea of the *IIA via EUI* is to express the i-th interval variable α_i^I in the following *affine form*:

$$\alpha_i^I = \alpha_{0,i} + \Delta\alpha_i \hat{e}_i^I \tag{A.1}$$

where $\hat{e}_i^I = [-1,+1]$ is the *EUI* which does not follow the rules of the *CIA*, i.e.:

$$\begin{aligned} &\hat{e}_i^I - \hat{e}_i^I = 0; \qquad \hat{e}_i^I \times \hat{e}_i^I = \left(\hat{e}_i^I\right)^2 = [1,1]; \\ &\hat{e}_i^I / \hat{e}_i^I = [1,1]; \quad \hat{e}_i^I \times \hat{e}_j^I = [-1,+1], \quad i \neq j; \\ &x_i \hat{e}_i^I \pm y_i \hat{e}_i^I = \left(x_i \pm y_i\right)\hat{e}_i^I; \\ &x_i \hat{e}_i^I \times y_i \hat{e}_i^I = x_i y_i \left(\hat{e}_i^I\right)^2 = x_i y_i [1,1]. \end{aligned} \tag{A.2a-f}$$

In these equations, $[1,1] = 1$ is the so-called unitary *thin interval* (Moore et al., 2009). It is worth emphasizing that the subscript i means that the *EUI*, $\hat{e}_i^I$, is associated to the i-th interval variable. By associating a different *EUI* to each interval variable, dependencies can be duly taken into account throughout calculations and the overestimation due to the *dependency phenomenon* can be drastically limited.

A Fail-Safe Design Approach Based on the Fracture Mechanical Analysis and Epistemic Uncertainty Quantification

Aleksandra Serafinska, Kaan Özenç, Michael Kaliske and Wolfgang Graf
Institute for Structural Analysis, Technische Universität Dresden, D-01062 Dresden,
aleksandra.serafinska@tu-dresden.de

Abstract: The developed method for a fail-safe optimal design of structures is based on a coupled approach of optimization involving a genetic algorithm, the fracture mechanical analysis, and uncertainty analysis enabling the quantification of epistemic uncertainty in the fracture process. The fail-safe structures are intended to retain their functionality even if subjected to certain damage conditions, e.g. a local failure of structural members. In the proposed approach, the failure process is modeled by means of the finite element analysis, employing the concept of discrete fracturing as well as the configurational mechanics based criteria. The investigations on safe failure are enhanced by the quantification of the influence of uncertainties. The uncertainties arising in the failure process of structures, which is governed by crack initiation and growth phenomena are not restricted to variability and randomness. In a structure designed as a system of coupled substructures, the crack initiation position is uncertain but not random, since it results from the boundary conditions change initiated by the occurrence of a certain failure scenario and damage of particular neighbouring structural members. For the modeling of this type of uncertainty, the uncertainty model fuzziness is applied. By means of the proposed method, the optimal design configuration is identified under the consideration of the uncertain crack propagation.

Keywords: fail-safe design, optimization, uncertainty model fuzziness, fracture mechanics

1. Introduction

In civil and mechanical engineering, the fail-safe design concepts are gaining on importance. Thus, for crucial structures, in parallel to standard design procedures aiming at providing sufficient load-bearing capacity, safe failure modes are planned and special design solutions are introduced to enforce an intended structural behavior in case of failure due to unforeseen events as extraordinary loading, impact, fatigue or material defects. Thereby, the main objective is to develop structures, which continue to perform its basic functions even under a certain damage level and are prevented from the catastrophic failure in form of chain reaction like sequential dysfunction of structural components. The fail-safe design strategy constitutes one of three engineering design concepts accounting for failure, next to the safe-life and the damage tolerance design principles (Dilger et al., 2009), (Wood and Engle, 1987), (Cazes, 2013).

The fail-safe design strategies are based upon the application of special design solutions as the redundancy of structural parts, multiple load paths or intentional weak links. Further solutions, considered also in the present contribution, are based on the application of crack arresters, which

hinder the crack propagation permitting solely the local failure of a substructure and preventing from damage escalation (Zhang et al., 2009). In parallel to the mentioned particular fail-safe design solutions, some systematic fail-safe design optimization approaches are introduced in (Sun et al., 1976), (Nguyen and Arora, 1982) and (Shechter, 1994). Though, the application of these approaches is limited to truss-like structures and the failure modeling is restricted to the failure of joints. In the present work, a fail-safe design optimization procedure is proposed, which involves failure modeling on the basis of a fracture mechanical solution and is thus applicable to a wider range of structures. In particular, the investigation of the failure process is introduced within a finite element framework by combination of discrete fracturing and configurational mechanics based criteria (Özenç and Kaliske, 2014), (Eshelby, 1951).

Furthermore, the proposed fail-safe design optimization approach is based upon the analysis of uncertainties in the fracture process. An established approach for the consideration of uncertainty of random nature in failure events is the probabilistic fracture mechanics, which is commonly applied for reliability assessment of structures (Rahman, 2001), (Rahman, 2002), (Novák et al., 2005), (Leonel et al., 2010). Further contributions on uncertainty consider a probabilistic fatigue crack growth model (Yang and Manning, 1996), (Besterfield et al., 1991), (Riahi et al., 2010) or investigate the size effect in probabilistic modeling of quasibrittle fracture (Bǎzant, 2001), (Vorechovský, 2004). In contrary, in the present work, nonstochastic uncertainty model − the model fuzziness (Möller and Beer, 2004), (Möller et al., 2000) is applied for the characterization of the crack initiation phenomenon in a structural system with coupled substructures.

The introduced fail-safe design optimization method is numerically realized as a coupled approach of a genetic algorithm based optimization, the fracture mechanical analysis and the fuzzy analysis. The interaction between the genetic algorithm and the fracture analysis enables to guide the uncertain crack path propagation direction into substructure preserved with crack arresters and thus to identify fail-safe designs, for which only local failures of substructures can occur instead of total failure of the system.

2. Fail-Safe Design Task

The exhibiting of a fail-safe function by a structure is understood as performing according to a predefined safe failure mode defined by a projected, not extensive failure of substructures, while the global system stability is maintained. In addition, the pursuation for the optimality implies that a design configuration is identified, for which the optimal performance within numerous objective functions, also related to safe failure, is expected. The safe failure modes are developed for a structure under the assumption, that the damage of particular substructures occurs in such a manner, that the neighbouring crucial structural elements, which substantially contribute to the global system stability keep performing in an undamaged condition. In the herein introduced fail-safe design strategy, a design concept of a substructure with damage accumulating function is developed, assuming that if this substructure is integrated within a system of coupled substructures it will hinder the progress of the failure mechanism towards crucial structural elements.

For numerical efficiency reasons, the presented fail-safe design optimization task can be solved within a two-step procedure involving: (i) the design optimization of the whole structure and

(ii) the subsequent detailled design of the damage accumulating element. The multi-objective design optimization task of the whole structure, solved in the first step, includes objective functions evaluated in an undamaged condition of the structure, e.g. minimal mass, deformations, production costs as well as in the damaged condition, focusing on obtaining an intended failure path/mode, which ends up in the damage accumulating element. In the second step of the fail-safe design procedure, the design optimization of the damage accumulating element is accomplished, with the initial design configuration identified within the first procedure step. Various loading cases and boundary condition changes of the damage accumulating element are taken into account, which are identified in the analysis of failure modes within the optimization of the whole structure.

The occurrence of a particular failure mode involves a dysfunction of specific substructures, joints or structural members, which are merged to the damage accumulating substructure. The resulting boundary condition changes within the damage accumulating substructure in form of support removal, support displacement or additional loads, lead to stress concentration and may provoke crack nucleation. In order to hinder possible crack propagation, structural elements in form of crack arresters are introduced within the damage accumulating substructure. In this contribution, the second step of the fail-safe design procedure is of main interest and thus a novel concept for the design of the damage accumulating substructure is provided.

For the structure mechanics based design optimization of the damage accumulating substructure, this substructure is considered as a body in the Euclidean space $\mathcal{B} \in \mathscr{E}^3$, surrounded by the boundary Γ, as shown in Figure 1. The body is subjected to body forces $\mathbf{b}$ and surface tractions $\mathbf{t}$, which are assigned to the part $\Gamma_F \in \Gamma$. At the part $\Gamma_b \in \Gamma$, displacement boundary conditions are prescribed. The body includes an initial crack of length γ_{in}, which arises in consequence of local stress concentrations induced by the occurrence of a failure mode. The controlling of partial damage in form of crack propagation and hindering its escalation to further structural components is obtained by the application of crack arresters. In the investigated damage accumulating substructure, n_c crack arresters are assembled, each with a boundary Γ_{Ai}, $i = 1, ..., n_c$ and a geometrical position vector $\boldsymbol{\chi}_{Ai}$ defined with respect to the reference point $P \in \mathcal{B}$. In Figure 1, the body $\mathcal{B}$ with a single crack arrester is presented as an example.

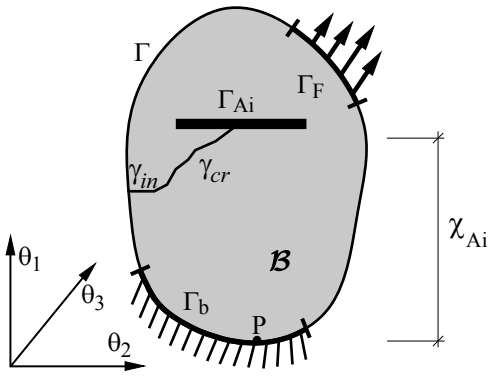

Figure 1. Structure mechanical configuration of the damage accumulating substructure.

The nonlinear multi-objective optimization problem of the damage accumulating substructure is defined as

$$\begin{aligned} \min_{\mathbf{x}_d \in X \subset \mathbb{R}^n} \quad & \mathbf{f}(\mathbf{x}_d, \tilde{\mathbf{p}}_a) = \{f_1(\mathbf{x}_d, \tilde{\mathbf{p}}_a), f_2(\mathbf{x}_d, \tilde{\mathbf{p}}_a), ...f_i(\mathbf{x}_d, \tilde{\mathbf{p}}_a), ..., f_m(\mathbf{x}_d, \tilde{\mathbf{p}}_a)\}, \\ & f_i(\mathbf{x}_d, \tilde{\mathbf{p}}_a) = \mathcal{K}\left(\tilde{\gamma}_{cr}(\mathbf{x}_d, \tilde{\mathbf{p}}_a, \mathcal{F})\right) \\ \textit{subject to} \quad & G^{\mathcal{M}}(\mathbf{x}_d, \tilde{\mathbf{p}}_a) = \nabla_X \cdot \mathbf{\Sigma}^t + \mathbf{B} = 0 \\ & g_k(\mathbf{x}_d, \tilde{\mathbf{p}}_a) \leq 0 \quad k = 1, 2, ..., p, \\ & h_l(\mathbf{x}_d, \tilde{\mathbf{p}}_a) = 0 \quad l = 1, 2, ..., q. \end{aligned} \tag{1}$$

The major optimization objective of the optimization task in Eq. (1) focuses on the identification of the geometrical configuration $\boldsymbol{\chi}_{Ai}$ of the crack arresters, so that the uncertain crack propagation $\tilde{\gamma}_{cr}(\mathbf{x}_d, \tilde{\mathbf{p}}_a, \mathcal{F})$ is always limited by the crack arrester. Within the definition of the major optimization objective $f_i(\mathbf{x}_d, \tilde{\mathbf{p}}_a)$, $\mathcal{K}$ represents a function utilized for the quantification of the uncertain crack propagation $\tilde{\gamma}_{cr}$, which will be discussed in Section 4. Further objective functions can be considered as well.

In Eq. (1), the objective functions $f_i, (i = 1, 2, ..., m)$ evaluate two types of input parameters, the design variables x_d and the uncertain a priori parameters $\tilde{p}_a$. They are represented by an n-dimensional design vector $\mathbf{x}_d = \{x_{d\,1}, x_{d\,2}, ..., x_{d\,n}\}^T$ and the s-dimensional vector of uncertain a priori parameters $\tilde{\mathbf{p}}_a = \{\tilde{p}_{a\,1}, \tilde{p}_{a\,2}, ..., \tilde{p}_{a\,s}\}^T$ respectively. In the presented optimization problem, $h_l(\mathbf{x}_d, \tilde{\mathbf{p}}_a) = 0$ denote nonlinear equality constraints and $g_k(\mathbf{x}_d, \tilde{\mathbf{p}}_a) \leq 0$ inequality constraints.

Due to the fact, that the major objective function considered in Eq. (1) evaluates the uncertain crack propagation function $\tilde{\gamma}_{cr}(\mathbf{x}_d, \tilde{\mathbf{p}}_a, \mathcal{F})$, the fracture mechanical analysis is applied for the solution of the optimization task. The crack propagation is governed by the energy minimization method on the basis of the configurational forces $\mathcal{F}$. The configurational forces are derived from the material momentum balance equation $G^{\mathcal{M}}$ and then applied for the energy minimization principle to determine the crack growth direction, compare (Özenç and Kaliske, 2014). The material balance equation $G^{\mathcal{M}}$ evaluates forces acting on material inhomogeneities of continuous media in the material space, compare (Eshelby, 1951), (Eshelby, 1975) and (Steinmann, 2000), in contrast to the balance laws formulated in the framework of classical Newtonian mechanics, which involve physical forces. The forces considered within $G^{\mathcal{M}}$ are denoted as configurational or material forces and defined as thermodynamical driving forces. In the optimization task in Eq. (1), the material balance equation $G^{\mathcal{M}}$ yielding the material forces is introduced as an optimization constraint. Thereby, $G^{\mathcal{M}}$ considers a stress measure conjugate to the material forces $\mathcal{F}$, the Eshelby stress tensor $\mathbf{\Sigma}$ as well as the material body force $\mathbf{B}$.

In subsequent sections, various aspects of the optimization task are discussed, as the formulation of the uncertain parameters related to crack initiation and growth and the definition of the objective functions. Finally, a solution concept for the presented fail-safe design optimization problem is provided.

3. Uncertain Crack Initiation and Propagation in Fail-Safe Structures

An important aspect of a fail-safe design strategy is the assessment of potential crack initiation location as well as the prediction of the crack propagation image, taking into account the uncertainties in the fracture processes. A major assumption of the introduced fail-safe design optimization approach is, that in a system with coupled substructures, the crack initiation location in the damage accumulating substructure is uncertain but not random, since it results from the boundary conditions change induced by the occurrence of a certain failure mode and failure of particular neighbouring structural elements. Thus, the nature of the crack initiation process in the context of safe failure of structures designed as a system of coupled substructures differs significantly from e.g. fatigue induced failure of independent systems, which is governed by the crack initiation at randomly distributed material inhomogeneities.

The crack initiation in the damage accumulating substructure is visualized in Figure 2. For the considered body $\mathcal{B}$, the boundary Γ_b with prescribed displacement boundary conditions is divided into three parts Γ_{b1}, Γ_{b2}, Γ_{b3}, whereas each part denotes a support or joint connecting $\mathcal{B}$ with neighbouring structural elements. Should the structure fail according to the first planned failure mode, the failure of support/joint associated with Γ_{b1} within the damage accumulating substructure is expected. Thereby, the consequence of the removal of the boundary part Γ_{b1} is the crack initiation at a position in body $\mathcal{B}$, which is shown in Figure 2 b). The most possible crack initiation location is marked with the black color and the crack initiation locations with gradually decreasing occurrence possibility are indicated by shading in the gray scale. Though, the occurrence of the second planned failure mode, provokes the removal of boundary Γ_{b2} and the uncertain crack initiation in a quite different part of the body $\mathcal{B}$, compare Figure 2 c). For the description of the crack initiation phenomena, the framework of the possibility theory is chosen.

The framework of the fuzzy set theory yields mathematical foundations for the theory of possibility (Dubois and Prade, 1980), (Zadeh, 1965). Especially, the fuzzy set theory based uncertainty model fuzziness is applicable if incomplete, limited statistical or subjective information is evaluated.

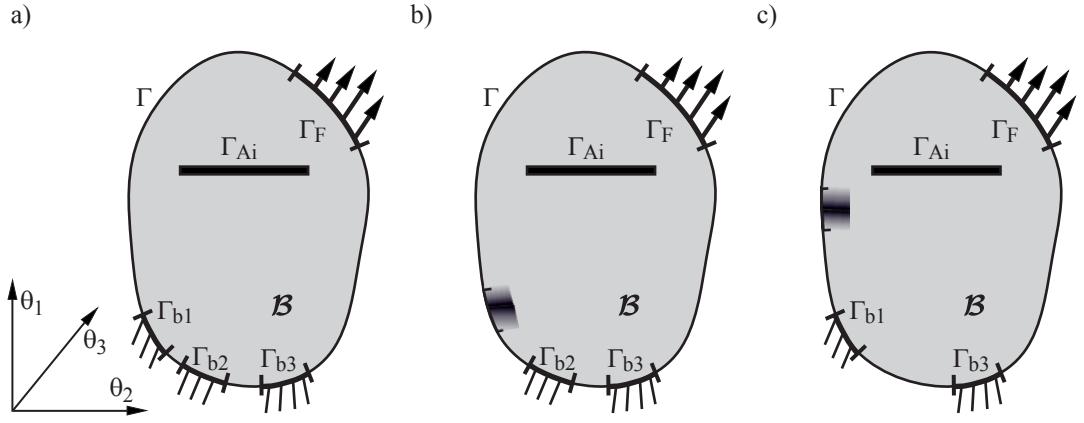

Figure 2. Crack initiation due to the boundary change.

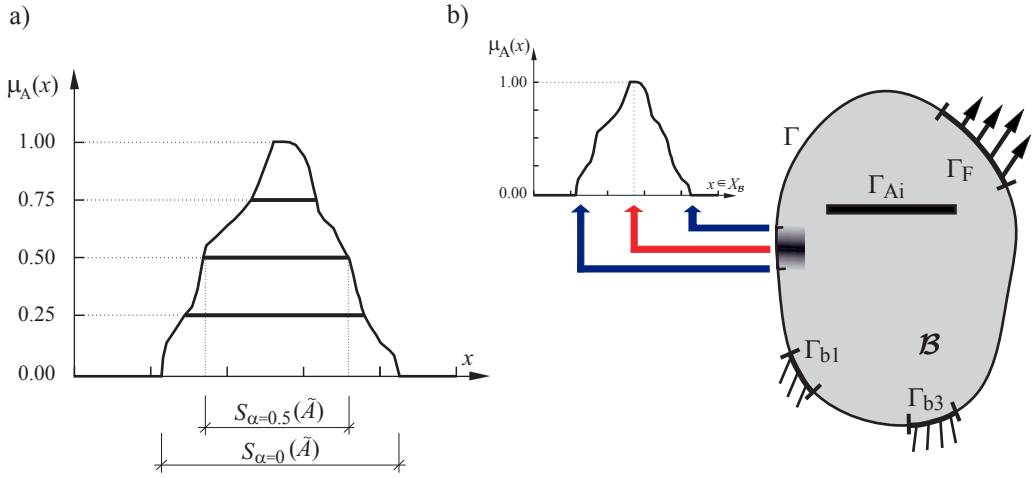

Figure 3. Definition of a fuzzy variable.

Since the information required for modelling the crack initiation position as an uncertain parameter is based on vaque data and/or stems from expert evaluations, its modeling by means of fuzzy sets is reasonable. The fuzzy set $\tilde{A}$ is defined as

$$\tilde{A} = \{(x, \mu_A(x)) \mid x \in X\}. \tag{2}$$

The gradual membership of the elements $x \in X$ to the fuzzy set $\tilde{A}$ is specified by a membership function μ_A, as visualized in Figure 3 a)

$$\mu_A : X \to [0, 1]. \tag{3}$$

The definition of the crack initiation position as a fuzzy set requires the assessment of a set of material points in a subregion of the body $X_{\mathcal{B}} \subseteq \mathcal{B}$ according to the crack initiation potential. The gradual assessment suceeds by means of the membership function μ_A, compare Figure 3 b). In order to provide an interpretation in the context of the possibility theory, a possibility measure Π in the measure space $[X_{\mathcal{B}}, \Sigma, \Pi]$ is assumed, with Σ as the σ-Algebra on $X_{\mathcal{B}}$. Thereby, the possibility measure Π denotes a subjective assessment of the possibility of the occurrence of an event, which is e.g. defined by the crack initiation at a particular point $x \in X_{\mathcal{B}}$. Consider a variable $\tilde{p}_a$ taking values in $X_{\mathcal{B}}$, which is characterized by the possibility distribution function $\pi_d(\tilde{p}_a)$. Thereby, $\pi_d(\tilde{p}_a)$ is defined to be equal to the membership function μ_A of the set $\tilde{A}$

$$\pi_d(\tilde{p}_a) = \mu_A. \tag{4}$$

Thus, an advantageous description of the crack initiation event is obtained since every realization x of the fuzzy variable $\tilde{p}_a$ is quantified by the possibility measure Π and has an assigned degree of possibility $\mu_A(x)$.

The herein presented fail-safe design procedure is based on the solution of the multi-objective optimization task, where the objective functions $f_i(\mathbf{x}_d, \tilde{\mathbf{p}}_a)$, $i = 1, ..., m$ evaluate uncertain input parameter, e.g. the uncertain crack initiation location. Especially, within each objective function $f_i(\mathbf{x}_d, \tilde{\mathbf{p}}_a)$, $i = 1, ..., m$ considered in Eq. (1), a mapping of a design vector $\mathbf{x}_d$, and uncertain parameters vector $\tilde{\mathbf{p}}_a$ onto uncertain structural responses $\tilde{z}_i = f_i(\mathbf{x}_d, \tilde{\mathbf{p}}_a)$ is accomplished by means of the fracture mechanical analysis

$$\begin{aligned} f_i : \mathbb{R}^n \times \mathcal{U}(\mathbb{R}^s) &\rightarrow \mathcal{U}(\mathbb{R}), \\ (\mathbf{x}_d, \tilde{\mathbf{p}}_a) &\mapsto \tilde{z}_i. \end{aligned} \tag{5}$$

In Eq. (5), $\mathcal{U}(\cdot)$ stands for the set of all fuzzy sets, defined respectively, on the space of uncertain parameters $\mathcal{U}(\mathbb{R}^s)$ and on the objective space $\mathcal{U}(\mathbb{R}) \in \mathbb{R}^m$. $\mathbb{R}^n$ denotes the space of design variables. The outputs of the objective functions $f_i(\mathbf{x}_d, \tilde{\mathbf{p}}_a)$, $i = 1, ..., m$ are uncertain structural responses $\tilde{z}_i \in \mathcal{U}(\mathbb{R}^m), i = 1, ..., m$ in form of fuzzy sets. The generation of $\tilde{z}_i$ is accomplished by means of the fuzzy analysis on the basis of the α-level optimization (Möller et al., 2000) and involves the discretization of both, the fuzzy input parameters $\tilde{p}_a$ and fuzzy responses $\tilde{z}_i$ into crisp sets $S_\alpha(\tilde{p}_a)$ and $C_\alpha(\tilde{z}_i)$

$$S_\alpha(\tilde{p}_a) = \{x \in \mathbb{R} : \ \mu_A \geq \alpha\}, \tag{6}$$

$$\tilde{p}_a = (S_\alpha(\tilde{p}_a))_{\alpha \in (0,1]}. \tag{7}$$

$$\tilde{z}_i = (C_\alpha(\tilde{z}_i))_{\alpha \in (0,1]}. \tag{8}$$

The uncertain structural responses $\tilde{z}_i$ can be obtained as fuzzy numbers or may exhibit time τ and space θ dependency and, thus, be characterized by uncertain functions in form of fuzzy processes $\tilde{z}_i(\tau)$, $\tau \in T = \mathbb{R}^4$ and fuzzy fields $\tilde{z}_i(\boldsymbol{\theta})$, $\boldsymbol{\theta} \in T$. The structural response, which is of main interest in this work is the uncertain crack propagation obtained as a fuzzy curve. According to the α-level discretization, the fuzzy crack propagation curve $\tilde{\gamma}_{cr}$ is defined by sets $C_\alpha(\tilde{\gamma}_{cr})$ of trajectories γ_{cr}

$$\tilde{\gamma}_{cr} = (C_\alpha(\tilde{\gamma}_{cr}))_{\alpha \in (0,1]}; \quad C_\alpha(\tilde{\gamma}_{cr}) = \left\{\gamma_{cr} \in \mathscr{E}^3 : \ \mu_z \geq \alpha\right\}. \tag{9}$$

Each trajectory γ_{cr} is equivalent to a deterministic realization of the uncertain propagation curve and corresponds to a deterministic fracture image, compare Figure 4. The set $C_\alpha(\tilde{\gamma}_{cr})$ assembles trajectories, which have at least the assigned membership $\mu_z \geq \alpha$. In addition, every deterministic crack propagation γ_{cr} can be assessed with respect to the possibility of occurrence $\pi_d = \mu_z$. Each trajectory γ_{cr} is defined as a set of n_θ points $\boldsymbol{\theta}_c^i$ in the body $\mathcal{B}$

$$\gamma_{cr} = \left\{\boldsymbol{\theta}_c^1; ..., \boldsymbol{\theta}_c^i, ..., \boldsymbol{\theta}_c^{n_\theta} \mid \boldsymbol{\theta}_c^i = [\theta_1, \theta_2, \theta_3] \in \ \mathcal{B}\right\}, \tag{10}$$

where the identification of the point $\boldsymbol{\theta}_c^{i+1}$, subsequent to the point $\boldsymbol{\theta}_c^i$, is based on the computation of the material force vector $\mathcal{F}$.

For the uncertain crack propagation $\tilde{\gamma}_{cr}$, the bounding curves $\tilde{\gamma}_{cr}^{\underline{b}}$, $\tilde{\gamma}_{cr}^{\overline{b}}$, which envelope all trajectories γ_{cr}, may be specified

$$\tilde{\gamma}_{cr}^{\underline{b}} = \min_{\boldsymbol{\theta}_c^{\tilde{\gamma}ij}|_j} [\gamma_{cr} \mid \gamma_{cr} \in C_{\alpha=0}(\tilde{\gamma}_{cr})], \tag{11}$$

$$\tilde{\gamma}_{cr}^{\bar{b}} = \max_{\boldsymbol{\theta}_c^{\bar{\wedge}ij}|_j} [\gamma_{cr} \mid \gamma_{cr} \in C_{\alpha=0}(\tilde{\gamma}_{cr})]. \tag{12}$$

In Eq. (11) and (12), $\boldsymbol{\theta}_c^{\bar{\wedge}ij}$ stands for a position vector projected from the three-dimensional Euclidean space $\mathscr{E}^3$ with dimensions denoted by $i, j, k \in \{1, 2, 3\} \mid i \neq j \neq k$ onto two-dimensional Euclidean space $\mathscr{E}^2$ with dimensions i, j. The bounding curves indicated by black dashed line in Figure 4, are evaluated within the fail-safe design optimization procedure.

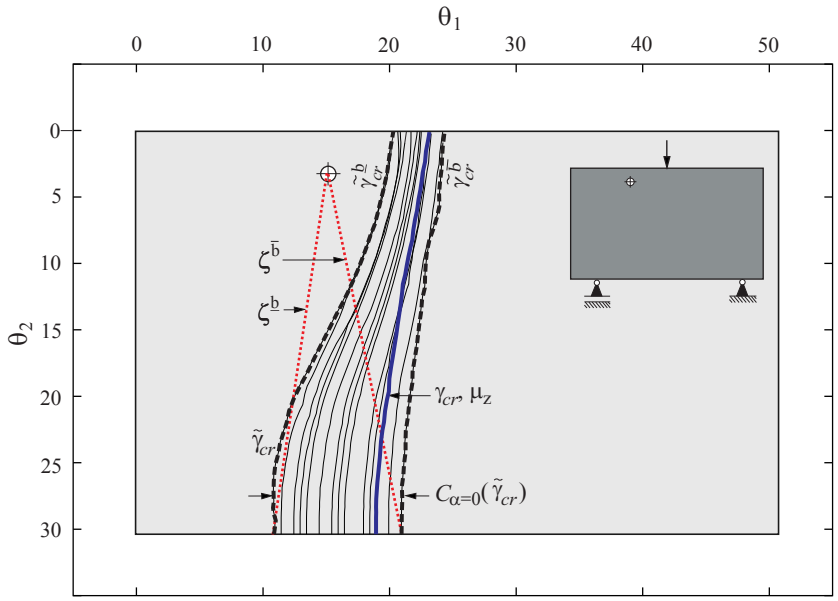

Figure 4. Fuzzy crack propagation curve.

4. Fail-Safe Design Optimization

In the following, the solution of the fail-safe optimal design problem, which is formulated as a the multi-objective optimization task with uncertain (fuzzy) parameters is presented. Since ordering of the objective function outputs is an inherent function of every optimization procedure, the order relations for the uncertain structural responses $\tilde{z}_i$, $\tilde{z}_i(\tau)$, $\tilde{\gamma}_{cr}$ need to be developed. The herein applied order is based on the application of the information reducing measures $\mathcal{M}_j : \mathcal{U}(\mathbb{R}) \to \mathbb{R}$, (Serafinska et al., 2013), (Graf et al., 2010), (Sickert et al., 2009).

Due to the utilization of information reducing measures $\mathcal{M}_j$ and the application of the scalarization approach for the multi-objective optimization problem in form of the weighted sum method, the objective function vector $\mathbf{f}(\mathbf{x}_d, \tilde{\mathbf{p}}_a)$ in Eq. (1) turns to

$$f(\mathbf{x}_d, \tilde{\mathbf{p}}_a) = \sum_{i=1}^{k} \sum_{j=1}^{l} w_{ij} \mathcal{M}_j(\tilde{z}_i) + \sum_{i=k}^{m-1} \sum_{j=l}^{u-1} w_{ij} \mathcal{K}_{ij}(\mathcal{M}_j(\tilde{z}_i(\tau))) + w_{mu} \mathcal{K}_{mu}(\mathcal{M}_u(\tilde{\gamma}_{cr})), \tag{13}$$

where $\tilde{z}_i = f_i(\mathbf{x}_d, \tilde{\mathbf{p}}_a)$ and w_{ij} are the weighting factors. In Eq. (13), the information reducing measures $\mathcal{M}_j$ are applied to the uncertain structural responses obtained as fuzzy quantities $\tilde{z}_i$, fuzzy functions $\tilde{z}_i(\tau)$ and fuzzy curves $\tilde{\gamma}_{cr}$. Thereby, for fuzzy quantities $\tilde{z}_i$, the measures $\mathcal{M}_j$ defined as the zeroth moment, the variance or the Shannon's entropy quantify the information content, e.g. the uncertainty of $\tilde{z}_i$ and reduce $\tilde{z}_i$ to a crisp value (Sickert et al., 2009). The quantification of the information content of an uncertain function/curve by means of $\mathcal{M}_j$ is equivalent to the identification of deterministic representatives of the fuzzy function/curve, important for a particular optimization objective. An example of representative curves are the deterministic bounding curves $\tilde{\gamma}_{cr}^{\underline{b}}$, $\tilde{\gamma}_{cr}^{\overline{b}}$ of the uncertain crack propagation $\tilde{\gamma}_{cr}$ shown in Figure 4

$$\mathcal{M}_u\left(\tilde{\gamma}_{cr}\right) = \left\{\tilde{\gamma}_{cr}^{\underline{b}}; \tilde{\gamma}_{cr}^{\overline{b}}\right\}. \tag{14}$$

A significant fail-safe design objective is the identification of a design with an optimal position of the crack arresters $\boldsymbol{\chi}_{Ai}$, so that all trajectories γ_{cr} of the uncertain crack propagation curve $\tilde{\gamma}_{cr}$ reach the boundary of the crack arrester Γ_{Ai}. Since all trajectories γ_{cr} of the uncertain crack propagation curve are located between the bounding curves $\tilde{\gamma}_{cr}^{\underline{b}}$, $\tilde{\gamma}_{cr}^{\overline{b}}$, the fail-safe criterion is satisfied if the bounding curves approach the boundary of the crack arrester. Thus, every bounding curve must be assessed with respect to the aspired propagation direction and path. Thereby, the aspired propagation path is defined a priori based on the assumption, that the propagation ends up at the crack arrester, as shown in Figure 4. In Eq. (13), the coincidence between bounding curves $\tilde{\gamma}_{cr}^{\underline{b}}$, $\tilde{\gamma}_{cr}^{\overline{b}}$ and the conjugate aspired crack propagation paths $\zeta^{\underline{b}}$, $\zeta^{\overline{b}}$ is quantified by the function $\mathcal{K}$ utilizing the Euclidean distance metric $d_{\mathscr{E}}$

$$\mathcal{K}_{mu}\left(\mathcal{M}_u\left(\tilde{\gamma}_{cr}\right)\right) = \sum_{l=1}^{n_\theta} P\left[d_{\mathscr{E}}\left(\tilde{\gamma}_{cr}^{\underline{b}}; \zeta^{\underline{b}}\right)\right] + \sum_{l=1}^{n_\theta} P\left[d_{\mathscr{E}}\left(\tilde{\gamma}_{cr}^{\overline{b}}; \zeta^{\overline{b}}\right)\right]. \tag{15}$$

In Eq. (15), n_θ stands for the number of discrete points $\boldsymbol{\theta}_c$ on the bounding curve of the uncertain crack propagation and P is the arbitrarily defined penalty function. The aspired crack curve, e.g. $\zeta^{\underline{b}}$, is specified on the basis of the initial conditions $\zeta^{\underline{b}\,0}$, which are known since they are derived from the definition of the uncertain crack initiation point as a fuzzy quantity $\tilde{p}_a$

$$\zeta^{\underline{b}\,0} = \boldsymbol{\theta}_c^0; \quad \boldsymbol{\theta}_c^0 = \min\left[\boldsymbol{\theta}_c \mid \boldsymbol{\theta}_c \in S_{\alpha=0}(\tilde{p}_a)\right]. \tag{16}$$

Further coordinate $\zeta^{\underline{b}\,n_\theta}$ of the aspired crack curve $\zeta^{\underline{b}}$ is prescribed on the boundary of the crack arrester and defined with respect to the location vector of the crack arrester $\boldsymbol{\chi}_{Ai}$

$$\zeta^{\underline{b}\,n_\theta} = \boldsymbol{\theta}_c^{n_\theta}; \quad \boldsymbol{\theta}_c^{n_\theta} = \boldsymbol{\chi}_{Ai}. \tag{17}$$

The interpolation between points $\zeta^{\underline{b}\,0}$ and $\zeta^{\underline{b}\,n_\theta}$ is defined e.g. as a linear function. The aspired crack propagation paths are indicated by a dashed red line in Figure 4. The optimization algorithm identifies an advantageous position of crack arresters, for which the distance between the aspired crack paths and the corresponding bounding curves of the uncertain crack propagation is minimized and all realizations γ_{cr} reach the boundary of crack arresters.

5. Numerical Realization

The numerical realization of the presented fail-safe design optimization concept is based upon a three level procedure implemented as a nested loop approach, compare Figure 5. Accordingly, the optimization constitutes the first level and the outer loop of the numerical procedure whereas the fuzzy analysis establishes the second level and the first inner loop. Within the fuzzy analysis, the fracture mechanical analysis in the finite element framework is executed.

The binary genetic algorithm applied at the optimization level, starts with initialization of the first population of design vectors ξ_ω, $\omega = 0$, and the vector of uncertain a priori parameters $\tilde{\mathbf{p}}_a$.

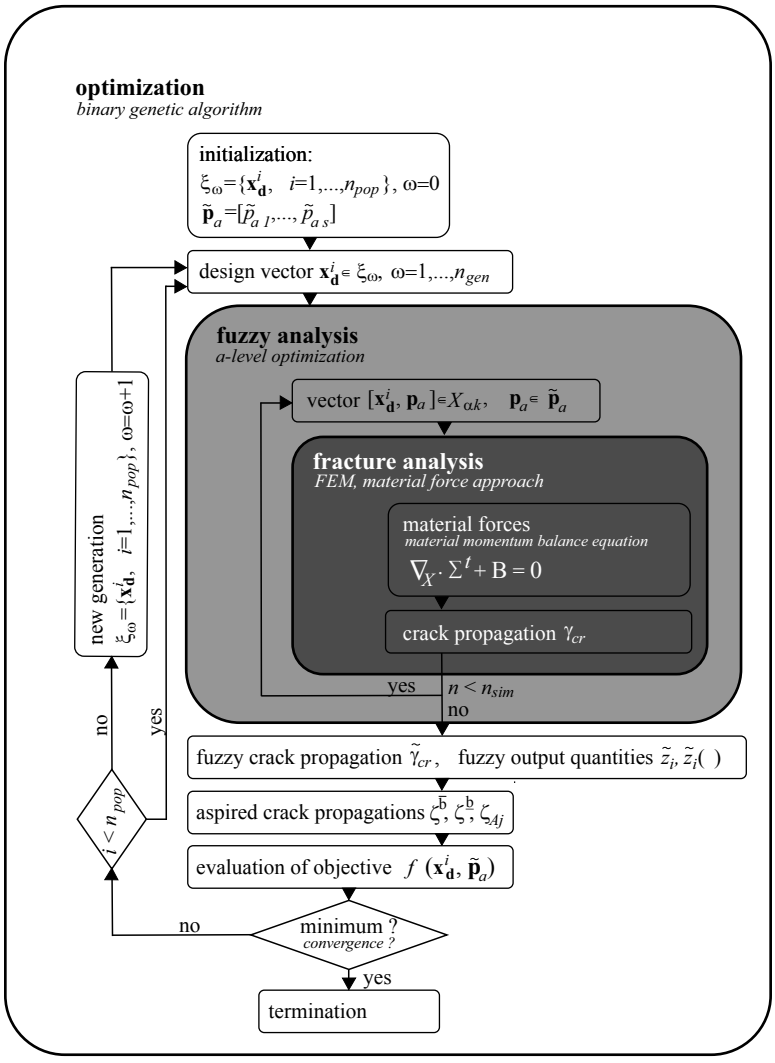

Figure 5. Schematic presentation of the optimization approach.

In the course of the optimization, for each design vector $\mathbf{x}_d^i$, $i = 1, ..., n_{pop}$ in the population ξ_ω, the fuzzy analysis is executed, yielding for every considered objective function $f_i(\mathbf{x}_d, \tilde{\mathbf{p}}_a)$ a fuzzy output quantity $\tilde{z}_i$, $\tilde{z}_i(\tau)$ or $\tilde{\gamma}_{cr}$, where $i = 1, ..., m-1$. The computation of fuzzy output quantities within the fuzzy analysis involves the determination of the shape of the membership function μ_z and the support ranges $C_{\alpha=0}(\tilde{z}_i)$. In the present approach, the fuzzy analysis is conducted by means of the α-level optimization procedure, introduced in (Möller et al., 2000). Thereby, the α-level optimization for the determination of the fuzzy crack propagation curve involves the Monte Carlo simulation. Especially, the Monte Carlo simulation is accomplished to identify the crack initiation points. The crack propagation curves resulting from the identified initiation points are evaluated at discrete spatial points to determine the extrema of the spatial dispersion of the uncertain crack propagation at each α-level.

Subsequently, the uncertain responses $\tilde{z}_i$, $\tilde{z}_i(\tau)$ and $\tilde{\gamma}_{cr}$ obtained for every considered design $\mathbf{x}_d^i$ are evaluated with the function $f(\mathbf{x}_d, \tilde{\mathbf{p}}_a)$ in Eq. (13). Since the formulation of $f(\mathbf{x}_d, \tilde{\mathbf{p}}_a)$ is facilitated by the information reducing measures $\mathcal{M}_j$, $f(\mathbf{x}_d, \tilde{\mathbf{p}}_a)$ yields a crisp output for a particular design $\mathbf{x}_d^i$. Obtaining of crisp outputs permits the ordering of conjugate designs within the binary genetic algorithm. After the evaluation of the function $f(\mathbf{x}_d, \tilde{\mathbf{p}}_a)$, the convergence criterion is verified. If the optimal design is found, the optimization terminates, else the next design is examined.

On the basis of the introduced coupling of the fuzzy analysis, the optimization algorithm and the fracture mechanical analysis, the genetic algorithm learns the features of the uncertain crack propagation and identifies the optimal configuration of the crack arresters.

6. Example

In the present example, the optimal geometrical configuration of crack arresters is determined for a concrete panel with dimensions 50.8 x 30.32 $[cm]$. Thereby, the crack arresting function is exhibited by the openings in the structure, e.g. the service pipes openings, which existence is required anyway. The optimization aims at the identification of the location of four openings $\boldsymbol{\chi}_{Ai}$, $i = 1, ..., 4$, described by six design variables a, b, c, d, e, f as shown in Figure 6.

The crack arrester position vectors $\boldsymbol{\chi}_{Ai}$ are specified with respect to the coordinate system with the origin in the reference point P. The considered design parameters are modelled as discrete variables, compare Table I. The diameter D of all openings is defined by 1.27 $[cm]$ and the magnitude of the initial crack length is set to $\gamma_{in} = 1.254$ $[cm]$. In the model, a linear elastic material characteristic is considered with the modulus of elasticity $E = 38000$ $[MPa]$, Poisson's ratio $\nu = 0.18$ and the fracture toughness $\mathcal{G}_c = 0.5$ $[N/mm]$.The crack initiation position $\theta_1^{\tilde{cr}}$ is considered as an uncertain parameter and modelled as a fuzzy triangular number, compare Figure 6 and Table I. In this example, the crack initiation is a consequence of a particular boundary change, e.g. a removal of an additional support in the bottom of the panel, as depicted in Figure 6.

The fracture analysis is performed with a monotonic displacement based loading at constant increments $\Delta d_z = 0.01$ $[mm]$ on a statically determinate structure, which is obtained after the removal of the additional support. In Figure 7, the crack propagation for the identified optimal design at different stages of the loading and a particular crack initiation position is visualized. At

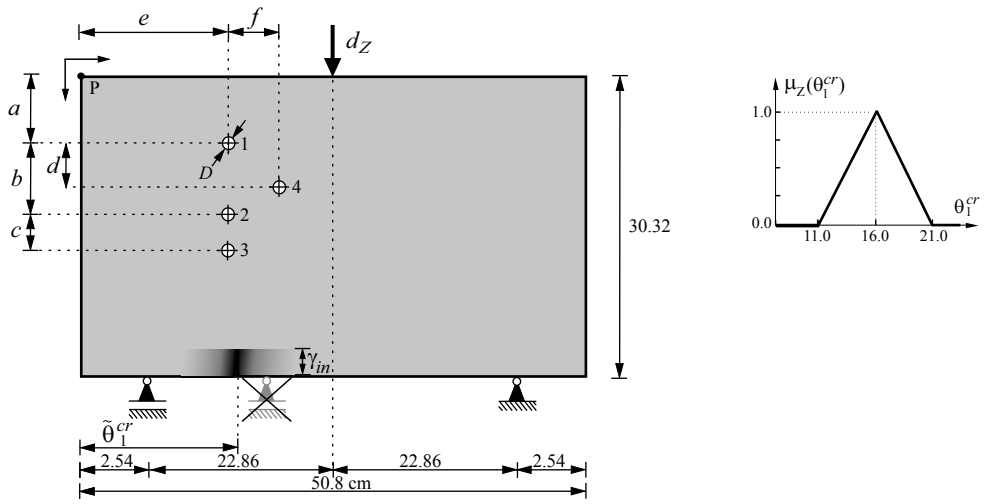

Figure 6. Parametrization of the panel design.

the nodes of the finite element model, the material force vectors are marked, whereas the vector at the crack tip defines the crack driving force.

The optimization accomplished by means of the binary genetic algorithm involves 20 generations of the algorithm and the population size of 25 genomes. The fuzzy analysis is executed considering the discretization of the fuzzy variable $\theta_1^{\tilde{cr}}$ into two α-level sets at $\alpha = 0$ $S_{\alpha=0}(\theta_1^{\tilde{cr}})$ and at $\alpha = 1$ $S_{\alpha=1}(\theta_1^{\tilde{cr}})$. The evaluation of the α-level set $S_{\alpha=0}(\theta_1^{\tilde{cr}})$, enables to account for all possibly appearing crack initiation locations. In addition, the proposed method permits to consider only the crack initiation positions with highest possibility by the evaluation of the α-level sets $S_\alpha(\theta_1^{\tilde{cr}})$ with $\alpha \approx 1$.

Table I. Definition of the design variables and uncertain parameters.

Design variables			
	interval	increment	unit
a	$[3.175, 8.255]$	$\Delta a = 2.54$	$[cm]$
b	$[2.54, 5.08]$	$\Delta b = 1.27$	$[cm]$
c	$[2.54, 5.08]$	$\Delta c = 1.27$	$[cm]$
d	$[0.00, 10.16]$	$\Delta d = 2.54$	$[cm]$
e	$[2.54, 27.94]$	$\Delta e = 5.08$	$[cm]$
f	$[2.54, 10.16]$	$\Delta f = 2.54$	$[cm]$
Fuzzy parameter			
$\tilde{p}_{a\,1} = \theta_1^{\tilde{cr}}$	$< 11.0; 16.0; 21.0 >$		$[cm]$

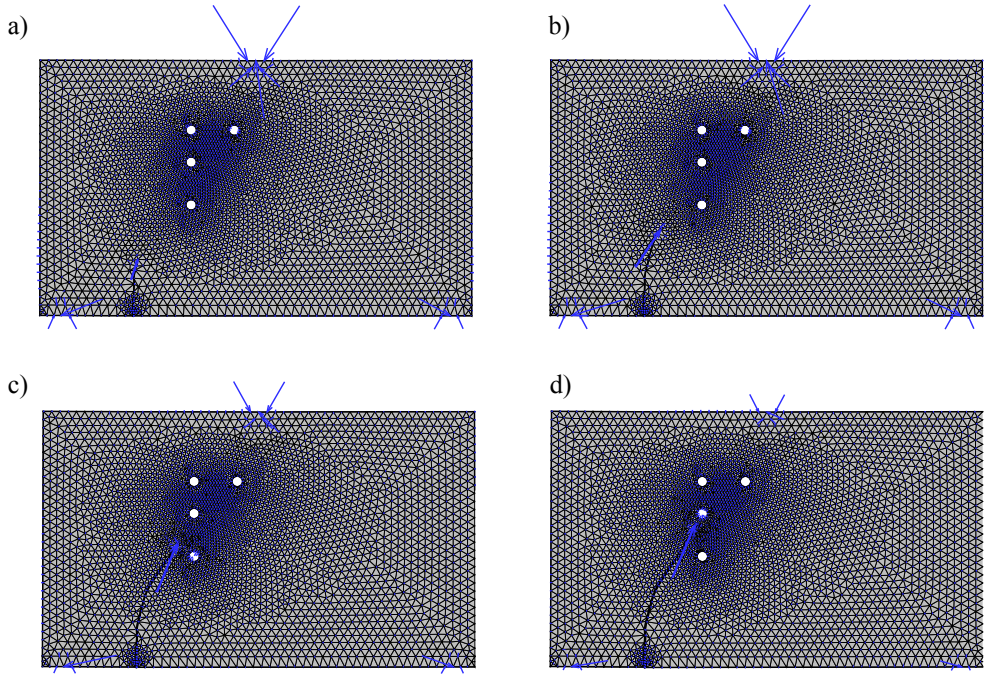

Figure 7. Crack propagation at different stages of the computation a) − d), at applied deformation of 0.70, 0.76, 0.87 and 0.95 $[mm]$ and the nodal material force vectors.

The α-level optimization is performed on the basis of the Monte Carlo simulation with 14 crack initiation locations evaluated for every design. The aspired crack propagation curves are specified as linear functions based on the points $\boldsymbol{\theta}_c^0$ and $\boldsymbol{\theta}_c^{n_\theta}$ available for each considered crack initiation point. The penalty function is defined as $P = [d_{\mathscr{E}}(\gamma_{cr\,j}; \zeta_{Ai})]^3$.

In Figure 8, the improvement of designs analyzed in subsequent optimization steps is visualized. For the design evaluated in the initial optimization step, which is presented in Figure 8 a), the disadvantageous configuration of the crack arresters implies that no crack propagation, i.e. no realization of the fuzzy crack propagation curve can be hindered. The enhancement of the fail-safe function is achieved for designs in Figure 8 b), c) analyzed in later optimization stages. In the progress of optimization, the fail-safe optimal design is identified with the crack arrester configuration limiting every crack growth determined by the fuzzy analysis. The optimal design, visualied in Figure 8 d), is characterized by the design variables configuration $a = 8.26$, $b = 3.81$, $c = 5.05$, $d = 0.00$, $e = 17.78$, $f = 5.08\,[cm]$ and the corresponding crack arrester position vectors $\boldsymbol{\chi}_{A1} = [17.78, 8.26]$, $\boldsymbol{\chi}_{A2} = [17.78, 12.06]$, $\boldsymbol{\chi}_{A3} = [17.78, 17.14]$, $\boldsymbol{\chi}_{A4} = [22.86, 8.26]$ $[cm]$. The FE models associated with the design configurations evaluated in the optimization are depicted in Figure 8 as well. Thereby, FE models with only one of the considered crack initiation points are visualized.

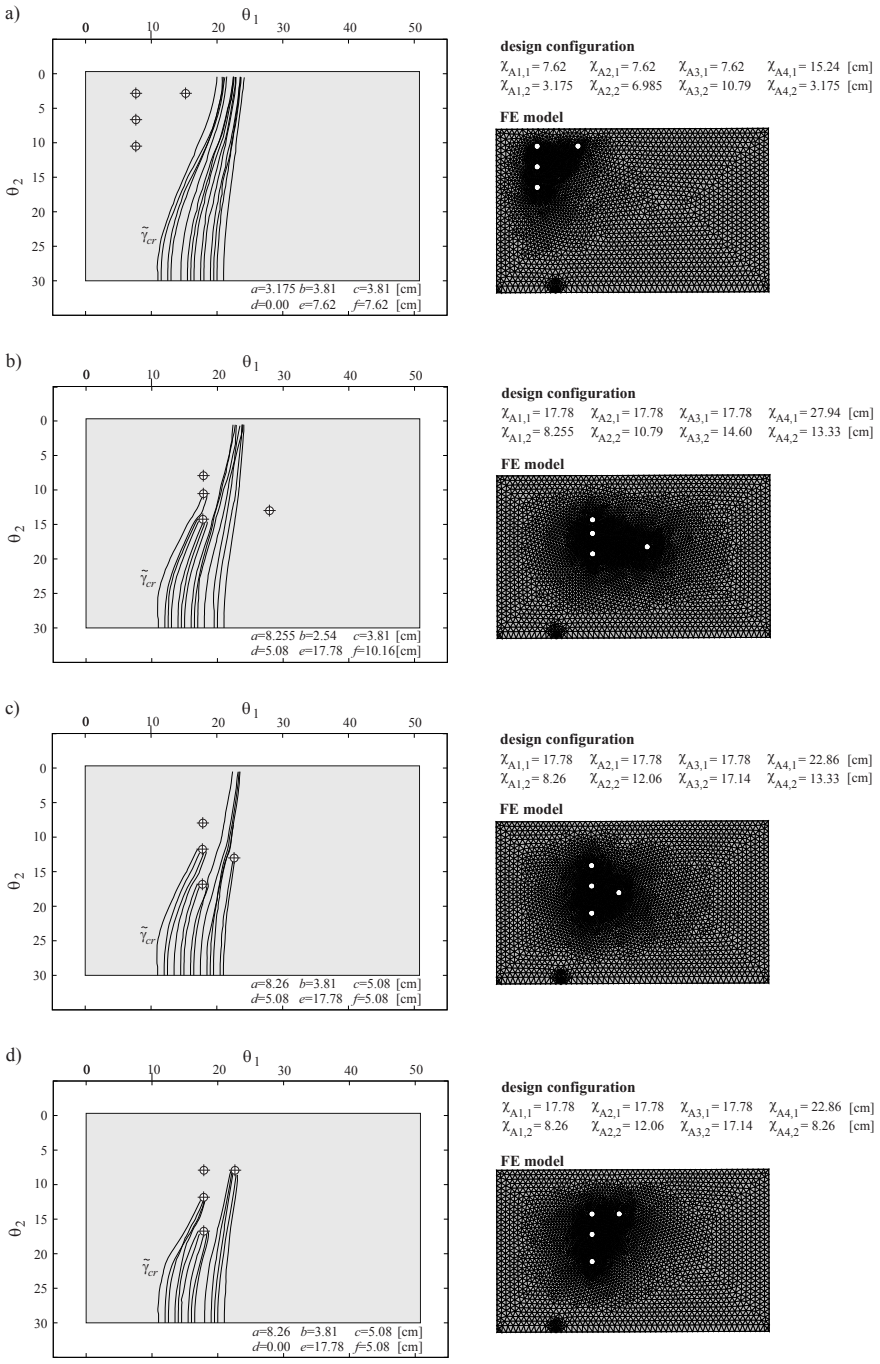

Figure 8. Fuzzy crack propagation curve for designs in subsequent generations of the optimization algorithm.

7. Conclusions

In the present contribution, a method for a fail-safe design optimization is presented, which is numerically realized as a coupled approach of optimization, fuzzy analysis and fracture mechanical analysis. For the investigations on safe failure, the uncertainties within the crack initiation and growth process are analyzed. The modelling of nonstochastic properties of the uncertain crack initiation position in a substructure belonging to the system of coupled substructures, succeeds by the application of the fuzzy set theory and the possibility theory framework. By taking into account the possibility of the occurrence of diverse crack propagation paths, the optimal configuration of the crack arresters can be identified in a systematic way by means of the genetic algorithm based design optimization procedure. The introduced approach enables the improvement of the prevention from undesired crack growth and damage escalation as well as contributes to the enhancement of structural durability and safety.

Acknowledgements

The support of the German Research Foundation (DFG) within the research project KA1163/13 "Design of durable tires under consideration of data uncertainty" is gratefully acknowledged.

References

Băzant, Z. Probabilistic modeling of quasibrittle fracture and size effect. In Corotis, R. B. (Ed.), *Proceedings of the 8th International Conference on Structural Safety and Reliability*, Lisse, 2001.

Besterfield, G. H., W. K. Liu, M. A. Lawrence, and T. Belytschko. Fatigue crack growth reliability by probabilistic finite elements. *Computer Methods in Applied Mechanics in Engineering*, 86:297–320, 1991.

Cazes, R. Damage Tolerance Design. In Bathias, C. and A. Pineau (Eds.), *Fatigue of Materials and Structures*. Wiley, Hoboken, 2013.

Dilger, R., H. Hickethier, and M. D. Greenhalgh. Eurofighter a safe life aircraft in the age of damage tolerance. *International Journal of Fatigue*, 31:1017–1023, 2009.

Dubois, D. and H. Prade. *Fuzzy Sets and Systems: Theory and Applications*. Academic Press, 1980.

Eshelby, J. D. The force on an elastic singularity. *Philosophical Transactions of the Royal Society London A*, 244:87–112, 1951.

Eshelby, J. D. The elastic energy-momentum tensor. *Journal of Elasticity*, 5:321–335, 1975.

Graf, W., J.-U. Sickert, S. Pannier, and M. Kaliske. Robust design with uncertain data and response surface approximation.. In Beer, M., Muhanna, R. L. and R. L. Mullen (Eds.), *Proceedings of the 4th International Workshop on Reliable Engineering Computing*, Singapore, 2010.

Leonel, E. D., A. Chateauneuf, W. S. Venturini, and P. Bressolette. Coupled reliability and boundary element model for probabilistic fatigue life assessment in mixed mode crack propagation. *International Journal of Fatigue*, 32:1823–1834, 2010.

Möller, B., W. Graf, and M. Beer. Fuzzy structural analysis using alpha-level optimization. *Computational Mechanics*, 26:547–565, 2000.

Möller, B. and M. Beer. *Fuzzy Randomness. Uncertainty in Civil Engineering and Computational Mechanics*. Springer, 2004.

Nguyen, D. T. and J. S. Arora. Fail-safe optimal design of complex structures with substructures. *Journal of Mechanical Design*, 104:861–868, 1982.

Novák ,D., M. Vorechovský, D. Lehký, R. Rusina, R. Pukl, and V. Červenka. Stochastic nonlinear fracture mechanics finite element analysis of concrete structures. In Augusti, G., Schuëller, G. I. and M. Ciampoli (Eds.), *Proceedings of the 9th International Conference on Structural Safety and Reliability*, Rotterdam, 2005.

Özenç, K. and M. Kaliske. An implicit adaptive node-splitting algorithm to assess the failure mechanism of inelastic elastomeric continua. *International Journal for Numerical Methods in Engineering*, 9:669–688, 2014.

Rahman, S. Probabilistic fracture mechanics: J-estimation and finite element methods. *Engineering Fracture Mechanics*, 68:107–125, 2001.

Rahman, S. and B. N. Rao. Probabilistic fracture mechanics by Galerkin meshless methods − part II: reliability analysis. *Computational Mechanics*, 28:365–374, 2002.

Riahi, H., P. Bressolette, and A. Chateauneuf. Random fatigue crack growth in mixed mode by stochastic collocation method. *Engineering Fracture Mechanics*, 77:3292–3309, 2010.

Serafinska, A., M. Kaliske, C. Zopf, and W. Graf. A multi-objective optimization approach with consideration of fuzzy variables applied to structural tire design. *Computers and Structure*, 116:7–19, 2013.

Shechter, A. Optimal fail-safe design of elastoplastic structures. *The American Institute of Aeronautics and Astronautics Journal*, 32:1333–1335, 1994.

Sickert, J.-U., S. Pannier, W. Graf, and C. Jenkel Robustness assessment of structures incorporating generalized uncertainty models. In Furuta, H., Frangopol, D. M. and M. Shinozuka (Eds.), *Proceedings of the 10th International Conference on Structural Safety and Reliability*, London, 2009.

Steinmann, P. Application of material forces to hyperelastostatic fracture mechanics. I. Continuum mechanical setting. *International Journal of Solids and Structures*, 37:7371–7391, 2000.

Sun, P. F., J. S. Arora, and E. J. Haug. Fail-safe optimal design of structures. *Engineering Optimization*, 2:43–53, 1976.

Vorechovský, M. *Probabilistic modeling of quasibrittle fracture and size effect.* PhD thesis, Brno University of Technology, 2004.

Wood, H. A. and R. M. Engle. USAF damage tolerant design handbook. Technical Report, United States Air Force, Structures and Dynamics Division, 1979.

Yang J. N. and S. D. Manning. A simple second order approximation for stochastic fatigue growth analysis. *Engineering Fracture Mechanics*, 53:677–686, 1996.

Zadeh, L. A. Fuzzy sets. *Information and Control*, 8:338–353, 1965.

Zhang, X., M. Boscolo, D. Figueroa-Gordon, G. Allegri, and P. E. Irving. Fail-safe design of integral metallic aircraft structures reinforced by bonded crack retarders. *Engineering Fracture Mechanics*, 76:114–133, 2009.

Numerical Simulation of Wooden Structures with Polymorphic Uncertainty in Material Properties

Ferenc Leichsenring, Wolfgang Graf and Michael Kaliske
Institute for Structural Analysis, TU Dresden, 01062 Dresden, Germany,
ferenc.leichsenring@tu-dresden.de

Abstract: Due to nature, uncertainties are inherently present in structural parameters such as loadings, boundary conditions or resistance of structural materials. Especially material properties and parameters of wood are strongly varying in consequence of growth and environmental conditions. The considered uncertainties can be classified into aleatoric and epistemic uncertainty. To include this variation in structural analysis, available data need to be modelled appropriately, e.g. by means of probability and furthermore fuzzy probability based random variables or fuzzy sets. Therefore, a limited empirical data basis for Norway spruce, obtained by experiments according to DIN EN 408, is stochastically analysed including correlation, sensitivity analyses and statistical tests. In order to comprehend uncertainties induced by estimating the distribution parameters, the stochastic approach has been extended with fuzzy distribution parameters to fuzzy probability based random variables according to (Möller and Beer, 2004; Möller et al., 2000). To cope with epistemic uncertainties for e.g. geometric parameters of knotholes, fuzzy sets are used. The consequence for wooden structures is determined by fuzzy stochastic analysis (Götz et al., 2015) in combination with a FEM simulation using a model suitable for characteristics of a timber structure by (Jenkel and Kaliske, 2014). The uncertain results (e.g. displacements, failure loads) constituted by the proposed holistic approach – defining the material properties based on an empirical data basis and the attempt of representing the uncertainties in material parameters and methods itself – will be discussed in terms of further processing in engineering tasks.

Keywords: polymorphic uncertainty, fuzzy randomness, stochastic modelling, wood mechanics, structural analysis

1. Introduction

Wooden structures underlie a fundamental data uncertainty in every engineering related matter. The material parameters of wood are strongly varying due to the natural growth and environmental conditions even within small pieces of wood. These aspects hold especially true for the material parameters defined at a macroscopic level like the elasticity moduli and material strengths considered in this contribution. The reason for the variation at the macroscopic level might be found in the anatomical structure of wood including the cellular level. To incorporate these characteristics, wood can be described on the mesoscale including the growth layer dependent spatial variability of material parameters, see e.g. (De Amicis et al., 2011), or even on a micro and nanoscale, see (De Borst et al., 2013). However, the material parameters on the nano and microscale are naturally

varying themselves. Regarding the design of timber structures according to EN 1995 (2010), global engineering material parameters are applied including further structural uncertainties e.g. in fibre orientation and knot hole size as well as distribution. Despite those uncertainties, it becomes necessary to assess the capabilities of a structure as well as characteristic variables for construction and design purposes. Methods for consideration of uncertainties in design of timber structures by means of randomness have been presented amongst others in (Fink and Köhler, 2014; Jenkel et al., 2015; Köhler et al., 2007; Spaethe, 1992).

In general, uncertainty can be classified into aleatoric and epistemic uncertainty. The combination of both yields polymorphic uncertainty, see e.g. (Götz et al., 2015). The first type includes e.g. the variations of material properties based on repetitive material tests. Due to a given amount of test results, the uncertainties can be represented by means of randomness, which in general satisfies statistical laws and possess a quasi objective information content. In this contribution, experiments performed on small specimens made of Norway spruce according to European standards are used as data basis. Epistemic uncertainties encounter non-statistical properties, information deficits and subjective influences. According to (Möller and Beer, 2004), epistemic uncertainties are further divisible into informal and lexical uncertainties. In this approach, geometric dimensions, knothole sizes and positions are defined as fuzzy sets according to the fuzzy set theory of (Zadeh, 1965).

Especially for insufficiently large observations, a statistical evaluation free of doubt is hard to constitute. Therefore, the use of fuzzy probability based random variables (*fp-r*), see (Götz et al., 2015; Pannier, 2011; Pannier et al., 2013), is proposed in order to encounter the uncertainty within the determination of stochastic parameters as well as representing the range of the response for deterministic fundamental solution. To approximate solutions of FE simulations, and analytical functions, artificial neural networks are hereby used as deterministic fundamental solution. To evaluate polymorphic uncertainty with respect to a wooden structure, a fuzzy stochastic analysis according to (Götz et al., 2015; Möller et al., 2007) is a valid approach, which yields to more realistic but uncertain result quantities.

This contribution is divided into five main sections. Firstly, a brief overview of mathematical fundamentals is given, regarding randomness, fuzziness and fuzzy randomness. The computational analysis procedure is explained as well. Approaches to model fuzzy distribution parameters for fuzzy probability based random variables are introduced. Hereafter, the data basis gathered from multiple experiments is presented together with the appropriate *fp-r* variables. Subsequently, a fuzzy stochastic analysis is applied on a wooden structure including knotholes.

2. Introduction of Uncertainty Models

The utilized uncertain structural analysis includes both, stochastic and fuzzy analysis. Therefore, the mathematical basis for each concept of uncertainty is introduced including the description of polymorphic uncertainty by means of fuzzy randomness.

2.1. Uncertainty models

In order to derive a numerical model for an adequate consideration of uncertainty, it is proposed to extend the common approach of stochastic modelling, used e.g. for material parameters, to fuzzy probability based random variables. Therefore, the fundamentals of randomness, fuzziness, covering epistemic uncertainty of e.g. geometric dimensions, and fuzzy probability based random variables are hereafter introduced, to incorporate the source and nature of present uncertainties.

2.1.1. *Randomness*

A random variable X is defined by the mapping $X: \Sigma \to \mathbb{R}$ fulfilling the condition

$$\forall I \in \mathcal{B}(\mathbb{R}) : X^{-1}(I) := \{\omega \in \Omega \mid X(\omega) \in I\} \in \Sigma \,, \tag{1}$$

whereas Ω correspondents with the set of elementary events ω, Σ is a σ-Algebra and P is the probability measure, satisfying the probability axioms of Kolmogorov. The observation space is represented by $(\mathbb{R}, \mathcal{B}(\mathbb{R}))$ including the Borel-σ-Algebra $\mathcal{B}(\mathbb{R})$. If X complies to the condition Eq. (1), an associated probability measure P_X is furthermore defined as

$$P_X : \mathcal{B}(\mathbb{R}) \to [0,1] : I \mapsto P_X(I) = P(X^{-1}(I)) \,. \tag{2}$$

The underlying distribution of the random variable X can be expressed by the cumulative distribution function F_X (cdf) and its derivative called probability density function f_X (pdf) for which holds

$$F_X(x) = \int_{-\infty}^{x} f_X(t)\mathrm{d}t \,. \tag{3}$$

Based on the assumption that f_X is continuous, the probability of an interval $I = [x_l, x_r]$ is related to F_X as follows

$$P_X(I) = F_X(x_r) - F_X(x_l) \,. \tag{4}$$

The probability distribution of random variables is usually described by means of parametrized distributions $F_X(x, \theta)$. Common distribution types as the Normal or Log.-Normal distribution will be further represented as parametric model with respect to suitable distribution parameters θ.

2.1.2. *Fuzziness*

Considering a precise set $A \subseteq \mathbb{R}$, the characterizing function $\xi(\cdot)$, in terms of precise sets also called indicator functions (Viertl, 1996), is defined by

$$\xi_A : \mathbb{R} \to \{0;1\}, x \mapsto: \begin{cases} 1, & x \in A \\ 0, & x \notin A \end{cases} \,. \tag{5}$$

Due to the imprecision of measurements, it becomes obvious that the definition of interval boundaries in this precise manner is a simple approach and not very realistic. Subsequently, the definition of precise sets has been enhanced to non-precise sets. For reasons of distinction, the characterizing function $\xi(\cdot)$ for non-precise data will be further expressed as membership function $\mu(\cdot)$ allowing

an assessment of the membership to an domain between $[0, 1]$. A fuzzy set $\tilde{A}$ can be expressed as set of ordered pairs

$$\tilde{A} = \{(x, \mu_{\tilde{A}}(x)) \mid x \in X, \mu_{\tilde{A}}(x) \geq 0\} \, . \tag{6}$$

To highlight the transformation from precise sets A to uncertain sets in $\mathbb{R}$, fuzzy sets will be further referred to as $\tilde{A}$. The fuzzy set $\tilde{A}$ can also be referred to as a fuzzy number $\tilde{x}$, see (Möller and Beer, 2004). The membership function $\mu(\cdot)$ of an uncertain variable is a real function of a real variable with the following properties

$$\mu : \mathbb{R} \to [0, 1] \, , \tag{7}$$

$$\exists \, x_0 \in \mathbb{R} : \mu(x_0) = 1 \, , \tag{8}$$

$$A_\alpha := \{x \in \mathbb{R} \mid \mu_{\tilde{A}}(x) \geq \alpha\} = [a_\alpha, b_\alpha] \, , \tag{9}$$

where the finite closed interval A_α is called α-cut of $\mu(\cdot)$ (Zadeh, 1971). The α-cut A_0 is called support of $\tilde{A}$. In this contribution, only convex fuzzy numbers according to (Möller and Beer, 2004; Pannier, 2011; Pannier et al., 2013) are considered. With respect to Eq. (9), all utilized fuzzy numbers are represented as either fuzzy triangular number

$$\tilde{x} = \langle a_0, x_0, b_0 \rangle \, , \tag{10}$$

or fuzzy trapezoidal interval number

$$\tilde{x} = \langle a_0, a_1, b_1, b_0 \rangle \, . \tag{11}$$

Both types of fuzzy numbers are illustrated in Fig. 1.

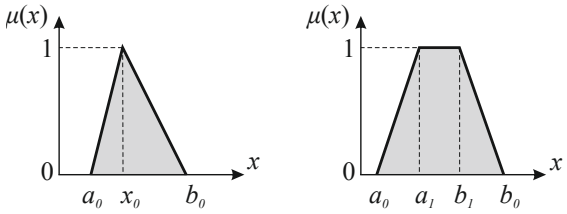

Figure 1. Fuzzy number $\tilde{x}$ as triangular and trapezoidal interval number.

2.1.3. *Fuzzy randomness*

The definition of fuzzy probability based random variables (*fp-r*) is founded on the assumption that the probability distribution of a random variable X according to Eq. (2) cannot be described exactly due to a lack of information, see e.g. (Götz et al., 2015; Pannier, 2011; Pannier et al., 2013). Thus, a fuzzy probability distribution and a fuzzy probability space $(\Omega, \Sigma, \hat{P})$ can be introduced. The fuzzy probability $\hat{P}$ is represented as family of α-cuts

$$\hat{P} = (P_\alpha)_{\alpha \in (0;1]} \, . \tag{12}$$

Each event $A \in \Sigma$ is related by P_α to an interval $[P_{\alpha,l}(A); P_{\alpha,r}(A)]$ for all $\alpha \in (0,1]$ such that the following condition is fulfilled

$$0 \leq P_{\alpha,l}(A) \leq P_{\alpha,r}(A) \leq 1 \; . \tag{13}$$

A fuzzy probability based random variable X is defined by the mapping of the fuzzy probability space onto the observation space $X : \Omega \to \mathbb{R}$. The fuzzy probability distribution $\hat{P}_X$ is formulated as family of mappings $\hat{P}_X = ((P_X)_\alpha)_{\alpha\in(0;1]}$, with

$$(P_X)_\alpha : \mathcal{B}(\mathbb{R}) \to \{[l,r] \mid 0 \leq l \leq r \leq 1\} : \tag{14}$$

$$I \mapsto P_\alpha(X^{-1}(I)) = [P_{\alpha,l}(X^{-1}(I)), P_{\alpha,r}(X^{-1}(I))] \; . \tag{15}$$

The fuzzy probability distribution might be represented by a fuzzy cumulative distribution function $\hat{F}_X$, which is again defined as family of α-cuts

$$\hat{F}_X = ((F_X)_\alpha)_{\alpha\in(0,1]} \tag{16}$$

$$(F_X)_\alpha = \{G : \mathbb{R} \to [0,1] \text{ cdf} \mid \forall x \in \mathbb{R} : \tag{17}$$

$$P_{\alpha,l}\left(X^{-1}((-\infty,x])\right) \leq G(x) \leq P_{\alpha,l}\left(X^{-1}((-\infty,x])\right)\} \; , \tag{18}$$

with an arbitrary cumulative distribution function $G(x)$. Each $G \in F_X$ is an original of $\hat{F}_X$. The applied cumulative distribution function G is usually defined by distribution parameters θ in terms of $G(x,\theta)$. Then, the fuzzy cumulative distribution function $\hat{F}_X$ can be described with fuzzy distribution parameters $\tilde{\theta} = (\theta_\alpha)_{\alpha\in(0,1]}$. For example, a two parametric distribution function with parameters θ_1 and θ_2 yields

$$\hat{F}_X = (\{F_{\theta_1\times\theta_2} \mid \theta_1 \in \tilde{\theta}_{1,\alpha}, \theta_2 \in \tilde{\theta}_{2,\alpha}\})_{\alpha\in(0,1]} \; . \tag{19}$$

This formulation is referred to as bunch parameter representation, since the fuzzy cumulative distribution and the fuzzy probability density function can be considered as assessed bunches of functions which are described by bunch parameters $\tilde{\theta}$.

2.2. Uncertain structural analysis

According to (Möller and Beer, 2004; Pannier, 2011), the so-called fuzzy stochastic analysis type I is utilized, in which the bunch parameter representation of fuzzy random variables is used. The general workflow is constituted in a three-loop computational model.

Initially, each input parameter X_i with $i = 1, \ldots, n$ is represented by a fuzzy distribution according to Eq. (19), where each distribution type is determined individually for each input dimension, see Section 3. The fuzzy analysis, performed in the outer loop, implies the α-discretization. A crisp space

$$\theta_{i,\alpha} = \{\theta_i \in \tilde{\theta}_i \mid \mu_{\tilde{\theta}_i}(\theta_i) \geq \alpha\} \subset \mathbb{R}^2 \tag{20}$$

is obtained for each α-level, carried out on $\tilde{\theta}_i = (\tilde{\theta}_{1,i} \times \tilde{\theta}_{2,i})$. Evidently, every set of bunch parameters θ_i is associated with a trajectory $F_{\theta_i}(x)$, see Fig. 2. In the inner loop of the computational model, for each trajectory a stochastic analysis is performed, which concludes, in combination with a given deterministic fundamental solution $f_{\mathcal{Z}} : \mathbb{R}^n \to \mathbb{R}^m$, to an empirical distribution $\bar{F}_j(z)$ for each

$$\theta_{i,\alpha} = \left\{ \theta_i \in \widetilde{\theta}_i \,|\, \mu_{\widetilde{\theta}_i}(\theta_i) \geq \alpha \right\} \subset \mathbb{R}^{n_{\theta_i}} \tag{4.70}$$

is obtained, whereas n_{θ_i} represents the number of bunch parameters per input variable. The membership function $\mu_{\widetilde{\theta}_i}(\theta_i)$ is determined according to Eq. 4.17 with $\theta_i = \{\theta_{i,1} \times \theta_{i,2} \times \ldots \times \theta_{i,n_{\theta_i}}\}$. From the deterministic space, a point can be picked containing a deterministic set of bunch parameters $\theta_i \in \theta_{i,\alpha}$, see Fig. 4.32. With this point, one trajectory $F_{\theta_i}(x)$ is determined and a real random variable $X_{\theta_i} \in X_i$ is described.

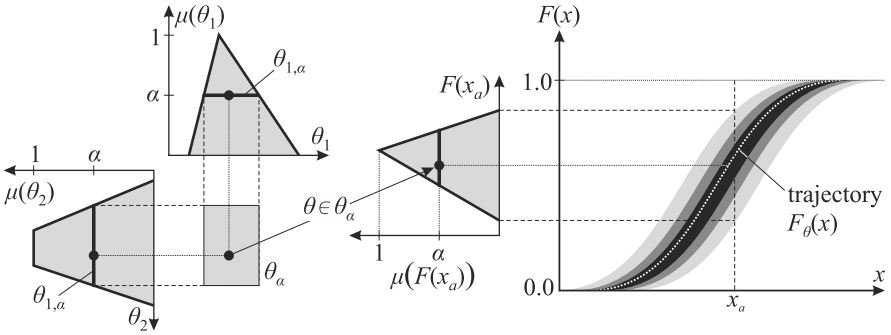

Figure 4.32: Fuzzy stochastic structural analysis: α-level discretization of bunch parameters and description of input variables by trajectories [105]

Figure 2. Trajectory regarding θ_i (Möller and Beer, 2004).

result set Z_j with $j = 1, \ldots, m$. To map the results at the appropriate α-level, it becomes necessary to condense the empirical distribution $\bar{F}(z)$ to a representative scalar value σ. As information reduction method, any descriptive statistical evaluation parameters such as standard deviation, mean, median, quantiles etc. are conceivable for this task. In order to determine the bounds of the associated α-level cut, a so-called α-level optimization (Möller et al., 2000) is necessary to be carried for the computation of $\{\sigma_{\min,\alpha}, \sigma_{\max,\alpha}\}$ as illustrated in Fig. 3. Conclusively, the fuzzy result variable $\tilde{\sigma}$ is used to represent the uncertain results of the chosen information reduction method. Therefore, the choice of method should be related to the problem under investigation and considered in the final interpretation of the gained results.

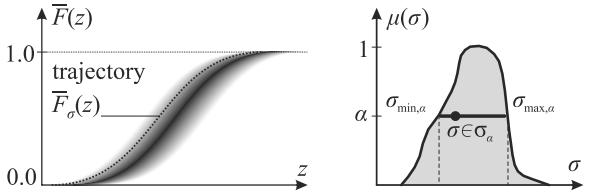

Figure 3. Distribution of z, representation with two reduction measurements (Möller and Beer, 2004).

3. Data Modelling

Since the proposed procedure of uncertain analysis is founded on *fp-r* variables for material parameters of wood, elements of statistics are necessary to determine stochastic parameters. Additionally, two approaches for modelling fuzzy distribution parameters as either triangular or trapezoidal interval numbers are introduced, whereas both methods base on the statistical evaluation of a given dataset.

3.1. Elements of mathematical statistics

To transform given test results into a distribution function, methods of inductive statistics are necessary. There are four distribution types considered in this contribution all of which are two-parametric such as $F_X(\theta_1, \theta_2)$. Beside the common Normal and Log.-Normal distribution, two extreme value distributions, Gumbel and Weibull, are considered. Point estimators are used to determine the distribution parameters. Methods of Moments (MoM) as well as Maximum-Likelihood Estimation (MLE) apply for the most common point estimation procedures (Köhler et al., 2007). The MoM is used since initial investigations revealed that especially for a small sample size of data the more robust MoM is sufficiently accurate considering the general variance within the data set itself.

The determination of a probability distribution function based on a given test results will be shown for the elasticity modulus in tangential direction E_t and is initially based on 45 test samples $\underline{E_t}$. An examination with the boxplot detects potential outliers ($1.5 \cdot$*inter quartile range*), see (Frigge et al., 1989). In order to determine the distribution parameters, the empirical mean value $\bar{m}(\underline{E_t})$ and empirical standard deviation $\bar{\sigma}(\underline{E_t})$ will be used.

For a real-valued continuous functions $f(x)$, the n-th moment is determined according to (Spaethe, 1992)

$$\mu_n = \int_{-\infty}^{\infty} (x - c)^n f(x) dx \ . \tag{21}$$

The mean value μ of $f(x)$ is equal to the first moment (with $c = 0$) and the variance σ^2 satisfies the second moment if $c = \mu$ (central moment). The moments depending on the parameters θ_1, θ_2 can be expressed as

$$\begin{aligned} \mu_1 &= g_1(\theta_1, \theta_2) \\ \mu_2 &= g_2(\theta_1, \theta_2) \ . \end{aligned} \tag{22}$$

The MoM defines the empirical moments $\bar{m}, \bar{\sigma}^2$ equal to the moments μ_1, μ_2 of true distribution with the result that the equation system

$$\begin{aligned} \bar{m} &= g_1(\hat{\theta}_1, \hat{\theta}_2) \\ \bar{\sigma}^2 &= g_2(\hat{\theta}_1, \hat{\theta}_2) \end{aligned} \tag{23}$$

leads to the parameter estimations $\hat{\theta}_1, \hat{\theta}_2$ for θ_1, θ_2. For continuous functions, the estimators based on the MoM fulfil the following properties, such as consistency

$$\lim_{n \to \infty} P(|\hat{\theta} - \theta| > \varepsilon) = 0 \ , \forall \ \varepsilon > 0 \ , \tag{24}$$

as well as being asymptotically unbiased

$$\lim_{n \to \infty} \mathrm{E}(\hat{\theta}) = \theta \ . \tag{25}$$

To test the conformity of the empirical distribution with an assumed distribution type, two statistical tests are performed, see e.g. (Rinne, 2008; Viertl, 1997), the Kolmogorov-Smirnov test (KS)

and the χ^2-test with focus on the KS test due to the sample size of $n^* = 44$. Both statistic tests belong to the category "Goodness of fit", which determines how well an empirical distribution suits a hypothetical distribution function. The KS test is based on the maximum difference between an empirical and hypothetical cumulative distribution, with the given KOLMOGOROV-SMIRNOV statistic for the null-hypothesis $H_0 : F_n(x) = F_0(x)$ for a continuous probability distribution

$$D_n = \sup_x |F_n(x) - F_0(x)| \ . \tag{26}$$

The critical value of the maximum difference with respected to the significance level α is approximately (for $n \geq 35$)

$$c_\alpha = \frac{\sqrt{\ln(\frac{2}{\alpha})}}{\sqrt{2n^*}} \ , \tag{27}$$

hence the null hypothesis will be rejected if $D_n > c_\alpha$ (Messay, 1951). Therefore, $F_0(x)$ can be assumed as the underlying distribution function for the empirical distribution with a certain sureness based on α, see Fig 4(b). The chosen criteria for rejecting the null hypothesis with the χ^2-test is the p-value χ^2_p of the χ^2-test statistic (Sellke et al., 2001). If $\chi^2_p < \alpha$, the hypothetical distribution is rejected.

Table I. Distribution parameters for E_t.

	GUMBEL	LOG.-NORMAL	NORMAL	WEIBULL
KS ($c_{0.05}$)	0.2047	0.2047	0.2047	0.2047
KS (D_n)	0.0862	0.0670	0.1412	0.1357
χ^2 (p-value)	0.8364	0.8367	0.5893	0,5036
parameter 1	$a = 0,0356$	$\mu_u = 5,6886$	$\mu = 297,63$	$\theta = 312,90$
parameter 2	$b = 281,45$	$\sigma_u = 0,1203$	$\sigma = 35,937$	$k = 9,9617$

As Table I shows, neither of the four distribution types is declined by both statistical tests, which yields to the assumption that all of the distributions are valid approximations for the test samples. Since the maximum absolute difference between the LOG.-NORMAL distribution and the empirical distribution is the lowest, a LOG.-NORMAL distribution (σ_u, μ_u, see Tab. I) can be considered as best fitting for $\underline{E_t}$. The four distribution types, represented by the probability density functions (parameters see Tab. I) are shown in Fig. 4(a) with the relative frequencies of $x \in \underline{E_t}$. The small positive skewness of the histogram might lead to the preference of the GUMBEL and LOG.-NORMAL distributions by the statistical tests.

3.2. PRINCIPLES OF MODELLING THE FUZZY PROBABILITY BASED RANDOM VARIABLES

Since multiple admissible distributions exist to describe an empirical distribution, it is likely that the chosen point estimators are not the most accurate way to determine the distribution parameters

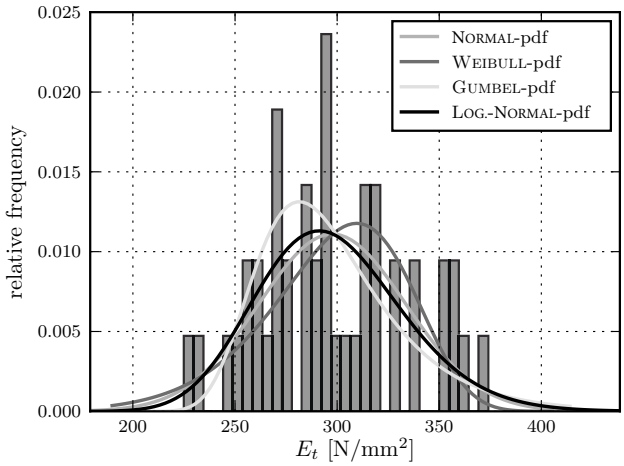

(a) Probability density functions and histogram of $\underline{E_t}$

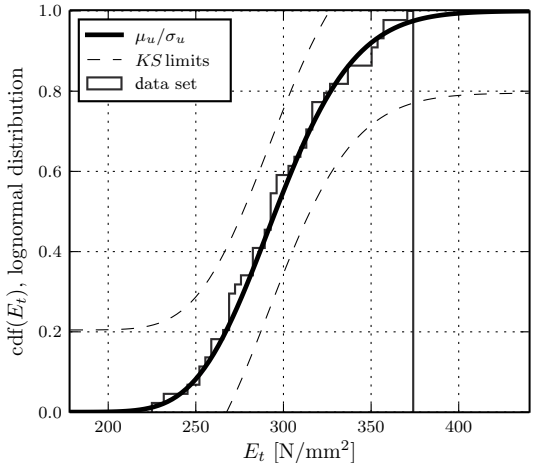

(b) Log.-Normal cumulative distribution function for E_t and empirical cumulative distribution of $\underline{E_t}$, limits for KS statistic Eq. (27)

Figure 4. All admissible distributions for E_t and the best fitting distribution within KS limits for $\alpha = 0.05$.

with respect to the uncertainty in the data. To define the bunch parameters of any chosen two-parametric fuzzy random based random variable

$$F_X = (\{F_{\theta_1 \times \theta_2} \mid \theta_1 \in \tilde{\theta}_{1,\alpha}, \theta_2 \in \tilde{\theta}_{2,\alpha}\})_{\alpha \in (0,1]} \,, \tag{28}$$

for $\alpha = 0$ and $\alpha = 1$, one of the following methods is used. A common approach for $\alpha = 0$ is based on interval estimation of a parameter θ. Assuming θ can vary within a defined confidence interval $[\vartheta_{\min}, \vartheta_{\max}]$

$$P_\theta(\vartheta_{\min} < \theta < \vartheta_{\max}) = (1 - \alpha) \,, \tag{29}$$

a set of the minimum and maximum values of parameters, according to the confidence level $(1-\alpha_s)$ might be used describing a set of distribution functions, see e.g. (Viertl, 1997). According to Eq. (28) and (29), the bounds of the support are defined as follows

$$\theta_{0,l} = \vartheta_{\min} \tag{30}$$

$$\theta_{0,r} = \vartheta_{\max} \,. \tag{31}$$

As described, one fuzzy parameter must hold $\{\exists\ \vartheta_0 \in \tilde{\theta} \mid \mu_{\tilde{\theta}}(\vartheta_0) = 1\}$. To obtain a so-called fuzzy triangular number, point estimators such as MLE, MoM are appropriate to gain ϑ_0. Therefore, the uncertain parameter will be further expressed as

$$\tilde{\theta}_{(\cdot)} = \langle \vartheta_{\min}, \vartheta_0, \vartheta_{\max} \rangle_{(\cdot)} \,. \tag{32}$$

Considering any point estimation of stochastic parameters for an empirical distribution with low sample sizes, it becomes obvious that this definition is accompanied by uncertainty as well. Consequently, an alternative definition to the one previously propagated must be found for input

dimensions with higher sensitivity relative to the investigated output dimension. Therefore, the error made by the point estimation has to be taken into account. Under the assumption that an admissible distribution type $F_X(\theta_1, \theta_2)$ fits the data set X, a sufficient amount of $n > 10^6$ samples

$$\bar{x} \in \bar{X}, P(\bar{X}) = F_X(\theta_1, \theta_2) \, , \tag{33}$$

should substitute the entire data set. To determine the deviation of the admissible parameter set from the actual provided data, the variation of mean and standard deviation of an extended original data set is computed with

$$X_i^* = X \cup \{\bar{x}_i\} \; \forall \; \bar{x}_i \in \bar{X} \; , \; i = \{1, \ldots, n\} \, , \tag{34}$$

$$\mu_i = \mathrm{E}[X_i^*] \, , \tag{35}$$

$$\sigma_i = \sqrt{\mathrm{Var}[X_i^*]} \, . \tag{36}$$

Hence, $\boldsymbol{\mu}^* = [\mu_1, \ldots, \mu_n]$ as well as $\boldsymbol{\sigma}^* = [\sigma_1, \ldots, \sigma_n]$ are two data sets containing the deflections of the first and second statistical moments. Concerning the longitudinal stiffness E_l, whereas the Weibull distribution can be considered as admissible, the distribution of the extended mean values (see Eq. (35)) is shown in Fig. 5(a). To evaluate the imprecision, the empirical quantiles μ_{q_5} and $\mu_{q_{95}}$ are chosen. With the same empirical quantiles of $\boldsymbol{\sigma}^*$ and the MoM, two parameter sets can be obtained

$$\mathrm{MoM} : \begin{cases} (\mu_{q_5}, \sigma_{q_5}) & \rightarrow (\vartheta_{1,\min_1}, \vartheta_{1,\min_2}) \\ (\mu_{q_{95}}, \sigma_{q_{95}}) & \rightarrow (\vartheta_{1,\max_1}, \vartheta_{1,\max_2}) \end{cases} \, . \tag{37}$$

Consequentially for each distribution parameter, a fuzzy trapezoidal interval number such as

$$\tilde{\theta}_{(\cdot)} = \langle \vartheta_{\min}, \vartheta_{1,\min}, \vartheta_{1,\max}, \vartheta_{\max} \rangle_{(\cdot)} \tag{38}$$

can be defined, whereas each α-cut A_1 is bounded by the corresponding distribution parameters in Eq. (37). The procedure is applied on material parameters of wood in Section 4. To observe the convergence properties, the fitting of admissible distribution parameters is performed on increasing samples size n_S for an arbitrary data set. In Fig. 5(b), a normalized error

$$\varkappa_{(\cdot)} = \frac{(q_{(\cdot)} - E[\mu^*])}{E[\mu^*]} \tag{39}$$

in relation to n_S is shown. Hence, based on the condition that for large n_S an admissible function exists, the following applies

$$\lim_{n_S \rightarrow \infty^+} \varkappa_{(\cdot)} = 0 \, , \tag{40}$$

as Fig. 5(b) illustrates. In terms of fuzzy numbers for stochastic parameters it yields $\vartheta_{1,min} = \vartheta_{1,max} = \vartheta_0$, whereby the fuzzy trapezoidal interval is reduced to a fuzzy triangular number.

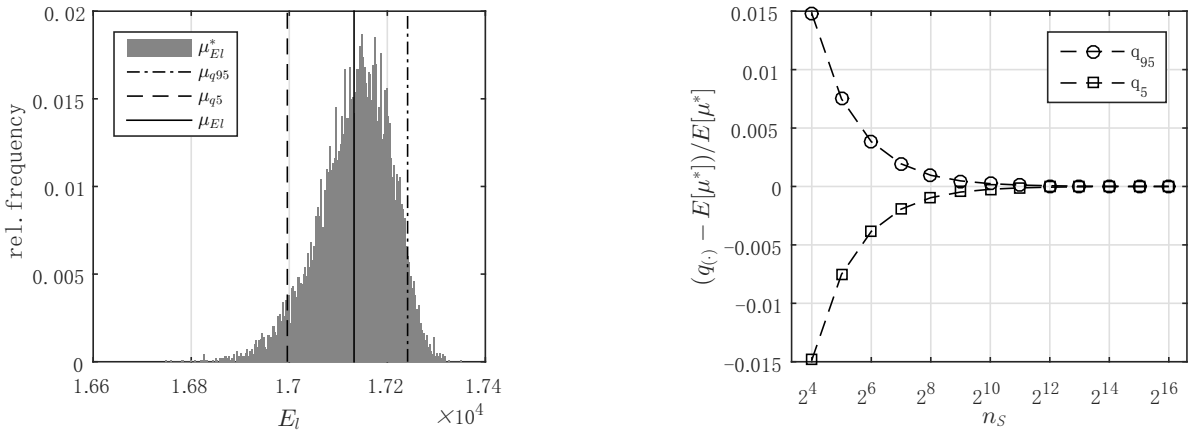

(a) Distribution of $\boldsymbol{\mu}^*$ (b) Convergence behaviour

Figure 5. Exemplary distribution of $\boldsymbol{\mu}^*$ (based on $\underline{E}_l$) and convergence behaviour of $\varkappa_{(\cdot)}$ related to increasing n_S.

4. Parameter Modelling and Data Basis

The introduced methods are applied to model the uncertainty of material parameters of wood subsequently. The mechanical behaviour of the anisotropic material wood differs significantly in the material directions radial r, tangential t and longitudinal l and strongly depends on the type of loading like tension t, compression c and shear loading v. In the structural analyses presented below, macroscopic material parameters taking into account these dependencies are utilized. The material parameters and their uncertain distributions are modelled on the basis of empirical data.

4.1. Data base situation

The data base applied in this contribution has been obtained in experiments described in (Jenkel et al., 2015; Ulrich and Seim, 2014). The investigated material parameters include the elasticity moduli and the material strengths in the material directions and depending on the type of loading. The tests have been carried out on small specimen, as far as possible free of inhomogeneities, according to European and German standards given in Tab. II. In the table, the number of samples (under consideration of outliers) as well as the empirical mean value $\bar{m}$ and standard deviation $\bar{\sigma}$ are given for each parameter. The total data sets are documented in (Jenkel et al., 2015; Ulrich and Seim, 2014).

The experiments are designed to take all samples independently on the basis of identical conditions (*i.i.d.* paradigm). For the parameters given in Tab. II, data sets should be obtained disregarding the interaction to other parameters. Especially density and moisture, as most relevant parameters influencing all material parameters of wood, should be blinded out. Thus, as far as possible, specimen of comparable density are used. The moisture is conditioned in climate chambers. To avoid size effects and obtain comparable parameters, identical specimen measures are applied

for most of the test series. Specimen with equal material directions are used in each test series considering all three material directions, except for the tensile strength perpendicular to grain.

Table II. Experimental basis according to (Jenkel et al., 2015; Ulrich and Seim, 2014).

parameter	E_r	E_t	E_l	$f_{t,90}$	$f_{t,l}$	$f_{c,r}$	$f_{c,t}$	$f_{c,l}$	f_v
standard	DIN 52192	DIN 52192	DIN 52185	EN 408	DIN 52188	DIN 52192	DIN 52192	DIN 52185	EN 408
samples	41	44	28	30	30	45	45	30	30
$\bar{m}\,[N/mm^2]$	656	298	17132	2.64	121.64	3.09	3.64	43.60	5.77
$\bar{\sigma}\ [N/mm^2]$	107	36	2211	0.33	18.20	0.23	0.43	2.07	0.73

4.2. Data modelling

The available data is evaluated statistically to model the material parameters as fuzzy probability based random variables. The best fitting distribution types for the data sets used in the examples presented below are given in Tab. III. Exemplarily, the longitudinal elasticity moduli E_l is represented by means of a Weibull distribution

$$\widehat{F}_{E_l} = \left(\left\{ F_{\theta \times k} \,|\, \theta \in \widetilde{\theta}_\alpha,\ k \in \widetilde{k}_\alpha \right\} \right)_{\alpha \in (0;1]}, \tag{41}$$

whereas the distribution parameters are modelled as fuzzy trapezoidal interval numbers according to Tab. III.The distribution is illustrated in Fig. 6. The black graphs in Fig. 6(a) are obtained using the *max*- and *min*-sets of the space of bunch parameters defined at $\alpha = 1$ marked by I and II in Fig. 6(b). The light grey graphs are computed with $\alpha = 0$ for the *max*- and *min*-sets of the bunch parameters marked by III and IV.

5. Example

The methods presented above are used subsequently to compute the ultimate load of a timber board containing knots at tensile loading are analysed under consideration of uncertainties in material and geometrical parameters. The material parameters are modelled as fuzzy probability based random variables (*fp-r*) while geometric parameters are described by fuzzy variables.

Knots in timber are remnants of branches in trees and can be considered as structural inhomogeneities. The size of knots and the boundary to the surrounding wood can often not be identified exactly. Thus, the size of the knots is regarded as being uncertain and modelled by means of fuzzy numbers. The board with dimensions $t \times b \times l = 18 \times 150 \times 350\,mm$ is analysed at uniform tensile loading as shown in Fig. 7. The aim is to compute the ultimate load. An FE analysis according to (Jenkel and Kaliske, 2014) is applied to generate an artificial neural feed forward network, which is used as deterministic fundamental solution $f_{\mathcal{Z}}$. Thereby, the knots and the surrounding wood are

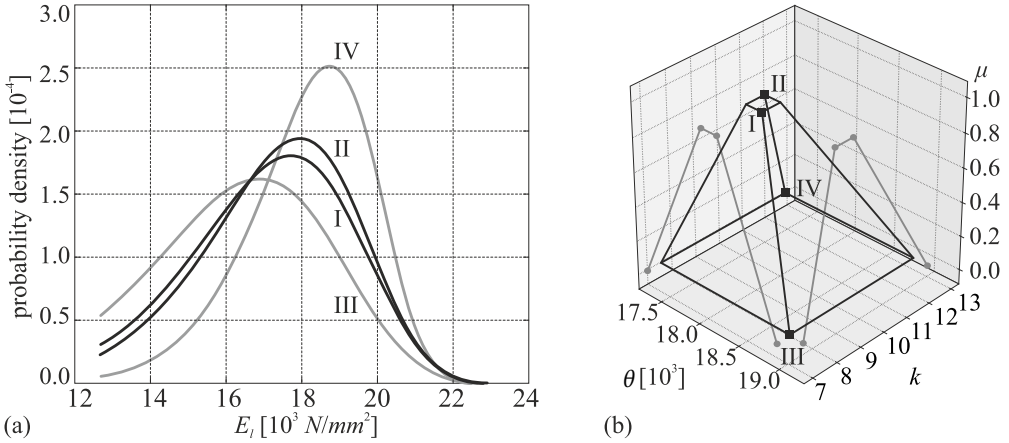

Figure 6. Fuzzy probability based random variable E_l: (a) fuzzy probability density function $\widehat{f}_{E_l}$ and (b) Cartesian product $\{\widetilde{\theta} \times \widetilde{k}\}$.

Table III. Evaluation of experimental data (all data in $[N/mm^2]$).

parameter	distribution type	fuzzy distribution parameters
E_l	Weibull	$\widetilde{\theta} = \langle 17256, 17790, 18326, 18785 \rangle$ $\widetilde{k} = \langle 7.529, 9.283, 10.99, 13.83 \rangle$
$f_{t,90}$	Weibull	$\widetilde{\theta} = \langle 2.6627, 2.7771, 2.8879 \rangle$ $\widetilde{k} = \langle 7.7578, 9.7439, 13.5851 \rangle$
$f_{t,l}$	Normal	$\widetilde{\mu} = \langle 114.45, 121.11, 125.37, 132.02 \rangle$ $\widetilde{\sigma} = \langle 14.491, 18.134, 21.248, 27.354 \rangle$
$f_{c,r}$	Gumbel	$\widetilde{a} = \langle 2.9097, 2.9687, 3.0375 \rangle$ $\widetilde{b} = \langle 4.9700, 5.9334, 7.7054 \rangle$
$f_{c,l}$	Log.-Normal	$\widetilde{\mu}_u = \langle 3.7554, 3.7737, 3.7917 \rangle$ $\widetilde{\sigma}_u = \langle 0.0395, 0.0491, 0.0559 \rangle$
f_v	Log.-Normal	$\widetilde{\mu}_u = \langle 1.6979, 1.7439, 1.7829 \rangle$ $\widetilde{\sigma}_u = \langle 0.0931, 0.1259, 0.1553 \rangle$

not distinguished by element edges, but by means of integration points. This smeared FE model is feasible since an individual coordinate system and material parameters can be assigned to every integration point of each finite element, compare (Zohdi and Wriggers, 2005). The board is simply discretized by a regular mesh with $2 \times 12 \times 30$ hexahedral 8-node finite elements, see Fig. 7. To improve the approximation of knots, three integration points are used in each direction per element. Due to the indirect representation of knots in the FE model, a fixed regular mesh can be applied

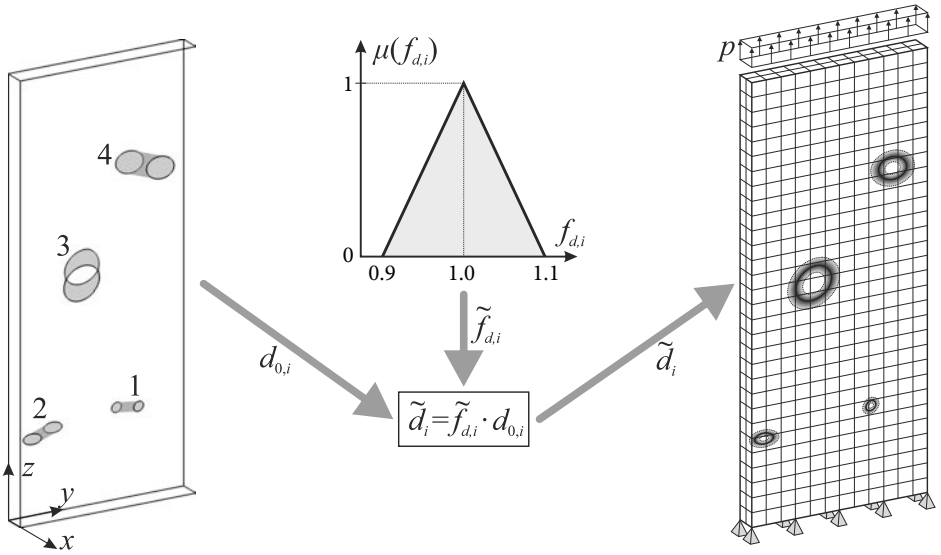

Figure 7. Original geometrical model and FE model with fuzzy sized knots due to fuzzy knot diameter $\widetilde{d}_i$.

in the uncertain analysis. Otherwise, a new mesh would need to be generated for each solution step due to changing knot size.

The board analysed here is experimentally investigated in (Stübi, 2001), whereas the knots are documented in size and position on the board surfaces. The procedure how to derive a geometrical model as shown in Fig. 7 from these measurements is presented in (Jenkel and Kaliske, 2014). For the given example, the knots are described as cylinders passing the board in different angles. The board contains 4 knots $i = \{1, 2, 3, 4\}$. The original knot diameters $d_{0,i}$ taken from (Jenkel and Kaliske, 2014; Stübi, 2001) are varied in-between $\pm 10\%$. Thus, four fuzzy knot diameters

$$\widetilde{d}_i = \widetilde{f}_{d,i} \cdot d_{0,i}, \quad i = \{1, 2, 3, 4\} \tag{42}$$

are introduced using fuzzy triangular numbers $\widetilde{f}_{d,i} = \langle 0.9, 1.0, 1.1 \rangle$ as knot factors, see Fig. 7.

Before the structural analysis is carried out, a material coordinate system representing the three material directions r, t and l needs to be assigned to every integration point. In general, the longitudinal direction is defined by the stem direction, the tangential direction by the growth rings and the radial direction by the medullary rays pointing to pith. In the area of branches, the fibre course, i.e. the longitudinal direction, is deviating from the stem direction. Therefore, the fibre course is computed by means of a streamline approach presented in (Jenkel and Kaliske, 2014) based on a flow-grain analogy. Since the knot diameters are varied, this computation has to be carried out for every solution step within the fuzzy stochastic structural analysis.

The ultimate load p_u is computed using a Tsai-Wu plasticity formulation with linear isotropic softening, see e.g. (Schmidt and Kaliske, 2009; Tsai and Wu, 1971). In the simulations, the load p is increased by small increments. If the total cross-section in an arbitrary region of the board is in the plastic regime, the load will decrease. The ultimate load is determined as maximum loading in the computed load-displacement dependencies $p_u = \max(p)$.

The material parameters are modelled based on the empirical data described above. In the applied elasto-plastic material model, the 9 material parameters described in Tab. II (E_l, E_r, E_t, $f_{c,r}$, $f_{c,t}$, $f_{c,l}$, $f_{t,90}$, $f_{t,l}$ and f_v) are utilized. In addition, the shear moduli, POISSON's ratios and the rolling shear strength are needed. Since these parameters are not investigated in the experiments, deterministic standard values are chosen in terms of $\nu_{rt} = 0.24$, $\nu_{tl} = \nu_{rl} = 0.45$ and $G_{rt} = 80\,N/mm^2$, $G_{tl} = G_{rl} = 800\,N/mm^2$ and $f_{v,rt} = 0.1 \cdot \bar{m}_{f_v}$ for all simulations.

Two configurations are considered, whereas the knots are modelled as holes ($k_{type} = 1$) and as being filled and fully connected to the surrounding wood ($k_{type} = 2$). If $k_{type} = 1$, the knot holes are approximated in the regular mesh using 1% of the values of the material parameters applied for the surrounding wood. If $k_{type} = 2$, the same material parameters as for the surrounding wood are applied for the integration points inside the knots, but with material coordinate systems defined by the longitudinal branch axes. The influence of the 9 material parameters and the four knot factors has been investigated on the basis of a Design of Experiments (DoE) for both configurations, $k_{type} = 1$ and $k_{type} = 2$. Beside the ultimate load p_u, the displacement $u_z(p_u)$ at the point of maximum load, obtained as mean value of the displacements in z-direction of all loaded nodes, is regarded as result quantity. The results are evaluated in sensitivity analyses using SOBOL indices (Sobol, 2001). In Fig. 8, the sensitivity measures of all input quantities are given.

The outcomes are similar for both knot configurations. The ultimate load p_u is influenced mostly by $f_{t,l}$ and f_v. The displacement at the point of ultimate load $u_z(p_u)$ is affected by E_l, $f_{t,l}$, f_v and slightly $f_{t,90}$. The influence of the knot factors seems to be rather small. The effects of the different factors might neutralize if one knot becomes larger while the other gets smaller. If $k_{type} = 2$, the knots have larger influence, probably due to their load bearing capacity. The SOBOL indices of the particular knot factors correspond to the original knot size. As a consequence of the sensitivity

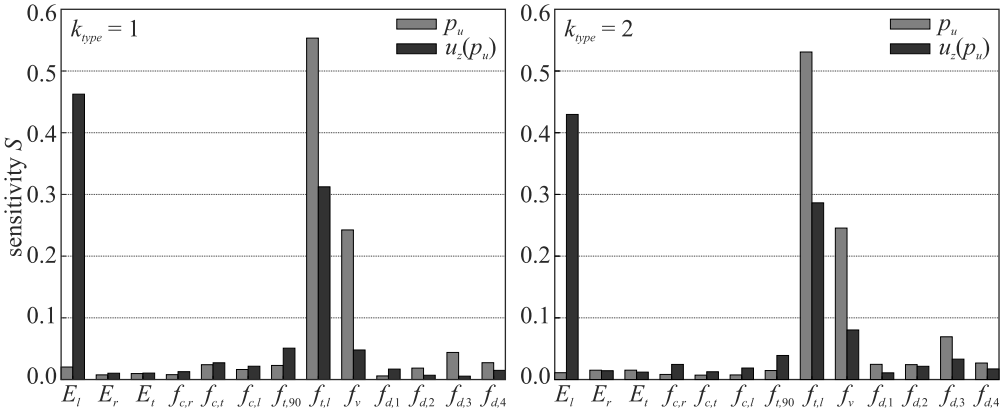

Figure 8. Sensitivity measures S of all input variables regarding the result values p_u and $u_z(p_u)$.

analysis, the longitudinal elasticity modulus E_l, the tensile strength perpendicular to grain $f_{t,90}$, the longitudinal tensile strength $f_{t,l}$ and the shear strength f_v are modelled as fuzzy probability based random variables using the best fitting distribution types identified in Tab. III. All other material parameters are modelled deterministically by their mean values according to Tab. II. A WEIBULL distribution is used to represent E_l, see Fig. 6. For $f_{t,l}$, a NORMAL distribution fits best

to the empirical data. Since these material parameters appear to be most relevant, the distribution parameters are described by means of fuzzy trapezoidal interval numbers, see Tab. III.

For each configuration ($k_{type} = 1, 2$), the ultimate load p_u is computed as fuzzy stochastic result quantity. Quantiles $\bar{q}_i$ are chosen to represent the uncertain distribution of p_u here. The α-level optimization is carried out on α-levels $\alpha = \{0, \frac{1}{6}, \frac{1}{3}, \frac{1}{2}, \frac{2}{3}, \frac{5}{6}, 1\}$ regarding $\bar{q}_1$, $\bar{q}_5$, $\bar{q}_{25}$, $\bar{q}_{50}$, $\bar{q}_{75}$, $\bar{q}_{95}$ and $\bar{q}_{99}$. The results of the simulation with $k_{type} = 1$ are illustrated in Fig. 9. The uncertain ultimate load p_u computed using $k_{type} = 2$ is depicted in Fig. 10.

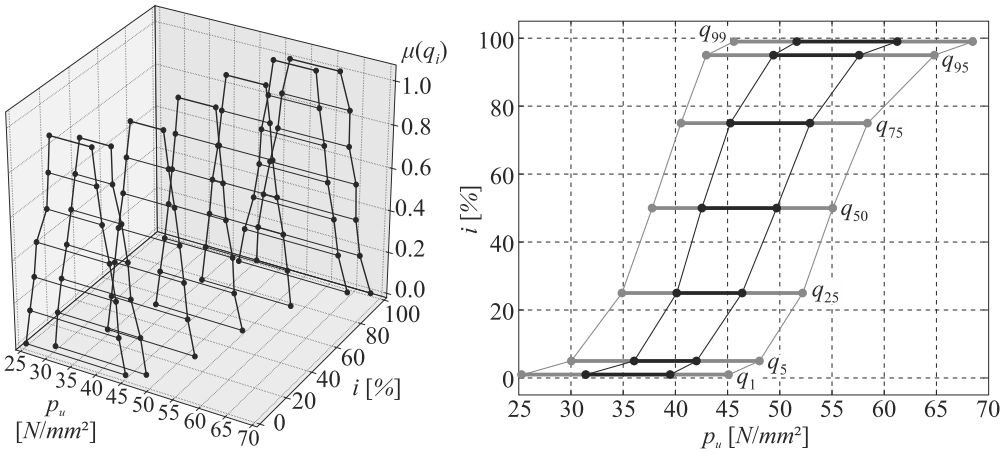

Figure 9. Uncertain distribution of p_u represented by fuzzy quantiles $\widetilde{\bar{q}}_i$ for $k_{type} = 1$.

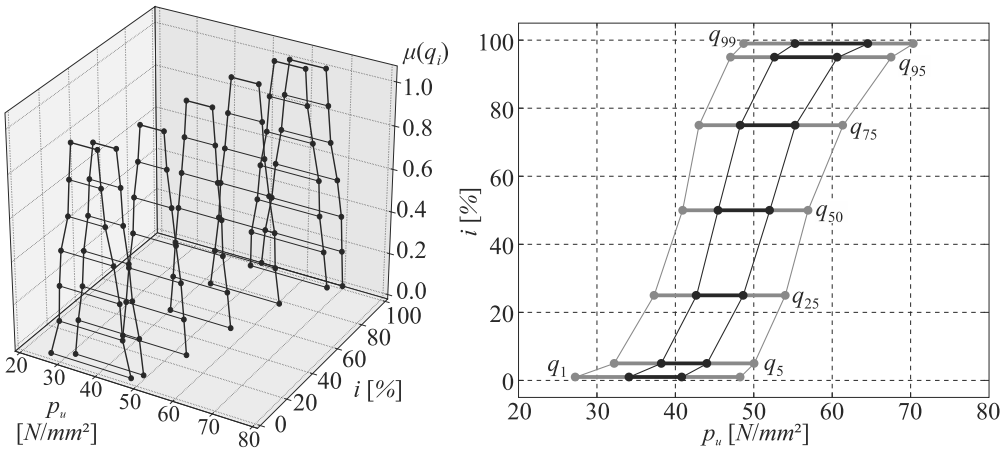

Figure 10. Uncertain distribution of p_u represented by fuzzy quantiles $\widetilde{\bar{q}}_i$ for $k_{type} = 2$.

In both figures, the fuzzy numbers for the particular quantiles $\widetilde{\bar{q}}_i$ with $i = \{1, 5, 25, 50, 75, 95, 99\}$ are depicted in 3D views. The black circles mark the bounds of each fuzzy number on each α-level. All fuzzy quantiles are obtained as kind of fuzzy trapezoidal interval numbers. In addition, a top view is given. The black lines represent the plateaus of the fuzzy trapezoidal interval numbers while

the grey lines represent the support. As can be seen in the top views, the uncertain distribution function of p_u is approximated by the quantiles.

For $k_{type} = 1$, smaller ultimate loads are computed as for $k_{type} = 2$, which is reasonable due to the load bearing capacity of the knots. The membership functions of the fuzzy quantiles are similarly shaped for both configurations. The range of the intervals computed for each quantile on each α-level is comparable for $k_{type} = 1$ and $k_{type} = 2$. Moreover, the uncertain distributions according to the top views in Figs. 9 and 10 are very similar, except that the distribution for $k_{type} = 2$ seems to be shifted to the right about 2-3 N/mm^2.

In this example, methods for the consideration of material and structural inhomogeneities are applied jointly revealing the advantages of the introduced uncertainty models. The results given in Figs. 9 and 10 include information, which could not have been achieved by application of a pure stochastic analysis.

6. Conclusion and Outlook

The uncertainty of material and structural parameters has manifold reasons. If the uncertainty of input parameters shall be considered realistically in a structural analysis, appropriate data models are needed. In this contribution, a general description with polymorphic uncertainty is utilized and further classified into aleatoric and epistemic uncertainty. The first type is described using randomness while the latter is represented by means of fuzziness. The combination of both yields fuzzy randomness which is ideally suited to describe the uncertainty of material parameters of wood. Although the natural variability of material parameters is identified with aleatoric uncertainty, an application of randomness is often not feasible due to the limitations of available data bases.

Methods to model empirical data by fuzzy randomness with focus on fuzzy probability based random variables are introduced. The procedure is applied to describe the uncertainty of macroscopic material parameters of wood. In addition, the uncertainty of geometrical and further structural parameters is represented using fuzzy variables. The procedure of a fuzzy stochastic structural analysis is described theoretically and demonstrated by an examples. In the structural analyses of wooden structures, information is considered which could not have been included in stochastic analyses nor a single deterministic structural analysis.

According to EN 1990 (2010), a semi-probabilistic safety concept is proposed for the future determination of partial safety factors. A stochastic analysis procedure as special case of the introduced methods can be used for the calibration of safety factors in a partial factor design concept. A failure probability might be prescribed, which is used to determine deterministic design values from the uncertain input parameters and results. These values simply need to be related to the characteristic values to define partial safety factors.

Although the uncertainty models fuzziness and fuzzy randomness are established in science, an application for the purpose of standardization seems improbable in short term. Actually, engineers demand a further simplification of the design rules instead of a wider range of methods (Seim et al., 2012). However, the evaluation of the uncertain results can give an additional input for the determination of less conservative safety factors and a better utilization of the load bearing capacity

of timber structures. Future work is necessary to get from the fuzzy stochastic structural analysis presented here to recommendations for a numerical design concept.

In uncertain structural analyses, uncertain results are computed containing all information provided due to the uncertain input parameters. Engineers require deterministic values to determine a structural design. Measures of central tendency as mean value and measures of dispersion as quantiles can be used to reduce the information of uncertain variables to deterministic values. Similar measures have been used in the fuzzy stochastic structural analysis to describe the uncertain distributions of the results. Due to the application of fuzzy randomness, the mean values and quantiles are obtained as uncertain quantities, which might need to be simplified themselves. Information reducing measures for fuzzy numbers are introduced e.g. in (Beer and Liebscher, 2008; Graf et al., 2009).

In this contribution, the idea is not to reduce the uncertainty but keep as much information as possible. If all available data are considered in the structural analyses, the influence of the uncertainty of the input parameters on the structural results can be evaluated. Engineers can obtain indication which input parameters deserve closer attention and might be modified to improve a structural design. Therefore, robustness analyses, such as in (Beer and Liebscher, 2008; Graf et al., 2009), and sensitivity analysis, see e.g. (Pannier and Graf, 2015), are powerful tools. Moreover, the procedures presented in this contribution can be used in structural optimization approaches as introduced in (Götz et al., 2015).

References

Beer, M. and M. Liebscher. Designing robust structures a nonlinear simulation based approach. *Computers and Structures*, 86:1102–1122, 2008.

De Amicis, R., M. Riggio, G. Girardi and M. Piazza. Morphology-based macro-scale finite-element timber models. *Computer-Aided Design*, 43:72–87, 2011.

De Borst, K., C. Jenkel, C. Montero, J. Colmars, J. Gril, M. Kaliske and J. Eberhardsteiner. Mechanical characterization of wood: An integrative approach ranging from nanoscale to structure. *Computers and Structures*, 127:53–67, 2013.

EN1990. Basis of structural design; German version. Beuth, Berlin, 2010.

EN1995NA. National Annex – Nationally determined parameters – Eurocode 5: Design of timber structures – Part 1-1: General – Common rules and rules for buildings. Beuth, Berlin, 2010.

Fink, G. and J. Köhler. Model for the prediction of the tensile strength and tensile stiffness of knot clusters within structural timber. *European Journal of Wood and Wood Products*, 72:331–341, 2014.

Frigge, M., D. C. Hoaglin and B. Iglewicz. Some implementations of the boxplot. *The American Statistician*, 43(1):50–54, 1989.

Götz, M., W. Graf and M. Kaliske. Numerical concepts for structural design with polymorphic uncertainty modelling. *International Journal of Reliability and Safety*, 9:112–131, 2015.

Graf, W., C. Jenkel, S. Pannier, J.-U. Sickert and F. Steinigen. Numerical structural monitoring with the uncertainty model fuzzy randomness. *International Journal of Reliability and Safety*, 3:218–234, 2009.

Jenkel, C. and M. Kaliske. Finite element analysis of timber containing branches – an approach to model the grain course and the influence on the structural behaviour. *Engineering Structures*, 75:237–247, 2014.

Jenkel, C., F. Leichsenring, W. Graf and M. Kaliske. Stochastic modelling of uncertainty in timber engineering. *Engineering Structures*, 99:296–310, 2015.

Köhler, J., J. D. Sorensen and M. H. Faber. Probabilistic modeling of timber structures. *Structural Safety*, 29:255–267, 2007.

Messay, F. J. The Kolmogorov-Smirnov test for goodness of fit. *Journal of the American Statistical Association*, 46(253):68–78, 1951.

Möller, B. and M. Beer. *Fuzzy Randomness – Uncertainty in Civil Engineering and Computational Mechanics*. Springer, Berlin, 2004.

Möller, B., W. Graf and M. Beer. Fuzzy structural analysis using α-level optimization. *Computational Mechanics*, 26:547–565, 2000.

Möller, B., W. Graf, J.-U. Sickert and U. Reuter. Numerical simulation based on fuzzy stochastic analysis. *Mathematical and Computer Modelling of Dynamical Systems*, 13:349–364, 2007.

Pannier, S. *Effizienter numerischer Entwurf von Strukturen und Prozessen bei Unschärfe*. Veröffentlichungen des Instituts für Statik und Dynamik der Tragwerke, H. 23, TU Dresden, 2011.

Pannier, S. and W. Graf. Sectional global sensitivity measure. *Reliability Engineering and System Safety*, 134:110–117, 2015.

Pannier, S., M. Waurick, W. Graf and M. Kaliske. Solutions to problems with imprecise data – an engineering perspective to generalized uncertainty models. *Mechanical Systems and Signal Processing*, 37:105–120, 2013.

Rinne, H. *Taschenbuch der Statistik*. Verlag Harri Deutsch, Frankfurt/M., 2008.

Schmidt, J. and M. Kaliske. Models for numerical failure analysis of wooden structures. *Engineering Structures*, 31:571–579, 2009.

Seim, W., M. Schick and L. Eisenhut. Simplified design rules for timber structures – drawback or progress. In Quenneville, P., editor, *World Conference on Timber Engineering*. University of Auckland, 2012.

Sellke, T., M. Bayarri and J. O. Berger. Calibration of p values for testing precise null hypotheses. *The American Statistician*, 55(1):62–71, 2001.

Sobol, I. M. Global sensitivity indices for nonlinear mathematical models and their monte carlo estimates. *Mathematics and Computers in Simulation*, 55:271–280, 2001.

Spaethe, G. *Die Sicherheit tragender Baukonstruktionen*. Springer-Verlag, Wien, 1992.

Stübi, T. *Gütesortierung von Schweizer Holz durch Kombination von mehreren Erkennungsmethoden*. Schweizerische Hochschule für die Holzwirtschaft, Biel, 2001.

Tsai, S. W. and E. M. Wu. A general theory of strength for anisotropic materials. *Journal of Composite Materials*, 5:58–80, 1971.

Ulrich, H. and W. Seim. *Experimentelle Prüfungen an Kleinproben aus Fichtenholz*. Fachgebiet Bauwerkserhaltung und Holzbau, Universität Kassel, 2014.

Viertl, R. *Statistical Methods for Non-Precise Data*. CRC-Press, Boca Raton, 1996.

Viertl, R. *Einführung in die Stochastik*. Springer, Wien, 1997.

Zadeh, L. A. Fuzzy sets. *Information and Control*, 8:338–353, 1965.

Zadeh, L. A. Similarity relations and fuzzy orderings. *Information Sciences*, 3:177–200, 1971.

Zohdi, T. I. and P. Wriggers. *Introduction to Computational Micromechanics*. Springer, Berlin, 2005.

Analysis of Truss Structures with Uncertainties: From Experimental Data to Analytical Responses

P. Longo[1)], N. Maugeri[1)], G. Muscolino[2)] and G. Ricciardi[2)]
[1)] Department of Engineering, University of Messina, Villaggio S. Agata, 98166 Messina, Italy, {plongo, nmaugeri}@unime.it

[2)] Department of Engineering and Inter-University Centre of Theoretical and Experimental Dynamics, University of Messina, Villaggio S. Agata, 98166 Messina, Italy, {gmuscolino, gricciardi}@unime.it

Abstract: This paper deals with the analysis of truss structures with uncertain elastic modulus under deterministic loads. The uncertain parameters, which characterize the elastic modulus, are determined by examining the experimental data obtained from tensile tests on several steel bars performed in the Laboratory of Structures and Materials of the Department of Engineering (University of Messina). Analyzing the experimental data, both the probabilistic and non-probabilistic models are examined. In the first case the random uncertainties are completely characterized through the knowledge of the probability density function, which is determined by applying the maximum entropy approach and compared with Gaussian model. In the second case the interval model is adopted and the uncertainties are characterized by the midpoint and deviation values. Finally, in order to compare the propagation of these two models of uncertainties, the response of a benchmark truss structure is evaluated and the results in terms of displacements are compared.

Keywords: probabilistic uncertainties, maximum entropy approach, interval analysis, rational series expansion

1. Introduction

In recent years it has been recognized that the analysis of structural systems should take into account all the relevant uncertainties present in the analyzed problem. Uncertainties associated with an engineering problem, due to the different sources, can be divided into two main groups: *random uncertainties* and *epistemic uncertainties* (Elishakoff and Ohsaki, 2010). The random uncertainties are completely characterized through the knowledge of the full set of its statistics (which could be moments, cumulants or other derived quantities) or, which is the same, through the knowledge of its *probability density function* (*PDF*). Despite their success, unfortunately the probabilistic approaches give reliable results only when sufficient experimental data are available to define the *PDF* of the fluctuating properties. If available information are fragmentary or incomplete so that only bounds on the magnitude of the uncertain structural parameters are known, non-probabilistic approaches can be alternatively applied. In the framework of non-probabilistic approaches the interval model, which stems from *interval analysis* (see e.g. Moore, 1966; Moore et al., 2009), may be considered as the most widely used analytical tool among non-probabilistic

methods (Muhanna and Mullen, 2001; Moens and Vandepitte, 2005). According to this approach, the fluctuating structural parameters are treated as interval numbers inside their lower and upper bounds.

In the framework of probabilistic approaches usually the uncertainties are assumed as stochastic variables modelled by Gaussian distributions. However, often, this distribution does not reflect the actual one. As a consequence the numerical results obtained by assuming the Gaussian approximations could be very far from the effective ones. On the contrary in this paper, starting from data obtained from experiments on several steel bars performed in the Laboratory of Structures and Materials of the Department of Engineering (University of Messina), the *PDF* of elastic modulus of the material is derived by applying the maximum entropy approach proposed by Alibrandi and Ricciardi (2008). Then the probabilistic response of a benchmark truss structures is determined once the inverse of the global stochastic stiffness matrix is evaluated in approximate explicit closed form by applying the recently proposed *Rational Series Expansion* (*RSE*) (Muscolino and Sofi, 2013; Muscolino et al., 2014). So operating a substantial computational savings over classical Monte Carlo Simulation (*MCS*) is obtained.

In the framework of interval analysis the midpoint and deviation values of the uncertain elastic modulus are determined by analyzing experimental data. Then, approximate explicit expressions of the bounds of the interval nodal displacements of the benchmark truss structures are derived by applying the so-called *Interval Rational Series Expansion* (*IRSE*) (Muscolino and Sofi, 2013; Muscolino et al., 2014) recently proposed to evaluate the explicit inverse of the global stiffness matrix with interval modifications.

2. Preliminary concepts and definitions

2.1. Equations Governing the Problem of Truss Structures

It is well known that the equilibrium equations of a truss structure with n unconstrained nodal displacements and m elements, subjected to known static loads, can be written as follows:

$$\begin{aligned} &\mathbf{C}^T\mathbf{Q}=\mathbf{f}\,; && \text{equilibrium equation;}\\ &\mathbf{Q}=\mathbf{R}\,\mathbf{q}\,; && \text{constitutive equation;}\\ &\mathbf{C}\,\mathbf{U}=\mathbf{q}. && \text{compatibility equation.} \end{aligned} \qquad (1a,b,c)$$

where $\mathbf{U}$ is the is the vector, of order n, of nodal displacements; $\mathbf{f}$ is the vector, of order n, collecting the external loads applied at the nodes; $\mathbf{Q}$ and $\mathbf{q}$ are the vectors , of order m, of internal forces and deformations respectively; $\mathbf{C}^T$ is the $n\times m$ equilibrium matrix and $\mathbf{R}$ is the $m\times m$ diagonal internal stiffness matrix. Let us now indicate with $\rho_j = E_j A_j / L_j$ the axial stiffness of the j-th element, where E_j, A_j and L_j are the Young elastic modulus, the area and the length of the j-th element, respectively. Let us assume now that $r \le m$ elements possess uncertain elastic modulus. Denoting with α_j the dimensionless fluctuation of the j-th uncertain elastic modulus around the nominal value, $E_{0,j}$, of the j-th element, such that $E_j = E_{0,j}\left(1+\alpha_j\right)$, one gets:

$$\rho_j = E_{0,j}\left(1+\alpha_j\right)A_j/L_j = \rho_{0,j}(1+\alpha_j) \tag{2}$$

where $\rho_{0,j} = E_{0,j}A_j/L_j$ is the nominal value of the axial stiffness of the *j*-thelement with $j = 1,2,\ldots,r \le m$. Then, the internal stiffness matrix $\mathbf{R}(\boldsymbol{\alpha})$ can be written as:

$$\mathbf{R}(\boldsymbol{\alpha}) = \mathbf{R}_0 + \sum_{j=1}^{r}\alpha_j\ \mathbf{l}_{E,j}\mathbf{l}_{E,j}^T, \tag{3}$$

where $\boldsymbol{\alpha}$ is the vector collecting the *r* uncertain dimensionless fluctuations α_j, $\mathbf{R}_0$ is the diagonal nominal internal stiffness matrix and $\mathbf{l}_{E,j}$ is a vector of order *n* with only the *j*-th element equal to $\sqrt{\rho_{0,j}}$ and the other ones equal to zero. Notice that the dyadic product $\mathbf{l}_{E,j}\mathbf{l}_{E,j}^T$ gives a change of rank one to the nominal internal stiffness matrix. After simple substitutions into Eqs. (1) the solving equilibrium equation, in the framework of the displacement method, can be written as:

$$\mathbf{K}(\boldsymbol{\alpha})\mathbf{U}(\boldsymbol{\alpha}) = \mathbf{f} \tag{4}$$

where $\mathbf{U}(\boldsymbol{\alpha})$ is the vector, of order n, of the unknown nodal displacement depending on uncertainties and $\mathbf{K}(\boldsymbol{\alpha})$ is the uncertain stiffness matrix which, by means of Eqs. (1), can be written as:

$$\mathbf{K}(\boldsymbol{\alpha}) = \mathbf{C}^T\mathbf{R}(\boldsymbol{\alpha})\ \mathbf{C} \tag{5}$$

Then, according to Eq. (3), the stiffness matrix $\mathbf{K}(\boldsymbol{\alpha})$, which possesses r uncertain parameters. can be rewritten as:

$$\mathbf{K}(\boldsymbol{\alpha}) = \mathbf{K}_0 + \sum_{j=1}^{r}\alpha_j\ \mathbf{K}_j\ = \mathbf{K}_0 + \Delta\mathbf{K}\left(\boldsymbol{\alpha}\right) \tag{6}$$

where $\mathbf{K}_0$ is the nominal stiffness matrix and $\mathbf{K}_j$ is a rank-one matrix defined respectively as:

$$\mathbf{K}_0 = \mathbf{C}^T\ \mathbf{R}_0\ \mathbf{C}\,; \quad \mathbf{K}_j = \mathbf{v}_j\ \mathbf{v}_j^T \tag{7a,b}$$

with the vector $\mathbf{v}_j$ given as:

$$\mathbf{v}_j = \mathbf{C}^T\ \mathbf{l}_{E,j} \tag{8}$$

Finally, the solution of Eq. (4) can be formally written as:

$$\mathbf{U}(\boldsymbol{\alpha}) = \mathbf{K}(\boldsymbol{\alpha})^{-1}\mathbf{f} \tag{9}$$

Because of the presence in Eq. (9) of the vector $\boldsymbol{\alpha}$, collecting the uncertain dimensionless fluctuations α_j, the solution of previous equation can be obtained efficiently if explicit expressions of the inverse of the random stiffness matrix $\mathbf{K}(\boldsymbol{\alpha})$ are known. To do this, in the next subsection a new series expansion is described.

2.2. Explicit Inverse of the Stiffness Matrix for Structural System with Rank-one Modifications

In order to derive the explicit expression of the inverse of the stiffness matrix, in this section a recently proposed series expansion, called *Rational Series Expansion* (*RSE*), is described (Muscolino and Sofi, 2013; Muscolino et al., 2014). The *RSE* has been obtained by properly modifying the Neumann series expansion in the case of structural systems with more rank-one modifications in the stiffness matrix. So operating an approximate explicit expression of the inverse of an invertible matrix with *r* modifications was derived. In particular, for truss structures, the matrix $\Delta\mathbf{K}(\boldsymbol{\alpha})$, which collects the rank-*r* change in the stiffness matrix, can be written as the superposition of *r* rank-one matrices as follows:

$$\Delta\mathbf{K}(\boldsymbol{\alpha}) = \sum_{i=1}^{r} \alpha_i \mathbf{v}_i \, \mathbf{v}_i^T \tag{10}$$

where the vector $\mathbf{v}_i$ has been defined in Eq. (8). Moreover, since the fluctuating dimensionless uncertainties are lesser than one, that is $|\alpha_s| \ll 1$, it is possible to evaluate in explicit form the approximate inverse of stiffness matrix by retaining only the first order term as follows:

$$\mathbf{K}(\boldsymbol{\alpha})^{-1} = \left[\mathbf{K}_0 + \sum_{i=1}^{r} \alpha_i \mathbf{v}_i \, \mathbf{v}_i^T \right]^{-1} \approx \mathbf{K}_0^{-1} - \sum_{i=1}^{r} \frac{\alpha_i}{1+\alpha_i d_i} \mathbf{D}_i \tag{11}$$

where the following quantities have been introduced:

$$d_i = \mathbf{v}_i^T \mathbf{K}_0^{-1} \mathbf{v}_i \, ; \quad \mathbf{D}_i = \mathbf{K}_0^{-1} \mathbf{v}_i \, \mathbf{v}_i^T \mathbf{K}_0^{-1} . \tag{12a,b}$$

Notice that Eq. (11) certainly holds if the following condition is satisfied:

$$|\alpha_i d_i| < 1. \tag{13}$$

2.3. Explicit Mean-value Vector and Covariance Matrix for Stochastic Uncertainties

This section addresses the problem of static analysis of structures in which the uncertainties are modelled as zero-mean stochastic independent variables $\tilde{\alpha}_i$, with assigned *Probability Density Function* (*PDF*) $p_{\tilde{\alpha}_i}(x)$, collected in the vector $\tilde{\boldsymbol{\alpha}}$. In this case the solution of equilibrium equations depend on stochastic variables, that is:

$$\mathbf{K}(\tilde{\boldsymbol{\alpha}}) \, \mathbf{U}(\tilde{\boldsymbol{\alpha}}) = \mathbf{f} \tag{14}$$

where the tilde denotes a stochastic quantity. By applying Eq. (11), the inverse of the stochastic matrix $\mathbf{K}(\tilde{\boldsymbol{\alpha}})$ can be evaluated as:

$$\mathbf{K}(\tilde{\boldsymbol{\alpha}})^{-1} = \left[\mathbf{K}_0 + \sum_{i=1}^{r} \tilde{\alpha}_i \mathbf{v}_i \, \mathbf{v}_i^T \right]^{-1} \approx \mathbf{K}_0^{-1} - \sum_{i=1}^{r} \frac{\tilde{\alpha}_i}{1+\tilde{\alpha}_i d_i} \mathbf{D}_i \tag{15}$$

where $\mathbf{K}_0$ is the stiffness matrix of the nominal system while d_i and $\mathbf{D}_i$ have been defined in Eq. (12).

Accordingly, the solution of the set of linear stochastic Eq. (14) can be written in the following approximate explicit form:

$$\mathbf{U}(\tilde{\boldsymbol{\alpha}}) \equiv \tilde{\mathbf{U}} = \mathbf{K}(\tilde{\boldsymbol{\alpha}})^{-1}\mathbf{f} \approx \mathbf{K}_0^{-1}\mathbf{f} - \sum_{i=1}^{r} \frac{\tilde{\alpha}_i}{1+\tilde{\alpha}_i d_i}\mathbf{D}_i\mathbf{f} \tag{16}$$

Finally, since zero-mean stochastic variables $\tilde{\alpha}_i$ are realistically assumed independent ones, the mean-value vector and the covariance matrix of the stochastic response vector $\tilde{\mathbf{U}}$ can be evaluated, respectively, as follows:

$$\begin{aligned} \boldsymbol{\mu}_{\tilde{\mathbf{U}}} &= \mathrm{E}\left\langle \tilde{\mathbf{U}} \right\rangle \approx \mathbf{K}_0^{-1}\mathbf{f} - \sum_{i=1}^{r} \mathrm{E}\left\langle \frac{\tilde{\alpha}_i}{1+\tilde{\alpha}_i d_i} \right\rangle \mathbf{D}_i\mathbf{f}; \\ \boldsymbol{\Sigma}_{\tilde{\mathbf{U}}} &= \mathrm{E}\left\langle \tilde{\mathbf{U}}\tilde{\mathbf{U}}^T \right\rangle - \boldsymbol{\mu}_{\tilde{\mathbf{U}}}\boldsymbol{\mu}_{\tilde{\mathbf{U}}}^T \approx \sum_{i=1}^{r} \left[\mathrm{E}\left\langle \left(\frac{\tilde{\alpha}_i}{1+\tilde{\alpha}_i d_i} \right)^2 \right\rangle - \left(\mathrm{E}\left\langle \frac{\tilde{\alpha}_i}{1+\tilde{\alpha}_i d_i} \right\rangle \right)^2 \right] \mathbf{D}_i\mathbf{f}\mathbf{f}^T\mathbf{D}_i \end{aligned} \tag{17a,b}$$

where $\mathrm{E}\langle \bullet \rangle$ is the stochastic operator defined as:

$$\mathrm{E}\left\langle \frac{\tilde{\alpha}_i}{1+\tilde{\alpha}_i d_i} \right\rangle = \int_{-\infty}^{\infty} \left[\frac{x}{1+x d_i} \right] p_{\tilde{\alpha}_i}(x)\,\mathrm{d}x; \quad \mathrm{E}\left\langle \left(\frac{\tilde{\alpha}_i}{1+\tilde{\alpha}_i d_i} \right)^2 \right\rangle = \int_{-\infty}^{\infty} \left[\frac{x}{1+x d_i} \right]^2 p_{\tilde{\alpha}_i}(x)\,\mathrm{d}x. \tag{18a,b}$$

Obviously, if the stochastic variable is defined in a finite interval $[a,b]$ the previous relationships can be rewritten as:

$$\mathrm{E}\left\langle \frac{\tilde{\alpha}_i}{1+\tilde{\alpha}_i d_i} \right\rangle = \int_{a}^{b} \left[\frac{x}{1+x d_i} \right] p_{\tilde{\alpha}_i}(x)\,\mathrm{d}x; \quad \mathrm{E}\left\langle \frac{\tilde{\alpha}_i}{1+\tilde{\alpha}_i d_i} \right\rangle^2 = \int_{a}^{b} \left[\frac{x}{1+x d_i} \right]^2 p_{\tilde{\alpha}_i}(x)\,\mathrm{d}x. \tag{19a,b}$$

The previous equations provide substantial computational savings over classical MCS method since they just involve the statistics of the random variables $\tilde{\alpha}_i \,/\left(1+\tilde{\alpha}_i d_i\right)$ without requiring the inversion of the global stochastic stiffness matrix. Furthermore, the closed-form expression of the random response in Eq. (16) enables one to evaluate higher-order statistical moments useful to determine the *PDF* of the response.

2.4. Explicit Bounds of the Response for Interval Uncertainties

Let us consider now the case in which the uncertainties are modelled with uncertain-but-bounded parameters modeled as interval variables. According to interval analysis, the vector $\boldsymbol{\alpha}$, of order *r*, in this case has to be defined as: $\boldsymbol{\alpha}^I = \left[\underline{\boldsymbol{\alpha}}, \overline{\boldsymbol{\alpha}}\right]$. In the following with the apex *I* is denoted an interval quantity. The vector $\boldsymbol{\alpha}^I$, collects the *r* uncertain-but-bounded symmetric fluctuations of axial stiffness around their nominal value and defines a *r*-dimension bounded convex set-interval vector of real numbers, such that

$\underline{\boldsymbol{\alpha}} \le \boldsymbol{\alpha} \le \overline{\boldsymbol{\alpha}}$ whose *i*-th element is α_i^I. Without loss of generality it is assumed the midpoint value vector, $\boldsymbol{\alpha}_0$, equals to **0**. Then the deviation amplitude vector, $\Delta\boldsymbol{\alpha}$, which collect the fluctuations around the midpoint is given as:

$$\boldsymbol{\alpha}_0 = \mathbf{0} \quad \Rightarrow \quad \Delta\boldsymbol{\alpha} = \frac{1}{2}\left(\overline{\boldsymbol{\alpha}} - \underline{\boldsymbol{\alpha}}\right) = \overline{\boldsymbol{\alpha}} = -\underline{\boldsymbol{\alpha}} \tag{20a,b}$$

where the symbols $\underline{\boldsymbol{\alpha}}$ and $\overline{\boldsymbol{\alpha}}$ denote the lower and upper bound vectors respectively. As a consequence of Eqs. (20), the following relationship holds for the generic interval variable

$$\alpha_i^I = \Delta\alpha_i \ \hat{e}_i^I \tag{21}$$

where $\hat{e}_i^I \triangleq [-1,+1] \quad (i = 1,2,\cdots,r)$ is the so-called *Extra Unitary Interval* (*EUI*) (Muscolino and Sofi, 2012; Muscolino and Sofi, 2013).

For deterministic static loads and uncertain-but-bounded parameters, the equilibrium Eq. (5) can be rewritten as:

$$\mathbf{K}(\boldsymbol{\alpha}^I)\,\mathbf{u}(\boldsymbol{\alpha}^I) = \mathbf{f} \tag{22}$$

It follows that the stiffness matrix $\mathbf{K}(\boldsymbol{\alpha}^I)$, depends only on deviation amplitude value of the *r* uncertain-but-bounded parameters and according to interval formalism is written as:

$$\mathbf{K}\left(\boldsymbol{\alpha}^I\right) = \mathbf{K}_0 + \sum_{i=1}^{r} \Delta\alpha_i \hat{e}_i^I \mathbf{v}_i \mathbf{v}_i^T = \mathbf{K}_0 + \sum_{i=1}^{r} \hat{e}_i^I \Delta\mathbf{K}_i \tag{23}$$

where:

$$\Delta\mathbf{K}_i = \Delta\alpha_i \mathbf{v}_i \mathbf{v}_i^T \tag{24}$$

The goal is now to find the narrowest interval $\mathbf{u}^I$ containing all possible response vectors $\mathbf{u}$, satisfying the equilibrium Eq. (22), when the vector $\boldsymbol{\alpha}$ assumes all possible values inside the interval vector $\boldsymbol{\alpha}^I$. The problem is formally solved as:

$$\mathbf{u}^I = \left(\mathbf{K}\left(\boldsymbol{\alpha}^I\right)\right)^{-1} \mathbf{f} \tag{25}$$

Since in structural engineering the stiffness matrix is regular and it can be assumed that the uncertainties are not large, so that $\Delta\alpha_i \ll 1 \ \forall i$, the inverse interval of the stiffness matrix, by applying the *Improved Interval Analysis* (Muscolino and Sofi, 2012), can be determined by the applying so called *Interval Rational Series Expansion* (*IRSE*) (Muscolino and Sofi, 2013; Muscolino and al., 2014) as (see Eq. (11)):

$$\mathbf{K}\left(\boldsymbol{\alpha}^I\right)^{-1} = \left(\mathbf{K}_0 + \sum_{i=1}^{r} \Delta\alpha_i \hat{e}_i^I \mathbf{v}_i \mathbf{v}_i^T\right)^{-1} \approx \mathbf{K}_0^{-1} - \sum_{i=1}^{r} \frac{\Delta\alpha_i \hat{e}_i^I}{1 + \Delta\alpha_i \hat{e}_i^I d_i} \mathbf{D}_i \tag{26}$$

Obviously, the accuracy of Eq. (26), which gives the explicit inverse of a matrix with r fluctuating parameters, depends on the magnitude of the fluctuations $\Delta\alpha_i$. Alternatively, Eq. (26) can be rewritten in the so-called affine form (Muscolino and Sofi, 2013) as:

$$\mathbf{K}\left(\boldsymbol{\alpha}^I\right)^{-1} = \left(\mathbf{K}_0 + \sum_{i=1}^{r} \Delta\alpha_i\, \hat{e}_i^I \mathbf{v}_i\, \mathbf{v}_i^T\right)^{-1} \approx \mathbf{K}_0^{-1} + \sum_{i=1}^{r} \left(a_{0,i} + \Delta a_i\, \hat{e}_i^I\right)\mathbf{D}_i \tag{27}$$

where $a_{0,i}$ and Δa_i are given by:

$$a_{0,i} = \frac{\left(\Delta\alpha_i\right)^2 d_i}{1-\left(\Delta\alpha_i\, d_i\right)^2} > 0; \quad \Delta a_i = \frac{\Delta\alpha_i}{1-\left(\Delta\alpha_i\, d_i\right)^2} > 0. \tag{28a,b}$$

Then the solution of Eq. (22) is given respectively as:

$$\mathbf{u}^I = \mathbf{K}\left(\boldsymbol{\alpha}^I\right)^{-1}\mathbf{f} \approx \mathbf{K}_0^{-1}\mathbf{f} + \sum_{i=1}^{r}\left(a_{0,i} + \Delta a_i\, \hat{e}_i^I\right)\mathbf{D}_i\mathbf{f} \tag{29}$$

Due to the monotonicity of the components of the vector $\mathbf{u}(\boldsymbol{\alpha}^I)$ with respect to the generic $\Delta\alpha_i$, the lower and upper bounds of displacements can be evaluated respectively as:

$$\underline{\mathbf{u}} = \mathbf{u}_0 - \Delta\mathbf{u}; \quad \overline{\mathbf{u}} = \mathbf{u}_0 + \Delta\mathbf{u} \tag{30a,b}$$

where the following vectors are introduced:

$$\mathbf{u}_0 = \mathbf{K}_0^{-1}\mathbf{f} + \sum_{i=1}^{r} a_{0,i}\,\mathbf{D}_i\,\mathbf{f}; \quad \Delta\mathbf{u} = \sum_{i=1}^{r}\Delta a_i\,\left|\mathbf{D}_i\,\mathbf{f}\right| \tag{31a,b}$$

with the symbol $|\bullet|$ which denotes the *component wise* absolute value.

3. Probability density function derived by experimental data

In the framework of structural engineering usually the uncertainties are assumed as stochastic variables modelled by Gaussian distributions. However, often, this distribution does not reflect the actual one. As a consequence the numerical results obtained by assuming the Gaussian approximations could be very far from the effective ones. To overcome this drawback, in this section, a method to derive the distribution coherent in some way with the histogram obtained analysing the results of a set of experimental data is presented. The method is based on the maximum entropy principle proposed by Alibrandi and Ricciardi (2008), which derived the effective *PDF* coherent with experimental data in terms of moments.

Let denote with $\hat{p}_{\tilde{X}}(x)$ the approximating *PDF* of the given random variable $\tilde{X}$, defined in a finite interval $[a,b]$, which can be written as superposition of basis *PDF* $\varphi_{\tilde{X}}^{(i)}(x;x_i,h_i)$:

$$\hat{p}_{\tilde{X}}(x) = \sum_{i=1}^{N} p_i\,\varphi_{\tilde{X}}^{(i)}(x;x_i,h_i) \tag{32}$$

where the *i*-th basis *PDF* $\varphi_{\tilde{X}}^{(i)}\left(x;x_i,h_i\right)$, having unitary area in the interval domain $[a,b]$, depends on the location x_i and bandwidth h_i. The location parameters are N points belonging to the domain $[a,b]$, chosen for sake of simplicity with a constant step $\Delta x = x_{i+1} - x_i$, (with $i = 1,2,\ldots,N-1$). In a similar way it has been assumed a constant bandwidth parameter $h_i = h = q\,\Delta x$, a good choice is $q = 2/3$.

The superposition of basis *PDF* (Eq. (32)) represents a *PDF* if and only if the coefficients p_i satisfy the following conditions:

$$\begin{cases} 0 \le p_i < 1, \quad i = 1 \ldots N \\ \sum_{i=1}^{N} p_i = 1 \end{cases} \tag{33}$$

Equations (32) and (33) show that a generic *PDF* can be expressed as a linear convex combination of simpler *PDF*s, whose coefficients have the meaning of probabilities. In order to evaluate the probabilities p_i, it is useful to rewrite Eq. (32) as follows:

$$\hat{p}_{\tilde{X}}\left(x\right) = \boldsymbol{\varphi}_{\tilde{X}}^{T}\left(x\right)\mathbf{p} \tag{34}$$

where $\boldsymbol{\varphi}_{\tilde{X}}^{T}\left(x\right) = \left[\varphi_{\tilde{X}}^{(1)}\left(x;x_1,\hbar\right),\varphi_{\tilde{X}}^{(2)}\left(x;x_2,\hbar\right),\cdots,\varphi_{\tilde{X}}^{(N)}\left(x;x_N,\hbar\right)\right]$ and $\mathbf{p}^T = \left[p_1,p_2,\cdots,p_N\right]$ are vectors of order N. Multiplying both sides of Eq. (34) by x^k (with $k = 0,1,2,\ldots,M$). and integrating over the domain, taking into account Eqs. (33), the following system of equations is obtained:

$$\begin{cases} \mathbf{1}^{\mathrm{T}}\mathbf{p} = 1 \\ \mathbf{M}\,\mathbf{p} = \boldsymbol{\mu} \end{cases} \tag{35a,b}$$

where $\mathbf{1}$ is a unit vector of order N, $\mathbf{M}$ is a matrix of order $M \times N$, whose elements, m_{ki}, are the moments of order k of the *i*-th basis *PDF* $\varphi_{\tilde{X}}^{(i)}\left(x;x_i,h_i\right)$:

$$m_{ki} = \int_a^b x^k\ \varphi_{\tilde{X}}^{(i)}\left(x;x_i,h_i\right)\mathrm{d}x \tag{36}$$

while $\boldsymbol{\mu}$ is a vector of order M collecting the k-th moment derived from experimental data. In the system of equations (Eq. (35)) the number of moments M gives the data information. Here it is assumed that only the lower six moments ($M \le 6$) can be derived with good accuracy from experimental data.

The number N of kernel densities gives the resolution for the recovery of the target *PDF* $p_{\tilde{X}}\left(x\right)$; as much as N increases, computational complexity grows; it's a good choice to select N in the range 20-100, being generally N lower than the N_s sample data.

To solve the system (Eq. (35)) the Maximum Entropy method is adopted, that leads to find the unique minimum of the free functional $H^{ME} = H\left(\lambda_1,\lambda_2,\ldots,\lambda_M\right)$, where λ_i is the *i*-th Lagrange multiplier, defined as (Alibrandi and Ricciardi, 2008):

$$H^{ME} = H\left(\lambda_1, \lambda_2, \ldots, \lambda_M\right) = \lambda_0 + \sum_{k=1}^{M} \lambda_k \cdot \mu_k \tag{37}$$

where

$$\lambda_0 = \lambda_0\left(\lambda_1, \lambda_2, \ldots, \lambda_M\right) = \ln\left[\sum_{i=1}^{N} \exp\left(-\sum_{k=1}^{M} \lambda_k \cdot x_i^k\right)\right] \tag{38}$$

is the normalization constant, that can be expressed as a function of $\lambda_1,\lambda_2,., \lambda_M$, and

$$\mu_k = \mu_k\left(\lambda_1, \lambda_2, \ldots, \lambda_M\right) = \frac{\sum_{i=1}^{N} x_i^k \cdot \exp\left(-\sum_{j=1}^{M} \lambda_j x_i^k\right)}{\sum_{i=1}^{N} \exp\left(-\sum_{j=1}^{M} \lambda_j x_i^k\right)} \tag{39}$$

The free function $H^{ME} = H\left(\lambda_1, \lambda_2, \ldots, \lambda_M\right)$ is convex with respect to the Lagrange multipliers $\lambda_1, \lambda_2, \ldots, \lambda_M$ and, as a consequence, it has an unique minimum , which can be obtained through a standard convex optimization algorithm, with a limited number of iterations.

The corresponding coefficients p_i can be computed as:

$$p_i = \exp\left(-\lambda_0 - \sum_{k=1}^{M} \lambda_k \cdot x_i^k\right) \tag{40}$$

where the Lagrange multipliers are solution of the Maximum Entropy optimization problem (Alibrandi and Ricciardi, 2008).

4. Numerical results versus experimental data

Aim of this study is to perform the analysis of truss structures with uncertain Young elastic modulus under deterministic loads by applying both probabilistic and non-probabilistic approaches. To do this the Young elastic modulus is determined by several experiments on steel bars performed in the Laboratory of Structures and Materials of the Department of Engineering (University of Messina). Tensile strength tests, according to UNI EN ISO 15630-1, were performed on 128 specimens, using universal machine, Galdabini VB47, Quasar 1200 and elastic modulus was computed by electronic extensometer micron motor (class 0.5 according to UNI EN ISO 9513). The main statistics of experimental data: *Coefficient of Variation* (*CoV*), $\mu_{\tilde{\alpha}} / \sigma_{\tilde{\alpha}}$; *skewness coefficient*, $\mu_{3,\tilde{\alpha}} / \sigma_{\tilde{\alpha}}^3$, and *excess kurtosis*, $(\mu_{4,\tilde{\alpha}} / \sigma_{\tilde{\alpha}}^4) - 3$, are reported in Table I.

In this section, the described procedure is applied to the benchmark truss structure depicted in Figure 1. The cross-sectional areas and Young's moduli of five bars are A_1=A_2=A_3=A_4=A_5=0.0009 [m^2] and $E_{0,1}$=$E_{0,2}$=$E_{0,3}$=$E_{0,4}$=$E_{0,5}$=2.1 10^6 [N/mm^2] respectively. In particular, first, in the framework of probabilistic approaches, the statistics of the response are evaluated by applying the proposed formulation and compared

with the same obtained by *Monte Carlo Simulation* (*MCS*). Then, by applying the *Improved Interval Analysis*, the bounds of nodal response in terms of displacements are evaluated.

Table I. Statistical results for Young Elastic Modulus from experimental data.

N. Samples	128
Mean: $\mu_{\tilde{\alpha}}$ [N/mm^2]	198110.68
Standard Deviation: $\sigma_{\tilde{\alpha}}$ [N/mm^2]	13868.14
Minimum [N/mm^2]	161742.41
Median [N/mm^2]	198147.39
Maximum [N/mm^2]	240816.20
CoV	0.07
Skewness Coefficient	0.4188
Excess Kurtosis	4.8246

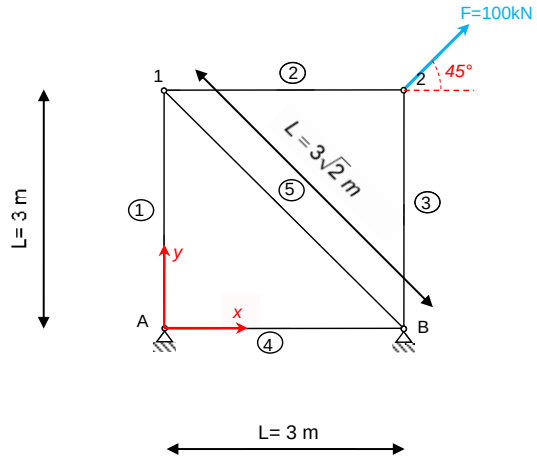

Figure 1. Sketch of benchmark truss system.

4.1. PROBABILISTIC APPROACH

In the framework of the probabilistic approach and according to the Chauvenet criterion for the selection of the effective experimental results (Barbato et al., 2011), the *Kernel PDF* of the Young elastic modulus is evaluated in the interval domain $[a,b]$ of existence of *PDF* which is chosen as $\left[\mu_{\tilde{\alpha}} - 4.0\sigma_{\tilde{\alpha}}, \mu_{\tilde{\alpha}} + 4.0\sigma_{\tilde{\alpha}}\right]$; then, to avoid numeric instability, the interval is normalized into the domain [0,1]. Finally the *Kernel PDF* is determined, according to Eq. (32), as a linear combination of 30 normal basis kernel densities, whose

coefficient p_i are computed by Eq. (40) once the Maximum Entropy optimization problem is solved (Alibrandi and Ricciardi, 2008).

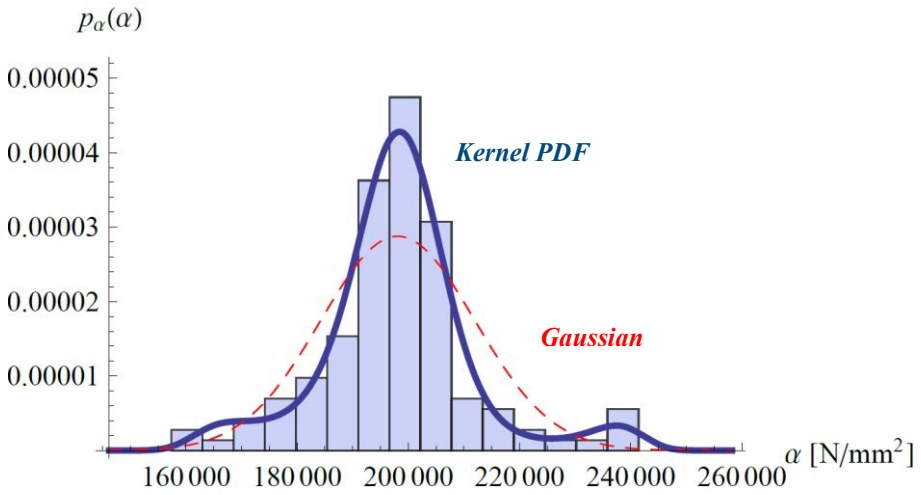

Figure 2. Comparison between *Kernel PDF*, *Gaussian PDF* and experimental data.

The *Kernel PDF* is depicted in Figure 2 together with the histogram of experimental data and the *Gaussian PDF* having same mean value and standard deviation of experimental data. Clearly this figure shows as the *Kernel PDF* better fits experimental data.

The nominal displacement vector $\mathbf{u}_0^N$ is evaluated as follows :

$$\mathbf{u}_0^N = \mathbf{K}_0^{-1}\mathbf{F} \tag{41}$$

obtaining:

$$\mathbf{u}_0^N = \begin{pmatrix} u_{x1} \\ u_{y1} \\ u_{x2} \\ u_{y2} \end{pmatrix} = \begin{pmatrix} 4.29699 \\ 1.12239 \\ 5.41939 \\ 1.12239 \end{pmatrix} [\text{mm}]; \tag{42}$$

To evaluate in explicit form the first two statistics of the response, the *Kernel PDF*, to satisfy the condition (13), has to be normalized into a lesser than 1 domain. This normalization has been performed by means of the following transformation:

$$\tilde{e} = \frac{\tilde{\alpha} - \mu_{\tilde{\alpha}}}{\mu_{\tilde{\alpha}}} \tag{43}$$

where $\mu_{\tilde{\alpha}}$ is the mean value of *Kernel PDF*. So operating the normalized *Kernel PDF* of uncertain elastic modulus, $p_E(\tilde{e})$, represented in Figure 3, lies into the interval domain $[-0.28, 0.28]$.

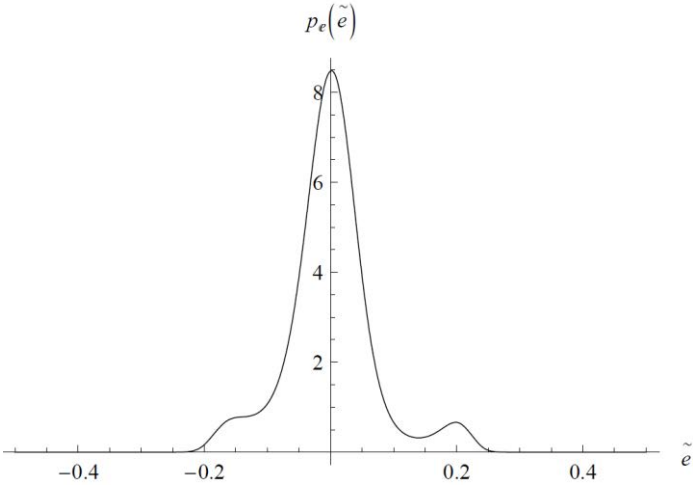

Figure 3. Normalized *Kernel PDF*.

To test the accuracy of proposed method, in Table II are reported the mean values, μ_{u_r} , and the standard deviations, σ_{u_r} , of displacements of studied structure, evaluated by means of Eqs. (17) and compared with the ones coming from *MCS*. In Table II the percentage errors are given, comparing the analytical data with the results obtained from *MCS* of 5000, 500 000, 1 000 000 samples. Negligible percentage errors confirm the accuracy of proposed method, provided a considerable reduction of the computational effort.

Table II. Comparison between stochastic results and Monte Carlo Simulation (Kernel Density).

Parameter [mm]	*analytical*	*MCS 5000*	*Error* [%]	*MCS 500000*	*Error* [%]	*MCS* 10^6	*Error* [%]
μ_{ux1}	4.31818	4.31884	0.0153	4.31854	0.0083	4.3180	-0.0037
μ_{uy1}	1.12793	1.12768	-0.0222	1.12796	0.0027	1.1280	0.0062
μ_{ux2}	5.44611	5.44564	-0.0086	5.44658	0.0086	5.4468	0.0127
μ_{uy2}	1.12793	1.12806	0.0115	1.12774	-0.0168	1.1280	0.0027
σ_{ux1}	0.23680	0.23715	0.1451	0.23677	-0.0114	0.2369	0.0355
σ_{uy1}	0.07893	0.07943	0.6288	0.07876	-0.2174	0.0789	-0.0390
σ_{ux2}	0.24961	0.25103	0.5669	0.24949	-0.0481	0.2496	0.0024
σ_{uy2}	0.07893	0.07801	-1.1898	0.07885	-0.1074	0.0789	0.0152

The same analytical approach has been applied assuming a *Gaussian PDF*. In Table III the percentage errors between analytical results and *MCS* with 1.000.000 samples are reported, confirming the accuracy of proposed method.

Table III. Comparison between stochastic results and Monte Carlo Simulation (Gaussian PDF).

Parameter[mm]	*analytical*	*MCS10*^{6}	*Error*[%]
μ_{ux1}	4.31834	4.31821	-0.0030
μ_{uy1}	1.12797	1.12807	0.0089
μ_{ux2}	5.44631	5.44601	-0.0055
μ_{uy2}	1.12797	1.12802	0.0044
σ_{ux1}	0.24032	0.240522	0.0856
σ_{uy1}	0.08011	0.0801257	0.0255
σ_{ux2}	0.25332	0.253463	0.0584
σ_{uy2}	0.08011	0.0801882	0.1034

Table IV summarizes the 3rd and 4th order central moments sorted by *MCS* using 10^6 samples, for the adopted densities.

Table IV. Comparison between 3rd and 4th order central momentsfor both PDF.

Parameter	*Kernel PDF*	*Gaussian PDF*
$\mu_{3,ux1}$ [mm^3]	0.0042728	0.0053643
$\mu_{3,uy1}$ [mm^3]	0.0001791	0.0002233
$\mu_{3,ux2}$ [mm^3]	0.0044510	0.0055959
$\mu_{3,uy2}$[mm^3]	0.0001784	0.0002263
$\mu_{4,ux1}$ [mm^4]	0.0138060	0.0111287
$\mu_{4,uy1}$ [mm^4]	0.0001831	0.0001398
$\mu_{4,ux2}$ [mm^4]	0.0160580	0.0134891
$\mu_{4,uy2}$[mm^4]	0.0001835	0.0001405

Such central moments combined with the *MCS* mean values and standard deviations are used to evaluate the *CoV*s, μ_u / σ_u, the skewness coefficients, $\mu_{3,u} / \sigma_u^3$, and excess kurtosis, $(\mu_{4,u} / \sigma_u^4) - 3$, of both *Kernel PDF* and *Gaussian PDF* in terms of displacements.

Due to nonlinear filtering of input data, it is well known that the expected structural response has property of non Gaussianity. Adopting the kernel density function, which takes in account of higher order

statistics of the input data, the structural response statistics of order higher than the second gives results which are different from the ones sorted by simply assuming the Gaussianity of input data (i.e. taking into account the input data statistics up to the second order). Such consideration justifies the need to take into account of input data statistics of higher order to the second, when it is interesting to well catch the non Gaussian character of structural response.

On the other hand, the non Gaussianity of the response in both cases is highlighted by slightly right-tailed shape with respect to the mean of responses, as indicated by skewness coefficient, given in Table V where it is clearly evident that, adopting the *Kernel PDF*, the sensible higher value of excess kurtosis is provided.

Table V. C.O.V., skewness coefficients and excess kurtosis of the responses.

Parameter	*Kernel PDF*	*Gaussian PDF*
μ_{ux1}/σ_{ux1}	0.055	0.056
μ_{uy1}/σ_{u1}	0.070	0.071
μ_{ux2}/σ_{ux2}	0.046	0.047
μ_{uy2}/σ_{uy2}	0.070	0.071
$\mu_{3,ux1}/\sigma^3_{ux1}$	0.3214	0.3855
$\mu_{3,uy1}/\sigma^3_{uy1}$	0.3646	0.4342
$\mu_{3,ux2}/\sigma^3_{ux2}$	0.2862	0.3437
$\mu_{3,uy2}/\sigma^3_{uy2}$	0.3625	0.4390
$\frac{\mu_{4,ux1}}{\sigma^4_{ux1}}-3$	1.3845	0.3253
$\frac{\mu_{4,uy1}}{\sigma^4_{uy1}}-3$	1.7249	0.3909
$\frac{\mu_{4,ux2}}{\sigma^4_{ux2}}-3$	1.1361	0.2683
$\frac{\mu_{4,uy2}}{\sigma^4_{uy2}}-3$	1.7246	0.3985

4.2. INTERVAL ANALYSIS

It is well known that when the information on experimental data is incomplete or fragmentary, the interval analysis is a very efficient method to evaluate the propagation of the uncertainties on structural response. To define the interval of uncertainty, the knowledge of the distribution function is not required but its bounds only. Furthermore, according to the philosophy of interval analysis, the measured data define an interval with full confidence that the value is within the interval, and not outside it. That is, it is not a

confidence interval or credibility interval. Rather, the interval represents sure bounds of the measurement, with full degree of confidence on experimental data (Ferson et al., 2007).

The starting point in using a bounded interval to model the measurement uncertainty is to acknowledge the intrinsic imprecision in measurement. In the studied truss structure, the population of experimental data is numerous, so that reliable results can be obtained by applying the probabilistic approach, described in the previous section. The aim of this section, is to compare the results provided by the probabilistic model with the ones evaluated by applying the *Improved Interval Analysis*. For this purpose, the first step is to define a reliable interval of the uncertain elastic modulus. A reasonable choice seems to be a normalized interval containing all experimental data, i.e. $[-0.28,+0.28]$, which has been chosen for Kernel PDF evaluation. In Table VI, the chosen values of *lower bound* (*LB*), $\underline{\alpha}$, and *upper bound* (*UB*), $\overline{\alpha}$, as well as the midpoint, $\mu_\alpha = (\overline{\alpha}+\underline{\alpha})/2$, deviation, $\Delta\alpha = (\overline{\alpha}-\underline{\alpha})/2$, and *Coefficient of Interval Uncertainty* (*C.I.U.*), $\Delta\alpha/\mu_\alpha$, are reported.

Table VI. Interval parameters for Young Elastic Modulus from experimental data (100% of experimental data).

$\underline{\alpha}$ [N/mm^2]	142638.10
$\overline{\alpha}$ [N/mm^2]	253583.26
μ_α [N/mm^2]	198110.68
$\Delta\alpha$ [N/mm^2]	110945.16
C.I.U.	0.28

The corresponding midpoint displacement vector $\mathbf{u}_0$ and the lower and the upper bounds of displacements vectors calculated by Eqs. (30) and (31) are given respectively as:

$$\mathbf{u}_0 = \begin{pmatrix} 4.66256 \\ 1.21788 \\ 5.88044 \\ 1.21788 \end{pmatrix} [\text{mm}] \quad \underline{\mathbf{u}} = \begin{pmatrix} 3.35701 \\ 0.87686 \\ 4.23387 \\ 0.87686 \end{pmatrix} [\text{mm}]; \quad \overline{\mathbf{u}} = \begin{pmatrix} 5.96811 \\ 1.55890 \\ 7.52701 \\ 1.55890 \end{pmatrix} [\text{mm}];$$

The difference between midpoint values and explicit mean value vectors for *Kernel PDF* and *Gaussian PDF*, reported in Table II and Table III, is reported in Table VII.

In Figures 4-7 the bounds of interval responses, in terms of displacement, sorted by *Improved Interval Analysis*, are compared with the results obtained in terms of confidence range displacements, calculated as the mean value ± three times standard deviation of stochastic results, coming out by assuming maximum entropy approach and adopting the normal distribution. These Figures show that for the analysed truss structure, the confidence range lie into the bounds defined by *Interval Analysis*, if an interval that includes all experimental data is chosen.

Table VII. Comparison between mean values and midpoint displacements.

Parameter [mm]	$\mathbf{u}_0$	$\boldsymbol{\mu}_{\tilde{U}}$ *(Kernel PDF)*	$\boldsymbol{\mu}_{\tilde{U}}$ *(Gaussian PDF)*	*Difference* [%] *(Kernel PDF)*	*Difference* [%] *(Gaussian PDF)*
μ_{ux1}	4.66256	4.31818	4.31834	7.3861	7.3826
μ_{uy1}	1.21788	1.12793	1.12797	7.3858	7.3825
μ_{ux2}	5.88044	5.44611	5.44631	7.3860	7.3826
μ_{uy2}	1.21788	1.12793	1.12797	7.3858	7.3825

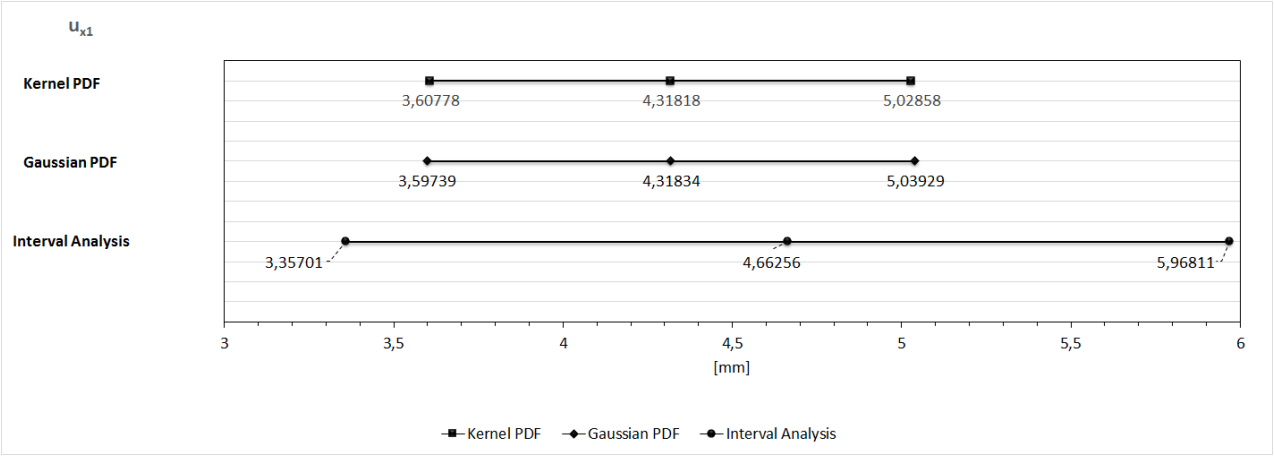

Figure 4. u_{x1}: interval analysis bounds and *Kernel* and *Gaussian PDF* $\mu_u \pm 3\sigma_u$.

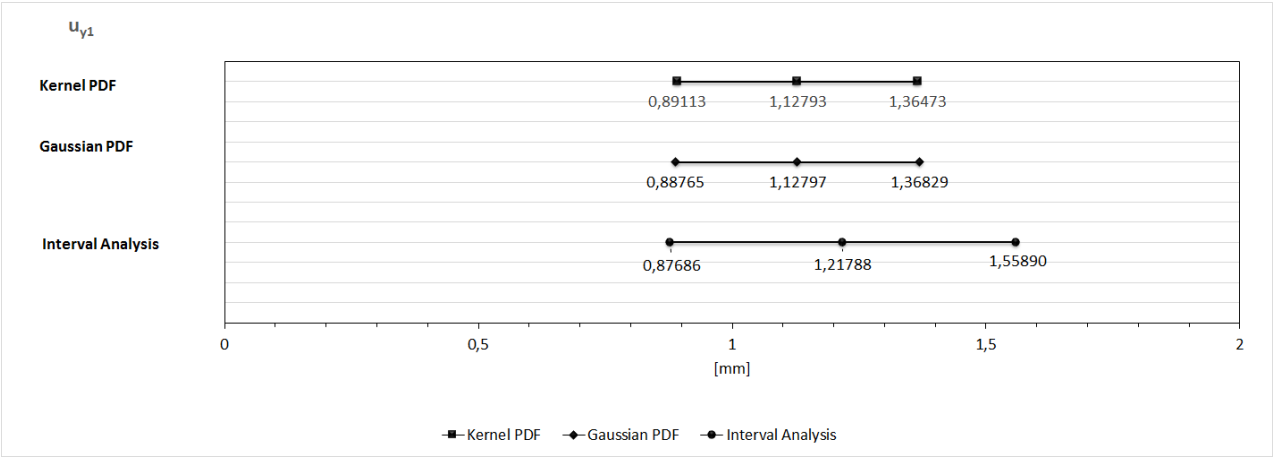

Figure 5.u_{y1}: interval analysis bounds and *Kernel* and *Gaussian PDF* $\mu_u \pm 3\sigma_u$.

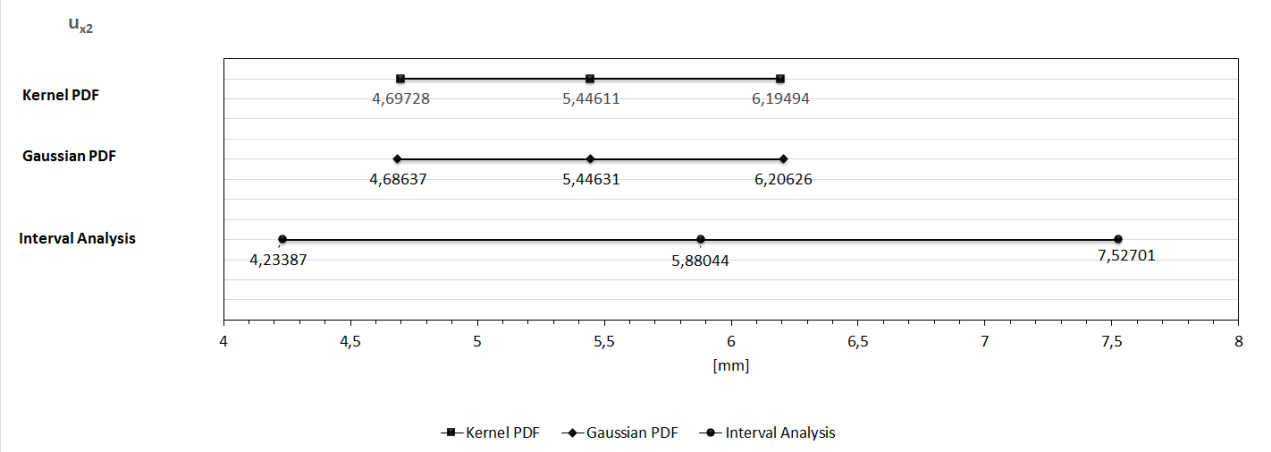

Figure 6. u_{x2}: interval analysis bounds and *Kernel* and *Gaussian PDF* $\mu_u \pm 3\sigma_u$.

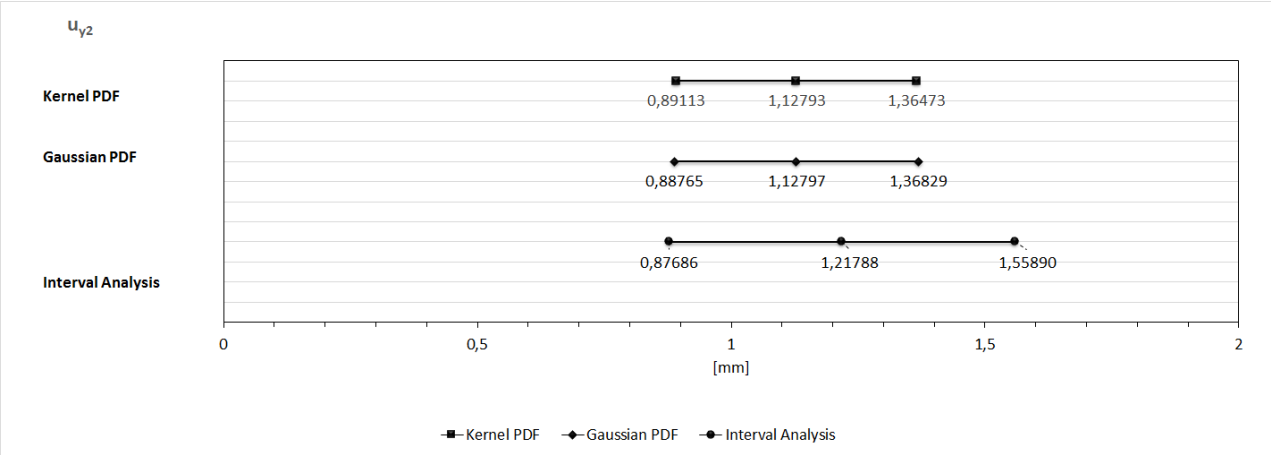

Figure 7. u_{y2}: interval analysis bounds and *Kernel* and *Gaussian PDF* $\mu_u \pm 3\sigma_u$.

5. Conclusions

Starting from tensile tests performed on steel bars, where elastic moduli are measured, the PDF of uncertain elastic modulus was recovered by maximum entropy approach. This function was adopted for the static analysis of a truss structure to evaluate stochastic structural response by means the *Rational Series Expansion* technique. The comparison with Monte Carlo Simulation results confirmed the accuracy of method.

In order to compare the results provided by the probabilistic model with the ones evaluated by applying the *Improved Interval Analysis*, the confidence range displacement, calculated as the mean value ± three

times standard deviation of stochastic results, is determined. Then the bounds of the response interval by applying the *Improved Interval Analysis* are evaluated. The comparison of two response intervals showed that the selected confidence range lies into the bounds defined by Interval Analysis if, for the uncertain elastic modulus, the interval that includes all experimental data is chosen.

References

Alibrandi U. and G. Ricciardi. Efficient evaluation of the pdf of a random variable through the kernel density maximum entropy approach. *International Journal for Numerical Methods in Engineering*, 75:1511–1548, 2008.

Barbato G., E. M. Barini, G. Genta and R. Levi. Features and performance of some outlier detection methods. *Journal of Applied Statistics*, 38:2133–2149, 2011.

Elishakoff I. and M. Ohsaki. Optimization and Anti-optimization of Structures under Uncertainty, Imperial College Press, London, 2010.

Ferson S., V. Kreinovich, J. Hajagos, W. Oberkampf and L. Ginzburg. *Experimental Uncertainty Estimation and Statistics for Data Having Interval Uncertainty*. SANDIA REPORT: SAND 2007-0939, 2007.

Moens, D. and D. Vandepitte. A Survey of Non-Probabilistic Uncertainty Treatment in Finite Element Analysis. *Computer Methods in Applied Mechanics and Engineering* 194:1527–1555, 2005.

Moore, R. E. *Interval Analysis*, Prentice-Hall, Englewood Cliffs, 1966.

Moore, R. E., R. B. Kearfott and M. J. Cloud. *Introduction to Interval Analysis*, SIAM, Philadelphia, USA, 2009.

Muhanna, R. L. and R. L. Mullen. Uncertainty in Mechanics: Problems-Interval-Based Approach. *Journal Engineering Mechanics ASCE* 127:557-566, 2001.

Muscolino G. and A. Sofi. Stochastic Analysis of Structures with Uncertain-but-Bounded Parameters via Improved Interval Analysis. *Probabilistic Engineering Mechanics* 28:152-163, 2012.

Muscolino, G. and A. Sofi. Bounds for the Stationary Stochastic Response of Truss Structures with Uncertain-but-Bounded Parameters. *Mechanical Systems and Signal Processing* 37:163-181, 2013.

Muscolino G., R. Santoro and A. Sofi. Explicit frequency response functions of discretized structures with uncertain parameters. *Computer and Structures*, 133:64-78, 2014.

Efficient Propagation of Imprecise Probabilities

Jiaxin Zhang and Michael D. Shields
Department of Civil Engineering, Johns Hopkins University, Baltimore, MD 21212, USA,
michael.shields@jhu.edu

Abstract: It is often the case that sparse statistical data prohibits the assignment of a precise probability distribution to a given uncertain variable. In these cases, conventional statistical approaches such as Bayesian inference provide uncertain probability distributions - or imprecise probabilities. For convenience, many probabilistic approaches assign a specific distribution based on Maximum Likelihood Estimation (MLE) or some other criteria. Yet propagation of this single MLE distribution ignores potentially importance uncertainty/variability in these variables. Meanwhile, some quasi-probabilistic approaches treat the uncertainties in the distribution using intervals (e.g. mean value of a distribution may be assigned an interval) and propagate a family of distributions to construct a probability-box (or p-box) to bound the probabilities (Beer et al., 2013). This approach is generally computationally very expensive requiring several Monte Carlo analyses to propagate a large number of distributions.

In this work, we propose an approach based on importance sampling to propagate imprecise probability distributions with a single Monte Carlo analysis. The approach uses Bayesian inference to quantify the imprecise probabilities - determining a set of possible candidate distributions (that may come from different families - e.g. normal, lognormal, gamma, etc.) weighted according to their probability of occurrence. We then identify an optimal sampling distribution that best represents all possible candidate distributions. Samples from this optimal sampling distribution are propagated using Monte Carlo simulation and are re-weighted according to the different candidate distributions. Hence, we achieve the propagation of many probability distributions with a single Monte Carlo simulation. A further advantage of the methodology is that the underlying probability models can be updated using Bayesian updating and propagation of these updated distributions does not require additional simulations. Instead, the weights associated with the existing simulations are updated directly to update the probability model of the solution.

Keywords: imprecise probability, Bayesian inference, importance sampling

1. Introduction

Modern engineering structures and systems, and the models used to represent them, are often characterized by a high degree of complexity. Modeling the influence of various physical phenomena in these systems presents a significant challenge. With the rapid growth of deterministic modeling capabilities, it is becoming widely acknowledged that predictive modeling capabilities can only be achieved by accounting for uncertainties in the modeling process. Therefore, uncertainty quantification plays an important role in computational modeling from design to reliability analysis and risk assessment of complex systems.

A prominent obstacle in uncertainty quantification is the discrepancy between the required information and the available information. This discrepancy is often caused by limitations in the ability to collect sufficient information/data to accurately assign values or probability models to all variables in the problem (i.e. the presence of epistemic uncertainty). For instance, naval ship structures are incredibly complex engineering systems that are subject to highly stochastic marine environments. Further complicating the analysis of these structures is that design specifications provide only nominal values for material and geometric variables and maintenance/inspections are sparse, qualitative, and cover only a small fraction of critical structural components. Although some powerful statistical tools can be used to enable probabilistic modeling given sufficient data of suitable quality, the available data in engineering practice are often limited and of poor quality, which prevents the identification of a precise probability model and its associated parameters.

Imprecise probability approaches have been widely employed and have proven to be effective tools to overcome the issues caused by vague, limited and equivocal information. A series of influential developments on generalized methods has been discussed in the literature (Helton and Oberkampf, 2004; Beer et al., 2013) from various perspectives, including Bayesian approaches (Der Kiureghian et al., 2009), interval methods (Moore and Bierbaum, 1979; Ferson and Hajagos, 2004; Ferson and Ginzburg, 1996), Dempster-Shafer evidence theory (Nelsen et al., 2004) and fuzzy theory (Dubois and Prade, 2005; Stein et al., 2013) among other approaches. More generally, attempts have been made to bring all of these components together under a unifying theory of imprecise probability, which is mainly part of the generalized framework of information theory (Walley, 1991; Walley, 2000). In this framework, probability theory is employed on behalf of stochastic variations in the system variables while epistemic uncertainties associated with the probability laws and their parameters are described using the concepts discussed above.

Traditional statistical inference is based on an assumed probability model (i.e. distribution type) and its parameters (e.g. mean and standard deviation) are estimated using observed data. When sufficient data is provided, these conventional approaches assign a specific distribution with parameters estimated using e.g. maximum likelihood estimation or method of moments. However, it may be impossible to identify a precise distribution type and its parameters given uncertainty due to limited data. This results in many possible/viable probability models with interval or probabilistic model parameters such that uncertainty propagation becomes a major challenge. Existing methods for propagation of imprecise probabilities are usually computationally intractable for all but the simplest problems because they typically require a large number of individual probability studies spanning the range of possible probability distributions and parameters.

This paper proposes an efficient methodology to propagate imprecise probability distributions using Bayesian inference and importance sampling with a single Monte Carlo study. An optimal sampling distribution is identified to represent all candidate distributions by minimizing the overall differences between the sampling distribution and the ensemble of candidate variable distributions characterized by the Hellinger distance and the total variation distance. Samples are generated by this optimal sampling distribution and re-weighted according to importance sampling to simultaneously propagate all candidate distributions. The method has the further advantage that the probability study can be updated directly as additional data is collected. This is enabled through Bayesian updating of the joint model parameter distribution and re-weighting of the samples according to the updated probability laws.

2. Review of Important Concepts

2.1. Bayesian inference

Bayesian inference holds a central position in data-driven uncertainty quantification and uncertainty propagation in engineering science. As a statistical method, Bayesian inference is used to obtain a posterior PDF $p(\boldsymbol{\phi}|\boldsymbol{d}, M)$ for the parameters $\boldsymbol{\phi}$ of a model class M using experimental observations $\boldsymbol{d}$. This is achieved through Bayes' rule

$$p(\boldsymbol{\phi}|\boldsymbol{d}, M) = \frac{p(\boldsymbol{d}|\boldsymbol{\phi}, M)p(\boldsymbol{\phi}, M)}{p(\boldsymbol{d}, M)} \tag{1}$$

where $p(\boldsymbol{\phi}, M)$ is the prior PDF that expresses existing knowledge (or lack thereof) about the parameters, $p(\boldsymbol{d}|\boldsymbol{\phi}, M)$ is the likelihood of observing the data $\boldsymbol{d}$ from the model class M with parameters $\boldsymbol{\phi}$, and $p(\boldsymbol{d}, M)$ is the evidence of model M and is equal to

$$p(\boldsymbol{d}, M) = \int p(\boldsymbol{d}|\boldsymbol{\phi}, M)p(\boldsymbol{\phi}, M)d\boldsymbol{\phi} \tag{2}$$

Evaluating $p(\boldsymbol{d}, M)$ is often a non-trivial task because the integration in Eq. (2) is usually analytical intractable for nonlinear and high-dimensional models. To overcome this issue, either Markov Chain Monte Carlo (MCMC) approaches are employed or conjugate distributions are utilized.

The posterior model parameters determined from Eq. (1) are stochastic and are presented in the form of a PDF. From this PDF, the model parameters are frequently assigned using maximum likelihood estimation (MLE) but this ignores the essential variability in distribution parameters, which may have an important role in the results of a probability study - especially when data are sparse, imprecise or limited. Furthermore, the selection of the model M itself is subject to question unless abundant data are provided or some some rationale is used to supply convincing evidence that a specific model form applies (e.g. Central Limit Theorem applies so the distribution should be normal). In the coming sections, we discuss issues of non-unique model selection and the simultaneous propagation of many models having uncertain parameters.

2.2. Model selection

In the case of sparse data, the selection of a probability model is a substantial challenge. Existing model selection procedures often rank the candidate models based on some widely accepted criteria. Most approaches of model selection can be categorized into three classes: (a) frequentist methods (Guyon et al., 2010), (b) Bayes factor method (Berger and Pericchi, 1996), and (c) methods based on information theory such as the Akaike information criterion (AIC) (Akaike, 1974) and Bayesian Information Criterion (BIC) (Schwartz, 1978). The AIC and BIC, defined as follows, are used here

$$\mathrm{AIC}(M) = 2p - 2L(\hat{\boldsymbol{\phi}}) \tag{3}$$

$$\mathrm{BIC}(M) = p\log n - 2L(\hat{\boldsymbol{\phi}}) \tag{4}$$

where L is the log-likelihood for model M, $\hat{\boldsymbol{\phi}}$ are the parameter values that maximize the likelihood function, p is the dimensionality of the parameter space, and n is the number of observations.

Minimizing the AIC and BIC corresponds to maximizing the posterior model probability for a large amount of data. Again, the AIC and BIC cannot provide an exact means of model selection (especially under limited data), but instead provide evidence that certain types may be valid while others are not.

2.3. Importance sampling

To improve the accuracy and reduce the cost of stochastic simulation approaches, diverse variance reduction techniques exist. One of the most widely-used approaches is Importance Sampling (IS). Based on the introduction of a proposal sampling density (referred to as the IS density), IS concentrates the computational effort in regions of the uncertain model parameter space that play a more important role in the overall probabilistic performance. Consider a system that involves some design variables $\boldsymbol{x}$ and stochastic model parameters $\boldsymbol{\theta}$. If the performance function of the system model is given by $f(\boldsymbol{x}, \boldsymbol{\theta})$, then the expected performance is computed as

$$\mathcal{L} = \int f(\boldsymbol{x}, \boldsymbol{\theta}) p(\boldsymbol{\theta}) d\boldsymbol{\theta} = E_p[f(\boldsymbol{x}, \boldsymbol{\theta})] \approx \frac{1}{N} \sum_{i=1}^{N} f(\boldsymbol{x}, \boldsymbol{\theta}_i) \tag{5}$$

where $\boldsymbol{\theta}_i$ are independent identically distributed ($i.i.d.$) samples drawn from $p(\boldsymbol{\theta})$, $E_p[\cdot]$ is the expectation under target distribution $p(\boldsymbol{\theta})$, and N is the number of samples. Importance sampling associated with proposal sampling density $q(\boldsymbol{\theta})$ transforms the integral to

$$\hat{\mathcal{L}} = \int f(\boldsymbol{x}, \boldsymbol{\theta}) \frac{p(\boldsymbol{\theta})}{q(\boldsymbol{\theta})} q(\boldsymbol{\theta}) d\boldsymbol{\theta} = E_q[f(\boldsymbol{x}, \boldsymbol{\theta}) \frac{p(\boldsymbol{\theta})}{q(\boldsymbol{\theta})}] \approx \frac{1}{N} \sum_{i=1}^{N} f(\boldsymbol{x}, \boldsymbol{\theta}_i) \frac{p(\boldsymbol{\theta}_i)}{q(\boldsymbol{\theta}_i)} \tag{6}$$

where $E_q[\cdot]$ is the expectation with respect to $q(\boldsymbol{\theta})$. The ratio $\omega(\boldsymbol{\theta}) = p(\boldsymbol{\theta})/q(\boldsymbol{\theta})$ can be interpreted as the weights of samples generated from $q(\boldsymbol{\theta})$. Selection of an efficient proposal sampling density will lead to significant improvement in accuracy (i.e. variance reduction). Conversely, poor IS density selection can increase variance. The optimal choice for the proposal sampling density is derived by minimizing the variance of the estimator $\hat{\mathcal{L}}$ as

$$q^*(\boldsymbol{\theta}) = \frac{|f(\boldsymbol{x}, \boldsymbol{\theta}) p(\boldsymbol{\theta})|}{\int |f(\boldsymbol{x}, \boldsymbol{\theta}) p(\boldsymbol{\theta})| \, d\boldsymbol{\theta}} \tag{7}$$

where $|\cdot|$ means the absolute value. In practice, this choice is intractable since it needs simulation of samples from a PDF that is proportional to the integrand of the expectation and the expectation itself.

2.4. Hellinger distance and total variation distance

As the choice of optimal sampling distribution is not feasible using Eq. (7), one way is to find a proposal sampling density that has a minimal difference with the optimal one. The Hellinger distance, as a special case of the Csiszár's ϕ-divergence (Csiszar, 1975), can be used to quantify the

difference between probability distributions $p(\boldsymbol{\theta})$ and $q(\boldsymbol{\theta})$ as

$$H(P,Q) = \left(\frac{1}{2}\int\left(\sqrt{p(\boldsymbol{\theta})} - \sqrt{q(\boldsymbol{\theta})}\right)^2 d\boldsymbol{\theta}\right)^{\frac{1}{2}} \tag{8}$$

One way to minimize the difference between two distributions is to find the distribution that produces the minimum Hellinger distance estimator (MHDE) (Beran, 1977). In order to obtain the solution of

$$\hbar = \arg\min \frac{1}{\sqrt{2}}\left\|\sqrt{p(\boldsymbol{\theta})} - \sqrt{q(\boldsymbol{\theta})}\right\|_2 \tag{9}$$

where $\|p-q\|_2 = \left(\int\left(\sqrt{p(\boldsymbol{\theta})} - \sqrt{q(\boldsymbol{\theta})}\right)^2 d\boldsymbol{\theta}\right)^{\frac{1}{2}}$ denotes the ℓ_2 norm, we instead use the square MHDE which is convenient for expressing the derivative of the optimal sampling distribution in the following section

$$\hbar^2 = \arg\min \frac{1}{2}\left\|\sqrt{p(\boldsymbol{\theta})} - \sqrt{q(\boldsymbol{\theta})}\right\|_2^2 \tag{10}$$

where $\|p-q\|_2^2 = \int\left(\sqrt{p(\boldsymbol{\theta})} - \sqrt{q(\boldsymbol{\theta})}\right)^2 d\boldsymbol{\theta}$ denotes the square ℓ_2 norm. This is achieved by constructing a nonparametric proposal density $q(\boldsymbol{\theta})$ and conducting an optimization with Eq. (10) as the objective.

3. Optimal Importance Sampling for Multiple Distributions

To date, importance sampling has always been used with a precisely specified target distribution $p(\boldsymbol{\theta})$. However, in the imprecise probability case caused by lack of data, the target distribution cannot be assigned precisely and therefore, the estimation of the optimal sampling distribution becomes a significant challenge. This work first utilizes a Bayeisan inference approach to quantify the imprecise probabilities by identifying several viable probability models M through AIC/BIC and retaining the distributions of their model parameters $\boldsymbol{\phi}$. From this, a series of possible candidate target distributions are assigned on the basis of their probability of occurrence. The fundamental difference with classical importance sampling is that a set of probabilistically weighted target distributions are taken into consideration. The crucial issue addressed in this study is how to select an optimal importance sampling density to effectively represent and propagate all candidate target distributions. To do so, we need to identify a sampling distribution that is as close as possible to the ensemble of target distributions.

Our object of maximizing the representativeness of the importance sampling distribution for multiple target distributions can be restated as minimizing the total difference between the importance sampling distribution and the ensemble of target distributions. This is the equivalent of minimizing the distance in the probability space. Utilizing the Hellinger distance, an overall square MHDE with uncertain distribution parameters and distribution types is proposed as

$$\hbar^2 = \arg\min \sum_{i=1}^{N_d}\int_{\boldsymbol{\phi}} \frac{1}{2}\left\|\sqrt{p_i(\boldsymbol{\theta}|\boldsymbol{\phi})} - \sqrt{q(\boldsymbol{\theta})}\right\|_2^2 d\boldsymbol{\phi} \tag{11}$$

where N_d is the number of candidate probability models defined through the target densities $p_i(\boldsymbol{\theta}|\boldsymbol{\phi})$ having parameters $\boldsymbol{\phi}$. An advantage of this Hellinger distance metric is that we can obtain the analytical solution for the optimal proposal sampling. If we set the derivative of the overall square MHDE $\hat{\hbar}^2$ with respect to $q(\boldsymbol{\theta})$ as

$$\frac{\partial \hat{\hbar}^2}{\partial q(\boldsymbol{\theta})} = \frac{\partial \sum_{i=1}^{N_d} \int_{\boldsymbol{\phi}} \frac{1}{2} \left(\sqrt{p_i(\boldsymbol{\theta}|\boldsymbol{\phi})} - \sqrt{q(\boldsymbol{\theta})} \right)^2 d\boldsymbol{\phi}}{\partial q(\boldsymbol{\theta})} \tag{12}$$

$$\frac{\partial \hat{\hbar}^2}{\partial q(\boldsymbol{\theta})} = \frac{1}{2} \sum_{i=1}^{N_d} \left(\frac{\partial \int_{\boldsymbol{\phi}} \left(\sqrt{p_i(\boldsymbol{\theta}|\boldsymbol{\phi})} - \sqrt{q(\boldsymbol{\theta})} \right)^2 d\boldsymbol{\phi}}{\partial q(\boldsymbol{\theta})} \right) \tag{13}$$

$$\frac{\partial \hat{\hbar}^2}{\partial q(\boldsymbol{\theta})} = \frac{1}{2} \sum_{i=1}^{N_d} \left(\frac{\partial \int_{\boldsymbol{\phi}} p_i(\boldsymbol{\theta}|\boldsymbol{\phi}) - 2\sqrt{p_i(\boldsymbol{\theta}|\boldsymbol{\phi}) q(\boldsymbol{\theta})} + q(\boldsymbol{\theta}) d\boldsymbol{\phi}}{\partial q(\boldsymbol{\theta})} \right) \tag{14}$$

$$\frac{\partial \hat{\hbar}^2}{\partial q(\boldsymbol{\theta})} = \frac{1}{2} \sum_{i=1}^{N_d} \left(\int_{\boldsymbol{\phi}} \left(1 - \sqrt{\frac{p_i(\boldsymbol{\theta}|\boldsymbol{\phi})}{q(\boldsymbol{\theta})}} \right) d\boldsymbol{\phi} \right) \tag{15}$$

For the special case of two parameter distributions with $\boldsymbol{\phi} = (\mu, \sigma)$ where μ and σ are the mean and standard deviation respectively, we have

$$\frac{\partial \hat{\hbar}^2}{\partial q(\boldsymbol{\theta})} = \frac{1}{2} \sum_{i=1}^{N_d} \left(\int_{\mu} \int_{\sigma} \left(1 - \sqrt{\frac{p_i(\boldsymbol{\theta}|\mu, \sigma)}{q(\boldsymbol{\theta})}} \right) d\mu d\sigma \right) \tag{16}$$

By partitioning the joint probability density of model parameters $p_i(\boldsymbol{\theta})$ for each distribution type, we extract a finite but representative number of candidate target distributions from the infinite set. The derivative can then be approximated using discretized means $\mu_j (j = 1, 2, ..., N_{mi})$ and standard deviations $\sigma_k (k = 1, 2, ..., N_{si})$ as

$$\frac{\partial \hat{\hbar}^2}{\partial q(\boldsymbol{\theta})} \approx \frac{1}{2} \sum_{i=1}^{N_d} \left(\sum_{j=1}^{N_{mi}} \sum_{k=1}^{N_{si}} \left(1 - \sqrt{\frac{p_i(\boldsymbol{\theta}|\mu_j, \sigma_k)}{q(\boldsymbol{\theta})}} \right) \right) \tag{17}$$

where $N_{mi} \times N_{si}$ represents the total number of uncertain distribution parameters for model class M_i (e.g. mean and standard deviation for two-parameter distributions). Setting $\frac{\partial \hat{\hbar}^2}{\partial q(\boldsymbol{\theta})} = 0$ and (for simplicity) assuming $N_{mi} = N_m \ \forall i$ and $N_{si} = N_s \ \forall i$, we have

$$\sum_{i=1}^{N_d} \sum_{j=1}^{N_m} \sum_{k=1}^{N_s} 1 - \sum_{i=1}^{N_d} \sum_{j=1}^{N_m} \sum_{k=1}^{N_s} \sqrt{\frac{p_i(\boldsymbol{\theta}|\mu_j, \sigma_k)}{q(\boldsymbol{\theta})}} = N_d \cdot N_m \cdot N_s - \frac{\sum_{i=1}^{N_d} \sum_{j=1}^{N_m} \sum_{k=1}^{N_s} \sqrt{p_i(\boldsymbol{\theta}|\mu_j, \sigma_k)}}{\sqrt{q(\boldsymbol{\theta})}} = 0 \tag{18}$$

Therefore, the optimal proposal sampling density will be

$$q^*(\boldsymbol{\theta}) = \left(\frac{\sum_{i=1}^{N_d} \sum_{j=1}^{N_m} \sum_{k=1}^{N_s} \sqrt{p_i(\boldsymbol{\theta}|\mu_j, \sigma_k)}}{N_d \cdot N_m \cdot N_s} \right)^2 \tag{19}$$

However, as a nonparametric model, q^* is not always a PDF that satisfies $\int q^*(\boldsymbol{\theta})d\boldsymbol{\theta} = 1$ unless all candidate target distributions are the same. Actually, all target distributions are different here, so it will be improper to choose $q^*(\boldsymbol{\theta})$ as the proposal sampling density. In order to ensure $q^*(\boldsymbol{\theta})$ is a valid PDF, we may alternatively consider the optimization according to the total variation distance $\Delta(P, Q)$ defined through the following ℓ_1 norm

$$\Delta(P, Q) = \max \|P - Q\|_1 = \frac{1}{2} \sum_{\boldsymbol{\theta}} |p(\boldsymbol{\theta}) - q(\boldsymbol{\theta})| \tag{20}$$

thanks to the following property stated by (Lindsay, 1994) relating it to the Hellinger distance

$$H^2(P, Q) \leq \Delta(P, Q) \leq \sqrt{2}H(P, Q) \tag{21}$$

Thus, an equivalent way to obtain the optimal proposal sampling distribution is to minimize the total variation distance in Eq. (20), which yields

$$\hat{q}^*(\boldsymbol{\theta}) = \frac{1}{N_d \cdot N_m \cdot N_s} \sum_{i=1}^{N_d} \sum_{j=1}^{N_m} \sum_{k=1}^{N_s} p_i(\boldsymbol{\theta}|\mu_j, \sigma_k) \tag{22}$$

where $\hat{q}^*(\boldsymbol{\theta})$ is a nonparametric density estimator that consists of multiple mixture distributions. If the weights of different distribution types and parameters are identical, the coefficient for each candidate target will be equal. More generally, the optimal proposal density can be written with different weighting coefficients

$$\hat{q}^*(\boldsymbol{\theta}) = \sum_{i=1}^{N_d} \sum_{j=1}^{N_m} \sum_{k=1}^{N_s} \lambda_{jk}^i \cdot p_i(\boldsymbol{\theta}|\mu_j, \sigma_k) \tag{23}$$

where λ_{jk}^i is the weighting coefficient for the i^{th} distribution type with parameters of the j^{th} mean and the k^{th} standard deviation, and satisfies

$$\sum_{i,j,k} \lambda_{jk}^i = 1 \tag{24}$$

These coefficients may be derived from probabilistic considerations that account for the probability of occurrence of distribution parameters and model classes from the provided data.

4. Propagation of Imprecise Probability

By the discussion above, there are theoretically infinite candidate target distributions. Even after discretization, thousands of candidate distributions remain. Existing algorithms are often very computationally intensive since individual probability studies (Monte Carlo analyses) are needed to propagate each distribution separately. The method proposed here utilizes importance sampling to propagate these thousands of distributions simultaneously through a single Monte Carlo study

by generating samples from the optimal proposal sampling density in Eq. (22), and reweighting the samples according to each target. Specifically, after sampling from $q^*(\boldsymbol{\theta})$, importance sampling estimators are constructed for each candidate target $p_i(\boldsymbol{\theta}|\mu_j, \sigma_k)$ according to Eq. (6) and denoted $\hat{\mathcal{L}}^i_{jk}, i = 1, \ldots, N_d, j = 1, \ldots, N_m, k = 1, \ldots, N_s$. Note that all estimates $\hat{\mathcal{L}}^i_{jk}$ are constructed from the same set of samples drawn from $q^*(\boldsymbol{\theta})$, greatly reducing the computational cost over existing methods.

This procedure generates a set of probability distributions for the system performance that can be further assessed probabilistically. Given the Bayesian nature of the model construction, each of the probability distributions has an associated probability of occurrence derived from the joint density of its model parameters $\boldsymbol{\phi}$. Consequently, these distributions provide a rich source of information that goes beyond, for example, probability bounds that are typically available (in the form of a p-box for instance) to give a fully probabilistic measure of the output. This can be used to evaluate quantities like the PDF/CDF for statistical quantities or probability of failure that account for uncertainties associated with insufficient data.

A final advantage of the proposed method is that it can be readily updated to incorporate new data as it is collected. Using Bayesian updating, the joint parameter distirbution $p(\boldsymbol{\phi})$ is updated and the associated candidate target distributions are updated. However, it is not strictly necessary to identify a new optimal sampling density and the existing samples can be used for uncertainty propagation by re-weighting according to the importance sampling weights with the new target densities. Note that this does not ensure a low-variance estimator. In fact, the sampling density after updating is no longer optimal and may yield an increase in variance. If necessary, this variance can be reduced by either adding samples from $q^*(\boldsymbol{\theta})$ or solving for a new optimal PDF and resampling.

5. Numerical Example

The proposed methodology and its application are illustrated by an example considering the probabilistic assessment of plate buckling strength with uncertain geometric and material parameters. Carlsen (Carlsen, 1977) derived an analytical expression to evaluate the normalized buckling strength ψ of a simply supported plate in uniaxial compression considering the effects of non-dimensional initial deflections δ_0 and residual stress ηt resulting from welding as

$$\psi = \frac{\sigma_b}{\sigma_0} = \left(\frac{2.1}{\lambda} - \frac{0.9}{\lambda^2}\right)\left(1 - \frac{0.75\delta_0}{\lambda}\right)\left(1 - \frac{2\eta t}{b}\right) \tag{25}$$

where σ_b is the stress at which buckling occurs, $\lambda = b/t\sqrt{\sigma_0/E}$ is referred to as the slenderness of the plate with width b, thickness t, yield stress σ_0, and elastic modulus E. These material and geometric variabilities are estimated from the data presented by Hess et al. (Hess et al., 2002) and Soares (Soares, 1988) as presented in Table 1. According to a global sensitivity analysis (Saltelli, 2008), the yield stress shows the highest influence on the buckling strength accounting for nearly half of its variance, and therefore will be the main concern of this work.

Table I. Statistics for plate material, geometry and imperfection variables from Hess et al. (Hess et al., 2002) and Soares (Soares, 1988).

Variables	Physical Meaning	Nominal Value	Mean	COV	Sensitivity Index
b	Width	24	0.992*24	0.028	0.017
t	Thickness	0.5	1.05*0.5	0.044	0.045
σ_0	Yield Strength	34	1.3*34	0.1235	0.482
E	Elastic Modulus	29000	0.987*29000	0.076	0.194
δ_0	Initial Deflection	0.35	1.0*0.35	0.05	0.043
η	Residual Stress	5.25	1.0*5.25	0.07	0.233

We start with a collection of 25 yield stress values synthetically generated according to a normal distribution with parameters given in Table I. All other variables are assumed deterministic and taking their mean values. Next, we use the AIC (Eq. (3)) and BIC (Eq. (4)) to select viable distribution types based on the limited data. Table II presents the AIC and BIC values for several candidate distribution types. Note that only the Rayleigh and Exponential distributions stand out as having particularly high AIC/BIC and therefore we do not consider these two types as representative of our data. This leaves 11 distribution types that we consider as viable.

Table II. The rank sequence of distribution type using AIC and BIC.

Rank sequence	Distribution type	Akaike Information Criterion (AIC)	Bayesian Information Criterion (BIC)
1	Inverse Gaussian	160.9097	163.3474
2	Birnbaum-Saunders	160.9122	163.3499
3	Lognormal	160.9450	163.3828
4	Gamma	161.3044	163.7422
5	Loglogistic	161.7626	164.2004
6	Nakagami	161.7886	164.2264
7	Rician	162.3961	164.8338
8	Normal	162.4284	164.8662
9	Logistic	162.8088	165.2465
10	Weibull	166.3174	168.7552
11	Extreme Value	170.0299	172.4676
12	Rayleigh	208.0995	209.3183
13	Exponential	241.5110	242.7299

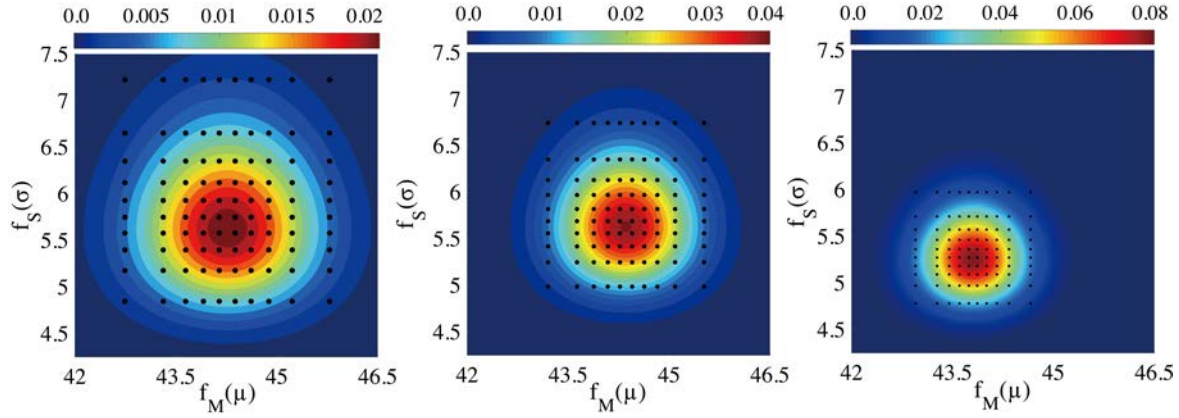

Figure 1. Joint posterior distribution for mean and standard deviation from Bayesian inference using datasets with 25 (left), 50 (middle) and 100 (right) yield stress values.

Using Bayesian inference, the joint posterior distribution of the mean and standard deviation are obtained from the initial 25 data. An equal partition of the joint probability distribution into a 10×10 grid yields 100 distinct values of the model parameters shown by the black dots in Figure 1. These pairs of mean and standard deviation values are then used with each of the 11 distribution types to produce a representative set of target distributions shown by the gray densities in Figure 2. When more data are collected, the joint posterior distribution of (μ, σ) is updated using Bayesian updating, as shown by the contours in Figure 1 for 25, 50, and 100 yield stress values. Again, the joint density is discretized through an equal partitioning of the probability space shown by the black dots.

The optimal sampling distribution is constructed analytically based on these 11 candidate target distributions and 100 possible parameter values (i.e. from a total of 1100 candidate target distributions - each equally probable). The optimal sampling density is shown by the black curve in Figure 2. The suite of distributions in Figure 2 are propagated through Eq. (25) by generating 5000 samples from the optimal sampling density and applying the importance sampling weights for each distribution. This propagation results in the gray band of CDFs for the compressive strength shown in Figure 3. Note that we do not update the optimal sampling density as data is gathered. This can be observed in Figure 2 where it is seen that the gray band of candidate target densities narrows but the black optimal sampling density remains the same. Hence, the optimal sampling density is no longer optimal in the right and middle images but remains sufficient for propagation and no new samples need to be generated. All of the CDFs shown in Figure 3 (from left to right) have been generated from the same 5000 random samples. Notice also that the band of CDFs in Figure 3 narrows considerably as additional yield stress values are collected. This is expected as the additional data reduces the epistemic uncertainty.

Next, consider that failure occurs when $\psi < 0.56$ - shown by the dashed vertical line in Figure 3. Given the equal partitioning of the probability space, each of the CDFs resulting from a given input distribution in Figure 3 is equally probable (note that the distribution types are not necessarily equally probable). We can therefore determine the empirical CDF of $P(\psi < 0.56)$ conditioned on the input distribution type as shown in Figure 4. Each of these CDFs has 100 values corresponding

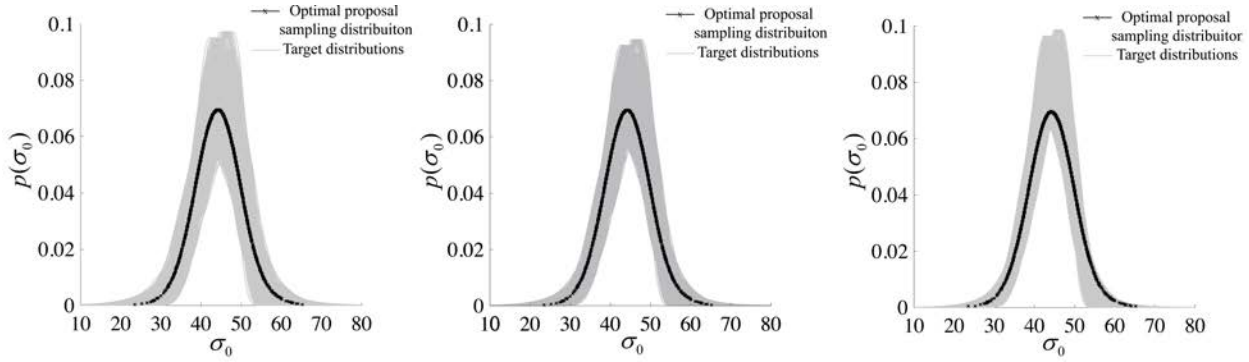

Figure 2. Ensemble of candidate target densities and the optimal proposal sampling density for yield stress from datasets with 25 (left), 50 (middle) 100 (right) yield stress values.

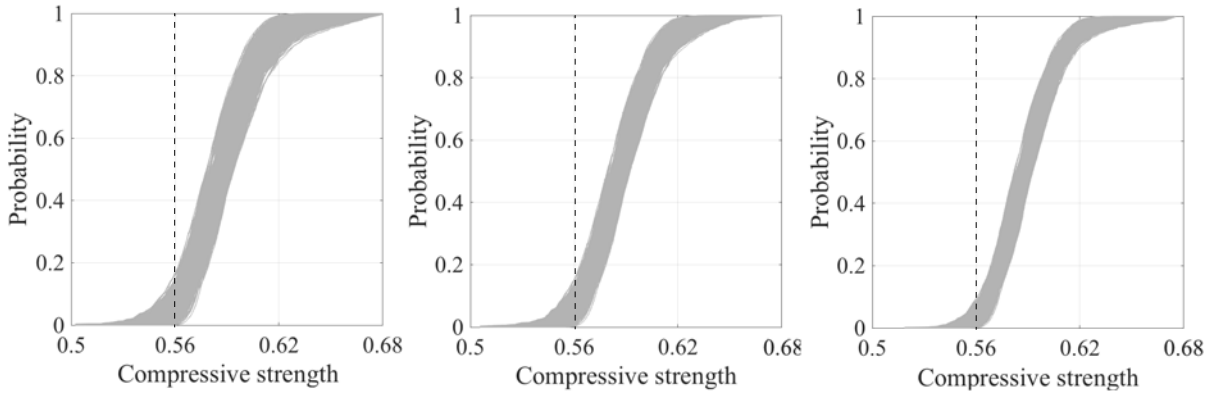

Figure 3. Ensemble of cumulative distribution functions with uncertain yield stress derived from propagation of uncertain probability models constructed using 25 (left), 50 (middle), and 100 (right) yield stress values.

to the 100 points in the 10×10 grid for the partitioning of the joint parameter probability space. Notice again that when there is little data, the CDFs are wide with $P(\psi < 0.56)$ in the range $[0, 0.18]$. However, as data is collected the range narrows considerably such that $P(\psi < 0.56)$ in the range $[0, 0.09]$. Theoretically, as a very large amount of data is collected these CDFs will converge toward a step function such that $P(\psi < 0.56)$ is known with certainty for each assumed input distribution.

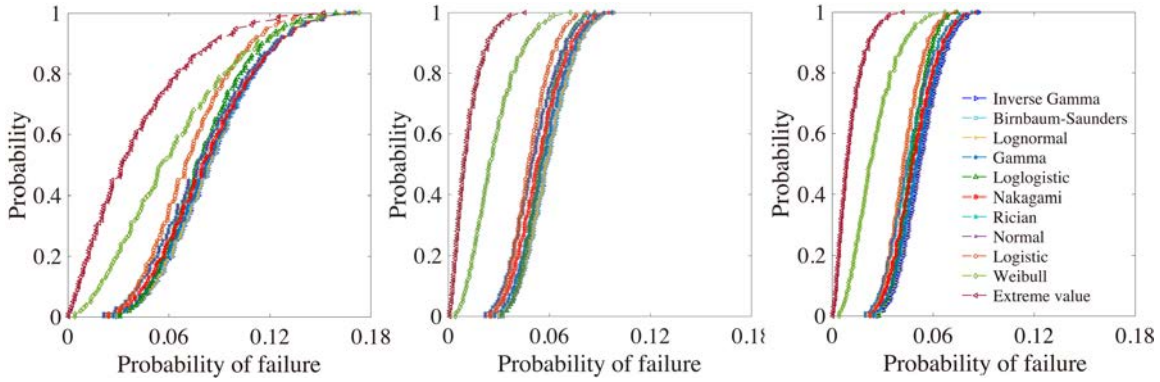

Figure 4. Empirical CDF of the probability of plate buckling failure $P(\psi < 0.56)$ with uncertain yield stress derived from propagation of uncertain probability models constructed using 25 (left), 50 (middle), and 100 (right) yield stress values..

6. Conclusion

Bayesian inference is used to quantify the uncertainty associated with a distribution derived from data. Yet, in the almost universal case of lack of complete data, the derived distribution cannot be precisely specified. We propose a efficient approach, based on Importance Sampling, for propagating uncertain probability distributions. The method identifies an optimal sampling distribution that is representative of the possible range of distributions and adaptively reweights the samples to simultaneously propagate the full range. An advantage of this approach is that the underlying probability models can be simply updated using Bayesian updating and we don't need additional simulations for propagation of the updated distributions. Instead, the existing simulations are reweighted and updated directly to update the proabability model.

Acknowledgements

The work presented herein has been supported by the Office of Naval Research under Award Number N00014-15-1-2754 with Dr. Paul Hess as program officer.

References

Beer, M., S. Ferson and V. Kreinovich. Imprecise probabilities in engineering analyse. *Mechanical Systems and Signal Processing*, 37(1-2):4–29, 2013.

Helton, J. C. and W. L. Oberkampf. Alternative representations of epistemic uncertainty. *Reliability Engineering and System Safety* , 85(1):1–10, 2004.

Der Kiureghian, A. and O. Ditlevsen. Aleatory or epistemic? Does it matter?. *Structural Safety* , 31(2):105–112, 2009.

Moore, R. E. and F. Bierbaum. *Methods and applications of interval analysis.* Vol. 2. Philadelphia: Siam, 1979.

Ferson, S. and J. G. Hajagos. Arithmetic with uncertain numbers: rigorous and (often) best possible answers. *Reliability Engineering and System Safety* , 85(1):135–152, 2004.

Ferson, S. and L. R. Ginzburg. Different methods are needed to propagate ignorance and variability. *Reliability Engineering and System Safety* , 54(2):133–144, 1996.

Nelsen, R. B., J. Hajagos, D. J. Berleant, J. Zhang, W. T. Tucker, L. R. Ginzburg and W. L. Oberkampf. *Dependence in probabilistic modeling, Dempster-Shafer theory, and probability bounds analysiss*. Sandia National Laboratories, 2004.

Ferson, S., V. Kreinovich, L. Ginzburg, D. S. Myers and K. Sentz. *Constructing probability boxes and Dempster-Shafer structures*. Vol. 835. Sandia National Laboratories, 2002.

Dubois, D. and H. Prade. *Interval-valued Fuzzy Sets, Possibility Theory and Imprecise Probability*. In EUSFLAT Conf, pages 314–319, 2005.

Stein, M., M. Beer and V. Kreinovich. Bayesian approach for inconsistent information. *Information sciences*, 245:96–111, 2013.

Walley P. Statistical reasoning with imprecise probabilities. London: Chapman and Hall, 1991.

Walley P. Towards a unified theory of imprecise probability. *International Journal of Approximate Reasoning*, 24(2):125–148, 2000.

Guyon, I., A. Saffari, G. Dror and G. Cawley. Model selection: Beyond the bayesian/frequentist divide. *The Journal of Machine Learning Research*,11:61–87, 2010.

Berger, J. O. and L. R. Pericchi. The intrinsic Bayes factor for model selection and prediction. *Journal of the American Statistical Association*, 91(433):109–122, 1996.

Akaike, H. A new look at the statistical model identification. *Automatic Control, IEEE Transactions on*, 19(6):716–723, 1974.

Schwarz, G. Estimating the dimension of a model. *The annals of statistics*, 6(2):461–464, 1978.

Csiszr, I. I-divergence geometry of probability distributions and minimization problems. *The Annals of Probability*, pages 146–158, 1975.

Beran, R. Minimum Hellinger distance estimates for parametric models. *The annals of statistics*, pages 445–463, 1977.

Lindsay, B. G. Efficiency versus robustness: the case for minimum Hellinger distance and related methods. *The annals of statistics*, pages 1081–1114, 1994.

Carlsen, C. Simplified collapse analysis of stiffened plates. *Norwegian Maritime Research*, 5(4):20–36, 1977.

Hess, P., D. Bruchman, I. Assakkaf and B. Ayyub. Uncertainties in material and geometric strength and load variables. *Naval Engineers Journal* , 114(2):139–166, 2002.

Soares, C. G. Uncertainty modelling in plate buckling. *Structural Safety* , 5(1):17–34, 1988.

Saltelli, A., F. Campolongo, J. Caliboni, D. Gatelli, F. Pennoni, M. Ratto, M. Saisana and S. Tarantola. Global Sensitivity Analysis: The Primer. John Wiley and Sons, Inc., 2008.

Approximation Concepts for Fuzzy Analysis in Structural Dynamics

Marcos Valdebenito[1)], Camilo Pérez[1)], Héctor Jensen[1)] and Michael Beer[2)]
[1)] *Department of Civil Engineering, Santa Maria University, Valparaiso, Chile*
{*marcos.valdebenito,hector.jensen*}*@usm.cl*
[2)] *Institute for Risk and Reliability, Leibniz Universität Hannover, Hannover, Germany / University of Liverpool, Liverpool, UK / Tongji University, Shanghai, China*
beer@irz.uni-hannover.de

Abstract: This contribution proposes a framework for performing fuzzy analysis for problems of structural dynamics. In order to avoid repeated structural analyses, a meta-model is used to represent the frequency response function (FRF) approximately. This meta-model comprises two different approximation levels. In the first level, approximate spectral properties (natural frequencies and mode shapes) are considered for calculating the FRF. In the second level, the mode shapes are approximated using a linear expansion with respect to the fuzzy variables of the problem, while the natural frequencies are also represented using a linear expansion but with respect to *intervening variables*. The fuzzy problem is solved using α-level optimization. A numerical example illustrates the accuracy and efficiency of the proposed scheme

Keywords: fuzzy analysis, structural dynamics, approximation concepts, intervening variables

1. Introduction

The so-called non traditional approaches for uncertainty quantification in engineering have gained considerable attention in the last years (Möller et al., 2000). In particular, interval analysis and fuzzy analysis offer the possibility of addressing problems where there is lack of knowledge or imprecision on the input parameters affecting the performance of a system. In this context, fuzzy analysis can be understood as a sequence of interval analyses. The value of applying fuzzy analysis is that it allows to identify sensitivities of the response of a structure with respect to the magnitude of imprecision of the input.
In spite of the evident advantages of fuzzy structural analysis, its application is not widespread. This is due to the fact that fuzzy analysis demands significant numerical efforts. In such scenario, this contribution presents an approach for performing fuzzy analysis of a particular class of problems, which is most efficient. The class of problems considered involve linear dynamical structural systems, which are analyzed using the frequency response function (FRF).
The efficient solution of problems of fuzzy structural dynamics has been the object of active research in the last few years. The approaches proposed for solving this problem can be broadly classified into two groups. The first group includes approaches that apply interval arithmetic. For example, in Modares et al., 2006, the intervals associated with natural frequencies of a structure comprising

interval parameters are calculated exactly using only two structural analyses by taking advantage of a formulation based on the Rayleigh quotient. Dessombz et al., 2001 apply an iterative algorithm for assessing the intervals associated with FRF functions; the algorithm addresses dependency issues of interval arithmetic. Manson, 2005 applies complex affine analysis for estimating the fuzzy FRF. Sim et al., 2007 propose an approach for calculating the FRF by considering exact bounds for the natural frequencies plus a first order Taylor expansion of the mode shapes. Muscolino et al., 2014 consider a *rational series expansion* in order to produce an accurate approximation of the FRF as an explicit function of the fuzzy variables.

The second group of strategies for fuzzy dynamic analysis includes approaches that apply optimization techniques, which attempt to identify the extrema of the structural response. For example, in Adhikari et al., 2011, the application of high dimensional model representation has been investigated in order to generate an explicit approximation of the fuzzy responses of interest. In Beer and Liebscher, 2008, a general framework for design under fuzziness is presented, which combines cluster analysis, an appropriate optimization strategy and robustness assessment. Adhikari and Khodaparast, 2014 propose a framework for fuzzy analysis combining the so-called Polynomial Chaos Expansion (PCE) in combination with a mode-based reduction strategy. Massa et al., 2008 propose an approach for solving fuzzy structural dynamics problems where natural frequencies and mode shapes are approximated using Padé rational functions. In addition to the two groups of strategies for fuzzy dynamic analysis mentioned above, it is interesting to note that a hybrid approach has been proposed by De Munck et al., 2008, where modal interval analysis (Moens and Vandepitte, 2004) and a response surface are applied simultaneously for estimating the intervals associated with the FRF.

The approach proposed in this contribution belongs to the second group mentioned above, i.e. it is formulated within the context of the α-level optimization strategy (Möller et al., 2000). In order to identify the minimum and maximum values of the structural response (for a given membership value α), the optimization algorithm introduced in (Li and Au, 2010) is considered, which is based on Subset Simulation (Au and Beck, 2001). In addition, the structural response is calculated approximately using a meta-model which approximates the frequency response function (FRF) explicitly with respect to the fuzzy input variables. This meta-model comprises two different approximation levels. In the first level, approximate spectral properties (natural frequencies and mode shapes) are considered for calculating the FRF. In the second level, the mode shapes are approximated using a linear expansion with respect to the fuzzy variables of the problem, while the natural frequencies are also represented using a linear expansion but with respect to *intervening variables* (Schmit and Farshi, 1974). The application of the latter type of variables has already been shown to provide accurate approximations within the context of fuzzy analysis for static structures (Valdebenito et al., 2016).

2. Formulation of the Problem

2.1. Fuzzy Variables and Structural Model

Consider a linear elastic structure modeled using the FE method (Bathe, 1996). In order to characterize this structure, there are $x_i,\ i = 1, \ldots, N_p$ fuzzy variables associated with structural properties (e.g. Young's modulus, cross section area, etc.) and $y_j,\ j = 1, \ldots, N_l$ fuzzy parameters associated with loads acting over the structure; $\mu_{\tilde{x}_i}(x_i),\ i = 1, \ldots, N_p$ and $\mu_{\tilde{y}_j}(y_j),\ j = 1, \ldots, N_l$ represent the membership functions associated with these fuzzy variables. It is assumed that the membership functions are convex. In the following, the fuzzy variables associated with structural properties and loads are grouped in vectors $\boldsymbol{x} = \langle x_1, x_2, \ldots, x_{N_p} \rangle^T$ and $\boldsymbol{y} = \langle y_1, y_2, \ldots, y_{N_l} \rangle^T$, respectively.
The structural system under study is characterized considering a total of N_d degrees-of-freedom. Then, the equation of motion relating structural properties, loads, displacements, velocities and accelerations of the FE model of the structure is:

$$\boldsymbol{M}(\boldsymbol{x})\ddot{\boldsymbol{u}}(t, \boldsymbol{x}, \boldsymbol{y}) + \boldsymbol{C}(\boldsymbol{x})\dot{\boldsymbol{u}}(t, \boldsymbol{x}, \boldsymbol{y}) + \boldsymbol{K}(\boldsymbol{x})\boldsymbol{u}(t, \boldsymbol{x}, \boldsymbol{y}) = \boldsymbol{f}(t, \boldsymbol{y}) \tag{1}$$

where t represents time; $\boldsymbol{M}(\boldsymbol{x})$, $\boldsymbol{C}(\boldsymbol{x})$ and $\boldsymbol{K}(\boldsymbol{x})$ are the mass, damping and stiffness matrices (dimension $N_d \times N_d$), where it is assumed $\boldsymbol{C}(\boldsymbol{x})$ corresponds to a classical damping matrix; $\ddot{\boldsymbol{u}}(t, \boldsymbol{x}, \boldsymbol{y})$, $\dot{\boldsymbol{u}}(t, \boldsymbol{x}, \boldsymbol{y})$ and $\boldsymbol{u}(t, \boldsymbol{x}, \boldsymbol{y})$ are the acceleration, velocity and displacement vector (dimension $N_d \times 1$); and $\boldsymbol{f}(t, \boldsymbol{y})$ is the load vector (dimension $N_d \times 1$). As both structural matrices and load vector depend on fuzzy variables, the structural response (e.g. displacement) also depends on these variables, i.e. the fuzziness in the structural properties and load propagates to the structural response. However, it should be noted that the membership function associated with the structural response cannot be calculated analytically (for almost all cases of practical interest).
Assume the load vector $\boldsymbol{f}(t, \boldsymbol{y})$ models a periodic loading and that it is of interest to determine the membership function associated with the steady-state displacement vector $\boldsymbol{u}_P(t, \boldsymbol{x}, \boldsymbol{y})$. Such problem can be solved most conveniently using the frequency response function (FRF), as described in the following. As the load vector is periodic, then it can be described as:

$$\boldsymbol{f}(t, \boldsymbol{y}) = \sum_{l=1}^{N_f} \boldsymbol{f}_l(\boldsymbol{y}) e^{i\omega_l(\boldsymbol{y})t} \tag{2}$$

where $\boldsymbol{f}_l(\boldsymbol{y})$ denotes the amplitude of the load vector with associated frequency $\omega_l(\boldsymbol{y})$; note both the amplitude and frequency may be dependent on the fuzzy vector $\boldsymbol{y}$. Then, the steady-state displacement vector is equal to:

$$\boldsymbol{u}_P(t, \boldsymbol{x}, \boldsymbol{y}) = \sum_{l=1}^{N_f} \boldsymbol{H}(\omega_l(\boldsymbol{y}), \boldsymbol{x}) \boldsymbol{f}_l(\boldsymbol{y}) e^{i\omega_l(\boldsymbol{y})t} \tag{3}$$

where $\boldsymbol{H}(\omega, \boldsymbol{x})$ is the so-called frequency response function (FRF) of dimension $N_d \times N_d$, which is defined as shown below (Craig and Kurdila, 2006).

$$\boldsymbol{H}(\omega, \boldsymbol{x}) = \sum_{r=1}^{N_m} \frac{\boldsymbol{\phi}_r(\boldsymbol{x}) \boldsymbol{\phi}_r^T(\boldsymbol{x})}{\omega_r(\boldsymbol{x})^2 - \omega^2 + i2\xi_r \omega \omega_r(\boldsymbol{x})} \tag{4}$$

In the above equation, N_m denotes the number of modes retained for dynamic analysis ($N_m \leq N_d$), ξ_r denotes the damping ratio associated with the r-th mode, while $\omega_r(\boldsymbol{x})$ and $\boldsymbol{\phi}_r(\boldsymbol{x})$ denote the r-th natural frequency and r-th mode shape, respectively. The natural frequencies and mode shapes are calculated by performing a dynamic structural analysis, which in this case involves solving the following eigenvalue/eigenvector problem.

$$\left(\boldsymbol{K}(\boldsymbol{x}) - \omega_r^2(\boldsymbol{x})\boldsymbol{M}(\boldsymbol{x})\right)\boldsymbol{\phi}_r(\boldsymbol{x}) = \boldsymbol{0},\ r = 1, \ldots, N_m \tag{5}$$

It is assumed that the mode shapes are orthonormal with respect to the mass matrix. The solution of the above problem can be numerically demanding, particularly for structures which comprise a large number of degrees-of-freedom.

2.2. α-Level Optimization

Recall the objective pursued is determining the membership function associated with the steady-state displacement vector. A possible means for determining such membership function is applying the so-called α-level optimization. In this manner, the membership function is represented in a discrete way. This implies that the values the displacement vector may assume are calculated at specific α-cuts, where α denotes the membership level under analysis (Beer, 2004); clearly, $0 < \alpha \leq 1$.

For applying α-level optimization, assume a specific cut α_k is selected and that the objective is determining the membership function of the n-th DOF of displacement vector $u_{P,n}$. This implies that the variables associated with structural parameters and loads are contained within the intervals $\underline{x}_{i,\alpha_k},\ i = 1, \ldots, N_p$ and $\underline{y}_{j,\alpha_k},\ j = 1, \ldots, N_l$, respectively. Note that under the assumption that the sets $\underline{x}_{i,\alpha_k}$ and $\underline{y}_{j,\alpha_k}$ are compact and convex, these sets are fully described by their minimum and maximum values (denoted with superscripts $(\cdot)^L$ and $(\cdot)^R$, respectively, see Figure 1). As there is a continuous mapping between the variables $(\boldsymbol{x}, \boldsymbol{y})$ and the output variable vector $\boldsymbol{u}_p$ (see Eq.(3)), the set $\underline{u}_{P,n,\alpha_k}$ is also fully described by its minimum and maximum value (denoted with superscripts $(\cdot)^L$ and $(\cdot)^R$, respectively, see Figure 1). These two extrema actually constitute two points of the membership function $\mu_{\tilde{u}_{P,n}}(u_{P,n})$ for the membership level α_k. Note that for determining the set $\underline{u}_{P,n,\alpha_k}$, it is necessary to solve two optimization problems (Moens and Vandepitte, 2005), i.e. minimization and maximization of the displacement given that the variables associated with structural properties and loading belong to the interval defined by their respective α-cuts. In order to visualize the α-level optimization strategy, Figure 1 contains a schematic representation where it is assumed that $N_p = N_l = 1$.

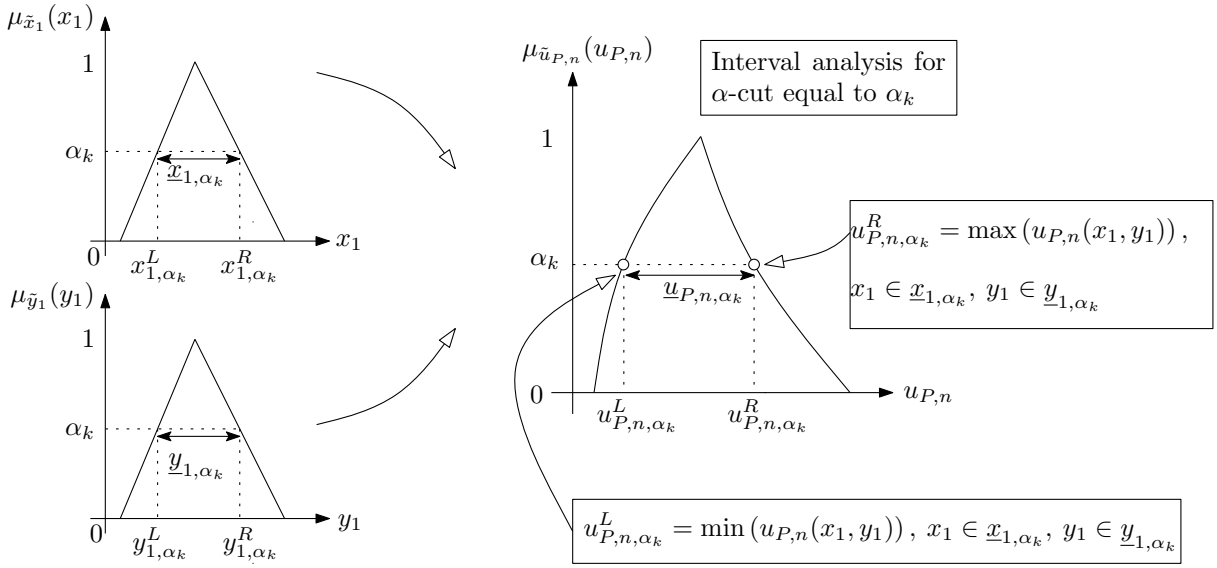

Figure 1. Schematic Representation of Fuzzy Analysis Applying α-level Optimization.

As noted from the above discussion, the application of α-level optimization demands solving two optimization problems (minimization and maximization) for each discrete α-cut being analyzed. For problems of practical interest, the numerical costs associated with this procedure can be considerable and even prohibitive, as it demands performing structural analyses for different values of the fuzzy variables. In order to reduce the aforementioned numerical costs, this contribution introduces a meta-model for the FRF function such that it can be evaluated with negligible effort. The details of the meta-model are discussed in the next section.

3. Approximate Representation of the Frequency Response Function

3.1. First Approximation Level

The most demanding step for evaluating the FRF function is calculating the spectral properties (i.e. natural frequencies and mode shapes). Therefore, in order to decrease the associated numerical costs, it is proposed to use a meta-model for evaluating the FRF that includes approximations of the spectral properties, as shown below.

$$\tilde{\boldsymbol{H}}(\omega,\boldsymbol{x}) = \sum_{r=1}^{N_m} \frac{\tilde{\boldsymbol{\phi}}_r(\boldsymbol{x})\tilde{\boldsymbol{\phi}}_r^T(\boldsymbol{x})}{\tilde{\omega}_r(\boldsymbol{x})^2 - \omega^2 + i2\xi_r\omega\tilde{\omega}_r(\boldsymbol{x})} \tag{6}$$

In the above equation, $\tilde{\boldsymbol{H}}$ denotes the approximate FRF, which is calculated using approximate spectral properties $\tilde{\omega}_r$ and $\tilde{\boldsymbol{\phi}}_r,\ r = 1,\ldots,N_m$.
The approximation proposed in Eq. (6) constitutes actually the first level of approximation of the proposed strategy. This corresponds to approximating an *intermediate quantity* (see, e.g. Jensen,

2000). This is an idea that has been used customarily in the field of structural optimization. Its basis is the following: as the FRF is a highly nonlinear function, attempting to approximate it explicitly in terms of the vector of structural parameters $\boldsymbol{x}$ would result quite challenging. In this context, *challenging* implies that probably higher order terms would be required for producing a sufficiently accurate approximation. In view of this issue, approximating an *intermediate quantity* is much more convenient, as this quantity may behave more linearly with respect to $\boldsymbol{x}$. In the context of the proposed meta-model, the intermediate quantity is actually the set of spectral properties.

3.2. Second Approximation Level

For the actual implementation of the meta-model proposed in Eq. (6), it is necessary to compute the approximate spectral properties. For approximating the mode shapes, it is proposed to apply a first order Taylor expansion, i.e.:

$$\tilde{\boldsymbol{\phi}}_r(\boldsymbol{x}) = \boldsymbol{\phi}_r\left(\boldsymbol{x}^0\right) + \sum_{i=1}^{N_p} \left.\frac{\partial \boldsymbol{\phi}_r}{\partial x_i}\right|_{\boldsymbol{x}=\boldsymbol{x}^0} \left(x_i - x_i^0\right) \tag{7}$$

where $\boldsymbol{x}^0$ is an expansion point.
For approximating the natural frequencies, a first order Taylor expansion is considered as well. However, instead of formulating the expansion directly with respect to $\boldsymbol{x}$, it is cast with respect to *intervening variables* $I_{r,i}(x_i),\ i = 1, \ldots, N_p$ (Prasad, 1983). These intervening variables are nonlinear functions with respect to x_i. The advantage of considering this strategy is that the quantity being approximated (in this case, the natural frequencies) behave more linearly with respect to $I_{r,i}(x_i)$ than with respect to x_i. Therefore, the approximation for the natural frequencies is the following.

$$\tilde{\omega}_r(\boldsymbol{x}) = \omega_r\left(\boldsymbol{x}^0\right) + \sum_{i=1}^{N_p} \left.\frac{\partial \omega_r}{\partial I_{r,i}}\right|_{\boldsymbol{x}=\boldsymbol{x}^0} \left(I_{r,i}\left(x_i\right) - I_{r,i}\left(x_i^0\right)\right) \tag{8}$$

For the case of fuzzy static structural analysis, it has been showed the so-called *exponential* intervening variable is most useful (Valdebenito et al., 2016). The exponential intervening variable possesses the form:

$$I_{r,i}\left(x_i\right) = x_i^{c_{r,i}} \tag{9}$$

where $c_{r,i}$ is a real constant. Thus, the approximation for the natural frequencies reduces to the following expression.

$$\tilde{\omega}_r(\boldsymbol{x}) = \omega_r\left(\boldsymbol{x}^0\right) + \sum_{i=1}^{N_p} \left.\frac{\partial \omega_r}{\partial x_i}\right|_{\boldsymbol{x}=\boldsymbol{x}^0} \frac{\left(x_i^0\right)^{1-c_{r,i}}}{c_{r,i}} \left(\left(x_i\right)^{c_{r,i}} - \left(x_i^0\right)^{c_{r,i}}\right) \tag{10}$$

In order to select the value of the constant $c_{r,i}$, the following criterion is proposed: the second-order derivatives of the exact natural frequency ω_r and of the approximate frequency $\tilde{\omega}_r$ should be equal at the expansion point. In mathematical terms, this criterion reads as follows.

$$\left.\frac{\partial^2 \omega_r}{\partial x_i^2}\right|_{\boldsymbol{x}=\boldsymbol{x}^0} = \left.\frac{\partial^2 \tilde{\omega}_r}{\partial x_i^2}\right|_{\boldsymbol{x}=\boldsymbol{x}^0},\ i = 1, \ldots, N_p \tag{11}$$

It can be shown that this criterion leads to the following expression for determining $c_{r,i}$, $i = 1, \ldots, N_p$.

$$c_{r,i} = 1 + x_i^0 \frac{\left.\frac{\partial^2 \omega_r}{\partial x_i^2}\right|_{\boldsymbol{x}=\boldsymbol{x}^0}}{\left.\frac{\partial \omega_r}{\partial x_i}\right|_{\boldsymbol{x}=\boldsymbol{x}^0}}, \; i = 1, \ldots, N_p \tag{12}$$

As the above equation may render values of $c_{r,i}$ which are too high in case the first derivative of the natural frequency is close to zero, it is suggested to limit the values $c_{r,i}$ may adopt within the range $[-3, 3]$.

3.3. Sensitivity of Natural Frequencies and Mode Shapes

The practical implementation of the approximations described in Section 3.2 demands evaluating the sensitivity of the spectral properties with respect to $\boldsymbol{x}$. The latter is a problem which is the subject of active research, see e.g. Lin and Lim, 1993. In particular, in this contribution, the approach proposed by Nelson, 1976 is implemented. A salient feature of this approach is that for calculating the sensitivity of the r-th natural frequency and mode shape, it requires only the information related with that frequency and mode shape. This is most convenient from a numerical viewpoint, as for large structural systems, usually $N_m \ll N_d$.

For presenting Nelson's method, consider Eq. (5). After differentiating this equation with respect to x_i and pre-multiplication by $\boldsymbol{\phi}_r^T(\boldsymbol{x})$, it is possible to determine the following explicit expression for the sensitivity of the natural frequency.

$$\frac{\partial \omega_r(\boldsymbol{x})}{\partial x_i} = \frac{1}{2\omega_r(\boldsymbol{x})} \boldsymbol{\phi}_r^T(\boldsymbol{x}) \left(\frac{\partial \boldsymbol{K}(\boldsymbol{x})}{\partial x_i} - \omega_r^2(\boldsymbol{x}) \frac{\partial \boldsymbol{M}(\boldsymbol{x})}{\partial x_i} \right) \boldsymbol{\phi}_r(\boldsymbol{x}) \tag{13}$$

In order to determine the sensitivity of the mode shape, consider again consider Eq. (5). After differentiating this equation with respect to x_i and arranging terms, it is possible to find the following expression.

$$\left(\boldsymbol{K}(\boldsymbol{x}) - \omega_r^2(\boldsymbol{x})\boldsymbol{M}(\boldsymbol{x})\right) \frac{\partial \boldsymbol{\phi}_r(\boldsymbol{x})}{\partial x_i} = -\left(\frac{\partial \boldsymbol{K}(\boldsymbol{x})}{\partial x_i} - \omega_r^2(\boldsymbol{x}) \frac{\partial \boldsymbol{M}(\boldsymbol{x})}{\partial x_i} \right) \boldsymbol{\phi}_r(\boldsymbol{x}) + 2\omega_r(\boldsymbol{x}) \frac{\partial \omega_r(\boldsymbol{x})}{\partial x_i} \boldsymbol{M}(\boldsymbol{x}) \boldsymbol{\phi}_r(\boldsymbol{x}) \tag{14}$$

For the above equation, assume that matrix $\left(\boldsymbol{K}(\boldsymbol{x}) - \omega_r^2(\boldsymbol{x})\boldsymbol{M}(\boldsymbol{x})\right)$ is denoted as $\boldsymbol{G}_r$ and that all terms of the right hand side are grouped in a vector $\boldsymbol{g}_{r,i}$. Then, the equation can be rewritten as follows.

$$\boldsymbol{G}_r \frac{\partial \boldsymbol{\phi}_r(\boldsymbol{x})}{\partial x_i} = \boldsymbol{g}_{r,i} \tag{15}$$

Note that $\boldsymbol{G}_r$ possesses rank $N_d - 1$ and nullspace $\boldsymbol{\phi}(\boldsymbol{x})$. Therefore, the sought sensitivity of the mode shape can be expressed as:

$$\frac{\partial \boldsymbol{\phi}_r(\boldsymbol{x})}{\partial x_i} = \boldsymbol{h}_{r,i} + \gamma_{r,i} \boldsymbol{\phi}_r(\boldsymbol{x}) \tag{16}$$

where $\boldsymbol{h}_{r,i}$ is any vector which fulfills $\boldsymbol{G}_r \boldsymbol{h}_{r,i} = \boldsymbol{g}_{r,i}$ and $\gamma_{r,i}$ is any real constant. In order to determine $\boldsymbol{h}_{r,i}$ and $\gamma_{r,i}$, the following procedure is proposed by Nelson, 1976.

1. $\boldsymbol{h}_{r,i}$ is determined by setting one of its component equal to some arbitrary value (e.g. equal to 1) and the other components are determined by solving the $N_d - 1$ equations associated with $\boldsymbol{G}_r \boldsymbol{h}_{r,i} = \boldsymbol{g}_{r,i}$.

2. $\gamma_{r,i}$ is determined by differentiating with respect to x_i the equation that ensures orthonormality of the mode shapes with respect to the mass matrix. This criterion yields the following expression for $\gamma_{r,i}$.

$$\gamma_{r,i} = -\boldsymbol{\phi}_r^T(\boldsymbol{x})\boldsymbol{M}(\boldsymbol{x})\boldsymbol{h}_{r,i} - \frac{1}{2}\boldsymbol{\phi}_r^T(\boldsymbol{x})\frac{\partial \boldsymbol{M}(\boldsymbol{x})}{\partial x_i}\boldsymbol{\phi}_r(\boldsymbol{x}) \tag{17}$$

It should be noted that the procedure for determining the sensitivity of the spectral properties proposed by Nelson, 1976 is valid whenever the natural frequencies are distinct. In case one or more natural frequencies possess multiplicity larger than one, it is possible to extend Nelson's method, as discussed by Dailey, 1989. The way this extension operates is as follows: the sensitivities associated with natural frequencies with multiplicity larger than 1 are calculated using eqs. (13) and (15), but in a matrix form, i.e. instead of calculating one sensitivity, m sensitivities are calculated simultaneously, where m is the multiplicity of the repeated natural frequency. It should be noted that the extension of Nelson's method proposed by Dailey, 1989 produces the second order derivatives of the natural frequencies as a byproduct. These second order derivatives are used to calculate the constants $c_{r,i}$ associated with the intervening variables (see Eq. (12)).
The interested readership is referred to Nelson, 1976 and Dailey, 1989 for details on the procedure for calculating the sensitivity of the spectral properties.

4. Subset Simulation for Optimization

The practical implementation of the α-level optimization approach demands applying an appropriate optimization algorithm for determining the extrema of the displacement function at each α-cut. The solution of this optimization problem is most challenging, as it may present local optima. In view of this challenge, this contribution applies Subset Simulation for optimization (Li and Au, 2010). This is a gradient free optimization algorithm that applies stochastic search for identifying the optimal solution.
Subset Simulation for optimization is applied following 5 steps. These steps are described briefly in the following, assuming it is applied for solving a maximization problem. For a detailed description, the reader is referred to Li and Au, 2010.

1. Introduce an *instrumental* probability density function (pdf) associated with the variables of the problem (in this case, the vectors $\boldsymbol{x}$ and $\boldsymbol{y}$). It is suggested that this instrumental pdf is set as a truncated Gaussian distribution.

2. Generate N samples of the variables $(\boldsymbol{x}, \boldsymbol{y})$ and evaluate for each of these samples the displacement of the structural system applying the meta-model for the FRF.

3. Select the pN samples of $(\boldsymbol{x}, \boldsymbol{y})$ which possess the largest associated displacement value. Note $0 < p < 1$. The selected samples are termed as *seed* samples.

4. Using the *seed* samples from the previous step and the modified Metropolis algorithm (see Au and Beck, 2001), generate $(1-p)N$ additional samples of $(\boldsymbol{x}, \boldsymbol{y})$ whose associated displacement value is equal or larger than any of the values selected in the previous step.

5. Check whether or not the algorithm has converged to the optimum solution. This is performed by assessing the standard deviation of the N samples of $(\boldsymbol{x}, \boldsymbol{y})$. In case convergence has been achieved, select the sample with largest value of the displacement as the optimal solution. Otherwise, return to step 3.

Figure 2 illustrates schematically the application of Subset Simulation for optimization. For simplicity, it is considered that $N_p = N_l = 1$. As noted from the Figure, first $N = 10$ samples of (x_1, y_1) are generated, which are marked with white circles. From these samples, the 2 samples with largest values of displacement are selected as seeds ($p = 0.2$). Then, using these 2 samples, 8 additional samples are generated by means of the Metropolis algorithm (gray circles).

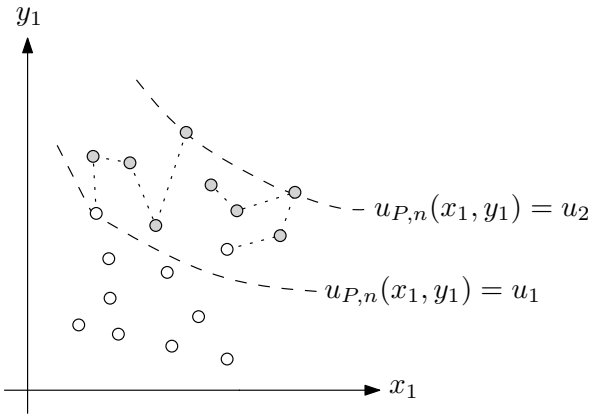

Figure 2. Schematic Representation of Subset Simulation for Optimization.

5. Example

In order to illustrate the application of the proposed strategy for fuzzy structural dynamic analysis, the following example is analyzed, which is taken from Beer and Liebscher, 2008. It consists of a steel beam which possesses distributed mass m and also a concentrated mass M, which is located at a distance l from the left support. The beam is subjected to an harmonic load $f(t, \boldsymbol{y})$, as illustrated in Figure 3. The objective of the example is determining the membership function associated with the maximum amplitude of the steady-state vertical displacement of the beam at the point where the load is applied.

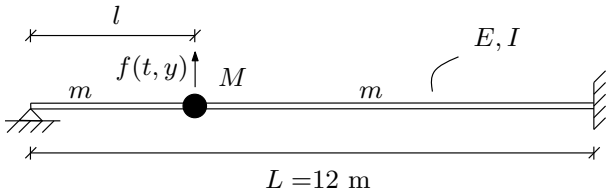

Figure 3. Steel beam subject to point load.

The fuzzy variables associated with the structural parameters of the problem are the position of the concentrated mass $l = x_1$ and the total mass $M_T = x_2$. Note the total mass is the summation of the distributed mass and the concentrated mass, which are defined as $m = M_T/3$ and $M = 2M_T/3$. The membership functions associated with x_1 and x_2 are shown in Figure 4.
The load is described as the superposition of two harmonic signals, i.e.:

$$f(t, \boldsymbol{y}) = y_1 \cos(y_2 \omega_1 t) + y_1 \cos(y_2 \omega_2 t) \tag{18}$$

where the frequencies are defined as $\omega_1 = 44$ [rad/s] and $\omega_2 = 66$ [rad/s]; and where y_1 and y_2 are fuzzy variables modeling the lack of knowledge on the amplitude and frequency of the loading, respectively. Their membership functions are defined in Figure 4.

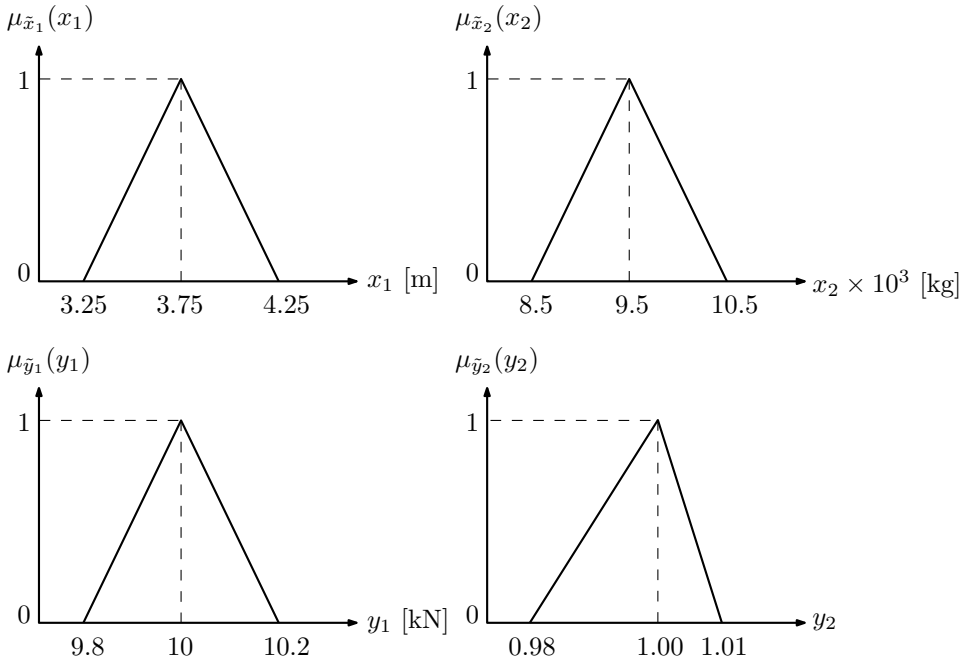

Figure 4. Membership functions of fuzzy variables.

The Young's modulus of the beam is $E = 210$ [GPa] and its second moment of area is $I = 1.5 \times 10^{-3}$ [m^4]. It is assumed that damping is negligible. In order to solve the problem, the beam model is discretized using 12 2D beam elements, which comprise a total of $N_d = 23$ degrees-of-freedom.

Figure 5 shows the results obtained for the problem in terms of the membership function of the maximum amplitude of the steady-state vertical displacement of the beam at the point where the load is applied. The membership function is calculated using the α-level optimization strategy for a total of 11 α-cuts. Subset Simulation for optimization was used to determine the minimum and maximum values of the displacement for each α-cut. Three different strategies were considered for calculating the steady-state displacement.

1. In order to obtain reference results, the displacement was calculated exactly, i.e. a structural analysis was carried out for each different value of the structural parameter vector $\boldsymbol{x}$. The obtained membership function is denoted as DO in Figure 5.

2. The proposed approach is used to calculated the displacement. This is denoted as P in Figure5.

3. The displacement is approximated considering a first order Taylor expansion of the natural frequencies without considering intervening variables. This is denoted as T in Figure 5. The objective of including this approximation is examining the advantages of including intervening variables for approximating the natural frequencies.

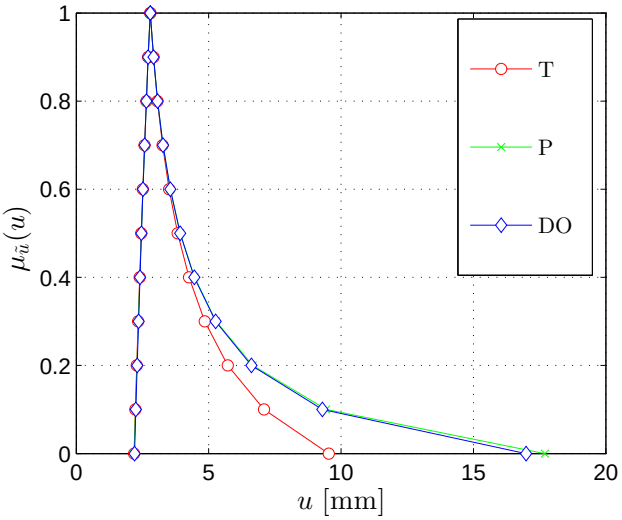

Figure 5. Membership function of amplitude of steady-state vertical displacement.

As noted from Figure 5, the proposed approach is capable of reproducing accurately the sought membership function. In this context, it should be noted that for applying the proposed approach, a single structural analysis plus a sensitivity analysis are required. This is remarkable, as it is possible to approximate the displacement with high quality and reduced numerical costs. In addition, it is seen from the Figure that the approximation T fails in approximating the displacement accurately. This result highlights the benefit of including intervening variables for approximating the natural frequencies.

6. Conclusions

This contribution has presented an approach for performing fuzzy structural analysis of linear dynamical systems. The key issue of the proposed approach consists in introducing a meta-model of the FRF which considers two different approximation levels. The results obtained in this contribution suggest the proposed approach can produce accurate results with a reduced number of structural analyses.
Although the results presented are most promising, further research efforts are required in order to determine the precise range of application of the proposed approach.

Acknowledgements

This research is partially supported by CONICYT (National Commission for Scientific and Technological Research) under grant number 1150009. This support is gratefully acknowledged by the authors.

References

Adhikari, S., R. Chowdhury, and M. Friswell. 'High dimensional model representation method for fuzzy structural dynamics'. *Journal of Sound and Vibration*, 330(7):1516–1529, 2011.

Adhikari, S. and H. Khodaparast. 'A spectral approach for fuzzy uncertainty propagation in finite element analysis'. *Fuzzy Sets and Systems*, 243:1–24. Theme: Fuzzy Intervals and Applications, 2014.

Au, S. and J. Beck. 'Estimation of Small Failure Probabilities in High Dimensions by Subset Simulation'. *Probabilistic Engineering Mechanics*, 16(4):263–277, 2001.

Bathe, K. *Finite Element Procedures.* New Jersey: Prentice Hall, 1996.

Beer, M. 'Uncertain structural design based on nonlinear fuzzy analysis'. *Journal of Applied Mathematics and Mechanics (ZAMM)*, 84(10-11):740–753, 2004.

Beer, M. and M. Liebscher. 'Designing robust structures – A nonlinear simulation based approach'. *Computers & Structures*, 86(10):1102–1122, 2008.

Craig, R. and A. Kurdila. *Fundamentals of Structural Dynamics.* Hoboken, New Jersey: Wiley, 2nd edition, 2006.

Dailey, R. 'Eigenvector derivatives with repeated eigenvalues'. *AIAA Journal*, 27(4):486–491, 1989.

De Munck, M., D. Moens, W. Desmet, and D. Vandepitte. 'A response surface based optimisation algorithm for the calculation of fuzzy envelope FRFs of models with uncertain properties'. *Computers & Structures*, 86(10):1080–1092, 2008.

Dessombz, O., F. Thouverez, J.-P. Laîné, and L. Jézéquel. 'Analysis of Mechanical Systems Using Interval Computations Applied to Finite Element Methods'. *Journal of Sound and Vibration*, 239(5):949–968, 2001.

Jensen, H. 'On the structural synthesis of uncertain systems subjected to environmental loads'. *Structural and Multidisciplinary Optimization,* 20(1):37–48, 2000.

Li, H. and S. Au. 'Design optimization using Subset Simulation algorithm'. *Structural Safety*, 32(6):384–392, 2010.

Lin, R. and M. Lim. 'Methods for Calculating Derivatives of Eigenvalues and Eigenvectors'. In: *11th International Modal Analysis Conference (IMAC XI)*, pages 1554–1558, 1993.

Manson, G. 'Calculating frequency response functions for uncertain systems using complex affine analysis'. *Journal of Sound and Vibration*, 288(3):487–521. Uncertainty in structural dynamicsUncertainty in structural dynamics, 2005.

Massa, F., K. Ruffin, T. Tison, and B. Lallemand. 'A complete method for efficient fuzzy modal analysis'. *Journal of Sound and Vibration*, 309(1-2):63–85, 2008.

Modares, M., R. Mullen, and R. Muhanna. 'Natural Frequencies of a Structure with Bounded Uncertainty'. *Journal of Engineering Mechanics*, 132(12):1363–1371, 2006.

Moens, D. and D. Vandepitte. 'An interval finite element approach for the calculation of envelope frequency response functions'. *International Journal for Numerical Methods in Engineering*, 61(14):2480–2507, 2004.

Moens, D. and D. Vandepitte. 'A survey of non-probabilistic uncertainty treatment in finite element analysis'. *Computer Methods in Applied Mechanics and Engineering*, 194(12-16):1527–1555, 2005.

Möller, B., W. Graf, and M. Beer. 'Fuzzy structural analysis using α-level optimization'. *Computational Mechanics*, 26(6):547–565, 2000.

Muscolino, G., R. Santoro, and A. Sofi. 'Explicit frequency response functions of discretized structures with uncertain parameters'. *Computers & Structures*, 133(0):64–78, 2014.

Nelson, R. 'Simplified calculation of eigenvector derivatives'. *AIAA Journal*, 14(9):1201–1205, 1976.

Prasad, B. 'Explicit constraint approximation forms in structural optimization. Part 1: Analyses and projections'. *Computer Methods in Applied Mechanics and Engineering*, 40(1):1–26, 1983.

Schmit, L. and B. Farshi. 'Some Approximation Concepts for Structural Synthesis'. *AIAA Journal*, 12(5):692–699, 1974.

Sim, J., Z. Qiu, and X. Wang. 'Modal analysis of structures with uncertain-but-bounded parameters via interval analysis'. *Journal of Sound and Vibration*, 303(12):29–45, 2007.

Valdebenito, M., C. Pérez, H. Jensen, and M. Beer. 'Approximate Fuzzy Analysis of Linear Structural Systems Applying Intervening Variables'. *Computers & Structures*, (162):116–129, 2016.

Structural Dynamic Response under Uncertainty - An Interval Finite Element Approach

Naijia Xiao[1)], Francesco Fedele[2)] and Rafi Muhanna[1)]
[1)] *School of Civil and Environmental Engineering, Georgia Institute of Technology, Atlanta, GA 30332, USA, {naijia.xiao, rafi.muhanna}@gatech.edu*
[2)] *School of Civil and Environmental Engineering and School of Electrical and Computer Engineering, Georgia Institute of Technology, Atlanta, GA 30332, USA, fedele@gatech.edu*

Abstract: An analysis of the structural dynamic response under uncertainty is presented. Uncertainties in load and material are modeled as intervals exploiting the interval finite element method (IFEM). To reduce overestimation and increase the computational efficiency of the solution, we do not solve the dynamic problem by an explicit step-by-step time integration scheme. Instead, our approach solves for the structural variables in the whole time domain simultaneously by an implicit scheme using discrete Fourier transform and its inverse (DFT and IDFT). Non-trivial initial conditions are handled by modifying the right-hand side of the governing equation. To further reduce overestimation, a new decomposition strategy is applied to the IFEM matrices, and both primary and derived quantities are solved simultaneously. The final solution is obtained using an iterative enclosure method, and in our numerical examples the exact solution is enclosed at minimal computational cost.

Keywords: interval finite element method, dynamic response, discrete Fourier transform, matrix decomposition, iterative enclosure method

1. Introduction

For any given physical system, uncertainties caused by measurement device or environmental conditions in the data acquisition process causes inconsistencies between the estimated and actual system behavior (Fernández-Martínez et al., 2013). Thus it is necessary to model and track the propagation of uncertainties in the system and to reliably evaluate the accuracy of the obtained solution. Conventional treatment of uncertainties involves the probability theory (Lutes and Sarkani, 2004), in which random variables are used to model the uncertainties encountered. In cases where enough measurement data is available and sufficient to reliably predict the nature of the uncertainties, probability approach is preferred. However, when there is not enough measurement data (Moens and Hanss, 2011; Zhang, 2005), as an alternative, one can turn to other available non-probabilistic approaches, such as Bayesian networks (Igusa et al., 2002; Soize, 2013; Unger and Könke, 2011), fuzzy sets (Adhikari and Khodaparast, 2014; Dehghan et al., 2006; Erdogan and Bakir, 2013; Klir and Wierman, 1999), evidence theory (Bai et al., 2013; Dempster, 1967; Jiang et al., 2013; Shafer, 1968), and intervals (Corliss et al., 2007; Do et al., 2014; Impollonia and Muscolino, 2011; Muhanna et al., 2007). Here the interval approach is adopted, in which uncertainties are modeled by interval

numbers characterized by their respective lower and upper bounds. More discussions on intervals and interval arithmetic can be found in Alefeld and Herzberger (1984), Kulisch and Miranker (1981), and Moore et al. (2009).

In this paper, an interval-based approach for the analysis of structural dynamic problems in the time domain is presented. In particular, the time-domain dynamics of elastic structures with uncertain geometric and material properties are studied. Uncertain parameter of the structure are modeled by intervals, and Interval Finite Element Method (IFEM) is implemented (Hu and Qiu, 2010; Qiu and Ni, 2010; To, 2012; Xia et al., 2010). The structure is governed by the following interval differential equation in the time domain,

$$\mathbf{K}\mathbf{u} + \mathbf{C}\dot{\mathbf{u}} + \mathbf{M}\ddot{\mathbf{u}} = \mathbf{f}, \tag{1}$$

where $\mathbf{K}$, $\mathbf{C}$, and $\mathbf{M}$ are respectively the stiffness, damping, and mass matrix of the structure, $\mathbf{u}$ is the unknown nodal displacement vector, $\dot{\mathbf{u}}$ and $\ddot{\mathbf{u}}$ are the corresponding nodal velocity and acceleration vector, $\mathbf{f}$ is the time-varying nodal equivalent load. From now on, *non-italic bold letters are used to denote interval variables.* The initial conditions are expressed in an interval form,

$$\mathbf{u}(0) = \mathbf{u}_0, \qquad \dot{\mathbf{u}}(0) = \mathbf{v}_0, \tag{2}$$

where $\mathbf{u}_0$ and $\mathbf{v}_0$ are the initial nodal displacement and velocity vector, respectively.

In practice, the differential Eq. (1) is solved at discrete time t_k, which are usually uniformly spaced in time. Conventional numerical integration approaches solve Eq. (1) recursively, viz. the solution at the current time t_k is obtained by using the solution in the previous time t_{k-1}. One notable example of the numerical integration method in structural analysis is the Newmark-β method (De Borst et al., 2012; Dokainish and Subbaraj, 1989; Paz, 1997). However, such recursive approach is not directly applicable for IFEM implementation, because overestimation due to interval dependency accumulates, and the yielded interval enclosure quickly become excessively wide and practically useless after a few iterations in time.

Alternatively, the transformation approach can be used (Bae et al., 2014; Yang et al., 2012). In the current method, the Discrete Fourier Transform (DFT) approach is adopted. A brief introduction on the DFT can be found in Santamarina and Fratta (2005). The governing Eq. (1) is transformed into the frequency domain using DFT, and the computed response is expressed back into the time domain using the corresponding inverse transform (Inverse Discrete Fourier Transform, IDFT). As a result, the solution vector at all time steps are obtained simultaneously.

In the following sections, first the deterministic solver based on the DFT approach is presented. Then the presented interval solver is introduced in detail. The governing Eq. (1) is reintroduced into a fixed-point form, and an iterative approach is adopted to obtain a sharp interval enclosure of the exact solution. Finally, the performance of the current method is compared with other available methods in a few numerical example.

2. Deterministic Dynamic Solver

In this section, the deterministic dynamic solver based on the DFT approach (Veletsos and Kumar, 1983; Veletsos and Ventura, 1985) is presented. The dynamic response of a linearly elastic structure is studied, which, after FEM discretization, is governed by

$$Ku + C\dot{u} + M\ddot{u} = f, \tag{3}$$

where K, C, and M are the stiffness, damping, and mass matrices of the structure, respectively, u is the nodal displacement vector, $\dot{u}$ and $\ddot{u}$ are the first and second derivatives of u with respect to the time (or, equivalently, nodal velocity and acceleration), and f is the nodal equivalent load. The initial condition is given by

$$u(0) = u_0, \qquad \dot{u}(0) = v_0. \tag{4}$$

The system is assumed discretized in time. The nodal equivalent load at discrete time t_k is given, and the goal is to solve for the nodal displacement vector u at t_k, as well as its derivatives $\dot{u}$ and $\ddot{u}$. That is, $f(t_k) = f_k,\ u(t_k) = u_k,\ \dot{u}(t_k) = \dot{u}_k,\ \ddot{u}(t_k) = \ddot{u}_k$. Usually, the time steps are uniformly spaced, viz. $t_k = k\Delta t$. The sampling interval Δt must be small enough to prevent any potential aliasing (Santamarina and Fratta, 2005). Let T be the total time length of the signal and N the total number, then $T = N\Delta t$.

In the discrete Fourier transform approach, DFT is applied to the discrete version of the governing Eq. (3) and transform it into

$$\left(-\omega_j^2 M + i\omega_j C + K\right) \mathcal{F}_t(u)_j = \mathcal{F}_t(f)_j, \tag{5}$$

where $i = \sqrt{-1}$ is the imaginary unit, $\omega_j = j\Delta\omega$ with $\Delta\omega = 2\pi/T$ being the fundamental frequency, $\mathcal{F}_t(u)_j$ and $\mathcal{F}_t(f)_j$ are the Fourier transform of the nodal displacement u_k and equivalent load f_k, respectively. Then the nodal displacement vector in the time-domain is obtained by applying the IDFT to $\mathcal{F}_t(u)_j$, viz.

$$u_n = \frac{1}{N}\sum_{j=0}^{N-1} \mathcal{F}_t(u)_j e^{-i(2\pi/N)jn} = \frac{1}{N}\sum_{j=0}^{N-1} G_j \mathcal{F}_t(f)_j e^{-i(2\pi/N)jn}, \tag{6}$$

where G_j is the inverse of the effective stiffness matrix in Eq. (5). To ensure that the final solution u_n is real, i.e., null imaginary part, G_j takes the following form,

$$G_j = \begin{cases} \left(-\omega_j^2 M + i\omega_j C + K\right)^{-1}, & 0 \le j < N/2; \\ \text{conjugate of } G_{N-j}, & N/2 \le j < N. \end{cases} \tag{7}$$

The above approach essentially solves for the stationary response of the structure caused by periodic loads with period T. The results are identical to the actual dynamic response with trivial initial conditions ($u_0 = v_0 = 0$) when enough zero-padding is attached. The length of the zero-padding, T_p, can be estimated from

$$e^{-\zeta\omega T_p} < \tau_{err}, \qquad \Rightarrow \qquad T_p > \frac{\ln \tau_{err}}{\zeta\omega}, \tag{8}$$

where τ_{err} is the error tolerance, ω is the lowest natural frequency of the structure, and ζ is the corresponding effective damping ratio. Let T_0 be the length of the original signal, then $T = T_0 + T_p$.

Non-trivial initial conditions can be modeled by modifying the equivalent load (Lee et al., 2005; Liu et al., 2015; Mansur et al., 2000). For initial displacement u_0, it is equivalent to add a constant load $f_{u0} = Ku_0$, which exist for the time interval $T_0 \leq t < T$. For initial velocity v_0, it is equivalent to add an impulse load $f_{v0} = Mv_0/\Delta t$, at time $t = 0$ for a duration of time Δt.

3. Interval Dynamic Solver

Assume the elastic structure under study contains uncertain parameters, which are modeled by intervals. The structural system is governed by Eqs. (1) and (2). For simplicity, the Rayleigh damping is adopted. The damping matrix

$$\mathbf{C} = \alpha_d \mathbf{M} + \beta_d \mathbf{K}, \tag{9}$$

where α_d and β_d are the Rayleigh damping coefficients. To reduce overestimation due to interval dependency, the interval matrix decomposition outlined before is adopted. Then DFT is used to transform the governing equation into a fixed-point form, which is further solved by a new variant of iterative enclosure method. Details on the current method are presented in the following subsections.

3.1. Interval matrix decomposition

The matrix decomposition strategy reduces overestimation due to interval dependency by avoiding multiple occurrences of the same interval variable in the formulation. The stiffness matrix $\mathbf{K}$, the mass matrix $\mathbf{M}$, and the stress-displacement matrix $\mathbf{S}$ are decomposed into

$$\mathbf{K} = A\mathrm{diag}(\Lambda\boldsymbol{\alpha})A^T, \qquad \mathbf{M} = A_m\mathrm{diag}(\Lambda_m\boldsymbol{\alpha}_m)A_m^T, \tag{10}$$

where A, Λ, A_m, and Λ_m are deterministic matrices, $\boldsymbol{\alpha}$ is the interval stiffness parameter vector that accounts for uncertainties in the stiffness matrix $\mathbf{K}$, and $\boldsymbol{\alpha}_m$ is the interval mass parameter vector that accounts for uncertainties in the mass matrix $\mathbf{M}$.

By combining the nodal equivalent load vector $\mathbf{f}_k$ at different time steps t_k, the interval load matrix $\mathbf{f}$ is obtained, whose k-th column is $\mathbf{f}_k$. When the structure is subject to external loading and the M-$\boldsymbol{\delta}$ method is adopted (Muhanna and Mullen, 2001), $\mathbf{f}$ is decomposed into

$$\mathbf{f} = F\boldsymbol{\delta}_t, \tag{11}$$

where F is a deterministic matrix, and $\boldsymbol{\delta}_t$ is the time-varying load uncertainty matrix. Usually it is necessary to distinguish the uncertainty in the magnitude of the load and the uncertainty in the time-history of the load. Thus $\boldsymbol{\delta}_t$ is further decomposed into an interval column vector $\boldsymbol{\delta}$ and an interval row vector $\mathbf{d}_t$, viz. $\boldsymbol{\delta}_t = \boldsymbol{\delta}\mathbf{d}_t$, where $\boldsymbol{\delta}$ models the uncertainties in the load magnitude and $\mathbf{d}_t$ models the uncertainties in the load time-history. Finally, the nodal equivalent load $\mathbf{f}$ is decomposed into

$$\mathbf{f} = (F\boldsymbol{\delta})\mathbf{d}_t. \tag{12}$$

Similarly, when the structure is subject to ground motion, $\mathbf{f}$ is decomposed into

$$\mathbf{f} = -\mathbf{M}\mathbf{a} = -\mathbf{M}q\boldsymbol{\delta}_t, \tag{13}$$

where $\boldsymbol{\delta}_t$ denotes the time-varying ground acceleration, $\mathbf{a}$ represents the resulting nodal acceleration of the structure, and q relates $\boldsymbol{\delta}_t$ to $\mathbf{a}$, viz. $\mathbf{a} = q\boldsymbol{\delta}_t$. By using the same decomposition for $\boldsymbol{\delta}_t$, and noting Eq. (10),

$$\mathbf{f} = -A_m \mathrm{diag}(\Lambda_m \boldsymbol{\alpha}_m) A_m^T q \boldsymbol{\delta} \mathbf{d}_t = A_m \left(\Lambda_m \boldsymbol{\alpha}_m \circ B_f \boldsymbol{\delta}\right) \mathbf{d}_t, \tag{14}$$

where $B_f = -A_m^T q$, and $a \circ b$ is the element-by-element Hadamard product of two vectors a and b.

When the initial conditions are non-trivial and modeled by intervals, as shown in Eq. (2), the corresponding nodal equivalent load $\mathbf{f}$ is given by

$$\mathbf{f} = \mathbf{K}\mathbf{u}_0 d_{u_0} + \mathbf{M}\mathbf{v}_0 d_{v_0}, \tag{15}$$

where d_{u_0} and d_{v_0} are two deterministic row vectors. d_{u_0} is zero for the time interval $0 \le t_k < T_0$ and unity for the time interval $T_0 \le t_k < T$, where T_0 and T are the length of the original and padded signal. d_{v_0} represents an impulse load which is $1/\Delta t$ at $t_k = 0$ and zero everywhere else. Noting the decomposition in Eq. (10),

$$\mathbf{f} = A\left(\Lambda\boldsymbol{\alpha} \circ A^T \mathbf{u}_0\right) d_{u_0} + A_m \left(\Lambda_m \boldsymbol{\alpha}_m \circ A_m^T \mathbf{v}_0\right) d_{v_0}, \tag{16}$$

which has a similar matrix form as Eq. (14). Thus the non-trivial initial conditions are treated in the same manner as ground accelerations.

3.2. Interval governing equations

To solve the interval differential Eq. (1), following the DFT approach outlined in Section 2, the equation is transformed into the frequency domain, viz.

$$\left(-\omega_j^2 \mathbf{M} + i\omega_j \mathbf{C} + \mathbf{K}\right) \mathcal{F}_t(\mathbf{u})_j = \mathcal{F}_t(\mathbf{f})_j, \tag{17}$$

where $\mathcal{F}_t(\mathbf{u})_j$ and $\mathcal{F}_t(\mathbf{f})_j$ are the Fourier transform of the nodal displacement $\mathbf{u}_k$ and equivalent load $\mathbf{f}_k$, respectively.

To include compatibility requirements and essential boundary conditions in the governing equation, and to ensure that the final solution has zero imaginary part, Eq. (17) is brought into the following equivalent form,

$$\begin{Bmatrix} \mathbf{K}_{\mathrm{eff},j} & C^T \\ C & 0 \end{Bmatrix} \begin{Bmatrix} \mathcal{F}_t(\mathbf{u})_j \\ \mathcal{F}_t(\boldsymbol{\lambda})_j \end{Bmatrix} = \begin{Bmatrix} \mathcal{F}_t(\mathbf{f})_j \\ 0 \end{Bmatrix}, \tag{18}$$

where $\mathbf{K}_{\mathrm{eff},j}$ is the effective stiffness matrix corresponding to the j-th frequency ω_j, namely

$$\mathbf{K}_{\mathrm{eff},j} = \begin{cases} -\omega_j^2 \mathbf{M} + i\omega_j \mathbf{C} + \mathbf{K}, & 0 \le j < N/2; \\ \text{conjugate of } \mathbf{K}_{\mathrm{eff},N-j}, & N/2 \le j < N, \end{cases} \tag{19}$$

C is the constraint matrix that imposes compatibility requirements and essential boundary conditions, and $\boldsymbol{\lambda}_k$ is the Lagrangian multiplier representing the internal forces and support reactions at t_k. By adopting the Rayleigh damping and the decomposition of $\mathbf{K}$ and $\mathbf{M}$ in Eq. (10), $\mathbf{K}_{\text{eff},j}$ can be decomposed into

$$\mathbf{K}_{\text{eff},j} = A_{\text{eff},j}\text{diag}\left(\Lambda_{\text{eff}}\boldsymbol{\alpha}_{\text{eff}}\right)B_{\text{eff}}, \tag{20}$$

where $A_{\text{eff},j}$ is a deterministic matrix depending on the frequency ω_j,

$$A_{\text{eff},j} = \begin{cases} \left\{(1+ib\omega_k)A \quad (-\omega_k^2 + ia\omega_k)A_m\right\}, & 0 \le j < N/2; \\ \text{conjugate of } A_{\text{eff},N-j}, & N/2 \le j < N, \end{cases} \tag{21}$$

and Λ_{eff}, B_{eff}, and $\boldsymbol{\alpha}_{\text{eff}}$ are time-invariant variables,

$$\Lambda_{\text{eff}} = \begin{Bmatrix} \Lambda & 0 \\ 0 & \Lambda_m \end{Bmatrix}, \quad B_{\text{eff}} = \begin{Bmatrix} A^T \\ A_m^T \end{Bmatrix}, \quad \boldsymbol{\alpha}_{\text{eff}} = \begin{Bmatrix} \boldsymbol{\alpha} \\ \boldsymbol{\alpha}_m \end{Bmatrix}. \tag{22}$$

Suppose the structure is subject to external loading, then

$$\mathcal{F}_t(\mathbf{f})_j = \mathcal{F}_t(F\boldsymbol{\delta}\mathbf{d}_t)_j = F\boldsymbol{\delta}\mathcal{F}_t(\mathbf{d}_t)_j. \tag{23}$$

Then Eq. (18) is equivalent to the following decomposed form

$$\begin{Bmatrix} K_{\text{eff},j0} & C^T \\ C & 0 \end{Bmatrix}\begin{Bmatrix} \mathcal{F}_t(\mathbf{u})_j \\ \mathcal{F}_t(\boldsymbol{\lambda})_j \end{Bmatrix} = \begin{Bmatrix} F \\ 0 \end{Bmatrix}\boldsymbol{\delta}\mathcal{F}_t(\mathbf{d}_t)_j - \begin{Bmatrix} A_{\text{eff},j} \\ 0 \end{Bmatrix}\text{diag}\Big(B_{\text{eff}}\mathcal{F}_t(\mathbf{u})_j\Big)\Lambda_{\text{eff}}\Delta\boldsymbol{\alpha}_{\text{eff}}, \tag{24}$$

by using the decomposition in Eqs. (20) and (23) and the following identities

$$\begin{aligned} A_{\text{eff},j}\text{diag}\left(\Lambda_{\text{eff}}\boldsymbol{\alpha}_{\text{eff}}\right)B_{\text{eff}}\mathcal{F}_t(\mathbf{u})_j &= A_{\text{eff},j}\Big(\Lambda_{\text{eff}}\boldsymbol{\alpha}_{\text{eff}} \circ B_{\text{eff}}\mathcal{F}_t(\mathbf{u})_j\Big) \\ &= A_{\text{eff},j}\text{diag}\Big(B_{\text{eff}}\mathcal{F}_t(\mathbf{u})_j\Big)\Lambda_{\text{eff}}\boldsymbol{\alpha}_{\text{eff}}, \end{aligned} \tag{25}$$

where $\Delta\boldsymbol{\alpha}_{\text{eff}}$ is the difference between $\boldsymbol{\alpha}_{\text{eff}}$ and the reference vector $\alpha_{\text{eff}0}$, viz. $\Delta\boldsymbol{\alpha}_{\text{eff}} = \boldsymbol{\alpha}_{\text{eff}} - \alpha_{\text{eff}0}$, and $K_{\text{eff},j0} = A_{\text{eff},j}\text{diag}(\Lambda_{\text{eff}}\alpha_{\text{eff}0})B_{\text{eff}}$.

When the structure is subject to ground motion, according to Eq. (14),

$$\begin{aligned} \mathcal{F}_t(\mathbf{f})_j &= A_f\left(\Lambda_m\boldsymbol{\alpha}_m \circ B_f\boldsymbol{\delta}\right)\mathcal{F}_t(\mathbf{d}_t)_j \\ &= \left(A_f\left(\Lambda_m\alpha_{m0} \circ B_f\boldsymbol{\delta}\right) + A_f\left(\Lambda_m\Delta\boldsymbol{\alpha}_m \circ B_f\boldsymbol{\delta}\right)\right)\mathcal{F}_t(\mathbf{d}_t)_j \\ &= F_0\boldsymbol{\delta}\mathcal{F}_t(\mathbf{d}_t)_j + A_f\text{diag}\Big(B_f\boldsymbol{\delta}\mathcal{F}_t(\mathbf{d}_t)_j\Big)\Lambda_m\Delta\boldsymbol{\alpha}_m, \end{aligned} \tag{26}$$

where $\Delta\boldsymbol{\alpha}_m$ is the difference between $\boldsymbol{\alpha}_m$ and the reference vector α_{m0}, viz. $\Delta\boldsymbol{\alpha}_m = \boldsymbol{\alpha}_m - \alpha_{m0}$, and $F_0 = A_f\text{diag}(\Lambda_m\alpha_{m0})B_f$. Then the generalized equivalent load in Eq. (18) is decomposed into

$$\begin{Bmatrix} \mathcal{F}_t(\mathbf{f})_j \\ 0 \end{Bmatrix} = \begin{Bmatrix} F_0 \\ 0 \end{Bmatrix}\boldsymbol{\delta}\mathcal{F}_t(\mathbf{d}_t)_j + \begin{Bmatrix} A_f \\ 0 \end{Bmatrix}\text{diag}\Big(B_f\boldsymbol{\delta}\mathcal{F}_t(\mathbf{d}_t)_j\Big)\Lambda_m\Delta\boldsymbol{\alpha}_m, \tag{27}$$

Eq. (18) is equivalent to the following decomposed form

$$\begin{Bmatrix} K_{\text{eff},j0} & C^T \\ C & 0 \end{Bmatrix} \begin{Bmatrix} \mathcal{F}_t(\mathbf{u})_j \\ \mathcal{F}_t(\boldsymbol{\lambda})_j \end{Bmatrix} = \begin{Bmatrix} F_0 \\ 0 \end{Bmatrix} \boldsymbol{\delta} \mathcal{F}_t(\mathbf{d}_t)_j \\ - \begin{Bmatrix} A_{\text{eff}} & A_f \\ 0 & 0 \end{Bmatrix} \text{diag}\left(\begin{Bmatrix} B_{\text{eff}} \mathcal{F}_t(\mathbf{u})_j \\ -B_f \boldsymbol{\delta} \mathcal{F}_t(\mathbf{d}_t)_j \end{Bmatrix} \right) \begin{Bmatrix} \Lambda_{\text{eff}} & \\ 0 & \Lambda_m \end{Bmatrix} \Delta\boldsymbol{\alpha}_{\text{eff}}. \tag{28}$$

Due to the similarities between the decomposition of the equivalent load in Eqs. (14) and (16), the above formulation can be extended to cases when the initial conditions are non-trivial.

3.3. Iterative enclosure method

To solve the interval linear system Eqs. (24) and (28), they are recast into the following form

$$K_{g,j} \mathcal{F}_t(\mathbf{u}_g)_j = F_g \boldsymbol{\delta} \mathcal{F}_t(\mathbf{d}_t)_j - A_{g,j} \text{diag}\Big(\mathcal{F}_t(\mathbf{v}_g)_j \Big) \Lambda_g \Delta\boldsymbol{\alpha}_{\text{eff}}, \tag{29}$$

where $K_{g,j}$, F_g, $A_{g,j}$, Λ_g are given deterministic matrices, $\mathbf{u}_g$ is the unknown interval vector, $\boldsymbol{\delta}$, $\mathbf{d}_t$, and $\Delta\boldsymbol{\alpha}_{\text{eff}}$ are given interval vectors, and $\mathbf{v}_g$ linearly depend on $\mathbf{u}_g$, viz. $\mathbf{v}_g = \mathbf{v}_0 + B_g \mathbf{u}_g$. Here subscripts $_j$ denotes variables associated with the j-th frequency ω_j. Note that matrices $K_{g,j}$ and $A_{g,j}$ are functions of the frequency ω_j. In the most general case, $\mathbf{u}_g$ includes $\mathbf{u}$ and $\boldsymbol{\lambda}$, and the auxiliary variable $\mathbf{v}_g$ includes $B_{\text{eff}}\mathbf{u}$, $-B_f\boldsymbol{\delta}\mathbf{d}_t$, and $A_s^T\mathbf{u}$.

Now introduce $G_j = K_{g,j}^{-1}$. Multiplying both sides of Eq. (29) by G_j yields

$$\mathcal{F}_t(\mathbf{u}_g)_j = (G_j F_g) \boldsymbol{\delta} \mathcal{F}_t(\mathbf{d}_t)_j - (G_j A_{g,j}) \text{diag}\Big(\mathcal{F}_t(\mathbf{v}_g)_j \Big) \Lambda_g \Delta\boldsymbol{\alpha}_{\text{eff}}. \tag{30}$$

Then $\mathbf{u}_g$ is obtained by applying the IDFT to both side of (30),

$$\mathbf{u}_{g,k} = \Big(\mathcal{F}_t^{-1}(G_j F_g) * \mathbf{d}_t \Big)_k \boldsymbol{\delta} - \Big(\mathcal{F}_t^{-1}(G_j A_{g,j}) * \text{diag}(\mathbf{v}_g) \Big)_k \Lambda_g \Delta\boldsymbol{\alpha}_{\text{eff}}, \tag{31}$$

where $(a*b)_k$ denotes the convolution between two discrete signals a_k and b_k. Eq. (31) can be recast into the following summation form,

$$\mathbf{u}_{g,k} = \left(\sum_{l=0}^{N-1} \mathcal{F}_t^{-1}(G_j F_g)_{k-l} \mathbf{d}_{t,l} \right) \boldsymbol{\delta} - \left(\sum_{l=0}^{N-1} \mathcal{F}_t^{-1}(G_j A_{g,j})_{k-l} \text{diag}(\mathbf{v}_{g,l}) \right) \Lambda_g \Delta\boldsymbol{\alpha}_{\text{eff}}. \tag{32}$$

Then a fixed-point form for $\mathbf{v}_{g,k}$ is obtained as

$$\mathbf{v}_{g,k} = \mathbf{v}_{0,k} + B_g \Big(\mathcal{F}_t^{-1}(G_j F_g) * \mathbf{d}_t \Big)_k \boldsymbol{\delta} - B_g \Big(\mathcal{F}_t^{-1}(G_j A_{g,j}) * \text{diag}(\mathbf{v}_g) \Big)_k \Lambda_g \Delta\boldsymbol{\alpha}_{\text{eff}}. \tag{33}$$

A guaranteed outer enclosure for $\mathbf{v}_{g,k}$ is obtained by iteratively using Eq. (33), starting from the trivial initial guess $\mathbf{v}_{g,k}^1 = \mathbf{v}_{0,k} + \big(\mathcal{F}_t^{-1}(G_j F_g) * \mathbf{d}_t \big)_k \boldsymbol{\delta}$. The iteration stops when no improvement in $\mathbf{v}_{g,k}^j$ is observed for two consecutive iterations, and the converged solution is denoted as $\mathbf{v}_{g,k}^n$. Then the outer solution $\mathbf{u}_{g,k}^{out}$ is obtained by substituting $\mathbf{v}_{g,k}$ in Eq. (31) with the converged solution $\mathbf{v}_{g,k}^n$.

The convolution between a deterministic signal and an interval signal is computed multiple times, as shown in Eqs. (31) and (33). To increase the computational efficiency and reduce overestimation in the final solution, the FFT-based fast interval convolution algorithm, proposed by Liu and Kreinovich (2010), is adopted. During the iteration in Eq. (33), only the radius of $\mathbf{v}_g$ is updated. All other vectors and matrices do not change after the first iteration.

4. Numerical Examples

The current IFEM algorithm is implemented using the interval MATLAB toolbox INTLAB (Rump, 1999). Interval enclosures of the structural responses of the following sample problems are calculated: *i*) a four-story rigid frame and *ii*) a simply supported truss. The performance of the current method is compared against other available methods in the literature: *i*) the endpoint combination method (EC) and *ii*) the Monte Carlo (MC) simulation. The results shows that the current method is applicable to the transient analysis of structural dynamic problems with uncertain parameters. Guaranteed interval enclosures of the exact structural responses in the time domain are obtained with small overestimations. In addition, the computational time is negligible when compared with other competing methods.

4.1. Four-story rigid frame

The first example is a four-story frame shown in Figure 1. The floors of the frame are assumed to be rigid enough to model the structure as an equivalent spring-mass system (shown in the right-hand side of Figure 1). The mass $\mathbf{m}_j$ and the inter-story shear stiffness $\mathbf{k}_j$ of each floor ($j = 1, \ldots, 4$) are modeled by independent interval variables, and given in Table I.

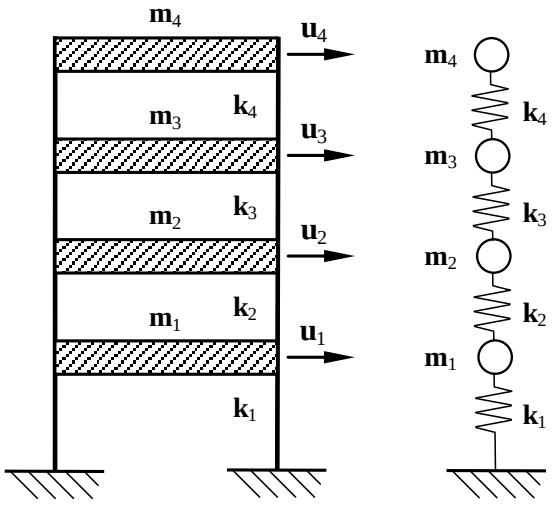

Figure 1. A four-story rigid frame and the equivalent spring-mass system.

Consider the structural response of the frame under a concentrated impact force acting on the top floor. The force has a duration of 4 s, and its variation during that time is deterministic, viz.

$$\mathbf{f}(t) = \begin{cases} \mathbf{P}\sin(\pi t/2), & 0 \le t \le 4 \text{ s}; \\ 0, & t > 4 \text{ s}, \end{cases} \tag{34}$$

where $\mathbf{P} = [0.99, 1.01]$ kN (2% uncertainty in the magnitude of the load). The damping matrix $\mathbf{C} = 0.5\mathbf{M} + 5 \times 10^{-3}\mathbf{K}$. The sampling rate is 100 Hz, so the sampling interval $\Delta t = 0.01$ s.

Figure 2 compares the lower and upper bounds of $\mathbf{u}_4$ for the first 10 s, obtained from the current method (IS, solid lines), Monte Carlo predictions (MC, dashed lines) from an ensemble of 10,000 simulations, the reference solution obtained from endpoint combination (EC, dash-dotted lines), and the deterministic solution (DS, dotted line). Note that IS always contains the reference solution EC, and MC is always contained by EC. In addition, the overestimation level of the current method

Table I. Interval mass and stiffness for the five-story rigid frame of Figure 1, including 1% uncertainties in mass, and 5% uncertainties in stiffness.

Floor	Mass (kg)			Stiffness (kN/m)		
	$\mathbf{m}_j$	mid $\mathbf{m}_j$	rad $\mathbf{m}_j$	$\mathbf{k}_j$	mid $\mathbf{k}_j$	rad $\mathbf{k}_j$
1	[5.416, 5.470]	5.443	0.027	[1.180, 1.240]	1.210	0.030
2	[5.416, 5.470]	5.443	0.027	[1.677, 1.763]	1.720	0.043
3	[5.416, 5.470]	5.443	0.027	[1.862, 1.958]	1.910	0.048
4	[5.416, 5.470]	5.443	0.027	[1.775, 1.865]	1.820	0.045

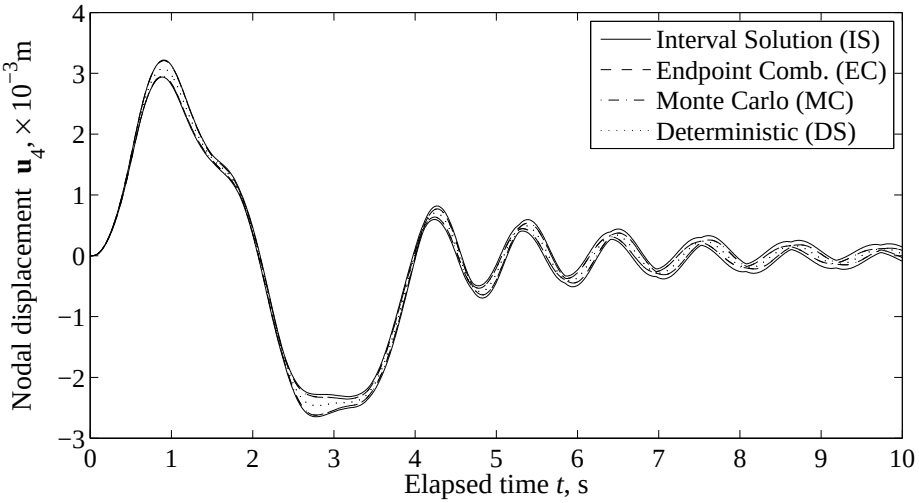

Figure 2. Lower and upper bounds of the nodal displacement $\mathbf{u}_4$ for the four-story frame of Figure 1 under a sinusoidal force: IS (solid lines) from the current method, EC (dashed lines), and MC (dash-dotted lines) from an ensemble of 10,000 simulations. Material uncertainty is 1% for mass, and 5% for stiffness. Load uncertainty is 2% for the magnitude.

slightly increases as the time increases. The MC solution is obtained using the DFT approach, which indistinguishable from the solution obtained from a recursive Newmark-β method.

Then the concentrated force $\mathbf{f}(t)$ is removed, and the structure is subject to non-trivial initial conditions. Figure 3 shows the nodal displacement $\mathbf{u}_4$ at the top floor for the first 10 s with non-trivial initial nodal displacement $\mathbf{u}_0$ (top) and nodal velocity $\mathbf{v}_0$ (bottom), respectively. Here 2%

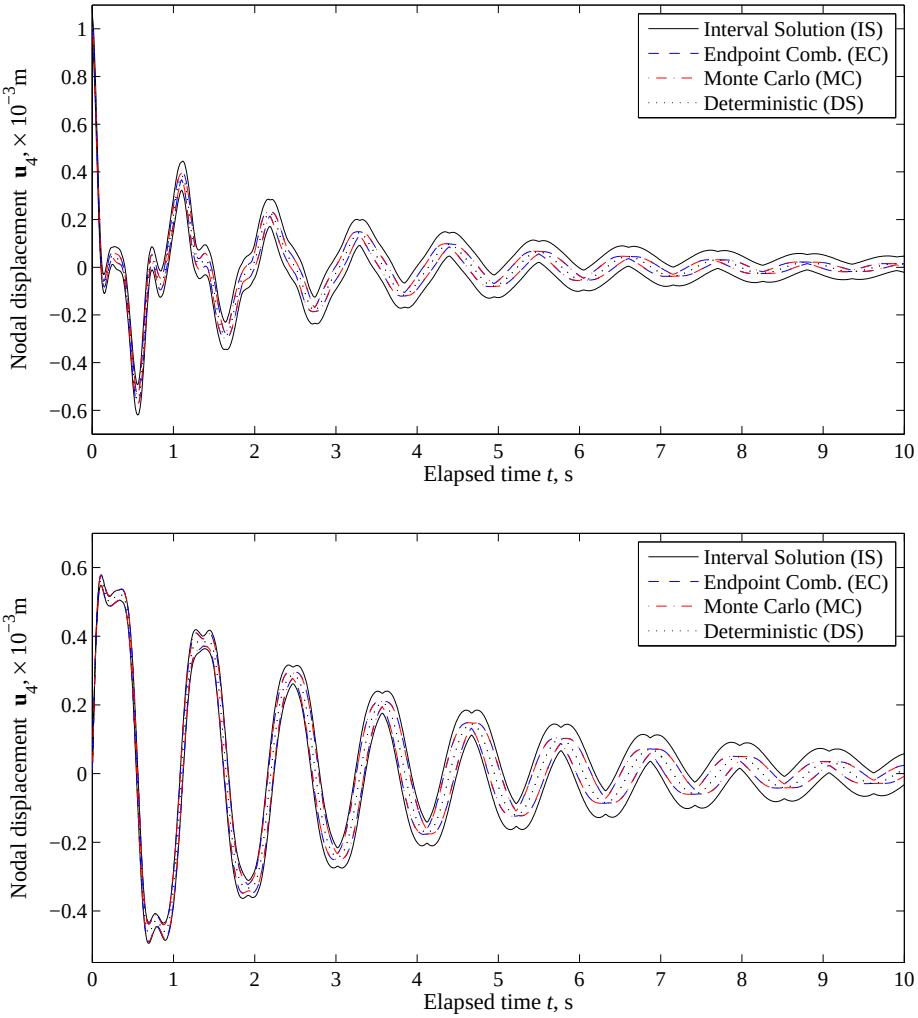

Figure 3. Lower and upper bounds of the nodal displacement $\mathbf{u}_4$ for the four-story frame of Figure 1 under non-trivial initial conditions: (top) non-trivial initial displacement $\mathbf{u}_0$, (bottom) non-trivial initial velocity $\mathbf{v}_0$. IS (black solid lines) from the current method, EC (blue dashed lines), and MC (red dash-dotted lines) from an ensemble of 10,000 simulations. Material uncertainty is 1% for mass, and 5% for stiffness. Uncertainty in the initial condition is 2% (see online version for colors).

uncertainty is considered for $\mathbf{u}_0$ and $\mathbf{v}_0$, viz.

$$\mathbf{u}_0 = \left\{ 0 \;\; 0 \;\; 0 \;\; 0 \;\; [0.99,\ 1.01] \right\}^T \times 10^{-3} \text{ m}; \tag{35}$$
$$\mathbf{v}_0 = \left\{ 0 \;\; 0 \;\; 0 \;\; 0 \;\; [0.99,\ 1.01] \right\}^T \times 10^{-2} \text{ m/s}.$$

Figure 3 shows that the high frequency components dissipate quickly. After about 3 s, the response of the structure is dominated by the lowest frequency vibration. Observe that the performance of the current method is the same as in the previous case. The obtained interval solution guarantees to enclose the reference solution (endpoint combination, EC), and the overestimation level increases slightly as the time increases. Thus non-trivial initial conditions are handled successfully.

4.2. Simply supported truss

The second example is a simply supported symmetric truss composed of 15 bars, as shown in Figure 4. The joints are labeled from 1 to 8, and the bars are labeled from 1 to 15. Time-varying concentrated load $\mathbf{P}$ acts at joint 5. Bars 1 to 3, 13 to 15 have the same cross section area $A = 1.0 \times 10^{-3}$ m^2, and all other bars, viz. bars 4 to 12, have smaller cross section area $A = 6.0 \times 10^{-4}$ m^2. All the bars are made of steel. They have the interval mass density $\boldsymbol{\rho}$ with midpoint value $\rho = 7.8 \times 10^3$ kg/m^3, and the interval Young's modulus $\mathbf{E}$ with midpoint value $E = 200$ GPa.

Fifteen bar elements are used to model the truss in Figure 4. Element mass density $\boldsymbol{\rho}$ and Young's modulus $\mathbf{E}$ are assumed independent, and they are modeled by 30 interval variables. The midpoint of the load $\mathbf{P}$ is a sinusoid with a frequency of 50 Hz and an amplitude of 200 kN, viz.

$$P = 200 \sin(100\pi t) \text{ kN}. \tag{36}$$

The damping matrix $\mathbf{C} = 20\mathbf{M} + 3 \times 10^{-5}\mathbf{K}$. The sampling rate is 10 kHz, so $\Delta t = 1 \times 10^{-4}$ s.

Then vertical displacement $\mathbf{v}_5$ at joint 5 is selected for comparison among the various methods mentioned previously. Consider 1% uncertainty for the magnitude and time-history of the load, as well as Young's modulus and mass density of each bar. Figure 5 plots the lower and upper

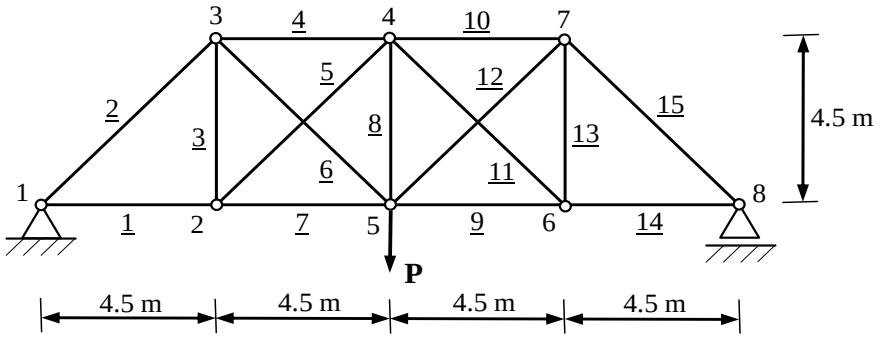

Figure 4. A simply supported symmetric truss subject to concentrated force.

bounds of $\mathbf{v}_5$ for the first 0.1 s obtained from the current method (IS, solid lines) and the Monte Carlo predictions (MC, dashed lines from the Newmark-β approach, and dash-dotted lines from the DFT approach) from an ensemble of 100,000 simulations. Observe that the current method obtains guaranteed enclosures of the MC prediction.

Figure 5 shows that the uncertainties in the structural responses increase significantly over time. This behavior is due to the fact that the load history uncertainties are modeled by independently varied intervals at different time steps. In the current example, this means 0.1 s $\times$ 10 kHz = 1,000 independent interval variables. As a result, the overall uncertainty level is much higher than 1%. This also explains the growing differences between IS and MC predictions over time. Figure 6 considers (top) 2% uncertainties in load time-history and (bottom) 2% uncertainties in load magnitude, Young's modulus, and mass density. Observe that in the bottom subplot, the uncertainties now do not increase over time, and the difference between IS and MC is much smaller than to top subplot. So it is indeed the increased number of interval variables that caused the increased uncertainty and the difference between IS and MC.

5. Conclusion

An interval finite element formulation is presented for the time-domain dynamic analysis of elastic structures with uncertain geometric and material properties. By using the Discrete Fourier Transform (DFT) and the Inverse Discrete Fourier Transform (IDFT), the given equivalent load and the final obtained structural responses are both given in the time domain, but the matrix inversion process is performed in the frequency domain. Ground motion and non-trivial initial conditions

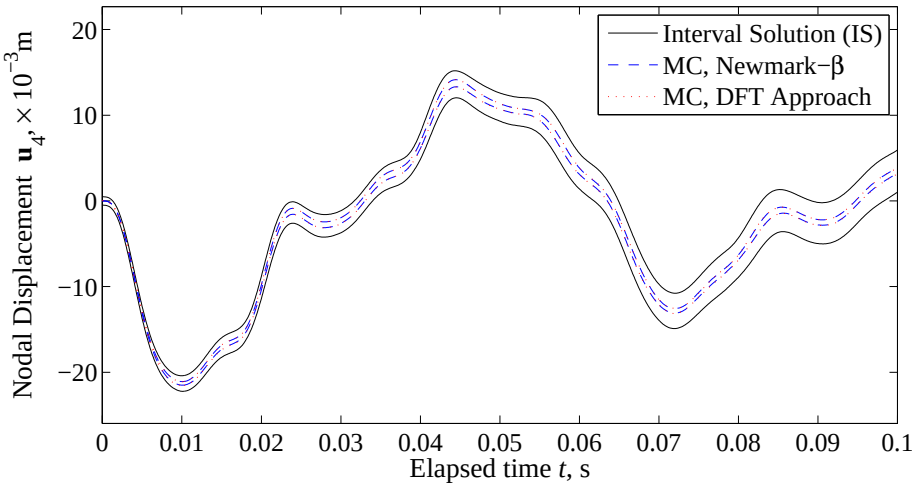

Figure 5. Lower and upper bounds of the nodal displacement $\mathbf{v}_5$ at joint 5 for the four-story frame of Figure 4 under external loads: IS (black solid lines) from the current method and MC predictions (blue dashed lines and red dotted lines) from an ensemble of 100,000 simulations. Parameter uncertainties are 1% for load magnitude, load history, Young's modulus, and mass density (see online version for colors).

are successfully handled via the introduction of the corresponding equivalent nodal forces. The resulting method is both efficient and widely applicable.

Uncertain parameters of the structure are modeled as intervals. The obtained interval enclosures guarantee to enclose the exact solution set with small overestimation, even for large uncertainty levels. Numerical examples show that the presented method gives guaranteed sharp bounds on the dynamic responses of the structure, even in cases when a large number of interval variables are present and other available methods give over-optimistic prediction on the lower and upper bounds.

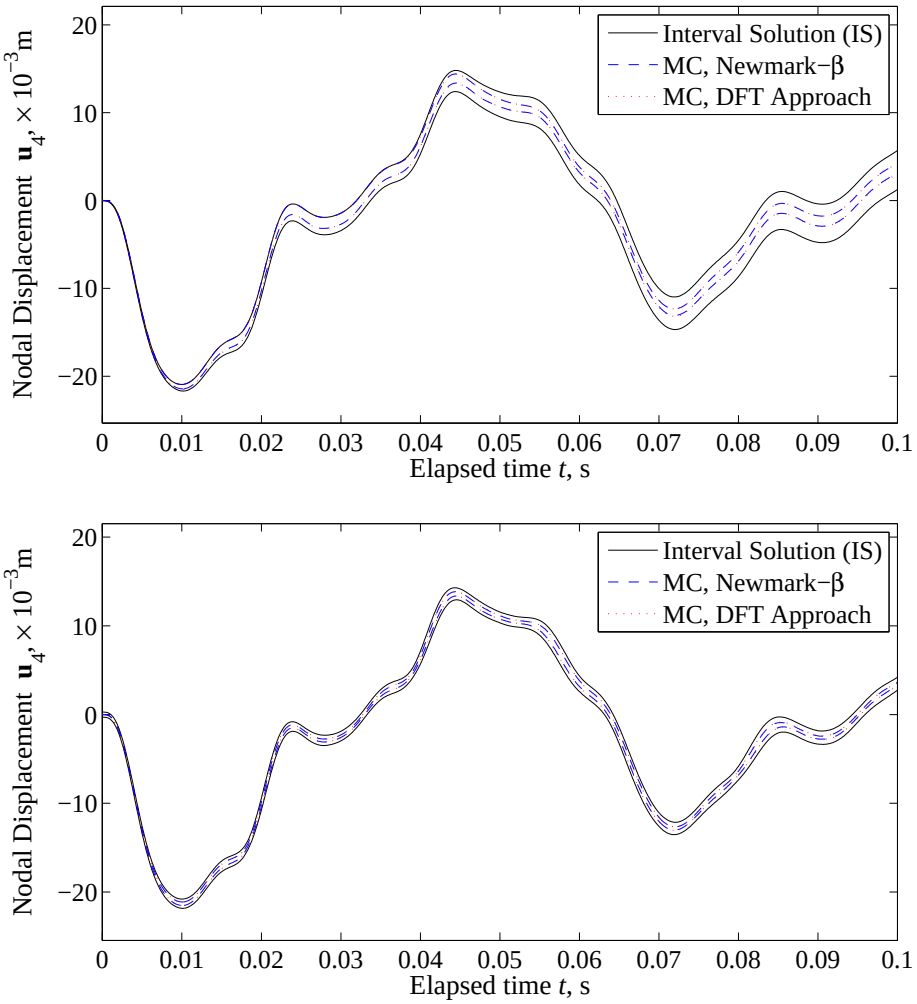

Figure 6. Lower and upper bounds of the nodal displacement $\mathbf{v}_5$ at joint 5 for the four-story frame of Figure 4 with: (top) 2% uncertainty only in load history; (bottom) 2% uncertainties in load magnitude, Young's modulus, and mass density. IS (black solid lines) from the current method and MC predictions (blue dashed lines and red dotted lines) from an ensemble of 100,000 simulations (see online version for colors).

References

Adhikari S. and H. H. Khodaparast. A spectral approach for fuzzy uncertainty propagation in finite element analysis. *Fuzzy Sets and Systems*, 243:1–24, 2014.

Alefeld, G. and J. Herzberger. *Introduction to Interval Computation*. Academic Press, 1984.

Bae, S. H., J. R. Cho, S. R. Bae and W. B. Jeong. A discrete convolutional Hilbert transform with the consistent imaginary initial conditions for the time-domain analysis of five-layered viscoelastic sandwich beam. *Computer Methods in Applied Mechanics and Engineering*, 268:245–263, 2014.

Bai, Y. C., C. Jiang, X. Han and D. A. Hu. Evidence-theory-based structural static and dynamic response analysis under epistemic uncertainties. *Finite Elements in Analysis and Design*, 68:52–62, 2013.

Corliss, G., C. Foley and R. B. Kearfott. Formulation for reliable analysis of structural frames. *Reliable Computing*, 13(2):125–147, 2007.

De Borst, R., M. A. Crisfield, J. J. C. Remmers and C. V. Verhoosel. *Nonlinear Finite Element Analysis of Solids and Structures*. John Wiley & Sons, 2012.

Dehghan, M., B. Hashemi and M. Ghatee. Computational methods for solving fully fuzzy linear systems. *Applied Mathematics and Computation*, 179(1):328–343, 2006.

Dempster, A. P. Upper and lower probabilities induced by a muilti-valued mapping. *The Annals of Mathematical Statistics*, 38:325–339, 1967.

Do, D. M., W. Gao, C. Song and S. Tangaramvong. Dynamic analysis and reliability assessment of structures with uncertain-but-bounded parameters under stochastic process excitations. *Reliability Engineering & System Safety*, 132:46–59, 2014.

Dokainish, M. A. and K. Subbaraj. A survey of direct time-integration methods in computational structural dynamics: I. Explicit methods. *Computers & Structures*, 32(6):1371–1386, 1989.

Erdogan, Y. S. and P. G. Bakir. Inverse propagation of uncertainties in finite element model updating through use of fuzzy arithmetic. *Engineering Applications of Artificial Intelligence*, 26(1):357–367, 2013.

Fernández-Martínez, J. L., Z. Fernández-Muñiz, J. L. G. Pallero, L. M. Pedruelo-González. From Bayes to Tarantola: new insights to understand uncertainty in inverse problems. *Journal of Applied Geophysics*, 98:62–72, 2013.

Hu, J. and Z. Qiu. Non-probabilistic convex models and interval analysis method for dynamic response of a beam with bounded uncertainty. *Applied Mathematical Modelling*, 34(3):725–734, 2010.

Igusa, T., S. G. Buonopane and B. R. Ellingwood. Bayesian analysis of uncertainty for structural engineering applications. *Structural Safety*, 24(2):165–186, 2002.

Impollonia, N. and G. Muscolino. Interval analysis of structures with uncertain-but-bounded axial stiffness. *Computer Methods in Applied Mechanics and Engineering*, 200(21):1945–1962, 2011.

Jiang, C., Z. Zhang, X. Han and J. Liu. A novel evidence-theory-based reliability analysis method for structures with epistemic uncertainty. *Computers & Structures*, 129:1–12, 2013.

Klir, G. J. and M. J. Wierman. *Uncertainty-Based Information - Elements of Generalized Information Theory*. Physica-Verlag, Heidelberg, 1999.

Kulisch, U. W. and W. L. Miranker. *Computer Arithmetic in Theory and Practice*. Academic Press, New York, 1981.

Lee, U., S. Kim and J. Cho. Dynamic analysis of the linear discrete dynamic systems subjected to the initial conditions by using an FFT-based spectral analysis method. *Journal of Sound and Vibration*, 288(1):293–306, 2005.

Liu, F., H. Li, W. Wang and B. Liang. Initial-condition consideration by transferring and loading reconstruction for the dynamic analysis of linear structures in the frequency domain. *Journal of Sound and Vibration*, 336:164–178, 2015.

Liu, G. and V. Kreinovich. Fast convolution and fast Fourier transform under interval and fuzzy uncertainty. *Journal of Computer and System Sciences*, 76(1):63–76, 2010.

Lutes, L. D. and S. Sarkani. *Random Vibrations: Analysis of Structural and Mechanical Systems*. Butterworth-Heinemann, 2004.

Mansur, W. J., J. A. M. Carrer, W. G. Ferreira, D. G. A. Claret and F. Venancio-Filho. Time-segmented frequency-domain analysis for non-linear multi-degree-of-freedom structural systems. *Journal of Sound and Vibration*, 237(3):457–475, 2000.

Moens, D. and M. Hanss. Non-probabilistic finite element analysis for parametric uncertainty treatment in applied mechanics: Recent advances. *Finite Elements in Analysis and Design*, 47(1):4–16, 2011.

Moore, R. E., R. B. Kearfott and M. J. Cloud. *Introduction to Interval Analysis*. Society for Industrial and Applied Mathematics, 2009.

Muhanna, R. L. and R. L. Mullen. Uncertainty in mechanics problems-interval-based approach. *Journal of Engineering Mechanics*, American Society of Civil Engineers, 127(6):557–566, 2001.

Muhanna, R. L., H. Zhang and R. L. Mullen. Combined axial and bending stiffness in interval finite-element methods. *Journal of Structural Engineering*, 133(12):1700–1709, 2007.

Paz, M. *Structural Dynamics: Theory and Computation*. Springer Science & Business Media, 1997.

Qiu, Z. and Z. Ni. An inequality model for solving interval dynamic response of structures with uncertain-but-bounded parameters. *Applied Mathematical Modelling*, 34(8):2166–2177, 2010.

Rump, S. M. *INTLAB - INTerval LABoratory*. Kluwer Academic Publishers, 77–104, 1999.

Santamarina, J. C. and D. Fratta. *Discrete Signals and Inverse Problems: an Introduction for Engineers and Scientists*. John Wiley & Sons, 2005.

Shafer, G. *A Mathematical Theory of Evidence*. Princeton University Press, Princeton, 1968.

Soize, C. Bayesian posteriors of uncertainty quantification in computational structural dynamics for low-and medium-frequency ranges. *Computers & Structures*, 126:41–55, 2013.

To, C. and W. Solomon. Response analysis of nonlinear multi-degree-of-freedom systems with uncertain properties to non-Gaussian random excitations. *Probabilistic Engineering*, 27(1):75–81, 2012.

Unger, J. F. and C. Könke. An inverse parameter identification procedure assessing the quality of the estimates using Bayesian neural networks. *Applied Soft Computing*, 11(4):3357–3367, 2011.

Veletsos, A. S. and A. Kumar. Steady-state and transient responses of linear structures. *Journal of Engineering Mechanics*, American Society of Civil Engineers, 109(5):1215–1230, 1983.

Veletsos, A. S. and C. E. Ventura. Dynamic analysis of structures by the DFT method. *Journal of Structural Engineering*, American Society of Civil Engineers, 111(12):2625–2642, 1985.

Xia, Y., Z. Qiu and M. I. Friswell. The time response of structures with bounded parameters and interval initial conditions. *Journal of Sound and Vibration*, 329(3):353–365, 2010.

Yang, Y., Z. Cai and Y. Liu. Interval analysis of dynamic response of structures using Laplace transform. *Probabilistic Engineering Mechanics*, 29:32–39, 2012.

Zhang, H. *Nondeterministic Linear Static Finite Element Analysis: an Interval Approach*. Georgia Institute of Technology, PhD Thesis, 2005.

Interval Model of Equilibrium Equations in Mechanics

Evgenija D. Popova
Institute of Mathematics and Informatics, Bulgarian Academy of Sciences, Acad. G. Bonchev str., block 8, 1113 Sofia, Bulgaria, epopova@math.bas.bg, epopova@bio.bas.bg

Abstract: The engineering demand for more realistic and accurate models involving interval uncertainties lead to a new interval model of equilibrium equations in mechanics, which is based on the algebraic completion of classical interval arithmetic called Kaucher arithmetic. The proposed approach replaces straightforward a deterministic model by an interval model in terms of proper and improper intervals, fully conforms to the equilibrium principle and provides sharper enclosure of the unknown quantities than the best known methods based on classical interval arithmetic. The paper presents the interval algebraic approach to equilibrium equations and demonstrates its applications to various practical problems.

Keywords: force equilibrium, modeling structures, interval arithmetic, proper and improper intervals

1. Introduction

The basic principle of static (or dynamic) equilibrium under general force systems is an essential prerequisite for many branches of engineering, such as mechanical, civil, aeronautical, bioengineering, robotics, and others that address the various consequences of forces, (Beer et al., 2010).

One main challenge for the models involving interval uncertainty is the overestimation of the system response. Nowadays, the most successful approaches for overestimation reduction are those that relate the dependency of interval quantities to the physics of the problem being considered, (Muhanna et al., 2013). Recently, a model of a bar subjected to multiple axial external loads, where load magnitudes are represented by intervals, is considered in (Elishakoff et al., 2015). Although the aim at providing interval model conforming to the principle of static equilibrium is not completely achieved by the proposed model, the paper demonstrates what are the challenges in this non-trivial task. A similar problem in the context of robotics is discussed in the IEEE P1788 working group on standardization of interval arithmetic, (Mazandarani, 2015). It is shown in (Elishakoff et al., 2015), (Mazandarani, 2015) that an interval model based entirely on the classical interval arithmetic, in its set-theoretic interpretation as proposed by Moore (1966), cannot provide a good estimation of the unknown quantities involved in interval equilibrium equations.

The demand for more accurate models involving interval uncertainties lead to an interval model of equilibrium equations in mechanics (Popova, 2016a), which is based on the algebraic completion of classical interval arithmetic, called also Kaucher or generalized interval arithmetic. It is proven that the proposed interval model always yields the narrowest interval enclosure and is in full conformance with the physical meaning of static equilibrium. The work (Popova, 2016a) is focused on justification

of the proposed interval model in one dimension, comparison to the approach of (Elishakoff et al., 2015), and applications to computing resultant forces. A next paper (Popova, 2016b) further develops the interval algebraic approach to models involving interval equilibrium equations by considering models of practical applications which reduce to systems of interval equilibrium equations where the number of the unknowns is equal to the number of the equations. The initial interval model is expanded by considering interval algebraic solution to the system of equilibrium equations, model properties are revealed and the quality of the interval algebraic solution is compared to the best interval solution enclosure obtained by classical interval arithmetic. The present paper summarizes all achieved by now and continues the applications of the model to problems where the number of equilibrium equations is less than the number of the involved unknown quantities.

The structure of the present paper is as follows. In the next section some basic notions and properties of the algebraic extension (Kaucher, 1980) of classical interval arithmetic are summarized. In Section 3 we present the new interval model, its generalization to systems of interval equilibrium equations involving as many unknowns as the number of the equations, and a methodology how to apply the interval algebraic approach when the number of equilibrium equations is less than the number of the involved unknown quantities. Numerical applications developed in details in Sections 4 and 5 illustrate the proposed interval algebraic approach, its conformance to the equilibrium principle, bring out its effectiveness and advantages over the approach based on classical interval arithmetic. Section 5 demonstrates the hybrid interval approach on a frame model example. The article ends by some conclusions.

2. The Algebraic Completion of $\mathbb{IR}$

The set of classical compact intervals $\mathbb{IR} = \{[a^-, a^+] \mid a^-, a^+ \in \mathbb{R}, a^- \leq a^+\}$, called also *proper* intervals, is extended in (Kaucher, 1980) by the set $\overline{\mathbb{IR}} := \{[a^-, a^+] \mid a^-, a^+ \in \mathbb{R}, a^- \geq a^+\}$ of *improper* intervals obtaining thus the set $\mathbb{KR} = \mathbb{IR} \bigcup \overline{\mathbb{IR}} = \{[a^-, a^+] \mid a^-, a^+ \in \mathbb{R}\}$ of all ordered couples of real numbers called *generalized* (extended or Kaucher) intervals. For a better understanding we denote the classical intervals by bold face letters (e.g., $\mathbf{a}$) and the intervals from $\mathbb{KR}$ by brackets (e.g., $[a]$). Of course, $\mathbf{a} \in \mathbb{IR} \subset \mathbb{KR}$, and thus $[b] = \mathbf{a} \in \mathbb{KR}$ is a correct assignment. The inclusion order relation between classical intervals $\subseteq$, $\leq$ is generalized for $[a], [b] \in \mathbb{KR}$ by $[a] \subseteq [b] \iff b^- \leq a^-$ and $\mathrm{a}^+ \leq \mathrm{b}^+$. Denote $\mathcal{T} := \{[a] \in \mathbb{KR} \mid [a] = [0, 0] \text{ or } \mathrm{a}^-\mathrm{a}^+ < 0\}$. For $[a] = [a^-, a^+] \in \mathbb{KR}$ and $[b] \in \mathbb{KR} \setminus \mathcal{T}$, define binary variables *direction* (τ) and "sign" (σ) by

$$\tau([a]) := \begin{cases} + & \text{if } \mathrm{a}^- \leq \mathrm{a}^+, \\ - & \text{if } \mathrm{a}^- > \mathrm{a}^+; \end{cases} \qquad \sigma([a]) := \begin{cases} + & \text{if pro } ([\mathrm{a}])^- \geq 0, \\ - & \text{otherwise.} \end{cases}$$

All elements of $\mathbb{KR}$ with positive direction are called proper intervals and the elements with negative direction are called improper intervals. An element-to-element symmetry between proper and improper intervals is expressed by the "Dual" operator. For $[a] = [a^-, a^+] \in \mathbb{KR}$, $\mathrm{Dual}([a]) := [a^+, a^-]$. For $[a], [b] \in \mathbb{KR}$,

$$\mathrm{Dual}(\mathrm{Dual}([a])) = [a], \tag{1}$$

$$\mathrm{Dual}([a] \circ [b]) = \mathrm{Dual}([a]) \circ \mathrm{Dual}([b]), \ \circ \in \{+, -, \times, /\}. \tag{2}$$

Define proper projection of a generalized interval $[a]$ onto $\mathbb{IR}$ by

$$\mathrm{pro}([a]) := \begin{cases} [a] & \text{if } \tau([\mathrm{a}]) = +, \\ \mathrm{Dual}([a]) & \text{if } \tau([\mathrm{a}]) = -. \end{cases}$$

The conventional interval arithmetic and lattice operations, as well as other interval functions are isomorphically extended onto the whole set $\mathbb{KR}$, (Kaucher, 1980). Thus,

$$[a] + [b] = [a^- + b^-, a^+ + b^+] \qquad \text{for } [\mathrm{a}], [\mathrm{b}] \in \mathbb{KR},$$

$$[a] \times [b] = \begin{cases} [a^{-\sigma([b]}b^{-\sigma([a])}, a^{\sigma([b]}b^{\sigma([a])}] & \text{if } [\mathrm{a}], [\mathrm{b}] \in \mathbb{KR} \setminus \mathcal{T} \\ [a^{\sigma([a]\tau([b])}b^{-\sigma([a])}, a^{\sigma([a]\tau([b]}b^{\sigma([a])}] & \text{if } [\mathrm{a}] \in \mathbb{KR} \setminus \mathcal{T}, [\mathrm{b}] \in \mathcal{T} \\ [a^{-\sigma([b]}b^{\sigma([b])\tau([a])}, a^{\sigma([b])}b^{\sigma([b])\tau([a])}] & \text{if } [\mathrm{a}] \in \mathcal{T}, [\mathrm{b}] \in \mathbb{KR} \setminus \mathcal{T} \\ [\min\{a^-b^+, a^+b^-\}, \max\{a^-b^-, a^+b^+\}] & \text{if } [\mathrm{a}], [\mathrm{b}] \in \mathcal{T}, \tau([\mathrm{a}]) = \tau([\mathrm{b}]) \\ 0 & \text{if } [\mathrm{a}], [\mathrm{b}] \in \mathcal{T}, \tau([\mathrm{a}]) \neq \tau([\mathrm{b}]), \end{cases}$$

wherein $++ = -- = +$, $+- = -+ = -$. Interval subtraction and division can be expressed as composite operations, $[a]-[b] = [a]+(-1)[b]$ and $[a]/[b] = [a] \times (1/[b])$, where $1/[b] = [1/b^+, 1/b^-]$ if $[b] \in \mathbb{KR} \setminus \mathcal{T}$. The restrictions of the arithmetic operations to proper intervals produce the familiar operations in the conventional interval space.

The generalized interval arithmetic structure possesses group properties with respect to the operations addition and multiplication. For $[a] \in \mathbb{KR}$, $[b] \in \mathbb{KR} \setminus \mathcal{T}$,

$$[a] - \mathrm{Dual}([a]) = 0, \qquad [b]/\mathrm{Dual}([b]) = 1. \tag{3}$$

The complete set of conditionally distributive relations for multiplication and addition of generalized intervals can be found in (Popova, 1998), (Popova, 2001). Here we present only one that will be used. For $[a], [b], [s] = ([a] + [b]) \in \mathbb{KR} \setminus \mathcal{T}$, $[c] \in \mathbb{KR}$

$$([a] + [b])[c]_{\sigma([s])} = [a]_{\sigma([a])} + [b]_{\sigma([b])}, \tag{4}$$

wherein $[a]_+ = [a]$, $[a]_- = \mathrm{Dual}([a])$. Addition operation in $\mathbb{KR}$ is commutative and associative; associativity does not hold true in (interval) floating point arithmetic. Lattice operations are closed with respect to the inclusion relation; handling of norm and metric are very similar to norm and metric in linear spaces, (Kaucher, 1980). Some other properties and applications of generalized interval arithmetic can be found in (Kaucher, 1980), (Markov et al., 1996), (Popova, 1998), (Popova, 2001), (Popova and Ullrich, 1996), (Shary, 2002) and the references given therein.

For $\mathbf{a} \in \mathbb{IR} \setminus \mathcal{T}$, define $\mathrm{Abs}\,(\mathbf{a}) = \{\mathbf{a} \text{ if } 0 \leq \mathbf{a}; -\mathbf{a} \text{ otherwise}\}$. Relative diameter of $\mathbf{a} \in \mathbb{IR}$ is defined as $a^+ - a^-$ if $0 \in \mathbf{a}$ and $(a^+ - a^-)/\min\{|a^-|, |a^+|\}$ otherwise. For $\mathbf{a} \subseteq \mathbf{b}$, the percentage by which $\mathbf{b}$ overestimates $\mathbf{a}$ is defined by

$$100(1 - \omega(\mathbf{a}))/\omega(\mathbf{b}), \qquad \omega(\mathbf{a}) := a^+ - a^-.$$

3. Interval Model of Equilibrium Equations

In this section the algebraic approach to equilibrium equations in mechanics is derived by considering two-dimensional problems involving several forces acting on a particle. The same approach with obvious modifications is applicable to three-dimensional problems and problems whose models involve other vector physical quantities possessing magnitude and direction such as velocities, accelerations, or momenta. Such problems will be illustrated in the next section. In the text of this paper forces (and other vector quantities) are denoted by underlining the letter used to represent it. This is necessary in order to distinguish vectors from the proper intervals, which are denoted by bold-face letters, and from the real-valued scalars. The magnitude of a vector will be denoted by the corresponding italic-face letter.

In the deterministic case of two- dimensional problems involving several forces, the determination of their resultant $\underline{R}$ is best carried out by first resolving each force into rectangular components. Choosing a rectangular coordinate system (Oxy), with unit vectors $\underline{i}, \underline{j}$, any force vector $\underline{F}$ can be resolved into rectangular components $\underline{F}_x = F_x\underline{i}$, and $\underline{F}_y = F_y\underline{j}$, so that $\underline{F} = F_x\underline{i} + F_y\underline{j}$. The scalar component F_x is positive when the vector component $\underline{F}_x$ has the same direction as the unit vector $\underline{i}$ (i.e., the same direction as the positive x axis) and is negative when $\underline{F}_x$ has the opposite direction. A similar conclusion may be drawn regarding the sign of the scalar component F_y. Denoting by F the magnitude of the force $\underline{F}$ and by θ the angle between $\underline{F}$ and the axis x, measured counterclockwise from the positive axis, we may express the scalar components of $\underline{F}$ as follows: $F_x = F\cos(\theta)$ and $F_y = F\sin(\theta)$, cf. any textbook in statics, e.g., (Beer et al., 2010). When more than one force act on a particle (or a rigid body), it is important to determine the resultant force, i.e., the single force $\underline{R}$ which has the same effect on the particle as the given forces. The resultant force $\underline{R}$ can be determined by:

1. choosing a rectangular coordinate system;
2. resolving the given forces into their rectangular components;
3. each scalar component R_x, R_y of the resultant $\underline{R}$ of several forces $\underline{F}_i$ acting on a particle is obtained by adding algebraically the corresponding scalar components of the given forces. That is, $R_x = \sum_i F_{x,i}$, $R_y = \sum_i F_{y,i}$, which gives $\underline{R} = R_x\underline{i} + R_y\underline{j}$.

Basing on the above, the one dimensional interval algebraic model for computing the resultant force (and reaction), developed in (Popova, 2016a), can be applied to two- and three-dimensional problems involving vector physical quantities.

*Theorem 1. (*Popova*,* 2016a*)* Consider a bar subjected to a finite number of loads $\underline{p}_1, \ldots, \underline{p}_k$ that may be applied in opposite directions and have uncertain magnitude $p_1 \in \mathbf{p_1}, \ldots, p_k \in \mathbf{p_k}$, $\mathbf{p}_i \geq 0$, $i = 1, \ldots, k$. Assume that a coordinate system (Ox) is chosen. Then,

(i) for every j, $1 \leq j \leq k$, we have $[N_j] = \sum_{i=1}^{j}[p_i]$, wherein

$$[p_i] = \begin{cases} \mathbf{p}_i & \text{if the direction of } \underline{p}_i \text{ is in the positive } x \text{ axis} \\ -\text{Dual}(\mathbf{p}_i) & \text{if the direction of } \underline{p}_i \text{ is opposite to the positive } x \text{ axis} \end{cases},$$

and $[r] = -\text{Dual}([N_k]) = -\text{Dual}(\sum_{i=1}^{k}[p_i])$.

(ii) The interpretation of $[N_j] \in \mathbb{KR}$, $1 \leq j \leq k$, and similarly of $[r]$, is as follows.

- If $[N_j] \in \mathcal{T}$, then $\underline{N}_j$ may have positive or negative direction and its magnitude varies in pro($[N_j]$).
- If $[N_j] \in \mathbb{KR} \setminus \mathcal{T}$, the magnitude of $\underline{N}_j$ varies in Abs(pro ([Nj])), while the direction of $\underline{N}_j$ coincides with the sign of $[N_j]$ (if $[N_j] \geq 0$ the direction of $\underline{N}_j$ is the positive x axis, otherwise it is opposite to the positive x axis).

Strong proof that Theorem 1 provides sharpest estimation of the resultant force and its reaction is given in (Popova, 2016a) along with a detailed discussion and examples.

Now we consider the interval algebraic model of equilibrium equations from a more general perspective. Assume that there is a deterministic model described by some equilibrium equation(s) that involve uncertain parameters varying within given proper intervals. Clearly, the unknowns in this model will be also uncertain and we search for proper intervals that are the sharpest interval estimations of these unknowns and that conform to the physics of the problem (statics or dynamic equilibrium). Conformance to static (dynamic) equilibrium means that the intervals found for the unknowns when replaced in the equation(s) and all operations are performed results in true equality(ies).

*Definition 1. (*Ratschek and Sauer*,* 1982*)* Interval *algebraic solution* to a (system of) interval equation(s) is an interval (interval vector) which substituted in the equation(s) and performing all interval operations in exact arithmetic[1] results in valid equality(ies).

Interval algebraic solutions do not exist in general in classical interval arithmetic (Ratschek and Sauer, 1982). Generalized interval arithmetic on proper and improper intervals $(\mathbb{KR}, +, \times, \subseteq)$ is the natural arithmetic for finding algebraic solutions to interval equations since it is obtained from the arithmetic for classical intervals $(IR, +, -, \times, /, \subseteq)$ via an algebraic completion. This is another justification of the proposed interval algebraic approach. Therefore, we embed the initial problem formulation in the interval space $(\mathbb{KR}, +\times, \subseteq)$, find an algebraic solution (if exists) and interpret the obtained generalized intervals back in the initial interval space $\mathbb{IR}$. This is a three steps procedure summarized below.

1. The **representation convention** for a model involving interval forces (and/or other physical quantities considered as vectors and possessing magnitude and direction) is:
   - a scalar force component F_x (F_y, F_z) involving any kind of uncertainty is represented by proper interval $\mathbf{F}_x$ ($\mathbf{F}_y$, $\mathbf{F}_z$) if the force component $\underline{F}_x$ ($\underline{F}_y$, $\underline{F}_z$) has the same direction as the positive x (y, z) coordinate axis;
   - a scalar force component F_x (F_y, F_z) involving any kind of uncertainty is represented by the improper interval Dual($\mathbf{F}_x$) (Dual($\mathbf{F}_y$), Dual($\mathbf{F}_z$)) if the force component $\underline{F}_x$ ($\underline{F}_y$, $\underline{F}_z$) has opposite direction to the corresponding positive x (y, z) coordinate axis.

[1] no round-off errors

2. **Computing**. Find the **algebraic solution** for the unknown(s) in $(\mathbb{KR}, +, \times, \subseteq)$. Conditions for existence of algebraic solution of interval linear equations are published in (Popova, 1998), (Shary, 2002). Numerical methods finding the algebraic solution to an interval linear system are discussed in (Markov et al., 1996), (Shary, 2002). For small systems, the approach based on *equivalent algebraic transformations* is transparent and will be used in this paper.

3. **Interpretation** of the obtained generalized intervals in the initial space $\mathbb{IR}$ is done according to the physics of the unknowns. If it is a force component, then Theorem 1 ii) is applied. In general the interpretation projects the generalized interval solution on $\mathbb{IR}$.

Since computing a resultant $\underline{R}$ of several forces $\underline{F_i}$ can be represented as a solution of the equilibrium equation $\sum_i \underline{F_i} - \underline{R} = 0$, Theorem 1 is a special case of the above more general interval algebraic approach.

If the deterministic model involves more unknowns than the number of equilibrium equations, other relations are obtained from the information contained in the statement of the problem. In this case the following hybrid approach should be applied. Let the number of the equilibrium equations be k and the number of the unknown quantities be n, $n > k$. From the statement of the problem we find $n - k$ additional relations involving (some of) the unknowns.

a. If the $n - k$ additional relations involve $n - k$ of the n unknowns, by methods of classical interval analysis find interval estimations of these $n - k$ unknowns. Then replace the obtained interval estimations in the interval model of the equilibrium equations and find the algebraic solution with respect to the remaining k unknowns.

b. Let $n - k$ additional relations involve $n - k + q$ of the unknowns. We consider q of the k equilibrium equations together with the $n - k$ additional relations in a way that the system involves $n - k + q$ unknowns. Then the process continues as in a. above.

This approach ensures that the unknown uncertain quantities are estimated in a way that the equilibrium equations are satisfied to a highest extent that corresponds to the initial uncertainties. Next two sections illustrate the proposed interval algebraic approach.

4. Numerical Applications

Here we consider models of practical applications which illustrate the application of interval algebraic approach to equilibrium equations and its properties. In order to avoid many technical details that will hamper the comprehension, no more than two dimensional problems are considered. The numerical results presented in this section are obtained by the *Mathematica*® package `directed.m` (Popova and Ullrich, 1996). JInterval library (Nadezhin and Zhilin, 2014) can be used for this purpose, too.

Example 1. Three horizontal forces are applied, as shown in Figure 1, to a vertical cast iron arm. Assume that the distances shown in Figure 1 are measured with 1% uncertainty. Determine the

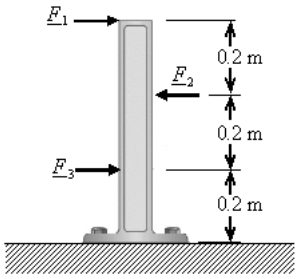

Figure 1. Horizontal forces applied to a vertical cast iron arm.

resultant of the forces, which are measured with 5% uncertainty, and the distance from the ground to its line of action when $F_2 = 700$N, $F_3 = 150$N, and a) $F_1 = 300$N, b) $F_1 = 550$N, c) $F_1 = 1200$N.

With a standard coordinate system, applying the representation convention, for the resultant force $\underline{R}$ we have

$$[R] = \mathbf{F}_1 - \mathrm{Dual}(\mathbf{F}_2) + \mathbf{F}_3.$$

The computation results in[2]

$$[R] = \begin{cases} [-237.5001, -262.4999] & \text{if a)} \\ [-2.27 \times 10^{-13}, 2.27 \times 10^{-13}] & \text{if b)} \\ [617.5000, 682.5001] & \text{if c).} \end{cases}$$

According to the interpretation convention the resultant force has magnitude $\mathbf{R} = \mathrm{Abs}(\mathrm{pro}([R]))$ and its direction is determined by the sign of $[R]$. That is, in case a) the magnitude varies in $[237.5001, 262.4999]$N, the direction is opposite to the direction of $\underline{F}_1$; in case b) the tiny fluctuations around zero are due to round-off errors and therefore the forces are in equilibrium ($R = 0$N); in case c) the magnitude varies in $[617.5000, 682.5001]$N and the direction of the resultant force coincides with the direction of $\underline{F}_1$.

For the moment $\underline{M}$ (and positive direction pointing the positive y coordinate axis) the representation convention gives

$$[M] = -\mathrm{Dual}(\mathbf{F}_1\mathbf{d}_1) + \mathbf{F}_2\mathbf{d}_2 - \mathrm{Dual}(\mathbf{F}_3\mathbf{d}_3),$$

wherein $\mathbf{d}_1 \in [0.6 \mp 6 \times 10^{-3}]$, $\mathbf{d}_2 \in [0.4 \mp 4 \times 10^{-3}]$, $\mathbf{d}_3 \in [0.2 \mp 2 \times 10^{-3}]$. The computation results in

$$[M] = \begin{cases} [65.8349, 74.2351] & \text{if a)} \\ [-75.2340, -84.8400] & \text{if b)} \\ [-442.0351, -498.4349] & \text{if c).} \end{cases}$$

According to the interpretation convention the moment $\underline{M}$ has the following magnitude $\mathbf{M}$ and direction. In case a) the magnitude is $[65.8349, 74.2351]$N.m and the direction points to the positive y axis; in case b) the magnitude is $[75.2340, 84.8400]$N.m and direction pointing opposite to the positive y axis; in case c) $\mathbf{M} = [442.0351, 498.4349]$N.m and the direction points opposite to the positive y axis.

[2] All computed numerical intervals are outwardly rounded to the intervals presented in the paper.

Then, the distance is $\mathbf{d} = \mathbf{M}/\mathbf{R}$ which gives $d_a \in [0.2508, 0.3126]$m in case a); $d_b = \infty$ in case b); and $d_c \in [0.6476, 0.8072]$m in case c).

Next example demonstrates the interval algebraic approach applied to systems of equilibrium equations where the number of the unknowns is equal to the number of the equations.

*Example 2. (*Popova*, 2016b)* A $[100 \pm 1]$ kg crate is suspended from a pulley that can roll freely on the support cable ACB and is pulled at a constant speed by cable CD, as shown in Figure 2. If $\alpha = 30°$, $\beta = 10°$ and the angles are measured with 1% uncertainty, determine the tension
(a) in the support cable ACB,
(b) in the traction cable CD.

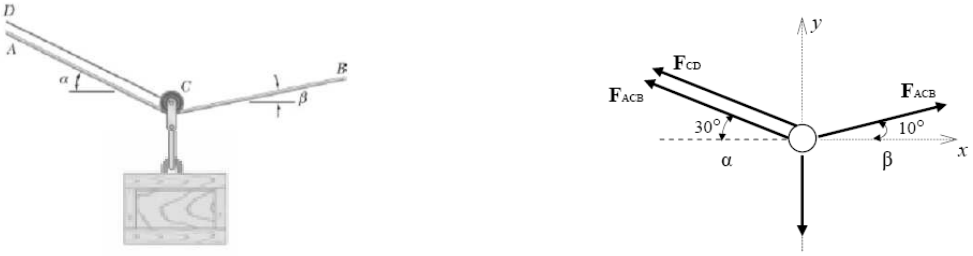

a) b)

Figure 2. a) A crate suspended from a pulley can roll freely on the support cable ACB and is pulled at a constant speed by cable CD; b) Free-body diagram.

The chosen coordinate system is presented on the free-body diagram in Figure 2. The deterministic equilibrium equations of force x and y components are

$$F_{\mathrm{ACB}} \cos(10°) - F_{\mathrm{ACB}} \cos(30°) - F_{\mathrm{CD}} \cos(30°) = 0, \tag{5}$$
$$F_{\mathrm{ACB}} \sin(10°) + F_{\mathrm{ACB}} \sin(30°) + F_{\mathrm{CD}} \sin(30°) - 100 \times 9.80665 = 0. \tag{6}$$

The representation convention gives the interval equilibrium equations

$$[F_{\mathrm{ACB}}] \cos([\beta]) - \mathrm{Dual}(\mathbf{F}_{\mathrm{ACB}} \cos([\alpha])) - \mathrm{Dual}(\mathbf{F}_{\mathrm{CD}} \cos([\alpha])) = 0, \tag{7}$$
$$[F_{\mathrm{ACB}}] \sin([\beta]) + [F_{\mathrm{ACB}}] \sin([\alpha]) + [F_{\mathrm{CD}}] \sin([\alpha]) - \mathrm{Dual}([99, 100] \times 9.80665) = 0, \tag{8}$$

wherein $[\alpha] = [29, 31]°$, $[\beta] = [9, 11]°$. We search for proper intervals $\mathbf{F}_{\mathrm{ACB}}$, $\mathbf{F}_{\mathrm{CD}}$, that satisfy Eqs. (7)–(8). First, we check the validity of the distributive relations for the first two additive terms in Eqs.(7) and (8). Since

$$[s_1] = \cos([\beta]) - \mathrm{Dual}(\cos([\alpha])) \in [0.121107, 0.116479] > 0,$$
$$[s_2] = \sin([\beta]) + \sin([\alpha]) \in [0.667387, 0.679895] > 0,$$

by Eq.(4), the system (Eqs. (7)–(8)) is equivalent to the system

$$[F_{\mathrm{ACB}}][s_1] - \mathrm{Dual}(\mathbf{F}_{\mathrm{CD}} \cos([\alpha])) = 0,$$
$$[F_{\mathrm{ACB}}][s_2] + [F_{\mathrm{CD}}] \sin([\alpha]) - \mathrm{Dual}([99, 100] \times 9.80665) = 0.$$

Remark 1. It is important that we check the distributive relations for every expression where we want to take a common interval variable out of brackets. For example, due to Eq. (4), and because $\cos([\alpha]) - \text{Dual}(\cos([\beta])) < 0$, the expression $[F_{\text{ACB}}]\cos([\alpha]) - \text{Dual}([F_{\text{ACB}}]\cos([\beta]))$ is equivalent to

$$\text{Dual}([F_{\text{ACB}}])\,(\cos([\alpha]) - \text{Dual}(\cos([\beta])))\,.$$

We add $[F_{\text{CD}}]\cos([\alpha])$ to the two sides of Eq. (7) and by Eq. (3) obtain the equivalent equation

$$[F_{\text{ACB}}][s_1] = [F_{\text{CD}}]\cos([\alpha]).$$

Dividing both sides of the last equation by $\text{Dual}(\cos([\alpha]))$, and due to Eq. (3), we obtain

$$[F_{\text{CD}}] = [F_{\text{ACB}}][s_1]/\text{Dual}(\cos([\alpha])). \tag{9}$$

We substitute the expression for $[F_{\text{CD}}]$ in Eq. (8). Since

$$[s_3] = [s_2] + \sin([\alpha])[s_1]/\text{Dual}(\cos([\alpha])) \;\in\; [5.25337, 5.57483] > 0,$$

due to the distributive relation, Eq. (8) is equivalent to

$$[F_{\text{ACB}}][s_3] - \text{Dual}([99, 100] \times 9.80665) = 0,$$

which is equivalent to

$$[F_{\text{ACB}}] = [99, 100] \times 9.80665/\text{Dual}([s_3]) \;\in\; [1317.51, 1324.97]. \tag{10}$$

Substituting Eq. (10) in Eq. (9), we obtain the second component of the algebraic solution to interval system (Eqs. (7)–(8))

$$[F_{\text{CD}}] \in [184.806, 177.669].$$

We are looking for proper algebraic solution to the interval equilibrium system. This restriction may not always be satisfied, as in the present example with respect to $[F_{\text{CD}}]$. Nevertheless, we interpret $[F_{\text{ACB}}]$ and $[F_{\text{CD}}]$ in $\mathbb{IR}$ as the corresponding proper intervals, namely,

$$\begin{aligned} \mathbf{F}_{\text{ACB}} &= \text{Abs}(\text{pro}([F_{\text{ACB}}])) \in [1317.51, 1324.97]\ \text{N}, \\ \mathbf{F}_{\text{CD}} &= \text{Abs}(\text{pro}([F_{\text{CD}}])) \in [177.669, 184.806]\ \text{N}. \end{aligned}$$

Since $[F_{\text{CD}}]$ is an improper interval, substituting $\mathbf{F}_{\text{ACB}}$ and $\mathbf{F}_{\text{CD}}$ into left sides of the Eqs. (7) and (8), we obtain much wider intervals involving zero, namely, $[6.16307, -6.20045]$ and $[-3.53667, 3.60141]$, respectively. The relative diameters of $\mathbf{F}_{\text{ACB}}$ and $\mathbf{F}_{\text{CD}}$ are 0.00565 and 0.0402, respectively.

Remark 2. Proper algebraic solution to the system (Eqs. (7)–(8)) can be obtained if, for example, we squeeze the interval $[\alpha]$ to the interval $[30 - 0.1, 30 + 0.1]$.

Now, we compare the solution $\mathbf{F}_{\text{ACB}}$, $\mathbf{F}_{\text{CD}}$, obtained by the discussed algebraic approach, to the solution obtained by classical interval arithmetic. The Eqs. (5) and (6) are rearranged to

$$\begin{aligned} &F_{\text{ACB}}\,(\cos(10^\circ) - \cos(30^\circ)) - F_{\text{CD}}\cos(30^\circ) = 0, \\ &F_{\text{ACB}}\,(\sin(10^\circ) + \sin(30^\circ)) + F_{\text{CD}}\sin(30^\circ) = 100 \times 9.80665 \end{aligned}$$

and the corresponding interval linear system that has to be solved is

$$\begin{pmatrix} \cos([\beta]) - \cos([\alpha]), & \cos([\alpha]) \\ \sin([\beta]) + \sin([\alpha]), & \sin([\alpha]) \end{pmatrix} \begin{pmatrix} F_{\mathrm{ACB}} \\ F_{\mathrm{CD}} \end{pmatrix} = \begin{pmatrix} 0 \\ [99, 100] \times 9.80665 \end{pmatrix}.$$

Since some interval parameters, e.g., $[\alpha]$, $[\beta]$, appear in more than one element of the matrix and/or the right-hand side vector, this is a parametric interval linear system. In classical interval arithmetic we search for a minimal outer interval estimation of the so-called united parametric solution set to the system. For $A(p)x = b(p)$, $p \in \mathbf{p}$, the united parametric solution set is

$$\Sigma = \{x \in \mathbb{R}^n \mid (\exists p \in \mathbf{p})(A(p)x = b(p))\}.$$

It can be proven, by method discussed in (Popova, 2006), that the united parametric solution set of the above system depends linearly on the interval parameters involved there. Therefore, one can find the minimal interval vector containing the united parametric solution set by finding the interval hull of the set of solutions to the point linear systems of equations obtained for the parameters taking values at all combinations of the corresponding interval end-points, the so-called combinatorial approach. Applying this approach, we find

$$\tilde{\mathbf{F}}_{\mathrm{ACB}} = [1293.33, 1349.74], \qquad \tilde{\mathbf{F}}_{\mathrm{CD}} = [175.743, 186.773],$$

whose relative diameters are respectively 0.04361 and 0.06276. Replacing $\tilde{\mathbf{F}}_{\mathrm{ACB}}$, $\tilde{\mathbf{F}}_{\mathrm{CD}}$ in the left-hand sides of the generalized interval equilibrium equations (Eqs. (7) and (8)), we obtain much wider intervals involving zero $[4.89652, -5.02244]$, $[-20.6303, 21.4392]$. There is no inclusion relation between $\mathbf{F}_{\mathrm{ACB}}$, $\mathbf{F}_{\mathrm{CD}}$ and $\tilde{\mathbf{F}}_{\mathrm{ACB}}$, $\tilde{\mathbf{F}}_{\mathrm{CD}}$. Nevertheless, judging from the value of the relative diameters and the extent to which the interval equilibrium equations are satisfied, we conclude that the interval algebraic approach applied to the equilibrium equations provides sharper interval estimations than the traditional approach based on classical interval arithmetic even in the present case when the algebraic solution to the interval equilibrium equations is not a proper interval vector.

Remark 3. In some deterministic models, e.g., when determine the forces in the members of a truss, in order to write the equilibrium equations one has to choose the direction of each of the unknown forces, cf. (Beer et al., 2010, Chapter 6). It cannot be determined until the solution is completed whether the guess was correct. To do that, the value found for each of the unknowns is considered: a positive sign means that the selected direction was correct; a negative sign means that the direction is opposite to the assumed direction. This convention is transparently applicable to the corresponding interval algebraic model which delivers the correct sign together with the interval magnitude.

5. Impact on Models of Structures

Example 3. After (Kulpa et al., 1998) consider a simple planar frame with three types of support and an external load distributed uniformly along the beam as shown in Figure 3 a).

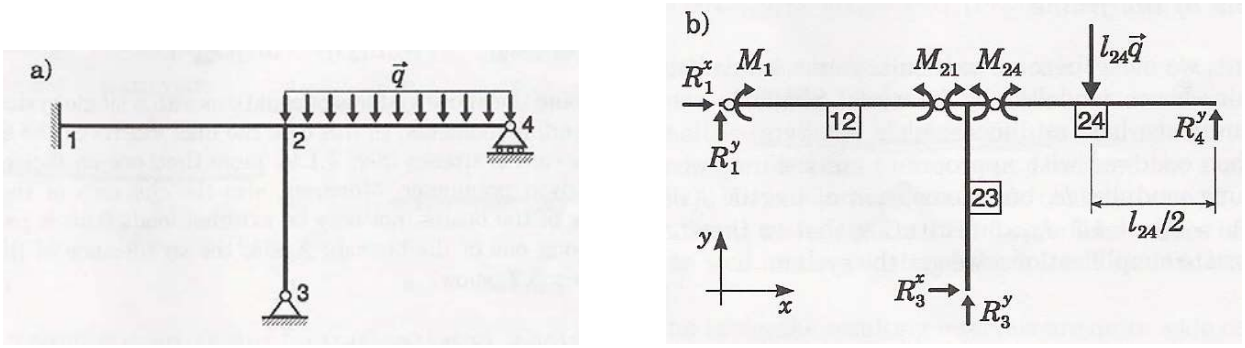

Figure 3. Planar frame (a) and its fundamental system of internal parameters (b), after (Kulpa et al., 1998).

Assuming small displacements and linear elastic material law, and using the method of forces, the frame is described in (Kulpa et al., 1998) by the following set of equilibrium equations for forces and bending moments, see Figure 3 (b).

$$R_1^x + R_3^x = 0, \tag{11}$$

$$R_1^y + R_3^y + R_4^y - ql_{24} = 0, \tag{12}$$

$$-M_1 + R_4^y(l_{12} + l_{24}) + R_3^y l_{12} + R_3^x l_{23} - ql_{24}(l_{12} + \frac{1}{2}l_{24}) = 0, \tag{13}$$

$$-R_1^y l_{12} - M_1 + M_{21} = 0, \tag{14}$$

$$R_4^y l_{24} - \frac{1}{2}ql_{24}^2 - M_{24} = 0. \tag{15}$$

The equilibrium equations involve more unknowns than the number of the equations. Then, the three canonical equations linking bending moments with material properties (Young modulus E and momentum of inertia J of the beam cross-section) of the beams are given by

$$\begin{pmatrix} \frac{l_{12}}{3E_{12}J_{12}} & \frac{l_{12}}{6E_{12}J_{12}} & 0 \\ \frac{l_{12}}{6E_{12}J_{12}} & \frac{l_{12}}{3E_{12}J_{12}} + \frac{l_{23}}{3E_{23}J_{23}} & \frac{-l_{23}}{3E_{23}J_{23}} \\ 0 & \frac{-l_{23}}{3E_{23}J_{23}} & \frac{l_{24}}{3E_{12}J_{12}} + \frac{l_{23}}{3E_{23}J_{23}} \end{pmatrix} \begin{pmatrix} M_1 \\ M_{21} \\ M_{24} \end{pmatrix} = \begin{pmatrix} 0 \\ 0 \\ \frac{-ql_{24}^3}{24E_{24}J_{24}} \end{pmatrix}. \tag{16}$$

The parameters of this frame will be given as dimensionless numbers. It is assumed that all the beams have the same Young modulus E and momentum of inertia J of the beam cross-sections are related by the formula $J_{12} = J_{23} = 1.5J_{24}$. The lengths of the beams and the load are considered to be uncertain with the following nominal values $l_{12} = l_{24} = 1$, $l_{23} = 0.75$, and $q = 10$. Substituting these into the Eqs. (11)–(16) for the frame and making appropriate simplifications, a parametric linear system described by the following relations is obtained

$$\frac{1}{2}a_{11} = a_{12} = a_{21} = a_{65} = -a_{74} = l_{12}$$

$$a_{22} = 2l_{12} + 2l_{23},\ a_{33} = 3l_{24} + 2l_{23},\ a_{66} = l_{12} + l_{24},\ a_{23} = a_{32} = -2l_{23},\ a_{68} = l_{23},\ a_{86} = l_{24}$$

$$a_{47} = a_{48} = a_{54} = a_{55} = a_{56} = -a_{61} = -a_{71} = a_{72} = -a_{83} = 1$$

$$b = (0,\ 0,\ -\frac{3}{8}q\,l_{24}^3,\ 0,\ q\,l_{24},\ q\,l_{24}(l_{12}+\frac{1}{2}l_{24}),\ 0,\ \frac{1}{2}q\,l_{24}^2)^\top.$$

It is assumed that there is no prestressing of the structure due to inexact dimensions of the beams. For that, the uncertainties are considered either as errors of measurements of the elements of the already existing structure, or else assume the structure will be assembled from inexact elements, but in a way that does not lead to prestressing (e.g., by slightly moving appropriate supports when necessary).

Usually, interval estimations for the unknown reactions and moments are found by bounding the united parametric solution set of the last system. In (Popova, 2006) it is proven that the united parametric solution set of the system (Eqs. (11)–(16)) depends linearly on the interval parameters. In (Popova, 2005, Table 8, column 2) the sharpest interval enclosing the solution set is reported for the parameters

$$l_{12} \in [0.995, 1.005],\ l_{24} \in [0.995, 1.005],\ l_{23} \in [0.74625, 0.75375], q \in [9.95, 10.05]. \tag{17}$$

The obtained enclosures are

Table I. Solution for moments and reactions of the planar frame system with 0.5% uncertain parameters after (Popova, 2005).

$\mathbf{M}_1$	$\mathbf{M}_{21}$	$\mathbf{M}_{24}$	$\mathbf{R}_1^x$
[.24479, .25530]	[-.51059, -.48958]	[-1.0171, -.98309]	[-.68421, -.64953]

$\mathbf{R}_1^y$	$\mathbf{R}_3^y$	$\mathbf{R}_4^y$	$\mathbf{R}_3^x$
[-0.76973, -0.73072]	[6.6698, 6.8309]	[3.9600, 4.0401]	[0.64953, 0.68421]

However, $\mathbf{R}_1^y + \mathbf{R}_3^y + \mathbf{R}_4^y - \mathbf{q}\mathbf{l}_{24} \in [-0.24, 0.24]$ and the equilibrium equation (Eq. (12)) is not satisfied.

In (Popova, 2005, Table 10, column 2) the sharpest intervals enclosing the solution set is reported for the the planar frame system with 1% uncertain lengths and 15 % uncertain load. In this case, the obtained interval estimations are such that $\mathbf{R}_1^y + \mathbf{R}_3^y + \mathbf{R}_4^y - \mathbf{q}\mathbf{l}_{24} \in [3.47, 3.48]$ and the equilibrium equation (Eq. (12)) is not satisfied, too.

In order to obtain more realistic interval estimations that satisfy the equilibrium equations (Eqs. (11)–(15)), we will apply the proposed interval algebraic approach. First, we find the exact interval hull of the united parametric solution set of the system (Eq. (16)) for the parameters (Eq. (17)) as shown in Table II.

Then, we replace the obtained intervals for $\mathbf{M}_1$, $\mathbf{M}_{21}$ and $\mathbf{M}_{24}$ in the proposed interval model of the equilibrium equations (Eqs. (11)–(15)) and find the algebraic solution for $\mathbf{R}_{1,3,4}^y$, $\mathbf{R}_{1,3}^x$, as follows. From Eq. (14)

$$[R_1^y] = (-\mathbf{M}_1 + \mathbf{M}_{21})/\mathrm{Dual}(\mathbf{l}_{12}) = -3\mathbf{M}_1/\mathrm{Dual}(\mathbf{l}_{12}) \in [-0.76055, -0.73954].$$

From Eq. (15)

$$[R_4^y] = (\mathbf{M}_{24} + \mathbf{q}\mathbf{l}_{24}^2/2)/\mathrm{Dual}(\mathbf{l}_{24}) \in [3.9279, 4.07192].$$

Table II. Solution for moments of the system (Eq. (16)) with 0.5% uncertain parameters.

$\mathbf{M}_1$	$\mathbf{M}_{21}$	$\mathbf{M}_{24}$
[.2452, .2548]	[-.5096, -.4905]	[-1.0171, -.98309]

From Eq. (12)

$$[R_3^y] = \mathbf{q}\mathbf{l}_{24} - [R_1^y] - \mathrm{Dual}([R_4^y]) \in [6.7118, 6.7889].$$

If the computations are done in exact (rational) arithmetic, so that there are no round-off errors, we will have

$$\mathrm{Dual}([R_1^y]) + [R_3^y] + [R_4^y] - \mathrm{Dual}(\mathbf{q}\mathbf{l}_{24}) = [0, 0].$$

From Eq. (13)

$$[R_3^x] = (\mathbf{q}\mathbf{l}_{24}(\mathbf{l}_{12} + \mathbf{l}_{24}/2) + \mathbf{M}_1 - \mathrm{Dual}([R_4^y](\mathbf{l}_{12} + \mathbf{l}_{24})) - \mathrm{Dual}([R_3^y]\mathbf{l}_{12}))/\mathrm{Dual}(\mathbf{l}_{23}) \in [.70557, .62824].$$

And from Eq. (11)

$$[R_1^x] = -\mathrm{Dual}([R_3^x]) \in [-.70557, -.62824].$$

$[R_3^x]$ is improper interval, so it should be interpreted as the corresponding proper one.

Denote by $\tilde{\mathbf{R}}^y_{1,3,4}$, $\tilde{\mathbf{R}}^x_{1,3}$ the sharpest enclosures obtained by classical interval approach and presented in Table I. Comparing the estimations of the reactions, got by the interval equilibrium model, to the reaction estimations $\tilde{\mathbf{R}}^y_{1,3,4}$, $\tilde{\mathbf{R}}^x_{1,3}$ we obtain

$$\begin{aligned}
\tilde{\mathbf{R}}^y_1 &\text{overdetermines } \mathbf{R}^y_1 \quad \text{by } 46.2\% \\
\tilde{\mathbf{R}}^y_3 &\text{overdetermines } \mathbf{R}^y_3 \quad \text{by } 52.2\% \\
\mathbf{R}^y_4 &\text{overdetermines } \tilde{\mathbf{R}}^y_4 \quad \text{by } 44.3\% \\
\mathbf{R}^x_{1,3} &\text{overdetermine } \tilde{\mathbf{R}}^x_{1,3} \quad \text{by } 55.2\%.
\end{aligned}$$

Note that the last two lines show that the classical interval estimates *underdetermine* the variation in reaction magnitude. This is especially dangerous.

Remark 4. Interval forces in the interval equilibrium model are like connected vessels — expanding some interval estimations shrinks the estimation of others, so that the equilibrium equations are always satisfied. This property is particularly important because not always we can obtain the sharpest interval estimations of the unknowns involved in the additional relations. To illustrate this property we take the values of $\mathbf{M}_{1,21,24}$ from Table I and round them outwardly to the second place after the decimal point as follows

$$\mathbf{M}_1 \in [24/100, 26/100], \quad \mathbf{M}_{21} \in [-52/100, -48/100], \quad \mathbf{M}_{24} \in [-102/100, -98/100]. \tag{18}$$

These intervals overestimate the intervals presented in Table II by $52.5, 52.5, 93.5\%$, respectively. Now, we repeat the above computations in the interval model of equilibrium equations and obtain slightly different intervals for $\mathbf{R}^y_{1,3,4}$, $\mathbf{R}^x_{1,3}$ which also satisfy the equilibrium equations.

Remark 5. Expanding the uncertainty cannot be unlimited. We illustrate this by the following example. Assume that in the input of interval estimates (Eq. (18)) we have a typing bug so that $\mathbf{M}_{24} \in [-102/100, -50/100]$. Then the computations in the interval model of equilibrium equations results in $[R_3^y] = [144/199, -16/597]$, $[R_1^x] = [-144/199, 16/597]$, both involving zero. The latter means that we cannot determine the direction of both reactions. Also the first equilibrium equation is not satisfied, $\mathbf{R}_1^x + \mathbf{R}_3^x \approx [-0.75, 0.75]$. Thus, if the interval model of equilibrium equations results in interval containing zero for some reaction magnitude, this might be due to wrong model or overestimation of some uncertain quantities.

Remark 6. The algebraic interval approach to equilibrium equations should be applied to all interval models (parametric interval systems of equations) involving equilibrium equations, for example to systems for both primary and derived variables (Rao et al., 2011). Keeping the equilibrium equations involving the same number of unknowns out of the parametric system that is solved by classical interval methods reduces the number of both equations and interval parameters in the latter, which additionally helps reducing the overestimation of the unknowns in the latter system.

6. Conclusion

The proposed interval algebraic model of equilibrium equations in mechanics contributes to the development of more realistic and accurate interval models that conform to the problem physics. The most attractive in the interval algebraic approach is its straightforward and transparent application to the deterministic model. By a simple representation convention one can easily transform a deterministic formulation into a unique interval arithmetic formulation in the interval space $(\mathbb{KR}, +, \times, \subseteq)$. Then in the same rich algebraic space one finds sharp algebraic solutions for the unknown quantities and interpret them in the original physical setting of the problem.

The proposed new interval model is demonstrated on various examples of practical problems whose models involve equilibrium equations and interval uncertainties. Along with guaranteed quantification of all sources of uncertainties, the new algebraic approach provides also sharper enclosure of the unknown quantities than the best known methods based on classical interval arithmetic. Contrary to classical interval approach, the algebraic one provides satisfaction of the equilibrium equations even for large parameter uncertainties.

The proposed interval model of equilibrium equations allows accounting for the dependencies between interval parameters from the very beginning of modeling process, as well as efficient reduction of the interval overestimation that may arise in more complicated models.

References

Beer F. P., E. R. Johnston, D. F. Mazurek, P. J. Cornwell and E. R. Eisenberg. *Vector Mechanics for Engineers: Statics and Dynamics*, 9th edition, McGraw-Hill, 2010.

Elishakoff I., S. Gabriele and Y. Wang. Generalized Galileo Galilei problem in interval setting for functionally related loads. *Archive of Applied Mechanics*, doi: 10.1007/s00419-015-1086-4

Kaucher E. Interval analysis in the extended interval space IR. *Computing Suppl.*, 2:33–49, 1980.

Kulpa, Z., A. Pownuk and I. Skalna. Analysis of linear mechanical structures with uncertainties by means of interval methods. *CAMES*, 5:443–477, 1998.

Markov S. M., E. D. Popova and C. P. Ullrich. On the solution of linear algebraic equations involving interval coefficients. In: Margenov S., Vassilevski P. (eds.) *Iterative Methods in Linear Algebra, II*, IMACS Series in Computational and Applied Mathematics 3, 216–225, 1996.

Mazandarani M. IEEE standard 1788-2015 vs. multidimensional RDM interval arithmetic. posting to IEEE P1788 working group, 2015. `http://grouper.ieee.org/groups/1788/email/msg08439.html`

Moore R. E. *Interval Analysis*. Prentice-Hall, Englewood Cliffs, N.J., 1966.

Muhanna R. L., M. V. Rama Rao and R. L. Mullen. Advances in interval finite element modelling of structures. *Life Cycle Reliability and Safety Engineering*, 2(3):15–22, 2013.

Nadezhin D. Y. and S. I. Zhilin. JInterval library: principles, development, and perspectives. *Reliable Computing*, 19:229–247, 2014.

Popova E. D. Algebraic solutions to a class of interval equations. *Journal of Universal Computer Science*, 4(1):48–67, 1998.

Popova E. D. Multiplication distributivity of proper and improper intervals. *Reliable Computing*, 7(2):129–140, 2001.

Popova E. D. Solving linear systems whose input data are rational functions of interval parameters. Preprint 3/2005, IMI-BAS, 2005. `http://www.math.bas.bg/~epopova/papers/05PreprintEP.pdf`

Popova E. D. Computer-assisted proofs in solving linear parametric problems. In *Proceedings of SCAN'06*, IEEE Computer Society Press, page 35, 2006.

Popova E. D. Improved solution to the generalized Galilei's problem with interval loads. *Archive of Applied Mechanics*, submitted 2016.

Popova E. D. Interval algebraic approach to equilibrium equations in mechanics. In Proceedings of 10th Annual Meeting of BGSIAM, submitted 2016.

Popova E. D. and C. P. Ullrich. Directed interval arithmetic in Mathematica. Implementation and applications. Technical Report 96-3, Universität Basel, Switzerland, 1996. `http://www.math.bas.bg/~epopova/papers/tr96-3.pdf`.

Rama Rao M. V., R. L. Mullen and R. L. Muhanna. A new interval finite element formulation with the same accuracy in primary and derived variables. *International Journal of Reliability and Safety*, 5(3-4):336–357, 2011.

Ratschek H. and W. Sauer. Linear interval equations. *Computing*, 26:105–115, 1982.

Shary S. P. A new technique in systems analysis under interval uncertainty and ambiguity. *Reliable Computing*, 8(5):321–418, 2002.

How to Estimate Amount of Useful Information, in Particular Under Imprecise Probability

Luc Longpré[1)], Olga Kosheleva[2)] and Vladik Kreinovich[1)]
[1)] *Department of Computer Science, University of Texas at El Paso, El Paso, TX 79968, USA, {longpre, vladik}@utep.edu*
[2)] *Department of Teacher Education, University of Texas at El Paso, El Paso, TX 79968, USA, olgak@utep.edu*

Abstract: Traditional Shannon's information theory describes the overall amount of information, without distinguishing between useful and unimportant information. Such a distinction is needed, e.g., in privacy protection, where it is crucial to protect important information while it is not that crucial to protect unimportant information. In this paper, we show how Shannon's definition can be modified so that it will describe only the amount of useful information.

Keywords: amount of information, entropy, utility, imprecise probabilities, interval uncertainty, useful information

1. Formulation of the Problem: Traditional Information Theory Does Not Distinguish Between Useful and Unimportant Information

To gauge the amount of information, we need to be able to gauge uncertainty. The more we learn, the more information we have about the world. Our ultimate goal is to gain a complete knowledge of the world, i.e., to reach a situation when we should be able, based on this knowledge, to answer any question that anyone may have about the future or past state of the world.

For example:

- one of the main objectives of meteorology is to be able to predict future weather;
- one of the main objectives of celestial mechanics is to predict future locations of celestial bodies and man-made satellites,
- etc.

In practice, we rarely have the *complete* information, we usually have only *partial* information, based on which we cannot uniquely reconstruct the state of the world and thus, cannot always find an answer to a question about the world. In other words, in practice, we have *uncertainty*.

Additional information allows us to decrease this uncertainty. It is therefore reasonable to gauge the amount of information in the new knowledge by how much this information decreases the original uncertainty. Thus, a natural way to gauge the amount of information is to estimate how

much this information decreases uncertainty. Hence, to gauge the amount of information, we need to be able to gauge the amount of uncertainty.

How to gauge the amount of uncertainty: idea. As we have mentioned earlier, uncertainty means that for some questions, we do not have a definite answer. Once we learn the answers to these questions, we thus decrease the original uncertainty. It is therefore reasonable to estimate the amount of uncertainty by the number of questions needed to eliminate this uncertainty.

Of course, not all questions are created equal. Some questions can have a simple binary "yes"-"no" question, some questions look for a more detailed answer – e.g., we can ask what is the value of a certain quantity. No matter what is the answer, we can describe this answer inside the computer and thus – since everything in the computer is represented as 0s and 1s – represent this answer as a sequence of 0s and 1s. Such a several-bits question can be represented as a sequence of on-bit questions:

- we can first ask what is the first bit of the answer,
- we can then ask what is the second bit of the answer,
- etc.

Since every question can thus be represented as a sequence of one-bit ("yes"-"no") questions, it is reasonable to measure uncertainty by the smaller number of such "yes"-"no" questions which are needed to eliminate this uncertainty – i.e., to uniquely determine the state of the corresponding system.

Let us recall how this idea can be transformed into exact formulas.

How to gauge uncertainty: finite case. Let us first consider the situation when we have finitely many N alternatives. In this case:

- if we ask one binary question, then we can get two possible answers (0 and 1) and thus, uniquely determine one of the two different states;
- if we ask two binary questions, then we can get four possible combinations of answers (00, 01, 10, and 11), and thus, uniquely determine one of the four different states;
- in general, if we ask q binary questions, then we can get 2^q possible combinations of answers, and thus, uniquely determine one of 2^q states.

So, to identify one of n states, the smallest number of binary questions q needed for this identification is the smallest value q for which $2^q \geq N$. This inequality is equivalent to $q \geq \log_2(N)$, and thus, the smallest number of binary questions is equal to the smallest integer which is greater than or equal to this logarithm, i.e., equal to $\lceil \log_2(q) \rceil$.

How to gauge uncertainty: finite case with known probabilities. In the previous text, we considered the situation when we have n alternatives about whose frequency we know nothing. In practice, we often know the probabilities $p_1, \ldots, p_n$ of different alternatives. In this case, instead of considering the *worst-case* number of binary questions needed to eliminate uncertainty, it is reasonable to consider the *average* number of questions.

This value can be described as follows. We have a large number N of similar situations with n-uncertainty.

- In $N \cdot p_1$ of these situations, the actual state is State 1.
- In $N \cdot p_2$ of these situations, the actual state is State 2,
- etc.

The average number of binary questions can be obtained if we divide the overall number of questions needed to determine the states in all N situations, by N.

Let us describe the uncertainty of this N-repetitions arrangement. Out of N situations, there are

$$\binom{N}{N \cdot p_1} = \frac{N!}{(N \cdot p_1)! \cdot (N - N \cdot p_1)!}$$

ways to select the situations in which the actual state is State 1. For each of these situations, there are

$$\binom{}{N \cdot p_1} = \frac{(N - N \cdot p_1)!}{(N \cdot p_2)! \cdot (N - N \cdot p_1 - N \cdot p_2)!}$$

ways to select, among the remaining $N - N \cdot p_1$ situations, $N \cdot p_2$ ones for which the actual state is State 2, etc. Thus, the overall number of possible arrangements is equal to the product

$$A = \frac{N!}{(N \cdot p_1)! \cdot (N - N \cdot p_1)!} \cdot \frac{(N - N \cdot p_1)!}{(N \cdot p_2)! \cdot (N - N \cdot p_1 - N \cdot p_2)!} \cdot \ldots =$$

$$\frac{N!}{(N \cdot p_1)! \cdot (N \cdot p_2)! \cdot \ldots \cdot (N \cdot p_n)!}.$$

To identify one of these A arrangements, we need to ask

$$Q = \log_2(A)$$

binary questions. For the above formula for A, we get

$$Q = \log_2(N!) - \sum_{i=1}^{n} \log_2((N \cdot p_i)!).$$

Here,

$$m! \sim \left(\frac{m}{e}\right)^m,$$

so

$$\log_2(m!) \sim m \cdot (\log_2(m) - \log_2(e)).$$

Thus,

$$Q = N \cdot \log_2(N) - N \cdot \log_2(e) - \sum_{i=1}^{n} (N \cdot p_i) \cdot \log_2(N \cdot p_i) + \sum_{i=1}^{n} (N \cdot p_i) \cdot \log_2(e),$$

and the average number $\overline{q}$ of "yes"-"no" questions is equal to

$$\overline{q} = \frac{Q}{N} = \log_2(N) - \log_2(e) - \sum_{i=1}^{n} p_i \cdot \log_2(N \cdot p_i) + \sum_{i=1}^{n} p_i \cdot \log_2(e).$$

Taking into account that $\log_2(N \cdot p_i) = \ln(N) + \ln(p_i)$, we get

$$\overline{q} = \log_2(N) - \log_2(e) - \sum_{i=1}^{n} p_i \cdot \log_2(N) - \sum_{i=1}^{n} p_i \cdot \log_2(p_i) + \left(\sum_{i=1}^{n} p_i\right) \cdot \log_2(e) =$$

$$\log_2(N) - \log_2(e) - \left(\sum_{i=1}^{n} p_i\right) \cdot \log_2(N) - \sum_{i=1}^{n} p_i \cdot \log_2(p_i) + \left(\sum_{i=1}^{n} p_i\right) \cdot \log_2(e).$$

Since $\sum\limits_{i=1}^{n} p_i = 1$, we get

$$\overline{q} = -\sum_{i=1}^{n} p_i \cdot \log_2(p_i).$$

This is the classical Shannon's formula for the amount of uncertainty (Shannon and Weaver, 1971).

How to gauge uncertainty: continuous case. In the continuous case, when the unknown(s) can take any of the infinitely many values from some interval, we need infinitely many binary questions to uniquely determine the exact value.

To estimate uncertainty, it then makes sense to consider the average number of questions needed to determine each value with a given accuracy $\varepsilon > 0$.

In other words, instead of determining the exact value x, we divide the real line into intervals $[x_i - \varepsilon, x_i + \varepsilon]$, where $x_{i+1} = x_i + 2\varepsilon$, and we want to find out to which of these intervals the actual value x belongs. For small ε, the probability p_i of belonging to the i-th interval is equal to $p_i \approx \rho(x_i) \cdot (2\varepsilon)$. Substituting this expression for p_i into the classical Shannon's formula, we get

$$\overline{q} = -\sum_{i=1}^{n} p_i \cdot \log_2(p_i) = -\sum_{i=1}^{n} \rho(x_i) \cdot (2\varepsilon) \cdot \log_2(\rho(x_i) \cdot (2\varepsilon)).$$

Using the fact that $\log(a \cdot b) = \log(a) + \log(b)$, we conclude that

$$\overline{q} = -\sum_{i=1}^{n} \rho(x_i) \cdot (2\varepsilon) \cdot \log_2(\rho(x_i)) - \sum_{i=1}^{n} \rho(x_i) \cdot (2\varepsilon) \cdot \log_2(2\varepsilon).$$

The first term in this sum has the form

$$-\sum_{i=1}^{n} \rho(x_i) \cdot \log_2(\rho(x_i)) \cdot (2\varepsilon) = -\sum_{i=1}^{n} \rho(x_i) \cdot \log_2(\rho(x_i)) \cdot \Delta x_i,$$

where we denoted $\Delta x_i \stackrel{\text{def}}{=} x_{i+1} - x_i$. One can easily see that this term is an integral sum for the interval $-\int \rho(x) \cdot \log_2(\rho(x))\, dx$ and thus, for small ε, is practically equal to this interval.

Similarly, the second term has the form

$$-\sum_{i=1}^{n} \rho(x_i) \cdot (2\varepsilon) \cdot \log_2(2\varepsilon) = -\log_2(2\varepsilon) \cdot \sum_{i=1}^{n} \rho(x_i) \cdot (2\varepsilon) = -\log_2(2\varepsilon) \cdot \sum_{i=1}^{n} \rho(x_i) \cdot \Delta x_i,$$

and is, thus, an integral sum for the integral $-\log_2(2\varepsilon) \cdot \int \rho(x)\, dx$. By the formula of complete probability, we have $\int \rho(x)\, dx = 1$, so the second term is simply equal to $-\log_2(2\varepsilon)$ and thus, the average number of binary questions $\overline{q}$ which is needed to determine x with accuracy ε is equal to

$$\overline{q} = -\int \rho(x) \cdot \log_2(\rho(x))\, dx - \log_2(2\varepsilon).$$

The first term in this expression does not depend on ε and thus, provides a good measure of how much uncertainty we have. This term

$$S \stackrel{\text{def}}{=} -\int \rho(x) \cdot \log_2(\rho(x))\, dx$$

was also introduced originally by Shannon and is known as *Shannon's entropy* (or simply *entropy*, for short) (Shannon and Weaver, 1971).

A similar formula holds in the multi-D case, when instead of a single variable x, we have a tuple of variables $\vec{x} = (x_1, \ldots, x_m)$:

$$\overline{q} = S - m \cdot \log_2(2\varepsilon),$$

where

$$S = -\int \rho(\vec{x}) \cdot \log_2(\rho(\vec{x}))\, d\vec{x}.$$

Need to distinguish between useful and unimportant information. Not all information is created equal:

- some pieces of information are useful, while
- other pieces of information are unimportant.

Whether the information is useful or not depends on what we plan to do with this information. For example:

- if we are interested in predicting weather in a given geographic area based on meteorological observations, then the specific colors at sunset or the colors and the smell of the fog are probably unimportant, while
- if we are analyzing polluting level, all this would be a very useful information.

Such distinction is important in privacy protection. A distinction between useful and irrelevant information is needed in privacy protection. Ideally, we would like to maintain full privacy, so that no one can gain any information about a person without his or her explicit permission. However, realistically, some information may be leaked. It is therefore important to distinguish between the cases when an important information was leaked and when an unimportant piece of information was leaked.

For example, if we want to keep the salaries private, then disclosing the higher bits of the salaries – i.e., in effect, the approximate values of the salaries – would be a major violation of privacy, while disclosing the lowest bits, i.e., number of cents in the annual salary, would be reasonably harmless.

It is therefore desirable to estimate the amount of *useful* information, i.e., information that affects the utility of different alternatives.

Such a distinction is also important in education. The distinction between relevant and irrelevant information underlies a successful training system designed by A. M. Zimichev et al. in the 1980s; see, e.g., (Zimichev, Kreinovich, et al., 1982; Zimichev, Kreinovich, et al., 1982a; Aló and Kosheleva, 2006). This system started with an attempt to resolve the following seeming contradiction.

On the one hand, the vast majority of pedagogues strongly supports the humanitarian belief that (almost) students are equal in their ability to learn. Some students may require different learning styles, different support environments, but the history of education has consistently shown that any group originally perceived as inferior in learning – be it by gender or by race or by country of origin – turns out to be as successful as everyone else. Standardized tests consistently prove that kids from different groups have, on average, the same ability to learn. There are big discussions on whether 10% differences between scores are meaningful or not, but the very size of these disputed differences confirms the big pictures: we are all born equally skilled in learning.

Based on the fact that we are all equally skilled in learning, one should expect that with advanced learning strategies, all kids should succeed equally in school. Alas, no matter how advanced is the pedagogical technique that we use in the actual classroom, usually, after each class, there is a big difference between how much different kids learned, difference often in the orders of magnitude.

Since this difference cannot be explained by the difference in the kid's ability to learn, then why is it there? and, most importantly, how can we overcome this difference and enable each kid to learn according to his or her full potential?

To understand the empirically observed difference, researchers decided to quantify how much the students recalled. They asked each student, after the class, to spend an hour or so writing down what this student remembered after the class, be it the material from the class, what was happening outside, etc. Then, the researchers tried their best to quantify this amount of information by counting it in bits.

When they counted the number of bits *relevant* to the material presented in the class (e.g., math), they got exactly the same order of magnitude difference as was expected. Surprisingly, however, when they counted the *total* amount of information, including both the information presented in the class and the irrelevant information (what was the teacher dressed in, what birds were signing, what kids at neighboring desks were saying, etc.), then the total amounts of information recalled by all the kids became approximately the same.

In other words, both the best learners and the worst learners remembered approximately the same amount of information, but the best learners remembered the material presented in the class, while the worst learners remembered a lot of irrelevant details but not what was taught.

2. How to Estimate the Amount of Useful Information: A Suggestion

Main idea. According to decision theory, the usefulness of each situation to a user can be described by a *utility function* $u(x)$; see, e.g., (Fishburn, 1969; Raiffa, 1970; Luce and Raiffa, 1989; Nguyen et al., 2009).

Therefore, we propose to count the number of binary questions that are needed to determine each of the unknown variables with accuracy sufficient to determine the utility u with a given accuracy $\varepsilon > 0$.

From this viewpoint, if some variable is irrelevant, then it does not affect the utility at all, so we should not waste binary questions trying to find the value of this variable. If some variable is slightly relevant, then a very crude estimate of this variable will provide us with ε-accuracy in $u(x)$ – and therefore, few questions will be needed. On the other hand, if a variable is highly relevant, then we need exactly as many questions as before.

Let us transform this idea into a precise definition. Let us describe how this idea can be transformed into a precise definition.

We will start with the case when we have only one variable x, and then continue with the multi-D case.

Towards a precise definition: 1-D case. In the 1-D case, if we know x with uncertainty Δx, then the resulting values of the utility is known with the uncertainty

$$u(x + \Delta x) - u(x) \approx u'(x) \cdot \Delta x,$$

where $u'(x)$ denotes the derivative of the utility function. Thus, to get the desired accuracy ε in describing utility $u(x)$, we need to determine x with accuracy $\Delta x = \dfrac{\varepsilon}{|u'(x)|}$.

In this case, we divide the real line into intervals

$$\left[x_i - \frac{\varepsilon}{|u'(x_i)|}, x_i + \frac{\varepsilon}{|u'(x_i)|}\right],$$

where

$$x_{i+1} = x_i + \frac{2\varepsilon}{|u'(x_i)|},$$

and we want to find out to which of these intervals the actual value x belongs. For small ε, the probability p_i of belonging to the i-th interval is equal to

$$p_i \approx \rho(x_i) \cdot \Delta x_i = \rho(x_i) \cdot \frac{2\varepsilon}{|u'(x_i)|},$$

where we denote $\Delta x_i \stackrel{\text{def}}{=} x_{i+1} - x_i$.

Substituting this expression for p_i into the classical Shannon's formula, we get the following formula for the average number of questions $\overline{q}$:

$$\overline{q} = -\sum_{i=1}^{n} p_i \cdot \log_2(p_i) = -\sum_{i=1}^{n} \rho(x_i) \cdot \Delta x_i \cdot \log_2\left(\rho(x_i) \cdot \frac{2\varepsilon}{|u'(x_i)|}\right).$$

Using the fact that $\log(a \cdot b) = \log(a) + \log(b)$, we conclude that

$$\overline{q} = -\sum_{i=1}^{n} \rho(x_i) \cdot \Delta x_i \cdot \log_2\left(\frac{\rho(x_i)}{|u'(x_i)|}\right) - \sum_{i=1}^{n} \rho(x_i) \cdot \Delta x_i \cdot \log_2(2\varepsilon).$$

The first term in this sum has the form

$$-\sum_{i=1}^{n} \rho(x_i) \cdot \log_2\left(\frac{\rho(x_i)}{|u'(x_i|}\right) \cdot \Delta x_i,$$

i.e., it is an integral sum for the interval

$$-\int \rho(x) \cdot \log_2\left(\frac{\rho(x)}{|u'(x)|}\right) dx$$

and thus, for small ε, is practically equal to this interval.

Similarly to the traditional Shannon's entropy case, the second term is equal to $-\log_2(2\varepsilon)$.

Thus, the average number of binary questions $\overline{q}$ which is needed to determine the utility $u(x)$ with accuracy ε is equal to

$$\overline{q} = -\int \rho(x) \cdot \log_2\left(\frac{\rho(x)}{|u'(x)|}\right) dx - \log_2(2\varepsilon).$$

The first term in this expression does not depend on ε and thus, provides a good measure of how much uncertainty we have. Thus, we arrive at the following conclusion.

1-D case: conclusion. The average number of binary questions needed to determine the utility $u(x)$ with given accuracy $\varepsilon > 0$ is equal to $\overline{q} = S_u - \log_2(2\varepsilon)$, where

$$S_u \stackrel{\text{def}}{=} -\int \rho(x) \cdot \log_2\left(\frac{\rho(x)}{|u'(x)|}\right) dx.$$

Thus, this quantity S_u can be viewed as the amount of useful information.

By using the fact that $\log(a/b) = \log(a) - \log(b)$, we conclude that

$$S_u = S + \int \rho(x) \cdot \log_2(|u'(x)|)\, dx,$$

where S is the traditional Shannon's entropy. The additional integral term is the mathematical expectation of $\log_2(|u'(x)|)$.

Discussion. In the particular case when $u(x) = x$, determining the utility with accuracy ε is equivalent to finding x with accuracy ε, so the new expression coincides with the traditional Shannon's entropy formula.

The smaller the derivative $|u'(x)|$, the less relevant the variable x – and the smaller the additional term and, thus, the amount S_u of useful information.

Multi-D case. In the multi-D case, for each of the variables x_j $(1 \le j \le m)$, the interval that guarantees accuracy ε in the utility has the width

$$\Delta x_j = \frac{2\varepsilon}{|u_{,j}|},$$

where we denoted

$$u_{,j} \stackrel{\text{def}}{=} \frac{\partial u}{\partial x_j}.$$

Thus, we divide the whole m-dimensional space into zones of volume

$$\Delta V = \frac{(2\varepsilon)^m}{\prod\limits_{j=1}^{m} |u_{,j}|}$$

and probability

$$p_i = \rho(\vec{x}_i) \cdot \frac{(2\varepsilon)^m}{\prod\limits_{j=1}^{m} |u_{,j}(\vec{x}_i)|}.$$

Substituting these probabilities into the Shannon's formula, we conclude that

$$\overline{q} = -\int \rho(\vec{x}) \cdot \log_2 \left(\frac{\rho(\vec{x})}{\prod\limits_{j=1}^{m} |u_{,j}(\vec{x})|} \right) dx - \log_2(2\varepsilon).$$

Thus, as an amount of useful information, we can take the value

$$S_u = -\int \rho(\vec{x}) \cdot \log_2 \left(\frac{\rho(\vec{x})}{\prod\limits_{j=1}^{m} |u_{,j}(\vec{x})|} \right) d\vec{x}.$$

By using the formula $\log(a/b) = \log(a) - \log(b)$, we can reformulate this formula in the following form:

$$S_u = S + \sum_{i=1}^{m} \int \rho(\vec{x}) \cdot \log_2(|u_{,j}(\vec{x})|)\, d\vec{x},$$

where S is the traditional Shannon's entropy and each additional term is the expected value of $\log_2(|u_{,j}(\vec{x})|)$, where $u_{,j}(\vec{x})$ is the j-th partial derivative of the utility function $u(\vec{x})$.

What if only have partial information about the probabilities. The above formulas assume that we have a complete knowledge of the corresponding probabilities. Specifically, these formulas assume that for every point $\vec{x}$, we know the corresponding value $\rho(\vec{x})$ of the probability density function.

In practice, however, we only have partial information about the probabilities. Specifically, instead of the exact value $\rho(\vec{x})$, we only know a lower bound $\underline{\rho}(\vec{x})$ and an upper bound $\overline{\rho}(\vec{x})$ on the actual (unknown) value $\rho(\vec{x})$, i.e., we only know that the the value $\rho(\vec{x})$ belongs to the interval $[\underline{\rho}(\vec{x}), \overline{\rho}(\vec{x})]$.

Many different probability distributions are consistent with this interval information. For different such distributions, in general, we get different values for the amount S_u of useful information.

We do not know which of the distributions are more probable and which are less probable. Thus, we do not know which values of S_u are more probable and which are less probable. In such situations, it makes sense to characterize the uncertainty by the worst-case scenario, i.e., by the largest of the corresponding values S_u:

$$\overline{S}_u \stackrel{\text{def}}{=} \max\left\{S_u : \underline{\rho}(\vec{x}) \le \rho(\vec{x}) \le \overline{\rho}(\vec{x}) \text{ for all } x \text{ and } \int \rho(\vec{x})\, d\vec{x} = 1\right\}.$$

To compute this largest value, we can take into account that the objective function S_u is concave and the corresponding domain

$$\left\{\rho(\vec{x}) : \underline{\rho}(\vec{x}) \le \rho(\vec{x}) \le \overline{\rho}(\vec{x}) \text{ for all } x \text{ and } \int \rho(\vec{x})\, d\vec{x} = 1\right\}$$

is convex. Thus, to compute the maximum $\overline{S}_u$, we can use one of the efficient convex optimization algorithms; see, e.g., (Bertsekas, 2015).

Comment. Algorithms for computing a similar bound $\overline{S}$ for the traditional Shannon's entropy S under such intervl uncertainty are presented in (Kreinovich, 1996; Xiang et al., 2007; Nguyen et al., 2012).

Acknowledgements

This work was supported in part by the National Science Foundation grants HRD-0734825 and HRD-1242122 (Cyber-ShARE Center of Excellence) and DUE-0926721, and by an award "UTEP and Prudential Actuarial Science Academy and Pipeline Initiative" from Prudential Foundation.

The authors are thankful to the anonymous referees for valuable suggestions.

References

Aló, R. and O. Kosheleva. Optimization Techniques under Uncertain Criteria, and Their Possible Use in Computerized Education, *Proceedings of the 25th International Conference of the North American Fuzzy Information Processing Society NAFIPS'2006*, pages 593–598, Montreal, Quebec, Canada, June 3–6, 2006.

Bertsekas, D. P. *Convex Optimization Algorithms*, Atthena Scientific, Belmont, Massachusetts, 2015.

Chirayath, V., L. Longpré and V. Kreinovich. Measuring privacy loss in statistical databases, In: H. Leung and G. Pighizzini (Eds.), *Proceedings of the Workshop on Descriptional Complexity of Formal Systems DCFS'2006*, pages 16–25, Las Cruces, New Mexico, June 21–23, 2006.

Fishburn, P. C. *Utility Theory for Decision Making*, John Wiley & Sons Inc., New York, 1969.

Kreinovich, V. Maximum entropy and interval computations, *Reliable Computing*, 2(1):63–79, 1996.

Luce, R. D. and R. Raiffa. *Games and Decisions: Introduction and Critical Survey*, Dover, New York, 1989.

Nguyen, H. T., O. Kosheleva and V. Kreinovich. Decision making beyond Arrow's 'impossibility theorem', with the analysis of effects of collusion and mutual attraction, *International Journal of Intelligent Systems*, 24(1):27–47, 2009.

Nguyen, H. T., V. Kreinovich, B. Wu and G. Xiang. *Computing Statistics under Interval and Fuzzy Uncertainty*, Springer Verlag, Berlin, Heidelberg, 2012.

Raiffa, H. *Decision Analysis*, Addison-Wesley, Reading, Massachusetts, 1970.

Shannon, C. E. and W. Weaver. *The Mathematical Theory of Communication*, University of Illinois Press, Chicago, Illinois, 1971.

Xiang, G., M. Ceberio and V. Kreinovich. Computing Population Variance and Entropy under Interval Uncertainty: Linear-Time Algorithms, *Reliable Computing*, 13(6):467–488, 2007.

Zimichev, A. M., V. Kreinovich, et al. *Automatic control system for psychological experiments*, Final Report on Grant No. 0471-2213-20 from the Soviet Science Foundation, Russian, 1982.

Zimichev, A. M., V. Kreinovich, et al. *Automatic system for quick education of computer operators*, Final Report on Grant No. 0471-0212-60 from the Soviet Science Foundation, 1980–82, Russian.

Limitations of Realistic Monte-Carlo Techniques in Estimating Interval Uncertainty

Andrzej Pownuk, Olga Kosheleva, and Vladik Kreinovich
Computational Science Program
University of Texas at El Paso, El Paso, TX 79968, USA
{*ampownuk,olgak,vladik*}*@utep.edu*

Abstract: Because of the measurement errors, the result $\widetilde{y} = f(\widetilde{x}_1, \ldots, \widetilde{x}_n)$ of processing the measurement results $\widetilde{x}_1, \ldots, \widetilde{x}_n$ is, in general, different from the value $y = f(x_1, \ldots, x_n)$ that we would obtain if we knew the exact values $x_1, \ldots, x_n$ of all the inputs. In the linearized case, we can use numerical differentiation to estimate the resulting difference $\Delta y = \widetilde{y} - y$; however, this requires $> n$ calls to an algorithm computing f, and for complex algorithms and large n this can take too long. In situations when for each input x_i, we know the probability distribution of the measurement error, we can use a faster technique for estimating Δy – namely, Monte-Carlo simulation technique. A similar Monte-Carlo technique is also possible for the case of interval uncertainty, but the resulting simulation is not realistic: this technique uses Cauchy distributions which can result in arbitrarily small or arbitrarily large values, while we know that each measurement error $\Delta x_i = \widetilde{x}_i - x_i$ is located within the corresponding interval. In this paper, we prove that this non-realistic character of interval Monte-Carlo simulations is inevitable: namely, that no realistic Monte-Carlo simulation can provide a correct bound for Δy.

Keywords: Monte-Carlo techniques, interval uncertainty

1. Need to Gauge Uncertainty of the Result of Data Processing: A Brief Reminder

Need for data processing. One of the main objectives of science is to predict the future state of the world, i.e., to predict the future values of the quantities that describe this future state. To make these predictions, we need to know how each of these future values y depends on the current values $x_1, \ldots, x_n$ of the related quantities, i.e., we need to know an algorithm $y = f(x_1, \ldots, x_n)$ that relates y to x_i.

Once we find this information, we can then use the results $\widetilde{x}_1, \ldots, \widetilde{x}_n$ of measuring the quantities x_i to compute an estimate $\widetilde{y} = f(\widetilde{x}_1, \ldots, \widetilde{x}_n)$ for the desired future value y.

For example, to predict tomorrow's temperature in El Paso y, we need to know today's temperature, wind speed and direction, and humidity in different locations inside El Paso and near El Paso; these values $x_1, \ldots, x_n$ are what we can use for this prediction. We can then use an appropriate method for solving the corresponding partial differential equation as the desired prediction algorithm $y = f(x_1, \ldots, x_n)$.

The weather example shows that the corresponding prediction algorithms can be very complicated; thus, we need to use high-performance computers for this data processing.

Other situations when we need data processing come from the fact that we also want to know the current state of the world, i.e., we want to know the current values of all the quantities that describe this state. Some of these quantities – like temperature in El Paso – we can measure directly. Other quantities, such as the temperature or the density deep inside the Earth, are difficult or even impossible to measure directly. To find the values of each such difficult-to-measure quantity y, a natural idea is to find related easier-to-measure quantities $x_1, \ldots, x_n$ that are related to the desired quantity y by a known dependence $y = f(x_1, \ldots, x_n)$, and then use the results $\widetilde{x}_1, \ldots, \widetilde{x}_n$ of measuring x_i to compute an estimate $\widetilde{y} = f(\widetilde{x}_1, \ldots, \widetilde{x}_n)$ for y.

Need to take uncertainty into account when processing data. In general, data processing means applying some algorithm $f(x_1, \ldots, x_n)$ to the values of the quantities $x_1, \ldots, x_n$, resulting in a value $y = f(x_1, \ldots, x_n)$.

Values x_i usually come from measurements. Measurement are never absolutely accurate; the measurement result $\widetilde{x}_i$ is, in general, different from the actual (unknown) value x_i of the corresponding quantity: $\Delta x_i \stackrel{\text{def}}{=} \widetilde{x}_i - x_i \neq 0$; see, e.g., (Rabinovich, 2005).

Because of the this, the computed value $\widetilde{y} = f(\widetilde{x}_1, \ldots, \widetilde{x}_n)$ is, in general, different from the ideal value $y = f(x_1, \ldots, x_n)$.

It is therefore desirable to estimate the accuracy $\Delta y \stackrel{\text{def}}{=} \widetilde{y} - y$. To estimate Δy, we need to have some information about the measurement errors Δx_i.

What do we know about the measurement errors Δx_i: two main situations. Traditional engineering approach to estimating the uncertainty of the results of data processing assumes that we know the probability distribution of each measurement error Δx_i, and that the corresponding random variables are independent; see, e.g., (Rabinovich, 2005).

In many practical situations, it is assumed that each Δx_i is normally distributed with zero mean and known standard deviation σ_i, but other distributions are also possible. In such situations, our goal is to find the probability distribution for Δy.

In many other practical situations, however, we only know the upper bound Δ_i on the absolute value $|\Delta x_i|$ of the measurement error: $|\Delta x_i| \leq \Delta_i$. In such situations, the only information that we have about the (unknown) actual value x_i is that thus value belongs to the interval $\mathbf{x}_i = [\widetilde{x}_i - \Delta_i, \widetilde{x}_i + \Delta_i]$.

Different values x_i from these intervals can lead, in general, to different values of $y = f(x_1, \ldots, x_n)$. Our goal is then to find the range $\mathbf{y}$ of all possible values of y:

$$\mathbf{y} = \{f(x_1, \ldots, x_n) : x_1 \in \mathbf{x}_1, \ldots, x_n \in \mathbf{x}_n\}.$$

The problem of computing this range $\mathbf{y}$ is one of the main problems of *interval computations*; see, e.g., (Jaulin et al., 2001; Moore, Kearfott, and Cloud, 2009; Rabinovich, 2005).

Possibility of linearization. In many practical situations, the measurement errors are relatively small. These are the cases that we will consider in this paper.

In such cases, we can safely ignore terms which are quadratic or higher order in Δx_i, and conclude that (Rabinovich, 2005)

$$\Delta y = \sum_{i=1}^{n} c_i \cdot \Delta x_i, \tag{1}$$

where

$$c_i \stackrel{\text{def}}{=} \frac{\partial f}{\partial x_i}. \tag{2}$$

What we do in this paper: main idea. In this paper, we recall the known methods of estimating the interval $\mathbf{y}$ under the linearization assumptions. Specifically, there are two classes of such methods:

- methods that use analytical or numerical differentiation, and
- methods that use Monte-Carlo simulations.

The problem with the existing Monte-Carlo methods is that they are not realistic: namely,

- while we know that each variable x_i can only take values *inside* the corresponding interval $\mathbf{x}_i$,
- the simulated values x_i can take values *outside* the interval $\mathbf{x}_i$.

In this paper, we prove that this non-realistic character of interval Monte-Carlo simulations is inevitable: namely, that no realistic Monte-Carlo simulation can produce the correct result $\mathbf{y}$.

Structure of the paper. We start, in Section 2, with recalling the existing methods for computing the interval $\mathbf{y}$. The explanation of why Cauchy distribution is used in this simulation – and not any other distribution – is given in a special Appendix.

In Section 3, we explain the problem with the existing Monte-Carlo method: that the corresponding simulations are not realistic. To emphasize why this is a problem, we recall Monte-Carlo techniques for the case of probabilistic uncertainty – which are realistic.

Finally, in Sections 4 and 5, we prove our main result: that in the case of interval uncertainty, the use of non-realistic Monte-Carlo techniques is inevitable. Specifically:

- in Section 4, we prove this result under the additional assumption that the simulated values Δx_i are independent, and then,
- in Section 5, we extend this result to the most general case, when we allow dependence between the simulated random variables.

2. Existing Methods for Computing the Interval Range: Linearization Case

Towards an explicit formula for the desired interval $\mathbf{y}$. The expression (1) for Δy attains its largest value when each of the terms $c_i \cdot \Delta x_i$ attains its largest possible value.

Each of these terms is a linear function of Δx_i on the interval $[-\Delta_i, \Delta_i]$. When $c_i \geq 0$, this linear function is increasing and thus, it attains its largest possible value when Δx_i is the largest, i.e., when $\Delta x_i = \Delta_i$. The corresponding value of the term $c_i \cdot \Delta x_i$ is $c_i \cdot \Delta_i$.

When $c_i < 0$, the linear function $c_i \cdot \Delta x_i$ is decreasing and thus, it attains its largest possible value when Δx_i is the smallest, i.e., when $\Delta x_i = -\Delta_i$. The corresponding value of the term $c_i \cdot \Delta x_i$ is $c_i \cdot (-\Delta_i) = (-c_i) \cdot \Delta_i$.

In both cases, the largest possible value of each term $c_i \cdot \Delta x_i$ is equal to $|c_i| \cdot \Delta_i$. Thus, the largest possible value Δ of the sum (1) is equal to

$$\Delta = \sum_{i=1}^{n} |c_i| \cdot \Delta_i. \tag{3}$$

Similarly, one can show that the smallest possible value of the sum (1) is equal to $-\Delta$. Thus, the range of possible values of Δy is the interval $[-\Delta, \Delta]$, and the range $\mathbf{y}$ of possible values of $y = \widetilde{y} - \Delta y$ is equal to

$$\mathbf{y} = [\widetilde{y} - \Delta, \widetilde{y} + \Delta]. \tag{4}$$

Thus, once we have the result $\widetilde{y} = f(\widetilde{x}_1, \ldots, \widetilde{x}_n)$ of data processing, to compute the desired range $\mathbf{y}$, it is sufficient to be able to compute the value Δ.

Case of analytical differentiation. In some cases, we have explicit expressions – or efficient algorithms – for the partial derivatives (2). In such cases, to compute Δ, we can first compute these derivatives c_i, and then apply the formula (3).

Numerical differentiation: idea. In many practical situations, we do not have algorithms for computing the derivatives c_i. This happens, e.g., when we use proprietary software in our computations – in this case, we cannot use neither formula for differentiation, nor automatical differentiation tools.

In such situations, we can use the fact that we are under the linearization assumption that thus, that for each i and $h_i \neq 0$, we have

$$f(\widetilde{x}_1, \ldots, \widetilde{x}_{i-1}, \widetilde{x}_i + h_i, \widetilde{x}_{i+1}, \ldots, \widetilde{x}_n) \approx f(\widetilde{x}_1, \ldots, \widetilde{x}_{i-1}, \widetilde{x}_i, \widetilde{x}_{i+1}, \ldots, \widetilde{x}_n) + h_i \cdot c_i. \tag{5}$$

If we move the term $\widetilde{y} = f(\widetilde{x}_1, \ldots, \widetilde{x}_i, \widetilde{x}_{i-1}, \widetilde{x}_{i+1}, \ldots, \widetilde{x}_n)$ to the left-hand side of the formula (5) and divide both sides of the resulting approximate equality by h_i, we conclude that

$$c_i \approx \frac{f(\widetilde{x}_1, \ldots, \widetilde{x}_{i-1}, \widetilde{x}_i + h_i, \widetilde{x}_{i+1}, \ldots, \widetilde{x}_n) - \widetilde{y}}{h_i}. \tag{6}$$

This is a known formula for numerical differentiation.

By using this formula, we get the following method for computing Δ.

Numerical differentiation: algorithm. We select some values $h_i \neq 0$. Then, we compute the values

$$c_i = \frac{f(\widetilde{x}_1, \ldots, \widetilde{x}_{i-1}, \widetilde{x}_i + h_i, \widetilde{x}_{i+1}, \ldots, \widetilde{x}_n) - \widetilde{y}}{h_i}. \tag{7}$$

Finally, we plug in these values into the formula (3) and get the desired estimate for Δ.

Numerical differentiation: computation time. The above algorithm contains $n + 1$ calls to the original data processing algorithm f:

– one call to compute $\widetilde{y}$ and

– n calls to compute n partial derivatives $c_1, \ldots, c_n$.

As we have mentioned earlier, the data processing algorithm f itself can be very time-consuming. The same weather prediction example shows that the number n of input variables can also be large, in hundreds or even thousands. As a result, the computation time needed for the numerical differentiation method can be very large.

Need for a faster method: idea. Since the numerical differentiation method takes too long time, it is desirable to come up with a faster method for computing Δ and $\mathbf{y}$.

Such a method is indeed known; see, e.g., (Kreinovich and Ferson, 2004). This method is based on using Cauchy distribution, with the probability density function

$$\rho_\Delta(x) = \frac{\Delta}{\pi} \cdot \frac{1}{1 + \dfrac{x^2}{\Delta^2}}. \tag{8}$$

Specifically, there is a known result about this distribution: that

– when we have several independent random variables Δx_i distributed according to Cauchy distribution with parameter Δ_i,

– then their linear combination $\sum\limits_{i=1}^{n} c_i \cdot \Delta x_i$ is also Cauchy distributed, with parameter

$$\Delta = \sum_{i=1}^{n} |c_i| \cdot \Delta_i.$$

This is exactly the desired formula (3). Thus, we can find Δ as follows:

– first, we several times simulate the inputs $\Delta x_i^{(k)}$ according to the Cauchy distribution;

– then, we plug in the corresponding simulated values $x_i^{(k)} = \widetilde{x}_i - \Delta x_i^{(k)}$ into the data processing algorithm $f(x_1, \ldots, x_n)$, producing the values $y^{(k)} = f(x_1^{(k)}, \ldots, x_n^{(k)})$;

– then, the differences $\Delta y^{(k)} = \widetilde{y} - y^{(k)}$ are also Cauchy distributed, with the desired parameter Δ.

The desired value Δ can then be determined, e.g., by using the Maximum Likelihood method, i.e., from the condition that

$$L \stackrel{\text{def}}{=} \prod_{k=1}^{N} \rho_\Delta(\Delta y^{(k)}) = \prod_{k=1}^{N} \frac{\Delta}{\pi} \cdot \frac{1}{1 + \dfrac{(\Delta y^{(k)})^2}{\Delta^2}} \to \max \tag{9}$$

Maximizing the likelihood L is equivalent to minimizing its negative logarithm $\psi \stackrel{\text{def}}{=} -\ln(L)$. Differentiating L with respect to Δ and equating the derivative to 0, we get the following formula:

$$\sum_{k=1}^{N} \frac{1}{1+\dfrac{(\Delta y^{(k)})^2}{\Delta^2}} = \frac{N}{2}. \tag{10}$$

To find Δ from this equation, we can use, e.g., the bisection method. Thus, we arrive at the following algorithm.

Monte-Carlo method for estimating the interval uncertainty: algorithm. We select the number of iterations N. For each iteration $k = 1, \ldots, N$, we do the following:

- First, we simulate $\Delta x_i^{(k)}$ based on Cauchy with parameter Δ_i. We can do this, e.g., by computing $\Delta_i^{(k)} = \Delta_i \cdot \tan(\pi \cdot (r_{ik} - 0.5))$, where r_{ik} is the result of a standard random number generator that generates the numbers uniformly distributed on the interval $[0, 1]$.
- After that, we compute the difference

$$\Delta y^{(k)} \stackrel{\text{def}}{=} \widetilde{y} - f(\widetilde{x}_1 - \Delta x_1^{(k)}, \ldots, x_n - \Delta x_n^{(k)}). \tag{11}$$

Now, we can find Δ by using bisection to solve the equation (10). Specifically, we start with $\underline{\Delta} = 0$ and $\overline{\Delta} = \max\limits_{1 \le k \le N} |\Delta y^{(k)}|$. For $\Delta = \underline{\Delta}$, the left-hand side of the formula (10) is smaller than $N/2$, while for $\Delta = \overline{\Delta}$, this left-hand side is larger than $N/2$. Thus, if we want to get Δ with the desired accuracy ε, while $\overline{\Delta} - \underline{\Delta} > \varepsilon$, we do the following:

- we compute $\Delta_{\text{mid}} = \dfrac{\underline{\Delta} + \overline{\Delta}}{2}$;
- we check whether

$$\sum_{k=1}^{N} \frac{1}{1+\dfrac{\left(\Delta y^{(k)}\right)^2}{\Delta_{\text{mid}}^2}} < \frac{N}{2}; \tag{12}$$

- if this inequality is true, we replace $\underline{\Delta}$ with the new value Δ_{mid}, leaving $\overline{\Delta}$ unchanged;
- if this inequality is not true, we replace $\overline{\Delta}$ with the new value Δ_{mid}, leaving $\underline{\Delta}$ unchanged.

In both cases, on each iteration, the width of the interval $\left[\underline{\Delta}, \overline{\Delta}\right]$ becomes twice smaller. Thus, in s steps, we decrease this width by a factor of 2^s. So, in a few steps, we get the desired value Δ. For example, to get the width $\le 0.1\%$ of the original one, it is sufficient to perform only 10 iterations of the bisection procedure.

Monte-Carlo method: computation time. In the Monte-Carlo approach, we need $N + 1$ calls to the data processing algorithm f, where N is the number of simulations.

Good news is that, as in statistical methods in general, the needed number of simulation N is determined only by the desired accuracy ε and does not depend on the number of inputs n. For example, to find Δ with relative accuracy 20% and certainty 95% (i.e., in 95% of the cases), it is sufficient to take $n = 200$ (Kreinovich and Ferson, 2004).

Thus, when the number of inputs n of the data processing algorithm f is large, the Monte-Carlo method for estimating interval uncertainty is much faster than numerical differentiation.

3. Problem: The Existing Monte-Carlo Method is Not Realistic

Monte-Carlo method for the case of probabilistic uncertainty. To explain the problem with the existing Monte-Carlo method for interval uncertainty, let us recall the Monte-Carlo method for the case of probabilistic uncertainty.

This method is used when we know the probability distributions $\rho_i(x|Deltax_i)$ for each Δx_i, and we know that these random variables are independent. In this case, to find the desired distribution for Δy, we several times $k = 1, \ldots, N$, do the following:

- we simulate n variables $\Delta x_i^{(k)}$ according to the corresponding probability distribution $\rho_i(\Delta x_i)$;
- then we simulate $x_i^{(k)} = \widetilde{x}_i - \Delta x_i^{(k)}$ for each i;
- we apply the data processing algorithm $f(x_1, \ldots, x_n)$ to the simulated values, resulting in $y^{(k)} = f(x_1^{(k)}, \ldots, x_n^{(k)})$;
- finally, we compute $\Delta y^{(k)} = \widetilde{y} - y^{(k)}$.

One can easily check that these differences $\Delta y^{(k)}$ have the same distribution as Δy. So, we can determine the desired probability distribution from the sample $\Delta y^{(1)}$, $\ldots$, $\Delta y^{(N)}$.

Monte-Carlo method for the case of probabilistic uncertainty is realistic. The above Monte-Carlo method is *realistic* in the following sense:

- we know that each measurement error Δx_i is distributed according to the probability distribution $\rho_i(\Delta x_i)$, and
- this is exactly how we simulate the measurement errors: to simulate each value $\Delta_i^{(k)}$, we use the exact same distribution $\rho_i(\Delta x_i)$.

In contrast, the Monte-Carlo method for the case of interval uncertainty is not realistic. In the case of uncertainty, all we know is that the measurement errors are always located within the corresponding interval $[-\Delta_i, \Delta_i]$. We do not know how frequently measurement errors will be observed in different parts of this interval. In other words, we do not know the probability distribution of the measurement errors – we only know that this (unknown) probability distribution is located on the interval $[-\Delta_i, \Delta_i]$ *with probability 1.*

With this in mind, a *realistic* Monte-Carlo simulation would mean that for simulating the values $\Delta_i^{(k)}$, we select a probability distribution is located on the corresponding interval $[-\Delta_i, \Delta_i]$ with probability 1. Instead, the existing Monte-Carlo method for interval uncertainty uses Cauchy distribution – and it is known that for this distribution, for any interval, there is a non-zero probability to be outside this interval, and thus, the *probability* to be inside the interval $[-\Delta_i, \Delta_i]$ *is smaller than 1.*

A natural question. A natural question is:

- is this a limitation of the existing method, and an alternative realistic Monte-Carlo method is possible for the case of interval uncertainty,
- or this is a limitation of the problem, and no realistic Monte-Carlo method is possible for interval uncertainty.

What we do in this paper. In the two remaining sections, we prove that the non-realistic character of the existing Monte-Carlo method for interval uncertainty is a limitation of the problem. In other words, we prove that no realistic Monte-Carlo is possible for the case of interval uncertainty.

4. Proof That Realistic Interval Monte-Carlo Techniques Are Not Possible: Case of Independent Variables

To prove the desired result, it is sufficient to consider a simple case. To prove the desired impossibility result – that no realistic Monte-Carlo algorithm is possible that would *always* compute the desired range $\mathbf{y}$ – it is sufficient to prove that we cannot get the correct estimate for *one* specific function $f(x_1, \ldots, x_n)$.

As such a function, let us consider the simple function $f(x_1, \ldots, x_n) = x_1 + \ldots + x_n$. In this case, all the partial derivatives are equal to 1, i.e., $c_1 = \ldots = c_n = 1$ and thus,

$$\Delta y = \Delta x_1 + \ldots + \Delta x_n. \tag{13}$$

If we assume that each variables Δx_i takes value from the interval $[-\delta, \delta]$, then the range of possible values of the sum is $[-\Delta, \Delta]$, where $\Delta = n \cdot \delta$.

Analysis of the problem. Under Monte-Carlo simulations, we have

$$\Delta y^{(k)} = \Delta x_1^{(k)} + \ldots + \Delta x_n^{(k)}. \tag{14}$$

We assumed that the probability distributions corresponding to all i are independent.

Since the original problem is symmetric with respect to permutations, the corresponding distribution is also symmetric, so all $\Delta_i^{(k)}$ are identically distributed. Thus, the value Δy is the sum of several (n) independent identically distributed random variables.

It is known that due to the Central Limit Theorem (see, e.g., (Sheskin, 2011)), when n increases, the distribution of the sum tends to Gaussian. So, for large n, this distribution is close to Gaussian.

The Gaussian distribution is uniquely determined by its mean μ and variance $V = \sigma^2$. The mean of the sum is equal to the sum of the means, so $\mu = n \cdot \mu_0$, where μ_0 is the mean of the distribution used to simulate each Δx_i. For independent random variables, the variance of the sum is equal to the sum of the variances, so $V = n \cdot V_0$, where V_0 is the variance of the distribution used to simulate each Δx_i. Thus, $\sigma = \sqrt{V} = \sqrt{V_0} \cdot \sqrt{n}$.

It is well known that for a normal distribution, with very high confidence, all the values are contained in a k-sigma interval $[\mu - k \cdot \sigma, \mu + k \cdot \sigma]$:

- with probability $\approx 99.9\%$, the value will be in 3-sigma interval,
- with probability $\approx 1 - 10^{-8}$, the value will be in the 6-sigma interval, etc.

Thus, with high confidence, all the values obtained from simulation are contained in the interval $[\mu - k \cdot \sigma, \mu + k \cdot \sigma]$ of width $2k \cdot \sigma = 2k \cdot \sqrt{V_0} \cdot \sqrt{n}$.

For large n, this interval has the size $\text{const} \cdot \sqrt{n}$. On the other hand, we want the range $[-\Delta, \Delta]$ whose width is $2\Delta = 2\delta \cdot n$. So, when n is large, the simulated values occupy a part of the desired interval that tends to 0:

$$\frac{2k \cdot \sqrt{V_0} \cdot \sqrt{n}}{2\delta \cdot n} = \frac{\text{const}}{\sqrt{n}} \to 0. \tag{15}$$

So, in the independence case, the impossibility is proven.

5. Proof That Realistic Interval Monte-Carlo Techniques Are Not Possible: General Case

To prove the desired negative result, it is sufficient to consider a simple case. Similarly to the previous section, to prove the impossibility result in the *general* case, it is also sufficient to prove the impossibility for *some* of the functions.

In this proof, we will consider functions

$$f(x_1, \ldots, x_n) = s_1 \cdot x_1 + \ldots + s_n \cdot x_n, \tag{16}$$

where $s_i \in \{-1, 1\}$.

For each of these functions,

$$\Delta y = s_1 \cdot \Delta x_1 + \ldots + s_n \cdot \Delta x_n, \tag{17}$$

so we have $c_i = s_i$. Similarly to the previous section, we assume that each of the unknowns Δx_i takes value from the interval $[-\delta, \delta]$, for some known value $\delta > 0$.

For each of these functions, $|c_i| = |s_i| = 1$, so the desired range is the same for all these functions and is equal to $[-\Delta, \Delta]$, where

$$\Delta = \sum_{i=1}^{n} |c_i| \cdot \Delta_i = n \cdot \delta. \tag{18}$$

Towards a precise formulation of the problem. Suppose that we want to find the range $[-\Delta, \Delta]$ with some relative accuracy ε. To get the range from simulations, we need to make sure that some of the simulated results are ε-close to Δ, i.e., that

$$\left|\sum_{i=1}^{n} s_i \cdot \Delta x_i^{(k)} - n \cdot \delta\right| \le \varepsilon \cdot n \cdot \delta, \tag{19}$$

or, equivalently,

$$n \cdot \delta \cdot (1-\varepsilon) \le \sum_{i=1}^{n} s_i \cdot \Delta x_i^{(k)} \le n \cdot \delta \cdot (1+\varepsilon). \tag{20}$$

We are interested in realistic Monte-Carlo simulations, for which $|\Delta_i^{(k)}| \le \delta$ for all i. Thus, we always have

$$\sum_{i=1}^{n} s_i \cdot \Delta x_i^{(k)} \le n \cdot \delta < n \cdot \delta \cdot (1+\varepsilon). \tag{21}$$

So, the right-hand inequality is always satisfied, and it is thus sufficient to make sure that we have

$$\sum_{i=1}^{n} s_i \cdot \Delta x_i^{(k)} \ge n \cdot \delta \cdot (1-\varepsilon) \tag{22}$$

for some simulation k.

For this inequality to be true with some certainty, we need to make sure that the probability of this inequality exceed some constant $p > 0$. Then, if we run $1/p$ simulations, then with high probability, the inequality will be satisfied for at least one of these simulations. Thus, we arrive at the following condition.

Definition. *Let $\varepsilon > 0$, $\delta > 0$, and $p \in (0,1)$. We say that a probability distribution on the set of all vectors*

$$(\Delta_1 \ldots, \Delta x_n) \in [-\delta, \delta] \times \ldots \times [-\delta, \delta] \tag{23}$$

is a (p, ε)-realistic Monte-Carlo estimation of interval uncertainty *if for every set of values $s_i \in \{-1, 1\}$, we have*

$$\mathrm{Prob}(s_1 \cdot \Delta x_1 + \ldots + s_n \cdot \Delta x_n \ge n \cdot \delta \cdot (1-\varepsilon)) \ge p. \tag{24}$$

Main Result. *Let $\delta > 0$ and $\varepsilon > 0$. If for every n, we have a (p_n, ε)-realistic Monte-Carlo estimation of interval uncertainty, then $p_n \le \beta \cdot n \cdot c^n$ for some $\beta > 0$ and $c < 1$..*

Comments.

– As we have mentioned, when the probability is equal to p, we need $1/p$ simulations to get the desired estimates. Due to the Main Result, to get a realistic Monte-Carlo estimate for the interval uncertainty, we thus need

$$\frac{1}{p_n} \sim \frac{c^{-n}}{\beta \cdot n} \tag{25}$$

simulations. For large n, we have

$$\frac{c^{-n}}{\beta \cdot n} \gg n + 1. \tag{26}$$

Thus, the above results shows that realistic Monte-Carlo simulations require even more computational time than numerical differentiation. This defeats the main purpose for using Monte-Carlo techniques, which is – for our problem – to decrease the computation time.

– It is worth mentioning that if we allow p_n to be exponentially decreasing, then a realistic Monte-Carlo estimation of interval uncertainty is possible: e.g., we can take Δx_i to be independent and equal to δ or to $-\delta$ with equal probability 0.5. In this case, with probability 2^{-n}, we get the values $\Delta x_i = s_i \cdot \delta$ for which

$$\sum_{i=1}^{n} s_i \cdot \Delta x_i = \sum_{i=1}^{n} \delta = n \cdot \delta > n \cdot \delta \cdot (1 - \varepsilon). \tag{27}$$

Thus, for this probability distribution, for each combination of signs s_i, we have

$$\mathrm{Prob}(s_1 \cdot \Delta x_1 + \ldots + s_n \cdot \Delta x_n \geq n \cdot \delta \cdot (1 - \varepsilon)) = p_n = 2^{-n}. \tag{28}$$

Proof of the main result. Let us pick some $\alpha \in (0, 1)$. Let us denote, by m, the number of indices i or which $s_i \cdot \Delta x_i > \alpha \cdot \delta$. Then, if we have

$$s_1 \cdot \Delta x_1 + \ldots + s_n \cdot \Delta x_n \geq n \cdot \delta \cdot (1 - \varepsilon), \tag{29}$$

then for $n - m$ indices, we have $s_i \cdot \Delta x_i \leq \alpha \cdot \delta$ and for the other m indices, we have $s_i \cdot \Delta x_i \leq \delta$. Thus,

$$n \cdot \delta \cdot (1 - \varepsilon) \leq \sum_{i=1}^{n} s_i \cdot \Delta x_i \leq m \cdot \delta + (n - m) \cdot \alpha \cdot \delta. \tag{30}$$

Dividing both sides of this inequality by δ, we get

$$n \cdot (1 - \varepsilon) \leq m + (n - m) \cdot \alpha, \tag{31}$$

hence $n \cdot (1 - \alpha - \varepsilon) \leq m \cdot (1 - \alpha)$ and thus,

$$m \geq n \cdot \frac{1 - \alpha - \varepsilon}{1 - \alpha}. \tag{32}$$

So, we have at least

$$n \cdot \frac{1 - \alpha - \varepsilon}{1 - \alpha} \tag{33}$$

indices for which Δx_i has the same sign as s_i (and for which $|\Delta x_i| > \alpha \cdot \delta$). This means that for the vector corresponding to a tuple $(s_1, \ldots, s_n)$, at most

$$n \cdot \frac{\varepsilon}{1 - \alpha - \varepsilon} \tag{34}$$

indices have a different sign than s_i.

It is, in principle, possible that the same tuple $(\Delta x_1, \ldots, \Delta x_n)$ can serve two different tuples $s = (s_1, \ldots, s_n)$ and $s' = (s'_1, \ldots, s'_n)$. However, in this case:

– going from s_i to $\text{sign}(\Delta x_i)$ changes at most $n \cdot \dfrac{\varepsilon}{1-\alpha-\varepsilon}$ signs, and

– going from $\text{sign}(\Delta x_i)$ to s'_i also changes at most $n \cdot \dfrac{\varepsilon}{1-\alpha-\varepsilon}$ signs.

Thus, between the tuples s and s', at most $2 \cdot \dfrac{\varepsilon}{1-\alpha-\varepsilon}$ signs are different. In other words, for the Hamming distance

$$d(s, s') \stackrel{\text{def}}{=} \#\{i : s_i \neq s'_i\}, \tag{35}$$

we have

$$d(s, s') \leq 2 \cdot n \cdot \frac{\varepsilon}{1-\alpha-\varepsilon}. \tag{36}$$

Thus, if

$$d(s, s') > 2 \cdot n \cdot \frac{\varepsilon}{1-\alpha-\varepsilon}, \tag{37}$$

then no tuples $(\Delta x_1, \ldots, \Delta x_n)$ can serve both sign tuples s and s'. In this case, the corresponding sets of tuples for which

$$s_1 \cdot \Delta x_1 + \ldots + s_n \cdot \Delta x_n \geq n \cdot \delta \cdot (1-\varepsilon) \tag{38}$$

and

$$s'_1 \cdot \Delta x_1 + \ldots + s'_n \cdot \Delta x_n \geq n \cdot \delta \cdot (1-\varepsilon) \tag{39}$$

do not intersect. Hence, the probability that the randomly selected tuple belongs to one of these sets is equal to the sum of the corresponding probabilities. Since each of the probabilities is greater than or equal to p, the resulting probability is equal to $2p$.

If we have M sign tuples $s^{(1)}, \ldots, s^{(M)}$ for which

$$d(s^{(i)}, s^{(j)}) > 2 \cdot \frac{\varepsilon}{1-\alpha-\varepsilon} \tag{40}$$

for all $i \neq j$, then similarly, the probability that the tuple $(\Delta x_1, \ldots, \Delta x_n)$ serves one of these sign tuples is greater than or equal to $M \cdot p$. On the other hand, this probability is ≤ 1, so we conclude that $M \cdot p \leq 1$ and $p \leq \dfrac{1}{M}$.

So, to prove that p_n is exponentially decreasing, it is sufficient to find the sign tuples whose number M is exponentially increasing.

Let us denote $\beta \stackrel{\text{def}}{=} \dfrac{\varepsilon}{1-\alpha-\varepsilon}$. Then, for each sign tuple s, the number t of all sign tuples s' for which $d(s, s') \leq \beta \cdot n$ is equal to the sum of:

– the number of tuples $\binom{n}{0}$ that differ from s in 0 places,

– the number of tuples $\binom{n}{1}$ that differ from s in 1 place, ...,

– the number of tuples $\binom{n}{\beta \cdot n}$ that differ from s in $\beta \cdot n$ places,

i.e.,

$$t = \binom{n}{0} + \binom{n}{1} + \ldots + \binom{n}{n \cdot \beta}. \tag{41}$$

When $\beta < 0.5$ and $\beta \cdot n < \dfrac{n}{2}$, the number of combinations $\binom{n}{k}$ increases with k, so $t \le \beta \cdot n \cdot \binom{n}{\beta \cdot n}$. Here,

$$\binom{a}{b} = \frac{a!}{b! \cdot (a-b)!}. \tag{42}$$

Asymptotically,

$$n! \sim \left(\frac{n}{e}\right)^n, \tag{43}$$

so

$$t \le \beta \cdot n \cdot \frac{\left(\dfrac{n}{e}\right)^n}{\left(\dfrac{\beta \cdot n}{e}\right)^{\beta \cdot n} \cdot \left(\dfrac{(1-\beta) \cdot n}{e}\right)^{(1-\beta) \cdot n}}. \tag{44}$$

One can see that the term n^n in the numerator cancels with the term $n^{\beta \cdot n} \cdot n^{(1-\beta) \cdot n} = n^n$ in the denominator. Similarly, the terms e^n and $e^{\beta \cdot n} \cdot e^{(1-\beta) \cdot n} = e^n$ cancel each other, so we conclude that

$$t \le \beta \cdot n \cdot \left(\frac{1}{\beta^\beta \cdot (1-\beta)^{1-\beta}}\right)^n. \tag{45}$$

Here,

$$\gamma \stackrel{\text{def}}{=} \frac{1}{\beta^\beta \cdot (1-\beta)^{1-\beta}} = \exp(S), \tag{46}$$

where

$$S \stackrel{\text{def}}{=} -\beta \cdot \ln(\beta) - (1-\beta) \cdot \ln(1-\beta) \tag{47}$$

is Shannon's entropy. It is well known (and easy to check by differentiation) that its largest possible values is attained when $\beta = 0.5$, in which case $S = \ln(2)$ and $\gamma = \exp(S) = 2$. When $\beta < 0.5$, we have $S < \ln(2)$, thus, $\gamma < 2$, and $t \le \beta \cdot n \cdot \gamma^n$ for some $\gamma < 2$.

Let us now construct the desired collection of sign tuples $s^{(1)}$, ..., $s^{(M)}$.

- We start with some sign tuple $s^{(1)}$, e.g., $s^{(1)} = (1, \ldots, 1)$.
- Then, we dismiss $t \le \gamma^n$ tuples which are $\le \beta$-close to s, and select one of the remaining tuples as $s^{(2)}$.
- We then dismiss $t \le \gamma^n$ tuples which are $\le \beta$-close to $s^{(2)}$. Among the remaining tuples, we select the tuple $s^{(3)}$, etc.

Once we have selected M tuples, we have thus dismissed $t \cdot M \le \beta \cdot n \cdot \gamma^n \cdot M$ sign tuples. So, as long as this number is smaller than the overall number 2^n of sign tuples, we can continue selecting.

This procedure ends when we have selected M tuples for which $\beta \cdot n \cdot \gamma^n \cdot M \geq 2^n$. Thus, we have selected

$$M \geq \left(\frac{2}{\gamma}\right)^n \cdot \frac{1}{\beta \cdot n} \tag{48}$$

tuples. So, we have indeed selected exponentially many tuples.

Hence,

$$p_n \leq \frac{1}{M} \leq \beta \cdot n \cdot \left(\frac{\gamma}{2}\right)^n, \tag{49}$$

i.e.,

$$p_n \leq \beta \cdot n \cdot c^n, \tag{50}$$

where

$$c \stackrel{\text{def}}{=} \frac{\gamma}{2} < 1. \tag{51}$$

So, the probability p_n is indeed exponentially decreasing. The main result is proven.

Acknowledgements

This work was supported in part by the National Science Foundation grants HRD-0734825 and HRD-1242122 (Cyber-ShARE Center of Excellence) and DUE-0926721, and by an award "UTEP and Prudential Actuarial Science Academy and Pipeline Initiative" from Prudential Foundation.

The authors are thankful to Sergey Shary and to the anonymous referees for their valuable suggestions.

References

Aczél, J. *Lectures on Functional Equations and Their Applications*, Dover, New York, 2006.

Jaulin, L., M. Kieffer, O. Didrit and E. Walter. *Applied Interval Analysis*, Springer, London, 2001.

Kreinovich, V. and S. Ferson. A new Cauchy-based black-box technique for uncertainty in risk analysis, *Reliability Engineering and Systems Safety*, 85(1–3):267–279, 2004.

Moore, R. E., R. B. Kearfott and M. J. Cloud. *Introduction to Interval Analysis*, SIAM Press, Philadelphia, Pennsylvania, 2009.

Rabinovich, S. G. *Measurement Errors and Uncertainty. Theory and Practice*, Springer Verlag, Berlin, 2005.

Sheskin, D. J. *Handbook of Parametric and Nonparametric Statistical Procedures*, Chapman and Hall/CRC, Boca Raton, Florida, 2011.

Appendix

A. Why Cauchy Distribution

Formulation of the problem. We want to find a family of probability distributions with the following property:

- when we have several independent variables $X_1, \ldots, X_n$ distributed according to a distribution with this family with parameters $\Delta_1, \ldots, \Delta_n$,
- then each linear combination $Y = c_1 \cdot X_1 + \ldots + c_n \cdot X_n$ has the same distribution as $\Delta \cdot X$, where X corresponds to parameter 1, and $\Delta = \sum\limits_{i=1}^{n} |c_i| \cdot \Delta_i$.

In particular, for the case when $\Delta_1 = \ldots = \Delta_n = 1$, the problem becomes even easier to describe, since then, we only need to find *one* probability distribution: corresponding to the value 1. In this case, the desired property of this probability distribution is as follows:

- if we have n independent identically distributed random variables $X_1, \ldots, X_n$,
- then each linear combination $Y = c_1 \cdot X_1 + \ldots + c_n \cdot X_n$ has the same distribution as $\Delta \cdot X_i$, where $\Delta = \sum\limits_{i=1}^{n} |c_i|$.

Let us describe all probability distributions that satisfy this property.

Analysis of the problem. First, we observe that from the above condition, for $n = 1$ and $c_1 = -1$, we conclude that $-X$ and X should have exactly the same probability distribution, i.e., that the desired probability distribution be symmetric with respect to 0 (even).

A usual way to describe a probability distribution is to use a probability density function $\rho(x)$, but often, it is more convenient to use its Fourier transform, i.e., in probabilistic terms, the *characteristic function* $\chi_X(\omega) \stackrel{\text{def}}{=} E[\exp(\mathrm{i} \cdot \omega \cdot X)]$, where $E[.]$ indicates the expected value of the corresponding quantity and $\mathrm{i} \stackrel{\text{def}}{=} \sqrt{-1}$.

The advantage of using a characteristic function is that for the sum $S = X_1 + X_2$ of two independent variables $X_1 + X_2$, we have

$$\chi_S(\omega) = E[\exp(\mathrm{i} \cdot \omega \cdot S)] = E[\exp(\mathrm{i} \cdot \omega \cdot (X_1 + X_2)] = E[\exp(\mathrm{i} \cdot \omega \cdot X_1 + \mathrm{i} \cdot \omega \cdot X_2)] =$$

$$E[\exp(\mathrm{i} \cdot \omega \cdot X_1) \cdot \exp(\mathrm{i} \cdot \omega \cdot X_2)]. \tag{51}$$

Since X_1 and X_2 are independent, the variables $\exp(\mathrm{i} \cdot \omega \cdot X_1)$ and $\exp(\mathrm{i} \cdot \omega \cdot X_2)$ are also independent, and thus,

$$\chi_S(\omega) = E[\exp(\mathrm{i} \cdot \omega \cdot X_1) \cdot \exp(\mathrm{i} \cdot \omega \cdot X_2)] = E[\exp(\mathrm{i} \cdot \omega \cdot X_1)] \cdot E[\exp(\mathrm{i} \cdot \omega \cdot X_2)] = \chi_{X_1}(\omega) \cdot \chi_{X_2}(\omega). \tag{52}$$

Similarly, for a linear combination $Y = \sum\limits_{i=1}^{n} c_i \cdot X_i$, we have

$$\chi_Y(\omega) = E[\exp(\mathrm{i}\cdot\omega\cdot Y)] = E\left[\exp\left(\mathrm{i}\cdot\omega\cdot\sum_{i=1}^{n} c_i\cdot X_i\right)\right] = E\left[\exp\left(\sum_{i=1}^{n}\mathrm{i}\cdot\omega\cdot c_i\cdot X_i\right)\right] =$$

$$E\left[\prod_{i=1}^{n}\exp\left(\mathrm{i}\cdot\omega\cdot c_i\cdot X_i\right)\right] = \prod_{i=1}^{n} E[\exp(\mathrm{i}\cdot(\omega\cdot c_i)\cdot X_i] = \prod_{i=1}^{n}\chi_X(\omega\cdot c_i). \tag{53}$$

The desired property is that the linear combination Y should have the same distribution as $\Delta\cdot X$. Thus, the characteristic function $\chi_Y(\omega)$ should be equal to the characteristic function of $\Delta\cdot X$, i.e., to

$$\chi_{\Delta\cdot X}(\omega) = E[\exp(\mathrm{i}\cdot\omega\cdot(\Delta\cdot X))] = E[\exp(\mathrm{i}\cdot(\omega\cdot\Delta)\cdot X)] = \chi_X(\omega\cdot\Delta). \tag{54}$$

By comparing expressions (53) and (54), we conclude that for all possible combinations $c_1,\ldots,c_n$, the desired characteristic function $\chi_X(\omega)$ should satisfy the equality

$$\chi_X(c_1\cdot\omega)\cdot\ldots\cdot\chi_X(c_n\cdot\omega) = \chi_X((|c_1|+\ldots+|c_n|)\cdot\omega). \tag{55}$$

In particular, for $n=1$, $c_1=-1$, we get $\chi_X(-\omega)=\chi_X(\omega)$, so $\chi_X(\omega)$ should be an even function. For $n=2$, $c_1>0$, $c_2>0$, and $\omega=1$, we get

$$\chi_X(c_1+c_2) = \chi_X(c_1)\cdot\chi_X(c_2). \tag{56}$$

The characteristic function should be measurable, and it is known that the only measurable function with the property (56) has the form $\chi_X(\omega)=\exp(-k\cdot\omega)$ for some k; see, e.g., (Aczél, 2006). Due to evenness, for a general ω, we get $\chi_X(\omega)=\exp(-k\cdot|\omega|)$. By applying the inverse Fourier transform, we conclude that X is Cauchy distributed.

Conclusion. The only distribution for which the independent-case Monte Carlo simulations lead to correct estimate of the interval uncertainty is the Cauchy distribution.

Voting Aggregation Leads to (Interval) Median

Olga Kosheleva[1] and Vladik Kreinovich[2]
[1] *Department of Teacher Education, University of Texas at El Paso, El Paso, TX 79968, USA, olgak@utep.edu*
[2] *Department of Computer Science, University of Texas at El Paso, El Paso, TX 79968, USA, vladik@utep.edu*

Abstract: When we have several results of measuring or estimating the same quantities, it is desirable to aggregate them into a single estimate for the desired quantities. A natural requirement is that if the majority of estimates has some property, then the aggregate estimate should have the same property. It turns out that it is not possible to require this for *all* possible properties – but we can require it for *bounds*, i.e., for properties that the value of the quantity is in between given bounds a and b. In this paper, we prove that if we restrict the above "voting" approach to such properties, then the resulting aggregate is an (interval) median. This result provides an additional justification for the use of median – in addition to the usual justification that median is the most robust aggregate operation.

Keywords: aggregation, voting aggregation, median, interval median

1. Formulation of the Problem

Need for aggregation. For many real-real problems, there are several different decision making tools. Each of these tools has its advantages and its limitations (otherwise, if a tool does not have any advantages, it would not be used). To combine the advantages of different tools, it therefore desirable to aggregate their results.

Voting as a natural approach to aggregation. One of the most widely used methods of aggregating several results is voting: if the majority of results satisfy a certain property, then we conclude that the actual value has this property; see, e.g., (Easley and Kleinberg, 2010; Regenwetter, 2009; Tang, 2015) and references therein.

For example, in a medical classification problem, if most classifiers classify the person's data as corresponding to pneumonia, we conclude that this person has pneumonia.

What we do in this paper. In this paper, we analyze how voting can be used to aggregate several numerical estimates.

This is not easy. To understand why this task is not easy, let us recall that a similar idea has been actively used in Artificial Intelligence.

Voting is closely related to the notions of "typical" in Artificial Intelligence. Voting is closely related to the notion of a "typical" object of a class, the notion actively studied in Artificial

Intelligence. Indeed, what is an intuitive meaning of a term "typical professor"? A natural meaning is that if most professors have some property, that a "typical" professor must have this property. For example, if most professors are absent-minded, then we expect a "typical" professor to be absent-minded as well.

If we know that a certain professor is a "typical" professor – or, in other words, not an abnormal professor – then whatever property normally holds for professors should hold for this particular professor as well. This line of reasoning is known as *non-monotonic reasoning*, and it is very important in Artificial Intelligence; see, e.g., (Halpern, 2003; Jalal-Kamai et al., 2012; Kreinovich, 2004; Kreinovich, 2012; Longpré and Kosheleva, 2012).

Related problem: no one is perfectly typical. This analogy can help us illustrate the problem related to the voting approach: while some professors may be *more or less* typical, no one is *absolutely* typical. For example, even if it turns out that we have found a professor who is typical (in the voting sense) in his/her appearance, in his/her habits, this professor's specific area of research – no matter what it is – will automatically make this professor not typical.

Indeed, it could be theoretical physics – but clearly, most professors are *not* theoretical physicists. It could be computational linguistics – but most professor are *not* computational linguists, etc.

This problem is why in Artificial Intelligence, there is a vast and ongoing literature analyzing how best to describe typical (not abnormal) objects.

2. Main Definitions and the First Result Explaining Why Voting Aggregation Is Not Easy

What is given. In the simplest case, we have several estimates $x_1, \ldots, x_n$ for the value of some physical quantity. We would like to combine these estimates into a single estimate x.

In more complex situations, we have several quantities that we would like to estimate. Let us denote the number of these quantities by q. In this case, we have several tuples $x_1, \ldots, x_n$, each of which estimates all q quantities: $x_i = (x_{i1}, \ldots, x_{iq})$. Our goal is to aggregate these estimates into a single estimate $x = (e_1, \ldots, e_q)$.

Let us describe voting aggregation in precise terms. Both for the 1-D case and for the multi-D case, we would like to select an estimate x that satisfies the following condition:

if the majority of the inputs $x_1, \ldots, x_n$ satisfies a property P,
then x should satisfy this property.

In mathematics, properties are usually described by sets: namely, each property P can be described by the set S of all the objects that satisfy this property. In these terms, the above condition takes the following form:

if the majority of the inputs $x_1, \ldots, x_n$ belong to a set S,
then x should belongs to this same set S.

In principle, we can formulate this condition for *all* possible sets, but in this case, as we have mentioned earlier, there may not exist any aggregate x that satisfies this property. Thus, it make

sense to consider the possibility of restricting this condition only to sets S from a certain class $\mathcal{S}$ of sets. So, we arrive at the following definition.

Definition 1. *Let $q \geq 1$, let $\mathcal{S}$ be a class of subsets of $\mathbb{R}^q$, and let $x_1, \ldots, x_n \in \mathbb{R}^q$.*

- *We say that an element $x \in \mathbb{R}^q$ is a* possible $\mathcal{S}$-aggregate *of the elements $x_1, \ldots, x_n$ if the following condition holds:*

  for every $S \in \mathcal{S}$, if the majority of x_i are in this set, then x should be in this set.

- *The set of all possible $\mathcal{S}$-aggregates is called the* $\mathcal{S}$-aggregate *of the elements $x_1, \ldots, x_n$.*

Let us first consider the case when we allow all properties (i.e., all sets). Let us first consider the case when we allow all possible sets $S \subseteq \mathbb{R}^q$, i.e., when $\mathcal{S}$ is equal to the class $U \stackrel{\text{def}}{=} 2^{\mathbb{R}^q}$ of *all* subsets of $\mathbb{R}^q$. In this case, as the following result shows, voting aggregation does not work – since the result set is often empty:

Proposition 1. *For every $q \geq 1$ and $n \geq 3$, if all n elements $x_1, \ldots, x_n$ are different from each other, then the U-aggregate of the elements $x_1, \ldots, x_n$ is empty.*

Proof. We will prove this by contradiction.

1°. Let us assume that the U-aggregate set is not empty. This means that there is an element x which is a possible U-aggregate of $x_1, \ldots, x_n$.

2°. All elements x_i belong to the set $\{x_1, \ldots, x_n\}$; thus, the majority of elements x_i belongs to this set as well. So, by definition of a possible aggregate, x should belong to this set. Thus, we must have $x = x_i$ for some i.

3°. Let us now consider the set of all the elements $x_1, \ldots, x_n$ except for the element x_i, i.e., the set $\{x_1, \ldots, x_{i-1}, x_{i+1}, \ldots, x_n\}$. Out of n elements $x_1, \ldots, x_n$, $n-1$ belong to this set. Since $n \geq 3$, these elements constitute the majority. Thus, by definition of a possible aggregate, the element x should belong to this new set – but since $x = x_i$, it doesn't.

This contradiction proves that the U-aggregate set is indeed empty.

Let us describe all the cases when the U-aggregate set is not empty. We can actually describe all the cases when the U-aggregate set is not empty, and explicitly describe how this aggregate set looks like. We will start with the cases $n = 1$ and $n = 2$ and then consider cases when $n \geq 3$.

Proposition 2. *For every $q \geq 1$:*

- *when $n = 1$ then the U-aggregate set of x_1 is $\{x_1\}$;*
- *when $n = 2$, then the U-aggregate set of x_1, x_2 is $\{x_1, x_2\}$.*

Proof.

1°. For $n \le 2$, the *majority* of x_i means *all* the elements x_i. Thus, the above condition means that for every set S, if $x_i \in S$ for all i, then we should have $x \in S$. This is trivially true for all elements x_i, so all elements x_i are indeed possible U-aggregates of $x_1, \ldots, x_n$.

2°. To complete the proof, let us show that no other elements are possible U-aggregates. Indeed, if x is a possible U-aggregate, then for the set $S = \{x_1, \ldots, x_n\}$, we have $x_i \in S$ for all i, and thus, we should have $x \in S$. So, x must indeed coincide with one of the elements x_i.

The proposition is proven.

Proposition 3. *For every $q \ge 1$ and for all odd $n \ge 3$:*

- *if the majority of elements $x_1, \ldots, x_n$ are equal to each other, then the U-aggregate set of $x_1, \ldots, x_n$ consists of this common element;*
- *in all other cases, the U-aggregate set is empty.*

Proof.

1°. Let us first consider the case when the majority of elements x_i are equal to each other.

1.1°. Without losing generality, we can assume that these elements are $x_1 = \ldots = x_k$ for some $k > n/2$. In this case, the majority of elements x_i belong to the set $\{x_1\}$. Thus, every possible U-aggregate x must belong to this set, and hence, x must be equal to x_1.

1.2°. Let us now prove that the element x_1 is a possible U-aggregate.

Indeed, if the majority of elements x_i belong to the set S, this means that at least some of the elements $x_1, \ldots, x_k$ must belong to this set – otherwise, we would not have a majority. Since the element x is equal to all of them, x belongs to this set S as well. Thus, x_1 is indeed a possible U-aggregate.

2°. Let us now consider the case when we do not have a majority of elements that are equal to each other. Let us show that in this case, the U-aggregate set is indeed empty.

Indeed, let x be a possible U-aggregate set. Since all elements x_i (and, thus, the majority of them) belong to the set $\{x_1, \ldots, x_n\}$, this implies that we should have $x \in \{x_1, \ldots, x_n\}$, i.e., x must be equal to one of the original inputs: $x = x_i$ for some i.

Since we do not have a majority of elements that are equal to each other, there are fewer than $n/2$ elements which are equal to x_i. Thus, the majority of elements $x_1, \ldots, x_n$ belong to the difference set $\{x_1, \ldots, x_n\} - \{x_i\}$. So, by the definition of a possible U-aggregation, the possible U-aggregate x should also belong to this set – but since $x = x_i$, it doesn't.

The contradiction proves that in this case, the U-aggregate set is indeed empty.

Proposition 4. *For every $q \ge 1$ and for all even $n \ge 4$:*

- *if the majority of elements $x_1, \ldots, x_n$ are equal to each other, then the U-aggregate set of $x_1, \ldots, x_n$ consists of this common element;*

- *if half of the elements $x_1, \ldots, x_n$ are equal to an element a, and the other half is equal to another element b, then the U-aggregate set is equal to $\{a, b\}$;*
- *if exactly half of the elements $x_1, \ldots, x_n$ is equal to an element a, and not all other elements are equal to each other, then the U-aggregate set is equal to $\{a\}$;*
- *in all other cases, the U-aggregate set is empty.*

Proof. The first and the last cases are proven in exactly the same way as in the proof of Proposition 3. Let us therefore consider the remaining two cases.

1°. Let us first consider the case when half of the elements $x_1, \ldots, x_n$ are equal to an element a, and the other half is equal to another element b.

1.1°. In this case, all elements x_i belongs to the set $\{a, b\}$. Thus, a possible U-aggregate x should also belong to this set. Thus, it should be equal either to a or to b.

1.2°. To complete the proof for this case, we need to prove that both a and b are indeed possible U-aggregates.

Indeed, if the majority of the elements x_i belong to a set S, then it cannot be only elements which are equal to a, since they do not form the majority. Thus, the set S must contain at least one element equal to b – i.e., we must have $b \in S$.

Similarly, if the majority of the elements x_i belong to a set S, then it cannot be only elements which are equal to b, since they do not form the majority. Thus, the set S must contain at least one element equal to a – i.e., we must have $a \in S$. So, indeed, both a and b are possible U-aggregates.

So, for this case, the proposition is proven.

2°. Let us now consider the case when exactly half of the elements $x_1, \ldots, x_n$ are equal to an element a, and not all other elements are equal to each other.

Without losing generality, we can describe this case as $x_1 = \ldots = x_{n/2} = a$, and $x_i \neq a$ for $i > n/2$.

Since not all elements x_i, $i > n/2$, are equal to each other, there is an element x_j which is different from $x_{n/2+1}$ (and both are different from a).

2.1°. Let us first prove that every U-aggregate element x must be equal to a.

Indeed, in this case, at least $n/2 + 1$ (majority) of elements x_i belong to the set $\{a, x_{n/2+1}\}$, so, for every U-aggregate x, we must have $x \in \{a, x_{n/2+1}\}$. Thus, x should be either equal to a or to $x_{n/2+1}$.

Similarly, at least $n/2 + 1$ (majority) of elements x_i belong to the set $\{a, x_j\}$, so, for every U-aggregate x, we must have $x \in \{a, x_j\}$. Thus, x should be either equal to a or to x_j.

Since we have selected x_j for which $x_j \neq x_{n/2+1}$, the condition that $x = a$ or $x = x_j$ is not satisfied when $x = x_{n/2+1}$. Thus, the option $x = x_{n/2+1}$ is not possible.

So, we conclude that, indeed, every U-aggregate element x must be equal to a.

2.2°. To complete the proof, let us show that the element a is indeed a possible U-aggregate.

Indeed, if the majority of elements $x_1, \ldots, x_n$ belong to a set S, this cannot be only elements different from a, since they do not form a majority. Thus, at least one of the elements equal to a must also belong to the set S, i.e., we should have $a \in S$. Thus, a is indeed a possible U-aggregate.

Discussion. Since in general, considering all the sets does not lead to a meaningful aggregation, we have to only allow sets from a certain family.

Structure of the paper. Let us start with considering all possible intervals. In Section 3, we analyze the 1-D case. In this case, as we will show, voting aggregation results in a median. In Section 4, we show that in the 1-D case, we cannot expand beyond intervals.

In Section 5, we extend the interval result to a multi-D case – and we also show that we cannot extend beyond multi-D intervals.

3. 1-D Interval-Based Voting Aggregation Leads to (Interval) Median

Let us first clarify what we mean by intervals.

Definition 2. *By an* interval*, we mean a finite closed interval* $[a, b] = \{x : a \le x \le b\}$ *corresponding to real numbers* $a \le b$*. The class of all interval will be denoted by* I*.*

Now, we need to clarify what we mean by a median.

Definition 3. *For every sequence of real numbers* $x_1, \ldots, x_n$*, let* $x_{(1)} \le \ldots \le x_{(n)}$ *denote the result of sorting the numbers* x_i *in increasing order.*

- *when* n *is odd, i.e., when* $n = 2k + 1$ *for some integer* k*, then by a* median*, we mean the value* $x_{(k+1)}$*;*
- *when* n *is even, i.e., when* $n = 2k$ *for some integer* k*, then by a* median*, we mean the interval* $[x_{(k)}, x_{(k+1)}]$*.*

The median will also be called an interval median*.*

Proposition 5. *For every sequence of numbers* $x_1, \ldots, x_n$*, the* I*-aggregate set is equal to the median.*

Comment. Median is indeed often used in data processing, since it is the most robust aggregation – i.e., the aggregation which is the least vulnerable to possible outliers; see, e.g., (Huber, 2004; Huber and Ronchetti, 2009; Rousseeuw and Leroy, 1987). Not surprisingly, median is used in econometrics, as a more proper measure of "average" ("typical") income than the mean (OECD, 2016) – since a single billionaire living in a small town increases its mean income without affecting the living standards of its inhabitants (see also (Kreinovich et al., 2015)).

Proof. In terms of intervals, the condition for a number x to be a possible I-aggregate takes the following form:

for every interval $[a, b]$, if the majority of the elements $x_{(i)}$ belong to this interval, then x should also belong to this interval.

1°. Let us first prove that every possible U-aggregate x should belong to the median set.

1.1°. Indeed, if $n = 2k + 1$, then the majority of elements $x_{(i)}$ belong to the interval $[x_{(1)}, x_{(k+1)}]$: namely, $k + 1$ elements $x_{(1)} \le \ldots \le x_{(k+1)}$. Thus, every possible U aggregate x must belong to the same interval, and thus, we must have $x \le x_{(k+1)}$.

Similarly, the majority of elements $x_{(i)}$ belong to the interval $[x_{(k+1)}, x_{(n)}]$: namely, $k+1$ elements $x_{(k+1)} \le \ldots \le x_{(n)}$. Thus, every possible U aggregate x must belong to the same interval, and thus, we must have $x \ge x_{(k+1)}$.

From $x \le x_{(k+1)}$ and $x \ge x_{(k+1)}$, we conclude that $x = x_{(k+1)}$, i.e., x coincides with the median.

1.2°. If $n = 2k$, then the majority of elements $x_{(i)}$ belong to the interval $[x_{(1)}, x_{(k+1)}]$: namely, $k+1$ elements $x_{(1)} \le \ldots \le x_{(k+1)}$. Thus, every possible U aggregate x must belong to the same interval, and thus, we must have $x \le x_{(k+1)}$.

Similarly, the majority of elements $x_{(i)}$ belong to the interval $[x_{(k)}, x_{(n)}]$: namely, $k + 1$ elements $x_{(k)} \le \ldots \le x_{(n)}$. Thus, every possible U aggregate x must belong to the same interval, and thus, we must have $x \ge x_{(k)}$.

So, we conclude that $x_{(k)} \le x \le x_{(k+1)}$, i.e., that x is indeed an element of the median interval $[x_{(k)}, x_{(k+1)}]$.

2°. To complete the proof, let us prove that every element of the interval median is indeed a possible I-aggregate. For this, we need to show that if an interval $[a, b]$ contains the majority of elements $x_{(i)}$, then it contains the interval median.

Let us prove it by considering two possible situations: when n is odd and when n is even.

2.1°. Let us show that in the odd case, when $n = 2k + 1$, if the interval $[a, b]$ contains the majority of the elements $x_{(i)}$, then $x_{(k+1)} \in [a, b]$, i.e., $a \le x_{(k+1)}$ and $x_{(k+1)} \le b$.

We will prove both inequalities by contradiction. If $a > x_{(k+1)}$, then the interval $[a, b]$ cannot contain any of the $k + 1$ elements $x_{(1)} \le \ldots \le x_{(k+1)}$, and thus, must contain no more than k remaining elements $x_{(k+2)}, \ldots, x_{(n)}$ – which do not form a majority.

Similarly, if $b < x_{(k+1)}$, then the interval $[a, b]$ cannot contain any of the $k+1$ elements $x_{(k+1)} \le \ldots \le x_{(n)}$, and thus, must contain no more than k remaining elements $x_{(1)}, \ldots, x_{(k)}$, which also do not form a majority.

Thus, if the interval $[a, b]$ contains the majority of elements $x_{(i)}$, then it must contain the median $x_{(k+1)}$ – and so, the median is a possible I-aggregate of the values $x_1, \ldots, x_n$.

2.2°. Let us show that in the even case, when $n = 2k$, if the interval $[a, b]$ contains the majority of the elements $x_{(i)}$, then $[x_{(k)}, x_{(k+1)}] \subseteq [a, b]$, i.e., $a \le x_{(k)}$ and $x_{(k+1)} \le b$.

We will prove both inequalities by contradiction. If $a > x_{(k)}$, then the interval $[a, b]$ cannot contain any of the k elements $x_{(1)} \le \ldots \le x_{(k)}$, and thus, must contain no more than k remaining elements $x_{(k+1)}, \ldots, x_{(n)}$ – which do not form a majority.

Similarly, if $b < x_{(k+1)}$, then the interval $[a, b]$ cannot contain any of the k elements $x_{(k+1)} \le \ldots \le x_{(n)}$, and thus, must contain no more than k remaining elements $x_{(1)}, \ldots, x_{(k)}$, which also do not form a majority.

Thus, if the interval $[a, b]$ contains the majority of elements $x_{(i)}$, then it must contain the median $[x_{(k)}, x_{(k+1)}]$ – and so, every element from the interval median is a possible I-aggregate of the values $x_1, \ldots, x_n$.

The proposition is proven.

What if we require strong majority? What if instead of requiring that a typical element x satisfy all the properties that are satisfied by a *simple majority* of inputs, we instead require that the property $P(x)$ is triggered only when we have a *strong majority*: e.g., when the proportion of values x_i satisfying this property is larger than a certain threshold $t > 0.5$?

In this case, we have a similar result.

Definition 4. *Let $q \geq 1$, let $\mathcal{S}$ be a class of subsets of $\mathbb{R}^q$, let $x_1, \ldots, x_n \in \mathbb{R}^q$, and let t be a number between 0.5 and 1.*

- *We say that an element $x \in \mathbb{R}^q$ is a* possible t-$\mathcal{S}$-aggregate *of the elements $x_1, \ldots, x_n$ if the following condition holds:*

  for every $S \in \mathcal{S}$, if more than $t \cdot n$ of x_i are in this set, then x should be in this set.

- *The set of all possible t-$\mathcal{S}$-aggregates is called the* t-$\mathcal{S}$-aggregate set *of the elements $x_1, \ldots, x_n$.*

Proposition 6. *For every sequence of numbers $x_1, \ldots, x_n$, and for every t, the t-I-aggregate set is equal to the interval $[x_{(n-k+1),(k)}]$, where k is the smallest integer greater than $t \cdot n$.*

Proof is similar to the proof of Proposition 5.

Another possible derivation of a median. Interval median can be also derived from other natural conditions:

- that it is a continuous function of $x_1, \ldots, x_n$,
- that it is invariant with respect to arbitrary strictly increasing or strictly decreasing re-scalings; such re-scalings which make physical sense: e.g., we can measure sound energy in Watts or in decibels – which are logarithmic units; and
- that this is the narrowest such operation – else we could, e.g., take an operation returning the whole range $\left[\min_i x_i, \max_i x_i\right]$.

Definition 5. *Let $n \geq 1$ be fixed. By an* aggregation operation*, we mean a mapping that maps each tuple of real numbers $x_1, \ldots, x_n$ into an interval $A(x_1, \ldots, x_n) = [\underline{a}(x_1, \ldots, x_n), \overline{a}(x_1, \ldots, x_n)]$, with the following properties:*

1. *this operation is* continuous*, i.e., both functions $\underline{a}(x_1, \ldots, x_n)$ and $\overline{a}(x_1, \ldots, x_n)$ are continuous;*
2. *this operation is* scale-invariant*, meaning that:*

- *for each strictly increasing continuous function* $f(x)$*, we have* $\underline{a}(f(x_1),\dots,f(x_n)) = f(\underline{a}(x_1,\dots,x_n))$ *and* $\overline{a}(f(x_1),\dots,f(x_n)) = f(\overline{a}(x_1,\dots,x_n))$*, and*
- *for each strictly decreasing continuous function* $f(x)$*, we have* $\underline{a}(f(x_1),\dots,f(x_n)) = f(\overline{a}(x_1,\dots,x_n))$ *and* $\overline{a}(f(x_1),\dots,f(x_n)) = f(\underline{a}(x_1,\dots,x_n))$*;*

3. *this operation is* the narrowest *meaning that if for some operation* $B(x_1,\dots,x_n)$ *that satisfies the properties* 1 *and* 2*, we have* $B(x_1,\dots,x_n) \subseteq A(x_1,\dots,x_n)$ *for all tuples, then* $B(x_1,\dots,x_n) = A(x_1,\dots,x_n)$*.*

Proposition 7. *Interval median is the only aggregation operation in the sense of Definition 5.*

Proof.

1°. One can easily check that the interval median operation $M(x_1,\dots,x_n)$ satisfies the properties 1 and 2 from Definition 5.

2°. To complete our proof, it is thus sufficient to prove that for every operation $A(x_1,\dots,x_n)$ that satisfies the properties 1 and 2, we have $M(x_1,\dots,x_n) \subseteq A(x_1,\dots,x_n)$.

Since the operation $A(x_1,\dots,x_n)$ is continuous, and every input $(x_1,\dots,x_n)$ with equal elements $x_i = x_j$ can be represented as a limit of inputs in which all elements are different, it is sufficient to consider the case when all the elements in the input are different, i.e., when $x_{(1)} < x_{(2)} \dots < x_{(n)}$.

We can now form a strictly increasing transformation $f(x)$ for which $f(x_{(i)}) = x_{(i)}$, and $f(x) \neq x$ for all other numbers x. Indeed:

– for $x_{(i)} \le x \le x_{(i+1)}$, we can take

$$f(x) = x_{(i)} + \left(\frac{x - x_{(i)}}{x_{(i+1)} - x_{(i)}}\right)^2 \cdot (x_{(i+1)} - x_{(i)}),$$

– for $x \le x_{(1)}$, we can take $f(x) = x_{(1)} - 2 \cdot (x_{(1)} - x)$, and

– for $x \ge x_{(n)}$, we take $f(x) = x_{(n)} + 2 \cdot (x - x_{(n)})$.

For this function, since $f(x_i) = x_i$ for all i, the condition $\underline{a}(f(x_1),\dots,f(x_n)) = f(\underline{a}(x_1,\dots,x_n))$ implies that $\underline{a}(x_1,\dots,x_n) = f(\underline{a}(x_1,\dots,x_n))$, i.e., that $f(z) = z$ for $z = \underline{a}(x_1,\dots,x_n)$. By our selection of the function $f(x)$, this means that $z = \underline{a}(x_1,\dots,x_n)$ must coincide with one of the values $x_{(i)}$. Similarly, the value $\overline{a}(x_1,\dots,x_n)$ must coincide with one of the values $x_{(j)}$. Thus, we have $A(x_1,\dots,x_n) = [\underline{a}(x_1,\dots,x_n), \overline{a}(x_1,\dots,x_n)] = [x_{(i)}, x_{(j)}]$ for some i and j.

From continuity, we can conclude that the corresponding indices i and j must be the same for all the tuples $x_1,\dots,x_n$ in which all elements are different – otherwise, we would have a discontinuity.

In particular, this means that for the tuple $x_i = i$, we have $A(1,2,\dots,n) = [i,j]$. The strictly decreasing function $f(x) = n+1-x$ keeps the tuple intact. Thus, scale-invariance implies that $A(1,2,\dots,n) = [n+1-j, n+1-i]$. This means that $j = n+1-i$, i.e., that we have $A(x_1,\dots,x_n) = [x_{(i)}, x_{(n+1-i)}]$. Here, we must have $i \le n+1-i$, i.e., $2i \le n+1$ and $i \le \dfrac{n+1}{2}$.

For odd $n = 2k + 1$, this means that $i \le k + 1$, thus $j = n + 1 - i \ge k + 1$, so indeed, $M(x_1, \ldots, x_n) = x_{(k+1)} \in [x_{(i)}, x_{(n+1-i)}] = A(x_1, \ldots, x_n)$.

For even $n = 2k$, this means that $i \le k$, thus $j = n + 1 - i \ge k + 1$, so indeed, $M(x_1, \ldots, x_n) = [x_{(k)}, x_{(k+1)}] \subseteq [x_{(i)}, x_{(n+1-i)}] = A(x_1, \ldots, x_n)$.

The proposition is proven.

4. 1-D Case: Can We Expand Beyond Intervals?

One can easily check that in our analysis, instead of closed intervals, we can consider general *convex subsets* of the real line – i.e., subsets S that, for every two real numbers a and x', contain all the numbers between x and x'. In addition to closed intervals, convex sets include open intervals, semi-open intervals, and intervals with infinite endpoints.

Can we go beyond intervals? It turns out that we cannot, as the following result shows.

Proposition 8. *Let a class $\mathcal{S}$ contain, in addition to all the intervals, a non-convex set S_0. Then, for $n = 3$ and for every $n \ge 5$, there exists values $x_1, \ldots, x_n$ for which the $\mathcal{S}$-aggregate set is empty.*

Proof.

1°. The fact that the set S_0 is not convex means that there exist points $a < b < c$ for which $a, c \in S_0$ but $b \notin S_0$. To construct the desired counterexample, we will then form sequences x_i in which some elements are equal to a, some to b, and some to c.

We will consider three possible cases: when $n = 3k$, when $n = 3k + 1$, and when $n = 3k + 2$.

2°. Let us first consider the case when $n = 3k$. In this case, we take k values equal to a, k values equal to b, and k values equal to c.

$2k$ of these values form a majority. Thus, the majority of elements x_i belong to the interval $[a, b]$, so any possible $\mathcal{S}$-aggregate x must also belong to this interval. Similarly, the majority of elements x_i belongs to the interval $[b, c]$, so x must also belong to the interval $[b, c]$. From $x \in [a, b]$ and $x \in [b, c]$, we conclude that $x \in [a, b] \cap [b, c] = \{b\}$, i.e., that $x = b$. However, also, the majority of elements are equal to a or to c and thus, belong to the set S_0. So, we should conclude that $x \in S_0$ – but the element $x = b$ does not belong to S_0.

This contradiction shows that in this case, $\mathcal{S}$-aggregate set is indeed empty.

3°. When $n = 3k + 1$ and $n > 4$, we get $k \ge 2$. In this case, we select k elements equal to a, k elements equal to b, and $k + 1$ elements equal to c. If we pick only two of these three groups of elements, we get at least $2k$ elements. So, to continue with the arguments similar to what we had in Part 2 of this proof, it is sufficient to make sure that $2k$ elements form a majority, i.e., that $2k > \dfrac{3k + 1}{2}$. This inequality is equivalent to $4k > 3k + 1$ and to $k > 1$ and is, thus, true. So, this case is proven as well.

4°. When $n = 3k + 2$ and $n > 4$, we get $k \ge 1$. In this case, we select k elements equal to a, $k + 1$ elements equal to b, and $k + 1$ elements equal to c. If we pick only two of these three groups of elements, we get at least $2k + 1$ elements. So, to continue with the arguments similar to what we

had in Part 2 of this proof, it is sufficient to make sure that $2k+1$ elements form a majority, i.e., that $2k+1 > \frac{3k+2}{2}$. This inequality is equivalent to $4k+2 > 3k+2$ and to $k > 0$ and is, thus, always true. So, this case is proven as well.

The proposition is proven.

Discussion. The above proposition excluded values $n = 1$, $n = 2$, and $n = 4$. For $n = 1$ and $n = 2$, as we have mentioned earlier, all the values x_i are possible aggregates even when we consider all possible sets S.

For $n = 4$, it is also possible to have a non-convex set S_0 for which the $(I \cup \{S_0\})$-aggregate set is always non-empty.

Proposition 9. *For $n = 4$, there exists a non-convex set S_0 for which the $(I \cup \{S_0\})$-aggregate set is always non-empty.*

Proof. Indeed, let us take a 2-point set $S_0 = \{0, 1\}$. In this case, majority means at least 3 elements. So, we must consider tuples of 4 elements in which 3 are equal to 0 or 1.

For $n = 4$, the interval median is the interval $[x_{(2)}, x_{(3)}]$. All these elements are possible I-aggregates. So, prove our result, it is sufficient to show that at least one of them is also a possible $\{S_0\}$-aggregate.

If two or fewer element x_i are equal to 0 or 1, then the S_0-related condition does not require anything from a possible aggregate element. The only time when this condition needs to be taken into account is when 3 out of the 4 elements $x_{(1)}, \ldots, x_{(4)}$ are equal to 0 or 1. In this case, however, at least one of the bounds $x_{(2)}$ and $x_{(3)}$ is equal to 0 or 1, and thus, belongs to the set S_0. This bound is therefore a possible $\{S_0\}$-aggregate – thus, the $(I \cup \{S_0\})$-aggregate set is indeed non-empty.

The proposition is proven.

5. Multi-D Interval-Based Voting Aggregation

Discussion. Let us now consider the multi-D situation. In this case, a natural multi-D analog of intervals are boxes.

Definition 6. *For every $q \geq 1$, by a* box*, we mean a set $[a_1, b_1] \times \ldots \times [a_q, b_q]$, where $[a_i, b_i]$ are intervals. The class of all boxes will be denoted by B.*

Proposition 10. *For every sequence of tuples $x_1, \ldots, x_n$, the B-aggregate set is the box*

$$M_1 \times \ldots \times M_q,$$

where for every i, M_i is the interval median of the i-th components $x_{1i}, \ldots, x_{ni}$.

Proof.

1°. Let us first prove that every possible B-aggregate tuple belongs to the median box $M_1 \times \ldots \times M_q$.

Let us fix one of the dimensions. Without losing generality, we can assume that this dimension is the first one. Then, we consider numbers $x_{11}, \ldots, x_{n1}$.

For all other dimensions $j \neq 1$, let us consider the largest possible boxes

$$[A_j, B_j] \stackrel{\text{def}}{=} \left[\min_k(x_{kj}), \max_k(x_{kj})\right]$$

that contain all given values x_{kj}.

For each possible B-aggregate tuple $x = (e_1, \ldots, e_q)$, the desired property holds for all the boxed of the type $[a_1, b_1] \times [A_2, B_2] \times \ldots \times [A_q, B_q]$. Since all other intervals forming this box are the largest possible, the condition that a tuple x_i is contained in this box is equivalent to the condition that $x_{i1} \in [a_1, b_1]$.

Thus, for these boxes, the definition of a possible B-aggregate of the tuples $x_1, \ldots, x_n$ implies that the first component e_1 of the tuple x is a possible I-aggregate of the components $x_{11}, \ldots, x_{n1}$. We already know that this implies that e_1 belongs to the interval median M_1 of these components.

Similarly, we can prove that e_2 belongs to M_2, etc., thus indeed $x \in M_1 \times \ldots \times M_q$.

2°. Vice versa, let us prove that every tuple $x \in M_1 \times \ldots \times M_q$ is a possible B-aggregate.

Indeed, let $x = (e_1, \ldots, e_q) \in M_1 \times \ldots \times M_q$, and let us assume that the majority of the tuples x_i belong to the box $B = [a_1, b_1] \times \ldots \times [a_q, b_q]$. This implies, for every component i, that the majority of the values $x_{1i}, \ldots, x_{ni}$ belong to the interval $[a_i, b_i]$. We already know, from the 1-D case, that this implies that $e_i \in [a_i, b_i]$ for every i. Thus, we indeed have

$$x = (e_1, \ldots, e_q) \in [a_1, b_1] \times \ldots \times [a_q, b_q] = B.$$

The proposition is proven.

Can we replace boxes with more general sets? Can we use more general sets, e.g., convex polytopes? In general, no, and here is a simple 2-D counter-example.

Definition 7. *Let P denote the class of all convex polytopes.*

Proposition 11. *For $q \geq 2$, and for $n = 3$ or $n \geq 5$, there exist an input $x_1, \ldots, x_n$ for which the P-aggregate set is empty.*

Proof. For $n = 3$, let us have $x_1 = (0, 0, 0, \ldots, 0)$, $x_1 = (0.1, 0.9, 0, \ldots, 0)$, and $x_3 = (1, 1, 0, \ldots, 0)$. Clearly here,

- the median M_1 of the first components 0, 0.1, and 1 is 0.1, and
- the median M_2 of the second components 0, 0.9, and 1 is 0.9.

For all other components, the median of the values 0, 0, and 0 is clearly 0.

Thus, the median box $M_1 \times M_2 \times M_3 \times \ldots \times M_q$ consists of a single point $x_2 = (0, 1.0.9, 0, \ldots, 0)$.

Here, the majority of the points (namely, x_1 and x_3) belong to the convex straight line segment $S = \{(x, x, 0, \ldots, 0) : 0 \leq x \leq 1\}$, but the median does not belong to this segment – and thus, if we add this segment to boxes, the resulting aggregate set will be empty.

For general n, we can have several points equal to $x_1 = (0, 0, 0, \ldots, 0)$, several points equal to $x_1 = (0.1, 0.9, 0, \ldots, 0)$, and several points equal to $x_3 = (1, 1, \ldots, 0)$ – just as we had in the proof of Proposition 8.

The proposition is proven.

Acknowledgements

This work was supported in part by the National Science Foundation grants HRD-0734825 and HRD-1242122 (Cyber-ShARE Center of Excellence) and DUE-0926721, and by an award "UTEP and Prudential Actuarial Science Academy and Pipeline Initiative" from Prudential Foundation.

The authors are thankful to the anonymous referees for valuable suggestions.

References

Easly, D. and J. Kleinberg. *Networks, Crowds, and Markets: Reasoning About a Highly Connected World*, Cambridge University Press, 2010.

Halpern, J. Y. *Reasoning about Uncertainty*, MIT Press, 2003.

Huber, P. J. and E. M. Ronchetti. *Robust Statistics*, Wiley, Hoboken, New Jersey, 2009.

Huber, P. J. *Robust Statistics*, Wiley, Hoboken, New Jersey, 2004.

Jalal-Kamali, A., O. Nebesky, M. H. Durcholz, V. Kreinovich and L. Longpré. Towards a "generic" notion of genericity: from "typical" and "random" to meager, shy, etc., *Journal of Uncertain Systems*, 6(2):104–113, 2012.

Kreinovich, V. Toward formalizing non-monotonic reasoning in physics: the use of Kolmogorov complexity and algorithmic information theory to formalize the notions 'typically' and 'normally' ", In: L. Sheremetov and M. Alvarado (eds.), *Proceedings of the Workshops on Intelligent Computing WIC'04 associated with the Mexican International Conference on Artificial Intelligence MICAI'04*, pages 187–194, Mexico City, Mexico, April 26–27, 2004.

Kreinovich, V. Negative results of computable analysis disappear if we restrict ourselves to random (or, more generally, typical) inputs, *Mathematical Structures and Modeling*, 25:100–113, 2012.

Kreinovich, V., H. T. Nguyen and R. Ouncharoen. From mean and median income to the most adequate way of taking inequality into account, In: V.-N. Huynh, V. Kreinovich, S. Sriboonchitta, and K. Suriya (eds.), *Econometrics of Risk*, Springer Verlag, pages 63–73, Berlin, Heidelberg, 2015.

Longpré, L. and O. Kosheleva. Towards unique physically meaningful definitions of random and typical objects, *Mathematical Structures and Modeling*, 26:49–56, 2012.

Organization for Economic Cooperation and Development (OECD), *OECD Statistics*, available at http://stats.oecd.org/

Regenwetter, M. Perspectives on preference aggregation. *Perspectives on Psychological Science*, 4(4):403–407, 2009.

Rousseeuw, P. and A. Leroy. *Robust Regression and Outlier Detection*, J. Wiley, New York, 1987.

Tang, K. Evolutionary ensemble learning in uncertain environments, *Proceedings of the 2015 IEEE Series of Symposia on Computational Intelligence SSCI'2015*, Cape Town, South Africa, December 7–10, 2015.

Uses of Methods with Result Verification for Simplified Control-Oriented Solid Oxide Fuel Cell Models

Ekaterina Auer and Stefan Kiel
University of Technology, Business and Design, Wismar, Germany, ekaterina.auer@hs-wismar.de

Abstract: Solid oxide fuel cells (SOFCs) represent a promising technology in the energy sector. One of their advantages is high efficiency. Improvements are necessary, for example, to be able to reduce their operating temperatures or to speed up starting times. Developing efficient control-oriented models for the SOFC temperature has also been in the focus of ongoing research. The goal here is to devise (global) dynamic models valid for a wide range of operating conditions instead of obtaining (linear) approximations of the behavior only for a certain mode of operation. The use of methods with result verification helps to address reliability of SOFC models and to take into account bounded uncertainty.

Dynamic SOFC models are systems of differential equations, the parameters of which have to be fitted to the available sensor data (usually, thousands of measurements). Normally, such differential equations do not have analytical solutions if we keep in mind the goal of devising models suitable for a wide range of operating conditions. In this paper, we point out two simplification possibilities possessing closed-form solutions along with their areas of validity. Moreover, we study their potential with respect to uncertainty handling with the focus on simulation. We perform a sensitivity analysis for different variants of the suggested simplifications. Finally, we consider uncertainty of different magnitudes in heat capacities of gases, which we propagate through the system using interval, affine and Taylor model based methods.

Keywords: methods with result verification, optimization, simulation, UniVerMeC, SOFC

1. Introduction

Modern engineering tasks pose high requirements on safety and reliability of a manufactured system. To check such requirements, developers often have to work with computer simulations of the system instead of the system itself (or even its prototype) in order to keep the costs low. For that purpose, a mathematical model for the system in question is developed and implemented on a computer. However, both the mathematical model of a complex system and its implementation are in general inexact and could introduce a considerable inaccuracy into the simulated outcome. Ideally, this inaccuracy has to be taken into account while checking the above mentioned requirements so that system verification, validation and uncertainty quantification gain more and more importance. In the last decades, the techniques and methodologies for that purpose initially suggested, for example, in (AIAA, 1998), have been studied, improved and extended continuously (e.g., (Oberkampf at al., 2003; Auer and Luther, 2009; Henninger et al., 2010)).

Assuming that the mathematical model is accurate enough, verification answers the question of whether the computer-obtained (numerical) outcome is the correct result of the model. That is, the question of whether the mathematical model and its associated implementation actually produce realistic results remains unanswered during verification, to be handled separately during system validation. Uncertainty handling helps to account for inherent stochasticity in or lack of knowledge about the system. For example, it is well-known that physical quantities such as lengths or masses can only be measured with a certain (small) inaccuracy so that the result is actually not a single real number but a (continuous) set of numbers. Methods for forward uncertainty quantification are able to propagate such input through the system, providing (an approximation of) the resulting output set.

A less widely known possibility to deal with inaccuracies in the model is to use methods with result verification, for example, interval analysis (Moore et al., 2009). Such methods prove mathematically that the outcome of a computer simulation is correct with respect to the underlying mathematical model. As a result, they usually supply a set of machine numbers which with absolute certainty contains the exact model outcome. Almost as a by-product, methods with result verification allow us to propagate bounded uncertainty in parameters directly through the implementation of the mathematical model (provided that the appropriate implementation exists). A common drawback is the possibility of too conservative bounds for the solution sets (e.g., between $-\infty$ and $+\infty$) resulting from the dependency problem or the wrapping effect (Lohner, 2001).

Current research (Rauh et al., 2015; Auer et al., 2012) shows that interval analysis helps to improve and develop control-oriented models for solid oxide fuel cells (SOFC) with the focus on reliability and uncertainty quantification. SOFCs are devices converting chemical energy into electricity using ceramics as the electrolyte. Working at high temperatures, they are sensitive to overheating, but can theoretically achieve the overall efficiency of up to 85%. General research goals in this area are, for example, the reduction of operating temperatures or a speed-up in the starting times. In recent years, developing efficient control-oriented models for the temperature of SOFCs has also been in the focus of ongoing research, see (Huang et al., 2012; Rauh et al., 2014). The goal here is to devise (global) dynamic models valid for a wide range of operating conditions instead of obtaining (linear) approximations of the behavior only for a certain mode of operation.

Dynamic SOFC models are systems of differential equations with many unknown parameters, for example, heat capacities of the involved gases. These quantities have to be chosen in such a way as for the model to reflect the experimental data (usually, thousands of measurements). The traditional approach in this case is to use the least squares optimization for parameters. One difficulty is that the differential equations representing the mathematical SOFC model do not have analytical solutions. That is, to measure the difference between the modeled and experimental result, which is necessary for the objective function of the least squares method, the modeled solution is either approximated by an analytical expression or obtained numerically, increasing the overall imprecision (cf. Section 2). Another difficulty is the necessity to compute the sum of squares of such differences for a large number of measurements, leading to various numerical problems.

An obvious approach to solve the first problem is to simplify the available models. In principle, it could be contradictory to the goal of obtaining models valid under various operating conditions. In (Auer at al., 2015), we pointed out two simplification possibilities for general SOFC models along with their corresponding validity areas. For these simplifications, we derived a closed form solution

and assessed the performance. In this paper, we carry out a sensitivity analysis for both variants and study their potential with respect to uncertainty handling (corresponding to the second difficulty mentioned above) using methods with result verification, in particular, Taylor models (Berz, 1995) and affine forms (de Figueiredo and Stolfi, 2004). Throughout the paper, we rely on the framework UniVerMeC (Kiel, 2014) which allows us to use the same models with different kinds of verified or floating point methods in an efficient way.

The structure of the paper is as follows. In the next section, we give a very brief overview of the theory on parameter identification for SOFC models. This does not include the details on how SOFC models are actually obtained, which can be found elsewhere (Huang et al., 2012). Although methods with result verification are less established in the engineering community, they are well-known in general, so that we omit their description and refer interested readers to (Moore et al., 2009). We specify the kinds of possible SOFC models from the point of view of verification and validation analysis as well as our understanding of the sensitivity analysis in this case in the remainder of Section 2. Section 3 provides the details on the above-mentioned simplification possibilities. In Section 4, we describe the most important features of UniVerMeC and use this tool to actually carry out the sensitivity analysis along with uncertainty quantification. In particular, we explore the potential for overestimation reduction provided by result verification with dependency tracking. A summary of the achieved results and an outlook on our future work conclude this paper.

2. Parameter Identification for SOFC Models

A model of an actual SOFC test rig consists of several subsystems each of which is modeled separately. They describe the behavior of the SOFC stack with respect to its thermodynamics, fluid mechanics, or electrochemistry. In this paper, we consider only the temperature model (Rauh et al., 2014; Rauh et al., 2015) based on general techniques from (Huang et al., 2012; Bove and Ubertini, 2008).

2.1. Modeling the SOFC Temperature

The overall procedure consists of three phases. First, a system of equations is developed to describe the temperature based on heat flow/energy balances over finite domains ("early lumping"). This system is used in combination with the finite volume method to obtain a system of ordinary differential equations (ODEs) for the temperature of the stack (including the behaviour of the preheaters) in the second step. The dimension of the resulting initial value problem (IVP) for the ODEs depends on the number of preheaters and on the coarseness of the discretization we consider. The IVP is used as the basis for the subsequent simulation and control of the SOFC stack in order to obtain global behaviour, in contrast to the traditional methodology (Bove and Ubertini, 2008) locally simplifying the system even further.

In this section, we focus on the third step, the parameter identification for the ODE-based thermal model using the least squares minimization. In general, there are many parameters needing identification, for example, specific heat capacities of the involved gases, reaction enthalpies or coefficients of heat convection. The first parameter group is usually quite large, since it is assumed that

a certain heat capacity c_{gas} is not a constant, but itself depends on the temperature. Since the actual dependency is unknown, it is approximated by polynomials of the second order in temperature θ:

$$c_{gas}(\theta) = c_{gas,0} + c_{gas,1} \cdot \theta + c_{gas,2} \cdot \theta^2 \quad , \tag{1}$$

which leads to three constant parameters per specific heat capacity. If such approximations are used, the right hand side of the resulting ODE system is a third-order polynomial in θ because it contains products of the type $c_{gas} \cdot \theta$. The actual equation for the temperature of the stack $\theta(t)$ has the general form

$$\dot{\theta}(t) = c_m^{inv} \left(c_{gases,AG}(\theta) \cdot \left(\theta_{AG}^{in}(t) - \theta(t) \right) + c_{gases,CG}(\theta) \cdot \left(\theta_{CG}^{in}(t) - \theta(t) \right) + f(\theta(t)) \right) \quad , \tag{2}$$

explained in more detail, for example, in (Rauh et al., 2013). Here, $f(\theta)$ contains components related to Ohmic losses and the heat flows between the stack and environment and of the overall chemical reaction, which are at most quadratic in temperature in case the reaction enthalpies are modeled similarly to (1). The symbols θ_{AG}^{in} and θ_{CG}^{in} denote the temperatures of anode and cathode gases, respectively (parameters which can be measured and recorded by SOFC test rig sensors). The constant c_m^{inv} is explained in Table I, and $c_{gases,AG}(\theta)$, $c_{gases,CG}(\theta)$ are the heat capacities of gases at the anode and cathode, respectively, modeled as in Eq. (1) for each of the involved gases. We studied this kind of model in (Auer et al., 2012; Kiel at al., 2013; Auer et al., 2014). In this paper, we simplify (2) as explained in Section 3 and study the resulting models. The rest of this section contains theory which can be applied generally to all temperature models of the type (2), simplified or not.

2.2. Parameter Identification for the SOFC Temperature

We obtain values for the parameters of the SOFC temperature model using the least squares minimization. If the goal is to verify the obtained optimum, the interval technique of global optimization (Hansen and Walster, 2004) can be employed. A common principle is to minimize the objective function J (or its worst-case value under uncertainty – its upper bound $\overline{J}$ in the interval case) with respect to parameters p:

$$J = \sum_{k=T_b}^{T_e} \sum_{i=1}^{N} \left(y_i(t_k, p) - y_{m,i}(t_k) \right)^2 \quad . \tag{3}$$

Here, $y(t_k, p)$ is the solution to the model equations (e.g., as given in Eqs. (8)–(12)) at the time t_k, $k = T_b, \ldots, T_e$. The notation $y_{m,i}(t_k)$, $i = 1 \ldots N$, signifies the measured values for the temperature. Without loss of generality, we assume that the N states that can be measured using the sensors of the SOFC test rig are the first N ones in the vector $y(t_k, p)$. In our context, $t_k = T_b, T_b + 1, \ldots, T_e$. That is, J quantifies deviations between the simulated results and the measured output vector acquired with $T = T_e - T_b$ samples and a constant sampling time $h = 1$s.

The solution $y(t, p)$ is obtained from the corresponding IVP and optimised with respect to the measured values. Depending on the number of finite volume elements that are used to discretize

the differential equations for the stack temperature, the resulting ODE system for this quantity has different number of equations. Until now, we considered one, three, and nine volume elements. If the preheater models consisting of M equations are used additionally (cf. e.g. Eqs. (8)–(11)), this results in systems of $1+M$, $3+M$, and $9+M$ equations, cf. (Rauh et al., 2013). Finer discretisations are possible in principle but are expensive computationally and rather unstable numerically. An empirically motivated additional condition is induced by the accuracy of the measurements:

$$y_i(t_k, p) \subseteq [y_{m,i}(t_k) - K_i, y_{m,i}(t_k) + K_i] =: [\Delta y_m(t_k)] \quad \text{for} \quad t_k = T_b, \ldots, T_e,\ i = 1 \ldots N \ , \tag{4}$$

with constants K_i chosen in accordance with the actual SOFC test rig. A traditional measure for comparing the quality of the identified parameter sets (because there could be many possibilities) is the root mean square error e given by

$$e = \sqrt{\frac{\sum_{k=T_b}^{T_e} (y_i(t_k) - y_{m,i}(t_k))^2}{T_e - T_b}} \tag{5}$$

for each solution component with the index $i \in \{1 \ldots N\}$ of $y(t)$ we are interested in.

In the most of our recent publications (e.g., (Auer et al., 2012; Kiel at al., 2013)), we solved the global optimisation problem (3) by verified approximation: The true solution $y(t, p)$ of the IVP was approximated by the explicit Euler method as

$$[y^{(k)}] := [y^{(k-1)}] + h \cdot f([y^{(k-1)}], [p]) \ , \tag{6}$$

where f denotes the right side of the IVP (componentwise). The approximation $[y^{(k)}]$ at t_k was substituted for the exact solution $y(t_k)$ in the objective function (Eq. (3)) with the sampling time of $h = 1s$ and the discretisation error ignored. Although we could not verify the whole process by applying interval optimisation procedures in this case, the approximated cost function

$$J_{app} = \sum_{k=T_b+1}^{T_e} \sum_{i=1}^{N} \left(y_i^{(k-1)} - y_{m,i}(t_k) + h \cdot f(y_i^{(k-1)}, p) \right)^2 \ , \tag{7}$$

where $y^{(T_b)}$ is the initial condition, was evaluated in a verified way and optimised using an interval algorithm available in UniVerMeC. Note that the first (and second) derivatives of J_{app} were computed exactly with the help of algorithmic differentiation. Although the control-oriented SOFC models are less complex than those based on, for example, partial differential equations, they are still complex enough so that their treatment with general-purpose verified global optimisation software is next to impossible. In particular, the summation in Eq. (3) is carried out for $T = 16628$ measurements which causes numerical problems even in the usual floating point based case. High times T are explained by the already mentioned general goal to produce models valid for a wide range of operating conditions.

2.3. Anaylsis of the Model Types; Sensitivity

From the point of view of verification and validation analysis, the optimization problem described above might take different forms which are verified to different extents. Generally, we can differentiate between four verification categories (Auer and Luther, 2009) summarized from the lowest to the highest verification extent as follows.

(C4) The implementation of the mathematical model is based on fixed point arithmetic or non-standard floating point arithmetic.

(C3) The implementation of the mathematical model uses standardized IEEE floating point arithmetic.

(C2) The implementation of the mathematical model uses verified techniques for several subtasks.

(C1) The implementation of the mathematical model uses verified techniques everywhere.

In the case of SOFC parameter identification, there are two general classification characteristics. The first one (F1) is the way the simulated solution $y(t_k, p)$ of the IVP is obtained in (3). The second characteristic (F2) is the kind of techniques the implementation relies on (essentially, verified or usual floating-point). Overall, we can discern the following model types:

(F1) How is $y(t_k, p)$ obtained in (3)?

- (F1.a) $y(t_k, p)$ is computed analytically (a closed-form solution)
- (F1.b) $y(t_k, p)$ is approximated by an analytic expression (e.g., using the Euler or Heun method) and the approximation error is neglected, cf. Eq. (7)
- (F1.c) $y(t_k, p)$ is computed using a "black box" numerical solver (no explicit expression for the solution)

(F2) What is the underlying technique for the implementation?

- (F2.a) Traditional floating point methods
- (F2.b) Interval analysis (with result verification; possibility to propagate bounded uncertainty through the system)
- (F2.c) Other techniques with result verification (e.g., affine arithmetic, Taylor models, etc.)

Note that forms F1.a and F1.c combined with F2.b or F2.c correspond to the complete verification of the model (C1), if optimisation is carried out in a completely verified way. If it is not possible to verify the optimum and a certain best suitable interval vector is chosen from the list of candidates produced by global optimisation according to a heuristic technique, then the corresponding degree is C2. In (Auer et al., 2012; Kiel at al., 2013), we were able to achieve the verification degree of C2 for SOFC temperature models of dimensions one and three (without considering preheaters) by using the variant F1.b&F2.b.

There are two more important notions in the context of verification and validation analysis: uncertainty quantification and sensitivity analysis. The task of the former is to quantify the uncertainty in the the model output from the uncertainty in the input (forward propagation) or vice versa (inverse). Generally, it is easier to solve the first problem than the second, so that there are a variety of probabilistic (e.g. Monte-Carlo) or non-probabilistic methods (interval or fuzzy analysis) developed for this purpose. The task of sensitivity analysis is to apportion the uncertainty in the model output to different sources of uncertainty in the model input (Saltelli et al., 2008). Here, a good indicator is considered to be the first derivative of the output with respect to the input we are interested in. The already mentioned framework UniVerMeC allows us to solve both tasks for different kinds of thermal models for SOFCs.

3. Possibile Simplifications

In a realistic situation, engineers often need a trade-off between a high degree of system reliability (or verification) and an acceptable computing time (or overall costs). That is, the models might need simplification if high verification degrees are requested in a real-time simulation or control. In this section, two obvious possibilities to simplify SOFC temperature models are described. Additionally, we provide closed form solutions to the suggested models. Note that using the computer algebra system MATLAB did not work very well for obtaining closed-form expressions (which had to be derived "by hand"). Although it was possible to compute them in MATLAB in some cases, the expressions were numerically unstable, leading to overflows with increasing times t.

3.1. Common Settings

We make several simplifying assumptions, some of which are used only for the purpose of clearer presentation and are not mandatory:

(S1) We consider the nitrogen as the only anode gas for the heating phase without any chemical reactions of gases (not mandatory)

(S2) We work with a single volume element to describe the temperature of the stack as a whole (mandatory for obtaining a closed form solution, at least under assumption S3.b)

(S3) We consider different approximations to the heat capacities $c(\theta)$ of the nitrogen (the anode gas) and the cathode gas (mandatory)

(S3.a) $c_{gas}(\theta) := c_{gas,0}$ is constant (corresponds to the model we denote by MPC1 in this paper)

(S3.b) $c_{gas}(\theta) := c_{gas,0} + c_{gas,1} \cdot \theta$ is linear (corresponds to the model MPL1)

In several cases, we take two preheaters into consideration since it improves the overall quality of SOFC models from the point of view of their control. It is possible include more preheaters into the overall model or do not consider them al all.

The parameters, variables, and control states still present in MPC1 and MPL1 are given by Table I. Those denoted by $\dot{m}$ describe mass flows of, for example, nitrogen. All *control variables* from

Table I are assumed to be piecewise constant. That is, we use the information from measurements to describe these values instead of modeling them by appropriate initial value problems (IVPs). These measurements are recorded each second (i.e., with the stepsize $h = 1$s) between $T_b = 362$ and $T_e = 17000$ (the heating stage of the experiment). In the same way, it is possible to use sensor data for the preheater output instead of the IVPs (8)–(11). All *parameters* are considered to be constant; their actual values are to be identified by an appropriate optimization procedure (cf. Section 2). For all *variables*, the corresponding initial values at the beginning of integration T_b are supposed to be known.

Because the control variables are piecewise constant, the model IVPs are solved separately in each time interval $[t_{n-1}, t_n]$, $t_n - t_{n-1} = 1$, $n = T_b + 1, \ldots, T_e$, since the stepsize for taking measurements is $h = 1$s. The initial values in the next step are the results from the previous step so that $t_0 = t_{n-1}$ for the time step t_n. If the possibility F2.b is used, we have to work with the interval hull of the values of the control variables, because we do not know the exact value inside (t_{n-1}, t_n), only in t_{n-1} and t_n.

3.2. Simplified Model MPC1: Constant Heat Capacities

The system of ODEs resulting from the assumptions S1, S2, S3.a is as follows (as a comparison, the general form under S2 is given in (Auer et al., 2012)):

$$\dot{y}_0 = T_{AG}^{inv} \cdot (u_1 - y_0) \tag{8}$$
$$\dot{y}_1 = T_{SL,AG}^{inv} \cdot (y_0 - y_1) \tag{9}$$
$$\dot{y}_2 = T_{CG}^{inv} \cdot (u_2 - y_2) \tag{10}$$
$$\dot{y}_3 = T_{SL,CG}^{inv} \cdot (y_2 - y_3) \tag{11}$$
$$\dot{\theta} = -c_m^{inv} \cdot (k_{const} - (c_{CG,0} \cdot y_3 + c_{N_2,0} \cdot y_1) + k_{lin}\theta) \ , \tag{12}$$

where k_a, k_{const} and k_{lin} are defined according to

$$\begin{aligned} k_a &= 234000\alpha_i + 448500\alpha_j + 345000\alpha_k \ , \\ k_{const} &= -\theta_A k_a \ , \\ k_{lin} &= k_a + \dot{m}_{CG}^{in} \cdot c_{CG,0} + \dot{m}_{N_2}^{in} \cdot c_{N_2,0} \ , \end{aligned}$$

and initial conditions $y_i(T_b) = y_i^{ic}$, $i = 0, 1, 2, 3$, $\theta(T_b) = \theta^{ic}$. The obtained ODE system is linear in temperature (including the preheater states). The equations (8)–(9) describe the first preheater (for the nitrogen), Eqs. (10)–(11) the second (for the cathode gas), and Eq. (12) the stack temperature. We can derive the simple closed form solution to the model:

$$y_0(t) = u_1 - (u_1 - y_0^{ic})e^{-T_{AG}^{inv}(t-t_0)} \tag{13}$$
$$y_1(t) = u_1 - \frac{T_{SL,AG}^{inv}}{T_{SL,AG}^{inv} - T_{AG}^{inv}}(u_1 - y_0^{ic})e^{-T_{AG}^{inv}(t-t_0)} + k_{N_2}e^{-T_{SL,AG}^{inv}(t-t_0)} \tag{14}$$

for the anode gas preheater, where $k_{N_2} = y_1^{ic} - u_1 + \frac{T_{SL,AG}^{inv}}{T_{SL,AG}^{inv} - T_{AG}^{inv}}(u_1 - y_0^{ic})$. The solution for the cathode gas preheater has the same form; only the parameters are different. (All labels "N_2" (or AG) in

Table I. Model parameters, control and state variables.

	Parameters (to identify)
α_i, α_j, α_k	coefficients of heat convection
$c_{N_2,0}$, $c_{N_2,1}$	heat capacity of nitrogen as $c_{N_2}(\theta) = c_{N_2,0}(+c_{N_2,1} \cdot \theta)$
$c_{CG,0}$, $c_{CG,1}$	heat capacity of the cathode gas as $c_{CG}(\theta) = c_{CG,0}(+c_{CG,1} \cdot \theta)$
T^{inv}_{AG}	inverse time constant of the anode gas preheater
T^{inv}_{CG}	inverse time constant of the cathode gas preheater
$T^{inv}_{SL,AG}$	inverse time constant of the anode gas supply line
$T^{inv}_{SL,CG}$	inverse time constant of the cathode gas supply line
c	specific heat capacity of the stack module
m	mass of the stack module
c^{inv}_m	$= 1/(c \cdot m)$
	Variables
$y_0 = v_{N_2}$	$\dot{m}^{in}_{N_2} \cdot \theta_{N_2}$ at the preheater outlet, $y_0(T_b) =: y^{ic}_0$
$y_1 = v^{in}_{N_2}$	$\dot{m}^{in}_{N_2} \cdot \theta^{in}_{N_2}$ at the stack inlet, $y_1(T_b) =: y^{ic}_1$
$y_2 = v_{CG}$	$\dot{m}^{in}_{CG} \cdot \theta_{CG}$ at the preheater outlet, $y_2(T_b) =: y^{ic}_2$
$y_3 = v^{in}_{CG}$	$\dot{m}^{in}_{CG} \cdot \theta^{in}_{CG}$ at the stack inlet, $y_3(T_b) =: y^{ic}_3$
θ	temperature of the stack, $\theta(T_b) =: \theta^{ic} = 293.9$K
	Control variables
$\dot{m}^{in}_{N_2}$	mass flow of anode gas (recorded data)
$\dot{m}^{in}_{CG}$	mass flow of cathode gas (recorded data)
θ_A	ambient temperature
θ^d_{AG}	desired temperature of the anode gas (recorded data)
θ^d_{CG}	desired temperature of the cathode gas (recorded data)
$u_1 = v^d_{N_2}$	desired $v_{N_2} = \theta^d_{AG} \cdot \dot{m}^{in}_{N_2}$
$u_2 = v^d_{CG}$	desired $v_{CG} = \theta^d_{CG} \cdot \dot{m}^{in}_{CG}$

Eqs. (13)–(14) should be changed to "CG".) If $T^{inv}_{SL,AG} = T^{inv}_{AG}$, we obtain trivial solutions $y_0(t) = y^{ic}_0$, $y_1 = y^{ic}_1$.

The solution for the temperature can be obtained after substituting into (12) the corresponding expressions for $y_3(t)$ and $y_1(t)$. Using variable separation and variation of the constant delivers the general solution form as

$$\theta(t) = \mathcal{I}_{N_2}(t) + \mathcal{I}_{CG}(t) + k_\theta e^{-c^{inv}_m \cdot k_{lin}(t-t_0)} - \frac{k_{const}}{k_{lin}} \ , \tag{15}$$

where

$$\mathcal{I}_{N_2}(t) := \frac{u_1 \cdot c_{N_2,0}}{k_{lin}} + c_m^{inv} \cdot c_{N_2,0} \cdot \left(- \frac{T_{SL,AG}^{inv}}{(T_{SL,AG}^{inv} - T_{AG}^{inv})(c_m^{inv} k_{lin} - T_{AG}^{inv})} (u_1 - y_0^{ic}) e^{-T_{AG}^{inv}(t-t_0)} + \frac{k_{N_2}}{c_m^{inv} k_{lin} - T_{SL,AG}^{inv}} e^{-T_{SL,AG}^{inv}(t-t_0)} \right) ,$$

$\mathcal{I}_{CG}(t)$ analogously, and $k_\theta = \theta^{ic} - \mathcal{I}_{CG}(t_0) - \mathcal{I}_{N_2}(t_0) + \frac{k_{const}}{k_{lin}}$. If $T_{SL,AG}^{inv} = T_{AG}^{inv}$ and $T_{SL,CG}^{inv} = T_{CG}^{inv}$, that is, if we have trivial solutions for the preheaters, the corresponding solution for the temperature is also trivial:

$$\theta(t) = -\frac{\tilde{k}_{const}}{k_{lin}} + \left(\theta^{ic} + \frac{\tilde{k}_{const}}{k_{lin}} \right) \cdot e^{-c_m^{inv} \cdot k_{lin} \cdot (t-t_0)} , \tag{16}$$

where $\tilde{k}_{const} = -\theta_A \cdot k_a - (c_{CG,0} \cdot y_3^{ic} + c_{N_2,0} \cdot y_1^{ic})$. This version of the solution is also useful if we assume that the preheaters are piecewise constant in time and employ the recorded sensor data instead of the dynamic model given by Eqs. (8)–(11).

In principle, we can use the same approach to obtain closed-form solutions for temperature models of higher dimensions with constant heat capacities. If the preheaters are assumed to be constant, the resulting linear system has only constant coefficients so that well-known techniques from the calculus can be employed. However, the expressions become very complicated. The numerical results from, for example, (Auer at al., 2015), suggest that there is almost no gain in using them even in the one dimensional case MPC1 from the point of view of the computing time for identification. One of their advantages is higher accuracy: better model parameter sets can be identified with their help. In (Auer at al., 2015a), we were able to identify the parameter set shown in Table II for the main parameters of interest of MPC1 with the root mean square measure $e = 3.5259$K. As a comparison, the best parameter set obtained for the non-simplified model of dimension one so far has the measure $e = 2.1641$K. Another advantage of MCP1 is the reduced computing time for pure simulation with known parameter sets. Our general conclusion about the model MPC1 is that it can be used efficiently in the context of an online simulation or control over relatively short time intervals. In Section 4, we will further explore the properties of this model by studying its sensitivity to parameters and its ability to account for parameter uncertainty.

Table II. The best obtained parameter sets for MPC1 and MPL1.

Model	c	$\alpha_i = \alpha_j = \alpha_k$	$c_{N_2,0}$	$c_{N_2,1}$	$c_{CG,0}$	$c_{CG,1}$	e
MPC1(F1.a&F2.a)	$4.53503 \cdot 10^6$	$1.49548 \cdot 10^{-3}$	$1.96452 \cdot 10^6$	–	$1.52826 \cdot 10^7$	–	3.5K
MPL1(F1.b&F2.a)	$3.38579 \cdot 10^4$	$3.60235 \cdot 10^{-5}$	$5.52725 \cdot 10^6$	-11221.8	$-8.88817 \cdot 10^4$	483.868	0.5K

3.3. Simplified Model MPL1: Linear Heat Capacities

The simplified model MPL1 relies on linear polynomial approximations for the heat capacities. Assuming that the preheater states are not constant inside the time interval (of width 1s) where other control variables are constant, we obtain a Riccati equation for the temperature which does not seem to have an analytical solution. For piecewise constant preheater states, we can derive a closed-form expression similarly to (Auer et al., 2014) as shown in the following.

If the preheater states are not constant, Eqs. (8)–(11) stay the same as for MPC1 from the previous section. The equation for the temperature θ turns into

$$\dot{\theta} = -c_m^{inv} \cdot (k_{const}(t) + k_{lin}(t)\theta + k_{sq}\theta^2) \tag{17}$$

where $k_{const}(t)$, $k_{lin}(t)$ depend on time and θ^2 appears on the right side of the equation with the constant coefficient k_{sq}:

$$\begin{aligned} k_{const}(t) &= -\theta_A k_a - (y_3(t)c_{CG,0} + y_1(t)c_{N_2,0}) \ \ (k_a \ \text{ as in Section 3.2}) \ , \\ k_{lin}(t) &= k_+ \dot{m}_{CG}^{in} \cdot c_{CG,0} + \dot{m}_{N_2}^{in} \cdot c_{N_2,0} - (y_3(t)c_{CG,1} + y_1(t)c_{N_2,1}) \ , \\ k_{sq} &= \dot{m}_{CG}^{in} \cdot c_{CG,1} + \dot{m}_{N_2}^{in} \cdot c_{N_2,1} \ . \end{aligned}$$

Now we have two additional parameters $c_{CG,1}$, $c_{N_2,1}$ as compared to MPC1, resulting from the fact that we represent heat capacities of gases as $c_{N_2}(\theta) = c_{N_2,0} + c_{N_2,1} \cdot \theta$, $c_{CG}(\theta) = c_{CG,0} + c_{CG,1} \cdot \theta$. Equation (17) is a Riccati equation. Since k_{sq} does not depend on time in our case, it can be transformed into a system of the following linear ODEs with non-constant coefficients:

$$\begin{pmatrix} y_4 \\ y_5 \end{pmatrix}' = \begin{pmatrix} 0 & 1 \\ -(c_m^{inv})^2 k_{const}(t) k_{sq} & -c_m^{inv} k_{lin}(t) \end{pmatrix} \cdot \begin{pmatrix} y_4 \\ y_5 \end{pmatrix} \ , \tag{18}$$

where the temperature θ equals $\dfrac{y_5}{c_m^{inv} k_{sq} y_4}$. The matrix in Eq. (18) does not necessarily commute with itself for given points of time t, s so that finding a closed-form expression in this case seems impossible. Therefore, we assume now that the preheaters behave as constant functions inside intervals of width 1s (piecewise constant on the whole) similarly to control variables. The values of y_1 and y_3 can be measured with the sampling frequency of 1s between T_b and T_e. The closed-form solution for the temperature equation with – now constant – coefficients k_{const}, k_{lin} and $y_1(t) = y_1^{meas}$, $y_3(t) = y_3^{meas}$ has different branches in dependence on $D = k_{lin}^2 - 4 \cdot k_{const} \cdot k_{sq}$:

$$\begin{aligned} D > 0: \ \theta(t) &= \frac{1}{k_{sq}} \left(\frac{\sqrt{D}}{1 - e^{-c_m^{inv}(t-t_0)\sqrt{D}} \cdot \left(1 - \dfrac{2\sqrt{D}}{2k_{sq}\theta^{ic} + k_{lin} + \sqrt{D}}\right)} - \frac{k_{lin} + \sqrt{D}}{2} \right) \ , \\ D < 0: \ \theta(t) &= \frac{\sqrt{-D}\tan\left(-\frac{\sqrt{-D}}{2} c_m^{inv}(t-t_0) + \theta^c\right) - k_{lin}}{2k_{sq}} \ , \ \theta^c = \operatorname{atan}\left(\frac{2k_{sq}\theta^{ic} + k_{lin}}{\sqrt{-D}}\right) \ , \\ D = 0: \ \theta(t) &= \frac{2\theta^{ic} + k_{lin}/k_{sq}}{2 + c_m^{inv}(t-t_0)(2k_{sq}\theta^{ic} + k_{lin})} - \frac{k_{lin}}{2k_{sq}} \ . \end{aligned} \tag{19}$$

From the definitions for k_{const}, k_{lin}, k_{sq} and the data, it is likely (but not certain) that D is positive. For the set of parameters obtained in MATLAB (F1.b&F2.a), we checked that to be so. However, the measure e for this parameter set and MPL1 is not satisfactory. If we take this set as starting values in UniVerMeC and use the model variant F1.b&F2.a, we obtain a much better parameter set (cf. Table II). Note that the measure e for this set is even better than that achieved by using the non-simplified model (Auer at al., 2015a). A drawback is that there is a branch change for the solution $\theta(t)$ in this case (from $D > 0$ to $D < 0$). However, this fact does not make any difference for the pure simulation. The difficulties would occur during stages in the verification and validation process requiring derivatives of θ (e.g. sensitivity analysis, uncertainty quantification with Taylor models). More information about that is in the next section. Our general conclusion is that MPL1 is a very promising simplification (both as F1.a and F1.b), which is able to handle a wide range of operating conditions in the same way as the non-simplified model. Moreover, it is faster and possesses a closed-form solution.

4. Uncertainty Quantification and Sensitivity Analysis for MPC1 and MPL1

In this section, we analyse the performance of the proposed simplified models MPC1 and MPL1 with respect to their ability to take into account uncertainty in model parameters during the simulation stage. That is, we assume that the parameters of the both models have already been identified as reported in (Auer at al., 2015a). We rely on the parameter values given by Table II which we obtained by using the interior point optimizer IPOPT (Wächter and Biegler, 1991) inside the framework UniVerMeC (Kiel, 2014). In this sense, the results of the parameter identification stage for these SOFC temperature models are not verified and have verification degree of C3 (cf. Section 2.3).

One possibility to quantify the uncertainty during the simulation stage is to use methods with result verification. This has an additional advantage: the produced simulation data are proven to be correct wrt. the considered mathematical model (i.e., do not contain any numerical errors). If there is no uncertainty in parameters, the simulation results – now nonetheless (tight) intervals containing the true solution – can be intersected with the sets given by Condition (4). If they stay inside the bounds of (4), the parameters obtained in the non-verified way mentioned above are validated. Both of the sets from Table II are valid in this sense.

To actually quantify the uncertainty, we consider variants F1.a and F1.b for MPC1 and MPL1 and three kinds of arithmetics with result verification (F2.b-F2.c). These are the interval arithmetic as implemented by C-XSC (Hofschuster et al., 2008), affine arithmetic implemented by Yalaa (Kiel, 2014), and Taylor model arithmetic from RiOT (Eble, 2007). The term "arithmetic" means that we need only basic operations such as addition along with several elementary functions such as the exponential (e^x). However, the combination F1.b&F2.b requires a verified solver for initial value problems, for which purpose we employ VNODE-LP (Nedialkov, 2002). At the moment, there are no other verified IVP solvers available in UniVerMeC where we implement the models and conduct computations during all stages of modeling and simulation cycle for SOFC temperature. That is, the combination F1.b&F2.c is possible in principle but not currently implemented inside UniVerMeC.

We have not mentioned variant F1.c so far, the reason being that it was found to be too slow (Pusch, 2013; Auer et al., 2014) even in its non-verified form F2.a. Additionally, it is not interesting from the point of view of the simulation stage since it is the same as for F1.b. The real advantage concerns the stage of parameter identification which is not in our focus in this paper.

The question of MPC1 and MPL1 sensitivity to parameters is also an interesting one. The answer allows us not only to apportion the output uncertainty to different inputs, but also to choose variables with dependency tracking (e.g., in affine or Taylor model arithmetic) efficiently. Therefore, this section is structured as follows. First, we outline the principles of the framework UniVerMeC in short. After that, we carry out sensitivity analysis for MPC1 and MPC2 using floating point arithmetic and algorithmic ("exact") differentiation as implemented in FADBAD++ (Stauning, 1997). Finally, we consider uncertainty in heat capacities of gases and propagate it through the system, which allows us to assess the usefulness of the considered models for that purpose.

4.1. UniVerMeC — An Interoperable Framework

Although originally developed for distance computations, the framework UniVerMeC works very well for the stages of parameter identification and simulation during the modeling and simulation cycle for SOFC temperature. Its major advantage consists in decoupling a computerized model from the arithmetic it works with. Usually, users have to decide which arithmetic their implementations are based on. The default choice is the floating-point arithmetic, although it has a number of disadvantages (for example, we cannot guarantee that the computed result is actually correct). Through its layered structure and, in particular, its adapter concept, UniVerMEC allows us to implement a mathematical model largely without the need to think about the kind of arithmetic we want to use. This helps to choose arithmetics according to the actual goal (e.g., offline verification as opposed to fast online simulation/control) and even combine verified and non-verified techniques in a meaningful way (e.g., floating-point parameter identification followed by interval simulation). Currently, UniVerMeC does not implement any stochastic methods or arithmetics. However, it can be extended in this way, which would provide even more possibilities for interoperable work.

UniVerMeC's layered structure is relaxed, that is, a layer can be skipped. The bottom layer *core* provides access to floating point, interval, and affine arithmetic as well as to Taylor models, which share a common interface but rely an different adapters. The next layer, *function*, allows us to represent scalar and vector-valued functions uniformly if their mathematical sense is supplied according to the formalization from (Kiel, 2014). This concept helps to evaluate a function with all arithmetics supported at the *core* layer. We introduce abstractions for derivatives, slopes, Taylor coefficients or contractors at this level, a list which advanced users can extend if necessary. The third layer is responsible for defining models in the framework, for example, the IVPs given in Section 3. It merges the relevant abstractions provided at the previous two layers into one entity. Specialized data structures for higher-level algorithms are at the fourth level, for example, those for special types of search space decomposition used in optimisation. Actual algorithms are implemented at the topmost level. UniVerMeC offers its own global optimisation algorithm *GlobOpt* based on that described in (Hansen and Walster, 2004). Additionally, external software such as IVP solvers or further optimisers can be interfaced at this level. For example, we interface the interior-point tool IPOPT for non-verified optimisation.

4.2. Sensitivity Analysis

Since UniVerMeC already implements the possibility to obtain derivatives for the models, it is easy to study different forms of MPC1 and MPL1 from this point of view. We chose to rely on floating point arithmetic in this case although we could have also used intervals or affine forms. The reason is that a number characterising the first derivative of the temperature $\theta(t)$ or the objective function J wrt. a certain parameter p gives us enough information to apportion uncertainty appropriately.

First, we consider the SOFC temperature $\theta(t)$ as modeled by MPL1 (cf. Eqs. (17) and (19)) in some detail. Since our simplifications concerned the heat capacities, we compute $\frac{\partial\theta(t_k)}{\partial c_{N_2,0}}$, $\frac{\partial\theta(t_k)}{\partial c_{N_2,1}}$, $\frac{\partial\theta(t_k)}{\partial c_{CG,0}}$, and $\frac{\partial\theta(t_k)}{\partial c_{CG,1}}$ for each point of time $t_k \in \{T_b, T_b+1, \ldots, T_e\}$. In Figure 1, the results are shown for F1.a (that is, Eq. (19)) on the left and F1.b (that is, Formula (6) in floating point with f defined by the right side of Eq. (17)) on the right. The Figure demonstrates that, out of the four mentioned parameters, both model variants are most sensitive to $c_{CG,1}$. On the whole, variant F1.b is much less sensitive to changes in parameters.

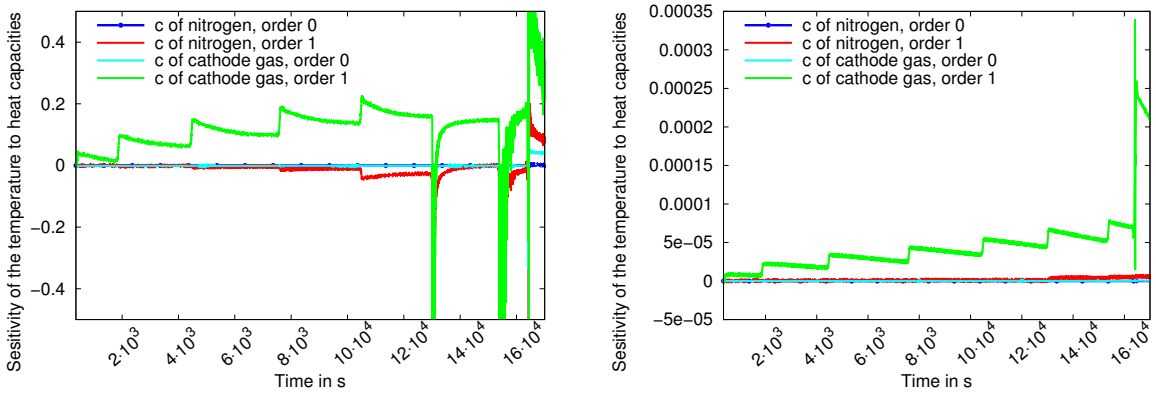

Figure 1. Sensitivity of the modeled SOFC temperature to the heat capacity of nitrogen and cathode gas for the model MPL1: exact solution on the left (F1.a), the Euler approximation on the right (F1.b).

Out of all possible parameters, MPL1 is most sensitive to α_i (equal to α_j and α_k in our setting). Instead of computing $\frac{\partial\theta(t_k)}{\partial p}$ for all relevant points of time, we now consider $\frac{\partial J}{\partial p}$ because, according to Formula 3, it essentially summarizes such plots as in Figure 1 in one number. The results for both MPL1 and MPC1 (as F1.a and F1.b) are given in Table III. Aside from demonstrating extreme sensitivity to α_i an all cases (which was also witnessed in experiment), it lets us observe that both variants of MPC1 are almost equally sensitive to changes in parameters, whereas there is a big difference for the variants of MPL1. The variant MPL1 as F1.b is the least sensitive one and, therefore, can be efficiently employed for parameter identification, the claim supported by the fact that the best parameter set so far was computed using this option. In Figure 2, we can see that MPL1 describes the measured data in the best way (both as F1.a and F1.b).

Table III. Sensitivities of the objective function J (cf. Eq. (3)) for the models MPC1 and MPL1 under F2.a.

J	$\left\lvert\frac{\partial J}{\partial c}\right\rvert$	$\left\lvert\frac{\partial J}{\partial \alpha_i}\right\rvert$	$\left\lvert\frac{\partial J}{\partial c_{N_2,0}}\right\rvert$	$\left\lvert\frac{\partial J}{\partial c_{N_2,1}}\right\rvert$	$\left\lvert\frac{\partial J}{\partial c_{CG,0}}\right\rvert$	$\left\lvert\frac{\partial J}{\partial c_{CG,1}}\right\rvert$
F1.a, MPL1	$2.93594 \cdot 10^{1}$	$3.8117 \cdot 10^{10}$	$4.9631 \cdot 10^{-2}$	$2.63897 \cdot 10^{1}$	1.46662	$1.26157 \cdot 10^{2}$
F1.b, MPL1	$4.76907 \cdot 10^{-3}$	$6.87924 \cdot 10^{5}$	$5.36099 \cdot 10^{-5}$	$2.20879 \cdot 10^{-2}$	$1.3089 \cdot 10^{-3}$	$5.25226 \cdot 10^{-1}$
F1.a, MPC1	$3.09309 \cdot 10^{-1}$	$2.44704 \cdot 10^{8}$	$8.48586 \cdot 10^{-2}$	–	$1.36277 \cdot 10^{-1}$	–
F1.b, MPC1	$3.09307 \cdot 10^{-1}$	$2.44754 \cdot 10^{8}$	$8.48573 \cdot 10^{-2}$	–	$1.36288 \cdot 10^{-1}$	–

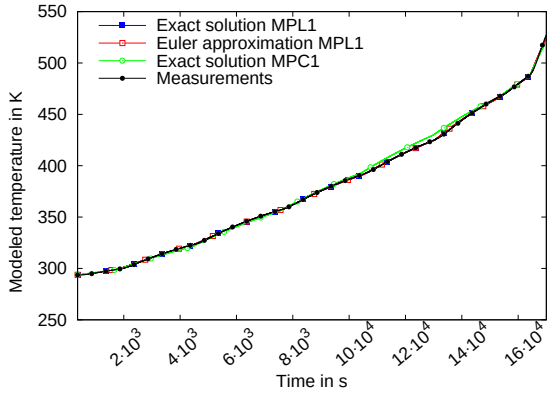

Figure 2. SOFC temperature modeled by MPL1 and MPC1 using F2.a in comparison to the measured data.

4.3. Uncertainty Quantification

We consider uncertainty of different magnitudes in parameters $c_{N_2,0}$ and $c_{CG,0}$ and try to propagate it through the models MPL1 and MPC1 (both as F1.a) using interval, affine, and Taylor model arithmetics. The variant F1.b as a pure approximation by Formula (6) is not feasible in this context because the deviation from the true solution would be too large. That is, to be accurate, we need to solve the corresponding simplified system (Eqs. (8)–(12) or Eq. (17)) numerically in this case. For comparison, we do this under uncertainty using the interval IVP solver VNODE-LP. Additionally, we measure the wall times needed for each relevant simulation. Our goal is to establish an uncertainty level in these parameters which would allow us enclose the measured data in a meaningful way, that is, not entirely because of overestimation effects.

The MPL1 solution from Eq. (19) takes preheaters into account only as measurements, whereas the exact solution in Eqs. (13),(14),(16) explicitly describes them. Besides, the solution in Eq. (19) has three different branches. To be able to enclose all possible states, it is necessary to compute the convex hull of enclosures of all three branches each time when the upper bound of D is not strictly less than zero or the lower bound of D is not strictly larger than zero. This fact makes MPL1 as F1.a more prone to overestimation than other variants, which is reflected in Figure 3, left. Only the uncertainty of $\pm 10^{-5}\%$ of the nominal parameter values of $c_{N_2,0}$ and $c_{CG,0}$ (cf. Table II) can be considered in interval arithmetic meaningfully, for both variants F.a and F.b (the

Table IV. Computing times for temperature simulations with exact solutions to models MPC1 and MPL1 under uncertainty $\pm U\%$ in $c_{N_2,0}$ and $c_{CG,0}$ using interval, affine, and Taylor model arithmetics. The last column shows times for the corresponding variant without the exact solution, obtained using interval-based solver VNODE-LP.

	Intervals	Affine forms	Taylor models	VNODE-LP
MPC1	0.34 s ($U = 10^{-4}$)	112.09 s ($U = 1$)	207 s ($U = 10$)	> 1 day ($U = 10^{-4}$)
MPL1	0.12 s ($U = 10^{-5}$)	23.34 s ($U = 50^{-5}$)	120.5* s ($U = 10^{-3}$)	228.42 s ($U = 10^{-5}$)

latter with VNODE-LP). Note that the nominal values for these parameters are of orders 10^6, 10^4 for the considered parameter set. The uncertainty of $\pm 10^{-4}\%$ leads to too large overestimation in the output $\theta(t)$, so that these enclosures are not useful. Affine forms (with a restart each 5 steps so that the dependencies are lost and the overall simulation is faster) can handle a slightly larger uncertainty of $\pm 50^{-5}\%$. Taylor models perform better with respect to uncertainty ($\pm 10^{-3}\%$) but have a different problem with the solution as in Eq. (19). The library RIOT we employ for Taylor model computations does not implement the elementary function *atan*, so that the branch containing it cannot be used and we have to stop computations.

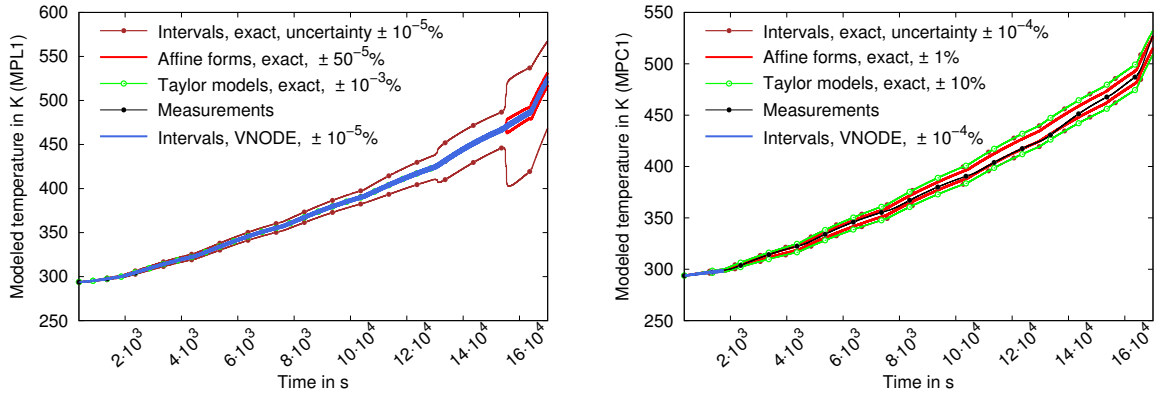

Figure 3. Upper and lower bounds of the temperature with uncertainty in $c_{N_2,0}$ and $c_{CG,0}$: MPL1 on the left and MPC1 on the right.

The model MPC1 behaves better with respect to uncertainty propagation (cf. Figure 3, right). Although interval arithmetic cannot handle more uncertainty than $\pm 10^{-4}\%$ in a meaningful way, affine forms propagate $\pm 1\%$ and $\pm 10\%$, respectively, despite large nominal values of $c_{N_2,0}$, $c_{CG,0}$ for the considered parameter set. The general form of the trajectory is preserved, and the measurement data are enclosed.

In Table IV, the computing times are shown. As a benchmark, we recorded the time necessary for 10 runs of each variant. The table gives the corresponding wall times divided by 10. Not surprisingly, the variant F1.b for both models is slow, extremely so for MPC1 (cf. the last column of the Table). Note that the speed in this case depends on the parameter set, since VNODE-LP implements

a dynamic stepsize control. That is, the simulation can be faster for a different parameter set; however, since the set from Table II had the closest fit for MPC1, we decided not to change it. The simulation reached $t_k = 1761$ s before we terminated it. As opposed to it, VNODE-LP could handle the variant F1.b for MPL1 in an acceptable time. However, the variant F1.a is still faster (especially for MPL1 because it does not have to handle the preheaters explicitly). Besides, we are able to use affine forms and Taylor models here, which achieve acceptable computing times. Note that the time for MPL1 with Taylor models is provided only as a reference for a different parameter set for which it does not become necessary to change the solution branch (so that we do not have to compute *atan* and the simulation is not terminated).

5. Conclusions

In this paper, we analysed two simplified versions of the one dimensional SOFC temperature model from the point of view of their performance during the simulation stage of the modeling and simulation process. The simplification concerned the heat capacities of gases, which were assumed to be constant (MPC1) or linear (MPL1) in temperature, respectively, as opposed to the normal version of the model operating with polynomials of order two. For MPC1 and MPL1, we were able to provide closed form expressions for the solutions (F1.a). Additionally, we analysed the performance of MPC1 and MPL1 when the obtained IVPs were solved numerically (F1.b). Having identified good parameter sets for both models, we performed a sensitivity analysis, which confirmed the experimentally observed fact that both models were very sensitive to changes in coefficients of heat convection. Since the simplifications concerned the heat capacities of the anode and cathode gases, we considered bounded uncertainties in them and propagated them through the system using interval, affine, and Taylor model based methods, which, in addition to the mentioned uncertainty quantification, allowed us to rule out the possibility of numerical errors during simulation.

The models MPC1 and MPL1 are now analysed almost completely from the point of view of simulation. The MPL1 is able to describe the measured data for wide ranges of operating conditions in the best way if no uncertainty in parameters is considered. The variant relying on the closed form expression is the fastest in all considered arithmetics, but less suitable for uncertainty propagation than the corresponding MPC1 one. Using the latter, we are able to process uncertainty of up to the order $\pm 10\%$ of the (large) nominal values of parameters under Taylor model arithmetic without much overestimation, whereas the former one is good for uncertainties up to $\pm 10^{-3}\%$. The problem is that the solution to MPL1 has different branches, which might lead to a large overestimation in "undecided" situations where a convex hull of all possibilities needs to be considered to ensure a verified result. Note that the nominal values are of orders up to 10^7 in the parameter sets with the smallest root mean square measures. The numerical variants of both models are actually too slow to propagate the uncertainty in real time simulations, especially for MPC1. However, they are less sensitive to changes in parameters, which makes them attractive at the (offline) identification stage of the process. An overall conclusion is that MPC1 can be efficiently used over shorter time intervals (especially with uncertainty, in which case it produces enclosures covering the data). MPL1 can compete with the usual non-simplified model from the point of view of data fit over long time intervals and is faster both as the closed-form and the numerical variant.

In our future work, we plan to explore the possibilities to speed up the parameter identification stage using the GPU. (Note that it would not be possible to employ the GPU for the classical simulation stage in our context since it is sequential in its nature — we need initial values as simulation results from the previous step to be able to proceed.) In (Auer et al., 2012; Auer et al., 2014), we have already applied that idea to the verified parameter identification for the non-simplified SOFC temperature model, achieving a significant speed-up. However, we were not able to verify the optimum because of overestimation, and the obtained candidate parameter sets were not very satisfactory with respect to the data fit. We hope that exact solutions to simplified models will help to verify the optimum, so that an overall verification degree of C1 can be achieved (in an acceptable time owing to the GPU). Moreover, it might be possible to employ the model variant F1.c which was dismissed until now because of very high computing times. This goal cannot be reached very easily for a technical reason: implementations of verified methods (e.g., interval analysis, etc.) on the GPU are still very rudimentary in comparison to those available for the CPU.

Acknowledgements

Thanks to A. Rauh and L. Senkel from the University of Rostock for providing measurement data for the SOFC test rig (available in Rostock) along with invaluable advice about the models.

References

AIAA. Guide for the Verification and Validation of Computational Fluid Dynamics Simulations. American Institute of Aeronautics and Astronautics (AIAA G-077-1998), 1998

Auer, E., S. Kiel, T. Pusch, and W. Luther. A Flexible Environment for Accurate Simulation, Optimization, and Verification of SOFC Models, in *Proc. of ASCE-ICVRAM-ISUMA, July 13–16, 2014*. Liverpool, UK, 2014.

Auer, E., S. Kiel, and A. Rauh. Verified Parameter Identification for Solid Oxide Fuel Cells, in *Proceeding of REC 2012*, pages 41–55, 2012.

Auer, E. and W. Luther. Numerical Verification Assessment in Computational Biomechanics, in *Proc. of Dagstuhl Seminar 08021: Numerical validation in current hardware architectures — From embedded systems to high-end computational grids*, Lecture Notes in Computer Science, pages 145–160, 2009.

Auer, E., L. Senkel, S. Kiel, and A. Rauh. Performance of Simplified Interval Models for Simulation and Control of SOFC, in Y. Tsompanakis et al., editors, *Proceedings of the Conference on Soft Computing Technology in Civil, Structural and Environmental Engineering*, Civil-Comp Press, Stirlingshire, UK, 2015.

Auer, E., L. Senkel, S. Kiel, and A. Rauh. Control-Oriented Models for SO Fuel Cells From the Angle of V&V: Analysis, Simplification Possibilities, Performance. *Special Issue of Proceedings of the Conference on Soft Computing Technology in Civil, Structural and Environmental Engineering*, 2015a, submitted.

Berz, M. Modern Map Methods for Charged Particle Optics. *Nucl. Instrum. Methods*, 363(1–2):100–104, 1995.

Bove, R. and S. Ubertini, editors. *Modeling Solid Oxide Fuel Cells.* Springer, Berlin, 2008.

Eble, I. Über Taylor-Modelle. PhD thesis, Universität Karlsruhe, 2007.

de Figueiredo, L. H. and J. Stolfi. Affine Arithmetic: Concepts and Applications. *Numerical Algorithms*, 34 (1–4):147–158, 2004.

Hansen, E. and G.W. Walster. *Global Optimization Using Interval Analysis.* Marcel Dekker, New York, 2004.

Henninger, H., S. Reese, A. Anderson, and J. Weiss. Validation of Computational Models in Biomechanics, in *Proceedings of the Institution of Mechanical Engineers, Part H: Journal of Eng. in Med.*, 224:801–812, 2010.

Hofschuster, W., W. Krämer, and M. Neher. C-XSC and Closely Related Software Packages, in Cuyt A. M., W. Krämer, W. Luther, and P. W. Markstein, editors, *Numerical Validation in Current Hardware Architectures LNCS 5492*:68–102, 2008.

Huang, B., Y. Qi, and A. Murshed. *Dynamic Modeling and Predictive Control in Solid Oxide Fuel Cells*. Wiley, 2012.

Kiel, S. UniVerMec – *A Framework for Development, Assessment, Interoperable Use of Verfied Techniques; with Applications in Distance Computation, Global Optimization, and Comparison Systematics*. PhD thesis, University of Duisburg-Essen, 2014.

Kiel, S., E. Auer, and A. Rauh. Uses of GPU Powered Interval Optimization for Parameter Identificationin the Context of SO Fuel Cells, in *Procedings of NOLCOS 2013*, pages 558–563, 2013.

Lohner, R. On the Ubiquity of the Wrapping Effect in the Computation of Error Bounds, in U. Kulisch, R. Lohner, A. Facius (Editors), *Perspectives on Enclosure Methods*, pages 201–218, Springer-Verlag, 2001.

Moore, R. E., R. B. Kearfott, and M. J. Cloud. Introduction to Interval Analysis. Society for Industrial and Applied Mathematics, Philadelphia, 2009.

Nedialkov, N. S. The Design and Implementation of an Object-Oriented Validated ODE Solver. Kluwer Academic Publishers, 2002.

Oberkampf, W. L., T. G. Trucano, and C. Hirsch: Verification, Validation, and Predictive Capability in Computational Engineering and Physics. Technical Report SAND2003-3769, Sandia National Laboratories, 2003.

Pusch, T. Umsetzung einer verifizierten Parameteridentifikation mit GUI Realisierung für Festoxidbrennstoffzellen, Master's thesis, Universität Duisburg-Essen, November 2013.

Rauh, A., L. Senkel, and H. Aschemann. Interval-Based Sliding Mode Control Design for Solid Oxide Fuel Cells with State and Actuator Constraints, in *IEEE Transactions on Industrial Electronics*, 2015.

Rauh, A., L. Senkel, E. Auer, and H. Aschemann. Interval Methods for the Implementation of Real-Time Capable Robust Controllers for Solid Oxide Fuel Cell Systems, *Mathematics in Computer Science*, 8(3–4):525–542, 2014.

Rauh, A., L. Senkel, J. Kersten, and H. Aschemann. Reliable Control of High-Temperature Fuel Cell Systems using Interval-Based Sliding Mode Techniques, *IMA Journal of Mathematical Control and Information*, 2014.

Saltelli, A., M. Ratto, T. Andres, F. Campolongo, J. Cariboni, D. Gatelli, M. Saisana, and S. Tarantola. Global Sensitivity Analysis: The Primer. Wiley, 2008

Stauning, O. Automatic Validation of Numerical Solutions. PhD thesis, September 1997.

Wächter, A. and L.T. Biegler. On the Implementation of an Interior-point Filter Line-search Algorithm for Large-scale Nonlinear Programming, *Math. Program.*, 106(1):25–57, 2006.

Structural Condition Assessment Using Imprecise Probability

Jamshid Mohammadi[1)], Mehdi Modares[1)] and Joshua Bergerson[2)]
[1)]*Illinois Institute of Technology, mohammadi@iit.edu, mmodares@iit.edu*
[2)]*Argonne National Laboratory, jbergerson@anl.gov*

Abstract: Investigating the condition of a structural system requires an accurate estimate of the applied load and the current condition of the structure. As such, the presence of uncertainty becomes significant; because the variations inherent in design parameters will significantly affect the reliability of the structure. Therefore, it is crucial to appropriately quantify uncertainty in the design parameters as well as perform structural reliability analyses for determining the condition of the structure and its failure potential. This paper presents a new method for condition assessment of structures, which exhibit polymorphic uncertainty in their design parameters. An imprecise probability approach is used to quantify the polymorphic uncertainty. Applying this technique to conventional methods, the reliability analysis of a structure is improved. By incorporating imprecise probability values in the reliability analysis process, bounds for the probability of failure are estimated and established. These bounds are then used as a measure for the condition assessment of the structure. A numerical example is provided to demonstrate the applicability of the developed method.

Keywords: structural dynamics, uncertainty, imprecise probability, p-box

1. Introduction

In structural engineering, the reliability and safety of a structure must be accurately assessed. Moreover, in order to achieve this reliability, the uncertainties present in both the structure and applied loads must be included in the analytical schemes. It is generally assumed in reliability analysis that all of the uncertainty is due to inherent stochasticity, known as aleatoric uncertainty, in the system and rather than due to modeling errors or faulty assumptions, known as epistemic uncertainty. This aleatoric uncertainty is accounted for using traditional theories of probability. Probabilistic methods require random variables to follow an assumed distribution, a requirement which often cannot be satisfied. One method of uncertainty modeling that avoids the shortcomings of traditional probabilistic modeling and other isomorphic uncertainty modeling methods is imprecise probability. Imprecise probability is a polymorphic uncertainty modeling method which involves setting possibilistic bounds on the cumulative distribution function describing uncertain parameters.

Numerous methods for reliability assessment of structural systems with uncertainty have been developed, the majority of which are based on traditional probability theories (isomorphic probabilistic approaches). Although theories of structural reliability are well-established, the practical application of the methods developed for reliability analysis is mathematically complicated. Moreover, the mathematical complexity increases dramatically as the number of structural components or modes of failure increases.

As a result, practicing engineers often resort to gross simplifications to overcome the complexity inherent in the general formulation of structural reliability. This leads to reliability predictions that have a significant level of error. In this work, a new method for reliability analysis of a structure using an imprecise probability approach is developed. This method offers a new direction for incorporating uncertainties in the analysis and relies on defining the uncertain parameters using imprecise probability structures. Due to its polymorphic approach, this method offers a more realistic and comprehensive yet simpler process of treating uncertainties than traditional probabilistic-based reliability analyses.

2. Review of Traditional Probabilistic Structural Reliability

2.1. Performance and Limit-State Analysis

Traditional structural reliability analyses seek to estimate the probability that a structure will be unable to withstand the applied loading, known as the probability of failure. Considering a performance function, Z, with multiple independent variables representing the design parameters, X_i (Ang and Tang, 2007):

$$Z = g(X_1, X_2, \ldots, X_n) \tag{1}$$

Using the performance function Z, the probability of failure can be defined as:

$$P_F = P(Z \leq z_o) \tag{2}$$

in which z_o is the performance limit defined as the minimum level of performance such that a structure is considered safe. Similarly, the probability of failure can be written as:

$$P_F = \int_{-\infty}^{z_o} f_z(z)dz \tag{3}$$

in which $f_z(z)$ is the probability density function (PDF) of the performance function Z in the multivariate space.

Many traditional reliability methods rely on the first order approximation, referred to as the First Order Reliability Method (FORM). This method yields sufficiently accurate results in cases where parameters X_i have small uncertainties. To enhance FORM, the Second Order Reliability Method (SORM) has also been developed. SORM also has limitations due to the increase in complexity of the analysis when the number of modes of failure increases or when there is a high level of correlation among parameters in the limit-state equation.

2.2. First Order Reliability Method (FORM)

In order to develop the general formulation for FORM, a first-order approximation on the performance function Z about the mean values, μ_i, of each design parameter is performed as:

$$Z = g(\mu_i) + \sum_{i=1}^{n} (X_i - \mu_i) \frac{\partial g(\mu_i)}{\partial X_i} \tag{4}$$

Assuming the variables X_i are independent, the mean, μ, and standard deviation, σ, of Z are defined as:

$$\mu = g(\mu_1, \mu_2, ..., \mu_n) \tag{5}$$

$$\sigma = \left(\sum_{i=1}^{n} c_i^2 \sigma_i^2 \right)^{1/2} \tag{6}$$

in which $c_i = \partial g(\mu_i) / \partial X_i$. FORM works well when uncertainties are small (say < 0.3).

Many performance functions exist. For example, considering a structure under a random load, S, and a random resistance, R, the performance function and performance limit can be written as:

$$Z = R - S \tag{7}$$

$$z_o = 0 \tag{8}$$

Therefore, the probability of failure is:

$$P_F = P(Z \leq 0) = \int_{-\infty}^{0} f_z(z) dz \tag{9}$$

The mean and standard deviation of Z are $\mu_Z = (\mu_R - \mu_S)$ and $\sigma_Z = \sqrt{\sigma_R^2 + \sigma_S^2}$, respectively.

Assuming S and R to be random variables defined by normal probability density functions, the probability of failure is:

$$p_F = \Phi\left(\frac{z_0 - \mu_Z}{\sigma_Z} \right) \tag{10}$$

in which Φ is the standard normal cumulative distribution function. Substitution for z_o, the mean, and the standard deviation of Z yields:

$$p_F = \Phi\left(\frac{\mu_S - \mu_R}{\sqrt{\sigma_R^2 + \sigma_S^2}} \right) \tag{11}$$

in which the probability of failure for the structure is evaluated based on the probabilistic values of the load and resistance.

When multiple modes of failure (m modes) are present, consideration of the two extreme cases of independence and perfect correlation among the modes allows for setting bounds on the probability of failure for the structure as:

$$\max(P_f^1, P_f^2, ..., P_f^m) \leq P_f \leq 1 - \prod_{j=1}^{m} (1 - P_f^j) \tag{12}$$

in which the lower bound is the case of perfect correlation between failure modes and the upper bound is the case of independence among failure modes. In order to ascertain the reliability of the structure, the upper bound (independence case) can be used for the reliability level of the structure.

3. Methodology

3.1. Formulation of Imprecise Probability Structural Condition Assessment

The polymorphic approach for obtaining the probability of failure enables more reliable structural condition assessment due to the consideration of polymorphic uncertainties in both the applied loads and resistance of the structure. The general algorithm for Imprecise Probability Structural Condition Assessment (IPSCA) is given below.

1. Determine the structure's modes of failure (e.g. bending, shear, deflection).
2. Determine the imprecise probability structure for the performance function for each failure mode. For each failure mode:
   a. Construct independent imprecise probability structures for the uncertain load and resistance.
   b. Perform random sampling on the CDF probability levels of uncertain load and resistance imprecise probability structures. For each realization *r* of the simulation:
      - Randomly select independent CDF values for load and resistance constructed imprecise probability structures and compute the corresponding interval load $\tilde{S}$ and interval resistance $\tilde{R}$ for the selected CDF values.
      - Determine and store interval bounds on the uncertain performance function.
   c. Repeat sufficiently large number of realizations to construct imprecise probability structure for uncertain performance function.
3. Determine the interval probability of failure for each failure mode by computing the performance function at the performance limit for each bound of the corresponding imprecise probability structure.
4. Determine the interval probability of failure of the structure using obtained intervals of probability of failure for each mode for two extreme cases of perfect correlation and independence among the modes as:

$$\max\left[\min(P_f^1), \min(P_f^2), ..., \min(P_f^m)\right] \le P_f \le 1 - \prod_{j=1}^{m}\left[1 - \max(P_f^j)\right] \tag{13}$$

5. Determine the maximum probability of failure as the upper bound of the interval probability of failure of the structure (independence case).

4. Example

In this section, an illustrative example is provided to demonstrate the applicability of the developed method in investigating the structural condition of a timber pedestrian bridge, shown in Figure 1. An increase in the bridge's live load (pedestrians using the bridge) in recent months has raised a concern over its safety.

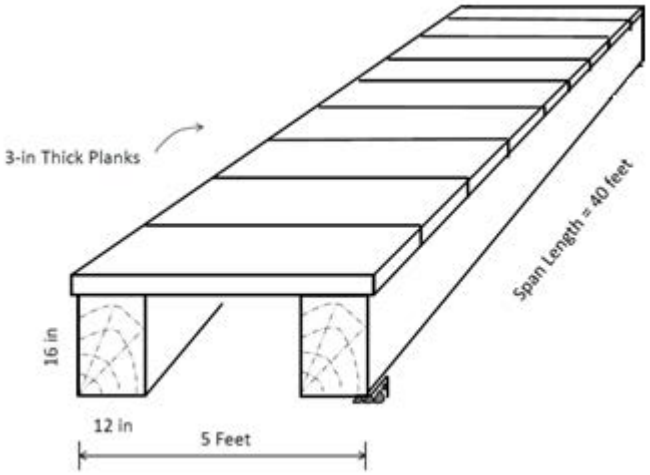

Figure 1. Schematics of a pedestrian bridge in the example.

4.1. PROBLEM PARAMETERS

The dominant modes of failure, as considered in this analysis, include bending, shear, and deflection modes of failure for the two beams. The input parameters are explained in detail in the authors' pervious work (Mohammadi and Modares, 2013). Based on the results from the previous analysis, Table I summarizes the probabilistic values (using Gaussian distributions) of the mean, μ, and standard deviation, σ, of the resistance and load for each failure mode.

Table I. Probabilistic values for load and resistance for considered failure modes.

Mode	Resistance		Load	
Bending	Bending Capacity		Applied Bending Stress	
	μ_R^b (psi)	σ_R^b (psi)	μ_S^b (psi)	σ_S^b (psi)
	6,990	1,820	1,730	416
Shear	Shear Capacity		Applied Shear Stress	
	μ_R^s (psi)	σ_R^s (psi)	μ_S^s (psi)	σ_S^s (psi)
	825	214	57.8	13.9
Deflection	Deflection Limit		Induced Deflection	
	μ_R^d (in)	σ_R^d (in)	μ_S^d (in)	σ_S^d (in)
	4.0	0	2.41	1.01

4.2. TRADITIONAL PROBABILITY ANALYSIS

The formulation for traditional probability analysis is used to compute the probability of failure for each failure mode (Eq. (11)). The results are summarized in Table II.

Table II. Probability of failure for each failure mode.

Mode	Probability of Failure, P_f
Bending	2.40×10^{-3}
Shear	1.73×10^{-4}
Deflection	5.77×10^{-2}

Considering the two extreme cases of perfect correlation and independence among the failure modes, the probability of failure for the structure can be bounded as (Eq. (12)):

$$0.0577 \le P_f \le 0.0602$$

In order to ascertain the reliability of the structure, the upper bound (independence case) can be used for the reliability level of the structure, $P_f = 0.0602$. It is worth noting that traditional probability analysis methods (including FORM) are not capable of considering uncertainties and variations in the mean or standard deviation of either load or resistance. The framework of imprecise probability structures allows for consideration of these uncertainties as depicted in the alternate solution of this example problem.

4.3. Imprecise Probability Structural Condition Assessment Analysis

The example problem is reanalyzed considering resistance and load values defined by imprecise probability structures for both the bending and shear failure modes. As the resistance value given in Table I for the deflection mode of failure is a code limit, it is not a random value, and thus only a deterministic CDF was used to model its value. An imprecise probability structure was also used to model the load (induced deflection) for the deflection mode of failure. All imprecise probability structures were generated by considering a ±10% shift in the mean values defining each random variable. Figures 2-4 depict the imprecise probability structures for load and resistance of bending, shear, and deflection modes, respectively (except for the resistance for the deflection failure mode).

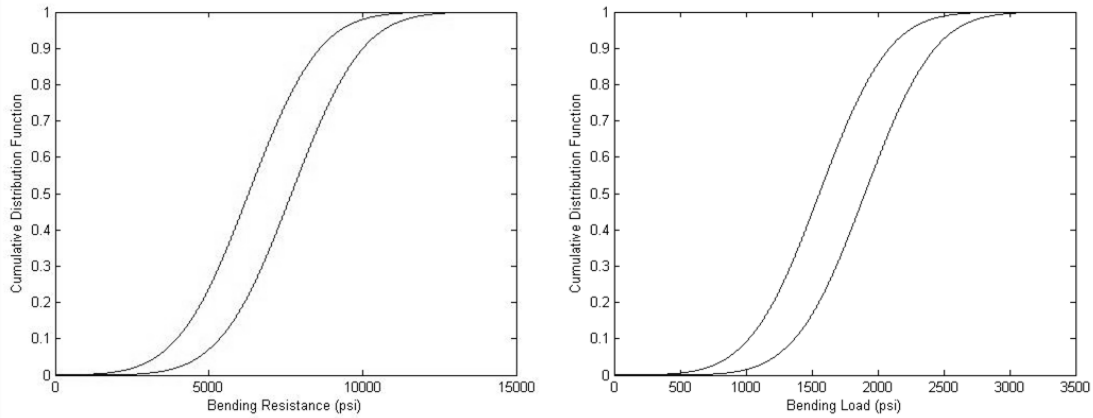

Figure 2. Imprecise probability structures for the resistance and load in bending mode.

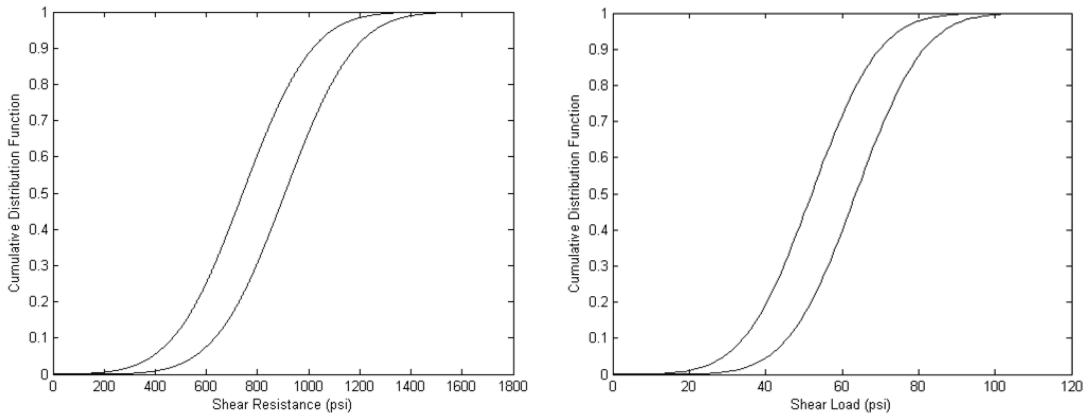

Figure 3. Imprecise probability structures for the resistance and load in shear mode.

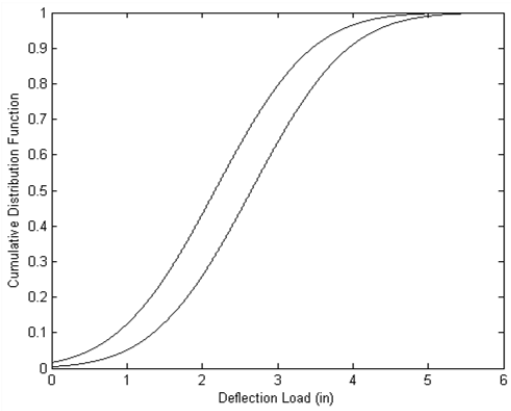

Figure 4. Imprecise probability structure for the induced deflection in the deflection mode.

4.4. SOLUTION

The Imprecise Probability Structural Condition Assessment (IPSCA) methodology was utilized for computing interval bounds on the probability of failure for each failure mode. These interval probabilities of failure were then used to compute an interval bound on the probability of failure of the structure. One million Monte Carlo realizations are performed and the interval bounds on the probability of failure for each failure mode and for the structure are determined (Table III).

Table III. Interval bounds on the probability of failure for each failure mode and for the structure.

Bending		*Shear*		*Deflection*		***Structure***	
Lower Bound	*Upper Bound*	*Lower Bound*	*Upper Bound*	*Lower Bound*	*Upper Bound*	***Lower Bound***	***Upper Bound***
4.76E-04	9.36E-03	3.00E-05	6.98E-04	3.50E-02	9.12E-02	**3.50E-02**	**1.00E-01**

4.5. OBSERVATIONS

As shown in Table III, the probability of failure of the structure is dominated by the single failure mode with the greatest probability of failure. Moreover, the results determined using IPSCA contain the FORM results, verifying the developed method.

5. Summary and Conclusions

In this work, a new method for reliability analysis of a structure using an imprecise probability approach is developed. This method, entitled Imprecise Probability Structural Condition Assessment (IPSCA), offers a new direction for incorporating uncertainties in condition assessment of structural systems. As IPSCA does not place restrictive assumptions typical in traditional probabilistic structural condition assessment methods, it provides a more realistic and comprehensive yet simpler process of treating uncertainties than traditional probabilistic-based reliability analyses. This method allows for uncertainty in the load and resistance for each mode of failure using imprecise probability structures. An example problem illustrating the application of the developed method demonstrated the application and computational feasibility of IPSCA. The simplicity of the proposed method makes it attractive for introducing uncertainty defined by imprecise probability into structural condition assessment procedures.

References

Ang, A. H.-S. and W. H. Tang. "Probability Concept in Engineering: Emphasis on applications to Civil and Environmental Engineering" Wiley, Hoboken, NJ., 2007.

Augenbaugh, J. M. and C. J. J. Paredis. "The Value of Using Imprecise Probabilities in Engineering Design." Journal of Mechanical Design, 128(4):969-979, 2006.

Ferson, S., V. Kreinovich, L. Ginzburg, D. S. Myers et al. Construction probability boxes and Dempster-Shafer structures, Tech. Rep. SAND2002-4015. Sandia National Laboratory, 2003.

Modares, M., R. L. Mullen and R. L. Muhanna. "Natural Frequencies of a Structure with Bounded Uncertainty." Journal of Engineering Mechanics, Dec. Ed., 1363-1371, 2006.

Mohammadi, J. and M. Modares. "Practical Approach to Using Uncertainties in Structural Condition Assessment." Practice Periodical on Structural Design and Construction, 18:155-164, 2013.

Muhanna, R. L. and R. L. Mullen. "Uncertainty in Mechanics Problems-Interval-Based Approach." Journal of Engineering Mechanics, June Ed., 557-566, 2001.

Oberkampf, W., J. Helton and K. Sentz. "Mathematical Representations of Uncertainty." AIAA Non-Deterministic Approaches Forum, AIAA 2001-1645. Seattle, 2001.

Williamson, R. and T. Downs. "Probabilistic Arithmetic I: Numerical Methods for Calculating Convolutions and Dependency Bounds." International Journal of Approximate Reasoning, 4:89-158, 1990.

Zhang, H., R. L. Mullen and R. L. Muhanna. "Finite Element Structural Analysis using Imprecise Probabilities Based on P-Box Representations." 4th International Workshop on Reliable Engineering Computing. Singapore, 211-225, 2010.

Why Min-Based Conditioning

Salem Benferhat[1)] and Vladik Kreinovich[2)]
[1)] *CRIL (Centre de Recherche en Informatique de Lens), CNRS – UMR 8188*
Université d'Artois, Faculté des sciences Jean Perrin
Rue Jean Souvraz, SP 18, F62307 Lens Cedex, France
benferhat@cril.univ-artois.fr
[2)] *Department of Computer Science, University of Texas at El Paso*
500 W. University, El Paso, Texas 79968, USA
vladik@utep.edu

Abstract: In many practical situations, we do not have full information about which alternatives are possible and which are not. In such situations, an expert can estimate, for each alternative, the degree to which this alternative is possible. Sometimes, experts can produce numerical estimates of their degrees, but often, they can only provide us with qualitative estimates: they inform us which degrees are higher, but do not provide us with numerical values for these degrees. After we get these degrees from the experts, we often gain additional information, because of which some alternatives which were previously considered possible are now excluded. To take this new information into account, we need to appropriately update the corresponding possibility degrees. In this paper, we prove that under several reasonable requirements on such an update procedure, there is only one procedure that satisfies all these requirements – namely, the min-based conditioning.

Keywords: imprecise knowledge, possibility distribution, conditioning, knowledge update, invariance

1. Formulation of the Problem

Need for ordinal-scale possibility degrees. It is often useful to describe, for each theoretically possible alternative ω from the set of all *theoretically* possible alternatives Ω, to what extent this alternative is, in the expert's opinion, *actually* possible.

Often, the only information that we can extract from experts is the qualitative one: which alternatives have a higher degree of possibility and which have lower degree. In some cases, we have a linear order between possible degrees, so all we know is the order of different alternatives, from the least possible to the most possible.

In principle, we could just use this order to process this information, but computers have been designed to process numbers – and they are still much better in processing numbers. So, to speed up processing of this data, degrees of possibility are usually described by numbers $\pi(\omega)$ from the interval $[0, 1]$: the higher the degree of possibility of an alternative ω, the larger the value $\pi(\omega)$.

These numbers by themselves do not have an exact meaning, the only meaning is in the order. So, in principle, the same meaning can be described if we apply any strictly increasing transformation to the interval $[0, 1]$.

Usually, some of this freedom is eliminated by the convention that the largest degree of possibility is set to 1; we can always achieve this with an appropriate transformation. Such possibility degrees are known as *normalized*. Thus, we arrive at the following definition (see, e.g., (Dubois et al., 1994; Dubois et al., 1998; Dubois and Prade, 1998; Gutierrez et al., 2014)):

Definition 1. *Let Ω be a finite Universe of discourse. A* possibility distribution *is a function $\pi : \Omega \to [0, 1]$ for which*

$$\max_{\omega \in \Omega} \pi(\omega) = 1.$$

Need for conditioning and normalization. Often, after we have learned the possibility degrees $\pi(\omega)$, we acquire an additional information, that some of the alternatives that we originally thought to be possible are actually not possible.

For example, we had originally the set Ω of possible suspects, but it turned out that some of the original suspects have alibis. As a result, the new list of suspects Ψ is smaller: $\Psi \subset \Omega$.

Let us now assume that for each of the suspects ω we had a numerical degree of this possibility $\pi(\omega)$ that this person committed the crime. Then, once we know that the list of suspects has narrowed, how to we change these possibility degrees?

In general, if we had a possibility distribution on a set Ω of possible alternatives, and we now learned that only alternatives from a subset $\Psi \subset \Omega$ are possible, how does this new information change our possibility degrees?

Of course, now that we learn that only alternatives from the smaller set Ψ are possible, we should set $\pi'(\omega) = 0$ for all $\omega \notin \Psi$. For all other alternatives $\sigma \in \Psi$, at first glance, it may sound reasonable to just retain the original possibility degrees, i.e., to take $\pi'(\omega) = \pi(\omega)$. However, we have an additional requirement, that the largest possibility degree should always be 1, and the above procedure does not always guarantee this requirement.

For example, if:

- we started with $\pi(a) = 0.4$, $\pi(b) = 0.5$, and $\pi(c) = 1.0$, and
- we learned that $\omega \in \Psi = \{a, b\}$,

then:

- if we simply take $\pi'(a) = 0.4$, $\pi'(b) = 0.5$, and $\pi'(c) = 0$,
- the largest of the resulting three degrees is not equal to 1.

It is therefore necessary to *normalize* the resulting degrees $\pi'(\omega)$, i.e., to transform them into new degrees for which the largest is 1. This transformation – that we will call a *conditioning operator* – should:

- take, as input, the original possibility distribution π, and
- generate the new probability distribution π'' that we will denote by $(\pi \mid \Psi)$.

According to Definition 1, a possibility distribution π is a function that assigns, to every alternative ω from the finite set Ω of possible alternatives, a value $\pi(\omega)$ from the interval $[0,1]$ – the value that describe the degree to which, according to the available information, the alternative ω is possible.

A function from a finite set is nothing else but a tuple. Thus, if we denote the elements of the finite set Ω by $\omega_1, \ldots, \omega_n$, then a possibility distribution is simply a tuple consisting of n values from the interval $[0,1]$: $\pi = (\pi(\omega_1), \ldots, \pi(\omega_n))$. In these terms, a conditioning operator is a mapping that takes one such tuple π as an input and returns a new tuple $\pi'' = (\pi \mid \Psi)$ as the output.

To get π'', one possibility is to divide all the values $\pi'(\omega)$ by the largest of these values. In the above example, the largest value is 0.5, so we get $\pi''(a) = \dfrac{0.4}{0.5} = 0.8$ and $\pi''(b) = \dfrac{0.5}{0.5} = 1$.

Another possibility is to replace the largest of the values $\pi'(\omega)$ by 1 and leave all other values unchanged. For the above example, this would mean that we take $\pi''(a) = 0.4$ and $\pi''(b) = 1$.

Let us describe a general definition of the corresponding operator.

Definition 2. *By a* conditioning operator*, we mean a mapping* $(\pi \mid \Psi)$ *that:*

- *inputs a possibility distribution* π *on a set* Ω *and a non-empty set* $\Psi \subseteq \Omega$*, and*
- *returns a new possibility distribution for which* $(\pi \mid \Psi)(\omega) = 0$ *for all* $\omega \notin \Psi$*.*

What are the reasonable conditioning operators?

2. Analysis of the Problem

Let us describe the desired properties of the conditioning operator.

First property: it should not matter how we previously judged alternatives that we now know to be impossible. A first reasonable requirement is that since alternatives $\omega \notin \Psi$ are excluded, their original possibility degrees should not affect the resulting degrees. In other words, if two original possibility distributions π and π' differ only by their values outside Ψ, then the conditioning should be the same.

C1. If $\pi_{|\Psi} = \pi'_{|\Psi}$, i.e., if $\pi(\omega) = \pi'(\omega)$ for all $\omega \in \Psi$, then

$$(\pi \mid \Psi) = (\pi' \mid \Psi).$$

Second property: order between possibility degree of different alternatives should not change. Another reasonable condition is that while the numerical values of possibility degrees may change, the order between these degrees should not change:

C2. If $\pi(\omega) < \pi(\omega')$ for some $\omega, \omega' \in \Psi$, then

$$(\pi \mid \Psi)(\omega) < (\pi \mid \Psi)(\omega').$$

C3. If $\pi(\omega) = \pi(\omega')$ for some $\omega, \omega' \in \Psi$, then

$$(\pi \mid \Psi)(\omega) = (\pi \mid \Psi)(\omega').$$

Third property: it should not matter whether we learn the new knowledge right away or in two steps. Often, we first learn some information, based on which the set of possible alternatives is limited to a subset $\Psi \subset \Omega$, and then learn some additional information according to which the set of possible alternatives is even smaller $\Psi' \subset \Psi$. In this case, :

- we first first condition the original degrees of possibility π with respect to Ψ, resulting in $\pi' = (\pi \mid \Psi)$, and then
- we condition π' with respect to the new set Ψ', resulting in $\pi'' = (\pi' \mid \Psi') = ((\pi \mid \Psi) \mid \Psi')$.

Alternative, we could learn both pieces of the information at the same time. In this situation, our reaction to this new information would replace the original possibility distribution π with $(\pi \mid \Psi')$.

In both cases, we gain the exact same new information, so the resulting changes in possibility degrees should be the same:

C4. If $\Psi' \subset \Psi$, then $((\pi \mid \Psi) \mid \Psi') = (\pi \mid \Psi')$.

Fourth property: alternatives which were originally considered impossible should not matter. Another condition is that if had an alternative ω_0 which we originally believed to be impossible – i.e., whose degree of possibility is 0 – then:

- this alternative should remain impossible after conditioning, and
- the possibility degrees of all other alternatives $\omega \neq \omega_0$ should remain the same, whether we keep the alternative ω_0 in the remaining set Ψ or whether we explicitly delete ω_0 from the set Ψ.

This property can be described as follows:

C5. If $\pi(\omega_0) = 0$ for some $\omega_0 \in \Psi$, then

$$(\pi \mid \Psi)(\omega_0) = 0 \text{ and } (\pi_{|\Psi - \{\omega_0\}} \mid \Psi) = (\pi \mid \Psi)_{|\Psi - \{\omega_0\}}.$$

Final property: invariance. As we have mentioned earlier, often, the only information that we can extract from the experts is which alternatives have a higher degree of possibility and which have a lower degree of possibility. In other words, what matters is the order between the degrees, not the numerical values of the degrees. So, the situations should not change if we simply apply some re-scaling that does not change the order (such as $x \to x^2$), i.e., if we apply some increasing one-to-one function $T : [0,1] \to [0,1]$ to transform each degree $\pi(\omega)$ into a degree $T(\pi(\omega))$. The corresponding re-scaled tuple will be denoted by $T\pi$: $(T\pi)(\omega) \stackrel{\text{def}}{=} T(\pi(\omega))$.

It is reasonable to require that the result of applying the conditioning operator not change if we apply such a re-scaling. In other words, the following two operations should leads to the exact same result:

– either we apply the conditioning in the original scale, i.e., transform π into $(\pi \mid \Psi)$, and then, apply the re-scaling T, resulting in $T(\pi \mid \Psi)$;

– or we first apply the re-scaling, resulting in $T\pi$, and then apply the conditioning, resulting in $(T\pi \mid \Psi)$.

Thus, we arrive at the following requirement:

C6. For every increasing one-to-one function $T : [0,1] \to [0,1]$, we have

$$(T\pi \mid \Psi) = T(\pi \mid \Psi).$$

Now, we are ready to formulate our main result.

3. Main Result

Proposition. *The only conditioning operator that satisfies the properties* **C1**–**C6** *is the min-based operator (*Dubois and Prade, 1984*;* Hisdal, 1978*) for which:*

- $(\pi \mid \Psi)(\omega) = 1$ *when* $\omega \in \Omega$ *and* $\pi(\omega) = \max\limits_{\omega' \in \Omega} \pi(\omega')$*;*
- $(\pi \mid \Psi)(\omega) = \pi(\omega)$ *when* $\omega \in \Omega$ *and* $\pi(\omega) < \max\limits_{\omega' \in \Omega} \pi(\omega')$*; and*
- $(\pi \mid \Psi)(\omega) = 0$ *when* $\omega \notin \Psi$*.*

Discussion. The usual derivation of the min-based conditioning (see, e.g., (Dubois et al., 1994)) is to interpret the degree $(A \mid B)$ as the maximal value for which $A \,\&\, B$ (with min as "and"-operation) has the same truth value as $(A \mid B) \,\&\, B$.

Our result shows that *maximality* can be replaced with *invariance* – which reflects the ordinal-scale character of the corresponding possibility degrees.

Proof.

1. It is easy to show that the min-based operator satisfies the properties **C1**–**C6**.

To complete the proof, we need to prove that, vice versa,

– every conditioning operator that satisfies these five properties

– is indeed the min-based operator.

To prove this statement, we will consider two possible cases:

– the case when the set Ψ contains some alternative ω for which $\pi(\omega) = 1$, and

– the case when the set Ψ does not contain any alternative ω for which $\pi(\omega) = 1$.

2. Let us first consider the case when the set Ψ contains some alternative ω for which $\pi(\omega) = 1$. In this case, the min-based formula leads to $(\pi \,|\, \Psi)(\omega) = \pi(\omega)$ for all $\omega \in \Psi$.

Let us show that this equality holds for all conditioning operators that satisfy the properties **C1**–**C6**.

2.1. If there is no $\omega_0 \in \Psi$ for which $\pi(\omega_0) = 0$, let us add such an element to our set Ω. According to Property **C5**, this will not change the result. Thus, without losing generality, we can safely assume that there is an element $\omega_0 \in \Psi$ for which $\pi(\omega_0) = 0$.

As for the values $\pi(\omega)$ for $\omega \notin \Psi$, we can use the property **C1** to replace them with zeros.

2.2. Let us sort values $\psi(\omega)$ corresponding to different alternatives $\omega \in \Psi$ in increasing order. We know that the resulting list of values includes 0 and 1, so this list has the form

$$v_1 = 0 < v_2 < \ldots < v_{k-1} < v_k = 1,$$

where k is the number of different values $\pi(\omega)$ corresponding to $\omega \in \Psi$.

Let us use property **C6** to prove that the values $(\pi \,|\, \Psi)$ should also be from this list. Indeed, let us consider the following strictly increasing function $T(v)$: for $v_i \le v \le v_{i+1}$, we take

$$T(v) = v_i + \left(\frac{v - v_i}{v_{i+1} - v_i}\right)^2 \cdot (v_{i+1} - v_i).$$

One can easily check that for this function, $T(v_i) = v_i$ for all i, so $T(\pi) = \pi$. Thus, the property **C6** implies that $T(\pi \,|\, \Psi) = (\pi \,|\, \Psi)$, i.e., that for each value $v = (\pi \,|\, \Psi)(\omega)$, we should have $T(v) = v$. But for the above function $T(v)$, the only such values are $v_1, \ldots, v_k$.

So, indeed, the values $v_1 < \ldots < v_k$ are mapped to the same k values. By properties **C2** and **C3**, equal values of $\pi(\omega)$ are mapped into equal values of $(\pi \,|\, \Psi)(\omega)$, and smaller values of $\pi(\omega)$ are mapped into smaller values of $(\pi \,|\, \Psi)(\omega)$. Thus, the values v_i' corresponding to v_i are also sorted in increasing order: $v_1' < \ldots < v_k'$. Each new value v_i' must coincide with one of the original values v_j. So, in the increasing list $v_1 < \ldots < v_k$ of k values, we have k new values v_i' which have the same order. This implies that v_1' must be the smallest of v_i, i.e., $v_1' = v_1$, that v_2' be the second smallest, i.e., $v_2' = v_2$, and, in general, $v_i' = v_i$, i.e., indeed, $(\pi \,|\, \Psi)(\omega) = \pi(\omega)$ for all $\omega \in \Psi$.

3. Let us now consider the case when the set Ψ does not contain some alternative ω for which $\pi(\omega) = 1$.

In this case, we can also add (if needed) an element ω_0 for which $\pi(\omega_0) = 0$, and sort the values $\pi(\omega)$ corresponding to $\omega \in \Psi$ into an increasing sequence $v_1 = 0 < v_2 < \ldots < v_k < 1$; the only difference is that in this case, the largest value v_k in this increasing sequence is smaller than 1.

One of the new values should be equal to 1. So, due to Properties **C2** and **C3**, only the largest degree v_k should be mapped into 1.

Similarly to Part 2 of this proof, we can prove that each of the the values v_1, …, v_{k-1} maps into one of the values v_1, …, v_k, and that if $v_i < v_j$, then $v_i' < v_j'$. By induction, we can prove that $v_i' \ge v_i$. Since we have only one additional value to move to, for each i, we have either $c_i' = v_i$ or $v_i' = v_{i+1}$. In other words, for each alternative, after conditioning, we will have either the same degree of possibility as before, or the next one.

Let use the Property **C4** to prove, by contradiction, that a value $v_i < v_k$ cannot be transformed into the next value v_{i+1}. Let us assume that, vice versa, there is an element $\omega_i \in \Psi$ for which $\pi(\omega_i) = v_i$ and $(\pi \,|\, \Omega)(\omega_i) = v_{i+1}$. To get a contradiction, let us consider the new set $\Omega^* = \Omega \cup \{\omega^*\}$, with a new element ω^*, and a new possibility distribution π^* for which:

- we have $v_i < \pi^*(\omega^*) < v_{i+1}$ and
- we have $\pi^*(\omega) = \pi(\omega)$ for all $\omega \neq \omega_i$.

Let us consider two conditionining paths from Ω^* to Ψ:

- in the first path, we go from Ω^* to Ω and then from Ω to Ψ;
- in the second path, we go from Ω^* to $\Psi^* \stackrel{\text{def}}{=} \Psi \cup \{\omega^*\}$ and then from Ψ^* to Ψ.

According to the Property **C4**, the resulting value $(\pi^* \,|\, \Psi)(\omega_i)$ should be the same for both paths.

In the first path, first, we go from Ω^* to Ω. This transition eliminates a single element ω^* for which $\pi^*(\omega^*) < 1$. Thus, according to Part 2 of this proof, all the possibility degrees of remaining elements remain unchanged. Thus, we have $(\pi^* \,|\, \Omega) = \pi$. We already know that $(\pi \,|\, \Psi)(\omega_i) = v_{i+1}$. Thus, due to Property **C4**, we have

$$(\pi^* \,|\, \Psi)(\omega_i) = ((\pi^* \,|\, \Omega) \,|\, \Psi)(\omega_i) = v_{i+1}.$$

On the other hand, in the second path, we first move from Ω^* to Ψ^*. In this transition, we have v_k transformed into 1, and the original value $\pi^*(\omega_i) = v_i$ can either remain the same, or it can be transformed to the next value which is now $\pi^*(\omega^*) < v_{i+1}$. In both cases, the new possibility degree is smaller than v_{i+1}: $\pi(\omega_i) < v_{i+1}$. When we then reduce the set Ψ^* to Ψ, then all the alternatives for which we originally had $\pi^*(\omega) = \pi(\omega) = v_k$ and now have $\pi'(\omega) = 1$ remain in the set. Thus, all other alternatives – including the alternative ω_i – according to Part 2 of this proof, retain their values. For ω_i, this implies that $(\pi' \,|\, \Psi)(\omega_i) = \pi'(\omega_i) < v_{i+1}$. Thus, we have $(\pi^* \,|\, \Psi)(\omega_i) = \pi'(\omega_i) < v_{i+1}$, which contradicts to the above equality $(\pi^* \,|\, \Psi)(\omega_i) = v_{i+1}$.

This contradiction shows that the transformation from v_i to v_{i+1} is indeed impossible. Thus, we have $v_i' = v_i$.

So, indeed, we have derive the min-based conditioning from the properties **C1**–**C6**. The proposition is proven.

Acknowledgements

This work was supported in part by the US National Science Foundation grants HRD-0734825, HRD-1242122, and DUE-0926721.

This work was performed when Salem Benferhat was visiting El Paso.

The authors are thankful to the anonymous referees for valuable suggestions.

References

Dubois, D., J. Lang and H. Prade. Possibilistic logic, In: D. Gabbay, C. J. Hogger, and J. A. Robinson (eds.), *Handbook of Logic in Artificial Intelligence and Logic Programming. Vol. 3. Nonmonotonic Reasoning and Uncertain Reasoning*, pages 439–513, Oxford University Press, New York, 1994.

Dubois, D., S. Moral and H. Prade. Belief change rules in ordinal and numerical uncertainty theories, In: D. Gabbay and P. Smets (eds.), *Handbook of Defeasible Reasoning and Uncertainty Management Systems, Vol. 1. Quantified Representation of Uncertainty and Imprecision*, pages 311–392, Kluwer Academic Publ., Dordrecht, 1998.

Dubois, D. and H. Prade. Fuzzy logics and the generalized modus ponens revisited, *Cybernetics and Systems*, 15:293–331, 1984.

Dubois, D. and H. Prade. Possibility theory: qualitative and quantitative aspects. In: D. Gabbay and P. Smets (eds.), *Handbook of Defeasible Reasoning and Uncertainty Management Systems, Vol. 1. Quantified Representation of Uncertainty and Imprecision*, pages 169–226, Kluwer Academic Publ. Dordrecht, 1998.

Gutierrez, L., M. Ceberio, V. Kreinovich, R. L. Gruver, M. Peña, M. J. Rister, A. Saldana, J. Vasquez, J. Ybarra and S. Benferhat. From interval-valued probabilities to interval-valued possibilities: case studies of interval computation under constraints, *Proceedings of the 6th International Workshop on Reliable Engineering Computing REC'2014*, Chicago, Illinois, pages 77–95, May 25–28, 2014.

Hisdal, E. Conditional possibilities: independence and non-interaction, *Fuzzy Sets and Systems*, 1:283–297, 1978.

Approximation of ECG Signals using Chebyshev Polynomials

Shashwati Ray and Om Prakash Yadav
Bhilai Institute of Technology, Durg-491001, (C.G.), India, shashwatiray@yahoo.com, opyadav@csitdurg.in

Abstract: The ECG (Electrocardiogram) signal represents electrical activity of heart and is recorded for monitoring and diagnostic purpose. These signals are corrupted by artifacts during acquisition and transmission predominantly by high frequency noise due to power line interference, electrode movements, etc. Addition of these noise change the amplitude and shape of the ECG signal which affect accurate analysis and hence need to be removed for better clinical evaluation. In this paper, ECG signal taken from MIT -BIH database is first denoised using Total Variation Denoising (TVD); using Majorization minimization (MM) optimization technique. ECG signals generate massive volume of digital data, so they need to be suitably compressed for efficient transmission and storage. Hence, for efficient compression the signal is segmented into various sections using Bottom-Up approach. The individual sections are then approximated using Chebyshev polynomials of suitable orders. The performance of the approximation technique is measured by computing the Maximum Absolute Error, the Compression Ratio, Root Mean Square Error, Percent Root Mean Square Difference and Percent Root Mean Square Difference Normalized. The results are also compared with other techniques as reported in the literature, where significant improvements in all the performance metrics are observed.

Keywords: ECG signal, total variation denoising, majorization-minorization, bottom-up, Chebyshev nodes, Chebyshev approximation

1. Introduction

The electrocardiogram (ECG) describes the electrical activity of the heart. It conveys information about structure of the heart and functions of its electrical conduction (Walraven, 2011). It is obtained as voltage variations by placing electrodes at specific positions on the chest, arms and legs. The ECG is characterized by a series of waves whose morphology and timing provide clinically useful information. The time pattern that characterizes the occurrence of successive heartbeats is also very important. The ECG signals are used to monitor drug and to detect metabolic disturbances. A systematic interpretation of the ECG signals prevents overlooking of important abnormalities of cardiac system like rhythm of heartbeats, size and position of chambers and the presence of any damage to the heart's muscle cells or conduction system, the effects of cardiac drugs, and the function of implanted pacemakers (Braunwald, 1997).

A single normal cycle of the ECG represents the successive atria depolarization/repolarisation and ventricular depolarization /repolarisation which occur with every heartbeat (Acharya et. al, 2007). These can be approximately associated with the peaks and troughs of the ECG waveform labelled P, Q, R, S, and T as shown in Figure 1.

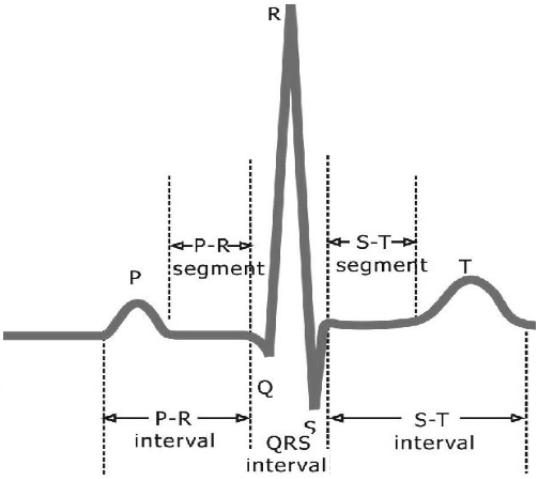

Figure 1. ECG Signal and its various waves.

The first step in the design of an ECG system involves understanding the nature of the signal that needs to be acquired. The ECG signal consists of low amplitude voltages in the presence of high offsets and noise. The common electrode used in ECG systems has a maximum offset voltage of 300mV. The actual desired signal is 0.5mV superimposed on the electrode offset. ECG Signal processing is a huge challenge since the actual signal value will be 0.5mV in an offset environment of 300mV. Other factors like AC power-supply interference, RF interference, electrode movement from surgery equipment, and implanted devices like pace makers and physiological monitoring systems can also impact accuracy (Bharadwaj and Kamath, 2011).

The amount of data involved in storage and transmission of digital ECG signals is quite large. So it needs to be adequately compressed in a way so that it can be accurately reconstructed. The ECG compression techniques are broadly classified as: direct methods, transform-based methods and parameter extraction methods (Jalaleddine et. al, 1990). In direct methods, the original ECG signal samples are compressed directly, and in transformation method the original samples are first transformed and then compressed. In parameter extraction methods, the features of the processed signal are extracted and then these features are used for the reconstruction of the signal (Jalaleddine et. al, 1990).

Various time domain compression algorithms like FAN, AZTEC, CORTES and SAPA etc can be found in the literature. These methods are based on the idea of extracting few significant signal samples to represent the signal and then decoding the same set of samples. These techniques are based on heuristics in the sample selection process. This makes them faster but suffer from suboptimality (Zahhad, 2011).

Several compression algorithms including polynomial approximations and polynomial interpolation have been proposed for ECG data compression. The advantage of polynomial approximation is that it requires only polynomial coefficient describing the data signal and is able to approximate the original ECG signal quite efficiently.

Polynomials of maximum degree 3, including spline functions have been proposed for ECG interpolation in (Karczewicz and Gabbouj, 1997). The representation of ECG signals using second degree quadratic polynomials is studied by Nygaard et al in (Nygaard et. al, 1999). High degree Legendre polynomials were used for ECG data compression (Philips, 1993; Colomer and Colomer, 1997; Tchiotsop et. al, 2007). Although Chebychev polynomials are widely used in mathematical interpolation and approximation, ECG signal compression through Chebychev polynomials are hardly found in the literature. In (Tchiotsop et. al, 2007) ECG data compression is done using Discrete Chebyshev Transform by segmenting the signal into blocks which consist of multiple cardiac cycles.

These methods are mainly focused on approximation of the entire ECG beat without paying attention to the importance of the intervals of the signal which is the case for vital signals. The signal is often broken into segments within which the signals can be considered stationary. In this way, each part can be analyzed or processed separately.

In this paper, we propose a computationally efficient method to model ECG signals through Chebyshev polynomials. The ECG signal contains an important noise component so a preprocessing is applied before the segmentation effectively takes place. The ECG signal is first denoised using Total Variation Denoising using Minimization-Majorization (TVD-MM) technique. In order to have a better compression ratio we must have a lower order of the polynomial. So, the denoised signal is then segmented into segments using Bottom-Up approach. Next, we model each segment independently using Chebyshev interpolation and combine them to reconstruct the complete signal.

The rest part of the paper is organized as follows: in section 2, we present the computational performance metrics to be applied to measure the efficiency of the method. In section 3 and 4, we give a brief introduction to Chebychev polynomials and Chebyshev interpolation. In section 5, we describe the proposed method along with the algorithm to achieve ECG data compression. In section 6, we present the implementation of our method on the ECG signals using the MIT-BIH arrhythmia database and discuss the results obtained. In the last section we give the conclusions regarding the presented approach.

2. Evaluation of Compression Method

Let N be the total number of the ECG samples and $p(x_i)$ and $f(x_i)$ represent the samples in original and reconstructed signal. In most ECG compression algorithms, the various performance metrics are as:

Root Mean Square Error ($RMSE$): is the average of the square of the errors (Sormno and Laguna, 2006)

$$RMSE = \sqrt{\frac{\sum_{i=1}^{N}(p(x_i) - f(x_i))^2}{N}} \tag{1}$$

Maximum Error ($Maxerror$): is the maximum error (Hadjileontiadis, 2006)

$$MaxError = \max_{N}(|(p(x_i) - f(x_i))|) \tag{2}$$

Compression Ratio (CR): is defined as the ratio between the number of bits needed to represent the original and the compressed signal (Zahhad et. al, 2010). We can also define it as the ratio between the number of samples needed to represent the original and the compressed signal.

$$CR = \frac{N}{n} \tag{3}$$

where n is the order of the interpolating polynomial

Percent Root Mean Square Difference (PRD): is the measure of acceptable fidelity (Zahhad et. al, 2010)

$$PRD\% = 100\sqrt{\frac{\sum_{i=1}^{N}(p(x_i) - f(x_i))^2}{\sum_{i=1}^{N} p(x_i)^2}} \tag{4}$$

Percent Root Mean Square Difference Normalized ($PRDN$): is the normalized version of PRD (Fira and Goras, 2008) and depends on the signal mean value p_m

$$PRDN\% = 100\sqrt{\frac{\sum_{i=1}^{N}(p(x_i) - f(x_i))^2}{\sum_{i=1}^{N}(p(x_i) - p_m)^2}} \tag{5}$$

3. Chebyshev polynomials

The Chebyshev polynomials (Gil et. al, 2007) of first type and degree n are defined in terms of trignometric cosine function as:

$$T_n(x) = \cos(n\cos^{-1}(x)) \text{ for } n \geq 0 \tag{6}$$

The expressions for Chebyshev polynomials are obtained from the recursive relation

$$\begin{aligned} T_0(x) &= 1 \\ T_1(x) &= x \\ T_{n+1}(x) &= 2xT_n(x) - T_{n-1}(x) \text{ for } n \geq 1 \end{aligned} \tag{7}$$

The Chebyshev polynomials of degree n, $T_n(x)$, has $n+1$ zeros in the interval [-1, 1], which can be calculated as

$$x_j = \cos\left(\frac{2j+1}{2n+1}\pi\right),\ 0 \leq j \leq n \tag{8}$$

The roots of the Chebyshev polynomial are also known as Chebyshev points or nodes. In the same interval the $n+1$ extrema of the polynomial $T_n(x)$ are located at

$$\widetilde{x_j} = \cos\left(\frac{\pi j}{n}\right),\ 0 \leq j \leq n \tag{9}$$

At all the maxima $T_n(x) = 1$, while at all the minima $T_n(x) = -1$. The Chebyshev polynomials are orthogonal in the interval $[-1, 1]$ over the weight $w(x) = \left(1 - x^2\right)^{-1/2}$. They also satisfy discrete orthogonality relationships. Other properties of Chebyshev polynomials can be found in (Szego, 1975).

4. Polynomial Approximation using Interpolation

A polynomial approximation problem is of finding a polynomial close to a given function and has the freedom to select the significant points. Once the significant points have been fixed, it is reduced to an interpolation problem that can be solved by polynomial interpolation (Birkhoff and Boor, 1965). Let $p(\mathbf{x})$ represent ECG segment vector of length N consisting of samples of $p(x_i)$ such that

$$p(\mathbf{x}) = \{p(x_0), p(x_1), ..., p(x_N)\}\ ,\ \mathbf{x} \in [a, b]$$

Given a set of $N + 1$ data points $(x_i, p(x_i))$ we want to construct a polynomial f of degree N with the property

$$f(x_i) \approx p(x_i),\ i = 0, 1, ...N$$

Suppose the interpolation polynomial is in the form

$$f(x) = a_N x^N + a_{N-1} x^{N-1} + ... + a_2 x^2 + a_1 x + a_0,\ x \in [a, b] \tag{10}$$

which means that

$$f(x_i) \approx p(x_i) \forall i \in \{0, 1, ...N\} \tag{11}$$

Substituting Eq.(11) in Eq.(10) we get a system of linear equations which in matrix form reads

$$\begin{bmatrix} x_0^N & x_0^{N-1} & \cdots & x_0 & 1 \\ x_1^N & x_1^{N-1} & \cdots & x_1 & 1 \\ \vdots & \vdots & & \vdots & \vdots \\ x_N^N & x_N^{N-1} & \cdots & x_N & 1 \end{bmatrix} \begin{bmatrix} a_N \\ a_{N-1} \\ \vdots \\ a_0 \end{bmatrix} = \begin{bmatrix} p(x_0) \\ p(x_1) \\ \vdots \\ p(x_N) \end{bmatrix} \tag{12}$$

The matrix on the extreme left is the Vandermonde's matrix. The system given by Eq.(12) would have a unique solution if the determinant of the Vandermonde matrix does not vanish (Bjorck and Pereyra, 1970). Solving this system for a_k we can construct the interpolating polynomial $f(x)$.

Alternatively we can write the required polynomial explicitly using Lagrange's formula (Yang et. al , 2005; Chan et al, 2001) as

$$f(x) = \sum_{i=0}^{N} f(x_i) \prod_{\substack{j=0 \\ j \neq i}}^{N} \frac{x - x_j}{x_i - x_j}, x \in [a, b] \tag{13}$$

Let us now construct yet another interpolating polynomial $p(x)$ by sampling $f(x)$ at n interpolation points such that $n < N$. We can estimate the difference between them, i.e., the interpolation error $E(x)$. Let Π_n denote the space of polynomials of degree$\leq n$, and let $C^{n+1}[a,b]$ denote the space of functions that have $n+1$ continuous derivatives on the interval $[a,b]$. Then from the truncation error from the Taylor series, we have this theorem:

Theorem 1: Let $f(x) \in C^{n+1}[a,b]$. Let $p(x) \in \Pi_n$ such that it interpolates $f(x)$ at the $n+1$ distinct points $x_0, ..., x_n \in [a,b]$. Then $\forall\ x \in [a,b]$, $\exists\ \xi \in [a,b]$ such that

$$E(x) = f(x) - p(x) = \frac{1}{(n+1)!} f^{(n+1)}(\xi) \prod_{j=0}^{n} (x - x_j)$$

where ξ is an intermediate point between x_0 and x_n (Caporale and Cerrato, 2008).

If we are free to choose the interpolating points $x_0, ..., x_n$ within this interval, then the product $\prod_{j=0}^{n} (x - x_j)$ can be minimized which in turn would minimize the interpolating error $E(x)$. This can be achieved by choosing interval as $[-1, 1]$ and the interpolating points x_j as the Chebyshev points (Yang et. al , 2005). The following theorem gives an estimate of the error for the above case.

Theorem 2: Assume that $p(x)$ interpolates $f(x)$ at $x_0, x_1, ..., x_n$. Also assume that these $n+1$ interpolation points are the $(n+1)$ roots of the Chebyshev polynomial of degree $T_{n+1}(x)$, which are given by Eq.(8). Then $\forall\ x \in [-1, 1]$,

$$|f(x) - p(x)| \leq \frac{1}{2^n (n+1)!} \max_{\xi \leq 1} |f^{n+1}(\xi)||$$

Our goal is not to approximate a function $p(x)$ on the interval $[-1, 1]$, but to approximate the values of the function $p(x)$ corresponding to the discrete set of points given by Eq.(8). An arbitrary function $p(x)$ can be approximated in the interval $[-1, 1]$ (Mason and Handscomb, 2002) by

$$p(x) = \sum_{k=0}^{n} c_k T_k(x), x \in [-1, 1] \tag{14}$$

where the coefficients c_j are defined as

$$\begin{aligned} c_0 &= \frac{1}{n+1} \sum_{j=1}^{n+1} p(x_j) \\ c_k &= \frac{2}{n+1} \sum_{j=1}^{n+1} p(x_j) T_k(x_j), k = 1, ..., n \end{aligned} \tag{15}$$

5. Proposed Method

The signal encounters various types of artifacts during acquisition, transmission and storage. The noises introduced are due to power line interference (PLI), body movements, electrode contacts, electromagnetic field interference, and respiration movements etc (Acharya et. al, 2007). Presence of noises in ECG signals degrades the signal quality and thus affects the visual diagnosis and feature extraction. Thus, noise removal becomes an essential part in ECG preprocessing for better performance in ECG analysis and diagnosis.

Total variation denoising (TVD) is an approach for noise reduction and preservation of sharp edges of signals. The total variation (TV) of a signal measures how much the signal changes between signal values. Total variation denoising (TVD) is based on the principle that signals with excessive and possibly spurious detail have high total variation. According to this principle, reducing the total variation of the signal subject to it being a close match to the original signal, removes unwanted detail whilst preserving important details such as edges. Unlike a conventional low-pass filter, TV denoising is defined in terms of an optimization problem. Here we first apply the majorization-minorization approach to optimize the total variation in the ECG signals (Yadav and Ray, 2015).

The purpose of the segmentation is to divide a signal to several segments with the same statistical characteristics such as amplitude and frequency. A segmentation algorithm has a global perspective that it produces the best Piecewise Linear Representation (PLR) of data with the least amount of error (Keogh et. al, 2001). Since statistical characteristic of ECG changes with time, so ECG signals are considered as non-stationary signals. Analysis of stationary signal is easier as compared to non- stationary signal so signal segmentation is applied as a pre-processing step for non-stationary signal analysis. Hence, we apply the The Bottom Up algorithm, also called as iterative merge which begins by dividing the original time series data of length n into a large number of segments and is consequently merged into bigger segments until stopping criteria is met (Yadav and Ray, 2016).

Since we are processing one segment, our working domain is in the interval $[a, b]$. So, we first transform the interpolation interval $y \in [-1, 1]$ using

$$x = \frac{(b-a)y + (a+b)}{2} \tag{16}$$

This converts the interpolation problem for $f(x)$ on $[a, b]$ into interpolation problem for $f(x) = g(x(y))$ in $y \in [-1, 1]$. The Chebyshev points in the interval $y \in [-1, 1]$ are the roots of the Chebyshev polynomial $T_n(y)$, i.e.,

$$y_j = \cos\left(\frac{2j+1}{2n+1}\pi\right),\ 0 \le j \le n$$

The corresponding $n+1$ interpolation points in the interval $[a, b]$ using Eq.(16) are now

$$x_j = \frac{(b-a)y_j + (a+b)}{2},\ 0 \le j \le n \tag{17}$$

The interpolation error now is given by

$$|f(x) - p(x)| \le \frac{1}{2^n(n+1)!}\left|\frac{b-a}{2}\right|^{n+1} \max_{\xi\in[a,b]}\left|f^{(n+1)}(\xi)\right|$$

In our method we need to construct the function $f(x)$ using Eq.(13) with all the N ECG samples of one segment. Then we find the Chebyshev nodes and subsequently the interpolating polynomial using these nodes. Next, we calculate the error and if the error is not within our tolerance, we increase the order. Since an ECG signal sampled value may not be available at the Chebyshev nodes, we derive this value by linear interpolation using adjacent ECG sampled values. We continue doing these operations till our error criterion is met.

We apply the same technique to all the segments and model each of them independently using Chebyshev interpolation method. We present here an algorithm to show the steps of our method.

Algorithm Chebyshev_poly_approx=Chebyshev_poly_approx (N, ε, $f(x)$, $p(x)$, $[a, b]$)
Inputs: $p(x)$, $[a, b]$, $\varepsilon = 10^{-3}$
Outputs: $f(x)$
BEGIN algorithm

1. Fix the order n of the Chebyshev approximation.
2. Transform the Chebyshev nodes on the domain $[a, b]$ and find the zeros or the Chebyshev nodes x_j using Eq.(17)
3. Find the function value $f(x_j)$ by linear interpolation using the adjacent integral points around x_j
4. Construct interpolating polynomial $f(x)$ using Eq.(13).
5. Calculate error $E(x) = \max |f(x) - p(x)|$
6. If $E > \varepsilon$ then $n = n + 1$ and go to step 2

END algorithm

6. Implementation and Results

An ECG signal is not linear, rather more curvaceous consisting of waves of various shapes. For testing the performance of our algorithm we conducted our tests in MATLAB environment. An ECG signal of duration 10 seconds with 8274 samples is taken from MIT-BIH (Goldberger et. al, 2000) arrhythmia database. Each file is sampled at 720Hz sampling frequency with 11 bits per sample of resolution. The denoised signal is obtained using the TVD approach. Since the ECG signal is quasi-stationary, segmentation plays very important role. The segmented points must be related with the diagonastical parameters, because they determine the diagonastical intervals and the wave amplitudes of the ECG. Peter Kovacs (Kovacs, 2012) had divided the ECG signal into 12 segments. In order to keep the model as simple as possible, number of segments should be minimal. So the number of segments has to be intelligently decided. Using Bottom Up approach we divide the denoised ECG signal into 10 segments so that the significant points and waves remain preserved at the time of approximation.

Since the shape of ECG is variable within and across patients, so all the segments cannot be approximated by a signal polynomial. Instead a number of polynomials are to be reconstructed depending upon the shape of segments. The proposed algorithm is implemented and tested over each segment of the ECG signal by choosing the order of polynomial in such a way so as to reduce the $MaxError$. Figure 2 to Figure 4 show the 10 original ECG signal segments and their approximated signals with their Chebyshev nodes marked as '$*$'. The original signal is shown in 'red' and the reconstructed signal is shown in 'blue'. Figure 5 shows the complete original and reconstructed signal.

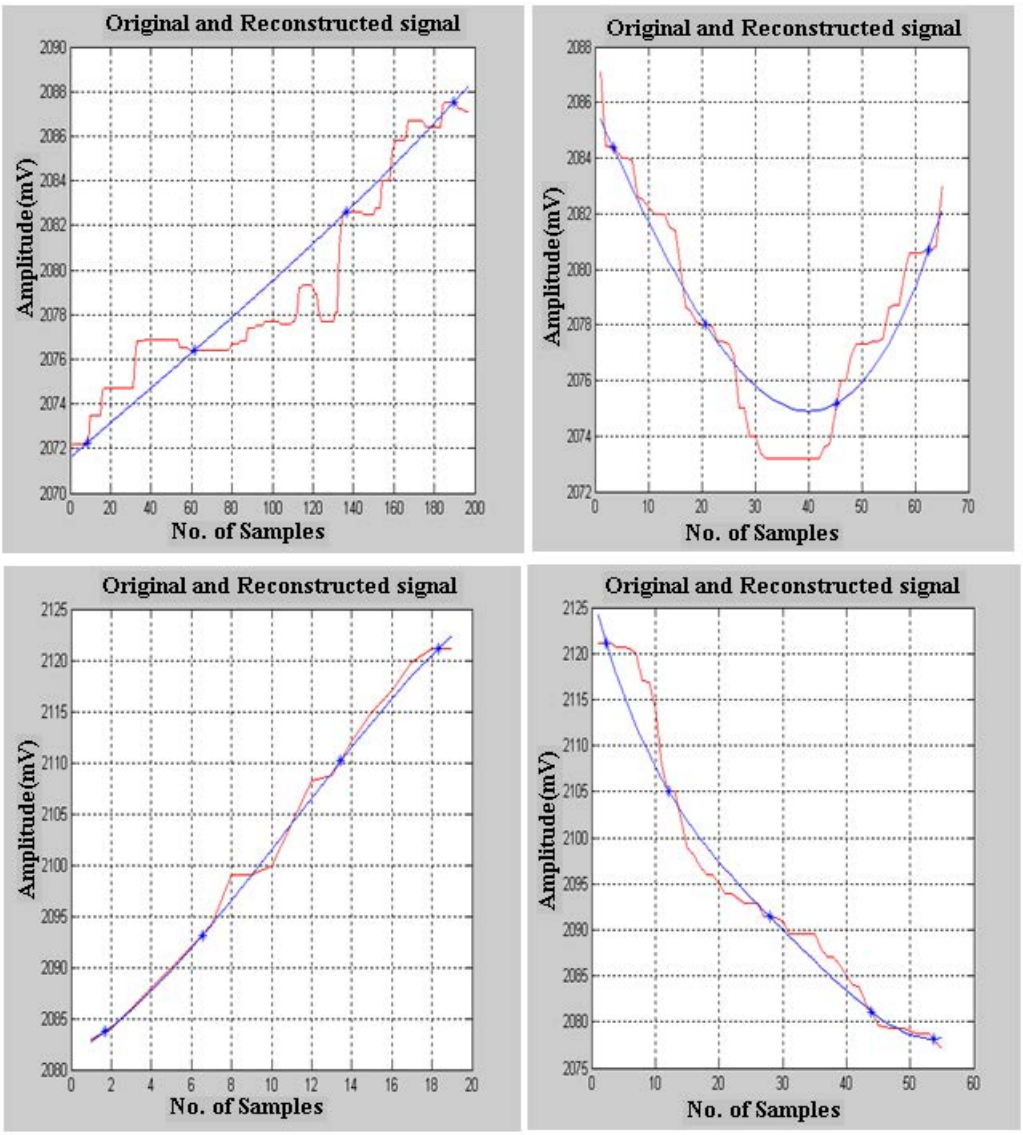

Figure 2. Segments 1 to 4 of Original and Reconstructed signals.

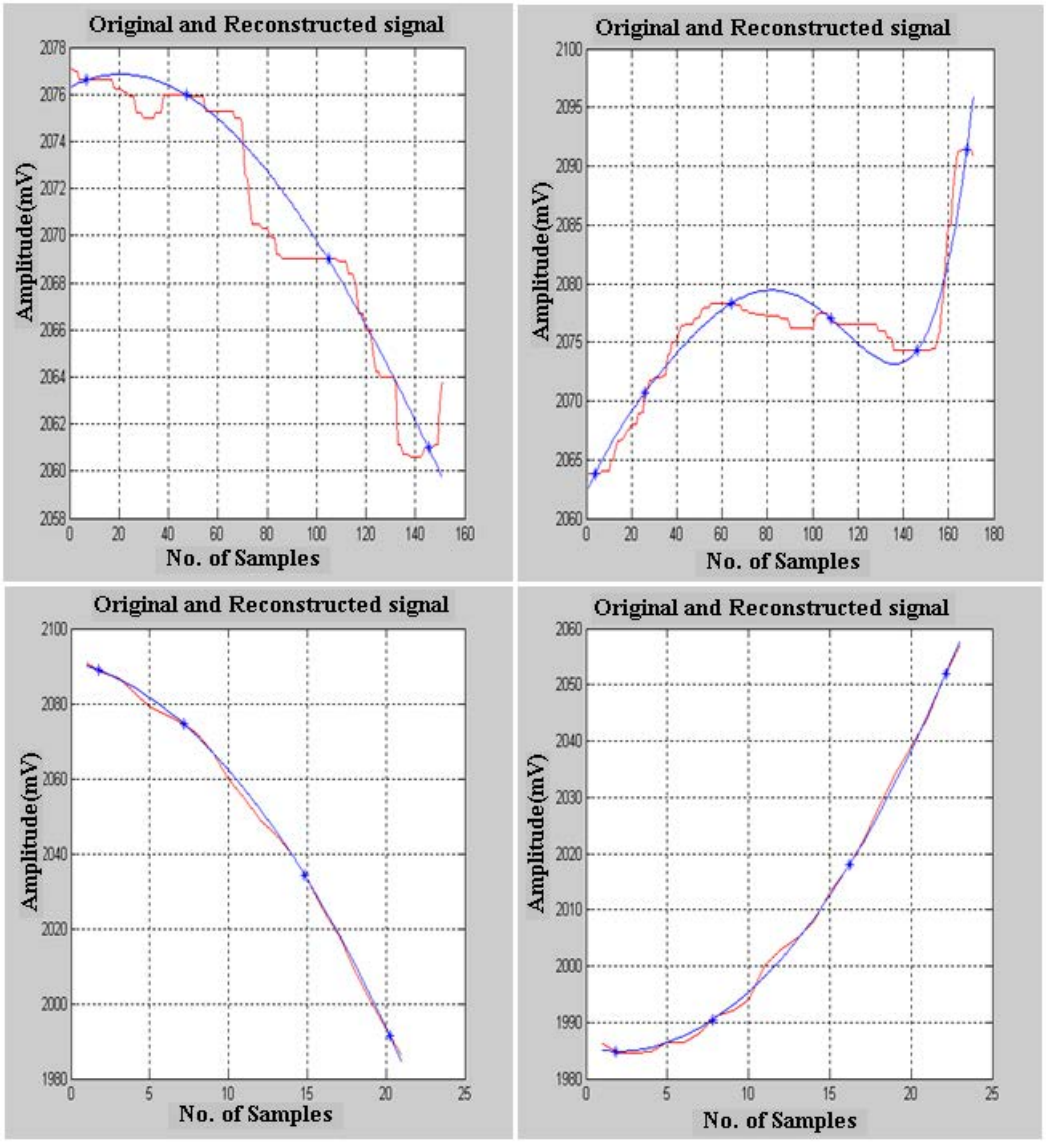

Figure 3. Segments 5 to 8 of Original and Reconstructed signals.

The performance of the Chebyshev approximation technique is measured in terms of CR, $RMSE$, $MaxError$, PRD and $PRDN$. Table I shows the results obtained for individual segments. The orders of the polynomials for each segment are chosen to retain the original shapes of the reconstructed signals. Compression ratios for linear sections are higher and can be approximated by third order Chebyshev polynomial with PRD approximately equal to 0.05. $MaxError$ for individual segments were also calculated and the highest is nearly 5.2 for segment number 6. ECG compression techniques with less than 10 % approximation error are considered to be medically

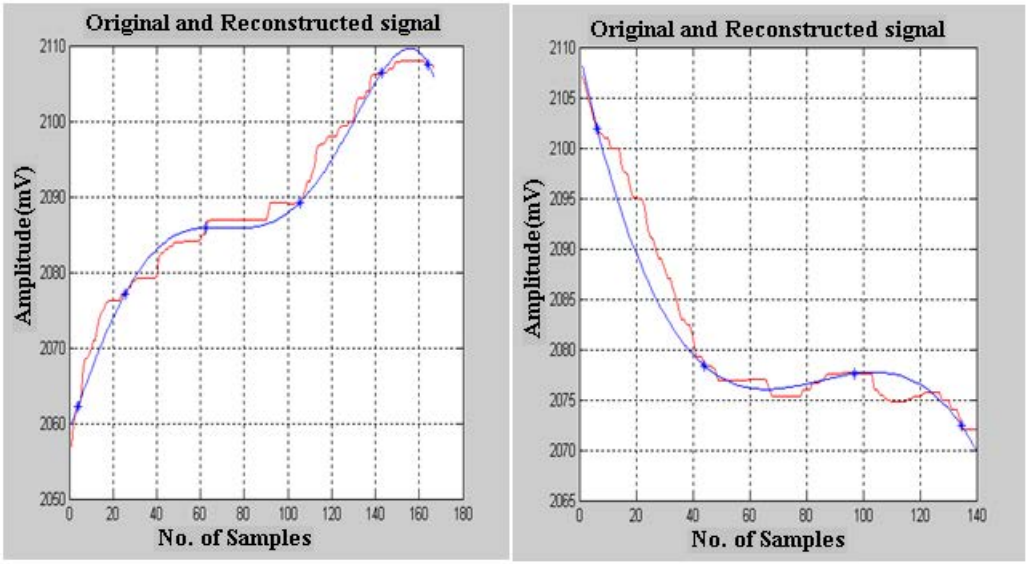

Figure 4. Segments 9 and 10 of Original and Reconstructed signals.

Table I. Performance metrics for all the segments.

Segment Number	Order n	N	CR	$RMSE$	$MaxError$	PRD	$PRDN$
1	3	197	65.67	1.5526	4.3348	0.0747	34.6824
2	3	65	21.67	1.2036	2.2892	0.0579	32.2823
3	3	19	06.33	0.9568	1.4826	0.0455	7.4977
4	4	55	14.75	2.7307	3.0925	0.1304	19.7871
5	3	151	50.33	1.3628	3.0040	0.0658	25.5228
6	5	171	34.20	1.7778	5.2056	0.0857	31.4943
7	3	21	7.00	1.4089	2.9302	0.0687	4.3420
8	3	23	7.67	0.9004	1.3611	0.0448	3.9164
9	5	167	33.40	1.8528	3.7423	0.0887	15.2980
10	3	140	46.67	2.3227	2.7732	0.1116	25.3066
Average	-	-	28.6683	1.6069	4.2298	0.0774	20.0130

accepted (Sandryhaila et. al, 2012). The maximum value of PRD is 0.13 for segment number 4 and average PRD obtained is 0.0774 which is also acceptable for ECG compression.

Similar approximation technique was used in (Yadav and Ray, 2013), but it was used on a simulated standard ECG signal with absolutely no noise, where one cycle of ECG signal was

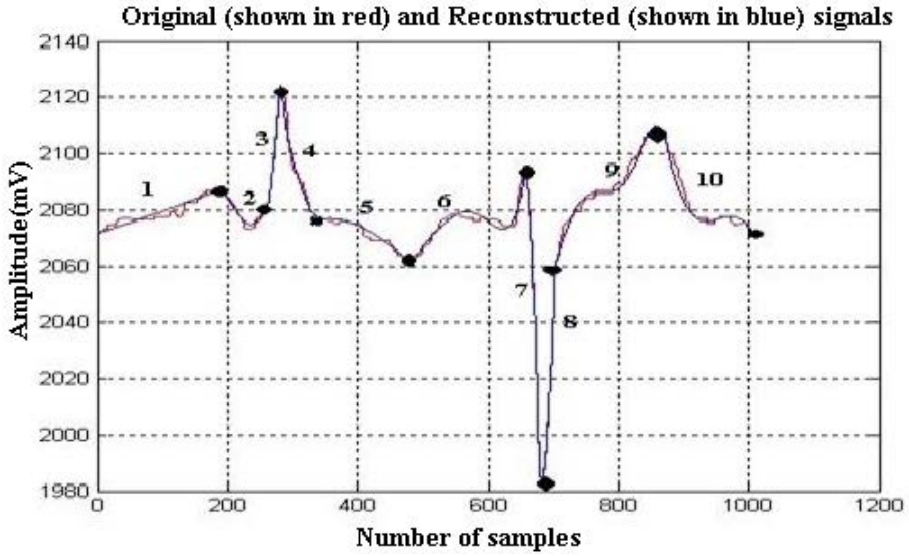

Figure 5. Original and Reconstructed ECG Signal with all its 10 segments.

segmented into seven sections on the basis of shape and duration of various waves of ECG. Hence, we have kept it outside the purview of our comparison.

The values of performance metrics obtained by the proposed method are much less than those shown in (Fira and Goras, 2008) with different ECG compression techniques, viz., Wavelet and Huffman, JPEG2000, SPHIT and other traditional techniques for one cycle of ECG signal. The mean value of CR obtained in (Fira and Goras, 2008) is 18.27 which is inferior than the average CR of 28.67 obtained by the proposed method. In (Tchiotsop et. al, 2007) ECG signals were approximated using Jacobi polynomials, where the highest compression achieved was 11. Hermite functions (Sandryhaila et. al, 2012) were also used to compress QRS complex of ECG signals and the average CR achieved was 11 with 25% approximation error. The results obtained by Sandryhailla et. al. were better than the results obtained by other transformation techniques. In (Jokic et. al, 2011) polynomial models of ECG signals were developed where the lowest and highest PRD observed were 3.5 and 10.8 respectively. In (Zahhad et. al, 2010) Discrete Wavelet Transform was used to compress ECG signals where the highest CR of 40 was achieved with PRD of 2.7, and lowest CR was 3.4 with PRD of 0.2 for one dataset. Hence, we can claim the proposed technique is quite suitable for ECG compression.

7. Conclusion

In this paper, a model is designed to compress ECG signals using Chebyshev polynomials. The signal was taken from MIT-BIH database which was denoised using the TVD-MM approach. Bottom-Up technique was then used to find the break points. The individual segments obtained were then approximated using Chebyshev polynomials. From the results, it was observed that the order of

Chebyshev polynomials depends upon the shape of various sections of ECG wave. Waves having zero or constant slope can be approximated by lower order Chebyshev polynomials, whereas waves having variable slopes require higher order Chebyshev polynomials. The approximated models are evaluated in terms of CR, $RMSE$, $MaxError$, PRD and $PRDN$. It was observed that the results obtained were superior than those reported in the existing literature. Also accuracy can be increased by breaking the complete signal into more number of segments at the cost of CR.

References

Acharya, U. R., J. S. Suri, J. A. Spaan and S. M. Krishnan. Advances In Cardiac Signal Processing. New York: Springer Berlin Heidelberg, 2007.

Bharadwaj, A. and U. Kamath. Techniques for accurate ECG signal processing. *EE Times*, 2011.

Birkhoff, G. and C. R. De Boor. Piecewise polynomial interpolation and approximation. *Approximation of functions*, 164–190, 1965.

Bjorck, A. and V. Pereyra. Solution of Vandermonde systems of equations. *Mathematics of Computation*, 24(112):893–903, 1970.

Braunwald, E. Heart Disease: A Textbook of Cardiovascular Medicine. Philadelphia: W.B. Saunders Co., 1997.

Caporale, M. Guglielmo and M. Cerrato. Chebyshev polynomial approximation to approximate partial differential equations. *,2008*

Chan, W. C. C., C. J. Chyan and H. M. Srivastava. The Lagrange polynomials in several variables. *Integral Transforms and Special Functions*, 12(2):139–148, 2001.

Clifford, G., L. Tarassenko and N. Townsend. One-pass training of optimal architecture auto-associative neural network for detecting ectopic beats. *Electronic Letters*, 37(18):1126–1127, 2001.

Colomer, A. and A. Colomer. Adaptive ECG data compression using Discrete Legendre Transform. *Digital Signal Processing* , 7(4):222-228, 1997.

Elascoa, M., B. Wengb and K. Barnerc. ECG signal denoising and baselinewander correction based on the empirical mode decomposition. *Computers in Biology and Medicine* , 38(2008):1–13, 2007.

Fira, C. M. and L. Goras. An ECG Signals Compression Method and Its Validation Using NNs. *IEEE Transactions on Biomedical Engineering*, 55(4):1319–1326, 2008.

Gil, A., J. Segura and N. Temme. Chebyshev Expansions:Numerical Methods for Special Functions Society for Industrial and Applied Mathematics , 51–86, 2007

Goldberger, A. L., L. Amaral, L. Glass, J. M. Hausdorff, P. C. Ivanov and R. Mark. PhysioBank and PhysioToolkit. *PhysioNet: Components of a New Research Resource for Complex Physiologic Signals*, e215-220, 2000.

Hadjileontiadis, L. J. Biosignals and Compression Standards *M.Health Springer US* ,277–292, ISBN: 978-953-307-185-5, 2006.

Jalaleddine, S. M. S., C. G. Hutches, R. D. Strattan and W. A. Cobberly. ECG data compression techniques A unified approach. *IEEE Transactions on Biomedical Engineering*, 37(4):293–343, 1990.

Jokic, S., V. Delic, Z. Peric, S. Krco and D. Sakac. Efficient ECG Modeling using Polynomial Functions.. *Signal Technology:Electronics and Electrical Engineering*, 4(110):121–124, 2011.

Karczewicz, M. and M. Gabbouj. ECG data compression by Spline approximation. *Signal Processing* , 59(1):43–59, 1997.

Kehagias, A., E. Nidelkou and V. Petridis. A dynamic programming segmentation procedure for hydrological and environmental time series. *Stochastic Environmental Research and Risk Assessment*, 20(1-2):77–94, 2006.

Keogh, E., S. Chu, D. Hart and M. Pazzani. An Online Algorithm for Segmenting Time Series:Data Mining. In *Proceedings ICDM,IEEE*, :289–296, 2001.

Kovacs, P. ECG Signal generator based on Geometrical features. *Annales Univ. Sci. Budapest., Sect. Comp.*, 37(2012):247–260, 2012.

Krimt, H. and H. D. Brooks. Feature -Based Segmentation of ECG Signals. *LIDS* , 2329,1996. *IEEE Trans. on Biomedical Engineering*, 47(7):849–856, 2000.

Mason, J. C. and D. C. Handscomb. Chebyshev polynomials ,CRC Press, 2002.

Moody, G. B. and R. G. Mark. QRS Morphology Representation and Noise Estimation using the Karhunen-Loeve Transform. *Computers in Cardiology*, pages 269–272, 1989.

Moody, G. B. and G. M. Roger. The MIT-BIH arrhythmia database on CD-ROM and software for use with it . *Computers in Cardiology*, 185–188, 1990.

Nygaard, R., D. Haughland and J. Husy. Signal compression by second order polynomials and piecewise non interpolating approximation. *Department of Electrical and Computing Engineering*, 2557 Ullandhang 4091 Stavanger, Norway, August, 1999.

Pan, J. and W. J. Tompkins. A Real-Time QRS Detection Algorithm. *IEEE Tansactions on Biomedical Engineering*, 230–233, 1985.

Philips, W. ECG data compression with time -warped polynomials. *IEEE Trans on Biomedical Engineering*, 40(11):1095–1101, 1993.

Rudin, L., S. Osher and E. Fatemi. Nonlinear Total Variation Based Noise Removal Algorithms. *Physica D*, 60:259–268, 1992.

Sandryhaila, A., S. Saba, M. Puschel and J. Kovacevic. Efficient Compression of QRS Complexes Using Hermite Expansion. *IEEE Transactions on Signal Processing*, 60(2):947–955, 2012.

Selesnick, I. Sparse Deconvolution (an MM algorithm), 2012.

Sorensen, J., J. Johannesen, U. Grove, K. Lundhus, J. P. Couderc and C. Graff. A Comparison of IIR and Wavelet Filtering for Noise Reduction of the ECG. *Computing in cardiology* , 37 :489–492, 2010.

Sormno, L. and P. Laguna. Electrocardiogram (ECG) Signal Processing Wiley Encyclopedia of Biomedical Engineering, 2006.

Spiegel, S., J. Gaebler, A. Lommatzsch, E. De Luca and S. Albayrak. Pattern Recognition And Classification For Multivariate Time Series. In *Proceedings of the fifth international workshop on knowledge discovery from sensor data: ACM*, 34–42, 2011.

Staudachera, M., S. Telserb, A. Amannc, H. Hinterhuberb and M. Ritsch-Marte. A new method for change-point detection developed for on-line analysis of the heart beat variability during sleep. *Physica A*, 349:586–592, 2005.

Szego, G. Orthogonal polynomials. *American Mathematical Society*, 23:38–57, 1975.

Tchiotsop, D., D. Wolf, V. Louisdorr and R. Husson. ECG data compression using Jacobi polynomials. *IEEE Engineering in Medicine and Biology Society* ,(29):1863–1867, 2007.

Walraven, G. Basic Arrhythmias (7th Edition edition.), 2011.

Yadav, O. P. and S. Ray. Total Variational Denoising of ECG Signals using Majorization-Minorization Technique. *Indian Control Conference. IIT Madras Chennai*, January, 2015.

Yadav, O. P. and S. Ray. Smoothening and Segmentation of ECG signals Using Total Variational Denoising Minimization-Majorization and Bottom-Up Approach. *International Conference on Computational Modeling and Security (CMS 2016),RLJIT, Bangalore*, February, 2016.

Yadav,O. P. and S. Ray. Modeling and Segmentation of ECG signals through Chebyshev polynomials. *International Journal of Advanced Research in Electrical, Electronics and Instrumentation Engineering*, 2(10), 2013.

Yang,W. Y., T.- S. Chung and J. Morris. Applied Numerical Methods Using Matlab. A JOHN WILEY and SONS, INC., Publications,Hoboken, New Jersey, 2005.

Zahhad, M. A. ECG Signal Compression Using Discrete Wavelet Transform Discrete Wavelet Transform : Theory and applications,143–168, ISBN: 978-953-307-185-5, 2011.

Zahhad, M. A., S. M. Ahmed and A. Zakaria. An ECG Signal Compression Technique Based on Discrete Wavelet Transform and QRS-Complex Estimation. *Signal Processing :An International Journal (SPIJ)*, 4(2):138–160, 2010.

Zifan, A., S. Saberi, M. H. Moradi and F. Towhidkhah. Automated ECG Segmentation Using Piecewise Derivative Time Warping. *International Journal of Biological and Medical Sciences*, 1(3):181–185, 2006.

Model-Order Reduction Using Interval Constraint Solving Techniques

Leobardo Valera and Martine Ceberio
Computer Science Department, The University of Texas at El Paso, El Paso, TX, 79968, USA,
{*lvalera, mceberio*}*@utep.edu*

Abstract: Many natural phenomena can be modeled as ordinary or partial differential equations. A way to find solutions of such equations is to discretize them and to solve the corresponding (possibly) nonlinear large systems of equations; see (Li and Chen, 2008).

Solving a large nonlinear system of equations is very computationally complex due to several numerical issues, such as high linear-algebra cost and large memory requirements. Model-Order Reduction (MOR) has been proposed as a way to overcome the issues associated with large dimensions, the most used approach for doing so being Proper Orthogonal Decomposition (POD); see (Schilders and Vorst, 2008). The key idea of POD is to reduce a large number of interdependent variables (snapshots) of the system to a much smaller number of uncorrelated variables while retaining as much as possible of the variation in the original variables.

In this work, we show how intervals and constraint solving techniques can be used to compute all the snapshots at once (I-POD); see (Granvilliers and Benhamou, 2006; Kreinovich and Ceberio, 2006; Moore and Kearfott, 2009). This new process gives us two advantages over the traditional POD method: 1. handling uncertainty in some parameters or inputs; 2. reducing the snapshots computational cost.

Keywords: Model-Order Reduction; Proper Orthogonal Decomposition; Large Nonlinear Systems of Equations; Interval Constraint Solving Techniques

1. Introduction

Many real life phenomena or situations can be represented by mathematic models. Because of the dynamic nature of these phenomena, the associated models could be, for instance, partial differential equations (PDEs). These kind of equations arise in many engineering problems describing phenomena such as the distribution of heat in a given rod or plate over time (heat equation), the description of waves like those of vibrating strings, and sound and water waves (wave equation), gas dynamics and traffic flow (Burgers' equation); see (Sharan and Pradhant, 2013; White, 2013).

A way to find an approximation of the solution of differential equations, either ordinary or partial, is to discretize the domain of the solution and to form a system of algebraic equations: this system of equations can be linear or nonlinear depending on the nature of the PDE.

In order to obtain a good accuracy in the approximation of the sought solution, the domain has to be discretized in many elements and nodes, leading to a large system of equations inheriting

several issues, such as: 1. not knowing about the existence and/or uniqueness of the solution of the system of equations, 2. storage, 3. high computational cost, 4. rounding errors.

To overcome these issues, several techniques have been developed to find a subspace where the an acceptable approximation of the solution of the system of equations lie. This process of identifying such subspace and reducing a large problem to a smaller one is known as **Model-Order Reduction (MOR)**.

Proper Orthogonal Decomposition (POD) is a broadly used and effective method to identify a reduced subspace and reduce the original large problem to a much smaller one. This method is based on Principal Component Analysis (PCA) (Cai and White, 2003; Marquez and Espinosa, 2013; Rathinam and Petzold, 2003). The idea behind POD consists in the following. First, identifying the function $U(x, t; \lambda)$, where x for solving the high dimensional Full-Order Model (FOM) for different values of its parameter, λ (chosen in a given interval or cartesian product of intervals). The function $U(x, t; \lambda)$ is defined in a space-temporal domain, where x represents the spatial variable and t the temporal one. For each parameter λ, after the FOM has been solved, m samples, $U(x, t_i, \lambda)$ are selected, commonly referred as snapshots, with $1 \leq i \leq m$. In this work, the instants of time at which the samples were selected were chosen in a uniform distribution. These snapshots are then arranged into a matrix A, which is factored: $A = U\Sigma V^T$, using Singular Value Decomposition (SVD). The basis of the reduced subspace is made of the first k columns, which are the ones that preserve most of the correlation.

Although POD is one of the most popular approaches to MOR, it presents several disadvantages, the main drawback being that it requires a series of offline computations in order to form the matrix of snapshots. The quality of the resulting reduced basis heavily depends on the choice of parameters and inputs, and on the accuracy of these over which the snapshots are computed.

In this work, we explored the idea of computing snapshots as a result of interval computations that we then sample: this leads us to one – interval – solving process as opposed to computing snapshots as a result of computations on sample parameters (many solving processes). This led to what we called an Interval-POD approach (IPOD), which has advantages beyond the mere computations of snapshots: if POD can handle intervals, it can therefore handle uncertainty as well. This would allow models to factor in uncertainty while still making it possible to process via MOR. Our preliminary tests show promise.

2. Background

Let us start by recalling the type of problems that we are attempting to solve. Many real-life phenomena are modeled and result in very large (most likely) nonlinear systems of equations that need to be solved. Solving these problems boils down to finding the zeroes of large-dimensional functions. Traditionally, finding zeroes of functions is achieved via the use of Newton methods.

In this section, we review basic notions about the components that motivate and make up our approach. Namely, we start by recalling the Newton's approach, which motivates the need to Model-Order Reduction. We then go over the MOR concept. Finally, we review interval computations and interval constraint solving techniques, as they are essential to our proposed IPOD.

2.1. The Newton Method

The Newton method is an iterative procedure that finds the zeroes of continuously differentiable functions $F : \mathbb{R}^n \to \mathbb{R}^n$. The formulation of the method is given by:

$$J_F(x_n)(x_{n+1} - x_n) = -F(x_n) \tag{1}$$

where $J_F(x_n)$ is the $n \times n$ Jacobian matrix of F.

If F is twice differentiable and the Hessian $\nabla^2 F(x)$ is Lipschitz continuous in a neighborhood of a solution x^* then:

1. if the initial point x_0 is sufficiently close to x^*, the sequence of iterations converges to x^*; and
2. the rate of convergence of $\{x_k\}$ is quadratic.

The Newton method is outlined in Table I:

Table I. Newton Method Outline.

Given an initial point x_0
`for i=1 until convergence`
Compute $F = F(x_0)$ and $J = J_F(x_0)$
Solve the linear system of equations: $J\Delta x = -F$,
Compute: $x_{i+1} = x_i + \Delta x$
`end for`

The Newton method converges if certain conditions are satisfied; for example, if a stationary initial point is chosen or if the approach oulined above enters in a cycle, the Newton method will not converge. Also, if the Jacobian matrix is singular or if any of its entries is discontinuous at the root, the convergence may fail. If the Jacobian is singular at the root of the function or the Hessian is not defined at it, the process may converge but not in q-quadratic order.

In addition to the above limitations of the Newton's approach, let us recall that the systems that are being considered for solution are of very large size. Not meeting a q-quadratic order of convergence is much more critical on such large spaces than it would be on smaller spaces.

To overcome all issues above mentioned, the solution is sought on a subspace where the convergence conditions are met, hence Model-Order Reduction.

2.2. Model-Order reduction

The main idea of the concept of Model Order Reduction (MOR) is as follows:

Let $T : V \to V$ be a bijective linear transformation. Then for every $b \in V$, there exists a unique $x \in V$ such that $T(x) = b$. Every linear transformation has a matrix representation (Hoffman, 1971). In this case, let us call A the matrix representation of T. Thus, finding x such that $T(x) = b$ is equivalent to solving the linear system:

$$Ax = b. \tag{2}$$

If the dimension of V is n, then Eq.(2) is a $n \times n$ linear system of n equations and n unknowns.

We can assure that there exists W, a subspace of V, whose dimension is $k \ll n$ and such that $x \in W$. This is true because, in particular, the subspace spanned by $\{x\}$ is a subspace of V, which contains x and whose dimension is $1 \ll n$.

Since W is a subspace of V, there exists a base $B = \{w_1, w_2, \ldots, w_k\}$ such that every element $w \in W$ can be expressed as a linear combination of the elements of B (Cotlar, 1974). In particular, if $w = x$,

$$x = \sum_{i=1}^{k} y_i w_i. \tag{3}$$

Since every base uniquely determines a subspace of V, we can, without loss generality, speak about subspace W and its base without difference. By writing Eq.(3) in matrix form, we obtain

$$Wy = x. \tag{4}$$

After substituting (4) in (2), we have:

$$(AW)y = b, \tag{5}$$

that can be solved using the normal equation (Bjork, 1996)

$$(AW)^T(AW)y = (AW)^T b, \tag{6}$$

which is itself a $k \times k$ linear system of equations. After we identify y, we can use Eq.(4) to find x.

Once the subspace is found, the approximation of the solution is given as the projection of it on the subspace obtained. This method truncates the solution of the original system to an appropriate basis. Let us illustrate this method by considering a basis transformation T that maps the original n-dimensional state space x into a vector that we will denote by

$$T(x) = \begin{pmatrix} T_1(x) \\ T_2(x) \end{pmatrix} = \begin{pmatrix} \hat{x} \\ \tilde{x} \end{pmatrix}$$

where $\hat{x}$ is k-dimensional. Suppose that T has at least a right-inverse. Let us denote $S = T^{-1}$ then S can be written as

$$S = (S_1 \;\; S_2)$$

and

$$\begin{aligned} I &= \begin{pmatrix} T_1 \\ T_2 \end{pmatrix} (S_1 \;\; S_2) \\ &= \begin{pmatrix} T_1 S_1 & T_1 S_2 \\ T_2 S_1 & T_2 S_2 \end{pmatrix} \qquad (7) \\ &= \begin{pmatrix} I_k & 0 \\ 0 & I_{n-k} \end{pmatrix}. \qquad (8) \end{aligned}$$

Since $T_1 S_1 = I_k$, we have $\Pi = S_1 T_1$ is an oblique projection along the kernel of T_1 onto the k-dimensional subspace that is spanned by the columns of the matrix S_1.

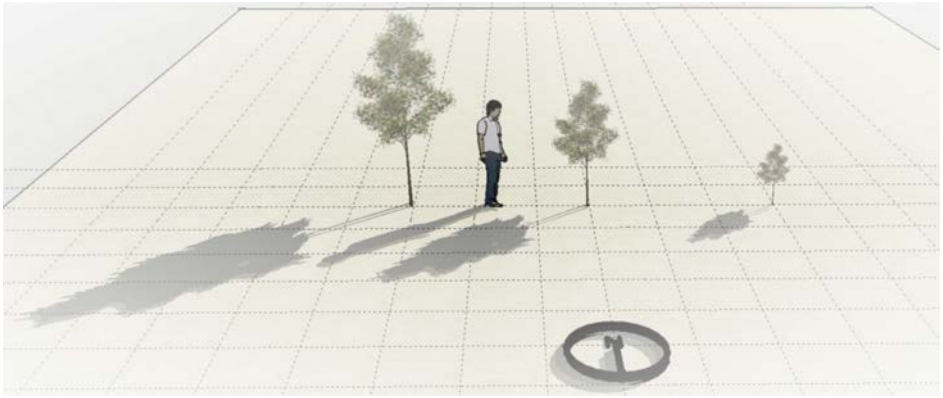

Figure 1. An oblique projection can be see as the shadow cast by objects on the ground when the sun is not directly vertical. Image taken from the site: http://www.schoolkitchengarden.com.au/design-your-garden/.

Let

$$\begin{array}{rcl} \dfrac{dx}{dt} & = & f(x,u), \\ y & = & g(x,u), \\ x(t_0) & = & x_0 \end{array} \tag{9}$$

be the dynamical system, where u is the input of the system, y is the output, x the so-called *state variable*. If we substitute the projection into the dynamical system Eq.(19), we obtain

$$\begin{array}{rcl} \dfrac{d\hat{x}}{dt} & = & T_1\hat{f}(S_1\hat{x} + S_2\tilde{x}, u), \\ y & = & \hat{g}(S_1\hat{x} + S_2\tilde{x}, u). \end{array} \tag{10}$$

The approximation occurs when we delete the terms involving $\tilde{x}$

$$\begin{array}{rcl} \dfrac{d\hat{x}}{dt} & = & T_1\hat{f}(S_1\hat{x}, u), \\ y & = & \hat{g}(S_1\hat{x}, u). \end{array} \tag{11}$$

In order to obtain a good approximation to the original system, the term $S_2\tilde{x}$ must be sufficiently small.

2.3. Interval Constraint Solving Techniques

The method that we are proposing in this article consists in expanding POD-based MOR techniques to interval computations (as we will describe in Section (4). Indeed, we aim to group the (possibly many) computational processes over the reals required to generate all snapshots into one single computational process over intervals that encompasses all computations over the reals.

In this subsection, we give a brief overview of interval computations and how to solve systems of equations that involve intervals; for more details about the field, please see (Moore and Kearfott, 2009).

2.3.1. *Computations with Intervals*
Let us start by pointing that in what follows, when mentioning intervals, we actually mean *closed intervals*. In addition, for simplicity, when we talk about intervals, we will talk about real-value-bounded intervals (not just floating-point-bounded intervals as is commonly the case when implemented on a computer).

So in this work, an interval X is defined as follows:

$$X = [\underline{X},\ \overline{X}] = \{x \in \mathbb{R} : \underline{X} \leq x \leq \overline{X}\}. \tag{12}$$

Operations on intervals are simply defined as follows: Since $x \in X$ means that $\underline{X} \leq x \leq \overline{X}$, and $y \in Y$ means that $\underline{Y} \leq y \leq \overline{Y}$ the followings operations are defined based on its infimum and supremum:

$$\textbf{Addition:}\ \ X + Y = [\underline{X} + \underline{Y}, \overline{X} + \overline{Y}] \tag{13}$$

$$\textbf{Substraction:}\ \ X - Y = [\underline{X} - \overline{Y}, \overline{X} - \underline{Y}] \tag{14}$$

$$\textbf{Multiplication:}\ \ X \cdot Y = [\min S, \max S],\ \text{where } S = \{\underline{XY}, \underline{X}\overline{Y}, \overline{X}\underline{Y}, \overline{XY}\} \tag{15}$$

As we observe above, combining intervals with addition, subtraction, and multiplication, always results in one interval. However, it is not always the case without extra care. For instance, the division of an interval by another one that contains 0 should result in two disjunct intervals. To avoid such cases with compromise the nature of traditional interval computations (according to which combining intervals should result in an interval), we generalize the combination of two intervals as follows:

$$\forall X, Y \text{ intervals},\ \ X \lozenge Y = \square\{x \lozenge y,\ \text{where } x \in X \text{ and } y \in Y\} \tag{16}$$

where $\lozenge$ stands for any arithmetic operator, including division, and $\square$ represents the hull operator.

More generally, when carrying out more general computations involving intervals, e.g., computing the interval value of a given function $f : \mathbb{R}^n \to \mathbb{R}$ on interval parameters (or a mix of interval and real-valued parameters), we have the following property:

$$f(X_1, \ldots, X_n) \subseteq \square\{f(x_1, \ldots, x_n),\ \text{where } x_1 \in X_1, \ldots, x_n \in X_n\} \tag{17}$$

where $f(X_1, \ldots, X_n)$ represents the range of function f over the domain $X_1 \times \ldots \times X_n$ and $\square\{f(x_1, \ldots, x_n),\ \text{where } x_1 \in X_1, \ldots, x_n \in X_n\}$ represents the smallest closed interval enclosing this range. Computing the exact range of f over intervals is therefore a very hard problem and instead, we approximate the range of f over domains using what we call an interval extension of f, which is in fact a surrogate interval function F.

Interval extensions of a given function f have to satisfy the following (very lose) property:

$$f(X_1, \ldots, X_n) \subseteq F(X_1, \ldots, X_n) \tag{18}$$

which to some extent would allow F to be the function that maps any input to the interval $[-\infty, +\infty]$. More pragmatically, the aim is to identify a function F that does not dramatically overestimate the range of our original function f (the closer to the range the better of course, but cost of achieving better range is also an issue). Many interval extensions exists. The most common one is the so-called natural extension, which is a simple interval extension of the syntactical expression of f: arithmetic operations are evaluated using interval rules as shown above, and any other single operator – e.g., power – has its own interval extension; see (Moore and Kearfott, 2009) for more details. Other extensions include Trombettoni et Al.'s occurrence grouping approach (Araya, Neveu, and Trombettoni, 2012). In this work, we use interval computations provided in RealPaver (Granvilliers and Benhamou, 2006) and the natural extensions this software provides.

2.3.2. *How to Solve Nonlinear Equations with Intervals?*
The premise of our approach is that we will replace several real-valued computational processes by one interval-based computational process by abstracting one real-valued parameter into an interval parameter. Each process (real-valued or interval) consists in solving a (most likely) nonlinear system of equations. In this subsection, we give the reader an overview of the way we proceed to solve a nonlinear system of equations that involves intervals.

We choose to solve nonlinear equations using interval constraint solving techniques. Constraint solving techniques allow to solve systems of constraints. Generally speaking, a constraint describes a relationship that its variables need to satisfy. A solution of a constraint is an assignment of values to the variables of the given constraint such that the relationship is satisfied.

In our case, each of our nonlinear equations $f_i(x_1, \ldots, x_n) = 0$ is a constraint: it establishes a relationship that the values of the variables should satisfy, in this case so that $f_i(x_1, \ldots, x_n)$ be equal to 0. Our system of nonlinear equations is therefore a system of constraints and our goal is to find values of the variables of this system that are such that: $\forall i,\ f_i(x_1, \ldots, x_n) = 0$.

Constraint solving techniques allow us to identify such values of the parameters that satisfy the constraints. Interval constraint solving techniques (Mackworth, 1977; Jaffar and Maher, 1994) produce a solution set (set of the solutions of the constraint system) that is interval in nature (this is what you will see in the graphs plotting our experimental results in Section (5)): it is a set of multi-dimensional intervals (or boxes whose dimension is n, the number of variables) that is guaranteed to contain all the solutions of the constraint problem (in our case, of the nonlinear system of equations).

The guarantee of completeness provided by interval constraint solving techniques comes from the underlying solving mode: a branch-and-bound (Kearfott, 2007) (or branch-and-prune for faster convergence (Caroa, Chablata, and Goldsztejnb, 2014)) approach that uses the whole search space as a starting point and successively assess the likeliness of finding solutions in the given domain (via interval computations) and possibly (if Branch and Prune) reduce it, and discard domains that are guaranteed not to contain any solution. *Note: while Branch-and-Bound algorithms only assess domains for likeliness of containing a solution (it is a keep or discard approach), Branch-and-Prune algorithms first use the constraints to reduce the domains to consistent domains (using appropriate*

consistency techniques based on interval computations) and the outcome (empty domain or not, small enough or not to be called a solution) decides whether to continue exploring the domain or not.

For instance, if on a given domain $D \subset \mathbb{R}$, any of the f_i is such that $0 \notin F_i(D)$, where F_i is an interval extension of f_i, then we can conclude that there is no zero of our system of equations in D and discard it altogether. In Table II, we outline the generic Branch-and-Bound approach, which is the underlying principle of search in interval constraint solving techniques, and allows to guarantee completeness of the search.

Table II. Generic Branch-and-Bound Algorithm.

Input: System of constraints $C = \{c_1, \ldots, c_k\}$, a search space D_0.
Output: A set *Sol* of interval solutions (boxes of size n, the number of variables)
Set *Sol* to empty
If $\forall i$, $0 \in F_i(D_0)$ then:
Store D_0 in some storage S[1]
While (S is not empty) do:
Take D out of S
If ($\forall i$, $0 \in F_i(D)$) then:
If (D is still too large[2]) then:
Split[3] D in D_1 and D_2
Store D_1 and D_2 in S
Else:
Store D in *Sol*
Return *Sol*

Using interval computations carries a lot of advantages, one of which being that the search can be guaranteed to be complete and that since intervals are used (interval computations to assess whether a domain is a viable option of not), uncertainty can easily be added and seamlessly handled. This however comes at a cost: interval solving processes are usually more computationally taxing that regular real-valued ones. Nevertheless, in what follows we will show that, when comparing our interval-based approach to real-valued processes that have to be repeated countless times, then the extra cost of interval computations is counterbalanced and our approach more computationally effective (as shown in Section 5).

[1] S could be a queue, a stack, a priority queue, etc.

[2] The size of the domain is a stopping criterion: once we have achieved a given precision ϵ, there is no need to keep exploring the domain, it is considered an interval solution.

[3] Literature is full of approaches to splitting, including splitting in more than two pieces. Here we assume that we split in two. The type of splitting (where? on which domain? or even in how many pieces?) does not affect the generic algorithm.

3. Proper Orthogonal Decomposition

In this section, we study the statistical procedure of Principal Component Analysis (PCA), which uses orthogonal transformation to convert a set of observations of possibly correlated Random Variables into a set of linearly uncorrelated ones with the largest possible variance, named principal components. The number of principal components is less than or equal to the number of the original random variables.

Using the same procedure as in (PCA), it is possible to find a set of linearly independent vectors from a set of linearly dependent ones, whose spanned space is practically the same. This procedure is named Proper Orthogonal Decomposition (POD), which we also describe here.

3.1. Principal Component Analysis

When information from a data sample is collected, usually we take the maximum number of variables. However, if we take too many variables from a data sample, for instance 20 variables, we must consider $\binom{20}{2} = 190$ possible correlation coefficients. If you have 40 variables that number is increased to 780. Obviously, in this case it is difficult to visualize relationships between variables. Another problem that arises is the strong correlation that often occurs between variables: if we take too many variables (which generally happens when much is not known about data, or we are only interested in exploratory tests), it is normal that they are related or they measure the same thing under different viewpoints. For example, in medical studies, blood pressure at the heart's outlet and out of the lungs are strongly related.

Therefore, it is necessary to reduce the number of variables. It is important to highlight that the concept of major information is related to the greater variability of the data or variance. The greater the variability (variance) of the data, the more information this data has.

Studying the relationships that exist between p correlated variables (which commonly measure information) transforms the original set of variables in another new set of uncorrelated variables together (that has no repetition or redundancy on the information) called a set of principal components.

3.2. Principal Components

Let us consider a number of variables $X = (x_1, x_2, \ldots, x_n)$ describing a group of objects or individuals and to calculate, from them, a new set of variables $(y_1, y_2, \ldots, y_n)$ uncorrelated with each other, whose variances will decrease gradually.

Each y_j (where $j = 1, \ldots, n$) is a linear combination of the original variables $x_1, x_2, \ldots, x_n$, i.e

$$\begin{aligned} y_j &= v_{1j}x_1 + v_{2j}x_2 + \ldots + v_{pj}x_n \\ &= Xv_j, \end{aligned}$$

where $v_j^{\mathrm{T}} = (v_{1j}, v_{2j}, \ldots, v_{pj})$ is a constant vector.

To keep the orthogonality of the transformation, we impose $||v_j|| = 1$.

The first component v_1 is calculated so y_1 has the greatest variance subject to the constraint that $||v_1|| = 1$. The second principal component v_2 is calculated so that the variables y_1 and y_2 are uncorrelated. Similarly are chosen $y_1, y_2, \ldots, y_p$, uncorrelated with each other.

The full principal components decomposition of X can therefore be given as

$$Y = XV,$$

where V is a $p \times p$ matrix whose columns are the eigenvectors of $X^T X$.

The principal component decomposition of X can be expressed in terms of singular value decomposition of X. Given

$$X = U\Sigma V^T,$$

then we have

$$\begin{aligned} Y &= XV \\ &= U\Sigma V^T V \\ &= U\Sigma. \end{aligned}$$

In practice, we initiate computations with p variables and we are left with a number of much smaller components that collect a large percentage of the variability. For instance, we take r variables, where r is the minimum positive integer such that:

$$\frac{\sum_{i=1}^{r} \sigma_i}{\sum_{i=1}^{p} \sigma_i} > tol.$$

where *tol* is an approximation of 1 by defect.

3.3. Proper Orthogonal Decomposition Method

Consider a parameterized static computational model described by large-scale linear system of discrete equations

$$A(\lambda)x = b. \tag{19}$$

Here we can see Eq.(19) as an input-output system, where λ is the input and the solution, $x(\lambda) \in \mathbb{R}^n$, is the output.

The idea behind this method is that, given a certain input, the solution $x(\lambda)$ of a system contains the behavior of the system (Schilders and Vorst, 2008). Therefore, the set of outputs serves as a starting-point for POD. The outputs are called *snapshots* and these must be given or be computed first.

Assume the set of snapshots S and the solution $x(\lambda^*)$ of Eq.(19) for a particular λ^* is in the subspace spanned by S. We assume that the columns of S are highly correlated, so we can apply principal components analysis (PCA) to obtain an uncorrelated number of columns, see 3.1, and thus to reduce the size of linear system of equations.

Consider the SVD of S

$$S = U\Sigma V^T \tag{20}$$

and

$$T = V\Sigma^{-1}U^T. \tag{21}$$

Define

$$T_1 = \sum_{i=1}^{k} v_i \sigma_i^{-1} u_i^T; \quad T_2 = \sum_{i=k+1}^{n} v_i \sigma_i^{-1} u_i^T,$$
$$S_1 = \sum_{i=1}^{k} u_i \sigma_i v_i^T; \qquad S_2 = \sum_{i=k+1}^{n} u_i \sigma_i v_i^T. \tag{22}$$

Conditions given by Eq.(22) are a particular case of conditions given in Eq.(7). We conclude that we get a good approximation of Eq.(19) if $S_2\tilde{x}$ is sufficiently small ($\tilde{x} = T_2(x)$) or equivalently if $\sigma_i \approx 0$ for $k+1 \leq i \leq n$.

To obtain a basis of W we have the algorithm in Table IV.

Table III. Computing a Proper Orthogonal Decomposition Basis.

In: Parameter λ's and *input-output system*
Out: Base of the subspace W
Solve the full-order model to several λ's.
For each λ, take one or more **snapshots**, which is the solution of Eq.(19) for some values of t, and store such snapshots in a matrix S. Compute the SVD of S: $[W, \Sigma, V] = svd(S)$.
Find k such that $\sigma = \frac{\sum_{i=1}^{k} \sigma_i}{\sum_{i=1}^{n} \sigma_i} > 0.99$.
Consider only the k first columns and redefine $W = W(:, [1:k])$.

Several problems have been solved by using this method (Willcox, 2002). As it has been said before, the POD is based on Principal Components Analysis. The reader who wants to read a little more about this can find a good source of information in (Jolliffe, 1986).

4. Interval Proper Orthogonal Decomposition (I-POD)

In this section, we present our Interval POD approach to solving large nonlinear systems of equations in a reduced subspace. Let us first recall once again the problem that we are solving.

Given a parametric system of equations (also known as the Full Order Model):

$$R(x, \lambda) = 0, \quad \lambda \in \mathbf{I} \tag{23}$$

where R can be either linear or nonlinear function $R : \mathbb{R}^n \to \mathbb{R}^n$, that might arise from the discretization of a set of partial differential equations and $\mathbf{I}$ is a fixed interval. The idea behind POD is to solve Eq.(23) for a sequence of values $\lambda_i \in \mathbf{I}$, i.e.,

$$R(x, \lambda_1) \; = \; 0,$$

$$\begin{aligned} R(x, \lambda_2) &= 0, \\ \vdots \quad &\quad \vdots \\ R(x, \lambda_n) &= 0, \end{aligned} \tag{24}$$

where $\lambda_i \in \mathbf{I}$, for $i = 1, 2, \ldots, n$. The main idea of this method is based on the high correlation between solutions for such values λ_i, so PCA techniques can be applied to obtain a smaller number of columns uncorrelated with the greatest of accumulated variance.

In this work, we propose an interval version of POD. The original idea behind this new Interval POD is that we aim to reduce the amount of work in solving the Full Order Model for many different values of the input parameters (λ). Instead we suggest and experimented solving the Full Order Model once on the entire interval containing all desirable values of λ.

This slight change in concept (many processes solving for many different values of λ vs. one process solving for an entire interval instead) has consequences in our ability to solve the Full Order Model. Now that an interval is part of the problem we are bound to use interval-computation-based solving techniques and we found interval constraint solving techniques to be very practical to do so.

More specifically, we are now solving:

$$R(x, \mathbf{I}) = 0, \tag{25}$$

which is a nonlinear system of equations with explicit uncertainty in the shape of an interval.

We called this variation of POD the **Interval Proper Orthogonal Decomposition (I-POD)** method.

5. Numerical Results

In this section, we describe and report on preliminary experiments of our IPOD method on two well-known problems: the Burgers' equation and the Transport equation. In each of these experiment, we aim to assess the ability of IPOD to generate snapshots that yield a reduced basis of quality enough that the solution of the reduced-order model yields a very small error (w.r.t. FOM solution) in comparison to what a similar process using POD achieves. Our experiments were conducted using MATLAB R2012b (8.0.0.783) on a laptop with 1.7 GHz intel core i7 and 8GB of RAM.

5.1. Burgers' Equation

Consider the Burgers' equation:

$$\frac{\partial U(x,t)}{\partial t} + \frac{\partial f(U(x,t))}{\partial x} = g(x), \tag{26}$$

where U is the unknown conserved quantity (mass, density, heat etc.), $f(U) = 0.5U^2$ and in this example, $g(x) = 0.02 \exp(0.02x)$. The initial and boundary conditions used with the above PDE

are: $U(x;0) \equiv 1$; $U(0;t) = 4$, for all $x \in [0;100]$, and $t > 0$.

Below, in Tables IV and V, we describe the procedure to obtain the snapshots and the reduced basis in the POD method for the Burgers' equation. We will then compared it with **I-POD**.

Table IV. Computing a Proper Orthogonal Decomposition Basis.

Initialize an empty matrix where we will collect the snapshots: Snap = [], and an initial $\lambda = 3.5$.

`For i= 2:100`,

Solve:
$$\begin{cases} \dfrac{\partial U(x,t)}{\partial t} + \dfrac{\partial f(U(x,t))}{\partial x} = g(x), \\ g(x) = 0.02\exp(0.02x) \\ U(x;0) \equiv 1, \text{ for all } x \in [0;100], \\ U(0;t) = \lambda_i, \text{ for } t > 0. \end{cases} \tag{27}$$

Collect snapshots:

From $t_1, t_2, \ldots, t_n$, select a subsequence[4] $t_{i1}, t_{i2}, \ldots, t_{ip}$.

Add new columns to the snapshot matrix Snap = [Snap $U(x,t_{i1})$ $U(x,t_{i2})$ $\ldots U(x,t_{ip})$].

Update λ: $\lambda_i = \lambda_{i-1} + 0.01$

Apply the principal component analysis, (SVD). Snap $= W\Sigma V^T$.

Select from W the principal components with the greatest accumulated variance:

$\sigma = 0$.

`for k=1:n` compute:

$\sigma = \sigma + \frac{\sigma_k}{\sum_{j=1}^{n} \sigma_j}$

If $\sigma > Tol$, $0 < Tol < 1$, break.

Select the first k columns of W and redefine it. $W = W(:,[1,2,\ldots,k])$.

The new W will be the reduced basis to apply the POD method.

We applied both previous procedures, POD and IPOD, to solve Eq. (26) and we obtained the results reported in the Table VI. We observe that there is no significant difference between the traditional method (using POD) and the method we propose (using IPOD) w.r.t. (1) the dimension of the subspace, (2) the time it takes to solve the problem once we have identified the reduced basis, and (3) the relative error compared with the FOM solution. The major two advantages of our proposed method are:

- the computational time it requires to obtain the snapshots: Our approach requires 68.52% less time than the original one and the quality of the snapshots our method generates is comparable to that generated by POD as observed in the relative error; and
- the ability to handle uncertainty: the interval that contains λ, handled at once by IPOD, is similar to uncertainty and is handled without problems. Further experiments will aim to

[4] In the experiment done in this work, $p = 5$ and the subsequence was a uniform random selection.

Table V. Computing a Proper Orthogonal Decomposition Basis Using IPOD.

Initialize a empty matrix where to collect the snapshots: Snap = [], and an initial $\lambda = 3.5$.

Solve:
$$\begin{cases} \dfrac{\partial U(x,t)}{\partial t} + \dfrac{\partial f(U(x,t))}{\partial x} = g(x), \\ g(x) = 0.02\exp(0.02x) \\ U(x;0) \equiv 1, \text{ for all } x \in [0;100], \\ U(0;t) = \mathbf{I}, \text{ for } t > 0. \end{cases} \tag{28}$$

The solution of Eq. (28) is an interval solution, i.e, for any $1 \leq x_0 \leq 100, 0 \leq t_0 \leq 50$, the value $U(x_0, t_0)$ is an interval. The infimum of such interval is defined $U_l(x_0, t_0)$ and $U_r(x_0, t_0)$ is the supremum. In that case, for all $1 \leq x \leq 100,\ 0 \leq t \leq 50$, $U(x,t) \in [U_l(x,t), U_r(x,t)]$, see Figure 3.

`For i=1:100`

Compute:

$U(x,t) = (U_r(x,t) - U_l(x,t))(\lambda - 3.5) + U_l(x,t)$

Collect snapshots:

From $t_1, t_2, \ldots, t_n$, select a subsequence[5] $t_{i1}, t_{i2}, \ldots, t_{ip}$.

Add new columns to the snapshot matrix Snap = [Snap $U(x,t_{i1})\ U(x,t_{i2})\ \ldots U(x,t_{ip})$].

Update λ: $\lambda_i = \lambda_{i-1} + 0.01$

Apply the principal component analysis, (SVD). Snap $= W\Sigma V^T$.

Select from W the principal components with the greatest accumulated variance:

$\sigma = 0$.

`for k=1:n` compute:

$\sigma = \sigma + \frac{\sigma_k}{\sum_{j=1}^{n} \sigma_j}$

If $\sigma > Tol$, $0 < Tol < 1$, break.

Select the first k columns of W and redefine it. $W = W(:, [1, 2, \ldots, k])$.

The new W will be the reduced basis to apply the POD method.

Table VI. Comparing POD and I-POD methods in solving a particular example of Burgers Equation.

Method	Tag 1	Tag 2	Tag 3	Tag 4
POD	300 secs	37	0.75 secs	$4.85E-4$
I-POD	94.45	36	0.75 secs	$5.76E-4$

Tag 1: Time computing the Reduced basis
Tag 2: Dimension of the Subspace
Tag 3: Time solving 26 using the obtained basis
Tag 4: $||u_{fom} - u_{rom}||/||u_{fom}||$

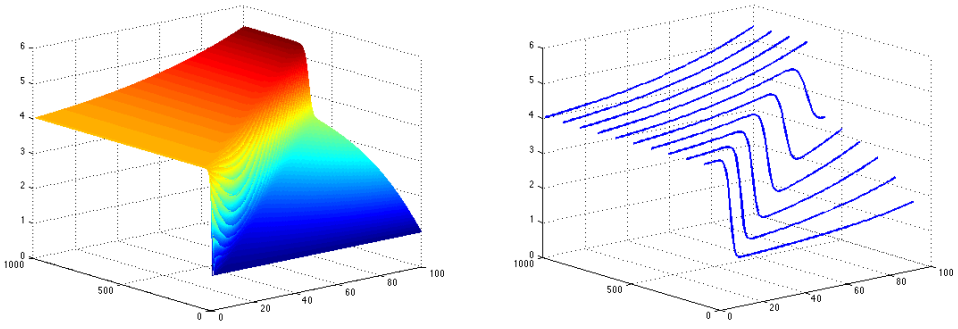

Figure 2. Solution of Eq.(27) for $\lambda = 4$, and some snapshots corresponding to this parameter.

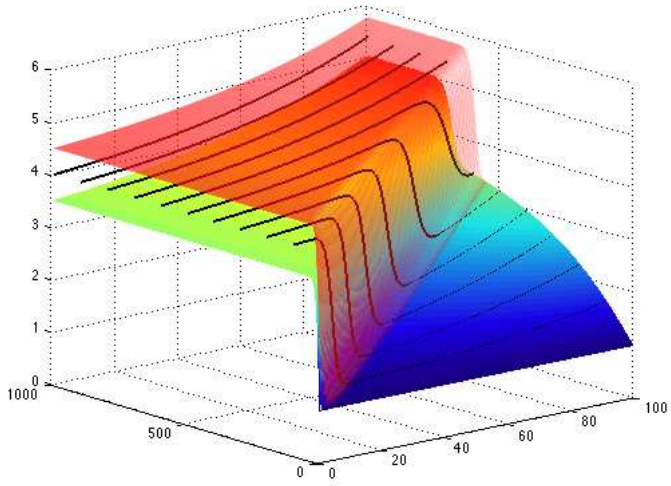

Figure 3. Infimum and supremum of the solution of Eq.(28), and some snapshots corresponding to $\lambda = 4$ are shown.

demonstrate that IPOD produces meaningful results also when there are other sources of uncertainty (beyond the interval for λ).

5.2. Transport Equation

The transport equation is a partial differential equation that models the concentration of a contaminant in the position x in at time t in a fluid that is flowing with velocity v in a thin straight tube whose ross section, denoted by A is constant. Such concentration will be denoted by $U(x,t)$. if the function $U(x,t)$ and its partial derivatives of order one are continuous functions of x and

[5] In the experiment done in this work, $p = 5$ and the subsequence was a uniform random selection.

t, and the fluid velocity v and the cross section of the tube, A, are constants, then the Transport Equation is reduced to:

$$\frac{\partial U}{\partial t} + v\frac{\partial U}{\partial x} = 0$$
$$(x,t) \in \Omega \tag{29}$$

Where Ω is a convex domain. In particular, we solve Eq.(29) with $U(x,t)$ subject to the following boundary and initial conditions:

$$U(0,t) = u(t) = -\sin(2\pi t) + \sin(\pi t) \tag{30}$$
$$U(x,0) = u(x) = \sin(2\pi x) + \sin(\pi x) \tag{31}$$

for all $t \in [0,1]$, and $x \in [0,1]$.

Using $v \in [0.5, 1.5]$ as the input parameter, we can proceed, similarly to how we did in the Burger Equation case, and compute, first, a basis using POD method, and later, using IPOD.

Comparative values are presented in Table VII:

Table VII. Comparing POD and I-POD methods in solving a particular example of Burgers Equation.

Method	Tag 1	Tag 2	Tag 3	Tag 4
POD	0.31 sec.	12	0.06 sec.	$7.97E-5$
I-POD	0.05 sec.	76	0.05 sec.	$1.81E-5$

Tag 1: Time computing the Reduced basis
Tag 2: Dimension of the Subspace
Tag 3: Time solving 29 using the obtained basis
Tag 4: $||u_{fom} - u_{rom}||/||u_{fom}||$

In this experiment, we observed that even when the dimension of the subspace is larger using the I-POD (76) than when using POD (12), the time needed to compute the reduced basis in I-POD is significantly less than the computing time needed using POD. Once, both basis are known, solving the reduced problem from POD or I-POD take the same time.

In Figure 4, we can observe the plot of the solution of the transport equation for time-steps 20, 40, 60, 80. In green and red are respectively the infimum and the supremum of the interval containing the solution.

6. Conclusions and Future Work

In this paper, we proposed and described a novel Model-Order Reduction approach that improves the well-known Proper Orthogonal Decomposition method (POD) by using Interval analysis and

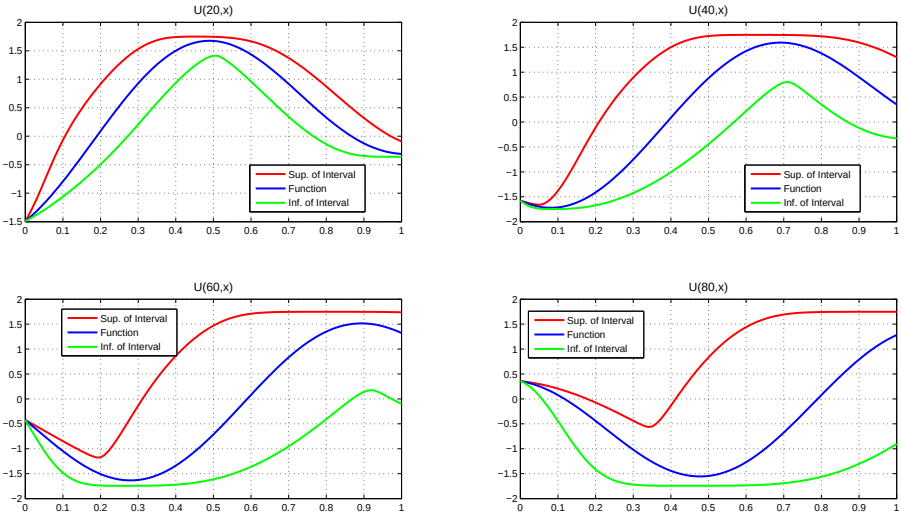

Figure 4. Solution of Eq.(29) for time-steps 20, 40, 60, 80, enclosed in the Interval solution.

Interval Constraint Solving Techniques. This new method called Interval Proper Orthogonal Decomposition (IPOD) was tested on two nonlinear partial differential equations problems: the Burgers' equation and the Transport equation. We observed and reported promising performance of IPOD, when compared to POD.

From this preliminary work, we draw the following research activities and directions. First, we do plan to challenge IPOD on problems whose solution is highly nonlinear, e.g., the Fitz-Hugh-Nagumo (FHN) problem. We also need to assess its relevance in handling and meaningfully solving problems with other sources of uncertainty. Finally, when having to handle uncertainty, achieving a relevant reduced basis is not all that needs to be modified from traditional approaches: once the space reduced, solving techniques (currently, namely, Newton-based methods) need to be extended to intervals. Although Interval Newton has been around for a long time (Moore and Kearfott, 2009; Hansen and Walster, 2004), Interval Newton on a reduced subspace is expected to present its set of challenges, including in particular, the likeliness of an empty solution set.

Acknowledgements

This work was supported by Stanford's Army High-Performance Computing Research Center funded by the army Research Lab, and by the National Science Foundation award #0953339.

References

Li, J. and Y. Chen. *Computational Partial Differential Equations Using MATLAB.* CRC Press, Las Vegas (NV), 2008.

Schilders, W. H and H. A. Vorst. *Model Order Reduction: Theory, Research Aspects and Applications.* Springer Science & Business Media, 2008.

Granvilliers, L. and F. Benhamou. *RealPaver: An Interval Solver using Constraint Satisfaction Techniques..* ACM TRANS. ON MATHEMATICAL SOFTWARE, 2006.

Kreinovich, V., G. Xian, M. Ceberio, at al. *Towards Combining Probabilistic and Interval Uncertainty in Engineering Calculations: Algorithms for Computing Statistics under Interval Uncertainty, and Their Computational Complexity.* Reliable Computing, 2006.

Moore, R. E, R. B. Kearfott and M. J. Cloud. *Introduction to Interval Analysis (1 edition)*, Philadelphia, PA: Society for Industrial and Applied Mathematics, 2009.

Sharan, M. and A. Pradhan. *A Numerical Solution of Burgers Equation Based on Multigrid Method*, International Journal of Advancements in Electronics and Electrical Engineering – IJAEEE, 2, 2013.

White. J. *A Trajectory Piecewise-Linear Approach to Model Order Reduction and Fast Simulation of Nonlinear Circuits and Micromachined Devices* in International Conference Computer Aided Design, pages 252–257, 2013.

Kelly, C. T. *Solving Nonlinear Equations with Newton's Method,* no 1 in Fundamentals of Algorithms, SIAM, ISBN 0-89871-546-6, 2003

Kelly, C. T. *Reduction of Model Order Based on Proper Orthogonal Decomposition for Lithium-Ion Battery Simulations,* Journal of the Electrochemical Society, 156:A154–A161, 2009.

Marquez, A. and J. Espinosa. *Model Reduction Using Proper Orthogonal Decomposition and Predictive Control of Distributed Reactor System, Model Reduction Using Proper Orthogonal Decomposition and Predictive Control of Distributed Reactor System,* Journal of Control Science and Engineering, Journal of Control Science and Engineering, p. e763165, 2013.

Rathinam, M. and A. Petzold. *A New Look at Proper Orthogonal Decomposition,* SIAM Journal on Numerical Analysis, 41, pages 1893–1925, 2003.

Björck, A. *Numerical Methods for Least Squares Problems*, Other Titles in Applied Mathematics, Society for Industrial and Applied Mathematics, January 1996.

Hoffman, K. and R. Kunze. *Linear Algebra*, Prentice-Hall, 1971.

Cotlar, M. and R. Cignoli. *Introduction to Functional Analysis*, North Holland Publishing Company and Elsevier Publishing Company, first edition ed., April 1974.

Willcox, K and J. Peraire. *Balanced model reduction via the proper orthogonal decomposition.* AIAA journal, 40(11):2323–2330, 2002.

Jolliffe, I. T. *Principal Component Analysis* Springer-Verlag. p. 487. doi:10.1007/b98835, ISBN 978-0-387-95442-4, 1986.

Hansen, E. and W. Walster. *Global Optimization using Interval Analysis,* Second Edition, Revised and Expanded. Marcel Dekker, Inc. New York, 2004.

Araya, I., B. Neveu and G. Trombettoni. *An interval extension based on occurrence grouping* Computing, 94(2):173-188, March 2012.

Hailer, A. *Verification of Branch and Bound Algorithms Applied to Water Distribution Network Design* Logos Verlag, Berlin, Dissertation, Technische Universitt Hamburg, Harburg, 2006.

Kearfott, R. B. *Verified branch and bound for singular linear and nonlinear programs: An epsilon-inflation process,* Available from the author, April 2007.

Jaffar, J. and M. Maher. *Constraint Logic Programming: a Survey* Journal of Logic Programming, 19/20:503–581, 1994.

Mackworth, A. K. *Consistency in Networks of Relations* Artificial Intelligence, 8(1):99–118, 1977.

Caroa, S., D. Chablata, A. Goldsztejnb, D. Ishiic and C. Jermannd. *A branch and prune algorithm for the computation of generalized aspects of parallel robots* Artificial Intelligence, 211:34–50, June 2014.

Hentenryck, V. P., D. McAllester and D. Kapur. *Solving Polynomial Systems Using a Branch and Prune Approach* SIAM J. Numer. Anal., 34(2):797–827, 1997.

On the Comparison of Two Novel Interval Field Formulations for the Representation of Spatial Uncertainty

Maurice Imholz[1)], Matthias Faes[2)], Jasper Cerneels[2)], Dirk Vandepitte[1)] and David Moens[2)]
[1)] *KU Leuven - Department of Mechanical Engineering, Celestijnenlaan 300, B-3000 Leuven*
[2)] *KU Leuven - Department of Mechanical Engineering, Technology campus De Nayer, B-2860 St.-Katelijne-Waver*

Abstract: This paper concerns the comparison of two established interval field methods for the representation of spatially varying non-determinism in an FE model: Inverse Distance Weighting (IDW) interpolation and the Local Interval Field Decomposition (LIFD) method. The comparison is first made from a theoretical point of view, highlighting the advantages of both techniques as compared to each other. Next, both IDW and LIFD are applied to a dynamical model of a U-shaped hollow tube and the resulting uncertain regions at the output side of the model are compared qualitatively. It is shown that both techniques are complementary to each other due to the trade-off in their ability to represent the uncertainty set at the output side of the model and the involved computational cost.

Keywords: interval fields, uncertainty, non-deterministic modelling

1. Introduction

In the context of integrating uncertainty and variability in Finite Element (FE) models, several advanced techniques for taking both inter- (between nominally identical parts) and intra-variability (spatial variability within one part) into account have recently been introduced. In the framework of possibilistic non-determinism, especially the theory of Interval Fields (IF) has been proven to show promising results. Following this approach, variability in the input parameters of the FE model is introduced as the superposition of a number of base vectors scaled by interval factors. In the recent past, two techniques for the construction of interval fields have been introduced by the authors: Inverse Distance Weighting interpolation (IDW) and the Local Interval Field Decomposition method (LIFD). In this paper, these two established interval field methods are compared in their ability to represent different uncertain input sets and the computational work required. Both techniques are compared theoretically, as well as applied to a dynamical model of a hollow U-shaped tube.

2. Interval Field Concepts

2.1. General framework

Uncertain parameters in FE models typically have a spatial character: material properties such as density and Young's modulus or geometric properties such as plate thickness are geometrically oriented in space. In the context of dealing with uncertainty in simulation models, these parameters can show variability over the spatial domain, referred to as *geometric variability*. In FE-models, such a geometric parameter is discretised to the elements, leading to a set of discrete values representing that parameter in each element of the model. According to the possibility of geometric variability, the value in each element can vary separately, leading to different values in each element. However, some degree of dependency will usually be present and the value in different elements can not vary independently. Here the interval concept poses a problem. The uncertainty in each element could be captured by an interval parameter marking the bounds of the variation, but interval parameters are by definition incapable of incorporating the dependency present in the spatial domain. To mark the uncertainty present in such *field parameters* using a possiblistic technique, the *interval field* concept can be used. In its simplest form, an interval field consists of basis functions $\phi(\mathbf{r})$ representing the dependency and interval coefficients α^I representing the uncertainty. The explicit formulation of the interval field is defined as:

$$y^I(\mathbf{r}) = \sum_{i=1}^{n} \alpha^I \phi_i(\mathbf{r}) \tag{1}$$

with n the number of basis functions employed in the representation.

2.2. The Local Interval Field Decomposition method

2.2.1. *General objective*

For this interval field definition, we start from a field parameter $u(\mathbf{r})$, with $\mathbf{r}$ the spatial coordinates. When applied to an FE-model, such a continuous parameter is discretised to the elements of the FE-mesh, leading to a set of discrete parameters. Within this set a certain amount of spatial dependency is always present. The parameter value assigned to elements in close proximity to each other will show more interdependence than elements further away. This poses a problem for defining a plausible possibilistic field: the field can easily be made non-deterministic by defining an interval parameter in each element marking the bounds of the uncertain parameter value in each element, but this completely disregards any dependency present and will always overestimate the true uncertainty within such a parameter.

In probabilistic context, the Karhunen-Loeve expansion (Vanmarcke, 1993) provides an elegant solution to this by using the eigenvectors of the covariance matrix of the field as basis functions for a decomposition method. The coefficients that emerge can be proven to be uncorrelated and even independent in case of a Gaussian distribution. To define the entries of the covariance matrix, the correlation length of the field can prove a valuable parameter, defined in Eq. 2:

$$COV(x(\mathbf{r}_1), x(\mathbf{r}_2)) = \exp\left(\frac{\|\mathbf{r}_1 - \mathbf{r}_2\|}{L_\rho}\right) \tag{2}$$

In possibilistic context, correlation is not defined since it is related to the joint probability distribution functions which are not defined in this case. In the possibilistic case, we only consider (in)dependency of parameters, a much wider term than correlation. Since correlation is undefined, a new global dependency parameter has to be defined that is compatible with the possibilistic approach. The parameter that will be used in the method described in this section will be the *maximum gradient of the field parameter* (Imholz et al., 2015a; Imholz et al., 2016a). Intuitively, this makes sense if we define the dependency between two parameters as the maximum difference that can occur between the two parameters. E.g. , consider two parameters a and b, for which an intervals a^I and b^I of equal size are defined. If $a = b$ over the entire interval reach, the parameters are perfectly dependent, whereas in the opposite case, when the parameters can take values independently, the maximum difference is $\overline{a} - \underline{a}$. Now consider parameters a and b as instances of the same field parameter $u(\mathbf{r})$ at places in close proximity $\mathbf{r}_a$ and $\mathbf{r}_b = \mathbf{r}_a + d\mathbf{r}$. The case of perfect dependency then corresponds to a gradient equal to zero, whereas the case of perfect independency corresponds to a high maximum gradient, making this a valid parameter to represent the dependency.

The purpose of the interval field should be to accurately represent the true uncertain set, taking into account the possible dependency within the field. In the case of perfect dependency, a single discrete variable would suffise to represent the field variable in the entire domain. However, in every other case, each element of the discretised mesh can (at least partially) determine it's own value. The *dimensionality of the uncertainty therefore equals the total number of elements in the mesh*, regardless of the degree of dependency. To ensure the entire uncertain set is captured by the field, the *dimensionality of the interval field should be at least equal to the number of elements.*

As a conclusion, the interval field will should keep the dimensionality intact, but will transform the initial set of dependent interval parameters located in each element of the mesh, to a new set with *independent* parameters, *that will obey a priorly set condition on the maximum gradient in the field.*

2.2.2. *Mathematical definition*

The mathematical definition below follows the one explained in (Imholz et al., 2015a) for a field parameter in a one-dimensional space. The LIFD in 1D will write the non-determistic field $u(r)$ as an interval field $u^I(r)$ in the form of Eq. 1 that obeys the following statements:

1. $\forall \tilde{r} \in \Omega : U_{min} \leq u(\tilde{r}) \leq U_{max}$
2. $\forall r \in \Omega : \left| \frac{\partial u(r)}{\partial r} \right| \leq G_{max}$
3. $\forall \tilde{u}(r) : \overline{u} - \underline{u} \leq D_{max}$

The parameters G_{max}, U_{min}, U_{max} and D_{max} can be independently set. The first statement demands that the absolute bounds on the field parameter U_{min} and U_{max} are never exceeded. The second statement demands that the norm of the gradient never exceeds a preset value. This statement accounts for the dependency in the field. The third statement puts a bound on the difference between the maximal and minimal value of any realisation of the interval field. The objective of the LIFD is to obey the statements using the four governing uncertainty parameters mentioned above with an explicit interval field description with *independent* interval coefficients.

The only freedom we have is the shape of the basis functions. In the 1D-case, the basis functions have the following properties:

1. All ϕ_i are identically shaped radial basis functions.
2. A single ϕ_i is positioned at each element at location $\mathbf{r}_i$ of the FE mesh.
3. All ϕ_i are piecewise second order polynomial functions so the first derivatives are continuous.

figure 1 illustrates the shape of a basis function and its first derivative. To comply with all demands, the following explicit field is proposed:

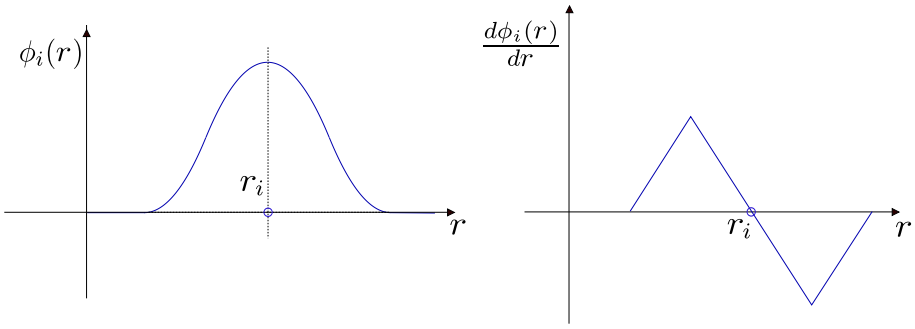

Figure 1. shape of a 1D radial basis function. Beyond a radius R from the center point, the basis function equals zero.

$$u^I(r) = C^I + \sum_{i=1}^{n} a \cdot 1_i^I \cdot \phi_i(r, R), \tag{3}$$

with $C^I = \langle \underline{C} | \overline{C} \rangle$ and $1_i^I = \langle 0|1 \rangle$ defined as the *unity* interval. The four controllable parameters are $\underline{C}$, $\overline{C}$, a and R. A unique mapping between these parameters and the four global uncertainty pararmeters is given by Eq. 4:

$$\begin{aligned} U_{max} &= \frac{a \cdot R}{dr} + \overline{C} \\ U_{min} &= \underline{C} \\ G_{max} &= \frac{a}{dr} \\ D_{max} &= \frac{a \cdot R}{dr} \end{aligned} \tag{4}$$

With dr the discretisation step of the mesh and R the effective radius of the basis functions. With these relations, the four global uncertainty parameters can be independently set, leading to a unique field definition as in Eq. 3.

2.2.3. *Adjustments*

For the purpose of dealing with bounded physical domains and local measurement data, a few adjustments can me made to the field mntionned above.

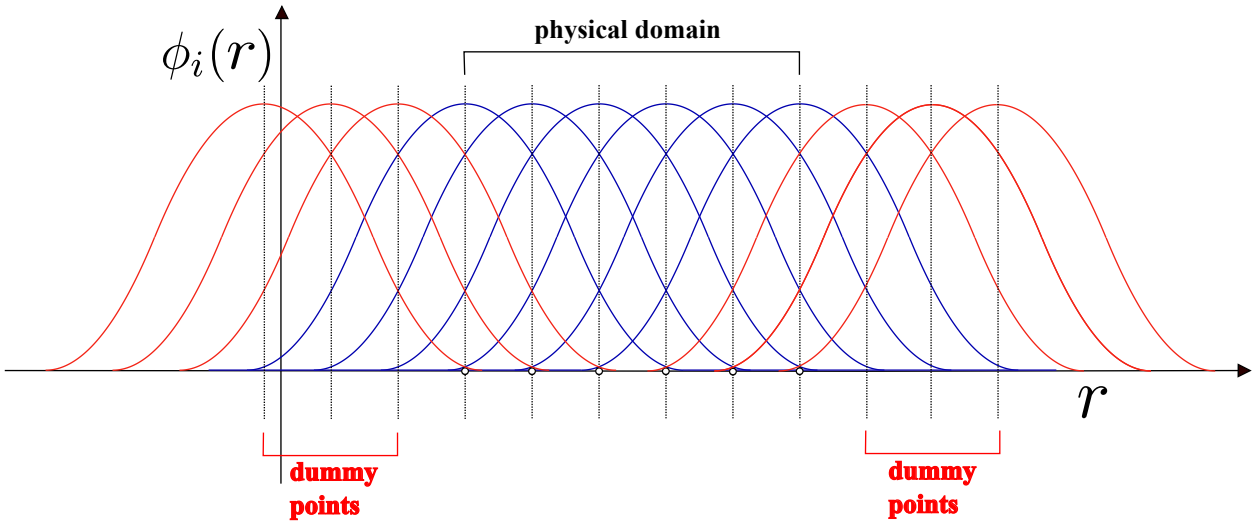

Figure 2. introduction of dummy points beoynd the physical domain in which non-physical basis functions are places, this to ensure the maximum gradient constraint is kept at the edges of the domain.

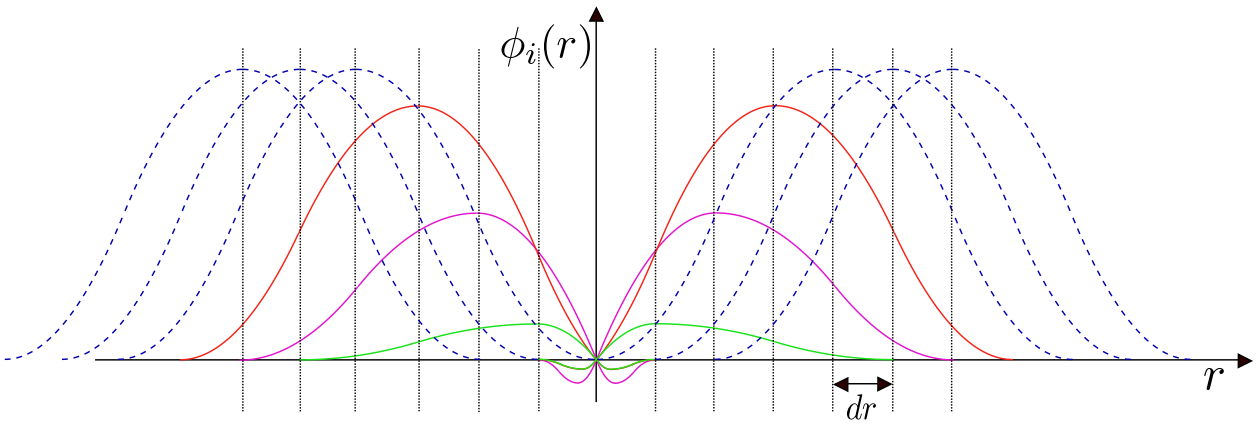

Figure 3. Adjustment of the basis function around a deterministic measurement point.

1. To ensure the maximum gradient constraint is kept over the entire domain, an adjustment is needed close to the edge of the domain. For points that lie within a distance R from a domain edge, the maximum constraint does not hold, because fewer basis functions have an effect in these points, leading to a smaller interval on the gradient in these points. To counter this, *dummy points* are added **beyond** the physical domain up to a distance R. The basis functions placed in these points lie partly in the physical domain and will ensure that the maximum

gradient constraint is kept over the entire physical domain. Figure 2 shows the dummy points beyond the physical domain.

2. Sometimes, local information can be available on the field parameter in a certain element, effectively fixing the value in that point. This limits the uncertain set to all realisations that smoothly run through this point. The shape function attached to this point is omitted, but to ensure the maximum gradient constraint is not violated, all base functions within a radius R of the point have to be adjusted as well. these adjustments are illustrated in figure 3.

2.3. Inverse Distance Weighting interpolation

Inverse Distance Weighting, as proposed by the authors in (De Mulder et al., 2012), constructs the base functions $\phi_i(\mathbf{r})$, needed for the explicit formulation of the Interval Field (1) based on the definition *a priori* selected locations $\mathbf{r}_i$ in the model geometry Ω. The selection of these locations $\mathbf{r}_i$ is based on the expert engineering knowledge of the analyst on where the uncertainty can be predicted within accurate bounds. The base functions are constructed following an inverse distance weighting, where it is assumed that the weight of an interval scalar α_i^I, defined at $\mathbf{r}_i$ decreases with the distance $\mathbf{r}$ from that respective location:

$$\phi_i(\mathbf{r}) = \frac{w_i(\mathbf{r})}{\sum_{j=1}^{n} w_j(\mathbf{r})} \tag{5}$$

,with n the number of base functions present in the interval field formulation. The weights $w_i(\mathbf{r})$ are calculated as the inverse of $d(\mathbf{r}_i, \mathbf{r})$ to the power of $p \in \mathbb{R}_{>0}$. $d(\mathbf{r}_i, \mathbf{r})$ is a distance measure between the location $\mathbf{r}_i$ where the interval is defined and the rest of the model $\mathbf{r}$. In the specific case of FE models, the concept of Euclidean distance is insufficient, as this yields non-physical paths between two points in the interpolation (De Mulder et al., 2012). It is therefore proposed to use a shortest path approach to calculate these distances.

An illustration of this concept is given in figure 4. The top graph of this figure shows all vertex realisations when three local intervals α_1^I, α_2^I and α_3^I are respectively defined at element 2, 4 and 8 in a 10 element 1D beam geometry, with $\alpha_1^I = [1.78; 1.85]$, $\alpha_2^I = [1.40; 1.75]$ and $\alpha_3^I = [1.3; 2.40]$. The middle graph shows the calculated weight functions $w_i(\mathbf{r})$ for the respective interval scalars and $p = 2$. Finally, the bottom graph shows the base functions $\phi_i(\mathbf{r})$ which are calculated based on the weighting functions for these locally defined interval scalars.

As can be noted, the locally defined intervals remain perfectly decoupled at the locations where they are defined, whereas the rest of the model can be seen as a weighted sum of their respective influences.

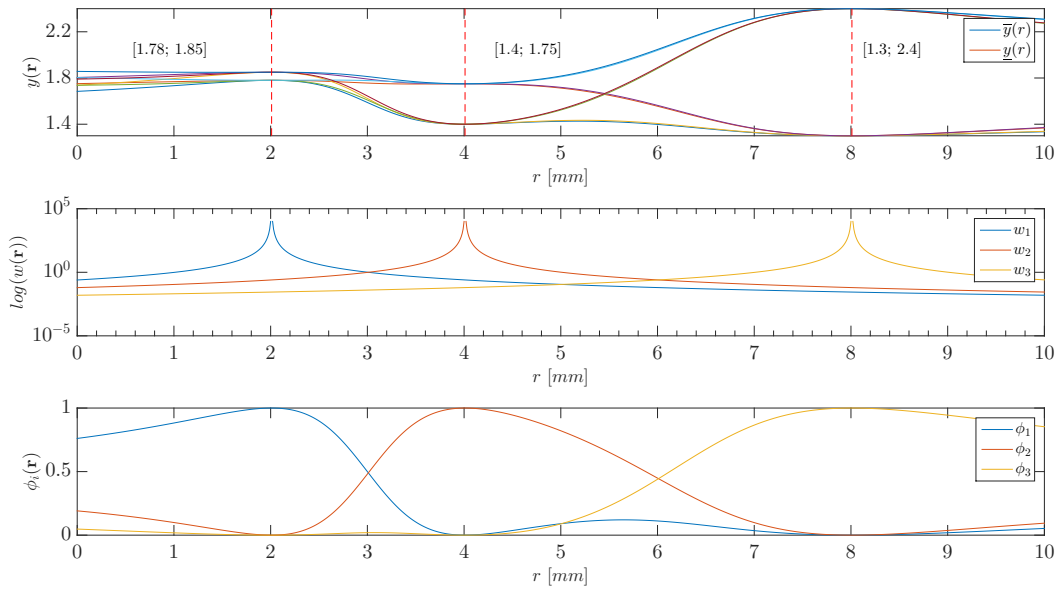

Figure 4. Illustration of the employed interpolation scheme. Top: vertex realisations of the resulting interval field, with the vertical lines indicating the locations of the interval scalars. Middle: Weight functions. Bottom: Base functions of the interval field, computed following Eq. 5.

3. Case Study

3.1. Object description and uncertainty definition

Both interval field formulations are applied to the dynamic analysis of a u-shaped tube. This tube is produced following a cold-forming process and hence the largest uncertainty is located in the bent part. Therefore, only this part is considered as uncertain in the following analysis. An illustration of this model is shown in figure 5. An FE model of this geometry is constructed using 75 beam elements and the model is solved for the first ten non-rigid eigenfrequencies.

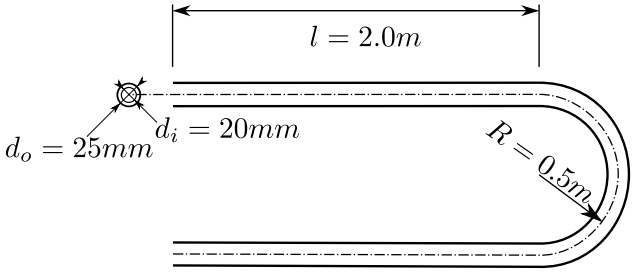

Figure 5. Illustration of the geometry of the u-shaped cold formed beam under consideration.

We assume the E-modulus of the tube is subject to uncertainty, ultimately limited to ±55% of the nominal value. The uncertain part of the tube is limited to the curved part, the straight ends are assumed to be deterministic. In the curved part, the two methods mentioned above are used to create an interval field for the 21 elements located there.

1. An interval field is defined by imposing that the interval scalars at elements 33 and 43 are both defined as $[93.12 \cdot 10^{09}\ Pa;\ 320.8 \cdot 10^{09}\ Pa]$ and is constructed following the IDW technique. Only the uncertainty between element 28 and 48 is regarded in the analysis. C_0 continuity in the realisations of Young's Modulus at the border between the *certain* and *uncertain* region is guaranteed by imposing infinitely thin intervals at elements 28 and 48. Propagation of the IDW interval field is performed following the vertex method (Dong and Shah, 1987). A maximum gradient of $5 \cdot 10^{05}\ MPa/m$ is thus obtained in the realisations of the IDW interval field. The interval field and its gradients for this model is shown in figure 6.

2. For the LIFD, an R-value equal to 0.3m (4 element-lengths) and a-value equal to $40 \cdot 10^3$ MPa provide limits that are similar to the IDW case. In the endpoints of the curved part, measurement points are introduced to fix the field there at the nominal value. This leads to an interval field description with 21 terms, one interval parameter and corresponding shape function in each element. Some realisations are given in figure 7. To propagate this field, a response surface is created using *coefficient fields*. Basically, this is a polynomial model that takes into account the dependency between E-moduli in adjacent elements by assuming the coefficients of the polynomial are continuous functions of the spatial coordinate r as well (Imholz et al., 2016a).

Obviously, the analysis using IDW is much more straightforward to perform and less time-consuming, as it only uses two uncertain independent variables. The LIFD attempts to capture the entire set of realisations that obey the maximum gradient constraint using 21 uncertain independent variables, at the cost of increased computational work. The uncertain set of the IDW is a subset of the uncertain set of the LIFD, which is realised by keeping the maximum derivative and maximum deviation equal between both approaches. As a result, the uncertain output set of eigenfrequencies obtained with IDW should be a subset of the uncertain output set obtained with LIFD.

3.2. RESULTING UNCERTAINTY ON THE EIGENFREQUENCIES

In both cases, the uncertain domain at the output is a region within a ten-dimensional domain containing the 10 eigenfrequencies. To allow for graphical verification, this domain is projected on some two-dimensional subdomains considering only two eigenfrequencies. Figure 8 shows the result of the vertex method computation for the IDW interval field. ω_m in this figure denotes one realisation of the input interval field, while C_m indicates the convex hull of the uncertainty region spanned by these realisations, as proposed by the authors in (Faes et al., 2016a; Faes et al., 2016b). Two vertex realisations ($[\underline{E};\overline{E}]$ and $[\overline{E};\underline{E}]$) of the IDW interval field are coincident due to the symmetry of both the IWD interval field and the model geometry, leading to a triangular uncertainty region in 10 dimensions.

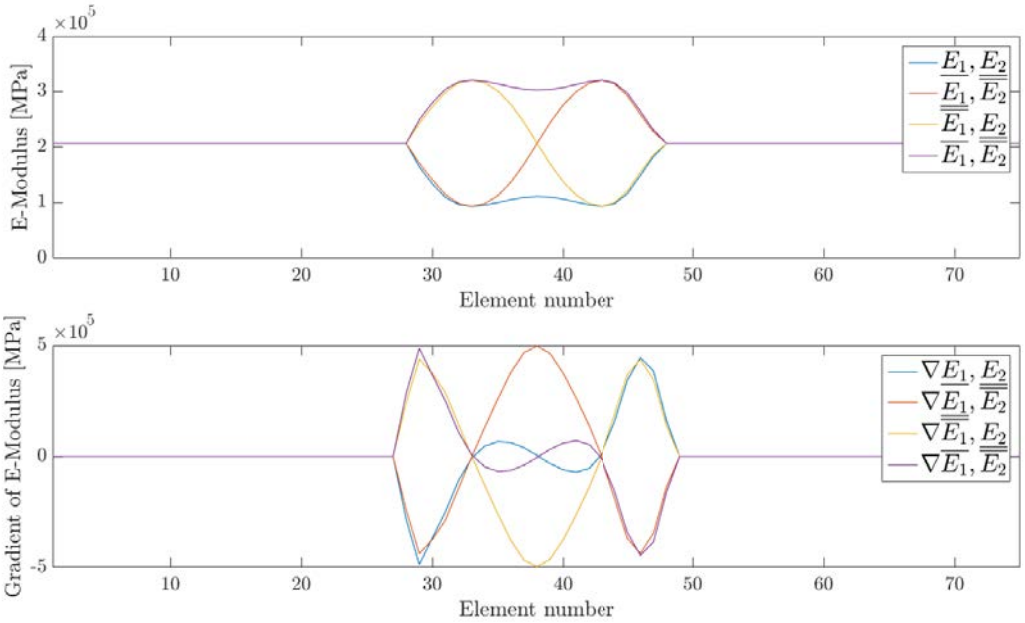

Figure 6. Top: Vertex realisations of the interval field obtained by regarding the spatial uncertainty between elements 28 and 48, obtained by interpolating $[93.12 \cdot 10^{09};\ 320.8 \cdot 10^{09}]$ and $[93.12 \cdot 10^{09};\ 320.8 \cdot 10^{09}]$ at elements 33 and 43. Bottom: gradients of the vertex realisations of the interval field.

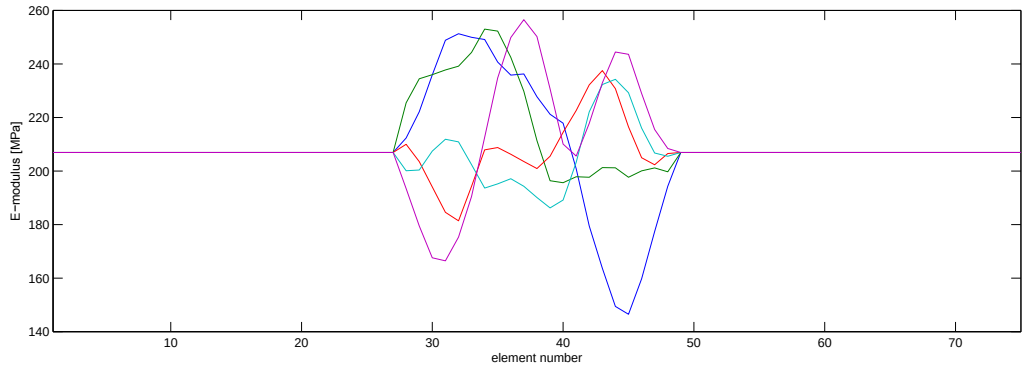

Figure 7. Some configurations generated by using the LIFD method.

For the LIFD, the vertex method is not applicable as the relatively large amount of variables (= 21) already amounts to over two million vertex points. Instead, a tracking algorithm was introduced by the authors in (Imholz et al., 2016b) that creates the 2D-projections of uncertain regions originating from *monotonous* problems directly. Starting in the minimum vertex point, where all inputs are at their minimal value, The upper bound curve is found by setting steps along a path that attempts to maximize the quantity $\frac{\partial \omega_y}{\partial E_i} / \frac{\partial \omega_y}{\partial E_i}$, whereas the lower bound curve is found

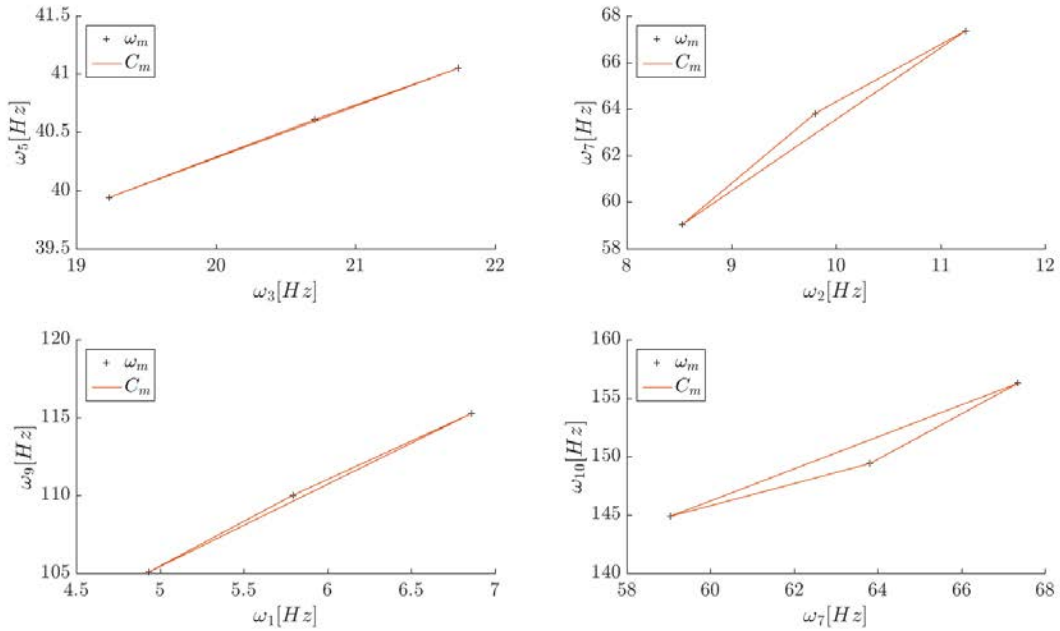

Figure 8. Two dimensional subdomains of the ten dimensional output space, obtained by performing the vertex method on the IDW interval field.

by setting steps along a path that attempts to minimize it. This approach is especially suited for identifying 'shuttle'-shaped uncertain regions, which are common for monotonous I/O-relations.

3.3. Observations

Figure 9 again shows the uncertain regions obtained from the IDW case, but the figure is expanded with the results of the LIFD-analysis. In this figure, the shuttle shapes can be seen very clearly. Our initial requirement that the IDW region should be a subset of the LIFD-region seems to be met. The uncertain region obtained from the LIFD is clearly much 'wider', indicating a less pronounced dependency between eigenfrequencies in the mid-vertex region (= half-way between the corner points). It is interesting to take a look at which realisations are responsible for this observation. If we look at the plot concerning ω_3 and ω_5, we are specifically interested in the point P, located on the upper bound curve. Figure 10 shows the input realisation that corresponds to this point. From the shape, we can see that IDW using only 2 uncertain parameters at the locations mentioned does not include this configuration in its uncertain set, and therefore it is not propagated to the output. Putting in an extra uncertain parameter in the middle in-between the two current parameters would solve this problem. However, the possibility remains that critical configurations in other frequency pairs remain neglected. Because LIFD takes into account all possible configurations bounded by the maximum gradient constraint, the LIFD-approach does not suffer from this problem. However, the increased dimensionality brings along problems of its own, leading to increased computational

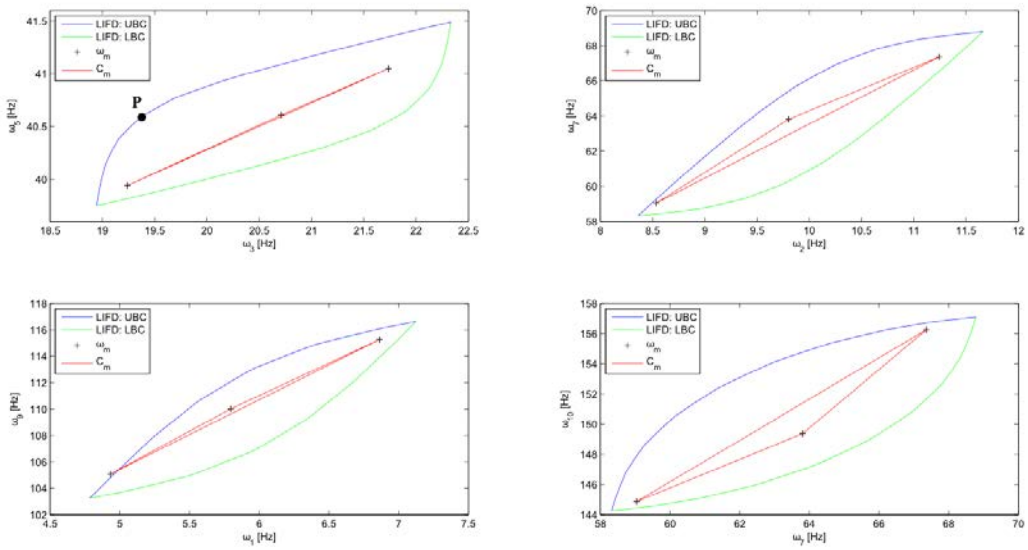

Figure 9. Two dimensional subdomains of the ten dimensional output space, both for the IDW and LIFD method. Upper left: frequency 3 and 5, upper right: frequency 2 and 7, lower left: frequency 2 and 9, lower right: frequency 7 and 10. UBC = upper bound curve, LBC = lower bound curve.

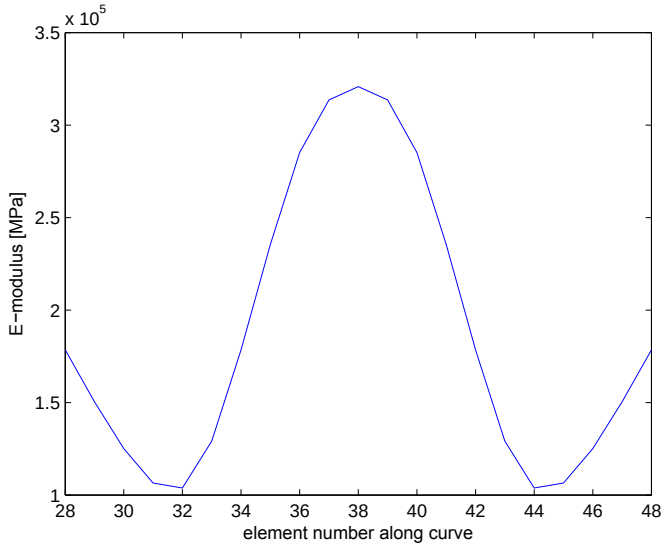

Figure 10. Realisation corresponding to the point P indicated in Figure 9.

work. The vertex method used by IDW only requires four FE-model evaluations (Actually only three, because two vertices are equal due to symmetry of the tube). The response surface used by

LIFD was build upon a sample set of 50 samples, after which the remaining work to compute the uncertain regions was neglectible. The efficient use of the coefficient functions prevents us from increasing the problem dimension to infeasible heights.

4. Conclusions

The importance of Uncertainty Quantification for the purpose of creating relaible designs cannot be stretched enough. This paper elaborated and compared two types of possiblistic uncertainty modelling using the interval as basic tool to represent non-deterministic parameters. Essentially, the concept of interval fields extend the use of intervals to geometric parameters by taking into acount possible spatial dependence within such a field. The two concept described here both approach the problem in a different manner: the IDW-method requires a preliminary choice of the locations where independent interval parameters will be placed in space, and then interpolates to all other points in the field. The LIFD starts from a global uncertainty definition by setting bounds on the maximum derivative and converts this to an interval field that puts an independent interval parameter in each point of the FE-mesh the field is defined on, thereby ensuring the entire uncertain set is captured at the cost of high dimensionality. As a final conclusion, one can say that IDW works well in problems were the sensitive points in the spatial domain are known beforehand and the number of output parameters is limited, since the sensitive points may vary for each output parameter. When multiple output parameters are considered, the LIFD provides a more robust approach to find the complete uncertain output set for a certain minimal gradient constraint.

References

De Mulder, W., D. Moens, D. Vandepitte. Modeling Uncertainty in the Context of Finite Element Models With Distance-Based Interpolation, in: Uncertainties 2012, Sao Paulo, Brazil, 2012.

Dong, W. and H. C. Shah. Vertex Method for Computing of Fuzzy Variables, Fuzzy Sets Systems, 24:65–78, 1987.

Faes, M., J. Cerneels, D. Vandepitte and D. Moens. Identification of Interval fields for spatial uncertainty representation in Finite Element models. Proceedings of the European Congress on Computational Methods in Applied Sciences and Engineering. Hersonissos, Greece, 5-10 June 2016.

Faes, M., J. Cerneels, D. Vandepitte and D. Moens. A convex set-based optimization scheme for the identification of Interval Field uncertainty in Finite Element models. Joint Annual Meeting of DMV and GAMM. Braunschweig, Germany, 7 - 11 March 2016.

Imholz, M., D. Vandepitte and D. Moens. Derivation of an input interval field decomposition based on expert knowledge using locally defined basis functions, proceedings of the 1st International Conference on Uncertainty Quantification in Computational Sciences and Engineering, Hersonissos, Greece, September 2015.

Imholz, M., D. Vandepitte and D. Moens. Analysis of the effect of uncertain clamping stiffness on the dynamical behaviour of structures using interval field methods, proceedings of ICUME 2015, Darmstadt, Germany, November 2015.

Imholz, M., D. Vandepitte and D. Moens. Application of interval fields to geometric output quantities of Finite Element models, proceedings of UNCERTAINTIES2016, Maresias, Brazil, February 216.

Imholz, M., D. Vandepitte and D. Moens. Dynamical analysis of plate models with uncertain structural properties using the interval field method, proceedings of ECCOMAS 2016, Hersonissos, Greece, June 2016.

Vanmarcke, E., Random Fields: analysis and synthesis, MIT Press, Cambridge, 1993.

Reliable Power Flow Analysis of Systems with Uncertain Data

Shashwati Ray[1)] and Shimpy Ralhan[2)]
[1)] *Bhilai Institute of Technolgy, Durg-491001, (C.G.), India, shashwatiray@yahoo.com*
[2)] *CV Raman University, Bilaspur, (C.G.), India, shimpys@gmail.com*

Abstract: The load flow is the most basic tool for investigating the requirements of a power system and understanding its performance with fixed transmission line parameters and for specified sets of load and generation values. The common formulation of the power flow problem has all the input data specified at a specific time and conditions with fixed values. However, these data are approximate and do not take the measurement errors in transmission line and variation in load demand into consideration. When the input conditions are uncertain, a reliable load flow solution is needed that incorporates the effect of data uncertainty. This paper addresses the problem of uncertainties in the input parameters by specifying them as compact intervals, taking into consideration the errors in modeling and measurement of transmission line parameters and also the continuous influence of load measurement errors and fluctuation in the load demand. The load flow or power flow equations are modeled as a set of nonlinear algebraic equations. These systems of equations are first linearized using Taylor Series expansion and the solution is obtained by the Krawczyk's method of interval arithmetic. The proposed methodology is implemented in MATLAB environment using the INTLAB toolbox. The method is applied to 3 bus, 14 bus, 30 bus and 57 bus IEEE test systems. The results obtained are bounded and thus help in providing an insight to the operation and future expansion of the power system. These results are also compared with those obtained with another iterative method for solving interval linear equation systems.

Keywords: interval mathematics, load flow analysis, uncertain data, Newton Raphson method, Intlab toolbox, Krawczyk's method

1. Introduction

The optimal load flow problem has had a long history in its development for more than 25 years. A generalized formulation of the economic dispatch problem including voltage and other operating constraints was introduced and was later named the optimal power or load flow problem (OPF) (Abdel-Hady and Abdel-Aal Hassan, 2012). Power flow studies are the backbone of power system analysis and design. They are necessary in planning and designing the future expansion of power systems as well as in determining the best operation of existing systems.

Modern power systems are operating under highly stressed and unpredictable conditions because of many issues like market-oriented reforms, consumer utility, measurement errors, use of renewable generation and electric vehicles, etc. The changes resulting from these uncertain factors lead to higher requirements for the reliability of power grids. In this situation, conventional methodologies cannot be applied, so robust and reliable methods become very essential.

The load flow problem in an electric power system is concerned with solving a set of static nonlinear equations describing the electric network performance. The problem is formulated on the basis of Kirchhoff's laws in terms of active and reactive power injections and voltages at each node in the system. Load flow studies or power flow studies is the basic tool for investigating the requirements of power system, viz., generation should be sufficient to meet demand and losses, bus voltages should be in specified range and reactive powers limits of generator buses should be within limits (Grainger and Stevenson, 1994). This information is essential for planning for future expansion such as adding new generator sites to meet increased load demand, operation of the current state of the system, exchange of power between utilities, etc.

The principal information obtained from a power flow study is the magnitude and phase angle of the voltage at each bus and the real and reactive power flow in each line (Hadi Saadat, 2002). As four quantities are involved, four independent constraints are required. In the load flow problem, the buses in the power grid are generally divided into three categories, i.e., slack bus, load bus PQ, and regulated or generator bus PV. A slack bus which is taken as reference is specified with both bus voltage magnitude and phase angle. A PQ bus which can typically be a substation or a power plant with fixed real and reactive power is specified with both active and reactive power injections. A PV bus which is usually a substation with adjustable reactive compensation devices or a power plant with reactive reserves is specified with real power injection and bus voltage magnitude. In reality, a power plant that has adequate capacity and is responsible for frequency control is often selected as a slack bus (Almeida et. al, 1994).

The mathematical formulation of the load flow problem results in a system of algebraic nonlinear equations where the input data are considered to be fixed for all time at all system conditions. However, in reality the models used in power flow analysis are only approximations. The network parameters are usually approximated even though the uncertainties may arise from variances in the model parameters of transmission system elements, such as resistance, reactance and/or capacitance values due to environmental conditions and measurement errors. Also, the specified variables, like real power at PV buses, are inaccurate as they may have measurement errors (Wang and Alvarado, 1994). Further, the demands can vary in a fast and disordered way. Moreover, the uncertainty in the input data can be enlarged due to both rounding and truncating processes that occur in numerical computations (Barboza, Dimuro and Reiser, 2004). Therefore, the final results obtained by conventional methods are wrongly implemented in the system. So, a more reliable power flow algorithm is required which allows the analysts to incorporate both the estimate in data and solution tolerance, i.e., the uncertainty in input parameters and the effect of propagation of data inaccuracies, thus obtaining a range of values for each output quantity (Vaccaro et.al, 2009; Vaccaro et. al, 2013).

Researchers and power engineers have recognized the importance of these uncertainties. Wang and Alvarado are the pioneers in this field where the authors have solved the interval nonlinear equations using the Newton operator and the Gauss Seidel method in (Wang and Alvarado, 1994). Later, in (Barboza, Dimuro and Reiser, 2004) load uncertainty has been dealt by solving the nonlinear equations using Krawczyk's method (Moore, 1966). Recently, many authors have used optimization techniques to address the existence of uncertainty in power flow problem (Dimitrovski and Tomsovic, 2004; Vaccaro et.al, 2009; Vaccaro et. al, 2010; Vaccaro et. al, 2013).

In order to overcome the aforesaid limitations and also control these numerical errors, we propose to apply the technique of interval arithmetic in the Newton-Raphson approach of power flow analysis. In this paper, we develop a methodology by taking into account the various uncertainties. Here, the input parameters are represented as intervals taking into consideration

- the errors in modeling and measurement of transmission line parameters.
- influence of the load measurement errors and fluctuation in the demand.

The nonlinear system is first linearized by the Newton Raphson method and then Krawczyk's method of interval mathematics is applied to solve the system of linearized equations. The implementation is performed in MATLAB environment, using the INTLAB toolbox developed by S. Rump (Rump, 1999). The proposed methodology is tested on 3 bus, 14 bus, 30 bus and 57 bus IEEE test systems.

The rest of the paper is organized as follows: Section II reviews some basic concepts related to interval arithmetic and interval systems. In Section III, we give the main characteristics of load flow problem. In Section IV we describe the interval arithmetic applied to the load flow problem with the proposed approach. In Section V, we give the results on the test problems followed by conclusion section.

2. Interval Arithmetic

Interval arithmetic, interval mathematics, interval analysis, or interval computation, is a method developed by mathematicians since the 1950s and 1960s as an approach to putting bounds on rounding errors and measurement errors in mathematical computation, thus developing numerical methods that yield reliable results. It is an arithmetic developed by R. E. Moore that is defined on sets of intervals instead on sets of real numbers (Moore, 1966). It combines interval arithmetic with analytic estimation techniques to compute the sharpest possible interval solution set which completely contains the true solution set. The power of interval arithmetic lies in its implementation on computers. It solves problems which are unsolvable by non-interval methods and has been used recently for global optimization, solving ordinary differential equations, linear systems, optimization, etc. Interval arithmetic is a logical extension of standard arithmetic that uses operators defined over real intervals.

Following the notations given by (Moore, 1966) and (Ralhan and Ray, 2013), let,

$$\mathbf{x} = [a, b] | a \leq b, a, b \in R \tag{1}$$

be a real interval where a is the infimum (lower endpoint) and b is the supremum (upper endpoint) of $\mathbf{x}$. The width of interval is defined as $w(\mathbf{x}) = a - b$. The midpoint of the interval is defined as $m(\mathbf{x}) = (a + b)/2$. For a n dimensional interval vector $\mathbf{x}^* = [\mathbf{x}_1, \mathbf{x}_2, ..., \mathbf{x}_n]$, the midpoint of interval vector $\mathbf{x}^*$ is given by $m(\mathbf{x}^*) = [m(\mathbf{x}_1), m(\mathbf{x}_2), ..., m(\mathbf{x}_n)]$. The width of interval vector is $w(\mathbf{x}^*) = [w(\mathbf{x}_1), w(\mathbf{x}_2), ..., w(\mathbf{x}_n)]$. A degenerate interval has both its lower and upper endpoints same.

Let $\mathbf{x}$= $[a, b]$ and $\mathbf{y}$= $[c, d]$ be two intervals. Let $+$, $-$, $*$ and / denote the operation of addition, subtraction, multiplication and division, respectively. If $\otimes$ denotes any of these operations for the arithmetic of real numbers x and y, then the corresponding operation for arithmetic of interval numbers $\mathbf{x}$ and $\mathbf{y}$ is,

$$\mathbf{x} \otimes \mathbf{y}=[\mathbf{x} \otimes \mathbf{y} \mid x \in \mathbf{x}, y \in \mathbf{y}]$$

The above definition is equivalent to the following rules:

$$\begin{aligned} \mathbf{x}+\mathbf{y} &= [a+c, b+d] \\ \mathbf{x}-\mathbf{y} &= [a-d, b-c] \\ \mathbf{x} * \mathbf{y} &= [\min(ac, bc, ad, bd), \max(ac, bc, ad, bd)] \\ \mathbf{x}/\mathbf{y} &= [\mathbf{x} * [1/d, 1/c]], 0 \notin \mathbf{y} \end{aligned}$$

.

An interval function $F(\mathbf{x}_1, \mathbf{x}_2, ..., \mathbf{x}_n)$ of intervals $\mathbf{x}_1, \mathbf{x}_2, ..., \mathbf{x}_n$ is an interval valued function of one or more variables. $F(\mathbf{x}_1, \mathbf{x}_2, ..., \mathbf{x}_n)$ is said to be an interval extension of a real function $f(x_1, x_2, ..., x_n)$ if $f(x_1, x_2, ..., x_n) \in \mathbf{F}(\mathbf{x}_1, \mathbf{x}_2, ..., \mathbf{x}_n)$, whenever $x_i \subset \mathbf{x}_i$ for all $i = 1, 2, ..., n$. F is said to be inclusion monotonic if,

$$x_i \subset y_i \Longrightarrow F(\mathbf{x}_1, \mathbf{x}_2, ..., \mathbf{x}_n) \subset F(\mathbf{y}_1, \mathbf{y}_2, ..., \mathbf{y}_n) \tag{2}$$

.

Also, $F(\mathbf{x}_1, \mathbf{x}_2, ..., \mathbf{x}_n)$ contains the range of $f(x_1, x_2, ..., x_n)$. Interval functions $F(\mathbf{x})$ can be constructed in any programming language in which interval arithmetic is implemented, viz., C/C++ and Fortran 90/95, Maple, MATLAB, etc. However, the computations are slow and costly. Computing an interval bound carries a cost of 2 to 4 times as much effort as evaluating $f(\mathbf{x})$ (Moore, 1966; Hansen, 1992). INTLAB implemented with MATLAB enables basic interval operations to be performed on real and complex interval scalars, vectors and matrices.

3. Load Flow Review

The power flow equations (Hadi Saadat, 2002; Chen et. al, 2008) to describe an n bus system shown in Figure 1, are formulated using the bus admittance matrix Y as:

$$I_i = \sum_{j=1}^{n} Y_{ij} V_j \tag{3}$$

where I_i is the current entering in bus i and Y_{ij} is the admittance between the i^{th} and j^{th} buses. These equations are established using the bus analysis which results in node voltages as independent variables.

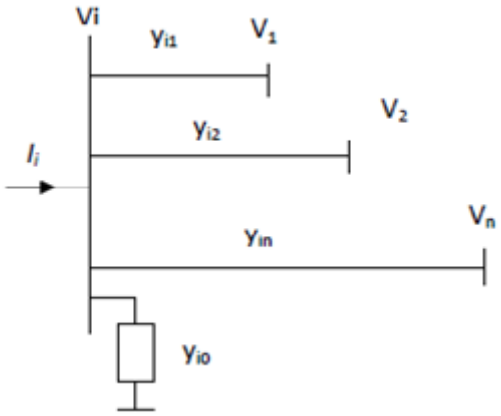

Figure 1. A Typical bus of Power system.

In polar form Eq.(3) is expressed as,

$$I_i = \sum_{j=1}^{n} |Y_{ij}| \angle \theta_{ij} |V_j| \delta_j \tag{4}$$

where, $|Y_{ij}|$ is the magnitude and $\angle\theta_{ij}$ is the angle of the admittance $|Y_{ij}|$ and $|V_j|$ is the magnitude and $\angle\delta_j$ is the phase angle of the voltage. The complex power at bus i is,

$$P_i - jQ_i = V_i^* I_i \tag{5}$$

P_i is the net real power injection and Q_i is the net reactive power injection at bus i

Again, from Eqs.(4) and (5),

$$P_i - jQ_i = |V_i| \angle - \delta_i \sum_{j=1}^{n} |Y_{ij}||V_j| \angle \theta_{ij} + \delta_j \tag{6}$$

Thus,

$$P_i = \sum_{j=1}^{n} |V_i||V_j||Y_{ij}| \cos(\theta_{ij} - \delta_i + \delta_j) \tag{7}$$

$$Q_i = \sum_{j=1}^{n} |V_i||V_j||Y_{ij}| \sin(\theta_{ij} - \delta_i + \delta_j) \tag{8}$$

The general practice in power flow studies is to identify the three types of buses in the network. At each bus i, out of the four quantities δ_i, $|V_i|$, P_i, and Q_i, two are specified and the remaining two are determined. Specified quantities are chosen according to the criteria explained in the following subsections.

3.1. Load Buses

At each non generator bus i, called a load bus or a PQ bus, both P_{gi} and Q_{gi} are zero and P_{di} and Q_{di} drawn from the system by the load are known from historical record, load forecast, or measurement, where the suffixes g and d denote generator and demand. Therefore, the two unknown quantities those to be determined are δ_i and $|V_i|$. Initially δ_i and $|V_i|$ are set as 0.0 and 1.0, respectively.

3.2. Voltage Controlled Buses

Any bus of the system at which the voltage magnitude is kept at a constant is said to be a voltage-controlled bus. A generator bus is usually called a voltage-controlled or a PV bus. A prime mover of any generator can control the amount of generated megawatts (MW), whereas generator voltage magnitude can be controlled by generators excitation system. Therefore, at each generator bus i both $|V_i|$ and P_{gi} may be properly specified. The two unknown quantities that must be determined are δ_i and Q_i. Initially δ_i is taken as 0.0.

3.3. Slack Bus

The voltage angle of a slack bus serves as a reference for the angles of all other bus voltages. Thus, the usual practice is to set δ_i to zero degree. Voltage magnitude of the slack bus $|V_i|$ is also specified. Therefore, the two unknown quantities P_i and Q_i must be determined during the load flow analysis.

3.4. Conventional Load Flow Problem Formulation

The set of equations given by Eq.(7) constitute a set of nonlinear algebraic equations as a function of voltage magnitude in per unit and phase angle in radians. Generalizing,

$$\begin{aligned} \mathbf{P}(|\mathbf{V}|, \delta) &= \mathbf{P}_s \\ \mathbf{Q}(|\mathbf{V}|, \delta) &= \mathbf{Q}_s \end{aligned} \tag{9}$$

If $(\mathbf{V}_k, \delta_k)$ is an initial estimate and $\Delta\mathbf{V}$ and $\Delta\delta$ are small deviations in voltage magnitudes and angles respectively, except the slack bus then,

$$\begin{aligned} \mathbf{P}(\mathbf{V}_k + \Delta\mathbf{V}, \delta_k + \Delta\delta) &= \mathbf{P}_s \\ \mathbf{Q}(\mathbf{V}_k + \Delta\mathbf{V}, \delta_k + \Delta\delta) &= \mathbf{Q}_s \end{aligned} \tag{10}$$

Expanding Eq.(10) in Taylor series about an initial estimate $(\mathbf{V}_k, \delta_k)$ and neglecting higher order terms, we obtain,

$$\begin{aligned} \mathbf{P}_{\mathbf{V}_k,\delta_k} + \Delta\mathbf{V}\frac{\partial \mathbf{P}_{\mathbf{V}_k,\delta_k}}{\partial \mathbf{V}} + \Delta\delta\frac{\partial \mathbf{P}_{\mathbf{V}_k,\delta_k}}{\partial \delta} - \mathbf{P}_s = 0 \\ \mathbf{Q}_{\mathbf{V}_k,\delta_k} + \Delta V\frac{\partial \mathbf{Q}_{\mathbf{V}_k,\delta_k}}{\partial \mathbf{V}} + \Delta\delta\frac{\partial \mathbf{Q}_{\mathbf{V}_k,\delta_k}}{\partial \delta} - \mathbf{Q}_s = 0 \end{aligned} \tag{11}$$

Hence,

$$\begin{bmatrix} \mathbf{P}_s - \mathbf{P}_{\mathbf{V}_k,\delta_k} \\ \mathbf{Q}_s - \mathbf{Q}_{\mathbf{V}_k,\delta_k} \end{bmatrix} = \begin{bmatrix} \frac{\partial \mathbf{P}_{\mathbf{V}_k,\delta_k}}{\partial \delta} & \frac{\partial \mathbf{P}_{\mathbf{V}_k,\delta_k}}{\partial \mathbf{V}} \\ \frac{\partial \mathbf{Q}_{\mathbf{V}_k,\delta_k}}{\partial \delta} & \frac{\partial \mathbf{Q}_{\mathbf{V}_k,\delta_k}}{\partial \mathbf{V}} \end{bmatrix} \begin{bmatrix} \Delta\delta \\ \Delta|\mathbf{V}| \end{bmatrix} \tag{12}$$

Elements of the Jacobian matrix are the partial derivatives of Eqs.(7) and (8) for $i = 2, ..., n$, evaluated at $(\mathbf{V}_k, \delta_k)$ and bus 1 is assumed to be the slack bus. Using the initial estimates given in Sections 3.1, 3.2 and 3.3, $\mathbf{P}_{\mathbf{V}_k,\delta_k}$ and $\mathbf{Q}_{\mathbf{V}_k,\delta_k}$ are calculated using Eqs.(7) and (8) respectively for each bus. Writing in compact form,

$$\begin{bmatrix} \Delta\mathbf{P} \\ \Delta\mathbf{Q} \end{bmatrix} = \begin{bmatrix} \mathbf{J}_1 & \mathbf{J}_2 \\ \mathbf{J}_3 & \mathbf{J}_4 \end{bmatrix} \begin{bmatrix} \Delta\delta \\ \Delta|\mathbf{V}| \end{bmatrix} \tag{13}$$

Therefore,

$$\begin{bmatrix} \Delta\delta \\ \Delta|\mathbf{V}| \end{bmatrix} = \mathbf{J}^{-1} \begin{bmatrix} \Delta\mathbf{P} \\ \Delta\mathbf{Q} \end{bmatrix} \tag{14}$$

Expressing Eq.(14) as,

$$\mathbf{J}\mathbf{x} = \mathbf{b} \tag{15}$$

where,

$$\mathbf{x} = \begin{bmatrix} \Delta\delta \\ \Delta|\mathbf{V}| \end{bmatrix} \tag{16}$$

$$\mathbf{J} = \begin{bmatrix} \mathbf{J}_1 & \mathbf{J}_2 \\ \mathbf{J}_3 & \mathbf{J}_4 \end{bmatrix} \tag{17}$$

and

$$\mathbf{b} = \begin{bmatrix} \Delta\mathbf{P} \\ \Delta\mathbf{Q} \end{bmatrix} \tag{18}$$

The above equations have inherent assumptions which include the factors, such as the three phase system is in balanced, steady-state condition so that the frequency and voltage are constant, the real and reactive power demands are known and specified precisely, the real power injection and voltage magnitude of generators are fixed, and the network topology and impedances are known precisely. But these are not valid, at least in true sense. The uncertainties may be induced by modeling errors due to the approximations in the values of the resistances, reactances and shunts in the models which are used to represent transmission lines and transformers. The practical power systems are very large with tens of thousands of buses. As a consequence, the probability of data errors increases dramatically with system size. Therefore, we take the data uncertainty into consideration by characterizing the load and transmission line parameters as a range of real values or a real interval instead of crisp values.

4. Load Flow Solution using Interval Method

As the uncertainties in the data could affect the deterministic power flow solution to a considerable extent, reliable solution algorithms that incorporate the effect of data uncertainties into the load flow analysis are therefore required. In this way, the uncertainty propagation effect is explicitly considered and the bounded values for power flow studies can be assessed. Thus, the voltages, angles and powers are obtained as intervals that include all computational errors and all the possible results obtained by computations with real numbers. The known real and reactive power injections P_i, Q_i, as well as other input line parameters are modeled as intervals that are estimated in the beginning of the process. The magnitude and angle of voltages are unknown intervals to be determined for all buses except the slack bus. In order to reach the solution, we use the Krawczyk method which is an iterative method to solve interval linear system of equations (Moore, Baker and Cloud, 2008; Hansen, 1992).

4.1. Krawczyk Method

The power flow equations (Eqs.(13), (14), and (15)) have been obtained after linearization using Taylor series expansion method. Since we have taken the uncertainty in the transmission line parameters, i.e, resistances and reactances, the Jacobian $\mathbf{J}$ is an interval matrix. Also, the variations in power lead to interval vectors (which are actually nonlinear in nature but are linearized). By using the Krawczyk method, along with interval arithmetic we can obtain the solution of the finite system of linear equations. Consider a system of finite system of linear equations represented as,

$$\mathbf{J}\mathbf{x} = \mathbf{b} \tag{19}$$

$$i, e., \quad \mathbf{x} = \mathbf{J}^{-1}\mathbf{b} \tag{20}$$

Let $\mathbf{Y}$ be an approximate inverse of $\mathbf{J}$, i.e.,

$$\mathbf{Y} \simeq \mathbf{J}^{-1} \tag{21}$$

Multiplying both sides of Eq.(19) by $\mathbf{Y}$. We have,

$$\mathbf{Y}\mathbf{J}\mathbf{x} = \mathbf{Y}\mathbf{b} \tag{22}$$

From Eq.(20) and Eq.(22), we get,

$$[\mathbf{I} - \mathbf{Y}\mathbf{J}]\mathbf{x} = \mathbf{J}^{-1}\mathbf{b} - \mathbf{Y}\mathbf{b} \tag{23}$$

Let us consider,

$$\mathbf{E} = \mathbf{I} - \mathbf{Y}\mathbf{J} \tag{24}$$

Therefore, Eq.(23) can be written as,

$$\mathbf{E}\mathbf{x} = \mathbf{x} - \mathbf{Y}\mathbf{b} \tag{25}$$

or,

$$\mathbf{x} = \mathbf{Y}\mathbf{b} + \mathbf{E}\mathbf{x} \tag{26}$$

The norm of an interval matrix say $\mathbf{A}$ is given by,

$$||\mathbf{A}|| = max_i \sum_j |\mathbf{A}_{ij}| \tag{27}$$

Since $\mathbf{E}$ is an interval matrix $||\mathbf{E}|| = \max_i \sum_j |E_{ij}|$. So if $||\mathbf{E}|| \leq 1$ using Eq.(27), then the sequence,

$$\begin{aligned} \mathbf{x}^{(k+1)} &= \mathbf{Yb} + \mathbf{Ex}^{(k)} \cap \mathbf{x}^{(k)}; k = 0, 1, 2, ... \\ \mathbf{x}_i^{(0)} &= [-1, 1]||\mathbf{Yb}||/(1 - ||\mathbf{E}||); i = 0, 1, ..., n \end{aligned} \tag{28}$$

is a nested sequence of interval vectors containing the unique solution to Eq.(19) for every interval matrix $\mathbf{J}$ and every interval vector $\mathbf{b}$. From Eq.(28) the new estimates for the bus voltage angle and magnitude are respectively obtained as,

$$\delta^{(k+1)} = \delta^(k) + \Delta\delta^(k) \tag{29}$$

$$|V^{(k+1)}| = |V^{(k)}| + \Delta|V^{(k)}| \tag{30}$$

Since nonlinearities in the power system can be said to be encompassed by intervals in the linearized system (Kearfott, 1991; Hansen, 1992), Eqs.(29) and (30) give us a bounded and converging solution for the non linear power flow equations.

5. Results

In this section we test the performance of the proposed method. For this we have carried out the tests on these standard systems, namely IEEE 3 bus, 14 bus, 30 bus and 57 bus test power systems from the Archive, by conventional load flow and interval load flow methods. We specify the loads and generation in Mega Watt (MW) and Mega Volt Ampere Reactive (MVAR), respectively, bus voltages in per unit, and their angles in degrees. Loads and generations are converted into per unit quantities on the base Mega Volt Ampere (MVA) selected. Three types of tests are performed on all the systems

1. Available data has been taken as fixed data without any uncertainty
2. Measurement error of 2% in the transmission line parameters was considered.
3. A 10% variation in active and reactive powers of load and generator were carried out.

The test cases considered are as given in the subsequent subsections. In this paper, we implement the methods in MATLAB environment using the INTLAB toolbox (Rump, 1999).

5.1. IEEE 3 bus system

The 3 bus network shown in Figure 2 consists of one load bus (PQ bus, bus 2), one generator bus (PV bus, bus 3) and a slack bus (reference bus, bus 1) and has three circuits whose parameters,

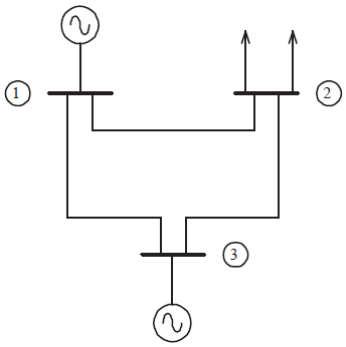

Figure 2. 3 Bus Test Case.

Table I. Line data for 3 bus test case.

Bus	Bus	$R_{p.u.}$	$X_{p.u.}$	$C(MVar)$	$Tr.TapSet.$
1	2	0.02	0.04	0	1
1	3	0.01	0.03	0	1
2	3	0.0125	0.025	0	1

i.e., resistance, reactance and capacitance are shown in Table I. Table II shows power flow data for the test case. Initially, we consider that the power at load bus is accurate and measurement errors are equal to zero.

With conventional Newton Raphson method we obtain the results as shown in Table III without considering any uncertainty in the input data. In the table we show the magnitude and angle of voltages at all system buses ($|V|$ is magnitude of bus voltage, δ is the angle in degrees), P_D and Q_D, P_G and Q_G are the active and reactive powers of load, generator and slack buses.

Then, we consider the existence of uncertainties in the values of the input data as mentioned above and Table IV and Table V show the results of the simulations performed using interval arithmetic. The active power at the slack bus for 2% variation in power load measurements is [1.4736, 2.8930] using intervals and by conventional method, it is 2.1482 p.u. which is inclusive in that range. Similarly, the reactive power at slack bus by conventional method is 1.4085 and interval value is [1.0008, 1.8217].

Table II. Bus data for 3 bus test case.

Bus	V(p.u.)	Angle (deg)	P_D	Q_D	P_G	Q_G	Q_{min}	Q_{max}	MVar
1	1.05	0	0	0	0	0	0	0	0
2	1.00	0	−4	−2.5	0	0	0	0	0
3	1.04	0	0	0	2	0	0	0	0

Table III. Load Flow Solution for 3 bus system with conventional Newton Raphson method.

Bus	$\|V\|$	δ(deg.)	P_D	Q_D	P_G	Q_G
1	1.05	0	0	0	2.1842	1.4085
2	0.97168	-0.04706	-4	-2.5	0	0
3	1.04	0.008705	0	0	2	1.4617

Table IV. Load Flow Solution for 3 bus Interval system with variation in load power.

Bus	$\|V\|$	δ(deg.)	Q_G
1	[1.0500, 1.0501]	[0.0000, 0.0000]	[1.0008, 1.8217]
2	[0.9637, 0.9797]	[-3.5040, -1.8889]	[0.0000, 0.0000]
3	[1.0400, 1.0401]	[-1.0924, 0.0948]	[0.1240, 2.7880]

5.2. IEEE 14 bus system

The 14 bus IEEE test case shown in Figure 3 has been analyzed in the same way. Table VI shows the results with the conventional Newton Raphson method. Table VII and Table VIII show the results of the simulations performed using Interval mathematics considering the existence of uncertainties in the values of the input data. The active power at the slack bus for 2% variation in power load measurements is [1.9931, 2.6583] using intervals and the interval value of reactive power at slack bus is [-0.2301, -0.0757].

5.3. IEEE 30 bus system

Next we consider 30 bus IEEE test case. Table IX and Table X show the results of the simulations performed using Interval mathematics considering the existence of uncertainties in the values of the input data. The active power at the slack bus for 2% variation in power load measurements

Table V. Load Flow Solution for 3 bus Interval system with variation in line parameters and load power.

Bus	$\|V\|$	δ(deg.)	Q_G
1	[1.0500, 1.0501]	[0.0000, 0.0000]	[1.0010, 1.8219]
2	[0.9637, 0.9797]	[-3.5024, -1.8880]	[0.0000, 0.0000]
3	[1.0400, 1.0401]	[-1.0918, 0.0949]	[0.1237, 2.7877]

Table VI. Load Flow Solution for 14 bus system with conventional Newton Raphson method.

Busno.	$V(p.u.)$	δ(deg.)	P_D	Q_D	P_G	Q_G
1	1.060	0.000	0.000	0.000	2.746	−0.238
2	1.045	−6.149	0.217	0.127	0.004	0.628
3	1.010	−13.781	0.942	0.190	0.000	0.272
4	1.014	−11.178	0.478	−0.039	0.000	0.000
5	1.017	−9.603	0.076	0.016	0.000	0.000
6	1.070	−15.283	0.112	0.075	0.000	0.216
7	1.050	−14.159	0.000	0.000	0.000	0.000
8	1.090	−14.159	0.000	0.000	0.000	0.246
9	1.034	−15.732	0.295	0.166	0.000	0.000
10	1.032	−15.935	0.090	0.058	0.000	0.000
11	1.047	−15.727	0.035	0.018	0.000	0.000
12	1.054	−16.136	0.061	0.016	0.000	0.000
13	1.047	−16.178	0.135	0.058	0.000	0.000
14	1.021	−16.952	0.149	0.050	0.000	0.000

Table VII. Load Flow Solution for 14 bus Interval system with variation in load power.

Bus	$\lvert V\rvert$	δ(deg.)	Q_G
1	[1.0600, 1.0601]	[0.0000, 0.0000]	[-0.2381, -0.0757]
2	[1.0449, 1.0450]	[-6.7794, -4.1951]	[-0.0671, 1.0016]
3	[1.0100, 1.0101]	[-14.3743, -11.1098]	[-0.1268, 0.6576]
4	[1.0110, 1.0176]	[-11.5647, -8.9499]	[0.0000, 0.0000]
5	[1.0143, 1.0202]	[-9.8895, -7.6405]	[0.0000, 0.0000]
6	[1.0700, 1.0701]	[-16.1462, -12.6894]	[-0.7583, 1.1850]
7	[1.0472, 1.0535]	[-14.8825, -11.6226]	[0.0000, 0.0000]
8	[1.0900, 1.0901]	[-14.8825, -11.6226]	[0.2152, 0.2748]
9	[1.0288, 1.0386]	[-16.6281, -13.0375]	[0.0000, 0.0000]
10	[1.0277, 1.0375]	[-16.8653, -13.2181]	[0.0000, 0.0000]
11	[1.0446, 1.0504]	[-16.6346, -13.0615]	[0.0000, 0.0000]
12	[1.0517, 1.0553]	[-17.1042, -13.4328]	[0.0000, 0.0000]
13	[1.0445, 1.0497]	[-17.1593, -13.4572]	[0.0000, 0.0000]
14	[1.0155, 1.0272]	[-18.0196, -14.1104]	[0.0000, 0.0000]

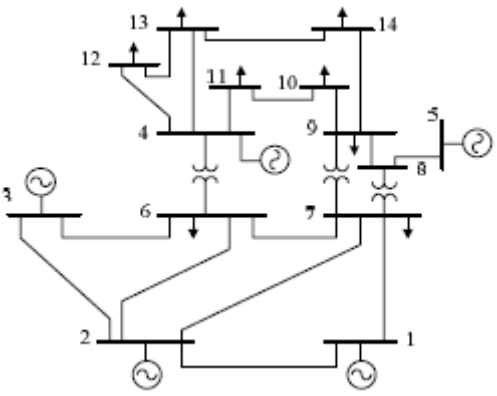

Figure 3. 14 Bus Test System.

Table VIII. Load Flow Solution for 14 bus Interval system with variation in line parameters and load power.

Bus	$\|V\|$	δ(deg.)	Q_G
1	[1.0600, 1.0601]	[0.0000, 0.0000]	[-0.2386, -0.0762]
2	[1.0449, 1.0450]	[-6.7826, -4.1989]	[-0.0669, 1.0019]
3	[1.0100, 1.0101]	[-14.3765, -11.1134]	[-0.1270, 0.6575]
4	[1.0110, 1.0176]	[-11.5672, -8.9534]	[0.0000, 0.0000]
5	[1.0143, 1.0202]	[-9.8922, -7.6440]	[0.0000, 0.0000]
6	[1.0700, 1.0701]	[-16.1464, -12.6910]	[-0.7584, 1.1849]
7	[1.0472, 1.0535]	[-14.8835, -11.6249]	[0.0000, 0.0000]
8	[1.0900, 1.0901]	[-14.8835, -11.6249]	[0.2152, 0.2749]
9	[1.0288, 1.0387]	[-16.6284, -13.0392]	[0.0000, 0.0000]
10	[1.0277, 1.0375]	[-16.8654, -13.2197]	[0.0000, 0.0000]
11	[1.0446, 1.0504]	[-16.6347, -13.0630]	[0.0000, 0.0000]
12	[1.0517, 1.0553]	[-17.1040, -13.4341]	[0.0000, 0.0000]
13	[1.0445, 1.0497]	[-17.1591, -13.4585]	[0.0000, 0.0000]
14	[1.0155, 1.0272]	[-18.0192, -14.1115]	[0.0000, 0.0000]

is [2.2425, 2.9780] using intervals which is inclusive in that range. Similarly, the reactive power at slack bus has interval value is [-0.2544,-0.0803] .

5.4. IEEE 57 BUS SYSTEM

Finally we consider 57 bus IEEE test case. In this case a measurement error of 2% in the transmission line parameters was assumed. Tables XI and XII show the results of the simulations performed using interval arithmetic considering the existence of uncertainties in the values of the input data. Next a 20% variation in active and reactive powers of load and generator were assumed. This was done

Table IX. Load Flow Solution for 30 bus Interval system with variation in load power.

Bus	$\|V\|$	δ(deg.)	Q_G
1	[1.0600, 1.0601]	[0.0000, 0.0000]	[-0.2544, -0.0803]
2	[1.0429, 1.0430]	[-6.3511, -4.6426]	[-0.0873, 1.0649]
3	[1.0186, 1.0244]	[-9.0298, -6.9783]	[0.0000,0.0000]
4	[1.0097, 1.0160]	[-10.9077, -8.4153]	[0.0000, 0.0000]
5	[1.0100, 1.0101]	[-16.1915, -12.5710]	[-0.2099, 0.9167]
6	[1.0096, 1.0145]	[-12.8548, -9.9412]	[0.0000, 0.0000]
7	[1.0011, 1.0058]	[-14.8170, -11.4820]	[0.0000,0.0000]
8	[1.0100, 1.0101]	[-13.6719, -10.5588]	[-0.6206, 1.2306]
9	[1.0464, 1.0556]	[-16.2159, -12.6518]	[0.0000, 0.0000]
10	[1.0365, 1.0522]	[-17.9750, -14.0733]	[0.0000, 0.0000]
11	[1.0820, 1.0821]	[-16.2159, -12.6518]	[0.1267, 0.1953]
12	[1.0530, 1.0617]	[-17.1766, -13.4283]	[0.0000, 0.0000]
13	[1.0709, 1.0710]	[-17.1766, -13.4283]	[0.0536, 0.1546]
14	[1.0362, 1.0487]	[-18.1762, -14.2064]	[0.0000, 0.0000]
15	[1.0307, 1.0449]	[-18.2662, -14.2903]	[0.0000, 0.0000]
16	[1.0381, 1.0513]	[-17.8166, -13.9444]	[0.0000, 0.0000]
17	[1.0311, 1.0472]	[-18.1645, -14.2121]	[0.0000, 0.0000]
18	[1.0193, 1.0366]	[-18.9491, -14.8180]	[0.0000, 0.0000]
19	[1.0160, 1.0345]	[-19.1381, -14.9658]	[0.0000, 0.0000]
20	[1.0203, 1.0383]	[-18.9045, -14.8000]	[0.0000, 0.0000]
21	[1.0229, 1.0413]	[-18.4906, -14.4464]	[0.0000, 0.0000]
22	[1.0235, 1.0418]	[-18.4724, -14.4368]	[0.0000, 0.0000]
23	[1.0183, 1.0361]	[-18.7160, -14.6088]	[0.0000, 0.0000]
24	[1.0112, 1.0319]	[-18.9230, -14.7373]	[0.0000, 0.0000]
25	[1.0098, 1.0279]	[-18.4728, -14.3749]	[0.0000, 0.0000]
26	[0.9902, 1.0122]	[-19.0010, -14.6834]	[0.0000, 0.0000]
27	[1.0185, 1.0330]	[-17.8839, -13.9411]	[0.0000, 0.0000]
28	[1.0080, 1.0135]	[-13.5871, -10.5278]	[0.0000, 0.0000]
29	[0.9965, 1.0154]	[-19.2754, -14.9973]	[0.0000, 0.0000]
30	[0.9837, 1.0053]	[-20.2658, -15.7635]	[0.0000, 0.0000]

to make a comparison of the performance of the proposed method with that of (Vaccaro et. al, 2013) and the results are shown in Tables XIII and XIV. From the results we can easily say that the bounds for the voltage and angles are comparable to that obtained in (Vaccaro et. al, 2013). The active power at the slack bus for 2% variation in power load measurements is [1.6903,5.9333] using the proposed technique which also includes the values obtained by the conventional method. Similarly, the reactive power at slack bus is [2.2970,3.1437].

Table X. Load Flow Solution for 30 bus Interval system with variation in variation in line parameters and load power.

Bus	$\|V\|$	δ(deg.)	Q_G
1	[1.0600, 1.0601]	[0.0000, 0.0000]	[-0.2554, -0.0813]
2	[1.0429, 1.0430]	[-6.3599, -4.6519]	[-0.0866, 1.0658]
3	[1.0186, 1.0244]	[-9.0411, -6.9902]	[0.0000,0.0000]
4	[1.0097, 1.0160]	[-10.9208, -8.4291]	[0.0000, 0.0000]
5	[1.0100, 1.0101]	[-16.1915, -12.5710]	[-0.2100, 0.9167]
6	[1.0096, 1.0145]	[-12.8703, -9.9576]	[0.0000, 0.0000]
7	[1.0011, 1.0058]	[-14.8317, -11.4978]	[0.0000,0.0000]
8	[1.0100, 1.0101]	[-13.6881, -10.5760]	[-0.6206, 1.2308]
9	[1.0464, 1.0556]	[-16.2297, -12.6667]	[0.0000, 0.0000]
10	[1.0365, 1.0522]	[-17.9878, -14.0874]	[0.0000, 0.0000]
11	[1.0820, 1.0821]	[-16.2297, -12.6667]	[0.1268, 0.1953]
12	[1.0530, 1.0617]	[-17.1885, -13.4416]	[0.0000, 0.0000]
13	[1.0709, 1.0710]	[-17.1885, -13.4416]	[0.0536, 0.1546]
14	[1.0362, 1.0487]	[-18.1879, -14.2195]	[0.0000, 0.0000]
15	[1.0307, 1.0449]	[-18.2780, -14.3036]	[0.0000, 0.0000]
16	[1.0381, 1.0513]	[-17.8287, -13.9580]	[0.0000, 0.0000]
17	[1.0311, 1.0472]	[-18.1770, -14.2260]	[0.0000, 0.0000]
18	[1.0193, 1.0366]	[-18.9609, -14.8313]	[0.0000, 0.0000]
19	[1.0160, 1.0345]	[-19.1500, -14.9792]	[0.0000, 0.0000]
20	[1.0203, 1.0383]	[-18.9166, -14.8137]	[0.0000, 0.0000]
21	[1.0229, 1.0413]	[-18.5032, -14.4604]	[0.0000, 0.0000]
22	[1.0236, 1.0418]	[-18.4851, -14.4508]	[0.0000, 0.0000]
23	[1.0184, 1.0361]	[-18.7280, -14.6224]	[0.0000, 0.0000]
24	[1.0112, 1.0319]	[-18.9357, -14.7514]	[0.0000, 0.0000]
25	[1.0099, 1.0279]	[-18.4867, -14.3903]	[0.0000, 0.0000]
26	[0.9903, 1.0122]	[-19.0147, -14.6987]	[0.0000, 0.0000]
27	[1.0185, 1.0330]	[-17.8987, -13.9573]	[0.0000, 0.0000]
28	[1.0080, 1.0135]	[-13.6048, -10.5465]	[0.0000, 0.0000]
29	[0.9965, 1.0155]	[-19.2896, -15.0131]	[0.0000, 0.0000]
30	[0.9837, 1.0053]	[-20.2796, -15.7789]	[0.0000, 0.0000]

6. Conclusion

In this study, a method for considering the uncertainties of the input parameters in the load flow solution for power systems has been presented. Based on interval arithmetic, the proposed methodology can consider the uncertainties in both the load demand and the transmission line parameters successfully. The solutions which we have obtained from the interval arithmetic based

Table XI. Load Flow Solution for 57 bus Interval system with variation in load power.

Bus no.	$V(p.u.)$	δ(deg.)	P_D	Q_D	P_G	Q_G
1	[1.06,1.06]	[0.00,0.00]	[0.55,0.55]	[0.17,0.17]	[1.69,5.93]	[2.29,3.14]
2	[1.00,1.00]	[-1.39,0.40]	[0.02,0.03]	[0.87,0.88]	[0.00,0.00]	[-2.16, −0.52]
3	[1.00,1.00]	[-8.89, −1.29]	[0.40,0.41]	[0.20,0.21]	[0.40,0.40]	[-4.00,4.72]
4	[0.99,0.99]	[-11.03, −1.53]	[0.00,0.00]	[0.00,0.00]	[0.00,0.00]	[0.00,0.00]
5	[0.99,0.99]	[-13.58, −1.25]	[0.12,0.13]	[0.04,0.04]	[0.00,0.00]	[0.00,0.00]
6	[1.00,1.00]	[-14.31,-0.73]	[0.74,0.75]	[0.02,0.02]	[0.00,0.00]	[-4.85,5.55]
7	[0.98,0.99]	[-13.82,1.49]	[0.00,0.00]	[0.00,0.00]	[0.00,0.00]	[0.00,0.00]
8	[1.00,1.00]	[-11.21,5.25]	[1.50,1.50]	[0.21,0.22]	[4.50,4.50]	[-4.10,3.23]
9	[1.00,1.00]	[-15.56, −0.99]	[1.20,1.21]	[0.25,0.26]	[0.00,0.00]	[-5.18,6.89]
10	[0.98,0.98]	[-16.43, −3.19]	[0.05,0.05]	[0.02,0.02]	[0.00,0.00]	[0.00,0.00]
11	[0.98,0.98]	[-15.03, −2.27]	[0.00,0.00]	[0.00,0.00]	[0.00,0.00]	[0.00,0.00]
12	[1.00,1.00]	[-14.95, −2.68]	[3.76,3.77]	[0.23,0.24]	[3.10,3.10]	[-4.47,5.05]
13	[0.97,0.98]	[-13.68, −2.59]	[0.17,0.18]	[0.02,0.02]	[0.00,0.00]	[0.00,0.00]
14	[0.97,0.98]	[-12.43, −2.62]	[0.10,0.10]	[0.05,0.05]	[0.00,0.00]	[0.00,0.00]
15	[0.99,1.00]	[-9.77, −2.12]	[0.21,0.22]	[0.05,0.05]	[0.00,0.00]	[0.00,0.00]
16	[1.00,1.01]	[-12.11, −3.14]	[0.42,0.43]	[0.02,0.03]	[0.00,0.00]	[0.00,0.00]
17	[1.02,1.03]	[-7.08, −2.30]	[0.41,0.42]	[0.08,0.08]	[0.00,0.00]	[0.00,0.00]
18	[0.98,0.99]	[-15.72, −5.26]	[0.27,0.27]	[0.09,0.09]	[0.00,0.00]	[0.00,0.00]
19	[0.95,0.97]	[-17.07, −6.00]	[0.03,0.03]	[0.00,0.00]	[0.00,0.00]	[0.00,0.00]
20	[0.95,0.97]	[-17.11, −5.79]	[0.02,0.02]	[0.01,0.01]	[0.00,0.00]	[0.00,0.00]
21	[0.991.01]	[-16.05, −4.71]	[0.00,0.00]	[0.00,0.00]	[0.00,0.00]	[0.00,0.00]
22	[0.99,1.02]	[-15.93, −4.57]	[0.00,0.00]	[0.00,0.00]	[0.00,0.00]	[0.00,0.00]
23	[0.99,1.01]	[-16.06, −4.59]	[0.06,0.06]	[0.02,0.02]	[0.00,0.00]	[0.00,0.00]
24	[0.97,1.00]	[-17.31, −4.15]	[0.00,0.00]	[0.00,0.00]	[0.00,0.00]	[0.00,0.00]
25	[0.92,0.96]	[-22.70, −8.59]	[0.06,0.06]	[0.03,0.03]	[0.00,0.00]	[0.00,0.00]
26	[0.94,0.96]	[-17.15, −3.80]	[0.00,0.00]	[0.00,0.00]	[0.00,0.00]	[0.00,0.00]
27	[0.97,0.98]	[-17.00, −2.22]	[0.09,0.09]	[0.00,0.00]	[0.00,0.00]	[0.00,0.00]
28	[0.98,1.00]	[-16.39, −1.20]	[0.04,0.04]	[0.02,0.02]	[0.00,0.00]	[0.00,0.00]
29	[1.00,1.01]	[-15.93, −0.51]	[0.17,0.17]	[0.02,0.02]	[0.00,0.00]	[0.00,0.00]
30	[0.90,0.95]	[-23.39, −9.16]	[0.03,0.03]	[0.01,0.01]	[0.00,0.00]	[0.00,0.00]
31	[0.88,0.93]	[-24.22, −9.95]	[0.05,0.05]	[0.02,0.02]	[0.00,0.00]	[0.00,0.00]
32	[0.91,0.95]	[-23.12, −9.56]	[0.01,0.01]	[0.00,0.00]	[0.00,0.00]	[0.00,0.00]
33	[0.91,0.95]	[-23.17, −9.58]	[0.03,0.03]	[0.018,0.01]	[0.00,0.00]	[0.00,0.00]
34	[0.94,0.97]	[-17.64, −5.58]	[0.00,0.00]	[0.00,0.00]	[0.00,0.00]	[0.00,0.00]
35	[0.95,0.98]	[-17.35, −5.43]	[0.05,0.06]	[0.02,0.03]	[0.00,0.00]	[0.00,0.00]
36	[0.96,0.99]	[-17.03, −5.25]	[0.00,0.00]	[0.00,0.00]	[0.00,0.00]	[0.00,0.00]
37	[0.97,1.00]	[-16.72, −5.09]	[0.00,0.00]	[0.00,0.00]	[0.00,0.00]	[0.00,0.00]
38	[1.00,1.02]	[-15.67, −4.51]	[0.14,0.14]	[0.07,0.07]	[0.00,0.00]	[0.00,0.00]
39	[0.97,0.99]	[-16.79, −5.12]	[0.00,0.00]	[0.00,0.00]	[0.00,0.00]	[0.00,0.00]
40	[0.96,0.99]	[-17.14, −5.30]	[0.00,0.00]	[0.00,0.00]	[0.00,0.00]	[0.00,0.00]
41	[0.99,1.00]	[-18.99, −5.75]	[0.06,0.06]	[0.02,0.03]	[0.00,0.00]	[0.00,0.00]
42	[0.95,0.97]	[-20.28, −6.90]	[0.07,0.07]	[0.04,0.04]	[0.00,0.00]	[0.00,0.00]
43	[1.01,1.02]	[-16.21, −3.31]	[0.02,0.02]	[0.01,0.01]	[0.00,0.00]	[0.00,0.00]
44	[1.01,1.02]	[-14.75, −4.31]	[0.11,0.12]	[0.01,0.01]	[0.00,0.00]	[0.00,0.00]
45	[1.03,1.04]	[-12.03, −3.21]	[0.00,0.00]	[0.00,0.00]	[0.00,0.00]	[0.00,0.00]

Table XII. Load Flow Solution for 57 bus Interval system with variation in load power (contd.).

Bus no.	$V(p.u.)$	δ(deg.)	P_D	Q_D	P_G	Q_G
46	[1.05,1.07]	[-13.67, −3.36]	[0.00,0.00]	[0.00,0.00]	[0.00,0.00]	[0.00,0.00]
47	[1.02,1.04]	[-14.51, −3.63]	[0.00,0.00]	[0.29,0.29]	[0.00,0.00]	[0.00,0.00]
48	[1.01,1.03]	[-15.03, −4.01]	[0.00,0.00]	[0.00,0.00]	[0.00,0.00]	[0.00,0.00]
49	[1.02,1.04]	[-16.32, −4.79]	[0.17,0.18]	[0.08,0.08]	[0.00,0.00]	[0.00,0.00]
50	[1.01,1.03]	[-17.47, −5.07]	[0.20,0.21]	[0.10,0.10]	[0.00,0.00]	[0.00,0.00]
51	[1.04,1.05]	[-17.42, −4.18]	[0.17,0.18]	[0.05,0.05]	[0.00,0.00]	[0.00,0.00]
52	[0.96,0.98]	[-17.60, −1.80]	[0.04,0.04]	[0.02,0.02]	[0.00,0.00]	[0.00,0.00]
53	[0.951,0.97]	[-18.29, −2.36]	[0.20,0.20]	[0.10,0.10]	[0.00,0.00]	[0.00,0.00]
54	[0.99,1.00]	[-17.83, −2.40]	[0.04,0.04]	[0.01,0.01]	[0.00,0.00]	[0.00,0.00]
55	[1.04,1.05]	[-16.95, −2.05]	[0.06,0.06]	[0.03,0.03]	[0.00,0.00]	[0.00,0.00]
56	[0.94,0.97]	[-20.45, −7.28]	[0.07,0.07]	[0.02,0.02]	[0.00,0.00]	[0.00,0.00]
57	[0.94,0.97]	[-20.91, −7.80]	[0.06,0.06]	[0.02,0.02]	[0.00,0.00]	[0.00,0.00]

Table XIII. Load Flow Solution for 57 bus Interval system with variation in load and generator power and in static reactive power.

Bus	$V(p.u.)$	δ(deg.)	P_D	Q_D	P_G	Q_G
1	[1.06,1.06]	[0.00,0.00]	[0.55,0.55]	[0.17,0.17]	[-0.42,8.06]	[2.00,3.72]
2	[1.00,1.00]	[-2.29,1.31]	[0.02,0.03	[0.87,0.88]	[0.00,0.00]	[-2.92,0.34]
3	[1.00,1.00]	[-12.69,2.50]	[0.40,0.41]	[0.20,0.21]	[0.40,0.40]	[-8.29,9.00]
4	[0.99,0.99]	[-15.78,3.20]	[0.00,0.00]	[0.00,0.00]	[0.00,0.00]	[0.00,0.00]
5	[0.99,0.99]	[-19.74,4.90]	[0.12,0.13]	[0.04,0.04]	[0.00,0.00]	[0.00,0.00]
6	[1.00,1.00]	[-21.10,6.05]	[0.74,0.75]	[0.02,0.02]	[0.00,0.00]	[-10.44,10.89]
7	[0.98,0.99]	[-21.48,9.15]	[0.00,0.00]	[0.00,0.00]	[0.00,0.00]	[0.00,0.00]
8	[1.00,1.00]	[-19.45,13.49]	[1.50,1.50]	[0.21,0.22]	[4.50,4.50]	[-10.65,8.50]
9	[1.00,1.00]	[-22.84,6.29]	[1.20,1.21]	[0.25,0.26]	[0.00,0.00]	[-12.92,14.76]
10	[0.97,0.99]	[-23.06,3.43]	[0.05,0.05]	[0.02,0.02]	[0.00,0.00]	[0.00,0.00]
11	[0.97,0.99]	[-21.40,4.09]	[0.00,0.00]	[0.00,0.00]	[0.00,0.00]	[0.00,0.00]
12	[1.00,1.000]	[-21.09,3.44]	[3.76,3.77]	[0.23,0.24]	[3.10,3.10]	[-9.96,9.89]
13	[0.97,0.99]	[-19.22,2.94]	[0.17,0.18]	[0.02,0.02]	[0.00,0.00]	[0.00,0.00]
14	[0.96,0.98]	[-17.34,2.28]	[0.10,0.10]	[0.05,0.05]	[0.00,0.00]	[0.00,0.00]
15	[0.99,1.00]	[-13.60,1.69]	[0.21,0.22]	[0.05,0.05]	[0.00,0.00]	[0.00,0.00]
16	[1.00,1.01]	[-16.59,1.33]	[0.42,0.43]	[0.02,0.03]	[0.00,0.00]	[0.00,0.00]
17	[1.01,1.03]	[-9.47,0.08]	[0.41,0.42]	[0.08,0.08]	[0.00,0.00]	[0.00,0.00]
18	[0.98,1.00]	[-20.95, −0.03]	[0.27,0.27]	[0.09,0.09]	[0.00,0.00]	[0.00,0.00
19	[0.94,0.98]	[-22.60, −0.47]	[0.03,0.03]	[0.00,0.00]	[0.00,0.00]	[0.00,0.00]
20	[0.93,0.98]	[-22.77, −0.12]	[0.02,0.02]	[0.01,0.01]	[0.00,0.00]	[0.00,0.00]

Table XIV. Load Flow Solution for 57 bus Interval system with variation in load and generator power and in static reactive power (contd.).

Bus	$V(p.u.)$	δ(deg.)	P_D	Q_D	P_G	Q_G
21	[0.98,1.03]	[-21.72,0.95]	[0.00,0.00]	[0.00,0.00]	[0.00,0.00]	[0.00,0.00]
22	[0.98,1.03]	[-21.61,1.10]	[0.00,0.00]	[0.00,0.00]	[0.00,0.00]	[0.00,0.00]
23	[0.98,1.03]	[-21.79,1.14]	[0.06,0.06]	[0.02,0.02]	[0.00,0.00]	[0.00,0.00]
24	[0.96,1.01]	[-23.89,2.42]	[0.00,0.00]	[0.00,0.00]	[0.00,0.00]	[0.00,0.00]
25	[0.90,0.98]	[-29.76,-1.535]	[0.06,0.06]	[0.03,0.03]	[0.00,0.00]	[0.00,0.00]
26	[0.92,0.97]	[-23.83,2.87]	[0.00,0.00]	[0.00,0.00]	[0.00,0.00]	[0.00,0.00]
27	[0.96,0.99]	[-24.38,5.15]	[0.09,0.09]	[0.00,0.00]	[0.00,0.00]	[0.00,0.00]
28	[0.98,1.01]	[-23.99,6.39]	[0.04,0.04]	[0.02,0.02]	[0.00,0.00]	[0.00,0.00]
29	[1.00,1.02]	[-23.64,7.19]	[0.17,0.17]	[0.02,0.02]	[0.00,0.00]	[0.00,0.00]
30	[0.88,0.97]	[-30.51, −2.04]	[0.03,0.03]	[0.010.01]	[0.00,0.00]	[0.00,0.00]
31	[0.85,0.96]	[-31.35, −2.82]	[0.05,0.05]	[0.02,0.02]	[0.00,0.00]	[0.00,0.00]
32	[0.88,0.98]	[-29.90, −2.78]	[0.01,0.01]	[0.00,0.00]	[0.00,0.00]	[0.00,0.00]
33	[0.88,0.98]	[-29.97, −2.79]	[0.03,0.03]	[0.019,0.01]	[0.00,0.00]	[0.00,0.00]
34	[0.92,0.99]	[-23.67,0.44]	[0.00,0.00]	[0.00,0.00]	[0.00,0.00]	[0.00,0.00]
35	[0.93,1.00]	[-23.31,0.53]	[0.05,0.06]	[0.02,0.03]	[0.00,0.00]	[0.00,0.00]
36	[0.94,1.00]	[-22.92,0.63]	[0.00,0.00]	[0.00,0.00]	[0.00,0.00]	[0.00,0.00]
37	[0.95,1.01]	[-22.54,0.71]	[0.00,0.00]	[0.00,0.00]	[0.00,0.00]	[0.00,0.00]
38	[0.99,1.03]	[-21.24,1.05]	[0.14,0.14]	[0.07,0.07]	[0.00,0.00]	[0.00,0.00]
39	[0.95,1.01]	[-22.63,0.71]	[0.00,0.00]	[0.00,0.00]	[0.00,0.00]	[0.00,0.00]
40	[0.94,1.00]	[-23.06,0.60]	[0.00,0.00]	[0.00,0.00]	[0.00,0.00]	[0.00,0.00]
41	[0.98,1.01]	[-25.61,0.86]	[0.06,0.06]	[0.02,0.03]	[0.00,0.00]	[0.00,0.00]
42	[0.94,0.99]	[-26.96, −0.21]	[0.07,0.07]	[0.04,0.04]	[0.00,0.00]	[0.00,0.00]
43	[1.00,1.02]	[-22.66,3.13]	[0.02,0.02]	[0.01,0.01]	[0.00,0.00]	[0.00,0.00]
44	[1.00,1.0388]	[-19.97,0.91]	[0.11,0.12]	[0.01,0.01]	[0.00,0.00]	[0.00,0.00]
45	[1.03,1.05]	[-16.44,1.19]	[0.00,0.00]	[0.00,0.00]	[0.00,0.00]	[0.00,0.00]
46	[1.04,1.07]	[-18.83,1.79]	[0.00,0.00]	[0.00,0.00]	[0.00,0.00]	[0.00,0.00]
47	[1.01,1.05]	[-19.94,1.79]	[0.00,0.00]	[0.29,0.29]	[0.00,0.00]	[0.00,0.00]
48	[1.00,1.04]	[-20.54,1.49]	[0.00,0.00]	[0.00,0.00]	[0.00,0.00]	[0.00,0.00]
49	[1.01,1.05]	[-22.08,0.97]	[0.17,0.18]	[0.08,0.08]	[0.00,0.00]	[0.00,0.00]
50	[1.00,1.04]	[-23.67,1.13]	[0.20,0.21]	[0.10,0.10]	[0.00,0.00]	[0.00,0.00]
51	[1.03,1.06]	[-24.04,2.43]	[0.17,0.18]	[0.05,0.05]	[0.00,0.00]	[0.00,0.00]
52	[0.96,0.99]	[-25.50,6.08]	[0.04,0.04]	[0.02,0.02]	[0.00,0.00]	[0.00,0.00]
53	[0.94,0.98]	[-26.25,5.59]	[0.20,0.20]	[0.10,0.10]	[0.00,0.00]	[0.00,0.00]
54	[0.99,1.01]	[-25.55,5.31]	[0.04,0.04]	[0.01,0.01]	[0.00,0.00]	[0.00,0.00]
55	[1.04,1.05]	[-24.40,5.39]	[0.06,0.06]	[0.03,0.01]	[0.00,0.00]	[0.00,0.00]
56	[0.93,0.99]	[-27.03, −0.70]	[0.07,0.07]	[0.02,0.02]	[0.00,0.00]	[0.00,0.00]
57	[0.92,0.99]	[-27.46, −1.25]	[0.06,0.06]	[0.02,0.02]	[0.00,0.00]	[0.00,0.00]

load flow method encompass all the solutions obtained from conventional load flow simulations thus guaranteeing the results. The solutions obtained by the proposed method provide more information in qualitative terms as the values obtained also include the unknown uncertainties. Conventional load flow solutions give only deterministic values which are approximated results.

Interval methods are often affected by overestimation, hence the computed error bounds become overly pessimistic. Even though (Vaccaro et. al, 2010) have stated that use of interval arithmetic in power flow analysis leads to solutions which are not useful for practical applications, alternative evaluation schemes can be applied to overcome this problem. The dependency problem and the wrapping effect are particular sources of overestimation in interval computations. Dependency problem occurs due to the failure of interval arithmetic to identify the different occurrences of the same variable. For reducing both the dependency problem and the wrapping effect, interval arithmetic has been extended with symbolic computations using Taylor models in (Neher, Jackson and Nedialkov, 2007). The dependency problem can be also eliminated by applying a suitable extension of the Jacobian matrix as discussed in (Kearfott, 1991). Consequently, this technique can be made computationally more robust and reliable, thus yielding better and accurate solutions.

Load flow analysis helps to ensure that cables, transformers, lines are sized properly to carry the variable load. From the results, it can be determined whether the system voltages remain within specified limits and the equipments are not getting overloaded. The profiles of bus voltages and angles help us to identify real and reactive power flows and minimize the transmission losses. Load flow studies become important in planning and expansion while ensuring that each generator runs within the specified limits and demand be met without overloading the power infrastructure. The reactive power bounds provide us an information regarding the injection of reactive power into the system, in order to keep the power factor close to unity.

Also, in the initial stages of planning and design studies of power systems, the proposed technique will be useful to save time, effort, and the resources required. The results obtained by the proposed method take into account the demand error which is very significant, whence, the load uncertainty is not accounted for, the load flow solutions obtained would be a 'snapshot' for a single specific configuration and operating conditions of the power system. If uneven variations in active and reactive powers in different buses are considered then we can arrive at a more realistic solution. The same is being considered as a part of the future work.

New techniques that are computationally robust and reliable are needed for the analysis of power systems with uncertainties, especially in view of the increasing use of renewable power sources, such as wind, hydro and solar power which are highly variable. However, using interval arithmetic computational requirements are greater than the conventional load flow methods.

References

Abdel-Hady, S. and M. Abdel-Aal Hassan. *Modern Optimization Techniques with Applications in Electric Power Systems Energy Systems*. Springer, New York, USA, 2012.

Almeida, K., F. P. Galiana and S. Soures. A general parametric optimal power flow. *IEEE Transactions on Power Syst*, 9:540–547, February, 1994.

Barboza, L. V., G. P. Dimuro and R. H. S. Reiser. Towards interval analysis of the load uncertainty in power electric systems. In, *Proc. 8th Int. Conf. Probabilistic Methods Applied to Power Systems*, September, 2004.

Chen, P., Z. Chen and B. Bak-Jensen. Probabilistic load flow: A review. In, *Proc. of Third Int. Conf. Electric Utility Deregulation and Restructuring and Power Technologies*, 1586-1591, April, 2008.

Dimitrovski, A. and K. Tomsovic. Boundary load flow solutions. *IEEE Transactions on Power Syst*, 19:348–355, Febraury, 2004.

Grainger, J. J. and W. D. Stevenson. *Power System Analysis.* McGraw Hill Edition, New York, 1994.

Hadi S. *Power System Analysis.* Tata McGraw Hill Edition, New Delhi, 2002.

Hansen, E. *Global Optimization using Interval Analysis.* Dekker, New York, 1992.

Kearfott, R. B. Decomposition of arithmetic expressions to improve the behavior of interval iteration for nonlinear systems. *Computing* , 47(2):169-191, June, 1991.

Kothari, D. P. and I. J. Nagrath. *Modern Power System Analysis.* McGraw Hill Edition, New Delhi, 2011.

Moore, R. E. *Interval Analysis.* Prentice-Hall, Englewood Cliffs, New Jersey, 1966.

Moore, R. E., R. Baker and M. J. Cloud. *Introduction to Interval Analysis.* SIAM, Philadelphia, 2008.

Neher, M., K. R. Jackson and N. S. Nedialkov. On Taylor model based integration of ODEs. *SIAM Journal on Numerical Analysis*, 45(1):236262, 2007.

Power System Test Case Archive [Online]. Available: http://www.ee.washington.edu/research/pstca.

Ralhan, S. and S. Ray. Directional Overcurrent Relays Coordination using Linear Programming Intervals: A Comparative Analysis. In, *Proc. of Annual IEEE India Conference (INDICON)*, 1–6, December, 2013.

Rump, S. M. Intlab-interval laboratory developments in reliable computing. *KluwerAcadmic Publishers*, Dordrecht, 1999.

Vaccaro, A., C. A. Canizares and D. Villacci. A Simple and Reliable Algorithm for Computing Boundaries of Power Flow Solutions due to System Uncertainties. In, *Proc. IEEE PowerTech, Bucharest*, 1–6, June, 2009.

Vaccaro, A., C. A. Canizares and D. Villacci. An affine arithmetic-based methodology for reliable power flow analysis in the presence of data uncertainty. *IEEE Transactions on Power Syst.*, 25(2):62463, May, 2010.

Vaccaro, A., C. A. Canizares and K. Bhattacharya. A Range Arithmetic-Based Optimization Model for Power Flow Analysis Under Interval Uncertainty. *IEEE TRANSACTIONS ON POWER SYSTEMS*, 28:1179-1186, May, 2013.

Wang, Z. and F. L. Alvarado. Interval arithmetic in power flow analysis. *IEEE TRANSACTIONS ON POWER SYSTEMS*, 7:1341–1349, August, 1992.

Bayesian Calibration of Lattice Discrete Particle Model for Concrete

Eliška Janouchová[1)], Anna Kučerová[1)], Jan Sýkora[1)], Jan Vorel[2)] and Roman Wendner[2)]
[1)] *Department of Mechanics, Faculty of Civil Engineering, Czech Technical University in Prague, Prague, Czech Republic, {eliska.janouchova,anna.kucerova,jan.sykora.1}@fsv.cvut.cz*
[2)] *Christian Doppler Laboratory LiCRoFast, Institute of Structural Engineering, University of Natural Resources and Life Sciences, Vienna, Austria, {jan.vorel,roman.wendner}@boku.ac.at*

Abstract: In lattice or particle formulations of models for quasi-brittle materials, a medium is discretized "a priori" according to an idealization of its internal structure. Geometrical parameters of particles or lattice equip these type of formulations with inherent characteristic lengths and they have the intrinsic ability of simulating the geometrical features of material internal structure. This allows the accurate simulation of damage initiation and crack propagation at various length scales, however, at increased computational costs. Here we employ the so-called Lattice Discrete Particle Model (LDPM) recently proposed by (Cusatis et al., 2011). LDPM was calibrated, and validated against a large variety of loading conditions in both quasi-static and dynamic loading conditions and it was demonstrated to possess superior predictive capability, see (Cusatis et al., 2011b). Nevertheless, the utilized calibration procedure was based on a hand-fitting, which complicates further practical applications of the model. Here we present a Bayesian inference of model parameters from experimental data obtained from notched three-point-bending tests and cube compression tests. The Bayesian inference allows to solve the inverse problem as well-possed and to quantify posterior uncertainty in parameters by combining a prior knowledge about the realistic parameter values and uncertainty contained in measurement errors. In particular, we obtain the posterior distributions by robust the Markov chain Monte Carlo sampling, where the computational burden, arising from repeated model simulations, is overcome by using a polynomial chaos-based surrogate of the LDPM.

Keywords: lattice discrete particle model, concrete, notched three point bending test, cube compression test, Bayesian inference, Markov chain Monte Carlo, polynomial chaos.

1. Introduction

In order to predict the behaviour of the structural system under the loading in a computational way, the corresponding numerical model has to be properly calibrated. In other words, parameters of the mathematical model of the system have to be estimated as accurately as possible to obtain realistic predictions, e.g. for usage in an appropriate reliability analysis or structural design optimisation. In this paper, the Lattice Discrete Particle Model (LDPM) is employed to accurately describe the macroscopic behaviour of concrete in elastic, fracturing, softening, and hardening regimes (Cusatis et al., 2011b; Cusatis et al., 2011a). To infer the model parameters from indirect experimental measurements one can proceed in two principally different ways. The traditional approach is deter-

ministic, while advances in surrogate modelling and increasing computational capacity of modern computers permitted many researches to focus on parameter identification in probabilistic setting.

The most common method of parameter estimation is based on fitting the response of the numerical model to the experimental data. This deterministic approach leads to optimising parameters so as to minimise the difference between the data and the model response. The optimisation problem is, however, often ill-posed and thus requires the employment of robust optimisation algorithms. The result of such optimisation process is only the single-point estimate of parameter values, as you can see in Figure 1b, thus any information beyond the mean values of parameters is omitted. Consequently, this deterministic inversion method does not provide any quantification of the uncertainty in parameter estimates which in fact exists and is caused by e.g. an insufficient number of observations and measurement errors. This contribution focuses on identification of epistemic (reducible, subjective, cognitive) uncertainty arising from our lack of knowledge (Oberkampf et al., 2002) which is supposed to be reduced by any new measurement according to the coherence of learning (Mantovan and Todini, 2006; Beven et al., 2007).

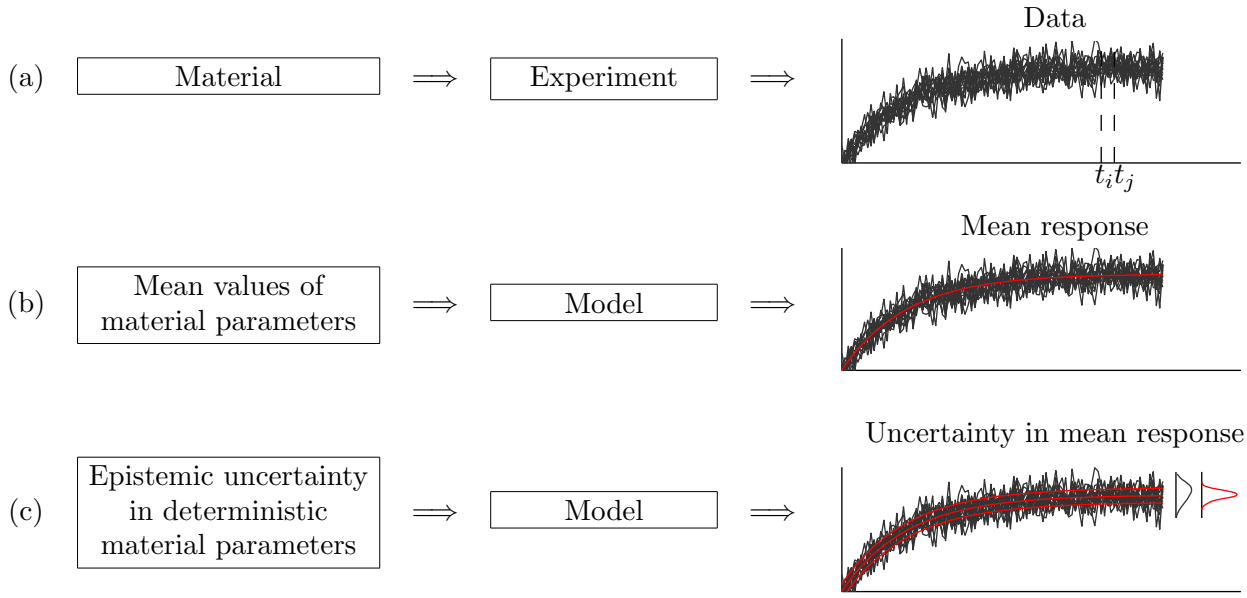

Figure 1. Scheme of an experiment and different approaches to parameter identification.

In the last decades probabilistic methods for stochastic modelling of uncertainties have become applicable thanks to a growing computational capacity of modern computers. The probabilistic approach restates the inverse problem as well-posed in an expanded stochastic space by modelling the parameters as well as the observations as random variables with their probability distributions (Kaipio and Somersalo, 2005). Several methods for the uncertainty quantification in probabilistic settings have been proposed in the literature. The last decade witnessed an intense development in the field of Bayesian updating of epistemic uncertainty (Figure 1c) in description of deterministic material or structural parameters, see e.g. (Marzouk et al., 2007). Here, a likelihood function is

established to quantify our confidence in observed data, with the goal to update our prior knowledge on model parameters (Gelman et al., 2004). The increasing popularity of Bayesian methods is motivated by developments in the field of spectral stochastic finite element method, which allows to alleviate the computational burden by surrogate models such as polynomial chaos expansions (Marzouk and Najm, 2009). The most commonly referred techniques of Bayesian inference in literature are based on the Markov chain Monte Carlo method (Marzouk et al., 2007), the Kalman filter (Rosić et al., 2013) or optimal transport maps (El Moselhy and Marzouk, 2012).

2. Bayesian Inference

Consider a stochastic problem

$$\boldsymbol{z}(\boldsymbol{x},\omega) = \boldsymbol{y}(\boldsymbol{x}) + \varepsilon(\omega), \tag{1}$$

with uncertain model parameters $\boldsymbol{x}$ and random observable data $\boldsymbol{z}$, which can be predicted by a model response $\boldsymbol{y}(\boldsymbol{x})$ besides a measurement error ε. In Bayesian statistics, probability represents a degree of belief about the parameter values (Tarantola, 2005). Combining the initial knowledge in the form of the prior distribution $p(\boldsymbol{x})$ and the experimental data as the likelihood function $p(\boldsymbol{z}|\boldsymbol{x})$ according to Bayes rule

$$p(\boldsymbol{x}|\boldsymbol{z}) = \frac{p(\boldsymbol{z}|\boldsymbol{x})p(\boldsymbol{x})}{p(\boldsymbol{z})} = \frac{p(\boldsymbol{z}|\boldsymbol{x})p(\boldsymbol{x})}{\int_{\boldsymbol{x}} p(\boldsymbol{z}|\boldsymbol{x})p(\boldsymbol{x})\mathrm{d}\boldsymbol{x}}, \tag{2}$$

we obtain the posterior distribution of the parameters. The mean values of the updated distribution are equal to the best guess of the parameters values with the uncertainty represented by the corresponding variance. However the posterior statistical moments cannot be generally computed analytically, because the identified distribution including the whole numerical model is too complicated.

To overcome this obstacle, we use Markov chain Monte Carlo sampling (MCMC) of the posterior distribution, which is a method based on a creation of an ergodic Markov chain of required stationary distribution equal to the posterior (Gilks et al., 2005; Geyer, 2011). There are different algorithms for constructing this chain (Spall, 2003), e.g. Gibbs sampler or Metropolis-Hastings algorithm, which avoids calculating of the normalisation constant in Eq. (2) by evaluating only ratios of target probabilities. Suitable setting of the proposal distribution for a random walk is important and can be evaluated on the basis of acceptance rate (Rosenthal, 2011) or autocorrelation, which is required to be minimal. The convergence speed of the procedure depends also on the appropriate choice of the starting point (Geyer, 2011). The essential advantage of this method is its versatility for usage with nonlinear models, when for an infinite number of samples it gives the exact solution. The disadvantage of this method is its high computational effort resulting from necessity of a high number of model simulations. In order to accelerate this sampling procedure in the identification process, the evaluations of a numerical model can be replaced by evaluations of a computationally efficient model surrogate.

2.1. Polynomial chaos expansion

In this contribution, we employ polynomial chaos expansion (PCE) for the approximation of the model response in the stochastic space (Marzouk et al., 2007), which has the following form:

$$\tilde{\boldsymbol{y}}(\boldsymbol{x}(\boldsymbol{\xi})) = \sum_{\alpha} \boldsymbol{\beta}_{\alpha} \psi_{\alpha}(\boldsymbol{\xi}), \tag{3}$$

where $\boldsymbol{\beta}_{\alpha}$ is a vector of PCE coefficients $\beta_{\alpha,i}$ corresponding to a particular component of the system response y_i. $\psi_{\alpha}(\boldsymbol{\xi})$ are multivariate polynomials. The expansion (Eq. (3)) is usually truncated to the limited number of terms n_{β}, which is very often related to the number of random variables $n_{\boldsymbol{x}}$ and to the maximal degree of polynomials n_{p} according to the relation

$$n_{\beta} = \frac{(n_{\mathrm{p}} + n_{\boldsymbol{x}})!}{n_{\mathrm{p}}! n_{\boldsymbol{x}}!}. \tag{4}$$

PCE can be used to approximate the response with respect to the probability distribution of the random variables $\boldsymbol{\xi}$. The convergence of the approximation error with the increasing number of polynomial terms is optimal in case of orthogonal polynomials of a special type corresponding to the probability distribution of the underlying variables (Xiu and Karniadakis, 2002). In particular, we employ Legendre polynomials associated with the uniform distribution.

The efficiency of this technique depends on computational requirements of the PCE construction and its consequent accuracy. In this contribution, the PCE coefficients are computed with help of linear regression (Blatman and Sudret, 2010a), which is based on a set of model simulations. The samples are drawn according to a stratified procedure called design of experiments (DoE), in particular well-known Latin hypercube sampling (LHS), which is able to respect the prescribed probability distributions (Janouchová and Kučerová, 2013).

2.2. Sensitivity analysis

Global sensitivity analysis (SA) is an important tool for investigating properties of complex systems. It is a valuable part of solution of an inverse problem such as a parameter identification, where the aim of SA can be estimating the influence of the identified parameters to the model response. SA provides some information about the relationship between the system outputs/model response and the system inputs/model parameters on their whole domain. Several approaches to SA have been developed, see e.g. (Saltelli et al., 2000) for an extensive review. The presented contribution is focused on Sobol sensitivity indices expressing an influence of chosen parameters on the response variance. Sobol indices can be analytically computed from the PCE coefficients (Blatman and Sudret, 2010b) according to the following relation

$$S^{\mathrm{PCE}}_{i_1,\ldots,i_s} = \frac{\sum_{\alpha \in \mathcal{I}_{i_1,\ldots,i_s}} \beta_{\alpha}^2 \mathbb{E}[\psi_{\alpha}^2(\boldsymbol{\xi})]}{\sum_{\alpha=1}^{n_{\beta}} \beta_{\alpha}^2 \mathbb{E}[\psi_{\alpha}^2(\boldsymbol{\xi})]}, \tag{5}$$

where $\mathbb{E}[\psi_{\alpha}^2(\boldsymbol{\xi})]$ is computed specifically for Legendre polynomials as

$$\mathbb{E}[\psi_{\alpha}^2(\boldsymbol{\xi})] = \int \psi_{\alpha}^2(\boldsymbol{\xi}) \mathrm{d}\mathbb{P}\psi(\boldsymbol{\xi}) = \int \cdots \int_{n_{\xi}} \prod_{j=1}^{n_{\xi}} (\psi_{\alpha,j}^2(\xi_j)) \mathrm{d}\mathbb{P}\psi(\xi_1) \cdots \mathrm{d}\mathbb{P}\psi(\xi_{n_{\xi}}) = \prod_{j=1}^{n_{\xi}} \frac{2}{2\alpha_{\xi_j} + 1}, \tag{6}$$

where α_{ξ_j} is a degree of ξ_j in a polynomial term ψ_α. $\mathcal{I}_{i_1,...,i_s}$ defines the polynomial terms depending only on $(\xi_{i_1}, ..., \xi_{i_s})$, i.e.

$$\mathcal{I}_{i_1,...,i_s} = \{\alpha_k = 0 \Longleftrightarrow k \notin (i_1, \ldots, i_s), \forall k = 1, \ldots, n_\xi\}. \tag{7}$$

3. Calibrated Material Model

In this section, the examined material model, used for the calibration, is briefly described. The material model, often employed to simulate quasi-brittle materials, is chosen to demonstrate the capability of aforementioned approach. This model is based on lattice or particle formulations in which materials are discretized "a priori" according to an idealization of their internal structure. Particle size and size of the contact area among particles, for particle models, as well as lattice spacing and cross sectional area, for lattice models, equip these type of formulations with inherent characteristic lengths and they have the intrinsic ability of simulating the geometrical features of material internal structure. This allows the accurate simulation of damage initiation and crack propagation at various length scales at the cost, however, of increased computational costs.

Earlier attempts to formulate particle and lattice models for fracture are reported in (Cusatis et al., 2003; Cusatis et al., 2006; Cusatis, 2011; Bažant et al., 1990; Yip et al., 2006) while the most recent developments were published in a Cement Concrete Composites special issue (Cusatis and Nakamura, 2011). A comprehensive discrete formulation for concrete was recently proposed by Cusatis and coworkers (Cusatis et al., 2011b; Cusatis et al., 2011a) who formulated the so-called Lattice Discrete Particle Model (LDPM). LDPM was calibrated, and validated against a large variety of loading conditions in both quasi-static and dynamic loading conditions and it was demonstrated to possess superior predictive capability.

In the present study the basic material properties of the tested concrete mix are kept constant for all simulations. Note that these parameters influence the generation of concrete meso-structure, see Table I. However, the seed number, governing the sampling of cumulative distribution func-

Table I. Values of parameters governing the generation of concrete meso-structure.

material property		unit	value
minimum particle size	d_0	mm	4
maximum particle size	d_a	mm	16
cement content	c	kg/m^3	240
water to cement ratio	w/c	-	0.83
aggregate to cement	a/c	-	8.83
Fuller coefficient	n_F	-	0.5
concrete density	ρ	kg/m^3	2400

tion of concrete granulometric distributions by a random number generator, is kept random. The distribution of particles influences the material response and is assumed to act as a noise in the response.

The parameters of the mathematical model which are kept constant or calibrated by the procedure described above are summarised in Table II.

Table II. Values of material model parameters used in the numerical simulations.

material property		unit	value (range)
normal modulus	E_0	MPa	$20000 - 70000$
shear-normal coupling	α	-	$0.2 - 0.3$
tensile strength	σ_t	MPa	$1.5 - 5$
tensile characteristic length	l_t	mm	$50 - 300$
softening exponent	n_t	-	$0.1 - 1$
shear/strength ratio	σ_s/σ_t	-	$1.5 - 8$
initial friction	μ_0	-	$0.001 - 0.5$
compressive strength	σ_{c0}	MPa	$\sigma_{c0} = 40\sigma_t$
transitional stress	σ_{N0}	MPa	$\sigma_{N0} = 240\sigma_t$
initial hardening modulus ratio	$H_{c0}/E0$	-	0.4
transitional strain ratio	κ_{c0}	-	4
deviatoric strain threshold ratio	κ_{c1}	-	1.0
deviatoric damage parameter	κ_{c2}	-	5.0
asymptotic friction	μ_∞	-	0.0
densification ratio	E_d/E_0	-	1.0
volumetric-deviatoric coupling	β	-	0

4. Results

The identification of the seven material model parameters for concrete is based on two types of experiments, specifically a uniaxial compression test and a notched three-point-bending test. The first experiment was repeated three times while the second one four times. For convenience and readability, data are presented in terms of nominal stress $_N$ and nominal strain ε_N. The most traditional tests to characterise concrete is the compression test performed on cubes of 150 mm side length. The nominal values are defined as

$$\sigma_N = \frac{F}{a^2} \quad \text{and} \quad \varepsilon_N = \frac{u}{a} \tag{8}$$

where F is the applied load, u denotes the load point displacement and a is the side length. The fracture properties of concrete are characterised by means of the notched three-point-bending test. The nominal stress and strain are

$$\sigma_N = \frac{3Fl}{dh^2} \quad \text{and} \quad \varepsilon_N = \frac{CMOD}{h} \tag{9}$$

where l stands for the beam span, h, d are the beam height and width, respectively. $CMOD$ is the crack mouth opening displacement measured over the notch.

Moreover, to eliminate the error in measurement caused by the testing machine stiffness, the inelastic part of the strain is used for the model calibration

$$\varepsilon_N^{\text{inel}} = \varepsilon_N - \sigma_N \left(1/K\right) \tag{10}$$

where K is the corresponding elastic stiffness. To capture the elastic properties of the model, the initial elastic part of the cube compression test is utilised.

The updated joint probability distribution of the parameters is formulated according to Bayes' formula as a product of prescribed uniform prior distribution with bounds given in Table III and likelihood function arising from the experimental errors, which are supposed to be normally distributed with zero mean values and standard deviations derived from the experimental data. Specifically, in the identification process we consider from the compression test the measured stress σ_N discretized into 250 strain steps with the error $\varepsilon \sim N(0, 8^2)$ and elastic stiffness K with error $\varepsilon \sim N(0, 2880^2)$, from the notched three-point-bending test the measured stress σ_N discretized into 250 strain steps with the error $\varepsilon \sim N(0, 2^2)$.

Table III. Prior bounds and identified statistical moments of parameters' distribution.

	E_0 [MPa]	α [-]	σ_t [MPa]	l_t [mm]	n_t [-]	σ_s/σ_t [-]	μ_0 [-]
			Prior				
MIN	20000	0.200	1.500	50.0	0.100	1.500	0.001
MAX	70000	0.300	5.000	300.0	1.000	8.000	0.500
			Identification				
MEAN	31183	0.297	2.236	166.6	0.910	3.192	0.063
STD	1998	0.003	0.193	17.8	0.037	0.338	0.051

The corresponding posterior distribution of the model parameters is obtained by MCMC sampling. Because the full numerical model simulation is computationally intensive (approx. 4 hours for the compression test and 10 hours for the bending test), the surrogate model has to be used. In this case of the stochastic model, the approximation can also serve for a purpose of eliminating the noise of the material model response caused by the random distribution of particles. We employ PCE in a form of Legendre polynomials of the third degree constructed by linear regression based on 200 simulations of the full model for prior parameter samples. Thanks to this approximation we obtain

500, 000 posterior samples in only few hours. The identified mean values of the parameters together with the corresponding epistemic uncertainties expressed by the posterior standard deviations are given in Table III. The updated univariate and bivariate marginal probability distributions are shown in Figure 2.

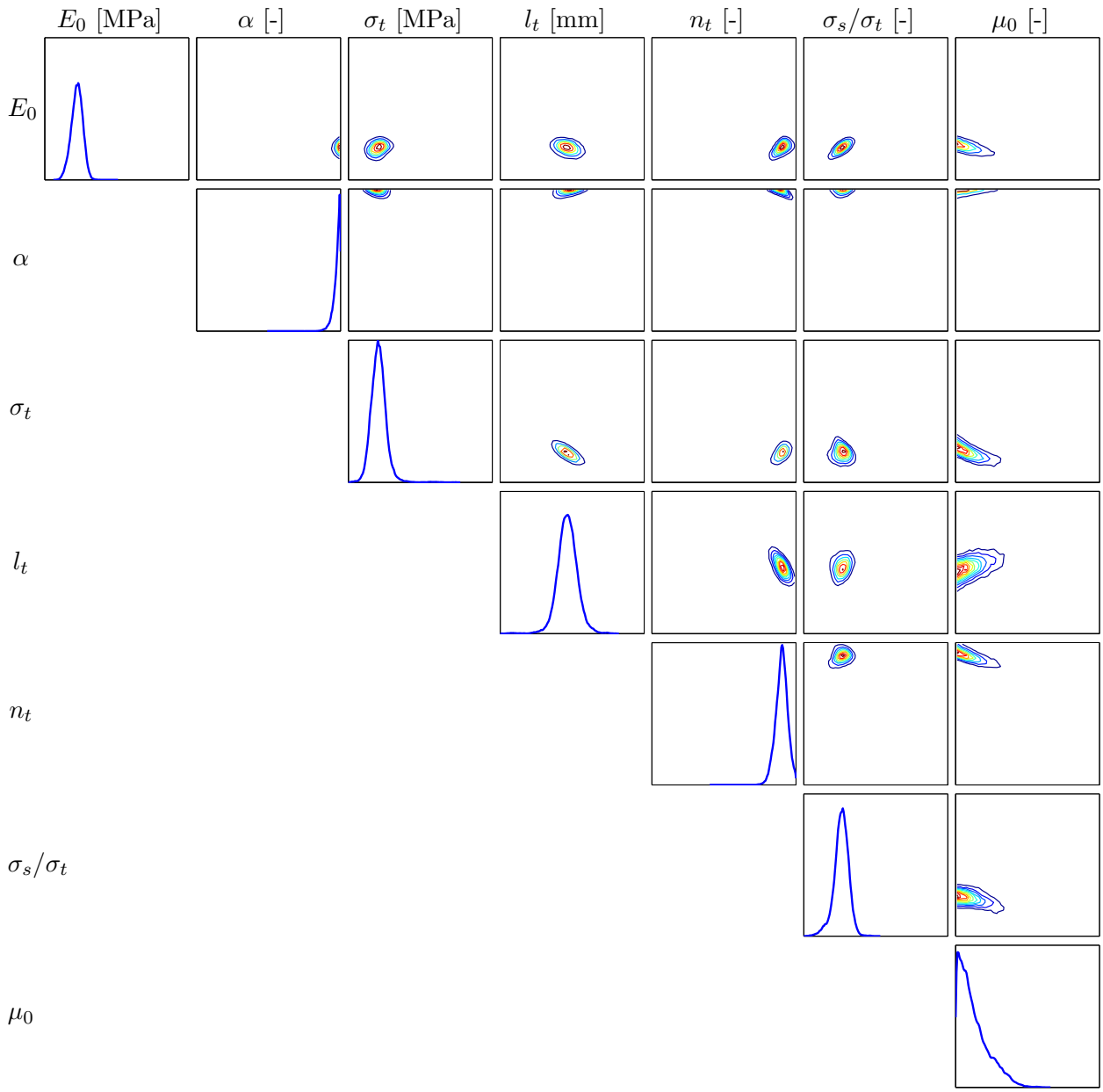

Figure 2. Identified 1D and 2D marginal pdfs of model parameters.

In order to validate the accuracy of the identification process, we compare the experimental data with the model response corresponding to the identified mean values of the model parameters which is shown in Figures 3 and 4. There are plotted five full stochastic model simulations and also the PCE-based response. As one can see, the PCE-based response fits the experimental data very well in the both experimental tests while the full numerical model response differs slightly in the case of the three-point-bending test and more significantly in the case of uniaxial compression test. It means that the used model approximation is not accurate enough. One reason can be a low degree of the polynomials or the training samples are not chosen properly. In Figures 3 and 4, there are also plotted the full numerical model simulations used for the approximation training. From these graphs the training curves seem to be appropriate because the experimental data do not lie outside the covered region.

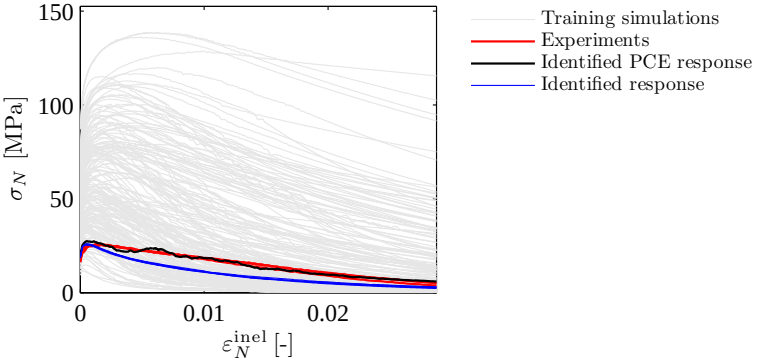

Figure 3. Comparison of experimental data and model response corresponding to the identified parameters for the uniaxial compression test.

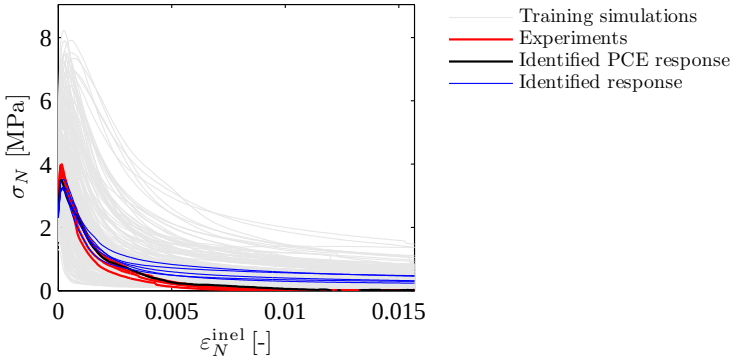

Figure 4. Comparison of experimental data and model response corresponding to the identified parameters for the notched three-point-bending test.

While the increasing part of the stress-strain diagrams is fitted satisfactorily, the approximation error is mainly related to their decreasing part. The problem can be explained with help of Figure 5 which shows a scatter diagram with maximal nominal stress σ_N on the vertical axis and area

below the considered stress-strain curve $A = \int \sigma \mathrm{d}\varepsilon$ on the horizontal axis. From this point of view, the experimental data lie outside the training simulations and the model approximation is forced to extrapolate.

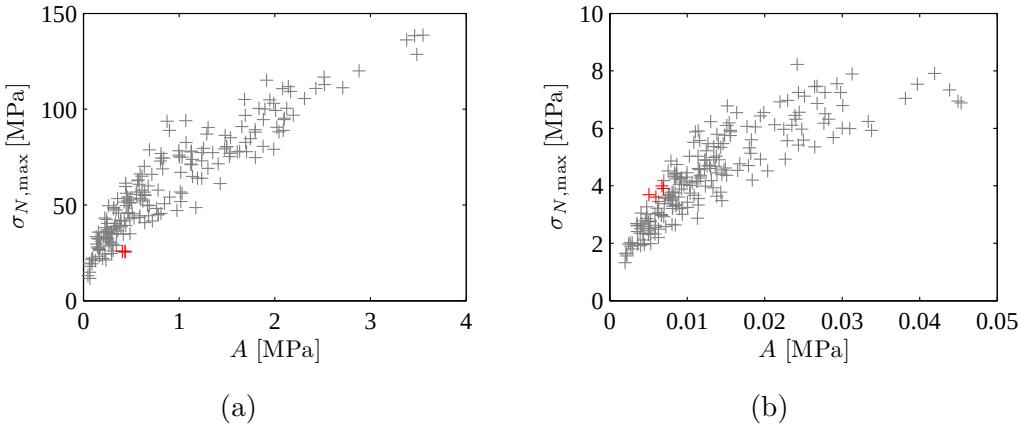

Figure 5. Comparison of integrals of training and experimental curves for uniaxial compression test (a) and three-point-bending test (b).

The unsuccessful calibration of the full model is apparently caused by the inappropriate prior parameters' distribution. The results of sensitivity analysis shown in Figure 6 can help us to estimate the model parameters, which are already identified well and which the decreasing part of the stress-strain curves is sensitive to so they probably cause the problematic approximation error.

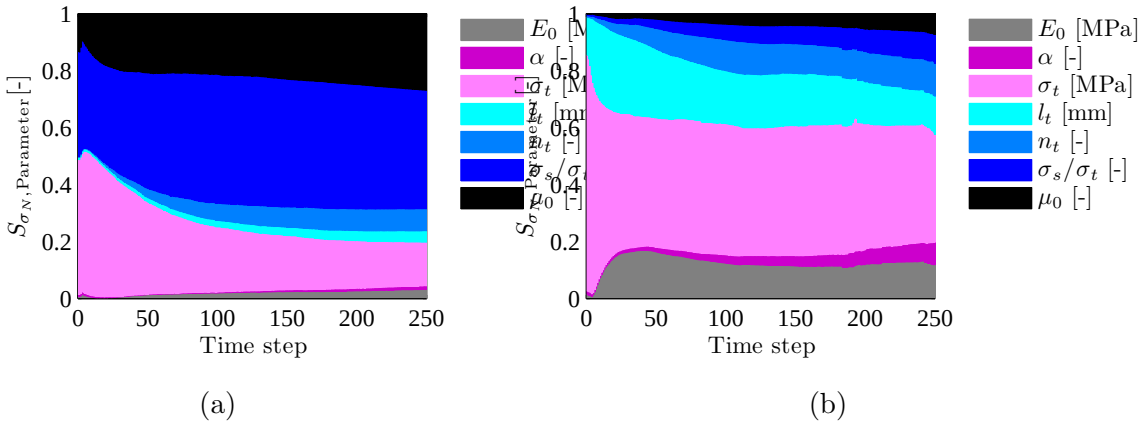

Figure 6. Sensitivity analysis for uniaxial compression test (a) and three-point-bending test (b) based on Sobol indices computed from PCE approximation.

We estimate that tensile strength σ_t and shear/strength ratio σ_s/σ_t can be identified well while softening exponent n_t, shear-normal coupling α and initial friction μ_0 can be the problematic parameters. The posterior mean values of the latter two are also very near to the upper bound of the prior uniform distribution which supports our assumption. Unfortunately, to this day we do not

have the necessary additional simulations to confirm this and provide an appropriate calibration of the examined material model.

5. Conclusions

The employed identification procedure is an efficient tool for calibration of nonlinear models allowing to take into account epistemic uncertainties caused by e.g. experimental errors or a small number of experimental data. Usage of PCE-based model approximation enables to handle the computational requirements of Markov chain Monte Carlo sampling of the posterior distribution. In this contribution, the calibration of the lattice discrete particle model for concrete does not succeed properly because of the inappropriate choice of prior range of the parameters values, which leads to the inaccurate approximation of the model response. In other words, the obtained parameters' distribution is correct with respect to the PCE-based model approximation, which however significantly differs from the full numerical model. This inaccuracy can be overcome by prescribing a new prior ranges for the evaluated parameters to obtain the necessary information for constructing the accurate model approximation.

Acknowledgements

The financial support of the Czech Science Foundation (Project No. 16-11473Y), the Grant Agency of the Czech Technical University in Prague (Project No. SGS16/037/OHK1/1T/11), the Austrian Federal Ministry of Economy, Family and Youth and the National Foundation for Research, Technology and Development is gratefully acknowledged.

References

Bažant, Z. P., M. R. Tabbara, M. T. Kazemi and G. Pijaudier-Cabot. Random particle model for fracture of aggregate or fiber composites Journal of Engineering Mechanics, 116:1686–1705, 1990.

Beven, K., P. Smith and J. Freer. Comment on "Hydrological forecasting uncertainty assessment: Incoherence of the GLUE methodology" by Pietro Mantovan and Ezio Todini. *Journal of Hydrology*, 338:315-318, 2007.

Blatman, G. and B. Sudret. An adaptive algorithm to build up sparse polynomial chaos expansions for stochastic finite element analysis. *Probabilistic Engineering Mechanics*, 25(2):183–197, 2010.

Blatman, G. and B. Sudret. Efficient computation of global sensitivity indices using sparse polynomial chaos expansions. *Reliability Engineering and System Safety*, 95:1216–1229, 2010.

Cusatis, G., D. Pelessone and A. Mencarelli. Lattice Discrete Particle Model (LDPM) for failure behavior of concrete. I: Theory. *Cement and Concrete Composites*, 33(9):881–890, 2011.

Cusatis, G., A. Mencarelli, D. Pelessone and J. Baylot. Lattice Discrete Particle Model (LDPM) for failure behavior of concrete. II: Calibration and validation. *Cement and Concrete Composites*, 33(9):891–905, 2011.

Cusatis, G., Z. P. Bažant and L. Cedolin. Confinement-shear lattice model for concrete damage in tension and compression: I. Theory Journal of Engineering Mechanics, 129:1439, 2003.

Cusatis, G., Z. P. Bažant and L. Cedolin. Confinement-shear lattice CSL model for fracture propagation in concrete Computer Methods in Applied Mechanics and Engineering, 195(52):7154–7171, 2006.

Cusatis, G. Strain-rate effects on concrete behavior International Journal of Impact Engineering, 38(4):162–170, 2011.

Cusatis, G. and H. Nakamura. Discrete modeling of concrete materials and structures Cement and Concrete Composites, 33(9):865–866, 2011.

Cusatis, G. and D. Pelessone and A. Mencarelli. Lattice Discrete Particle Model (LDPM) for failure behavior of concrete. I: Theory Cement and Concrete Composites, 33(9):881–890, 2011.

Cusatis, G. and A. Mencarelli and D. Pelessone and J. Baylot. Lattice Discrete Particle Model (LDPM) for failure behavior of concrete. II: Calibration and validation, Cement and Concrete Composites, 33(9):891–905, 2011.

El Moselhy, T. A. and Y. M. Marzouk. Bayesian inference with optimal maps. *Journal of Computational Physics*, 231(23):7815–7850, 2012.

Frank Xu, X. A multiscale stochastic finite element method on elliptic problems involving uncertainties. *Computer Methods in Applied Mechanics and Engineering*, 196:2723–2736, 2007.

Gelman, A., J. B. Carlin, H. S. Stern and D. B. Rubin. *Bayesian data analysis*. Chapman & Hall/CRC, 2004.

Geyer, C. J. *Handbook of Markov Chain Monte Carlo*. Chapman & Hall/CRC, 2011.

Gilks, W. R., S. M. Deland, B. M. Rutherford, K. V. Diegert and K. F. Alvin. Markov Chain Monte Carlo. In *Encyclopedia of Biostatistics*, Chichester, UK: John Wiley, 75(3):333–357, 2005.

Janouchová, E. and A. Kučerová. Competitive Comparison of Optimal Designs of Experiments for Sampling-based Sensitivity Analysis. *Computers & Structures*, 124:47–60, 2013.

Kaipio J. and E. Somersalo. *Statistical and Computational Inverse Problems*. New York: Springer-Verlag, 2005. 339 p. Applied mathematical sciences. ISBN 03-872-2073-9.

Mantovan P. and E. Todini. Hydrological forecasting uncertainty assessment: Incoherence of the GLUE methodology. *Journal of Hydrology*, 330:368-381, 2006.

Marzouk,Y. M., H. N. Najm and L. A. Rahn. Stochastic spectral methods for efficient Bayesian solution of inverse problems. *Journal of Computational Physics* 224:560-586, 2007.

Marzouk, Y. M. and H. N. Najm. Dimensionality reduction and polynomial chaos acceleration of Bayesian inference in inverse problems. *Journal of Computational Physics*, 228:1862-1902, 2009.

Oberkampf, W. L. et al. Error and uncertainty in modeling and simulation. *Reliability Engineering and System Safety*, 75:333-357, 2002.

Rosenthal, J. S. Optimal Proposal Distributions and Adaptive MCMC. In *Handbook of Markov Chain Monte Carlo*, Chapman & Hall/CRC, 93–140, 2011.

Rosić, B. V. et al. Parameter Identification in a Probabilistic Setting. *Engineering Structures*, 50:179-196, 2013.

Saltelli, A., K. Chan and E. M. Scott. *Sensitivity analysis*. NY:Wiley, 2000.

Spall, J. C. Estimation via Markov Chain Monte Carlo. *IEEE Control Systems Magazine*, 23(2):34–45, 2003.

Tarantola, A. *Inverse problem theory and methods for model parameter estimation*. Philadelphia, PA: Society for Industrial and Applied Mathematics, 348 p., 2005.

Xiu, D. and G. E. Karniadakis. The Wiener–Askey Polynomial Chaos for Stochastic Differential Equations. *SIAM Journal on Scientific Computing*, 24(2):619–644, 2002.

Yip, M., Z. Li, B. Liao and J. E. Bolander. Irregular lattice models of fracture of multiphase particulate materials International journal of fracture, 140(1):113–124, 2006.

Acceleration of Robust Experiment Design using Sobol Indices and Polynomial Chaos Expansion

Anna Kučerová[1)], Jan Sýkora[1)], Eliška Janouchová[1)], Daniela Jarušková[2)] and Jan Chleboun[2)]

[1)] *Department of Mechanics, Faculty of Civil Engineering, Czech Technical University in Prague, 16629 Prague, Czech Republic, {eliska.janouchova,anna.kucerova,jan.sykora.1}@fsv.cvut.cz*

[2)] *Department of Mathematics, Faculty of Civil Engineering, Czech Technical University in Prague, 16629 Prague, Czech Republic, {daniela.jaruskova,jan.chleboun}@cvut.cz*

Abstract: In practice, laboratory experiments are still mostly designed by trial and error method using the expert knowledge of the material model to be calibrated. This is, however, a difficult task in the case of advanced models developed to simulate engineering problems by non-linear finite element techniques. Ruffio et al. (2012) proposed method for optimisation of model-based design of experiments using robust evolutionary algorithms. Such a method, however suffers from the high computational demands, which make their application to non-linear finite element (FE) simulations difficult. In this contribution we present a novel method introducing surrogate of FE model based on polynomial chaos expansion (PCE) and global formulation of sensitivity matrices. PCE-based surrogates bring two principal advantages. First, they allow to overcome the computational burden of many times repeated FE simulations within the process of experiment design optimisation. Second, they allow fast analytical evaluation of Sobol indices or response variances, which can be used for quantification of global sensitivity of measured quantities to identified parameters. The advantages and drawbacks of the proposed method are demonstrated on a simple problem of two-dimensional nonstationary linear heat transfer. The goal of the experiment design is to find optimal positions of three thermocouples so as to identify the volumetric thermal capacity and the conductivities in the two principal directions while considering uncertainties in the prescribed loading conditions, positions of thermocouples and measurements errors.

Keywords: robust experiment design, global sensitivity, Sobol indices, polynomial chaos, evolutionary optimisation

1. Introduction

The last decade has witnessed growing interest in the development of models that can describe materials response more realistically. This has inspired many new ideas in phenomenological model building, in which the subscale phenomena are accounted for by internal parameters. However, up to the present time, the majority of such advanced models is of a limited practical use, because they are difficult to calibrate by conventional experiments. An experiment design is often done by the trial and error method using the expert, often heuristic, knowledge on the calibrated model.

Such efforts result in a series of single-purpose tests and manual or optimisation-based fitting of measured data. In the case of complex phenomenological models, however, such an approach is often not feasible or results in excessive financial and time costs due to a high number of experiments. Thus, the model complexity brings the need for the design of new experimental procedures. Such problem goes far beyond traditional curve-fitting procedures, as the key issue is to ensure that all model parameters are correctly calibrated by activating all relevant phenomena during the experiment. In addition, the procedure must be robust with respect to inevitable experimental inaccuracies.

The topic of optimal experiment design was mostly addressed by researchers from the field of chemical engineering (Franceschini and Macchietto, 2008; Telen et al., 2012) or theoretical biology (Lindner and Hitzmann, 2006; Van Derlinden et al., 2010). The developed methods, however, suffer from two principal shortcomings:

- they aim at experiments designed for calibration of models with linear relation between the parameters and response and
- they consider inevitable errors on experimental observations, but completely neglect possible errors in parameters of the experiment arising due to its imperfect realisation.

These reasons significantly limit the use of the methods to the case of complex nonlinear material models calibrated from imprecise experiments. Therefore, our goal is to extend the existing methods towards non-linear models under consideration of all the inevitable sources of errors.

To facilitate the following discussion, we introduce a scheme of an experiment suitable for material model calibration in Figure 1. Such an experiment deals with three types of variables: (i)

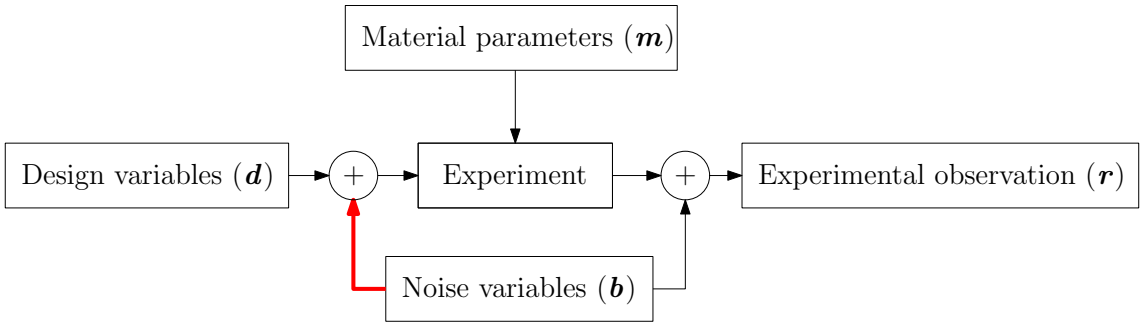

Figure 1. Experimental design problem.

material properties ($\boldsymbol{m}$) to be identified, e.g. thermal conductivity, heat capacity or water vapour resistance, (ii) design variables ($\boldsymbol{d}$) include loading types (e.g. prescribed temperature, moisture flux or heat transfer on boundary) and loading magnitude as well as positions of sensors (thermometers, hygrometers etc.) and (iii) noise ($\boldsymbol{b}$). As emphasized by red arrow, the noise variables must affect not only the experiment output characterizing measurement errors, but also the design variables so as to represent the imperfect realisation of the experiment (imprecise positioning of sensors or imperfections in prescribed loading conditions). The design variables are the only variables controlled by the experiment designer.

The goal of such a process is to find the experiment configuration defined by design variables $\boldsymbol{d}$, which (i) activates all the phenomena described by the investigated material model (i.e. is maximally sensitive to all model parameters $\boldsymbol{m}$) and (ii) reflects the technological aspects, limitations and inherent experimental errors $\boldsymbol{b}$. Hence, we speak about *model-based experiment design*, which needs to be (i) **optimal** in terms of the maximum information content on investigated parameters and (ii) **robust** to be minimally influenced by experimental errors. Both criteria – optimality and robustness – may be expressed by sensitivities of experimental observations $\boldsymbol{r}$ to given material properties and noise variables, respectively, leading to the following definition of the optimisation process:

$$\max_{\boldsymbol{d}} \ \mathbf{S}_{\boldsymbol{r},\boldsymbol{m}} \,, \tag{1}$$

$$\min_{\boldsymbol{d}} \ \mathbf{S}_{\boldsymbol{r},\boldsymbol{b}} \,, \tag{2}$$

$$\text{s.t.} \quad \boldsymbol{m} \in \mathscr{M}, \boldsymbol{b} \in \mathscr{B}, \boldsymbol{d} \in \mathscr{D} \,, \tag{3}$$

where $\mathbf{S}_{\boldsymbol{r},\boldsymbol{m}}$ and $\mathbf{S}_{\boldsymbol{r},\boldsymbol{b}}$ stand for a sensitivity measures of observations $\boldsymbol{r}$ to material properties $\boldsymbol{m}$ and noise variables $\boldsymbol{b}$, respectively. $\mathscr{M}$ is a feasible domain of material parameters typically defined by an expert on the investigated material model in terms of feasible intervals. The feasible domains of design variables $\mathscr{D}$ and noise variables $\mathscr{B}$ are supposed to be given by an expert in experimentation commonly in the form of feasible intervals for design variables and mean and variance of noise variables.

All methods reviewed in (Franceschini and Macchietto, 2008) or in many more recent articles (e.g. (Hametner et al., 2013)) completely omit the imperfections in experimental configuration and compute the sensitivities $\mathbf{S}_{\boldsymbol{r},\boldsymbol{m}}$ as local derivatives. The sensitivities are then organised into the information matrix quantifying the information content of the experiment and measurement errors enter into the information matrix simply as a scaling factors of the computed sensitivities $\mathbf{S}_{\boldsymbol{r},\boldsymbol{m}}$. Different optimality criteria are then proposed as a scalar measure of the information matrix used as an objective function for the experiment design optimisation process.

The authors in (Ruffio et al., 2012) employ the method for robust experiment design considering the uncertainties related to design variables or other known parameters of the experiment. The uncertainties are included in the modified Fisher information matrix and a new optimality criterion is proposed to quantify the information content of the experiment.

The remaining important drawback of all the presented methods consists in computing local derivatives-based sensitivities. In case of nonlinear relation between observations $\boldsymbol{r}$ and investigated parameters $\boldsymbol{m}$, the local sensitivity can be evaluated only for a given values of parameters $\boldsymbol{m}$ and thus their values can be estimated only approximately. One often employed solution is the so-called worst case or maximin approach computing the sensitivities in a set of points and optimising the experimental design so as to maximise the minimal obtained sensitivity (Asprey and Macchietto, 2002; Ruffio et al., 2012). Such a sensitivity estimate is rough, but can be quickly evaluated in case of analytically derived sensitivities. However, if a numerical computation of derivatives is inevitable, such evaluation of sensitivities becomes computationally prohibitive especially during an optimisation process requiring large number of iterations.

This limitation can be overcome by two novelties proposed in this paper. The first one consist in employment of global sensitivities quantifying the sensitivity over the whole prescribed domain of all the involved parameters. In particular, for a given set of controlled design variables $\boldsymbol{d}$, the sensitivity

is evaluated over the domains $\mathscr{B}$ and $\mathscr{M}$ defined as probability distributions (typically normal and uniform) of the respective noise and material parameters. There are different criteria measuring the global sensitivity, mostly based on the computationally expensive sampling procedure, see e.g. (Helton et al., 2006) for a thorough review. Certain time savings may be achieved by optimised sampling as presented by our team members in (Janouchová and Kučerová, 2013), but the predictions in case of high dimensional domains will be still too costly. To overcome this obstacle, the second novelty of our approach concerns the introduction of computationally cheap surrogate models, commonly used in the field of robust design optimisation of structures (Beyer and Sendhoff, 2007; Jurecka, 2007) to replace time consuming structural simulations within the optimisation process. Here we focus on polynomial chaos-based surrogates, which allow for fast analytical evaluation of Sobol indices without the need for exhaustive sampling (Blatman and Sudret, 2010). The global sensitivity measures thus come as the by-product of surrogate construction.

In this paper we follow the work of Ruffio et al. (2012) and compare our proposed global sensitivity-based strategy with their robust worst case scenario-based approach using local sensitivities. We also elaborate the same numerical example of two-dimensional nonstationary linear heat transfer. In this example, the goal of the experiment design is to find optimal positions of three thermocouples so as to identify the volumetric thermal capacity and the conductivities in the two principal directions while considering uncertainties in the prescribed loading conditions, positions of thermocouples and measurements errors.

2. Inverse Problem - Nonlinear Regression with Random Parameters

We consider a nonlinear model of an experiment resulting in multiple observations $\boldsymbol{f}(\boldsymbol{d}, \boldsymbol{b}_d, \boldsymbol{m}) = (\dots, f_i(\boldsymbol{d}, \boldsymbol{b}_d, \boldsymbol{m}), \dots)^{\mathrm{T}}$. Here $\boldsymbol{b}_d$ denotes a vector of random parameters with prescribed probability distribution quantifying our uncertainty related to experimental setting (e.g. imperfections in values of boundary conditions or loading, imperfections in sensors positioning etc.). Moreover, the experimental observations $\boldsymbol{r}(\boldsymbol{d})$ are also contaminated by measurement errors $\boldsymbol{b}_r$ and thus we write:

$$\boldsymbol{r}(\boldsymbol{d}) = \boldsymbol{f}(\boldsymbol{d}, \boldsymbol{b}_d, \boldsymbol{m}) + \boldsymbol{b}_r \,. \tag{4}$$

We suppose that the true value of material parameters $\boldsymbol{m}$ to be identified is $\boldsymbol{m}^* \in \mathscr{M}$, where $\mathscr{M}$ is some given feasible domain of material properties. The estimate $\widehat{\boldsymbol{m}}$ is generally defined as a least square solution given as

$$\widehat{\boldsymbol{m}} = \underset{\boldsymbol{m} \in \mathscr{M}}{\operatorname{argmin}} \sum_i \left(r_i - f_i(\boldsymbol{d}, \boldsymbol{b}_d, \boldsymbol{m})\right)^2 \,, \tag{5}$$

which is however nontrivial to obtain when the model $\boldsymbol{f}(\boldsymbol{d}, \boldsymbol{b}_d, \boldsymbol{m})$ is a nonlinear function of $\boldsymbol{m}$ and some robust optimisation algorithm will be necessary. Moreover, uncertainty in parameters $\boldsymbol{b}_d$ resulting in uncertainty in the obtained estimate $\widehat{\boldsymbol{m}}$ is also difficult to obtain due to the nonlinearity of the model w.r.t. random parameters $\boldsymbol{b}_d$ and generally will require some Monte Carlo-based sampling procedure.

Here we consider an approximate solution of the inverse problem based on the first order Taylor development of the model $\boldsymbol{f}(\boldsymbol{d}, \boldsymbol{b}_d, \boldsymbol{m})$ around the solution $(\widehat{\boldsymbol{m}}, \overline{\boldsymbol{b}_d})$ given as

$$\boldsymbol{f}_{\overline{\boldsymbol{b}_d}, \widehat{\boldsymbol{m}}}(\boldsymbol{d}, \boldsymbol{b}_d, \boldsymbol{m}) = \boldsymbol{f}(\boldsymbol{d}, \overline{\boldsymbol{b}_d}, \widehat{\boldsymbol{m}}) + \mathbf{S}_{\boldsymbol{b}_d}(\boldsymbol{b}_d - \overline{\boldsymbol{b}_d}) + \mathbf{S}_{\boldsymbol{m}}(\boldsymbol{m} - \widehat{\boldsymbol{m}}) \,, \tag{6}$$

where

$$\mathbf{S}_{\boldsymbol{b}_d} = \mathbf{S}_{\boldsymbol{b}_d}(\boldsymbol{d}, \overline{\boldsymbol{b}_d}, \widehat{\boldsymbol{m}}) = \begin{bmatrix} \frac{\partial f_1(\cdot)}{\partial b_{d,1}} & \frac{\partial f_1(\cdot)}{\partial b_{d,2}} & \cdots \\ \frac{\partial f_2(\cdot)}{\partial b_{d,1}} & \frac{\partial f_2(\cdot)}{\partial b_{d,2}} & \cdots \\ \vdots & \vdots & \ddots \end{bmatrix} \quad \text{and} \quad \mathbf{S}_{\boldsymbol{m}} = \mathbf{S}_{\boldsymbol{m}}(\boldsymbol{d}, \overline{\boldsymbol{b}_d}, \widehat{\boldsymbol{m}}) = \begin{bmatrix} \frac{\partial f_1(\cdot)}{\partial m_1} & \frac{\partial f_1(\cdot)}{\partial m_2} & \cdots \\ \frac{\partial f_2(\cdot)}{\partial m_1} & \frac{\partial f_2(\cdot)}{\partial m_2} & \cdots \\ \vdots & \vdots & \ddots \end{bmatrix} \tag{7}$$

denote the sensitivity matrices to noise parameters $\boldsymbol{b}_d$ and identified material properties $\boldsymbol{m}$, respectively.

Using this linearisation, the least square solution (Eq. (5)) can be obtained explicitly as

$$\widehat{\boldsymbol{m}}(\boldsymbol{d}, \boldsymbol{b}_d, \boldsymbol{b}_r) = \left(\mathbf{S}_{\boldsymbol{m}}^{\mathrm{T}}\mathbf{S}_{\boldsymbol{m}}\right)^{-1}\mathbf{S}_{\boldsymbol{m}}^{\mathrm{T}}\left[\boldsymbol{r}(\boldsymbol{d}) - \boldsymbol{f}(\boldsymbol{d}, \overline{\boldsymbol{b}_d}, \widehat{\boldsymbol{m}}) - \mathbf{S}_{\boldsymbol{b}_d}(\boldsymbol{b}_d - \overline{\boldsymbol{b}_d}) + \mathbf{S}_{\boldsymbol{m}}\widehat{\boldsymbol{m}}\right] \tag{8}$$

and the variance covariance matrix of $\widehat{\boldsymbol{m}}$ is then given as

$$\mathrm{cov}(\widehat{\boldsymbol{m}}) = \left(\mathbf{S}_{\boldsymbol{m}}^{\mathrm{T}}\mathbf{S}_{\boldsymbol{m}}\right)^{-1}\mathbf{S}_{\boldsymbol{m}}^{\mathrm{T}}\left[\mathrm{cov}(\boldsymbol{b}_r) + \mathbf{S}_{\boldsymbol{b}_d}\mathrm{cov}(\boldsymbol{b}_d)\mathbf{S}_{\boldsymbol{b}_d}^{\mathrm{T}}\right]\mathbf{S}_{\boldsymbol{m}}\,. \tag{9}$$

3. Robust Experiment Design

As described in previous section, the inverse problem considering the random noise parameters and nonlinear model w.r.t. to both the noise parameters $\boldsymbol{b}_d$ as well as to the identified material properties $\boldsymbol{m}$ is computationally nontrivial and generally requires some sampling procedure for evaluating the resulting uncertainty in parameter estimates. In the phase of experiment preparation, the goal is to design the experiment leading to minimal uncertainty in the parameter estimates. This generally leads to even more complex optimisation problem, where each iteration of a robust optimisation algorithm involves a solution of the underlying inverse problem.

3.1. Local sensitivity-based robust experiment design

Ruffio et al. (2012) suggest a procedure based on the linearisation described in previous section, where uncertainty in parameter estimates is expressed by variance covariance matrix obtained explicitly according to Eq. 9. The authors further propose the so-called *F-optimality* criterion, which is similar to commonly used *A-optimality* criterion given as

$$A(\boldsymbol{d}, \widehat{\boldsymbol{m}}) = \mathrm{trace}\left(\left[(\mathbf{S}_{\boldsymbol{m}}\mathrm{diag}(\widehat{\boldsymbol{m}}))^{\mathrm{T}}(\mathbf{S}_{\boldsymbol{m}}\mathrm{diag}(\widehat{\boldsymbol{m}}))\right]^{-1}\right) = \sum_i \left(\frac{\widehat{\sigma_{m_i}}}{\widehat{m_i}}\right)^2 \tag{10}$$

and which is equivalent to the sum of relative variances. The difference consists in considering the effect of the noise parameters, which is neglected by the A-optimality derived only from the sensitivity matrix $\mathbf{S}_{\boldsymbol{m}}$. The F-optimality, on the other hand, is derived from the variance covariance matrix (Eq. (9)) as

$$F(\boldsymbol{d}, \widehat{\boldsymbol{m}}, \overline{\boldsymbol{b}}) = \sqrt{\mathrm{trace}\left((\mathrm{cov}(\widehat{\boldsymbol{m}})\mathrm{diag}(\widehat{\boldsymbol{m}})^{-1})^{\mathrm{T}}(\mathrm{cov}(\widehat{\boldsymbol{m}})\mathrm{diag}(\widehat{\boldsymbol{m}})^{-1})\right)} = \sqrt{\sum_i \left(\frac{\widehat{\sigma_{m_i}}}{\widehat{m_i}}\right)^2}\,, \tag{11}$$

where variances $\widehat{\sigma_{m_i}}$ involves the effect of all noise parameters $\boldsymbol{b}$.

The F-criterion has, however, two significant drawbacks. First is the aforementioned approximative linearisation of the nonlinear model of the experiment. Second concerns the requirement of a prior guess about the values of the identified parameters $\overline{\boldsymbol{m}}$, for which the local derivatives in Eq. (7) are computed. To overcome the latter drawback, Ruffio et al. (2012) propose more robust *FR-criterion* based on the principle of worst case scenario considering for identified parameters some prescribed feasible domain. In particular, instead of evaluating the F-criterion at one single point $\overline{\boldsymbol{m}}$, they consider a set of possible solutions M given by the so-called *central star design points*, which are the points in the center of the considered feasible hypercube and in the center of all its facets, i.e. $M = \{\overline{\boldsymbol{m}}, \overline{\boldsymbol{m}} + \delta m_i \boldsymbol{e}_i, \overline{\boldsymbol{m}} - \delta m_i \boldsymbol{e}_i\}$ where vectors $\boldsymbol{e}_i$ represent canonical base in parameter domain. Figure 2 shows the set of possible solutions in case of three identified parameters.

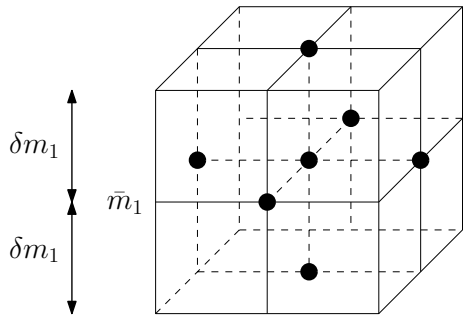

Figure 2. Set of possible solutions M considered for evaluation of robust FR criterion.

The FR-criterion is then given as maximal value of F-criterion obtained for a set of possible solutions M, i.e.

$$F_M(\boldsymbol{d}, \bar{\boldsymbol{b}}) = \max\left\{F(\overline{\boldsymbol{m}}, \bar{\boldsymbol{b}}, \boldsymbol{d}), F(\overline{\boldsymbol{m}} - \delta \boldsymbol{m}_i \boldsymbol{e}_i, \bar{\boldsymbol{b}}, \boldsymbol{d}), F(\overline{\boldsymbol{m}} + \delta \boldsymbol{m}_i \boldsymbol{e}_i, \bar{\boldsymbol{b}}, \boldsymbol{d})\right\} . \tag{12}$$

The FR-criterion increases the robustness of the obtained solution w.r.t. prior guess about the values of identified parameters, but this robustness is still limited as the central star design points M are only very rough approximation of the feasible domain for the identified parameters $\mathscr{M}$. The approximation quality can be obviously improved by increasing number of points in the set M (e.g. full factorial design points involving the corners of the hypercube), but it leads to significant increase of computational effort due to multiple evaluations of the F-criterion. Here we have to emphasize that computational complexity of F-criterion consists in evaluation of local derivatives in Eq. (7), which can be very fast if an explicit analytical expression is available. Otherwise – and very commonly in finite elements-based models – numerical and much more computationally demanding evaluation is inevitable.

3.2. Global sensitivity-based robust experiment design

In this contribution, we propose a new formulation of an optimality criterion in robust experiment design optimisation, which is derived to achieve two goals. First, we aim at increasing the robustness

of the criterion by considering whole feasible domain for identified parameters $\mathscr{M}$ and not only its rough approximation based on central star design points. Second, we focus on computational feasibility in case of complex nonlinear models of material behaviour. To that purpose, we propose a new criterion based on global sensitivity matrix consisting of Sobol indices derived analytically from coefficients of polynomial chaos-based approximation of model responses.

So as to build a polynomial chaos expansion, we consider all problem variables $(\boldsymbol{d}, \boldsymbol{b}, \boldsymbol{m})$ as random variables with prescribed probability distribution. In case of design variables and material properties, where only feasible domain is typically prescribed, we consider those variables as uniformly distributed within the feasible domain. As the noise variables are often defined as normally distributed variables, we assume that all the variables can be transformed into the standard normal variables $\boldsymbol{\xi}$ via linear (in case of normally distributed noise variables) or nonlinear (i.e. exponential in case of uniformly distributed design variables and material properties) transformation as $(\boldsymbol{d}, \boldsymbol{b}, \boldsymbol{m}) = \boldsymbol{g}(\boldsymbol{\xi} = (\boldsymbol{\xi_d}, \boldsymbol{\xi_b}, \boldsymbol{\xi_m}))$. We further assume all the problem variables $\boldsymbol{\xi}$ to be statistically independent. For an appropriate evaluation of Sobol indices, which correspond to proportional variances of model response, we need to involve all the relevant variables in our model of the experiment including measurement errors $\boldsymbol{b}_r$. Therefore we rewrite the Eq. (4) as

$$\boldsymbol{r}(\boldsymbol{d}) = \boldsymbol{f}(\boldsymbol{d}, \boldsymbol{b}, \boldsymbol{m})\,, \tag{13}$$

where vector $\boldsymbol{b} = (\boldsymbol{b}_d, \boldsymbol{b}_r)$. According to Doob-Dynkin lemma (Bobrowski, 2005), the model response $\boldsymbol{f}(\boldsymbol{d}, \boldsymbol{b}, \boldsymbol{m}) = \boldsymbol{f}(\boldsymbol{\xi})$ is a random vector which can be expressed in terms of the same random variables $\boldsymbol{\xi}$. Since $\boldsymbol{\xi}$ are independent standard Gaussian random variables, Wieners polynomial chaos expansion (PCE) based on multivariate Hermite polynomials[1] – orthogonal in the Gaussian measure – $\{H_\alpha(\boldsymbol{\xi})\}_{\alpha\in\mathcal{J}}$ is the most suitable choice for the approximation $\widetilde{\boldsymbol{f}}(\boldsymbol{\xi})$ of the model response $\boldsymbol{f}(\boldsymbol{\xi})$, see (Xiu and Karniadakis, 2002), and it can be written as

$$\widetilde{\boldsymbol{f}}(\boldsymbol{\xi}) = \sum_{\alpha\in\mathcal{J}} \boldsymbol{f}_\alpha H_\alpha(\boldsymbol{\xi})\,, \tag{14}$$

where $\boldsymbol{u}_\alpha$ is a vector of PC coefficients and the index set $\mathcal{J} \subset \mathbb{N}_0$ is a finite set of non-negative integer sequences with only finitely many non-zero terms, i.e. multi-indices, with cardinality $|\mathcal{J}| = R$. Of course, if any other type of standard random variables is more suitable (such as uniform variables), the Hermite polynomials can be replaced by other type of polynomial orthogonal w.r.t. chosen probability measure (e.g. Legendre polynomials in case of uniform variables).

Construction of PCE-based approximation is of course much more complex than construction of the first order Taylor series. Nevertheless, we recall again that the local sensitivities in Taylor development need to be recomputed for any new choice of design variables within the process of experiment optimisation. In our approach, the PCE constructions is, however, the computationally most demanding step, which needs to be done only once, before starting the experiment optimisation. Computational feasibility can be also achieved by considering low polynomial order in PCE (however with the risk of insufficient accuracy of the resulting approximation) or by employing

[1] We assume the full PCE, where number of polynomials r is fully determined by the degree of polynomials p and number of random variables s according to the well- known relation $r = \frac{(s+p)!}{(s!p!)}$.

efficient algorithms for computing PC coefficients, see e.g. (Xiu, 2009). One advantage of PCE-based model approximation is that it is well developed for nonlinear models based on finite element method. But the true beauty of PCE consists in the possibility of an analytical derivation of global sensitivity matrix based on Sobol indices, see (Blatman and Sudret, 2010), according to

$$S_{f_k,\xi_i} = \frac{\sum_{\boldsymbol{\alpha}\in\mathcal{I}_i} f_{k,\alpha}^2 \mathbb{E}[H_{\boldsymbol{\alpha}}^2(\boldsymbol{\xi})]}{\sum_{\boldsymbol{\alpha}\in\mathcal{J}\setminus\{\mathbf{0}\}} f_{k,\boldsymbol{\alpha}}^2 \mathbb{E}[H_{\boldsymbol{\alpha}}^2(\boldsymbol{\xi})]}, \tag{15}$$

where $\mathcal{I}_i$ determines the polynomials involving the terms depending only on ξ_i and polynomial degrees of other variables are null, i.e.

$$\mathcal{I}_i = \{\boldsymbol{\alpha} \in \mathbb{N}^s : 0 \leq \sum_{j=1}^{s} \alpha_j \leq p, \alpha_l = 0 \Longleftrightarrow l \notin (i), \forall l = 1, \ldots, s\}, \tag{16}$$

and

$$\mathbb{E}[H_{\boldsymbol{\alpha}}^2(\boldsymbol{\xi})] = \int H_{\boldsymbol{\alpha}}^2(\boldsymbol{\xi}) \mathrm{d}\mathbb{P}(\boldsymbol{\xi}) = \int \cdots \int_s \prod_{j=1}^{s} (H_{\alpha,j}^2(\xi_j)) \mathrm{d}\mathbb{P}(\xi_1) \cdots \mathrm{d}\mathbb{P}(\xi_s) = \prod_{j=1}^{s} p_{\alpha,j}!, \tag{17}$$

where $p_{\alpha,j}$ is a polynomial degree of variable ξ_j in the polynomial $H_{\boldsymbol{\alpha}}$.

As we aim at using the Sobol indices as components of global sensitivity matrix to be used for formulation of an optimality criteria, we introduce a simple new type of Sobol indices, so-called additive sensitivity indices (ASI), which consist of the sensitivity indices of the considered variable and a part of the sensitivity indices corresponding to the variable's combination with another variables, these indices are divided by the number of appeared variables to get their particular part. The formula for the additive sensitivity indices is

$$S_{f_k,\xi_i}^* = \frac{\sum_{\boldsymbol{\alpha}\in\mathcal{I}_i} f_{k,\boldsymbol{\alpha}}^2 \mathbb{E}[H_{\boldsymbol{\alpha}}^2(\boldsymbol{\xi})] + \sum_{\boldsymbol{\alpha}\in\mathcal{I}_i^*} {}^1\!/_{n_i^*} f_{k,\boldsymbol{\alpha}}^2 \mathbb{E}[H_{\boldsymbol{\alpha}}^2(\boldsymbol{\xi})]}{\sum_{\boldsymbol{\alpha}\in\mathcal{J}\setminus\{\mathbf{0}\}} f_{k,\boldsymbol{\alpha}}^2 \mathbb{E}[H_{\boldsymbol{\alpha}}^2(\boldsymbol{\xi})]}, \tag{18}$$

where n_i^* is a number of variables included in the polynomials from the set $\mathcal{I}_i^*$ defining all the polynomials involving ξ_i except the polynomials from $\mathcal{I}_i$, i.e.

$$\mathcal{I}_i^* = \{\boldsymbol{\alpha} \in \mathbb{N}^s : 0 \leq \sum_{j=1}^{s} \alpha_j \leq p, \boldsymbol{\alpha}_i \neq 0 \ \wedge \boldsymbol{\alpha}_l \neq 0 \Longleftrightarrow l \neq i, \forall l = 1, \ldots, s\}. \tag{19}$$

The reason is that original Sobol indices do not involve sensitivity to mixed terms involving multiple variables, which can be, however, significant and thus we do not want to neglect them. On the other hand, total sensitivity indices account for mixed terms in every index corresponding to variable present in the term. It means that sensitivity to these mixed terms will be accounted in the sensitivity matrix several times. This can lead to increased emphasis to mixed terms in comparison to terms depending uniquely on a single variable. The proposed ASI thus aim at including the sensitivity to all combinations of model variables along with their equalised significance. As a result, the sum of all ASI obtained for a chosen response component is equal to one and the indices

can be viewed as relative indices providing proportional significance of particular model variables for the response component.

In Eq. (14), the PCE is constructed also as a function of standardised design variables $\boldsymbol{\xi_d}$, but the sensitivity to those variables is of course not relevant for the experiment design. Design variables are involved only to allow an immediate analytical reconstruction of PCE as a function of only material properties and noise variables for given choice of design variables. At each step of an experiment design optimisation, the design variables $\boldsymbol{\xi_d}$ in PCE (Eq. (14)) are replaced by specific values $\boldsymbol{\xi_d^\chi}$ chosen by the governing optimisation algorithm resulting in simpler PCE given as

$$\widetilde{\boldsymbol{f}}_{\boldsymbol{\xi_d^\chi}}(\boldsymbol{\xi_m}, \boldsymbol{\xi_b}) = \widetilde{\boldsymbol{f}}(\boldsymbol{\xi})|_{\boldsymbol{\xi_d}=\boldsymbol{\xi_d^\chi}} . \tag{20}$$

Based on Eq. (20), we can define the global sensitivity matrix oppositely as a function of chosen values of design variables $\boldsymbol{\xi_d^\chi}$, which were handled as constants so far:

$$\mathbf{S}^*(\boldsymbol{\xi_d^\chi}) = \begin{bmatrix} \cdots & S^*_{f_1,\xi_{m_i}}(\boldsymbol{\xi_d^\chi}) & \cdots & S^*_{f_1,\xi_{b_i}}(\boldsymbol{\xi_d^\chi}) & \cdots \\ \cdots & S^*_{f_2,\xi_{m_i}}(\boldsymbol{\xi_d^\chi}) & \cdots & S^*_{f_2,\xi_{b_i}}(\boldsymbol{\xi_d^\chi}) & \cdots \\ & \vdots & & \vdots & \end{bmatrix} . \tag{21}$$

Here, sum of each line equals again to one and particular indices provide again the proportional significance of particular model variable (given by matrix column) to particular response component (given by matrix line). As the goal is to maximise the sensitivity to material properties and minimise the sensitivity to noise variables, from the formulation of global sensitivity matrix given in Eq. 21 it follows that maximising the sensitivity to material properties results in minimising the sensitivity to noise variables as by product. Hence, it is sufficient to evaluate only the part of sensitivity matrix corresponding to material properties given as

$$\mathbf{S}^*_{\boldsymbol{m}}(\boldsymbol{\xi_d^\chi}) = \begin{bmatrix} \cdots & S^*_{f_1,\xi_{m_i}}(\boldsymbol{\xi_d^\chi}) & \cdots \\ \cdots & S^*_{f_2,\xi_{m_i}}(\boldsymbol{\xi_d^\chi}) & \cdots \\ & \vdots & \end{bmatrix} , \tag{22}$$

where the sum of indices in each line is smaller or optimally equal to one.

As a last step we need to formulate a scaler-valued optimality criterion as some norm of the sensitivity matrix $\mathbf{S}^*_{\boldsymbol{m}}$. Since the commonly used optimality criteria such as A-optimality, D-optimality, E-optimality or others are derived for application to local sensitivity matrix obtained in linear design problem, their meaning is not fully preserved when applied to global sensitivity matrix. Therefore some further deeper research for suitable optimality criterion in case of global sensitivity matrix needs to be executed. It is, however, beyond the scope of this paper and we apply those criteria directly and only compare their behaviour on the illustrative example described in the following chapter. In particular, we implement these criteria in the following way:

$$A^*(\mathbf{S}^*_{\boldsymbol{m}}) = \operatorname{trace}\left(\left[(\mathbf{S}^*_{\boldsymbol{m}})^{\mathrm{T}}\,\mathbf{S}^*_{\boldsymbol{m}}\right]^{-1}\right) , \tag{23}$$

$$D^*(\mathbf{S}^*_{\boldsymbol{m}}) = \det\left((\mathbf{S}^*_{\boldsymbol{m}})^{\mathrm{T}}\,\mathbf{S}^*_{\boldsymbol{m}}\right) , \tag{24}$$

$$E^*(\mathbf{S}^*_{\boldsymbol{m}}) = \operatorname{cond}\left((\mathbf{S}^*_{\boldsymbol{m}})^{\mathrm{T}}\,\mathbf{S}^*_{\boldsymbol{m}}\right) , \tag{25}$$

respectively. And we emphasise that once the PCE-based approximation of model response is constructed, the criteria are defined as explicit analytical functions of design variables which make the optimisation of experiment design very computationally efficient. The criteria can of course be non-smooth or multi-modal, but any evolutionary algorithm requiring high number of iterations can be successfully applied. Here, in particular, we apply real-valued genetic algorithm GRADE extended by niching strategy CERAF allowing him to escape from local extremes (Kucerova, 2007).

4. Numerical Example

We use the example of experiment design problem elaborated in (Ruffio et al., 2012) and previously in (Sawaf et al., 1995). The example deals with two-dimensional linear nonstationary heat problem govern by energy balance equation

$$C\frac{\partial\theta}{\partial t} = \lambda_x\frac{\partial^2\theta}{\partial x^2} + \lambda_y\frac{\partial^2\theta}{\partial y^2} \tag{26}$$

on the spatial domain given as $0 \leq x \leq l_x = 5$ cm and $0 \leq y \leq l_y = 5$ cm and time domain given as $0 \leq t \leq \tau = 60$ s, see Figure 3.

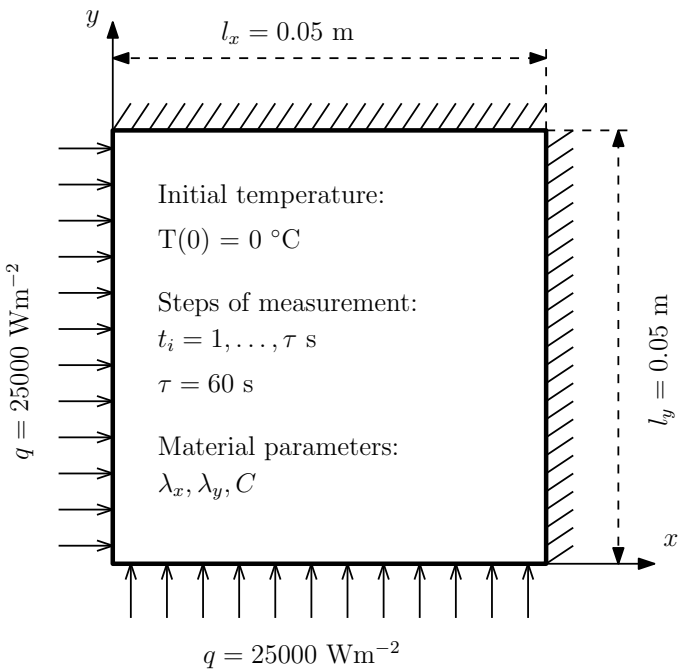

Figure 3. Experiment setup.

The boundary and initial conditions are defined by

$$-\lambda_x \frac{\partial \theta}{\partial x}(x=0) = q, \qquad -\lambda_y \frac{\partial \theta}{\partial y}(y=0) = q \tag{27}$$

$$-\lambda_x \frac{\partial \theta}{\partial x}(x=l_x) = 0, \qquad -\lambda_y \frac{\partial \theta}{\partial y}(y=l_y) = 0 \tag{28}$$

$$\theta(x,y,0) = 0\,, \tag{29}$$

where $q = 25000\mathrm{Wm}^{-2}$. The specimen consists of an orthotropic homogeneous material with three material parameters to be identified: two thermal conductivities λ_x and λ_y in principal directions and the thermal volumetric capacity C, i.e. $\boldsymbol{m} = (\lambda_x, \lambda_y, C)$. Their a priori selected feasible domains are

$$\lambda_x \in [0.3; 0.7] \quad \mathrm{Wm}^{-1}\mathrm{K}^{-1} \tag{30}$$

$$\lambda_y \in [3.0; 7.0] \quad \mathrm{Wm}^{-1}\mathrm{K}^{-1} \tag{31}$$

$$C \in [1400000; 1800000] \quad \mathrm{Jm}^{-3}\mathrm{K}^{-1} \tag{32}$$

The temperature is supposed to be measured by three sensors, each performing 60 measurements with the acquisition period $\Delta t = 1$ s. The aim of the experiment design problem is to find the optimal positions of the three sensors, i.e. $\boldsymbol{d} = (d_{x1}, d_{y1}, d_{x2}, d_{y2}, d_{x3}, d_{y3})$.

Once the experiment is realised, its parameters will not be exactly at designed values and thus we assume several parameters as random variables to account for the underlying noise. Therefore we consider following noise variables within the process of experiment design optimisation, see Figure 4:

- Heat flux density q is supposed to be constant during the measuring time period, but its mean value is perturbed by the normally distributed noise b_q with the zero mean and standard deviation $\sigma_q = 50\ \mathrm{Wm}^{-2}$.
- Temperature sensors provide results disturbed by additive Gaussian measurement noise b_r with zero mean and standard deviation $\sigma_r = 0.1°\mathrm{C}$.
- Sensors are supposed to be placed at designed positions $\boldsymbol{d}$ which are subject also to Gaussian noise $\boldsymbol{b}_x$ with zero mean and standard deviations $\sigma_{xi} = \sigma_{yi} = 0.5$ mm.

Ruffio et al. (2012) profits from the simplicity of the elaborated example consisting in possibility to derive the model response and local sensitivity matrix analytically. On the other hand, we want to present more realistic scenario, where experiment simulation involves finite elements-based discretisation. First, we transform all the involved variables into standard Gaussian variables $(\boldsymbol{\xi_m}, \boldsymbol{\xi_d}, \boldsymbol{\xi}_{b_q}, \boldsymbol{\xi}_{\boldsymbol{b}_x}, \boldsymbol{\xi}_{\boldsymbol{b}_r})$. Then we write the discretised model as

$$\mathbf{A}(\boldsymbol{\xi_m}, \boldsymbol{\xi}_{b_q})\boldsymbol{u} = \boldsymbol{q} \tag{33}$$

and we construct its PCE-based approximation in every response component as

$$\tilde{\boldsymbol{u}}(\boldsymbol{\xi_m}, \boldsymbol{\xi}_{b_q}) = \sum_{\alpha \in \mathcal{I}} \boldsymbol{\beta}_\alpha \psi_\alpha(\boldsymbol{\xi_m}, \boldsymbol{\xi}_{b_q})\,. \tag{34}$$

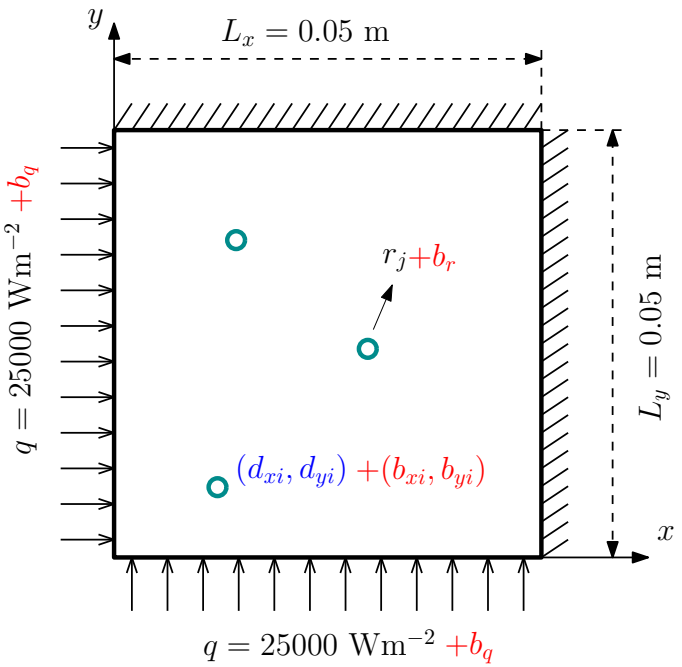

Figure 4. Design and noise variables considered in experiment design optimisation problem.

To obtain the temperature values corresponding to k-th sensor, we have to determine a specific finite element, where the sensor is located, and the polynomial expansions in its nodes

$$\tilde{\boldsymbol{u}}_k(\boldsymbol{\xi}_m) = (\tilde{u}_1(\boldsymbol{\xi}_m), \tilde{u}_2(\boldsymbol{\xi}_m), \tilde{u}_3(\boldsymbol{\xi}_m))^{\mathrm{T}}\,, \tag{35}$$

see Figure 5. By evaluating shape functions $\boldsymbol{N}_k(\boldsymbol{d}_k(\boldsymbol{\xi}_d))$ and their gradient $\mathbf{B}_k(\boldsymbol{d}_k(\boldsymbol{\xi}_d)) = \boldsymbol{\nabla}\boldsymbol{N}_k(\boldsymbol{d}_k(\boldsymbol{\xi}_d))$

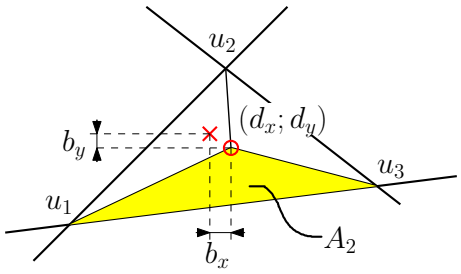

Figure 5. Scheme of a triangular finite element with the interior sensor at coordinates $(d_x + b_x, d_y + b_y)$.

(with $\boldsymbol{\nabla} = (\nabla x, \nabla y)^{\mathrm{T}}$) at the designed position of a sensor $\boldsymbol{d}_k = (d_x, d_y)$ as

$$\boldsymbol{N}_k(\boldsymbol{d}_k(\boldsymbol{\xi}_d)) = (N_1(\boldsymbol{d}_k(\boldsymbol{\xi}_d)), N_2(\boldsymbol{d}_k(\boldsymbol{\xi}_d)), N_3(\boldsymbol{d}_k(\boldsymbol{\xi}_d))) = \left(\frac{A_1(\boldsymbol{\xi}_d)}{A}, \frac{A_2(\boldsymbol{\xi}_d)}{A}, \frac{A_3(\boldsymbol{\xi}_d)}{A}\right) \tag{36}$$

we obtain an explicit function for model response component corresponding to chosen position of sensor including all relevant noise variables as

$$\begin{aligned}\widetilde{f}_k(\boldsymbol{\xi}_m, \boldsymbol{\xi}_d, \boldsymbol{\xi}_b) &= \boldsymbol{N}_k(\boldsymbol{\xi}_d)\tilde{\boldsymbol{u}}_k(\boldsymbol{\xi}_m) + \boldsymbol{b}_d(\boldsymbol{\xi}_b)\left[\mathbf{B}_k(\boldsymbol{\xi}_d)\right]\tilde{\boldsymbol{u}}_k(\boldsymbol{\xi}_m) + b_r(\xi_{b_r}) = \\ &= \left[\boldsymbol{N}_k(\boldsymbol{\xi}_d) + \boldsymbol{b}_d(\boldsymbol{\xi}_b)\left[\mathbf{B}_k(\boldsymbol{\xi}_d)\right]\right]\tilde{\boldsymbol{u}}_k(\boldsymbol{\xi}_m) + b_r(\xi_{b_r})\,, \end{aligned} \tag{37}$$

which is in fact also a polynomial expansion and can be written as

$$\widetilde{f}_k(\boldsymbol{\xi}_m, \boldsymbol{\xi}_d, \boldsymbol{\xi}_b) = \sum_{\alpha\in\mathcal{I}} \boldsymbol{\beta}_\alpha \psi_\alpha(\boldsymbol{\xi}_m, \boldsymbol{\xi}_d, \boldsymbol{\xi}_b)\,. \tag{38}$$

In this polynomial expansion, we treat the design variables as constants and get an explicit formulation for global sensitivity matrix according to Eq. (22), which can be then quickly evaluated at every iteration of the experiment design optimisation process.

5. Results

As the first numerical study we compare the performance of optimality criteria defined in Eqs. (23) – (25) and the A^*, D^* and E^*-optimal designs are plotted in the first three columns of Table I, respectively. All these designs are selected as best among the set of local optima determined by GRADE+CERAF algorithm. Last two columns are occupied by two best locally optimal solutions presented in (Ruffio et al., 2012). All experiment designs are employed in a single simulated experiment, where true values of material parameters are given according to (Ruffio et al., 2012) as

$$\begin{aligned}\lambda_x^* &= 0.6\,\mathrm{Wm^{-1}C^{-1}}\,,\\ \lambda_y^* &= 4.7\,\mathrm{Wm^{-1}C^{-1}}\,,\\ C^* &= 1700000\,\mathrm{Jm^{-3}C^{-1}}\,.\end{aligned}$$

In the local sensitivity-based approach, an initial guess about the values of material properties is required for computing the local sensitivities. This guess again according to (Ruffio et al., 2012) is

$$\begin{aligned}\overline{\lambda_x} &= 0.5\,\mathrm{Wm^{-1}C^{-1}}\,,\\ \overline{\lambda_y} &= 5.0\,\mathrm{Wm^{-1}C^{-1}}\,,\\ \overline{C} &= 1600000\,\mathrm{Jm^{-3}C^{-1}}\,.\end{aligned}$$

In order to compare the quality of particular experiment designs, an inverse analysis is performed in a simplified – linearised – way as described in Section 2 and parameter estimates along with their variances are computed according to Eqs. (8) and (9). Resulting relative variances in parameter estimates obtained for particular experimental designs are written in Table I.

By comparing these results we may conclude that the applied optimality criteria do not differ too significantly. Especially A^*- and D^*-optimality provide very similar results. The E^*-optimality outperforms the others by providing almost half of the variances obtained by A^*- and D^*-optimality.

Table I. Comparison of experimental designs within a single inverse analysis.

	$A^*(\mathbf{S}^*_{\boldsymbol{m}})$	$D^*(\mathbf{S}^*_{\boldsymbol{m}})$	$E^*(\mathbf{S}^*_{\boldsymbol{m}})$	$F(\boldsymbol{d}, \widehat{\boldsymbol{m}}, \overline{\boldsymbol{b}})$:U1	$F(\boldsymbol{d}, \widehat{\boldsymbol{m}}, \overline{\boldsymbol{b}})$:U2
	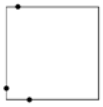	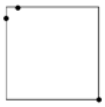	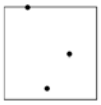	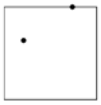	
$\sigma_{\lambda_x}/\lambda_x$	19.1%	20.2%	12.1%	4.6 %	8.0 %
$\sigma_{\lambda_y}/\lambda_y$	16.2%	13.7%	5.6%	7.5 %	2.9 %
σ_C/C	10.3%	10.4%	5.1%	2.9 %	2.0 %

Nevertheless, the E^*-optimality does not outperform the results obtained by Ruffio et al. using the problem linearisation and local sensitivity matrix.

One possible explanation is that the true values of the material properties are very close the starting guess used for computation of local sensitivities. Therefore we have performed a set of 25 simulated experiments for changing values of material properties on a regular grid $5x5x5$ within the feasible domain. For each experiment, the same inverse analysis was executed as in the first example and minimal and maximal values of estimated parameter variances are listed in Table II.

Table II. Case study: min-max.

	$\sigma_{\lambda_x}/\lambda_x$	$\sigma_{\lambda_y}/\lambda_y$	σ_C/C
$F(\boldsymbol{d}, \widehat{\boldsymbol{m}}, \overline{\boldsymbol{b}})$:U2	7.9 – 31.9 %	1.7 – 6.3 %	1.53 – 4.3 %
$A^*(\mathbf{S}^*_{\boldsymbol{m}})$	17.6 – 22.0 %	15.3 – 24.2 %	8.63 – 17.3 %
$D^*(\mathbf{S}^*_{\boldsymbol{m}})$	18.5 – 25.2 %	10.5 – 20.2 %	8.55 – 16.4 %
$E^*(\mathbf{S}^*_{\boldsymbol{m}})$	10.6 – 14.4 %	2.5 – 6.2 %	3.26 – 7.2 %

Here it can be already concluded that the E^*-optimal design has a comparable quality to U2-design obtained by Ruffio et al. and it still outperforms the A^*-optimal and D^*-optimal designs.

6. Conclusions

The proposed contribution presents a new method for designing robust and optimal experiments, which is developed with regard on its practical applicability to finitThe proposed contribution presents an original method for designing robust and optimal experiments, which is developed with regard on its practical applicability to finite element-based models and its computational feasibility. The method is based on an explicit formulation of global sensitivity matrix, which constituents are defined as Sobol indices derived analytically from the polynomial chaos-based approximation of model response. Employing higher order polynomials in model surrogate allows to account for

the nonlinearity of the model as well as for the prescribed large feasible domain of the material properties to be estimated. No prior expert guess about specific parameter values is needed as it is in the case of local sensitivity-based procedure described in (Ruffio et al., 2012). Construction of the higher order polynomial surrogate is of course computationally intensive task. Nevertheless, development of efficient computational tools for polynomial chaos-based uncertainty propagation is a scientific topic still atracting the attention of many researchers pushing forward the process in this field. Moreover, the construction of the PCE-based surrogate needs to be carried out only once before the actual start of the experiment design process. During the optimisation, only very fast evaluation of Sobol indices defined explicitely from the PC coefficients is needed at each iteration of the optimisation process.

The proposed method is compared here with the local sensitivity-based method on a simple example of nonstationary linear heat transfer. It is shown that the both method provides very similar values of variances of parameter estimates. The comparison is now, however, very modest. We suspect that the model of the experiment on the feasible domain of material properties is here only mildly nonlinear and thus the robustness of the proposed method cannot be fully appreciated. Moreover the comparison is performed using the linearised inverse analysis, while full Monte Carlo-based inverse analysis would be also more appropriate to verify the quality of the obtained experimental designs. These topic will be thus next steps in our future work.

Acknowledgements

The financial support of the Czech Science Foundation (Project No. 15-07299S) is gratefully acknowledged.

References

Asprey, S. P. and S. Macchietto. Designing robust optimal dynamic experiments. *Journal of Process Control*, 12:545–556, 2002.

Beyer, H.-G. and B. Sendhoff. Robust optimization - a comprehensive survey. *Comput. Methods Appl. Mech. Engrg.*, 196:3190–3218, 2007.

Blatman, G. and B. Sudret. Efficient computation of global sensitivity indices using sparse polynomial chaos expansions. *Reliability Engineering & System Safety*, 95(11):1216–1229, 2010.

Bobrowski, A. *Functional analysis for probability and stochastic processes: an introduction.* Cambridge University Press, 2005.

Franceschini, G. and S. Macchietto. Model-based design of experiments for parameter precision: State of the art. *Chemical Engineering Science*, 63:4846–4872, 2008.

Hametner, Ch., M. Stadlbauer, M. Deregnaucourt, S. Jakubek and T. Winsel. Optimal experiment design based on local model networks and multilayer perceptron networks. *Engineering Applications of Artificial Intelligence*, 26:251–261, 2013.

Helton, J., J. Johnson, C. Sallaberry and C. Storlie. Survey of sampling-based methods for uncertainty and sensitivity analysis. *Reliab Eng Syst Safe*, 91(10–11):1175–1209, 2006.

Janouchová, E. and A Kučerová. Competitive comparison of optimal designs of experiments for sampling-based sensitivity analysis. *Computers & Structures*, 124:47–60, 2013.

Jurecka, F. *Robust Design Optimization Based on Metamodeling Techniques*. PhD thesis, Technische Universität München, Germany, 2007.

Kučerová, A. *Identification of nonlinear mechanical model parameters based on softcomputing methods*. PhD thesis, Ecole Normale Supérieure de Cachan, Laboratoire de Mécanique et Technologie, France, 2007.

Lindner, P. F. O. and B. Hitzmann. Experimental design for optimal parameter estimation of an enzyme kinetic process based on the analysis of the fisher information matrix. *Journal of Theoretical Biology*, 238:111–123, 2006.

Ruffio, E., D. Saury and D. Petit. Robust experiment design for the estimation of thermophysical parameters using stochastic algorithms. *International Journal of Heat and Mass Transfer*, 56(11–12):2901–2915, 2012.

Sawaf, B., M. N. Özisik and Y. Jarny. An inverse analysis to estimate linearly temperature dependent thermal conductivity components and heat capacity of an orthotropic medium. *International Journal of Heat and Mass Transfer*, 38(16):3005–3010, 1995.

Telen, D., F. Logist, E. Van Derlinden, I. Tack and J. Van Impe. Optimal experiment design for dynamic bioprocesses: A multi-objective approach. *Chemical EngineeringScience*, 78:82–97, 2012.

Van Derlinden, E., K. Bernaerts and J. F. Van Impe. Simultaneous versus sequential optimal experiment design for the identification of multi-parameter microbial growth kinetics as a function of temperature. *Journal of Theoretical Biology*, 264:347–355, 2010.

Xiu, D. Fast Numerical Methods for Stochastic Computations: A Re- view. *Communications in Computational Physics*, 5(2–4):242–272, 2009.

Xiu, D. and G. E. Karniadakis. The Wiener–Askey Polynomial Chaos for Stochastic Differential Equations. *SIAM Journal on Scientific Computing*, 24(2):619–644, 2002.

Multi-Objective Reliability-Based Design Optimization using Subset Simulation Enhanced by Meta-Models

Adéla Pospíšilová and Matěj Lepš
Department of Mechanics, Faculty of Civil Engineering, Czech Technical University in Prague, Prague 6, 16629, Czech Republic

Abstract: This paper deals with double-looped reliability-based design optimization (RBDO), in which the system reliability is assessed within the inner loop and a designing process is performed in the outer loop. A common approach expressed as single-objective optimization is transformed into a multi-objective case providing results as an approximation of the Pareto front composed of the compromising solutions between cost and reliability. The double-loop formulation of RBDO provides the most accurate approximation of the Pareto front but is computationally demanding even if advanced simulation techniques are used for rare failure events. Nowadays, a *Subset simulation* is a popular method to obtain an estimate of small failure probabilities. Despite the reduction in evaluation time using a Subset simulation when compared to a crude Monte Carlo method, the computational effort is still high with a complex model as a performance function, e.g. a finite element model. The computational model can be replaced by its surrogate in order to reduce the computational costs. This *meta-model* fits the responses evaluated by the original model for the predetermined data, so called a Design of Experiment (DoE). Since the design variables change with every iteration and a meta-model is utilized for a reliability assessment, the meta-model is trained only in the vicinity of the relevant design variable which makes the meta-model computationally faster and more precise. The DoE is updated by selected points from subset simulation samples with respect to two criteria: first, beneficial samples are located in the vicinity of the limit state, which divides the space into a safe region and a failure domain, and second, these samples should also be placed in the sparsest position of the DoE. The described method is illustrated on a classical RBDO benchmark with two objective functions; the first objective is a cost function to be minimized, the second objective is a structural reliability expressed by a reliability index to be maximized. The quality is assessed by comparison to an asymptotic sampling and a Monte Carlo simulation all with responses obtained by an original model and local meta-models.

Keywords: multi-objective optimization, reliability-based design optimization, radial basis functions meta-models, non-dominated sorting genetic algorithm II, asymptotic sampling, subset simulation.

1. Introduction

Structural optimization is a process that seeks the best design under some predefined constraints. A deterministic model is usually unrealistic due to the uncertain inputs such as material properties, a structural topology, loadings etc. The optimal design with deterministic variables often terminates

at a boundary between the failure domain and the safe domain and even a small perturbation in inputs can lead to a fatal failure. For that reason, the model uncertainties are introduced; the parameter uncertainties are associated with the input data whereas the structural uncertainties express that the model need not clearly describe the physics of the problem. Optimization under uncertainties looks into two main tasks; the first task called *robust design optimization* deals with the everyday fluctuations in inputs and provides a design with a minimum price that is less sensitive to small perturbations in inputs; the second task known as *reliability-based design optimization* concentrates on worse-case scenarios and offers an economical design with large safety.

In reliability-based design optimization (RBDO), the most challenging task is to evaluate a probability constraint or a probability objective. For such a reliability assessment, it is required to evaluate a structural response several times with different settings of uncertain parameters and design variables, which is the most computer power demanding part of the problem. It is possible to evaluate a probability of failure analytically only for special types of problems, e.g. by Gauss quadrature approaches, Laplace Approximation approaches, etc., which is limiting for RBDO applications. An exact computation is impractical (Aoues and Chateauneuf, 2010). Approximation techniques such as a First-order reliability method (FORM) (Hasofer and Lind, 1974), and simulation techniques such as crude Monte Carlo (MC) (Metropolis and Ulam, 1949) and variance reduction techniques are commonly used. FORM is very often preferred for its speed and relatively few necessary evaluations of the structural response. The drawback is that the obtained reliability assessment is inaccurate for low probabilities of failure and for highly non-linear problems. There are two preferred formulations of FORM in RBDO, that proceed from a key idea that a reliability index is the shortest distance between the most probable failure point (MPFP) and the origin in a standard normal space and therefore it is an optimization task. First, the reliability index approach (RIA) (Enevoldsen and Sørensen, 1994) is a classical reliability formulation, in which the quadratic form of MPFP is minimized such that a limit state function value is less than or equal to a predefined threshold value. Second, performance measure approach (PMA) (Tu, Choi and Park, 1999) is defined as an inverse approach, in which limit state function is minimized such that the quadratic form of MPFP is equal to a predefined threshold value. This formulation is more stable because it is easier to minimize a complicated objective function subject to a simple constraint. Since the expansion of a computing power, the simulation techniques are becoming popular in RBDO, such as Monte Carlo simulation (Papadrakakis, Lagaros and Plevris, 2005), a subset simulation (Valdebenito and Schuüeller, 2010) or an importance sampling (Beaurepaire et al, 2013).

Reliability-based design optimization can be formulated by two linked loops. An optimizer provides a design in the outer loop, for which a probability of failure is evaluated in the inner loop. The double-looped procedure allows a very accurate safety appraisal of each design without any kind of approximation. However, this formulation suffers from large computational demands if a classical Monte Carlo method is used. Fortunately, advanced simulation techniques such as an asymptotic sampling (Bucher, 2009) and a subset simulation (Au and Beck, 2001) can be used for the reliability assessment and the accuracy can be almost maintained with the drastic computational effort reduction.

Although the speed-up is achievable with the advanced simulation techniques, a structural response can be still quite computationally demanding and an approximation of an original structural

model has to be implemented. The original model can be replaced by some model of the original model that has a very similar behaviour; however, it is less time consuming to evaluate. Those models of models are called *meta-models* or *surrogate models* and they require just few evaluations of the costly original function. Those evaluations are then used to create the meta-model. Proper locations for an original model evaluation (called *support points*) have to be chosen properly usually by a *Design of Experiments* (DoE) (Montgomery, 1997; Janouchová and Kučerová, 2013) with support points usually uniformly distributed in the whole design space. The accuracy of a meta-model is dependent on several factors such as a number of dimensions, non-linearity of the structural response model, a number of support points, etc.

The initial DoE can be created by as many support points as many times the original model can be evaluated or the initial DoE can be sparse and adaptively improved (*updated*) in interesting locations, subsequently. A type of an update is dependent on a purpose of the meta-model within the meaning of optimization. A meta-model replacing an original model in an objective function is updated differently from the meta-models replacing original models in constraints. For a meta-model utilization in a reliability assessment in RBDO, several updating methods are published in the literature such as Efficient global reliability analysis (Bichon et al, 2008) or Active Kriging using Monte Carlo simulation (Echard, Gayton and Lemaire, 2011). These updating methods are strictly oriented to Kriging meta-models and their error estimate, however, Kriging is not always the best option for the original model substitution (Jin, Chen and Sompson, 2001).

For a reliability assessment in RBDO, the most important region in any model is the boundary between the safe and the failure domain, called a *limit state*. A good meta-model should be the most precise especially around this boundary. If an initial DoE is sparse and it is subsequently adaptively refined, new support points should be placed partly in the vicinity of the limit state, partly in the location with the highest sparsity of DoE. These requirements can be formulated into multi-objective optimization with two objectives to search an optimal position of the new support points in DoE. The first one is the distance to the limit state; the second one is the space-filling property of the DoE, which is optimized by maximizing the minimal interpoint distance (i.e. the Maximin approach). The optimization routine runs repeatedly and obtained Pareto-optimal solutions are added into the existing DoE to get the updated meta-model, see more details in (Pospíšilová, Myšáková and Lepš, 2013). The benefits of this method are that this procedure is independent on a meta-model type, one global meta-model covers the whole design space and it can be treated as the original model, the update is run in parallel, and the DoE is updated with several support points at the same time. The main drawback is that the whole design space is large and the number of support points in DoE has to be enourmous to obtain the similar accuracy with the original model. It has a consequence in needed computational effort; since more samples are used for the interpolating meta-model construction, the more computational effort is necessary. In (Pospíšilová, and Lepš, 2015), we started to use several local meta-models instead of one global meta-model. Small meta-models are trained for every single design of RBDO. These meta-models are built from samples that are in the vicinity of the proposed design by the optimizer and therefore are relevant to that proposal. Evaluations of these tiny meta-models are very fast and can be repeated as many times as necessary by the sampling method with no limitations. The main drawback of the proposed methodology was that the chosen reliability assessment method, an asymptotic sampling, needed larger meta-models because of sequentially scaling random variables over the standard deviation

to predict a reliability index. If selected points in DoE for meta-model construction are too few, an asymptotic sampling requires an extrapolation of the meta-model and the resulting reliability assessment is not trustworthy. This paper deals with the incorporation of another reliability assessment method, a subset simulation, into RBDO enhanced by local meta-models introduced in (Pospíšilová, and Lepš, 2015). We expect the possibility of construction of smaller meta-models for the reliability evaluation and following speed-up of finding the approximation of the Pareto front in RBDO.

2. Methodology

2.1. From Single- to Multi-objective Double-looped Reliability-based Design Optimization

Reliability-based design optimization provides a design that is economical as well as reliable in presence of uncertainties. Many formulations of objective functions have been proposed, however, minimization of the total cost of the structure is a frequently used model comprising the initial cost together with the failure risk. This failure risk is defined as the cost of failure multiplied by the probability of failure and because of obstacles in assessing monetary values to all failure consequences (e.g. placing a monetary value on human life) (Frangopol, 1985), an alternative formulation is possible as

$$\min_{\mathbf{d}\in\mathbb{D}} \quad C(\mathbf{d}), \tag{1}$$

$$\text{s. t.} \quad H_i(\mathbf{d}) \leq 0,\ i = 1, \ldots, n_e, \tag{2}$$

$$\beta_j(\mathbf{x}, \mathbf{d}) \geq \beta_j^{tol},\ j = 1, \ldots, n_p. \tag{3}$$

The objective function $C(\cdot)$ is to be minimized with optimal values of design variables arranged in a vector $\mathbf{d}$ that contains deterministic variables or probability distribution parameters (e.g. the mean of random variables). Design variables are chosen from the design space $\mathbb{D}$. All deterministic constraints $H_i(\cdot)$ has to be less than or equal to zero where i is from 1 to n_e and n_e is the total number of constraints. A generalized reliability index $\beta_j(\cdot)$ has to be greater than or equal to a prescribed tolerable threshold β_j^{tol}; generally, β is defined as an inverse cumulative distribution function of the standard normal distribution $\beta = \Phi^{-1}(1 - p_F)$, where p_F is a probability of failure. The influence of uncertain parameters arranged in a vector $\mathbf{x}$ is taken into consideration in these constraints. A number of events n_p is equal to one in the simplest cases.

Multi-objective formulation of the reliability-based design optimization task provides larger room for a decision maker, whereas single-objective formulation forces a researcher to constrain the search space before an optimization procedure is started. The multi-objective formulation addressed here is stated as follows:

$$\min_{\mathbf{d}\in\mathbb{D}} \quad C(\mathbf{d}), \tag{4}$$

$$\max_{\mathbf{d}\in\mathbb{D}} \quad \beta_j(\mathbf{x}, \mathbf{d}),\ j = 1, \ldots, n_p, \tag{5}$$

$$\text{s. t.} \quad H_i(\mathbf{d}) \leq 0,\ i = 1, \ldots, n_e. \tag{6}$$

The reliability constraint in a single-objective formulation is freed to an objective function in a multi-objective formulation. Together with the first objective function $C(\cdot)$, the multi-objective formulation contains two conflicting objectives now and the trade-off between the structural safety and the cost has to be find as the Pareto front from which the most preferable solution is identified afterwards by a decision maker.

A double-loop approach deals with a designing process in an outer loop; an optimizer proposes a combination of design variables $\mathbf{d}^{(k)}$ in each optimization step k and deterministic constraints $H_i(\mathbf{d}^{(k)})$ together with reliability indexes $\beta_j(\mathbf{x}, \mathbf{d}^{(k)})$ are evaluated. A reliability assessment is appraised for each combination of design variables $\mathbf{d}^{(k)}$ in an inner loop to obtain $\beta_j(\mathbf{x}, \mathbf{d}^{(k)})$. The inner loop consists of N_s evaluations of a structural response $g(\mathbf{x}^{(s)}, \mathbf{d}^{(k)})$ with different values of random variables $\mathbf{x}^{(s)}$, with $s = 1, \ldots, N_s$.

2.2. Subset simulation

A subset simulation (Au and Beck, 2001) is a novel methodology that is based on a formulation of the failure event F as an intersection of the intermediate failure events F_m. The rare event problem is then reformulated as series of more frequent events that are easier to solve. The probability of failure is as follows

$$p_F = \text{Prob}[F_1] \cdot \prod_{m=2}^{M} [F_m | F_{m-1}]. \tag{7}$$

The failure probability of the first intermediate domain is evaluated by a classical Monte Carlo method with hundreds of samples N. These samples are sorted in an ascending order and a limit state function $y = g(\cdot)$ is relaxed such that $\text{Prob}[F_1]$ is equal to a predefined value p_0. The limit state function value of the $(p_0 \cdot N)^{\text{th}}$ sample is a relaxed threshold $y_1^\star$ in sorted Monte Carlo samples. The first $(p_0 \cdot N)$ samples are used as seeds for the simulation of samples from conditional probabilities by a Markov chain Monte Carlo (MCMC) with a modified Metropolis algorithm. In each level m, samples obtained by MCMC are sorted and first $(p_0 \cdot N)$ samples serve as seeds in the $(m+1)^{\text{th}}$ step together with a proper relaxation of the limit state function by value $y_m^\star$. The last level M is reached if the failure probability of the M^{th} step with the original limit state is greater than p_0; in other words, if the $y_M^\star$ changes its sign.

2.3. Radial basis functions model

Radial basis functions model (RBF) approximates a complicated true function as a sum of easier basis functions that are symmetrical and centered on a set of support points (Forrester, 2008). For noise-free data, the model is

$$\hat{y}(\mathbf{x}) = \mathbf{w}^T \boldsymbol{\psi} = \sum_{i=1}^{n_c} w_i \psi(||\mathbf{x} - \mathbf{c}^{(i)}||), \tag{8}$$

where $\mathbf{w}$ is a weighting vector, $\boldsymbol{\psi}$ is a vector of length n_c holding evaluated basis functions on Euclidean distances between the prediction $\mathbf{x}$ and centres of basis functions $\mathbf{c}$. Basis functions can be

fixed or parametric and are chosen by user according to the type of the original function; frequently used basis functions are Gaussian, Hardy multiquadrics, Inverse multiquadrics, C^n Matérn etc. We use Gaussian parametric bases

$$\psi(r) = \exp\left(\frac{-r^2}{2\sigma^2}\right) \tag{9}$$

where parameters σ are found by an optimization algorithm. Centres of basis functions can be made identical with the Design of Experiments $\mathbf{c}^{(i)} = \mathbf{x}^{(i)}$ and parameters in a weighting vector are evaluated from the system of linear equations $\mathbf{\Psi w} = \mathbf{y}$ where each element of Gram matrix $\mathbf{\Psi}$ is $\Psi_{i,j} = \psi(||x^{(i)} - x^{(j)}||),\ i,j = 1,\ldots,n$; n is a number of points in the DoE, $\mathbf{y}$ is a vector of responses evaluated with the original model or function and $\mathbf{w}$ is again a weighting vector.

2.4. Adaptive retrieval of new support points

A whole methodology is depicted in Figure 1 and it is taken over from (Pospíšilová, and Lepš, 2015). First of all, primary Design of Experiment $\mathcal{Q}$ is constructed. In our previous work (Pospíšilová, Myšáková and Lepš, 2013), we have found out that Halton sequences (Kocis, 1997) are efficient, fast and well distributed, thus we used them for every uniform design in this work. The true response function g(·) that should be computationally very expensive in real-life optimization problems (e.g. FEM simulation) is used to calculate responses $\mathcal{G}$ for DoE $\mathcal{Q}$. Therefore the DoE should be relatively sparse to save up the computational time. This data-set is saved as Dataset 1 $[\mathcal{Q}, \mathcal{G}]$ for the following meta-modeling. The optimizer proposes one individual $\mathbf{d}^{(k)}$ or a set of individuals (in case of population algorithm) in each generation k. In this paper, every individual has a meaning of the mean of a random variable. For each individual, deterministic functions as well as the reliability assessment are evaluated. Deterministic functions are not so computationally problematic for the most cases and if so, they are calculated only once for each individual. The reliability assessment, however, complicates the computational speed. Since we use a sampling approach for probability of failure estimation, we calculate the response function repeatedly. The response function is therefore substituted by a surrogate model, that is uniquely built by $\mathscr{S}(\cdot)$ for each individual $\mathbf{d}^{(k)}$ as $\overline{g}(\cdot)$, thus every individual has its own meta-model and individuals do not share them. The meta-model is set-up from DoE data-set points $\mathcal{Q}$ that are nearby the individual $\mathbf{d}^{(k)}$; the selection of the dataset is labeled as $\mathbf{Q}^{\mathbf{d}^{(k)}}$. We use the *k-nearest neighbors algorithm*[1] (Friedman, 1977) for the proximity assessment where only the prescribed number of points have to be specified. We found out that one tenth of the all DoE points is sufficient but this setting vary from problem to problem. However, the tenth is a good initial guess. The estimation of the probability of failure $p_F(\mathbf{d}^{(k)})$ as well as a value of the cost function $C(\mathbf{d}^{(k)})$ are given back to the optimization algorithm. In case that we do not want to utilize the knowledge about the problem provided by the meta-model and reflect it into the DoE, the optimization algorithm will continue up to the N_k step in the described way.

The reliability simulation method samples around the design variable and the reliability assessment needs the response in these samples. The difference between the response and the limit value of the admissible occurrence is called *limit state function* (LSF) in this paper. The most substantial part of the limit state function is the *limit state*, i.e. the frontier between the safe and failure region,

[1] We use knn-search implemented in Matlab.

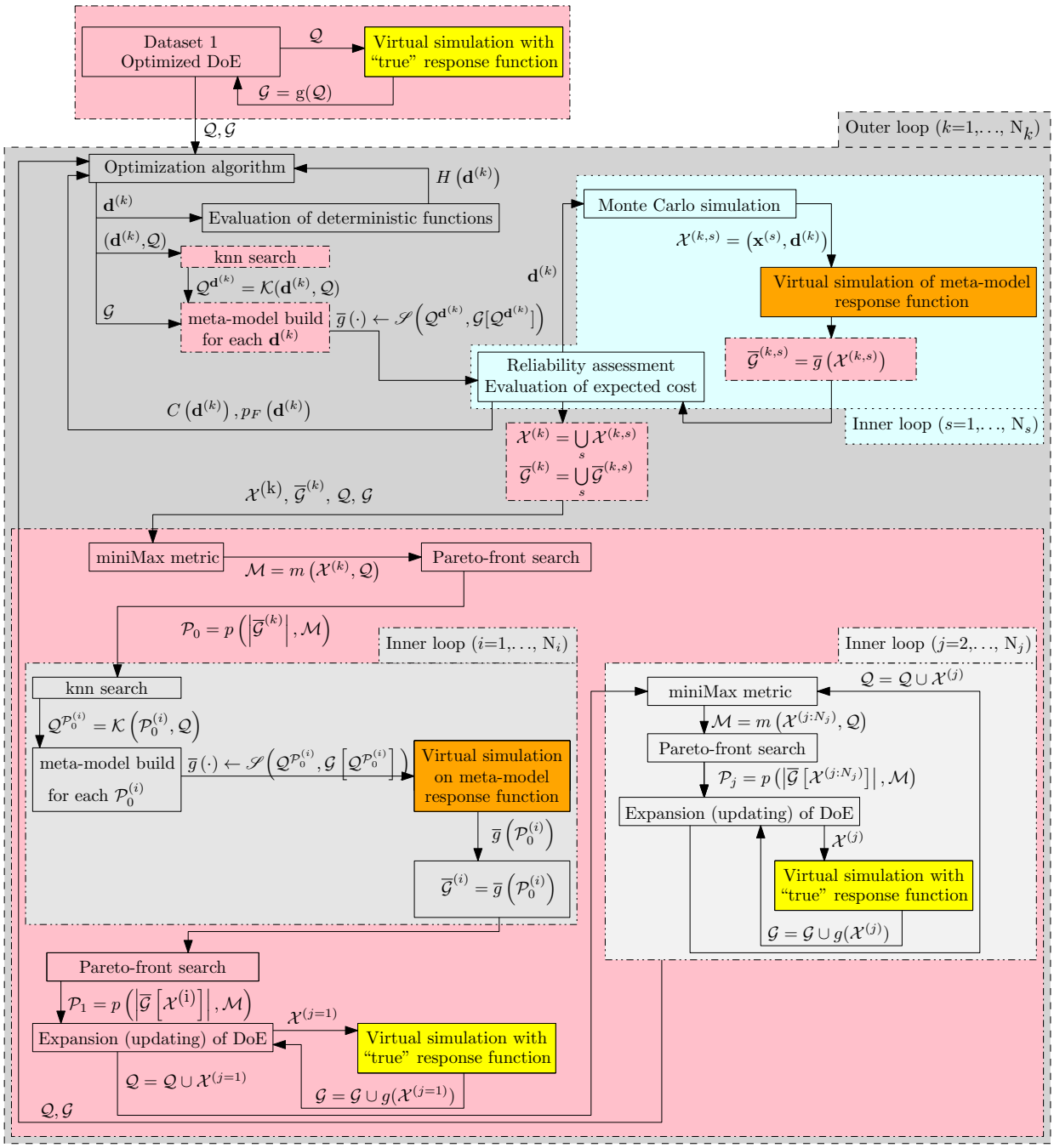

Figure 1. Schematic representation of a double-loop RBDO problem extended to the meta-model update.

sometimes called the *limit state surface*. The meta-model has to be very exact here. Generally, the accuracy of the meta-model is increased by addition of new samples into the DoE $\mathcal{Q}$ including their "true" responses of the original model. Since the original model is still not the solution of the real life problem, we use the quotation marks here. However, this response is more reliable than the meta-model response. New samples to DoE have to be added into the vicinity of the limit state; this is the first criterion. We already know the meta-model responses of the Monte Carlo samples and therefore we choose those new updating points from the Monte Carlo sample set. Every single sample from the reliability sampling method and its response value are therefore stored into $\mathcal{X}^{(k)}$ and $\overline{\mathcal{G}}^{(k)}$, respectively. These new samples should be also placed into the area with the deficient knowledge to uncover more possible limit states. For this second criterion, the miniMax metric m is used, which is the distance to the closest sample in sense of a diameter of the maximum inscribed hypersphere, and it is evaluated and stored in $\mathcal{M}$ for all Monte Carlo samples $\mathcal{X}^{(k)}$ with regard to the original DoE $\mathcal{Q}$. These two criteria are antagonistic, therefore the Pareto front $\mathcal{P}_0$ of the best incomparable solutions is calculated. It is possible to update DoE with the Pareto set (the corresponding coordinates in the design space for the Pareto front), however, the response of the meta-model has not to be accurate enough. Therefore, new meta-model is made for each point in the Pareto set so that the knn-search is carried out again and the one tenth of the closest points is chosen for the meta-model construction. These meta-models are therefore used to get a better meta-model response for the Pareto set. Since the distances to the limit state were recalculated, the Pareto front has to be found again as $\mathcal{P}_1$. In case that the meta-modeling response was good enough, the Pareto front $\mathcal{P}_1$ is the same as previous $\mathcal{P}_0$. In other case, the Pareto set is reduced. The first point of the Pareto set $\mathcal{P}_1$ is added into the final DoE $\mathcal{Q}$ and the "true" model response $g(\cdot)$ is calculated. Since the DoE is changed, the miniMax metric is again recalculated. The second criterion for the update is changed, therefore the new Pareto front $\mathcal{P}_j$ has to be found. If the j^{th} point of the $\mathcal{P}_1$ is still in the Pareto front $\mathcal{P}_j$, it is embedded into the DoE $\mathcal{Q}$ and the "true" response for this sample is computed. The DoE is therefore extended in every k^{th} step of the optimization algorithm.

3. Examples

This example utilizing mathematical functions was chosen to demonstrate the efficiency of the proposed methodology. The study of the single-objective optimization behaviour utilizing a surrogate model was carried out by (Lee and Jung, 2008) and the study of the decoupling approach by (Chen et al, 2013). The optimization problem of the original single-objective optimization problem is to

$$\begin{aligned} \min \quad & f_1 = (\mu_{X_1} - 3.7)^2 + (\mu_{X_2} - 4)^2 && (10)\\ \text{s.t.} \quad & g_1(\mathbf{X}) = -X_1 \sin(4X_1) - 1.1X_2 \sin(2X_2) && (11)\\ & g_2(\mathbf{X}) = X_1 + X_2 - 3 && (12) \end{aligned}$$

Stochastic variables X_1 and X_2 have a normal distribution with the mean values μ_{X_1} and μ_{X_2}, respectively, and both have a standard deviation equal to 0.1. They are statistically independent.

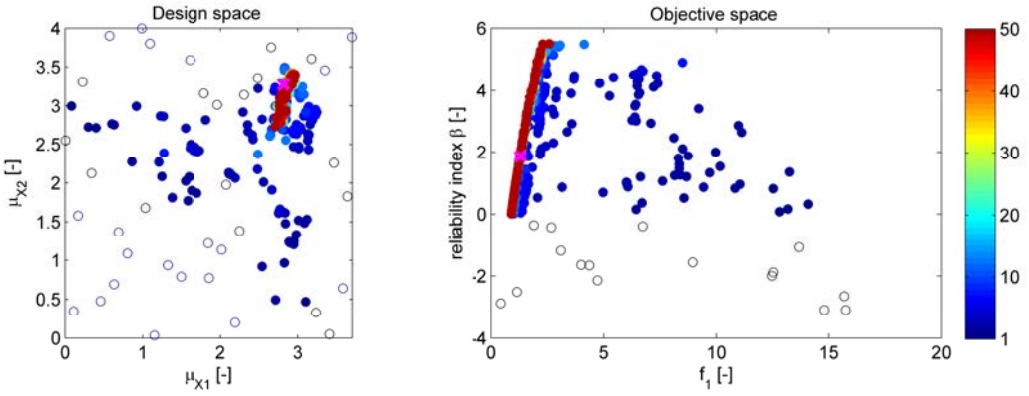

Figure 2. Optimization progression for 50 individuals and 50 generations. Every generation has a different shade depicted in the color bar on the right; the darkest blue color is used for the initial generation, claret wine for the very last generation. The Pareto front was constrained from both sides for β index from 0 to 5.5 that correspond to a failure probability 0.5 and approx. $2 \cdot 10^{-8}$, respectively. Those solutions that did not fulfilled those constraints are depicted with empty circles. The magenta cross is the single-objective optimum found by (Chen et al, 2013), which lies on the Pareto front.

Design variables are represented by both mean values μ_{X_1} and μ_{X_2}. They are in ranges of $0 \leq \mu_{X_1} \leq 3.7$ and $0 \leq \mu_{X_2} \leq 4$, respectively.

This single-objective optimization problem can be reformulated as a multi-objective one considering minimization of the first objective function and maximization of the reliability index of the given mathematical problem

$$\min \quad f_1 = (x_1 - 3.7)^2 + (x_2 - 4)^2 \tag{13}$$

$$\max \quad \beta \tag{14}$$

$$\text{considering LSF} \quad \min \begin{pmatrix} -x_1 \sin(4x_1) - 1.1 x_2 \sin(2x_2) \\ x_1 + x_2 - 3 \end{pmatrix} \tag{15}$$

$$0 \leq x_1 \leq 3.7, \quad 0 \leq x_2 \leq 4. \tag{16}$$

The algorithm utilizing local meta-models described in the previous section was used to obtain a final approximation of the Pareto set and the Pareto front. We use Non-dominated sorting genetic algorithm II (Deb, 2002) as a basis multi-objective algorithm with a simulated binary crossover operator (Deb, 1995), a Gaussian mutation operator and a tournament selection operator; probabilities of the operator utilization for creating offspring populations are 0.9, 0.5 and 1, respectively. The number of individuals was set to 50 as well as the number of total generations. The progress of the optimization is depicted in Figure 2. The convergence to the approximated the Pareto-optimal set and front is relatively fast; 20 generations would be sufficient from total 50 generations.

These approximations are compared with resulting the Pareto sets and the Pareto fronts gained by different computational methods in Figure 3. The squares symbols serve for visualisation of meta-model utilization while dots symbols are used for the original analytical function application. The analytical function was affordable for reliability-based design optimization in this benchmark

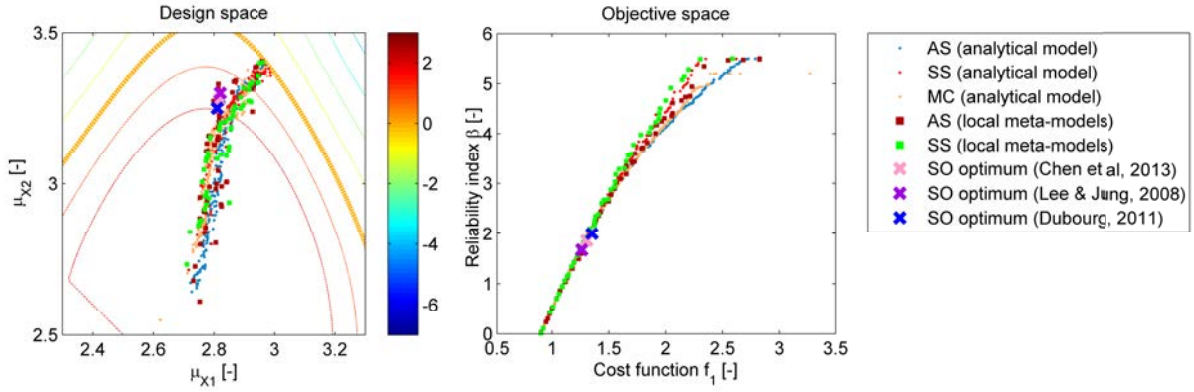

Figure 3. Comparison of Pareto set approximations (left) and Pareto front approximations (right) by several computational methods. The results without use of any meta-models are depicted by dots; an Asymptotic sampling (AS, blue dots), a Subset simulation (SS, red dots), and a Monte Carlo simulation (MC, orange dots) were used to approximate the reliability index. The results with use of local meta-models are drawn by squares; an Asymptotic sampling (claret squares), and a Subset simulation (green squares) were again utilized to approximate the reliability index. Crosses represent single objective optima found in literature; the pink cross is for the optimum taken from (Chen et al, 2013), the violet cross represents the optimum from (Lee and Jung, 2008), and the blue cross depicts the optimum taken from (Dubourg, 2011).

because its evaluation is fast; in case that a structural response is evaluated via a finite element model, a meta-model utilization is inevitable for reasonable results. The orange dot symbols represent an approximation that should be the most precise since a Monte Carlo simulation together with the original analytical function was used. A setting for the number of samples for a Monte Carlo method was contingent on the failure probability pre-evaluation $p_{F,AS}$ by an Asymptotic sampling. This probability $p_{F,AS}$ was then used to predict a number of samples for a Monte Carlo simulation $100/p_{F,AS}$ with a coefficient of variation approximately 10%. Since we used Halton sequences instead of an ordinary pseudo-random number generator, the predicted coefficient of variation should be even smaller. The visible distinction between individual methods is particularly in the upper part of the Pareto front for higher numbers of a reliability index; up to β-index equal to 3, there is no dramatic difference between individual reliability methods as well as between the analytical model and the meta-model utilization. The cross symbols serve for visualisation of single-objective optima found in literature; the original problem was restricted to the reliability index equal to two.

If the analytical model is compared with meta-models utilization and the same reliability assessment method is used, an asymptotic sampling variant has the largest discrepancy in the upper part of the Pareto front. The principal problem is in an interconnection between the asymptotic sampling and local meta-models. Large reliability indices require larger number of scaling steps of standard deviations and therefore a meta-model has to be more complex or it has to extrapolate. A problematic situation is depicted in Figure 4 on the left. Almost the whole design space is included in the sampling space for a β-index prediction and since only a small neighbourhood of the mean values was selected to construct a local meta-model, the resulting reliability index is unreliable. Therefore, a subset simulation was employed together with local meta-models since it makes use of

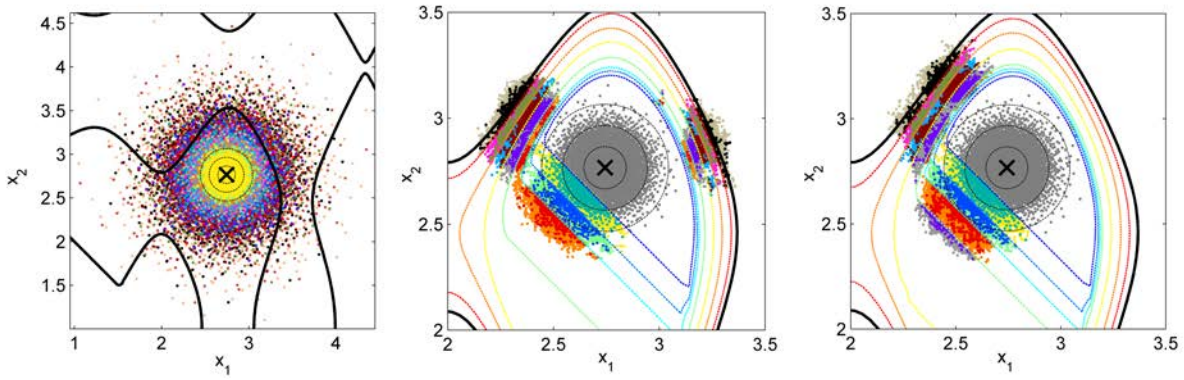

Figure 4. Comparison of sampling methods for a reliability assessment in the same mean values of variables, $\mu_{X1} = 2.74$ and $\mu_{X2} = 2.71$ (the black cross). The bold solid line is the limit state, black dashed circles mark the mean values plus one, two, and three standard deviations, respectively. An asymptotic sampling (left) needed standard deviation scaling 13 times, samples with the same standard deviation are depicted with the same colour. A subset simulation (middle, right) shows instability in selection of sampling directions. Colours of samples serve for differentiation of levels as well as with their seeds. Coloured dashed contours distinguish different $y_m^\star$ threshold levels. Each subset simulation assessment comprised eight levels.

narrower neighbourhood for meta-model training in which the only problem is the instability of the selection of the subsequent random walks directions, see Figure 4 in the middle and on the right. A subset simulation method proceeds in the steepest descent direction. A fixed portion of samples is taken from samples generated in the previous step and sorted in the ascending order serves for initial seeds in a random walk. Since a pseudo-random generator sampler does not always hit all possible directions to all most probable failure points, some important region can be omitted. This is again illustrated in Figure 4 middle and right, where two independent runs of a subset simulation with the same setting are shown.

The comparison of adaptively added support points into DoE between subset simulation samples and asymptotic sampling samples is depicted in Figure 5 by grey triangles. A subset simulation (Figure 5 right) uses narrower surroundings around the mean values for the reliability index prediction than an asymptotic sampling. An optimization procedure is moving mostly inside the safe space (depicted by orange and red contours) with the individuals representing mean values of random variables in latter generations; this is the reason for so many points added into the safe domain and around the limit state utilizing a subset simulation samples. On the other hand, an asymptotic sampling utilizes a wider space for the β-index prediction than a subset simulation (Figure 5). It is problematic for local meta-models but profitable for exploration of possible limit state locations. An update utilizing a subset simulation samples omitted the part of the limit state on the right of the design space where a potential optima can be placed. Nevertheless, the exploration by a subset simulation samples was sufficient for this benchmark and resembling Pareto sets were obtained with both simulation methods. The only but crucial difference is in β-indices approximations; a subset simulation using local meta-models seems to be more stable than an asymptotic sampling as depicted in Figure 3.

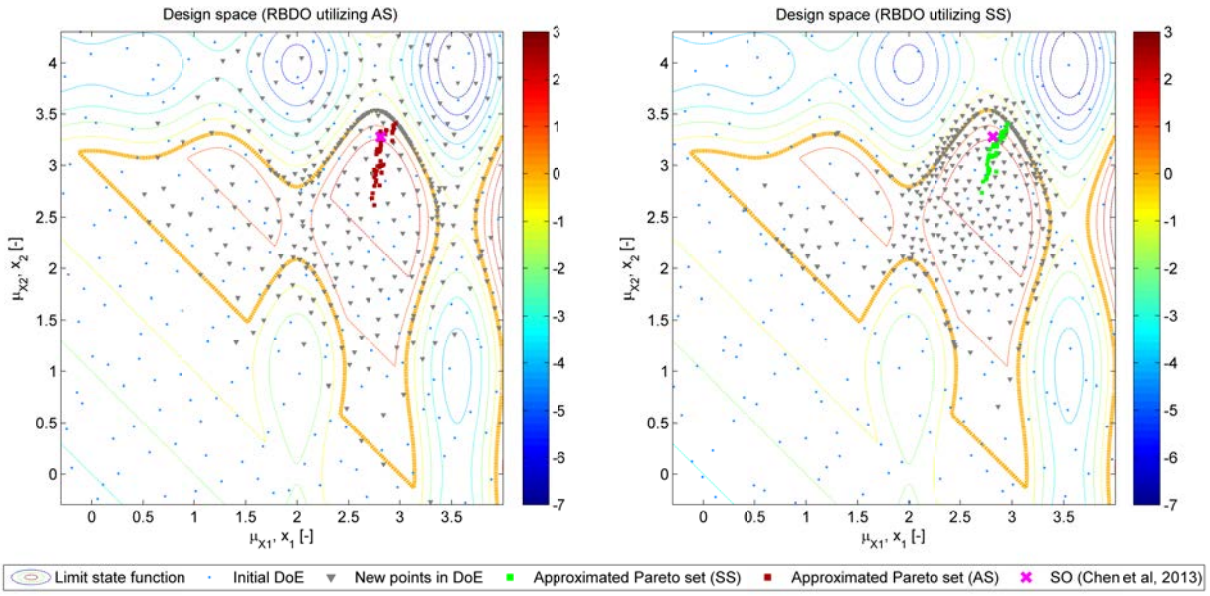

Figure 5. The design space after optimization. An initial Design of Experiments (DoE) is depicted by blue dots whereas adaptively added points to DoE are represented by grey triangles. The red squares (left) or green squares (right) serve for the Pareto set approximation selected from the last generation of NSGA-II; a single objective optimum taken from (Chen et al, 2013) used for a comparison is depicted by the magenta cross. The limit state function serves only for illustrative purposes, it was evaluated only in points of DoE. Two reliability assessment methods are compared; an Asymptotic sampling (left) enables to explore the design space in breath whereas a Subset simulation (right) concentrates samples added to DoE more narrowly around the individuals from an optimization algorithm.

4. Conclusions

Reliability-based design optimization searches for a design that is both economical and reliable. Since reliability index approximation requires plenty of structural responses computations, the most challenging task in RBDO is to evaluate a probability constraint or a probability objective. Even if any advanced simulation method is used to predict a reliability index, a meta-model utilization is necessary for designing real-life structures. One global meta-model for the whole design space needs an enormous number of support points to get a response similar to the original model. If more samples are used for the interpolating meta-model construction, the more computational effort is necessary and, moreover, numerical problems can be expected. A candidate design optimum usually does not need a whole design domain to predict safety of this design, and therefore local meta-models can be incorporated to speed-up an optimization of the designing process. We utilized two reliability assessment sampling methods together with local meta-models; an asymptotic sampling in our previous work (Pospíšilová, and Lepš, 2015) and a subset simulation in this paper. Both of these methods approximate a reliability index and a probability of failure and both methods are dependent on the shape of the limit state in the vicinity of the most probable failure point. In an

asymptotic sampling, the higher the predicted reliability index is the wider neighbourhood of mean values is employed and thus the larger local meta-model is necessary. For that reason, a subset simulation requiring narrower neighbourhood for a β-index prediction is more profitable together with local meta-models. The resulting Pareto fronts obtained with the original response model and with local meta-models almost overlap themselves, which implies that the meta-models provide sufficient accuracy of response values with beneficial speed-up of a response evaluation.

Another speed-up can be obtained via parallel evaluations. Since the proposed method is multi-level, partitioning is also available in different levels. Although we use a Non-dominated sorting genetic algorithm II, the algorithm is still population-based and reliability indices can be evaluated for each individual in parallel. Several different strategies can be used such as global parallelization, coarse grains, and fine grains, which differ in communication inside a population (Alba and Tomassini, 2002). The partitioning in population level is inherent but load balancing is complicated because of different computational efforts for different values of reliability indices. Since we use sampling methods for a reliability assessment, these samples can also be evaluated in parallel. A subset simulation utilizes a modified Metropolis algorithm with plenty of short Markov chains. All these chains can be evaluated again in parallel. Since each level in a subset simulation is dependent on the previous level exclusive of the first level, the partitioning via levels is not straightforward. An asymptotic sampling uses several Monte Carlo simulations with diverse standard deviations of random variables in Gaussian space. All these Monte Carlo levels contain a small number of samples. The minimum number of the levels is set up in advance, therefore the partitioning is possible in whole Monte Carlo simulations. The number of samples in every Monte Carlo level is known in advance as well and therefore, every Monte Carlo sample can be evaluated in parallel. The partitioning inside a sampling reliability assessment method is beneficial since the load to each threat can be decomposed with equal modular unit.

Acknowledgements

This work was supported by Czech Science Foundation, grant No. 15-07299S and by the Grant Agency of the Czech Technical University in Prague, grant No. SGS16/037/OHK1/1T/11.

References

Aoues, Y. and A. Chateauneuf. Benchmark study of numerical methods for reliability-based design optimization. *Structural and multidisciplinary optimization*, 41(2):277–294, 2010.

Hasofer, A. M., and N. C. Lind. Exact and invariant second-moment code format. *Journal of the Engineering Mechanics division*, 100(1):111–121, 1974.

Metropolis, N. and S. Ulam. The Monte Carlo method. *Journal of the American statistical association*, 44(247):335–341, 1949.

Tu, J., K. K. Choi and Y. H. Park. A new study on reliability-based design optimization. *Journal of mechanical design*, 121(4):557–564, 1999.

Enevoldsen, I. and J. D. Sørensen. Reliability-based optimization in structural engineering. *Structural safety*, 15(3):169–196, 1994.

Papadrakakis, M., N. Lagaros and V. Plevris. Design optimization of steel structures considering uncertainties. *Engineering Structures*, 27(9):1408–1418, 2005.

Beaurepaire, P., H. Jensen, G. Schuüeller and M. Valdebenito. Reliability-based optimization using bridge importance sampling. *Probabilistic Engineering Mechanics*, 34:48–57, 2013.

Valdebenito, M. and G. Schuüeller. Reliability-based optimization considering design variables of discrete size. *Engineering Structures*, 32(9):2919–2930, 2010.

Bucher, C. Asymptotic sampling for high-dimensional reliability analysis. *Probabilistic Engineering Mechanics*, 24(4):504–510, 2009.

Au, S. K. and J. L. Beck. Estimation of small failure probabilities in high dimensions by subset simulation. *Probabilistic Engineering Mechanics*, 16(4):263–277, 2001.

Montgomery, D. C. *Design and analysis of experiments*. Wiley New York, 1997.

Janouchová, E. and A. Kučerová. Competitive comparison of optimal designs of experiments for sampling-based sensitivity analysis. *Computers & Structures*, 124:47–60, 2013.

Bichon, B., M. Eldred, L. Swiler, S. Mahadevan and J. McFarland. Effcient global reliability analysis for nonlinear implicit performance functions. *AIAA journal*, 46(10):2459–2468, 2008.

Echard, B., N. Gayton and M. Lemaire. AK-MCS: An active learning reliability method combining Kriging and Monte Carlo simulation. *Structural Safety*, 33(2):145–154, 2011.

Jin, R., W. Chen and T. W. Simpson. Comparative studies of metamodelling techniques under multiple modelling criteria. *Structural and Multidisciplinary Optimization*, 23(1):1–13, 2001.

Pospíšilová, A., E. Myšáková and M. Lepš. Multi-Objective Adaptive DoE for RBDO. In D. Novák and M. Voěechovský, editors, *Proceedings of the 11th International Probabilistic Workshop*, pages 325–336. Ing. Vladislav Pokorný LITERA, Brno, Czech Republic, 2013.

Pospíšilová, A. and M. Lepš. Multi-Objective Reliability-Based Design Optimization utilizing an Adaptively Updated Surrogate Model. In Y. Tsompanakis, J. Kruis and B.H.V. Topping, editors, *Proceedings of the Fourth International Conference on Soft Computing Technology in Civil, Structural and Environmental Engineering*, Paper 8. Civil-Comp Press, Stirlingshire, UK, 2015.

Frangopol, D. M. Structural optimization using reliability concepts. *Journal of Structural Engineering*, 111:2288–2301, 1985.

Forrester, A., A. Sobester and A. Keane. *Engineering design via surrogate modelling: A practical guide*. John Wiley & Sons, 2008.

Kocis, L. and W. J. Whiten. Computational investigations of low-discrepancy sequences. *ACM Transactions on Mathematical Software TOMS*, 23(2):266–294, 1997.

Friedman, J. H., J. L. Bentley and R. A. Finkel. An algorithm for finding best matches in logarithmic expected time. *ACM Transactions on Mathematical Software (TOMS)*, 3(3):209–226, 1977.

Chen, Z., H. Qiu, L. Gao and P. Li. An optimal shifting vector approach for efficient probabilistic design. *Structural and Multidisciplinary Optimization*, 47(6):905–920, 2013.

Lee, T. H. and J. J. Jung. A sampling technique enhancing accuracy and efficiency of metamodel-based RBDO: constraint boundary sampling. *Computers & Structures*, 86(13):1463–1476, 2008.

Deb, K., A. Pratap, S. Agarwal and T. Meyarivan, A fast elitist multi-objective genetic algorithm: NSGA-II. *IEEE Transactions on Evolutionary Computation*, 6:182–197, 2002.

Deb, K. and R. B. Agrawal. Simulated binary crossover for continuous search space. *Complex Systems*, 9(3):115–148, 1995.

Chin, D. N. *Adaptive surrogate models for reliability analysis and reliability-based design optimization*. PhD thesis, Université Blaise Pascal Clermont II, 2011.

Alba, E. and M. Tomassini. Parallelism and evolutionary algorithms. *IEEE Transactions on Evolutionary Computation*, 6(5):443–462, 2002.

Application of Voronoi Weights in Monte Carlo Integration with a Given Sampling Plan

M. Vořechovský, V. Sadílek, and J. Eliáš
Faculty of Civil Engineering, Brno University of Technology, Brno, Czech republic

Abstract: The standard way to numerically calculate integrals such as the ones featured in estimation of statistical moments of functions of random variables using Monte Carlo procedure is to: (i) perform some sampling from the random vector, (ii) perform an approximation to the integrals using averages of the functions evaluated at the selected sampling points. If the N_{sim} points are selected with an equal probability (with respect to the joint distribution function) such as in Monte Carlo sampling, the averages use equal weights $1/N_{\text{sim}}$. The problem with Monte Carlo sampling is that the estimated values exhibit a large variance due to the fact that the sampling points are usually not spread uniformly over the domain of random variables. One way to improve the accuracy would be to perform a more advanced sampling.

The paper explores another way to improve the Monte Carlo integration approach: by considering unequal weights. These weights are obtained by transforming the sampling points into sampling probabilities (points within a unit hypercube), and subsequently by associating the sampling points with weights obtained as volumes of regions/cells around the sampling points within a unit hypercube. These cells are constructed by the Voronoi tessellation around each point. Supposedly, this approach could have been considered superior over the naive one because it can suppress inaccuracies stemming from clusters of sampling points.

Keywords: Monte Carlo sampling, estimation of statistical moments, Voronoi tesselation, weighted average, probability weights

1. Introduction

Monte Carlo estimation of statistical integrals is encountered in numerous applications. A typical example is the computer exploration of functions that feature random variables. These random variables form an N_{var}-dimensional vector, where N_{var} is the number of random variables considered. In computer experiments the first step is a selection of optimal sample set, i.e. selection of N_{sim} points from the N_{var} dimensional space. These points then form the sampling plan which is a $N_{\text{sim}} \times N_{\text{var}}$ matrix. The methods used for formulating the plan of experimental points are collectively known as Design of Experiments (DoE). The purpose of DoE is to provide a set of points lying inside a chosen *design domain* that are optimally distributed; the optimality of the sample depends on the nature of the problem. Various authors have suggested intuitive goals for good designs, including "good coverage", the ability to fit complex models, many levels for each factor/variable, and good projection properties. At the same time, a number of different mathematical criteria have been put forth for comparing designs.

The design of experiments is typically performed in a hyper-cubical domain of N_{var} dimensions, where each dimension/variable, U_v, ranges between zero and one ($v = 1, \ldots, N_{\text{var}}$). This *design domain* is to be covered by N_{sim} points as evenly as possible as the points within the design domain represent sampling probabilities. The probability that the i-th experimental point will be located inside some chosen subset of the domain must be equal to V_S/V_D, with V_S being the subset volume and V_D the volume of the whole domain (for unconstrained design $V_D = 1$). Whenever this is valid, the design criterion will be called *uniform*. Even though such uniformity is conceptually simple and intuitive on a qualitative level, it is somewhat complicated to describe and characterize it mathematically. Though some problems do not require this uniformity, it is the crucial assumption in Monte-Carlo integration and its violation may lead to significant errors (Eliáš and Vořechovský, 2016; Vořechovský and Eliáš, 2015).

There exist many other criteria of optimality of the sampling plan: e.g. the Audze-Eglājs (AE) criterion (Audze and Eglājs, 1977) later generalized into the so-called ϕ criterion, the Euclidean MaxiMin and MiniMax distance between points, various measures of discrepancy, criteria based on correlation (orthogonality), designs maximizing entropy and many others. It should also be noted that an experimental design can be also obtained via so-called "quasi-random" low-discrepancy sequences (deterministic versions of MC analysis) that can often achieve reasonably uniform sample placement in hypercubes (Niederreiter, Halton, Sobol', Hammersley, etc.).

As mentioned above, the selection of the sampling points is a crucial step when evaluating approximations to integrals as is performed in Monte Carlo simulations (numerical integration), where equal sampling probabilities inside the design domain are required.

In this article, it is assumed that the sampling points have already been selected and they are not spread uniformly over the design domain. A typical example may be a sample selected using crude Monte Carlo sampling. The article considers the possibility to improve quality of Monte Carlo estimation with such a given sample. The only possibility to improve the estimations of the integrals is to vary the weights associated with individual sampling points. Motivated by the MiniMax criterion of optimality and also by various numerical integrating schemes, we explore the possibility to improve the quality of statistical estimations using Voronoi tessellation, i.e. a particular form of partitioning of the design domain around given sampling points. The *design domain* to be partitioned is the unit hypercube described above and therefore the volumes around individual sampling points represent weights (probabilities) to be used in the weighted averages that estimate the integrals.

2. Statistical Moment Estimation Using Monte Carlo Sampling

As mentioned in the introduction, one of the frequent uses of DoE is *statistical sampling* for Monte Carlo integration. We present the application of statistical sampling to the problem of estimating statistical moments of a function of random variables. In particular, a deterministic function, $Z = g(\boldsymbol{X})$, is considered, which can be a computational model or a physical experiment. Z is the uncertain response variable (or generally a vector of the outputs). The vector $\boldsymbol{X} \in \mathbb{R}^{N_{\text{var}}}$ is considered to be a random vector of N_{var} continuous marginals (input random variables describing uncertainties/randomness) with a given joint probability density function (PDF).

Estimation of the statistical moments of variable $Z = g(\boldsymbol{X})$ is, in fact, an estimation of integrals over domains of random variables weighted by a given joint PDF of the input random vector, $f_{\boldsymbol{X}}(\boldsymbol{x})$. We seek the statistical parameters of $Z = g(\boldsymbol{X})$ in the form of the following integral:

$$\mathrm{E}[S[g(\boldsymbol{X})]] = \int_{-\infty}^{\infty} \dots \int_{-\infty}^{\infty} S[g(\boldsymbol{x})] \, \mathrm{d}F_{\boldsymbol{X}}(\boldsymbol{x}) \tag{1}$$

where $\mathrm{d}F_{\boldsymbol{X}}(\boldsymbol{x}) = f_{\boldsymbol{X}}(\boldsymbol{x}) \cdot \mathrm{d}x_1 \, \mathrm{d}x_2 \, \cdots \, \mathrm{d}x_{N_{\mathrm{var}}}$ is the infinitesimal probability ($F_{\boldsymbol{X}}$ denotes the joint cumulative density function) and where the particular form of the function $S[g(\cdot)]$ depends on the statistical parameter of interest. For example, to gain the mean value of $g(\cdot)$, $S[g(\cdot)] = g(\cdot)$; higher statistical moments of Z can be obtained by integrating polynomials of $g(\cdot)$. The probability of failure (an event defined as $g(\cdot) < 0$) is obtained in a similar manner: $S[\cdot]$ is replaced by the Heaviside function (or indicator function) $H[-g(\boldsymbol{X})]$, which equals one for a failure event ($g < 0$) and zero otherwise. In this way, the domain of integration of the PDF is limited to the failure domain.

In Monte Carlo sampling, which is the most prevalent statistical sampling technique, the above integrals are numerically estimated using the following procedure: (i) draw N_{sim} realizations of $\boldsymbol{X}$ that share the same probability of occurrence $1/N_{\mathrm{sim}}$ by using its joint distribution $f_{\boldsymbol{X}}(\boldsymbol{x})$; (ii) compute the same number of output realizations of $S[g(\cdot)]$; and (iii) estimate the desired parameters as arithmetical averages. We now limit ourselves to independent random variables in vector $\boldsymbol{X}$. The aspect of the correct representation of the target joint PDF of the inputs mentioned in item (i) is absolutely crucial. Practically, this can be achieved by reproducing a *uniform distribution* in the design space (unit hypercube) that represents the space of sampling probabilities.

Assume now a random vector $\boldsymbol{U}$ that is selected from a multivariate uniform distribution in such a way that its independent marginal variables U_v, $v = 1, \dots, N_{\mathrm{var}}$, are uniform over intervals $(0; 1)$. A vector with such a multivariate distribution is said to have an "independence copula" (Nelsen, 2006)

$$C(u_1, \dots, u_{N_{\mathrm{var}}}) = \mathrm{P}(U_1 \leq u_1, \dots, U_{N_{\mathrm{var}}} \leq u_{N_{\mathrm{var}}}) = \prod_{v=1}^{N_{\mathrm{var}}} u_v \tag{2}$$

These uniform variables can be seen as sampling probabilities: $F_{X_v} = U_v$. The joint cumulative distribution function then reads $F_{\boldsymbol{X}}(\boldsymbol{x}) = \prod_v F_{X_v} = \prod_v U_v$, and $\mathrm{d}F_{\boldsymbol{X}}(\boldsymbol{x}) = \prod_v \mathrm{d}U_v$. The individual random variables can be obtained by inverse transformations

$$\{X_1, \dots, X_{N_{\mathrm{var}}}\} = \{F_1^{-1}(U_1), \dots, F_{N_{\mathrm{var}}}^{-1}(U_{N_{\mathrm{var}}})\} \tag{3}$$

and similarly the realizations of the original random variables are obtained by the component-wise inverse distribution function of a point $\boldsymbol{u}$ (a realization of $\boldsymbol{U}$) representing a sampling probability

$$\boldsymbol{x} = \{x_1, \dots, x_{N_{\mathrm{var}}}\} = \{F_1^{-1}(u_1), \dots, F_{N_{\mathrm{var}}}^{-1}(u_{N_{\mathrm{var}}})\} \tag{4}$$

With the help of this transformation from the original to the uniform joint PDF, the above integral in Eq. (1) can be rewritten as

$$\begin{aligned} \mathrm{E}[S\left[g\left(\boldsymbol{X}\right)\right]] &= \int_0^1 \dots \int_0^1 S\left[g\left(\boldsymbol{x}\right)\right] \, \mathrm{d}C(u_1, \dots, u_{N_{\mathrm{var}}}) \\ &= \int_{[0,1]^{N_{\mathrm{var}}}} S\left[g\left(\boldsymbol{x}\right)\right] \prod_{v=1}^{N_{\mathrm{var}}} \mathrm{d}U_v \end{aligned} \tag{5}$$

so that the integration is performed over a unit hypercube with uniform unit density.

We now assume an estimate of this integral by the following statistic (the average computed using N_{sim} realizations of $\boldsymbol{U}$, namely the sampling points $\boldsymbol{u}_j$ $(j = 1, \dots, N_{\mathrm{sim}})$)

$$\mathrm{E}[S\left[g\left(\boldsymbol{X}\right)\right]] \approx \frac{1}{N_{\mathrm{sim}}} \sum_{i=1}^{N_{\mathrm{sim}}} S\left[g(\boldsymbol{x}_i)\right] \tag{6}$$

where the sampling points $\boldsymbol{x}_i = \{x_{i,1}, \dots, x_{i,v}, \dots, x_{i,N_{\mathrm{var}}}\}$ are selected using the transformation in Eq. (4), i.e. $x_{i,v} = F_v^{-1}(u_{i,v})$, in which we assume that each of the N_{sim} sampling points $\boldsymbol{u}_i$ $(i = 1, \dots, N_{\mathrm{sim}})$ were selected with the same probability of $1/N_{\mathrm{sim}}$. Violation of the uniformity of the distribution of points $\boldsymbol{u}_i$ in the unit hypercube may lead to erroneous estimations of the integrals.

If the sampling points are not selected carefully with respect to equal probabilities in the design domain, the possibility to improve the accuracy in Eq. (6) is to use weights different from $1/N_{\mathrm{sim}}$. These weights reflect the probability content of the cells around individual sampling points

$$\mathrm{E}[S\left[g\left(\boldsymbol{X}\right)\right]] \approx \sum_{i=1}^{N_{\mathrm{sim}}} S\left[g(\boldsymbol{x}_i)\right] \cdot w_i \tag{7}$$

The proposed approach aims at finding appropriate weights that are calculated considering the spatial distribution of the points. Obviously, unvisited regions of the design domain can not be explored by a nonuniform design. Partitioning the space into cells around the given sampling points may help to reduce probabilities associated with points that are participating in clusters of points. Voronoi tessellation has been selected for partitioning of the design space into volumes that are used as the weights w_i, $i = 1, \dots, N_{\mathrm{sim}}$. The following section describes the Voronoi tessellation procedures.

3. Weights Obtained as Volumes of Voronoi Regions

The weights associated with the design points are considered as volumes of Voronoi regions (Aurenhammer, 1991) computed on the sampling points. The Voronoi tessellation in N_{var}-dimensional space results in N_{sim} convex polyhedrons $\mathcal{V}_i$ that encloses all the points that are closer to i-th

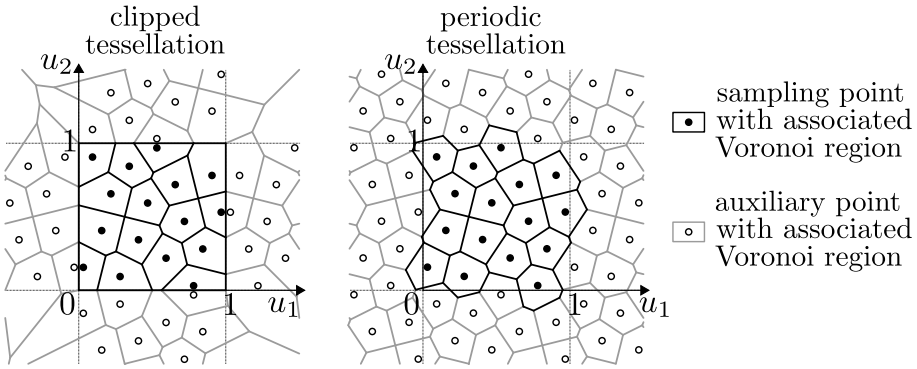

Figure 1. Example of clipped and periodic tessellation for $N_{\mathrm{var}} = 2$ and $N_{\mathrm{sim}} = 16$ with help of reflected and periodically repeated auxiliary points, respectively.

sampling point than any other. Defining the distance of point $\boldsymbol{u}$ from sampling point $\boldsymbol{u}_i$ as $d_i(\boldsymbol{u})$, the Voronoi region associated with i-th sampling point can be formally defined as

$$\mathcal{V}_i = \left\{ \boldsymbol{u} \in \mathbb{R}^{N_{\mathrm{var}}} \mid \forall\, j \neq i : d_i(\boldsymbol{u}) \leq d_j(\boldsymbol{u}) \right\} \tag{8}$$

Two alternatives of Voronoi tessellation that differ in the boundary regions are investigated:

– *clipped* Voronoi tessellation that is limited to the unit hypercube only

$$\mathcal{V}_i = \left\{ \boldsymbol{u} \in \langle 0,\, 1 \rangle^{N_{\mathrm{var}}} \mid \forall\, j \neq i : d_i(\boldsymbol{u}) \leq d_j(\boldsymbol{u}) \right\} \tag{9}$$

– *periodic* Voronoi tessellation which assumes that every sampling point is periodically repeated in the space along all the dimensions.

These two different concepts are demonstrated in Figure 1. The reason for studying the *periodic* tessellation is that the authors have shown recently (Eliáš and Vořechovský, 2016; Vořechovský and Eliáš, 2015) that the presence of boundaries in the hypercubical design domain cause problems. Briefly, one may think of a problem of packing (hyper)balls into a (hyper)cube. It is clear that the boundary is responsible for a kind of wall-effect. It has been shown (Eliáš and Vořechovský, 2016; Vořechovský and Eliáš, 2015) that this problem can be removed by considering periodic extension of the design domain. The balls then permeate through the boundaries without interacting with them, see Figure 1 right.

The *clipped* Voronoi diagrams (Chan et al., 1995; Yan et al., 2013) are used mostly for construction of meshes and therefore available software to compute such tessellation is limited to two and three dimensional space. A similar situation exists for *periodic* Voronoi tessellation (Yan et al., 2011; Rycroft, 2009). In the field of design of experiments more than three variables (factors) can be present and therefore the tessellation must be performed in higher dimensions. In this contribution, Qhull software (Barber et al., 1996) is utilized for both clipped and periodic tessellations because it can compute Voronoi tessellation for arbitrary dimension. On the other hand, it cannot work directly with neither *clipped* nor *periodic* boundary condition and therefore simple tricks are used.

These tricks consist in manipulations of the design domain (together with the sampling points contained) by adding new design domains around it. In order to obtain the *clipped* structure, the design domain is extended by reflecting the original design domain along each dimension. There are two reflections of the original unit interval along each dimension to obtain intervals $\langle -1,\, 0\rangle$ and $\langle 1,\, 2\rangle$. Therefore, the tessellation is performed on $N_{\text{sim}}\left(1+2^{N_{\text{var}}}\right)$ points. The use of reflection automatically provides edges between cells that coincide with the boundary of the original design domain and therefore the volumes outside the design domain can be ignored. The use of reflection to obtain clipped tessellation was proposed in (Pronzato and Müller, 2012).

The *periodic* structure is obtained by periodic extension (replication) of the original design domain along each direction and additionally the replication must be performed to obtain all the "corner" domains to fill a hypercube $\langle -1,\, 0\rangle^{N_{\text{var}}}$. Therefore, $N_{\text{sim}}\cdot 3^{N_{\text{var}}}$ points in total are used for the periodic tessellation.

The computational times needed for the both tessellation types can be substantially reduced if it involves only reflected or periodically repeated points that are close to the original hypercube, because only these points affects the tessellation inside the hypercube. Unfortunately, no effective algorithm has been developed yet to identify such points and therefore the full set of points must be involved for certainty.

In both alternatives, the weights for individual sampling points are the volumes of regions surrounding points. There are three algorithms available for the volume computation: (i) direct integration, (ii) Monte-Carlo integration and (iii) division into simplexes for which analytical formula is available. The first two algorithms are nicely elucidated in (Ong et al., 2003). Here, we perform the third algorithm. Each Voronoi region is (with a help of the Qhull) divided into simplexes. Each simplex has $N_{\text{var}}+1$ vertices denoted $\boldsymbol{v}_i$. The total volume of the region is simply the sum of simplex volumes, that are calculated based on the determinant of coordinate matrix.

$$V_{\text{simplex}} = \left| \frac{1}{N_{\text{var}}!} \begin{pmatrix} \boldsymbol{v}_1 - \boldsymbol{v}_0 \\ \boldsymbol{v}_2 - \boldsymbol{v}_0 \\ \vdots \\ \boldsymbol{v}_{N_{\text{var}}} - \boldsymbol{v}_0 \end{pmatrix} \right| \tag{10}$$

These volumes are used directly as weights of sampling points enclosed withing these cells.

4. Frequency Analysis of Weights

It turns out to be important to see (i) whether the weights are very scattered compared to $1/N_{\text{sim}}$ and, (ii) whether their magnitude tend to depend on the position inside the domain. This is achieved by studying $N_{\text{run}} = 1000$ realizations of samples, each having N_{sim} points within an N_{var}-dimensional hypercube. For each sample, both types of Voronoi tessellation is constructed and the weights are statistically processed.

The results will be presented for two sampling schemes: the classical (crude) Monte Carlo sampling without any optimization (MC-RAND) and LHS (Latin Hypercube Sampling) optimized using the periodic criterion (LHS-PAE). PAE stands for an enhanced version of the Audze-Eglais criterion, see (Eliáš and Vořechovský, 2016; Vořechovský and Eliáš, 2015).

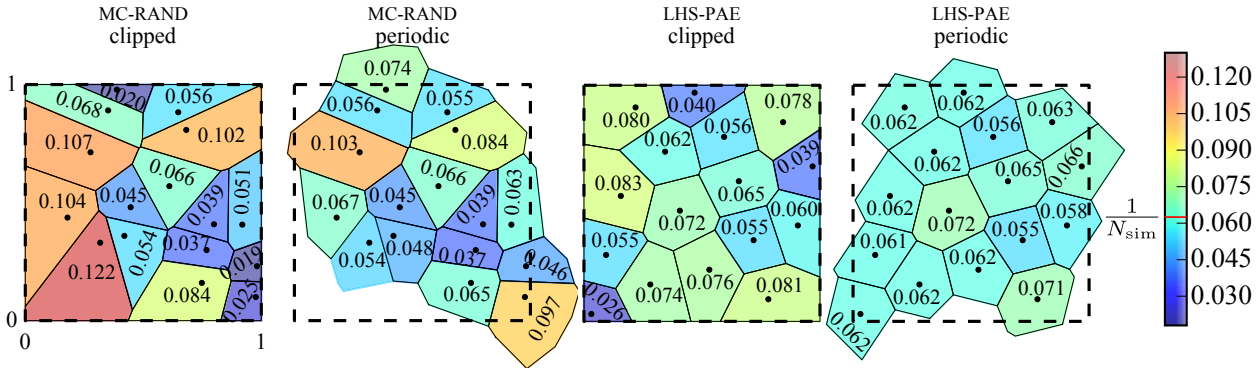

Figure 2. Voronoi weights for MC-RAND and LHS-PAE sampling plans ($N_{\text{var}} = 2$, $N_{\text{sim}} = 16$). Comparison of the *clipped* and *periodic* tessellations.

Figure 2 shows one sample (N_{sim}=16) of a bivariate random vector U_v for both sampling schemes. For the two sampling schemes, both types of Voronoi diagrams (*clipped* and *periodic*) are constructed and visualized with colors depending on the area. The LHS-PAE sampling plans show more uniform distribution of points because the PAE-optimized LH-sampling better avoids clustering and limit the occurrence of empty regions. Therefore, the cells in LHS-PAE have similar volumes and the sampling points are closer to the centers of Voronoi regions. The small differences among weights in LHS-PAE with *periodic* tessellation suggest that weighting will not make much difference in comparison with integrals evaluated using equal weights $1/N_{\text{sim}}$. The MC-RAND sampling plans suffer from point clustering and therefore, high variability in volumes of the Voronoi cells is observed. It should be noticed that the choice of tessellation (*clipped* vs. *periodic*) affects only the boundary regions while the central part of the hypercube is identical.

In order to judge about the spatial distribution of weights within the design domain, the above-mentioned N_{run}=1000 realizations of samples accompanied by Voronoi tessellations were prepared and for each spatial location, the mean value and standard deviation of weights occurring at that location have been calculated. The weights (volumes of Voronoi regions V_{simplex} in a hypercube) depend on the type of tessellation but they are independent of the sampling method (MC vs. LHS). The bivariate histograms in Figure 3 document the dependency of the mean value and the standard deviation of Voronoi region volumes on the position of the sampling point in a square. In the case of *clipped* tessellation, both the mean value and the standard deviation of weights are not uniform in the hypercube. Three zones can be distinguished: (a) the boundary region where the mean value (shown in blue) of weights is underestimated. The boundary strip is followed/balanced by (b) zone parallel to the boundary where the weights are overestimated (see the yellow to red color) and finally, (c) the bulk zone sufficiently far from the boundary, where the weights (volumes) are constant on average. The width of the two boundary zones is decreasing with increasing sample size N_{sim}.

Such a biased representation of different regions in the hypercube partitioned by the *clipped* tessellation must have consequences in Monte Carlo integration. If the points are sampled uniformly, and that is indeed the case of both MC-RAND and LHS-PAE, some error must be introduced due to introduction of nonuniform weighting. If the functions are sensitive to inaccuracies in representation

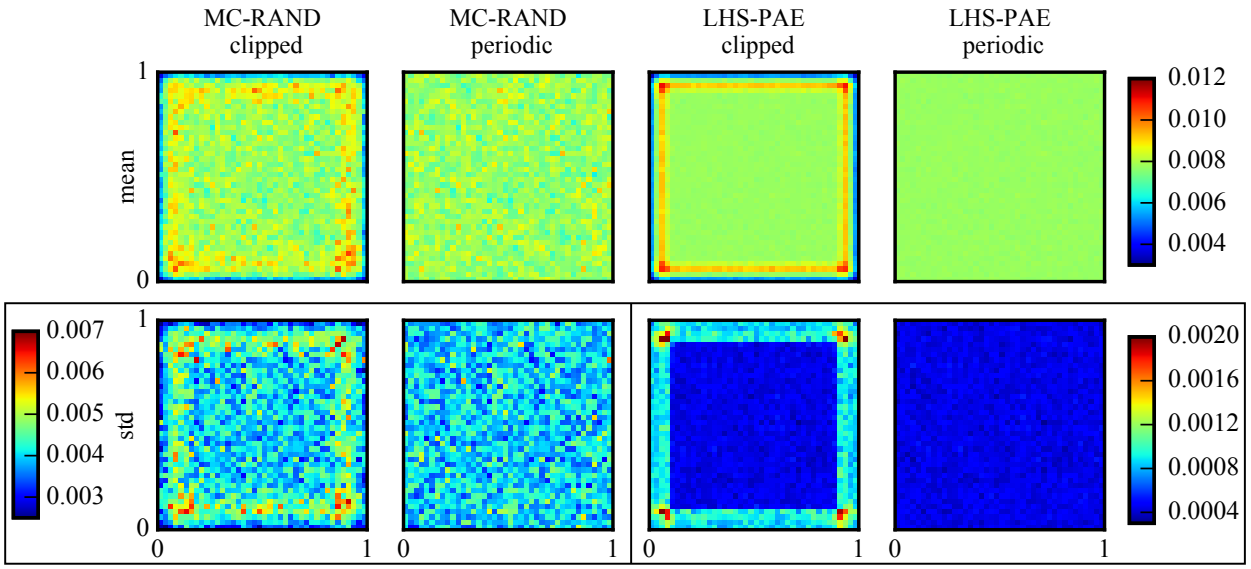

Figure 3. Bivariate histograms of the mean value and the standard deviation of cell volumes for both sampling plans and both tessellation alternatives ($N_{\text{var}} = 2$, $N_{\text{sim}} = 16$ and $N_{\text{run}} = 1000$ realizations).

of the boundary regions, their weighted MC integration may yield biased results. Therefore we conclude that the *clipped* tessellation generally should not be used for weighting in MC integration.

The *periodic* tessellation provides more promising bivariate histograms: no bias around the boundaries is visible for both MC-RAND and LHS-PAE sampling schemes. The statistics of the weights do not depend systematically on the position in the hypercube.

5. Numerical Examples of MC Integration & Discussion

This section studies whether weighting in MC integrals based on the Voronoi tessellation improves the quality of the estimates. Three basic transformations g of standard independent Gaussian random variables X_v, $v = 1, \ldots, N_{\text{var}}$ have been selected for the numerical study. The following array presents formulas of the three functions (first column), the analytical solutions for the mean values (second column) and standard deviations (third column):

$$Z_{\text{sum}} = g_{\text{sum}}(\boldsymbol{X}) = \sum_{v=1}^{N_{\text{var}}} X_v^2 \qquad \mu_{\text{sum}} = N_{\text{var}} \qquad \sigma_{\text{sum}} = \sqrt{2N_{\text{var}}} \tag{11}$$

$$Z_{\text{exp}} = g_{\text{exp}}(\boldsymbol{X}) = \sum_{v=1}^{N_{\text{var}}} \exp(-X_v^2) \qquad \mu_{\text{exp}} = \frac{\sqrt{3}}{3} N_{\text{var}} \qquad \sigma_{\text{exp}} = \sqrt{N_{\text{var}}} \sqrt{\frac{\sqrt{5}}{5} - \frac{1}{3}} \tag{12}$$

$$Z_{\text{prod}} = g_{\text{prod}}(\boldsymbol{X}) = \prod_{v=1}^{N_{\text{var}}} X_v \qquad \mu_{\text{prod}} = 0 \qquad \sigma_{\text{prod}} = 1 \tag{13}$$

The two sampling schemes studied above (MC-RAND and LHS-PAE) have been used to prepare $N_{\text{run}} = 1000$ sampling plans for various sample sizes N_{sim} and dimensions N_{var}. Each sample set is accompanied by both types of tessellations – *periodic* and *clipped*.

The performance of the approaches to estimate the integrals will be demonstrated by showing their ability to estimate the mean value and standard deviation of the transformed variable $Z = g(\boldsymbol{X})$. The estimated mean value and standard deviation are denoted as $\bar{\mu}_Z$ and $\bar{\sigma}_Z$, respectively:

$$\bar{\mu}_Z = \sum_{i=1}^{N_{\text{sim}}} g(\boldsymbol{x}_i) \cdot w_i \tag{14}$$

$$(\bar{\sigma}_Z)^2 = \frac{N_{\text{sim}}}{N_{\text{sim}} - 1} \sum_{i=1}^{N_{\text{sim}}} (g(\boldsymbol{x}_i) - \bar{\mu}_Z)^2 \cdot w_i \tag{15}$$

The term $N_{\text{sim}}/(N_{\text{sim}} - 1)$ is a standard adjustment that makes the sample variance unbiased. Analogical adjustment terms are known for higher statistical moments of random variables, see e.g. (Cramér, 1945). When the individual sampling points have unequal weights, similar correction terms have recently been derived (Rimoldini, 2014). The corrections use terms calculated as sums of pth powers of weights: $V_p = \sum_{i=1}^{N_{\text{sim}}} w_i^p$. For example, in the case of estimation of variance $(\bar{\sigma}_Z)^2$, the term $N_{\text{sim}}/(N_{\text{sim}} - 1)$ is replaced by $V_1^2/\left(V_1^2 - V_2\right)$. The corresponding unweighted form can be achieved by direct substitution of $w_i = 1/N_{\text{sim}}$. This results in $V_p = 1/{N_{\text{sim}}}^{p-1}$ (or simply $V_p = N_{\text{sim}}$) for all p, leading to the known formulas for sample-size unbiased moments (Cramér, 1945). We note that in the case of functions studied in the present paper, the enhancement using V_p makes almost no change compared to the results obtained with considering all $V_p = N_{\text{sim}}$.

Three approaches to the weighting in Monte-Carlo type numerical integration are compared:

- *uniform* weights that assign each design point a constant weight $w_i = 1/N_{\text{sim}}$,
- *clipped* Voronoi weights that assign weights according to the "volumes" of Voronoi regions obtained using the *clipped* tessellation,
- *periodic* Voronoi weights that use *periodic* Voronoi tessellation.

Based on the study focused on spatial distribution of weights within the design domain, one might expect that the *periodic* tessellation may or may not deliver improvement while the *clipped* tessellation must lead to biased MC integration when used to perform weighting. The results of numerical study are presented in Figure 4 for all three functions, two estimated statistical moments, two sampling schemes and three alternatives of weighting. Each alternative presents a line of the average with a scatter-band (shaded area) obtained as the mean value ± one standard deviation – both computed using $N_{\text{run}} = 1000$ realizations. A three dimensional domain has been selected: $N_{\text{var}} = 3$.

The standard procedure employing *uniform* weights leads to convergence to the exact value as expected. The estimator variance decreases with increasing N_{sim}.

The *clipped* Voronoi weights provide poor estimates as expected. Although the variance is generally lower than in case of *uniform* weights, the average converges significantly slower. The

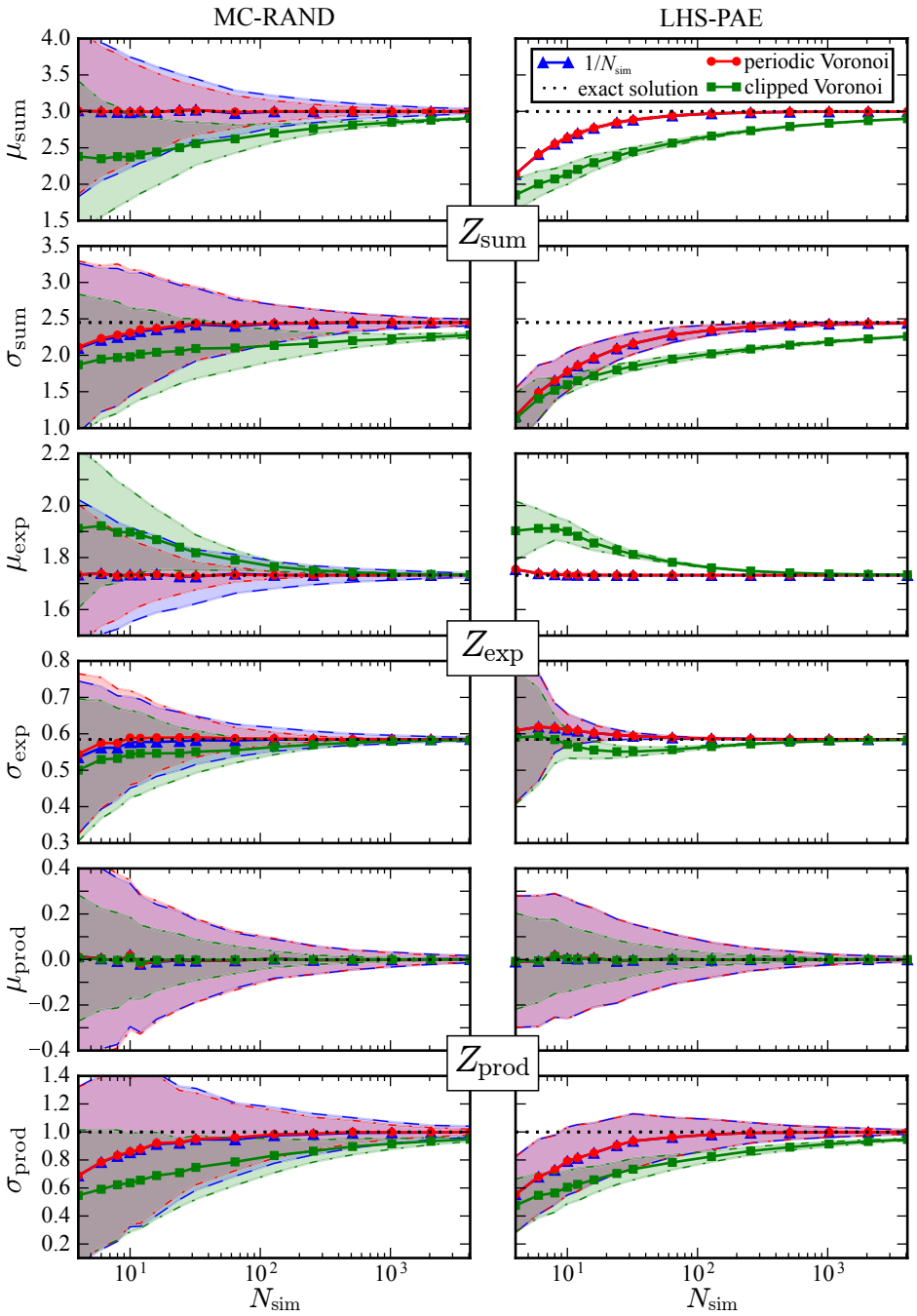

Figure 4. Convergence of the estimated mean values and standard deviations of the three transformed variables g_{sum}, g_{exp} and g_{prod}, computed for $N_{\text{var}} = 3$. Left column: MC-RAND, Right column: LHS-PAE.

reason is the improper volumes of boundary cells, the boundary zones are underestimated followed by the overestimated zone (see e.g. the bivariate histograms in Figure 3). It eventually also converges to the correct solution as the biased boundary region gets narrower with increasing N_{sim}.

Application of the *periodic* Voronoi diagram to obtain weights for calculation of statistics of the transformed random variable Z provides, on average, similar convergence to the exact value as observed with *uniform* weights. Also the variance of the estimator is similar. In fact, the variance of estimators seems to be slightly improved for MC-RAND sampling scheme, however, considering the relatively high computational cost related to evaluation of periodic Voronoi weights, the improvement is not worth the effort.

6. Conclusions

This paper studied two alternatives of Voronoi tessellation in an attempt to improve Monte-Carlo integration for small N_{sim} by weighting individual sampling points. The weights were obtained as volumes of the Voronoi cells – the regions surrounding the sampling points in the design domain (unit hypercube).

Weighting using the *clipped* Voronoi tessellation (a tessellation limited to the design domain) was found inapplicable due to problems related to the presence of boundaries of the unit hypercube. The tessellation results in systematic appearance of underestimated regions near the boundaries followed by regions with over-weighted regions.

The *periodic* tessellation slightly improves the integration if the location of sampling points is not optimized such as in the case for crude Monte Carlo sampling. However, the minor improvement does not outweigh the additional effort spend on the evaluation of the volumes of the regions and the tessellation.

Acknowledgements

The authors acknowledge financial support provided by projects nos. 16-22230S and GA14-10930 “SPADD” supported by the Czech Science Foundation.

References

Audze, P. and V. Eglājs. New approach for planning out of experiments. In *Problems of Dynamics and Strengths*, 35:104–107, Russian, 1977.

Aurenhammer, F. Voronoi Diagrams - A Survey of a Fundamental Geometric Data Structure. *ACM Computing Surveys*, 23(3):343–405, 1991.

Barber, C.B., D.P. Dobkin and H.T. Huhdanpaa. The Quickhull algorithm for convex hulls. *ACM Transactions on Mathematical Software*, 22(4):469–483, 1996. http://www.qhull.org

Chan, T.M.Y., J. Snoeyink and Ch.K. Yap. Output-sensitive construction of polytopes in four dimensions and clipped Voronoi diagrams in three. *In: Proceedings of the sixth annual ACM–SIAM symposium on discrete algorithms*, 282–291, 2013.

Cramér, H. *Mathematical Methods of Statistics*. Princeton landmarks in mathematics and physics, 1945.

Eliáš, J. and M. Vořechovský. Modification of the Audze–Eglajs criterion to achieve a uniform distribution of sampling points. *Advances in Engineering Software*, under review.

Nelsen, R.B. *An Introduction to Copulas*, volume XIV of *Springer Series in Statistics*. Springer, 2nd edition, 2006.

Ong, H.L., H.C. Huang and W.M. Huin. Finding the exact volume of a polyhedron. *Advances in Engineering Software*, 34(6):351–356, 2003. doi:10.1016/S0965-9978(03)00030-9.

Pronzato, L. and W.G. Müller. Design of computer experiments: space filling and beyond. *Statistics and Computing*, 22(3):681–701, 2012. doi:10.1007/s11222-011-9242-3.

Rimoldini, L. Weighted skewness and kurtosis unbiased by sample size and Gaussian uncertainties. *Astronomy and Computing*, 5:1–8, 2014. doi:10.1016/j.ascom.2014.02.001.

Rycroft, Ch.H. Voro++: a three-dimensional Voronoi cell library in C++. Documentation of the Voro++ software, 2009.

Vořechovský, M. and J. Eliáš. Improved formulation of AudzeEglajs criterion for space-filling designs.In: *Proc. of 12th International Conference on Applications of Statistics and Probability in Civil Engineering*, ICASP12, Vancouver, Canada, July 12–15, 2015.

Yan, D.-M., K. Wang, B. Lévy and L. Alonso. Computing 2D Periodic Centroidal Voronoi Tessellation. *In: 8th International Symposium on Voronoi Diagrams in Science and Engineering*, 2011. doi:10.1109/ISVD.2011.31.

Yan, D.-M., W. Wang, B. Lévy and Y. Liu. Efficient Computation of Clipped Voronoi Diagram for Mesh Generation. *Computer-Aided Design*, 45(4):843–852, 2013. doi:10.1016/j.cad.2011.09.004.

Static Analysis of Structural Systems with Uncertain Parameters Using Probability-Box

Naijia Xiao[1)], Robert Mullen[2)] and Rafi Muhanna[1)]
[1)] *School of Civil and Environmental Engineering, Georgia Institute of Technology, Atlanta, GA 30332, USA, {naijia.xiao, rafi.muhanna}@gatech.edu*
[2)] *Department of Civil and Environmental Engineering, University of South Carolina, Columbia, SC 29208, USA, rlm@sc.edu*

Abstract: A static analysis of structural systems with uncertain parameters is presented. Uncertain load and material parameters of the system are modeled by probability-boxes (or p-boxes), which do not require complete information about the statistical nature of the underlying random process. Arithmetic operations on p-boxes yield guaranteed lower and upper bounds on the probability distribution of the solution, regardless of the dependency among those uncertain parameters. In this paper, both load and material uncertainties for the first time are handled using a non-Monte-Carlo p-box approach that guarantees to enclose the exact solution. The governing linear equations are solved by an iterative approach that exploits a fixed-point formulation of the system of linear equations. In order to reduce overestimation and obtain the tightest bounds possible, a decomposition of the stiffness matrix of the structure is adopted. The resulting formulation gives guaranteed lower and upper bounds of the probability distribution of the structural responses, at a high computational efficiency and a low overestimation level.

Keywords: uncertainty, probability-box, matrix decomposition, iterative enclosure method

1. Introduction

Real systems contains uncertainties that cause discrepancy between the performance of the theoretical model and the real system (Fernández-Martínez et al., 2013). Conventional treatment of uncertainties involves probability theory, which models uncertain parameter in the system using random variables (Kolmogorov, 1950). This probabilistic approach successfully handles problems when the statistical nature of the uncertainty is well understood. Thus it is suitable when only allegoric uncertainties are present. However, when the nature of the uncertainty is not well understood and epistemic uncertainties are present (Moens and Hanss, 2011; Zhang, 2005), alternative approaches are proposed, such as Bayesian network (Igusa et al., 2002; Soize, 2013), fuzzy sets (Dehghan et al., 2006; Klir and Wierman, 1999), evidence theory (Dempster, 1967; Shafer, 1968), and intervals (Alefeld and Herzberger, 1984; Kulisch and Miranker, 1981; Moore et al., 2009; Muhanna et al., 2007).

The probability-box approach (or more compactly, p-box) integrates the conventional probability theory with the concept of intervals (Augustin and Hable, 2010; Beer, et al., 2013; Ferson, 2002). A p-box gives the lower and upper bounds on the cumulative distribution function (CDF) for an

uncertain variable. It is subject to any legitimate CDF within the given lower and upper bounds. Hence a traditional random variable can be interpreted as a p-box with zero width, and an interval can be interpreted as a rectangular p-box with constant width (Ferson, 2002).

One of the advantage of the p-box approach is the incorporation of bounded dependence information. In application of conventional probability theory, dependence of two random variables are simplified to their covariance or correlation coefficient (Cui and Blockley, 1990; Davis and Hall, 2003; Lucas, 1995). For linear dependence, the correlation coefficient is either 1 (perfect dependence) or -1 (opposite dependence). For independent variables, the correlation coefficient is 0. Then information about the covariance or correlation is used to analyse the random variables under consideration. Complete information about dependence is given by a joint probability distribution. However, it is often measured by limited information as covariance correlation coefficient (Ferson, et al., 2004). For instance, it is easy to construct two random variables that has 0 correlation coefficient but nonlinear dependence. Thus a more vigorous approach is required when available data is scarce and the consequence is high.

The p-box approach is designed to consider unknown dependence between random variables (Ferson, et al., 2004; Williamson, 1989). The p-box approach uses copulas (Kimeldorf and Sampson, 1975; Nelsen, 1999; Sklar, 1959), which gives complete information about the dependence of two random variables. Specifically, lower and upper bounds of the copula is used when performing binary arithmetic operations on p-boxes, such as addition, subtraction, multiplication, and division. In addition, due to the duality theorem (Frank and Schweizer, 1979; Williamson, 1989), the convolution of p-box, which is originally performed on the bounds of the CDF for given value on the random variable, can be performed on the bounds of the random variable for a given probability level. This significantly improves computational efficiency and facilitates discretization. Detailed discussion on p-boxes and their arithmetic operations can be found in Ferson (2002) and Williamson (1989).

In this paper, the p-box approach is applied to solve structural static problems with uncertain parameters. Both uncertainties in load and in material are considered. To reduce overestimation, a decomposition strategy (Muhanna and Mullen, 2001; Xiao, 2015) is presented, and a fixed-point formulation (Xiao, 2015; Xiao, et al., 2015) is implemented to solve the resulting governing linear system. To illustrate the performance of the current method, two numerical examples are solved, and the solutions are compared with those obtained from other available methods such as the interval Monte Carlo method (Zhang, et al., 2012). The results show that the current algorithm yields a tight p-box that encloses the solution, regardless of the dependence of the random variables.

2. Preliminaries on P-Boxes

A probability-box (or p-box) is useful to describe random variables whose probability distributions are not fully known. The p-box approach provides a rigorous way to account for uncertainty in our (lack of) knowledge of the random variables under study (Ferson, et al., 2004) by accounting for unknown dependence of the random variables. Arithmetic operations on p-boxes are developed in a way consistent with conventional probability theory (Ferson, 2002; Williamson, 1989). In the following subsections, some background information about p-boxes are introduced.

2.1. Description of a p-box

A p-box is defined by its lower and upper bounds on the cumulative distribution function (CDF) $\underline{F_X}(x)$ and $\overline{F_X}(x)$. It represents all legitimate random distributions whose CDF lie within that range. For a given value of x, the lower bound $\underline{F_X}(x)$ means the lowest probability that the random variable X is smaller than x, and the upper bound $\overline{F_X}(x)$ means the highest probability that X is smaller than x (Williamson, 1989).

The inverse functions of $\underline{F_X}(x)$ and $\overline{F_X}(x)$ gives the respective upper and lower bounds of a range $[\underline{x}, \overline{x}]$ of the random variable X for a given probability level F_X. For a given value of F_X, $\overline{F_X}^{-1}(F_X)$ is the smallest x such that the probability of X is smaller than x is F_X, and $\underline{F_X}^{-1}(F_X)$ is the largest, where superscript $^{-1}$ means inverse function. Note that the lower bound function $\underline{F_X}(x)$ corresponds to the upper bound $\overline{x}$ for a given F_X, and *vice versa*.

For a discrete description of a p-box, a list of triples $[m_i, \underline{x}_i, \overline{x}_i]$ are used (Dubois and Prade, 1991; Zhang, et al., 2012), where m_i are the probability masses, and $[\underline{x}_i, \overline{x}_i]$ are the associated intervals. The i-th probability mass m_i can be viewed as the probability that the i-th focal element $[\underline{x}_i, \overline{x}_i]$ is the range of x. For convenience, the probability masses have the same value for all focal elements, i.e., $m_i = 1/m$, where m is the number of focal elements in the discretization.

2.2. Dependency and copulas

The complete dependence information between two random variables are described by their joint probability distribution, which can be specified by a joint probability density function or a joint cumulative distribution function (Ferson, et al., 2004; Nelsen, 1999; Sklar, 1959). Because we are primarily dealing with CDF in p-boxes, the latter approach is adopted here.

For given random variables X and Y, any joint cumulative distribution function $F_{XY}(X, Y)$ can be expressed in terms of marginal distribution functions $F_X(x)$ and $F_Y(y)$ via the introduction of a 2D mapping $C(a, b) : [0, 1] \times [0, 1] \mapsto [0, 1]$

$$F_{XY}(X, Y) = C\left(F_X(x), F_Y(y)\right). \tag{1}$$

In the above equation, the 2D mapping $C(u, v)$ is a copula, satisfying the following requirements:

- $C(a, 0) = C(0, a) = 0$ and $C(a, 1) = C(1, a) = a$ for all $a \in [0, 1]$;
- $C(a_1, b_1) + C(a_2, b_2) - C(a_1, b_2) - C(a_2, b_1) \geq 0$ for all $a_1, a_2, b_1, b_2 \geq 0$ such that $a_1 \leq a_2$ and $b_1 \leq b_2$.

Any arbitrary copula $C(u, v)$ satisfies

$$W(u, v) \leq C(u, v) \leq M(u, v), \tag{2}$$

where $W(u, v) = \max(u + v - 1, 0)$ and $M(u, v) = \min(u, v)$ are the lower and upper Fréchet-Hoeffding bounds for any copula, respectively (Fréchet, 1951; Hoeffding, 1940). The lower bound $W(u, v)$ represents an opposite dependence between two distributions, and the upper bound $M(u, v)$

represents a perfect dependence. As a side note, independent case is represented by the copula $\Pi(u, v) = uv$. The dual of a copula is defined as

$$C^*(u, v) = u + v - C(u, v). \tag{3}$$

Parametrized copulas can be used to model dependence of different strength. One class of copulas, the Archimedean class, is associative and admits an explicit formula (Nelsen, 1999). The Archimedean copula has the following form

$$C_\theta(u, v) = \psi_\theta^{-1}\left(\psi_\theta(u) + \psi_\theta(v)\right), \tag{4}$$

where $\psi_\theta : [0, 1] \mapsto [0, \infty)$ is the generator function, which is continuous, strictly decreasing, convex, and $\psi_\theta(1) = 0$. Some of the most important families of Archimedean copulas include:

– The Clayton family (Clayton, 1978), with generator function $\psi_\theta(x) = (x^{-\theta} - 1)/\theta$,

$$C_\theta(u, v) = \left(u^{-\theta} + v^{-\theta} - 1\right)^{-1/\theta}, \tag{5}$$

where $\theta \geq -1$. The perfect dependence corresponds to $\theta = \infty$, the opposite dependence is $\theta = -1$, and the independent case is $\theta = 0$.

– The Frank family (Frank, 1979), with generator function $\psi_\theta(x) = \ln\left(\frac{e^{-\theta} - 1}{e^{-x\theta} - 1}\right)$,

$$C_\theta(u, v) = \frac{1}{\theta} \ln\left(1 + \frac{(e^{-u\theta} - 1)(e^{-v\theta} - 1)}{e^{-\theta} - 1}\right), \tag{6}$$

where $\theta \in \mathbb{R}$. The perfect dependence corresponds to $\theta = -\infty$, the opposite dependence is $\theta = \infty$, and the independent case is $\theta = 0$.

The above discussion is restricted to bivariate case for two random variables X and Y, but the idea can be easily extended to multi-variate case as well.

2.3. Arithmetic operations on p-boxes

For a single p-box X, its negation, its reciprocal, and its multiplication with a real number are all p-boxes. For instance, consider its negation $Y = -X$. Assume the lower and upper bound functions are $\underline{F_X}(x)$ and $\overline{F_X}(x)$, respectively. Then

$$\underline{F_Y}(y) = 1 - \overline{F_X}(-y), \qquad \overline{F_Y}(y) = 1 - \underline{F_X}(-y). \tag{7}$$

If the discrete description is used, and the focal elements are $[\underline{x}_i, \overline{x}_i]$, the results are

$$[\underline{y}_i, \overline{y}_i] = [-\overline{x}_{m+1-i}, -\underline{x}_{m+1-i}], \tag{8}$$

where m is the number of focal elements.

For two p-boxes X and Y, the result of their arithmetic binary operations, such as addition, subtraction, multiplication, and division, is also a p-box. The result depends on the lower and upper

bounds of their respective CDF's, as well as the copula between X and Y. According to Williamson (1989), for two p-boxes X and Y, the lower and upper bounds of the CDF of the sum $Z = X + Y$ are given by

$$\underline{F_Z}(z) = \sup_{v \in \mathbb{R}} C\big(\underline{F_X}(z-v), \underline{F_Y}(v)\big), \qquad \overline{F_Z}(z) = \inf_{v \in \mathbb{R}} C^*\big(\overline{F_X}(z-v), \overline{F_Y}(v)\big), \tag{9}$$

where $C(u, v)$ is the known lower bound of the copula between X and Y, and $C^*(u, v)$ is its dual. For discrete description, the i-th focal element of the sum, i.e., $[\underline{z}_i, \overline{z}_i]$, is given by

$$\underline{z}_i = \sup_{j,\, k \in C_i^*} (\underline{x}_j + \underline{y}_k), \qquad \overline{z}_i = \inf_{j,\, k \in C_i} (\overline{x}_j + \overline{y}_k), \tag{10}$$

where $j, k \in C_i$ means that j and k satisfy $\frac{i-1}{m} \in C([\frac{j-1}{m}, \frac{j}{m}], [\frac{k-1}{m}, \frac{k}{m}])$, and $j, k \in C_i^*$ means that j and k satisfy $\frac{i}{m} \in C^*([\frac{j-1}{m}, \frac{j}{m}], [\frac{k-1}{m}, \frac{k}{m}])$. For the Fréchet-Hoeffding lower bound copula $W(u, v) = \max(u + v - 1, 0)$, Eq. (10) becomes

$$\underline{z}_i = \sup_{j \in [1,\, i]} (\underline{x}_j + \underline{y}_{i+1-j}), \qquad \overline{z}_i = \inf_{j \in [i,\, m]} (\overline{x}_j + \overline{y}_{i+m-j}) \tag{11}$$

For multiple p-boxes X_i, when the dependence coefficient θ is constant, both the addition and the multiplication are associative. The results do not depend on the order of the arithmetic operations performed. Operations on vector and matrix with p-box entries can be defined accordingly. However, for each binary arithmetic operation ($+$, $-$, $\times$, or $\div$), the corresponding dependence coefficient θ or the copula $C_\theta(u, v)$ in general must be specified. In practice, this is not always possible. Hence the usual practice is to specify θ corresponding to the lower and upper bounds of the copulas. For positive dependence, the lower bound $\underline{\theta} = 0$ and the upper bound $\overline{\theta} = \infty$ for both the Clayton family and the Frank family. For negative dependence, $\underline{\theta} = -\infty$ and $\overline{\theta} = 0$ for the Clayton family, and $\underline{\theta} = -1$ and $\overline{\theta} = 0$ the Frank family. In both cases, the independent case is included as a subset. Hence the yielded solution considers the least favorable circumstances possible and encloses the solutions assuming independence, as observed in the comparison with the interval Monte Carlo solution (Zhang, et al., 2012) in the numerical example section.

For a more comprehensive discussion on arithmetic operations of p-boxes, we refer to the work of Ferson (2002) and Williamson (1989). In particular, Ferson (2002) considers binary arithmetic operations under the independence assumption.

3. Finite Element Formulation

Many engineering problems can be reduced to solving the following linear system of equations. For instance, for structural static analysis, after a displacement-based Finite Element (FE) discretization (Bathe and Wilson, 1976; Cook, et al., 2007), the system governing equation is

$$\mathbf{K}\mathbf{u} = \mathbf{f}, \tag{12}$$

where $\mathbf{K}$ is the stiffness matrix, $\mathbf{f}$ is the equivalent load vector, and $\mathbf{u}$ is the unknown displacement vector. The goal is to solve for the unknown displacement vector $\mathbf{u}$ when the external load and the

structure itself are given. When the system contains uncertain parameters, and those parameters are modeled by p-boxes, matrix $\mathbf{K}$ and vector $\mathbf{f}$ contain p-box entries. As a result, the unknown vector $\mathbf{u}$ also contains p-box entries. The goal of the current section is to develop an algorithm to solve the linear system Eq. (12) when p-box entries are present.

Following our previous work on interval linear systems (Xiao, 2015), to reduce overestimation in the interval of the final solution, the stiffness matrix $\mathbf{K}$ and the equivalent load vector $\mathbf{f}$ are decomposed into a form that minimize the multiple occurrences of the same p-box (Muhanna and Mullen, 2001). In addition, parametrized copulas are introduced to model dependence among uncertain parameters. Finally, the linear system Eq. (12) is solved using an iterative approach (Neumaier and Pownuk, 2007) by transforming the governing equation into a fixed-point form. Detailed discussions are presented in the following subsections.

3.1. Matrix decomposition strategy

The following decomposition of the stiffness matrix $\mathbf{K}$ and the equivalent load vector $\mathbf{f}$ is presented

$$\mathbf{K}^P = \mathbf{A}\,\mathrm{diag}\left(\mathbf{\Lambda}\boldsymbol{\alpha}^P\right)\mathbf{A}^T, \qquad \mathbf{f}^P = \mathbf{F}\boldsymbol{\delta}^P, \tag{13}$$

where the superscripts ^{P} emphasize that these variables contain p-box entries. After decomposition, all the p-box entries are included in vectors $\boldsymbol{\alpha}^P$ and $\boldsymbol{\delta}^P$. The above decomposition eventually reduce the overestimation of the final solution and helps to obtain a tighter bounds, as illustrated in the numerical simulation section.

In practice, the decompositions in Eq. (13) are performed at the element level before assembly. First the element stiffness matrix $\mathbf{K}_e^P$ and the element nodal equivalent load vector $\mathbf{f}_e^P$ are computed. Their decompositions yield the element matrices $\mathbf{A}_e$, $\mathbf{\Lambda}_e$, $\mathbf{F}_e$, $\boldsymbol{\alpha}_e^P$, and $\boldsymbol{\delta}_e^P$. These are further assembled into their global counterparts $\mathbf{A}$, $\mathbf{\Lambda}$, $\mathbf{F}$, $\boldsymbol{\alpha}^P$, and $\boldsymbol{\delta}^P$. During the assembly, the element-by-element (EBE) (Rama Rao, et al., 2011) assembly is adopted.

For the standard two-node plane truss elements, assume the Young's modulus E^P are modeled as p-boxes. The corresponding element stiffness matrix $\mathbf{K}_e^P$ is given by

$$\mathbf{K}_e^P = \begin{Bmatrix} E^PA/L & 0 & -E^PA/L & 0 \\ 0 & 0 & 0 & 0 \\ -E^PA/L & 0 & E^PA/L & 0 \\ 0 & 0 & 0 & 0 \end{Bmatrix}. \tag{14}$$

where L is the element length. Then $\boldsymbol{\alpha}_e^P$ contains the only p-box E^P in the element, and the corresponding $\mathbf{A}_e$ and $\mathbf{\Lambda}_e$ are given by

$$\mathbf{A}_e = \left\{-1 \;\; 0 \;\; 1 \;\; 0\right\}^T, \qquad \mathbf{\Lambda}_e = \left\{A/L\right\}, \qquad \boldsymbol{\alpha}_e^P = \left\{E^P\right\}. \tag{15}$$

The element nodal equivalent load vector $\mathbf{f}_e^P$ is decomposed into the form $\mathbf{f}_e^P = \mathbf{F}_e\boldsymbol{\delta}_e^P$ using the M-$\boldsymbol{\delta}$ method (Muhanna and Mullen, 2001). Thus the p-box terms in the element load uncertainty vector $\boldsymbol{\delta}_e^P$ is completely separated from the deterministic part $\mathbf{F}_e$ of the equivalent load.

In the element-by-element assembly, the structure is modeled by separated elements and common nodes that connect the elements. As a result, the structural nodal displacement vector $\mathbf{u}^P$ is a

collection of all the element nodal displacement vectors $\mathbf{u}_e^P$, and the nodal displacement vector $\mathbf{u}_n^P$ of the common nodes. Then the global stiffness matrix $\mathbf{K}^P$ and nodal equivalent load $\mathbf{f}^P$are assembled from their element counterparts

$$\mathbf{u}^P = \begin{Bmatrix} \mathbf{u}_e^P \\ \vdots \\ \mathbf{u}_e^P \\ \mathbf{u}_n^P \end{Bmatrix}, \qquad \mathbf{K}^P = \begin{Bmatrix} \mathbf{K}_e^P & & & \\ & \ddots & & \\ & & \mathbf{K}_e^P & \\ & & & 0 \end{Bmatrix}, \qquad \mathbf{f}^P = \begin{Bmatrix} \mathbf{f}_e^P \\ \vdots \\ \mathbf{f}_e^P \\ \mathbf{f}_n^P \end{Bmatrix}, \tag{16}$$

where $\mathbf{f}_n^P$ denotes concentrated forces applied directly on the common nodes. The assembly of $\mathbf{A}$, $\mathbf{\Lambda}$, $\mathbf{F}$, $\boldsymbol{\alpha}^P$, and $\boldsymbol{\delta}^P$ is similar. Note that $\mathbf{K}^P$ is a singular matrix.

To eliminate singularity in $\mathbf{K}^P$, the compatibility requirements and boundary conditions are collected into the form of a constraint equation $\mathbf{C}\mathbf{u}^P = \mathbf{0}$, which is enforced by the introduction of a Lagrangian multiplier $\boldsymbol{\lambda}^P$ into the energy functional $\mathbf{\Pi}^P$ of the system. The resulting governing equation of the system becomes

$$\begin{Bmatrix} \mathbf{K}^P & \mathbf{C}^T \\ \mathbf{C} & \mathbf{0} \end{Bmatrix} \begin{Bmatrix} \mathbf{u}^P \\ \boldsymbol{\lambda}^P \end{Bmatrix} = \begin{Bmatrix} \mathbf{f}^P \\ \mathbf{0} \end{Bmatrix}. \tag{17}$$

Noting the decomposition of $\mathbf{K}^P$ and $\mathbf{f}^P$, the above equation becomes

$$\left(\begin{Bmatrix} \mathbf{A} \\ \mathbf{0} \end{Bmatrix} \mathrm{diag}(\mathbf{\Lambda}\Delta\boldsymbol{\alpha}^P) \begin{Bmatrix} \mathbf{A}^T & \mathbf{0} \end{Bmatrix} + \begin{Bmatrix} \mathbf{K}_0 & \mathbf{C}^T \\ \mathbf{C} & \mathbf{0} \end{Bmatrix} \right) \begin{Bmatrix} \mathbf{u}^P \\ \boldsymbol{\lambda}^P \end{Bmatrix} = \begin{Bmatrix} \mathbf{F} \\ \mathbf{0} \end{Bmatrix} \boldsymbol{\delta}^P, \tag{18}$$

where $\Delta\boldsymbol{\alpha}^P = \boldsymbol{\alpha}^P - \boldsymbol{\alpha}_0$, and $\mathbf{K}_0 = \mathbf{A}\mathrm{diag}(\mathbf{\Lambda}\boldsymbol{\alpha}_0)\mathbf{A}^T$. Preferably, $\boldsymbol{\alpha}_0$ is chosen as the midpoint of the mean of $\boldsymbol{\alpha}^P$. The Lagrangian multiplier $\boldsymbol{\lambda}^P$ denotes negative internal forces between element nodes and common nodes, when the constraint is a compatibility condition; $\boldsymbol{\lambda}^P$ denotes reactions at the supports, when the constraint is an essential boundary condition (Cook, et al., 2007).

3.2. Iterative enclosure approach

The decomposed governing Eq. (18) can be brought into the following compact form

$$\mathbf{K}_{g0}\mathbf{u}_g^P = \mathbf{F}_g\boldsymbol{\delta}^P - \mathbf{A}_g \,\mathrm{diag}\left(\mathbf{\Lambda}\Delta\boldsymbol{\alpha}^P\right)\mathbf{A}_g^T\mathbf{u}_g^P. \tag{19}$$

By defining $\mathbf{G} = \mathbf{K}_{g0}^{-1}$, the above equation is rewritten into the following fixed-point form

$$\mathbf{u}_g^P = (\mathbf{G}\mathbf{F}_g)\boldsymbol{\delta}^P - (\mathbf{G}\mathbf{A}_g)\left(\mathbf{A}_g^T\mathbf{u}_g^P \circ \mathbf{\Lambda}\Delta\boldsymbol{\alpha}^P\right), \tag{20}$$

where the following equality has been used

$$\mathrm{diag}\left(\mathbf{\Lambda}\Delta\boldsymbol{\alpha}^P\right)\mathbf{A}_g^T\mathbf{u}_g^P = \mathrm{diag}\left(\mathbf{A}_g^T\mathbf{u}_g^P\right)\mathbf{\Lambda}\Delta\boldsymbol{\alpha}^P = \mathbf{A}_g^T\mathbf{u}_g^P \circ \mathbf{\Lambda}\Delta\boldsymbol{\alpha}^P, \tag{21}$$

where $\circ$ means the element-by-element product of two vectors. The auxiliary variable $\mathbf{v}^P = \mathbf{A}_g^T\mathbf{u}_g^P$, the following fixed-point form is more suitable for developing an iterative scheme

$$\mathbf{v}^P = (\mathbf{A}_g^T\mathbf{G}\mathbf{F}_g)\boldsymbol{\delta}^P - (\mathbf{A}_g^T\mathbf{G}\mathbf{A}_g)\left(\mathbf{v}^P \circ \mathbf{\Lambda}\Delta\boldsymbol{\alpha}^P\right). \tag{22}$$

To obtain a guaranteed enclosure of $\mathbf{v}^P$, we start from the initial guess $\mathbf{v}_0^P = (\mathbf{A}_g^T\mathbf{G}\mathbf{F}_g)\boldsymbol{\delta}^P$, and proceed using the following approach

$$\mathbf{v}_{i+1}^P = (\mathbf{A}_g^T\mathbf{G}\mathbf{F}_g)\boldsymbol{\delta}^P - (\mathbf{A}_g^T\mathbf{G}\mathbf{A}_g)\left(\mathbf{v}_i^P \circ \boldsymbol{\Lambda}\Delta\boldsymbol{\alpha}^P\right). \tag{23}$$

The iteration stops when $\mathbf{v}_i^P$ stops improving. Final solution $\mathbf{u}_{gn}^P$ is obtained by substituting $\mathbf{A}_g^T\mathbf{u}_g^P$ in Eq. (20) with the converged $\mathbf{v}_n^P$.

In the calculation, to reduce the overestimation, the deterministic matrices $(\mathbf{G}\mathbf{F}_g)$ and $(\mathbf{G}\mathbf{A}_g)$ in Eq. (20) and $(\mathbf{A}_g^T\mathbf{G}\mathbf{F}_g)$ and $(\mathbf{A}_g^T\mathbf{G}\mathbf{A}_g)$ in Eq. (23) are prepared before the iteration starts. The initial guess $\mathbf{v}_0^P$ is obtained by multiplying the deterministic matrix $(\mathbf{A}_g^T\mathbf{G}\mathbf{F}_g)$ with the p-box vector $\boldsymbol{\delta}^P$. During each iteration, firstly $\boldsymbol{\Lambda}\Delta\boldsymbol{\alpha}^P$ is obtained by multiplying the deterministic matrix $\boldsymbol{\Lambda}$ with the p-box vector $\Delta\boldsymbol{\alpha}^P$; secondly $\boldsymbol{\Lambda}\Delta\boldsymbol{\alpha}^P$ is multiplied element-by-element with the p-box vector $\mathbf{v}_i^P$ to yield $\left(\mathbf{v}_i^P \circ \boldsymbol{\Lambda}\Delta\boldsymbol{\alpha}^P\right)$; thirdly $\left(\mathbf{v}_i^P \circ \boldsymbol{\Lambda}\Delta\boldsymbol{\alpha}^P\right)$ is multiplied with the deterministic matrix $(\mathbf{A}_g^T\mathbf{G}\mathbf{A}_g)$, which is further subtracted to the initial guess $(\mathbf{A}_g^T\mathbf{G}\mathbf{F}_g)\boldsymbol{\delta}^P$. For each arithmetic operations ($+$, $-$, $\times$, or $\div$) in the calculation, if the two operands are known to be positively dependent, $\theta = 0$ for both the Clayton family and the Frank family; if they are know to be negative dependent, $\theta = -\infty$ for the Clayton family and $\theta = -1$ for the Frank family.

3.3. Random field modeling

In the above discussion, the p-box vector $\boldsymbol{\alpha}^P$ contains Young's modulus for each element, and the p-box vector $\boldsymbol{\delta}^P$ contains all the concentrated forces and distributed forces for each element. Usually these variables cannot vary independently, and it is necessary to describe this dependence among entries in $\boldsymbol{\alpha}^P$, $\boldsymbol{\delta}^P$, and other variables such as the displacement vector $\mathbf{u}^P$, the Lagrangian multiplier $\boldsymbol{\lambda}^P$, and the auxiliary variable $\mathbf{v}^P$.

In conventional probability theory, such dependence is described by the covariance or correlation of random variables. Then covariance decomposition technique (or kernel decomposition) such as the Karhumen-Loève expansion (Ghanem and Spanos, 1991; Zhang and Ellingwood, 1994) is applied to the auto-covariance function (or auto-covariance matrix in the discrete case). The goal is to either reduce the number of independent variables required to model the entire random field, or increase the computational efficiency of the algorithm. However, as pointed out by Ferson, et al. (2004), this is usually an over-simplification of the dependence of random variables in reality. The covariance or correlation between two random variables is insufficient to describe the dependence. Instead, a joint probability distribution in the form of either a joint distribution density function or a copula is required to completely describe it.

In this paper, the Clayton family of copulas $C_\theta(u, v)$ and their duel $C_\theta^*(u, v)$ are used to model dependence between random field variables such as Young's modulus (entries in $\boldsymbol{\alpha}^P$) and distributed load (entries in $\boldsymbol{\delta}^P$), as well as other variables such as $\boldsymbol{\alpha}^P$, $\boldsymbol{\delta}^P$, $\mathbf{u}^P$, $\boldsymbol{\lambda}^P$, and $\mathbf{v}^P$. The yielded solution provides guaranteed lower and upper bounds on the CDF's of the quantities of interest. In the following numerical simulation section, a discussion on the performance of the proposed hierarchical structure of the dependence modeling is presented.

4. Numerical Examples

The algorithm discussed previously is implemented in the MATLAB environment. Two structural problems are solved to illustrate the performance of the presented method: *i*) a fixed-end bar subject to axial deformation and *ii*) a simply supported symmetric 15-bar truss. The current method is compared with *i*) an interval Monte Carlo method (see Zhang, et al. (2012) for more detail) and *ii*) an analytical solution (only available for the first example). The results show that the current method is able to yield a conservative enclosure of the solution p-box with little overestimation, considering any dependence among the uncertain variables.

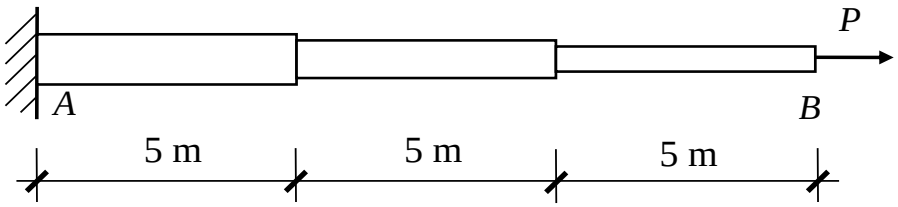

Figure 1. A fixed-end bar subject to axial load at the free end.

4.1. A fixed-end bar

The first example is a fixed-end bar subject to concentrated load P at the free end, as shown in Figure 1. The p-box for P is bounded from a normal distribution with an interval mean value $\mu_P = [99, 101]$ kN and a standard deviation $\sigma_P = 2$ kN. The total length of the bar is 15 m, which can be divided into three segments of equal length (i.e., $L = 5$ m for each). For each segment, the cross section areas are $A_1 = 0.015$ m^2, $A_2 = 0.012$ m^2, and $A_3 = 0.010$ m^2, respectively. The bar is made of copper, and Young's moduli E_i ($i = 1, 2, 3$) of the bar are modeled as p-boxes bounded by normal distributions. The interval mean value $\mu_E = [109, 111]$ GPa and the standard deviation $\sigma_E = 2$ GPa. The actual interval mean and standard deviation of P and E_i are given in Table I.

Table I. Bounds on the mean and standard deviation of the contained CDF's in the p-boxes. P - concentrated load; E_i - Young's moduli of the bar in Figure 1.

	Concentrated load, kN			Young's moduli, GPa	
	Mean μ_P	Standard deviation σ_P		Mean μ_E	Standard deviation σ_E
P	[98.86, 101.14]	[1.142, 3.136]	E_1	[108.9, 111.1]	[1.142, 3.136]
			E_2	[108.9, 111.1]	[1.142, 3.136]
			E_3	[108.9, 111.1]	[1.142, 3.136]

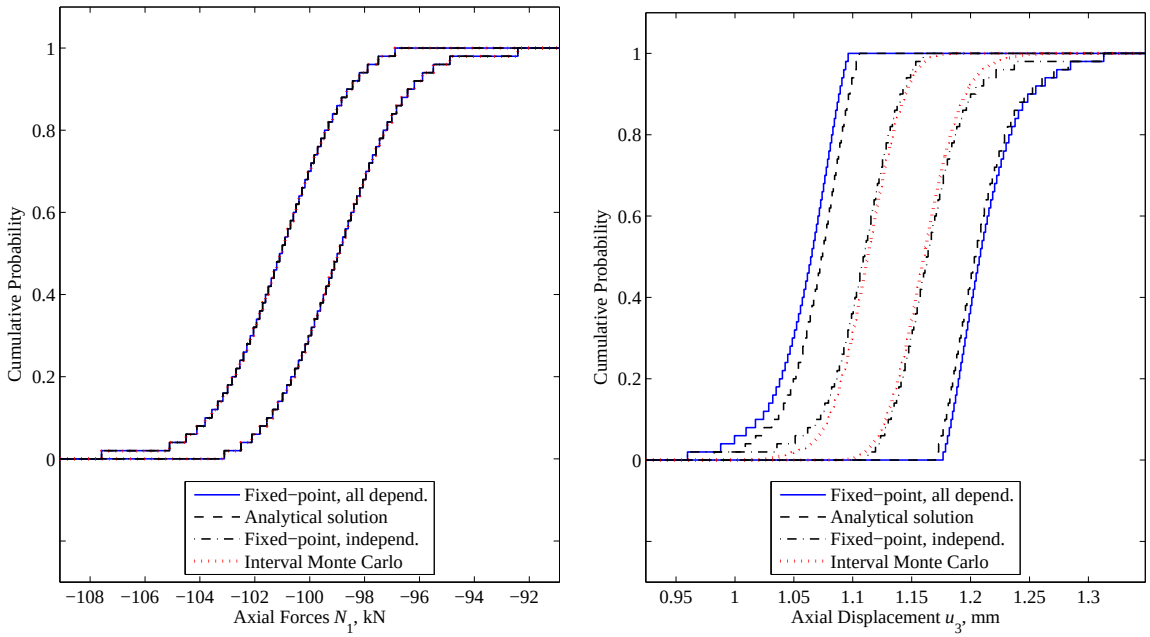

Figure 2. P-box solution for the axial force N_1 (left half) and axial displacement u_3 (right half) of the fixed-end bar of Figure 1, obtained from different method: the current method assuming all dependency (solid lines), the analytical solution (dashed lines), the current method assuming independence (dash-dotted lines), and the interval Monte Carlo method from an ensemble of 100,000 simulations (dotted lines).

A simplified version of the algorithm proposed by Ferson, et al. (2005) is adopted to calculate the interval bounds of mean and standard deviation. In the FEM discretization, the bar is modeled by three truss elements. Since the bar is subject to axial deformation only, lateral displacement is restrained.

The problem has four uncertain parameters, i.e., the concentrated load P and the Young's moduli E_i for each element. Now consider any dependence between the load and the Young's moduli and a positive dependence among E_i. The analytic solution to the problem is available. The structure is statically determinate. The axial force in the bar is equal to the concentrated load P. The nodal axial displacements

$$u_1 = P\left(\frac{L}{E_1A_1}\right), \quad u_2 = P\left(\frac{L}{E_1A_1} + \frac{L}{E_2A_2}\right), \quad u_3 = P\left(\frac{L}{E_1A_1} + \frac{L}{E_2A_2} + \frac{L}{E_3A_3}\right). \tag{24}$$

Solutions obtained from the current method, the interval Monte Carlo method, and the analytical solution from Eq. (24) are compared with each other. To ensure the accuracy of the solution, 50 focal elements are used in the discretization process. The interval Monte Carlo method include 100,000 simulations, in which the interval solver described in the thesis of Xiao (2015) is used.

All solutions report the same axial force, as shown in the left half of Figure 2. This is not surprising, because the current method can handle load uncertainty without any overestimation

Table II. Bounds on the mean and standard deviation of the contained CDF's in the p-boxes. N_1 - axial force; u_i - axial displacements of the bar in Figure 1.

	Axial force N_1, kN		Axial displacement u_1, mm	
	Mean μ_{N_1}	Standard deviation σ_{N_1}	Mean μ_{u_1}	Standard deviation σ_{u_1}
Current, all depend.	[−101.13, −98.87]	[1.142, 3.136]	[0.2864, 0.3197]	[0.0000, 0.0244]
Reference (analytical)	[−101.13, −98.87]	[1.142, 3.136]	[0.2880, 0.3190]	[0.0000, 0.0227]
Current, independ.	[−101.13, −98.87]	[1.142, 3.136]	[0.2953, 0.3108]	[0.0030, 0.0172]
Interval Monte Carlo	[−101.14, −98.88]	[1.127, 3.096]	[0.2965, 0.3098]	[0.0036, 0.0145]
	Axial displacement u_2, mm		Axial displacement u_3, mm	
	Mean μ_{u_2}	Standard deviation σ_{u_2}	Mean μ_{u_3}	Standard deviation σ_{u_3}
Current, all depend.	[0.6381, 0.7255]	[0.0000, 0.0595]	[1.0586, 1.2141]	[0.0000, 0.1033]
Reference (analytical)	[0.6436, 0.7232]	[0.0000, 0.0551]	[1.0689, 1.2100]	[0.0000, 0.0954]
Current, independ.	[0.6637, 0.6999]	[0.0048, 0.0380]	[1.1055, 1.1673]	[0.0068, 0.0631]
Interval Monte Carlo	[0.6672, 0.6970]	[0.0063, 0.0303]	[1.1120, 1.1617]	[0.0094, 0.0482]

due to the adoption of the M-$\boldsymbol{\delta}$ method proposed by Muhanna and Mullen (2001). The right half of Figure 2 compares the axial displacements u_3 at the free end from different methods. Note that solution obtained from the current method enclose the analytical solution, with very small overestimation, while the interval Monte Carlo solution is enclosed by the current method a with very large underestimation.

To illustrate that the difference is indeed caused by the inclusion of all dependency of random variables, not by the overestimation in the current method, the solution obtained from the current method assuming independence between random variables is added in Figure 2. Its difference with the interval Monte Carlo solution is very small. Table II compares the interval bounds of the mean and standard deviation of the axial force N_1 and axial displacements u_1, u_2, and u_3 obtained from different methods. Some of the lower bounds of the standard deviation obtained from the current method and the analytical solution are zero. This is consistent with the observation that those p-boxes are able to enclose step functions, which correspond to zero standard deviation (the smallest possible bound of the standard deviation of any probability distribution).

Table III. Computational time of the fixed-end bar (Example 4.1) and the simple truss (Example 4.2) for different methods.

	Fixed-end bar (s)	Simple truss (s)
Fixed-point, all dependency	0.41	13.20
Fixed-point, independent	0.07	2.27
Interval Monte Carlo	573.93	907.68
Analytical solution	0.01	N/A

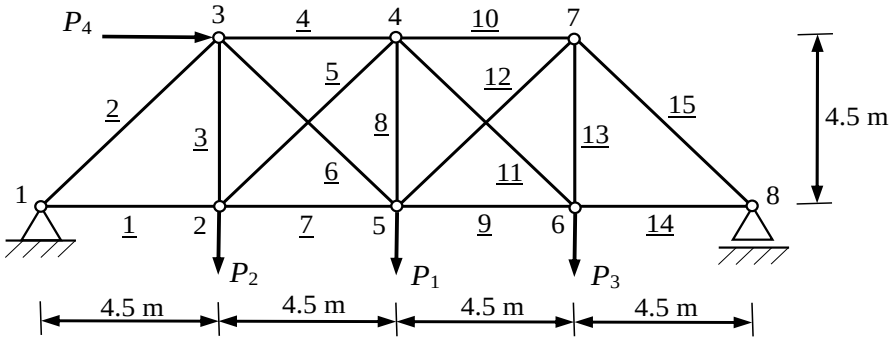

Figure 3. An 8-joint 15-bar symmetric simple truss subject to point loads.

Table III lists the computational time of the current example (and the next example) for different methods. The current method is more efficient than the interval Monte Carlo method.

4.2. A symmetric simple truss

The second example is a simply supported symmetric truss composed of 15 bars, as shown in Figure 3. The joints are labeled from 1 to 8, and the bars are labeled from $\underline{1}$ to $\underline{15}$. Point loads P_1, P_2, P_3, and P_4 are applied at joints 5, 2, 6, and 3, respectively. They are bounded by normal distributions with interval mean values $\mu_{P_1} = [199, 201]$ kN, $\mu_{P_2} = \mu_{P_3} = [99, 101]$ kN, and $\mu_{P_4} = [89, 91]$ kN and standard deviation $\sigma_{P_1} = \sigma_{P_2} = \sigma_{P_3} = \sigma_{P_4} = 2$ kN. Bars $\underline{1}$ to $\underline{3}$, $\underline{13}$ to $\underline{15}$ have the same cross section area $A = 1.0 \times 10^{-3}$ m^2, and all other bars, that is, bars $\underline{4}$ to $\underline{12}$, have a smaller cross section area $A = 6.0 \times 10^{-4}$ m^2. All the bars are made of steel and their Young's moduli E_i are modeled by p-boxes bounded by normal distributions with an interval mean value $\mu_E = [198, 202]$ GPa and a standard deviation $\sigma_E = 4$ GPa. The corresponding actual mean and standard deviation of P_i and E_i are given in Table IV.

Assume that the concentrated loads can be any dependence, and the Young's moduli of the bars are positively dependent with each other. No further assumptions are made. The axial forces in bar $\underline{2}$ and bar $\underline{8}$ (i.e., N_2 and N_8) and the displacements at node 5 (i.e., u_5 and v_5) are solved and

Table IV. Bounds on the mean and standard deviation of the contained CDF's in the p-boxes. P_i - concentrated loads; E_i - Young's moduli of the truss in Figure 3.

	Concentrated load, kN			Young's moduli, GPa	
	Mean μ_P	Standard deviation σ_P		Mean μ_E	Standard deviation σ_E
P_1	[198.87, 201.13]	[1.142, 3.136]	E_i	[197.7, 202.3]	[2.285, 6.271]
P_2	[98.87, 101.13]	[1.142, 3.136]			
P_3	[98.87, 101.13]	[1.142, 3.136]			
P_4	[88.87, 91.13]	[1.142, 3.136]			

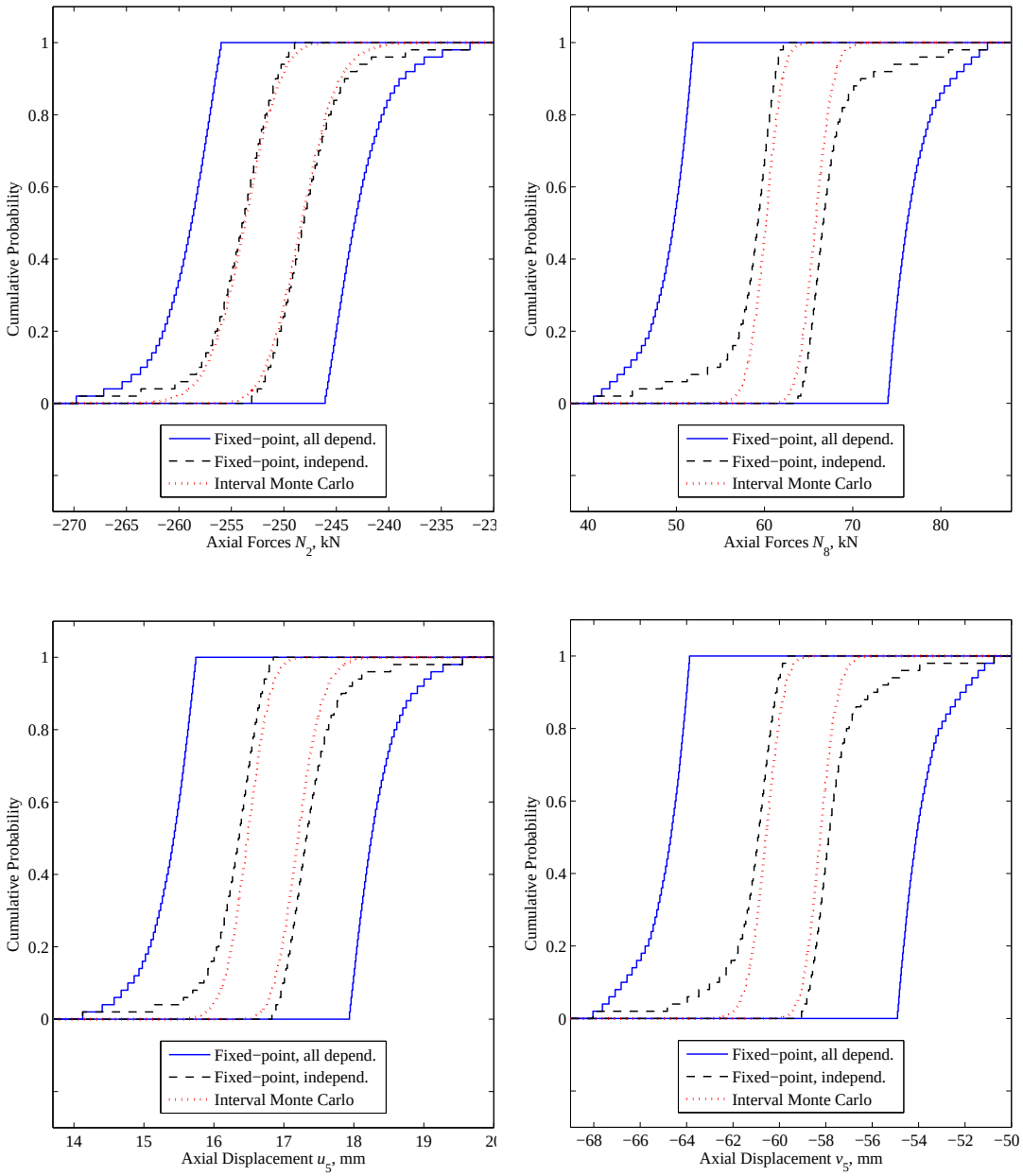

Figure 4. P-box solution for the axial force N_2 (upper left) and N_8 (upper right) and nodal displacements u_5 (lower left) and v_5 (lower right) of the symmetric simple truss of Figure 3, obtained from: the current method assuming positive dependence for E_i (solid lines), the current method assuming independence (dashed lines), and the interval Monte Carlo method from an ensemble of 100,000 simulations (dotted lines).

depicted in Figure 4. Again, 50 focal elements are used to discretize the p-box. Because there is no simple analytical solution, the current method is compared with the interval Monte Carlo method obtained from 100,000 simulations. For all the results, solution from the current method is wider than the interval Monte Carlo solution and always contains it, even for the deterministic axial force N_2. This is not surprising, because the current method considers any dependence between the random variables, while the interval Monte Carlo method can only consider the independent case. Again, the solution obtained from the current method assuming independence between random variables is very close to the interval Monte Carlo solution.

5. Conclusion

A new method is presented to solve linear system of equations with p-box entries, together with an application to structural static problems for plane trusses. Uncertainties in the system are modeled as p-boxes, which represent random variables whose CDF lie within the bounds of the p-boxes. The results are also presented in the form of p-boxes. To reduce overestimation in the obtained bounds, a matrix decomposition strategy and a fixed-point formulation are adopted, which are originally used for solving interval linear systems. Numerical examples illustrate that the performance of the current method is satisfactory.

Though the discussion is currently restricted to static analysis trusses, one of the simplest of structure forms, the formulation can be extended to more complicated structures such as frames, plane problems, plates, shells, etc., as well as other types of analysis such as frequency response analysis, vibration analysis, transient analysis, structural damage detection, etc. The introduction of p-boxes in the modeling of uncertainties in these problems will provide useful information about the bounds on the statistical properties of the random variables, regardless of the dependence of the uncertain parameters involved.

References

Alefeld, G. and J. Herzberger. *Introduction to Interval Computation*. Academic Press, 1984.

Augustin, T. and R. Hable. On the impact of robust statistics on imprecise probability models: A review. *Structural Safety*, 32:358–365, 2010.

Beer, M., S. Ferson and V. Kreinovich. Imprecise probabilities in engineering analyses. *Mechanical Systems and Signal Processing*, 37:4–29, 2013.

Bathe, K. and E. L. Wilson. *Numerical Methods in Finite Element Analysis*. Prentice-Hall, Inc., Englewood Cliffs, New Jersey, 1976.

Clayton, D. G. A model for association in bivariate life tables and its application in epidemiological studies of familial tendency in chronic disease incidence. *Biometrika*, 65(1):141–151, 1978.

Cook, R. D., D. S. Malkus, M. E. Plesha and R. J. Witt. *Concepts and Applications of Finite Element Analysis*. John Wiley & Sons, 2007.

Cui, W. C. and D. I. Blockley. Interval probability theory for evidential support. *International Journal of Intellegent Systems*, 5(2):183–192, 1990.

Davis, J. P. and J. W. Hall. A software-supported process for assembling evidence and handling uncertainty in decision-making. *Decision Support Systems*, 35:414–433, 2003.

Dehghan, M., B. Hashemi and M. Ghatee. Computational methods for solving fully fuzzy linear systems. *Applied Mathematics and Computation*, 179(1):328–343, 2006.

Dempster, A. P. Upper and lower probabilities induced by a muilti-valued mapping. *The Annals of Mathematical Statistics*, 38:325–339, 1967.

Dubois, D. and H. Prade. Random sets and fuzzy interval analysis. *Fuzzy Sets of Systems*, 42:87–101, 1991.

Fernández-Martínez, J. L., Z. Fernández-Muñiz, J. L. G. Pallero and L. M. Pedruelo-González. From Bayes to Tarantola: new insights to understand uncertainty in inverse problems. *Journal of Applied Geophysics*, 98:62–72, 2013.

Ferson, S. *RAMAS Risk Calc 4.0 Software: Risk Assessment with Uncertain Numbers*. Applied Bimathematics, Setauket, New York, 2002.

Ferson, S., L. Ginzburg, V. Kreinovich, L. Longpré and M. Aviles. Exact bounds on finite populations of interval data. *Reliable Computing*, 11(3):207–233, 2005.

Ferson, S., R. B. Nelsen, J. Hajagos, D. J. Berleant, J. Zhang, W. T. Tucker, L. R. Ginzburg and W. L. Oberkampf. Dependence in probabilistic modeling, Dempster-Shafer theory, and probability bounds analysis. *Sandia Report, SAND2004-3072*, 2004.

Frank, M. On the simultaneous associativity of and $F(x, y)$ and $x + y - F(x, y)$. *Aequationes Mathematicae*, 19:194–226, 1979.

Frank, M. J. and B. Schweizer. On the duality of generalized infimal and supremal convolutions. *Rendiconti dí Matematica Series*, 4(12):1–23, 1979.

Fréchet, M. Sur les tableaux de corrélation dont les marges sont données. *Annales de l'Université de Lyon. Section A: Sciences Mathématiques et Astronomie*, 9:53–77, 1951.

Ghanem, R. and P. D. Spanos. *Stochastic Finite Elements: A Spectral Approach*. Springer-Verlag, Berlin, 1991.

Hoeffding, W. Scale-invariant correlation theory. *Collected Works of Wassily Hoeffding*, N. I. Fisher and P. K. Sen (eds.), Springer-Verlag, New York, 1940.

Igusa, T., S. G. Buonopane and B. R. Ellingwood. Bayesian analysis of uncertainty for structural engineering applications. *Structural Safety*, 24(2):165–186, 2002.

Kimeldorf, G. and A. Sampson. Uniform representations of bivariante distributions. *Communications in Statistics*, 4:617–627, 1975.

Klir, G. J. and M. J. Wierman. *Uncertainty-Based Information - Elements of Generalized Information Theory*. Physica-Verlag, Heidelberg, 1999.

Kolmogorov, A. N. *Foundations of the Theory of Probability*. Chelsea Publishing Company, New York, 1950.

Kulisch, U. W. and W. L. Miranker. *Computer Arithmetic in Theory and Practice*. Academic Press, New York, 1981.

Lucas, D. J. Default correlation and credit analysis. *Journal of Fixed Income*, 4(4):76–87, 1995.

Moens, D. and M. Hanss. Non-probabilistic finite element analysis for parametric uncertainty treatment in applied mechanics: Recent advances. *Finite Elements in Analysis and Design*, 47(1):4–16, 2011.

Moore, R. E., R. B. Kearfott and M. J. Cloud. *Introduction to Interval Analysis*. Society for Industrial and Applied Mathematics, 2009.

Muhanna, R. L. and R. L. Mullen. Uncertainty in mechanics problems – interval-based approach. *Journal of Engineering Mechanics*, American Society of Civil Engineers, 127(6):557–566, 2001.

Muhanna, R. L., H. Zhang and R. L. Mullen. Combined axial and bending stiffness in interval finite-element methods. *Journal of Structural Engineering*, 133(12):1700–1709, 2007.

Nelsen, R. B. *An Introduction to Copulas*. Lecture Notes in Statistics 139, Springer-Verlag, New York, 1999.

Neumaier, A. and A. Pownuk. Linear systems with large uncertainties, with applications to truss structures. *Reliable Computing*, 13(2):149–172, 2007.

Rama Rao, M. V., R. L. Mullen and R. L. Muhanna. A new interval finite element formulation with the same accuracy in primary and derived variables. *International Journal of Reliability and Safety*, 5(3/4):336–367, 2011.

Shafer, G. *A Mathematical Theory of Evidence*. Princeton University Press, Princeton, 1968.

Sklar, A. Fonctions de répartition à n dimensions et leurs marges. *Publications de L'Institut de Statistiques de l'Université de Paris*, 8:229–231, 1959.

Soize, C. Bayesian posteriors of uncertainty quantification in computational structural dynamics for low-and medium-frequency ranges. *Computers & Structures*, 126:41–55, 2013.

Williamson, R. C. *Probabilistic Arithmetic.* University of Queensland, PhD Thesis, 1989.

Xiao, N. *Interval Finite Element Approach for Inverse Problem under Uncertainty.* Georgia Institute of Technology, PhD Thesis, 2015.

Xiao, N., R. L. Muhanna, F. Fedele and R. L. Mullen. Uncertainty analysis of static plane problems by intervals. *SAE International Journal of Materials and Manufacturing*, 8:374–381, 2015.

Zhang, H. *Nondeterministic Linear Static Finite Element Analysis: an Interval Approach.* Georgia Institute of Technology, PhD Thesis, 2005.

Zhang, J. and B. Ellingwood. Orthogonal series expansions of random fields in reliability analysis. *Journal of Engineering Mechanics (ASCE)*, 120:2660–2677, 1994.

Zhang, H., R. L. Mullen and R. L. Muhanna. Structural analysis with probability-boxes. *International Journal of Reliability and Safety*, 6(1/2/3):110–129, 2012.

Real-Time Prediction of Structural Processes with Polymorphic Uncertain Data

Ba Trung Cao, Steffen Freitag and Günther Meschke
Institute for Structural Mechanics, Ruhr University Bochum, Universitätsstr. 150, 44801, Bochum, Germany, ba.cao@rub.de, steffen.freitag@sd.rub.de, guenther.meschke@rub.de

Abstract: The focus of this paper is on the development and comparison of two interval approaches for real-time predictions of high dimensional structural processes, i.e. the prediction of uncertain time variant displacement fields of a structure due to a few steering parameters. The approaches are developed for simulation supported steering of mechanized tunneling processes but can also be applied to similar problems in structural mechanics. Using interval data for uncertainty quantification in mechanized tunneling is motivated by the geotechnical reports of tunnel projects, where often ranges for the geotechnical data (dimension of soil layers) and some soil parameters (e.g. modulus of elasticity, friction angle) are provided. For real-time simulations with interval data, two surrogate modeling strategies (Proper Orthogonal Decomposition and Artificial Neural Networks) are combined to substitute the structural simulation model, which is in the presented application a process oriented 3D finite element (FE) model for shield tunneling taking into account all relevant components of the construction process. The hybrid surrogate model is trained in the offline (design) stage with patterns of interval data obtained with an optimization based interval analysis. However, this approach is time consuming and not suitable for real-time predictions of high dimensional output data, e.g. nodal displacements of a FE model. For real-time steering in the online (construction) stage, the optimization based interval analysis is replaced by a direct prediction with interval data using either midpoint-radius representation or lower-upper-bound representation of intervals. Both approaches are presented in the paper and compared within a verification example and an application example in mechanized tunneling. It is also demonstrated, how these new surrogate modeling approaches for time variant interval fields can be applied in case of polymorphic uncertain date (combination of interval and stochastic parameters) within the probability-box (p-box) approach using interval Monte Carlo Simulation.

Keywords: surrogate models, real-time prediction, interval, probability box, finite element analysis

1. Introduction

Mechanized tunneling in urban areas must always consider the effect of the construction process on the built environment, e.g. the risk of damage of existing buildings or infrastructure on the surface. Currently, FE simulations are more commonly used in a deterministic framework to investigate and predict the structural behavior in mechanized tunneling processes. For reliability analyses taking the uncertainty of geotechnical parameters into account, multiple runs of the simulation model are required, at least a few hundreds within optimization approaches for interval or fuzzy analyses or

up to 10^6 within Monte Carlo simulations, e.g., to predict failure probabilities. Hence surrogate models are required to replace the FE simulation models with the aim to maintain the prediction performance and to reduce the computation time significantly, especially for real-time applications.

Recently, in (Freitag et al., 2015), reliability analyses approaches in mechanized tunneling were presented, taking polymorphic uncertain geotechnical data by means of stochastic numbers, intervals and interval stochastic numbers into account. The analyses are performed with a hybrid surrogate model (i.e. a combination of Proper Orthogonal Decomposition (POD) and Recurrrent Neural Networks (RNN)), for deterministic input-output mappings within optimization based interval analyses and interval stochastic analyses using Particle Swarm Optimization(PSO). The hybrid surrogate model has the capability to predict (extrapolate) tunneling induced uncertain time and spatially varying surface settlements, see also (Cao et al., 2016). Based on the RNN predictions at selected monitoring points of the settlement field, the Gappy POD (GPOD) method is utilized to approximate the complete surface settlement field. The optimization based interval analysis approach is useful for reliability assessment in the design stage of a project, because the computational time is between one and several hours using a standard laptop and increases dramatically especially for a large number of outputs (e.g. settlements at all surface points). This is because of the fact, that for each output two separate optimization problems have to be solved to compute the corresponding lower and upper interval bounds.

In order to support the steering of the tunnel boring machine (TBM) during the tunnel construction, the computation time of optimization based approaches may be inappropriate since the computational time needs to be significantly smaller than the time required for one tunnel ring construction stage, which is typically in the range between 2-4 hours. Therefore, a real-time prediction should be performed in the ranges of seconds to some minutes to investigate the influence of the steering parameters onto the outputs, e.g. surface settlements. This can be achieved by solving the independent optimization tasks for each output in parallel, e.g. using a computer cluster or by direct interval computations. Here, two interval computation approaches are presented.

The first approach is based on the midpoint-radius representation and is described in detail in (Freitag et al., 2016). The idea is to develop separate surrogate models for predicting the midpoints and the radiuses of the intervals. For the midpoints, the approach is identical to (Freitag et al., 2015). Meanwhile, the radiuses are restricted to positive numbers. This is satisfied by selecting activation functions with only positive outputs in the RNN part and by applying the Non-Negative Matrix Factorization (NNMF) in the GPOD part of the hybrid surrogate model.

The second approach is based on the lower-upper bound representation of intervals. Whereas the computation of the interval bounds with RNNs using interval arithmetic can directly be adopted from (Freitag et al., 2011) (RNNs for fuzzy data), two separate surrogate models for the lower and upper bound predictions are developed for the GPOD part, respectively. First, the upper bounds are computed with the same approach as presented in (Freitag et al., 2015). But for the lower bounds prediction, a constraint, not to exceed the upper bound, is defined within the GPOD approach.

The structure of this paper is organized as follows. Section 2 provides a short overview of the process-oriented FE model for numerical simulations of mechanized tunneling processes. Polymorphic uncertain data models are introduced in Section 3. In Section 4, the concept of the hybrid surrogate modeling strategy for time variant interval fields in mechanized tunneling is explained. Consequently, Section 5 presents how interval data are processed with the surrogate model. The

verification and comparison of the two approaches with an analytical solution and an application example are finally shown in Section 6.

2. Numerical Simulation of Mechanized Tunneling Processes

A process-oriented, three-dimensional, FE model is applied to simulate the tunneling process. The simulation model is based on (Kasper and Meschke, 2004) and has been further developed to the simulation model `ekate`, see e.g. (Nagel et al., 2010), using a more advanced and flexible software architecture within the object-oriented FE framework KRATOS. All relevant components involved in the mechanized tunneling process are considered, i.e the soil layers, existing structures, the shield machine, the segmented lining, the face support, and the tail void grouting. The FE model follows the tunneling construction stages during the numerical simulation, see also (Meschke et al., 2013).

The soil is modeled as a three or two phase material for partially or fully saturated soils respectively, see (Nagel and Meschke, 2010). A surface-to-surface contact algorithm (Laursen, 2002), which allows for a smooth advancement of the machine is employed to simulate the movement of the TBM through the soil. Face support and grouting pressures are applied to ensure the stability of the tunnel face due to distortions caused by the excavation process and to reduce ground loss behind the tapered shield, respectively. The tail void grout is described as a fully saturated two-phase material considering hydration-dependent material properties of the cementitious grouting material as proposed in (Meschke, 1996). This formulation allows to model the infiltration of fluid grout into the surrounding soil. After each TBM advance, the excavation at the cutting face, the tail void grouting and the erection of a new lining ring during standstill are taken into account by deactivation of soil elements an adjusting all boundary conditions to the new situation. The effect of existing structures at the surface is accounted by adopting substitute models with equivalent thickness and stiffness. In (Ninić, 2015), the model has been employed to perform in-depth investigations of soil-structure interactions during mechanized tunneling processes.

3. Polymorphic Uncertain Data

Polymorphic uncertainty modeling allows to combine several uncertainty concepts to consider aleatoric and epistemic sources of uncertainties within one numerical simulation, see e.g. (Graf et al., 2014). The input space can be a combination of intervals, fuzzy numbers and stochastic numbers (i.e. each input parameter is described by diverse uncertainty models), or some input parameters are polymorphic uncertain itself, e.g. defined as p-boxes or fuzzy stochastic numbers. Both situations of polymorphic uncertain input parameters can be treated in a similar way within numerical simulations and require to combine stochastic and non-stochastic simulation approaches and finally lead to imprecise stochastic responses (outputs), e.g. p-boxes, fuzzy stochastic numbers, interval or fuzzy failure probabilities. In this paper, it is focused on real-time simulations with interval data and its possible application within the p-box approach.

3.1. Intervals

Geotechnical parameters with epistemic sources of uncertainty can be quantified by intervals or fuzzy numbers. Here, it is focused on intervals

$$\bar{x} = [{}_l x,\ {}_u x] \ , \tag{1}$$

which are ranges with lower bounds ${}_l x$ and upper bounds ${}_u x$. The intervals can directly be obtained from geotechnical reports, which often contain possible ranges for the expected geotechnical parameters. An alternative to the lower-upper bound representation of intervals is the midpoint-radius representation, where the midpoint ${}_m x$ and radius ${}_r x$ of an interval $\bar{x}$ is defined as

$${}_m x = \frac{{}_l x + {}_u x}{2} \tag{2}$$

and

$${}_r x = \frac{{}_u x - {}_l x}{2} \ . \tag{3}$$

Interval arithmetic (Moore., 1979), the transformation method (Hanss, 2002), or optimization approaches, see e.g. (Möller et al., 2000), can be utilized to compute with intervals. The interval finite element method (IFEM) (Muhanna et al., 2007; Rao et al., 2011) has been developed for applications in structural mechanics, see also (Moens and Vandepitte, 2005; Moens and Hanss, 2011) for an overview.

3.2. Probability Boxes

The probability box (p-box) approach, see e.g. (Ferson et al., 2003), allows to define imprecise stochastic numbers by a lower bound ${}_l F(x)$ and an upper bound ${}_u F(x)$ cumulative distribution function (cdf). In general, arbitrary stochastic models, including empirical distributions, can be used for the lower and upper bound cdf. Each distribution, which is inside the p-box is valid.

3.3. Computing with Intervals and Stochastic Numbers

In order to compute with inputs defined as intervals and stochastic numbers, a combination of stochastic and interval analysis is required. This can be performed by a stochastic analysis with interval samples, e.g. by means of Interval Monte Carlo Simulation (Zhang et al., 2010). For each interval sample, the structural response has to be computed by optimization-based interval analysis or by approaches based on interval arithmetic, such as IFEM. In (Freitag et al., 2013), a surrogate modeling approach based on artificial neural networks is presented, which is applied to replace a time consuming optimization-based FE interval analysis within an Interval Monte Carlo Simulation to compute p-boxes of structural responses and also fuzzy failure probabilities. This idea is extended to a hybrid surrogate modeling approach for real-time surface settlement field predictions in mechanized tunneling.

4. Hybrid Surrogate Modeling Approach

During the tunnel advancement process, it is required to predict the surface settlement field in real-time to support the decision of choosing appropriate operational parameters such as grouting and support pressures. In (Freitag et al., 2015), a surrogate modeling strategy combining POD and RNN approaches is proposed to predict time-variant high-dimensional outputs (surface settlement fields) in mechanized tunneling. This hybrid surrogate model, which has been developed for deterministic real-time input-output mappings in (Cao et al., 2016), is extended for predictions with interval data in this paper. In Table I the proposed surrogate modeling strategy for interval data is summarized.

Table I. Hybrid surrogate modeling approach to predict time-variant interval settlement fields.

Offline stage
1: Create a numerical model representing a tunnel section
2: Define intervals for geotechnical parameters $\bar{\mathbf{X}}$ and scenarios for deterministic steering parameters ${}^{[n]}\mathbf{P}$
3: Run numerical simulations with different realizations of input parameters
4: Store the numerical results of the deterministic settlement fields
5: Define intervals of the geotechnical parameter $\bar{\mathbf{X}}$
6: Perform interval analysis (optimization approach) for different patterns of $\bar{\mathbf{X}}$ and scenarios of deterministic steering parameters ${}^{[n]}\mathbf{P}$ using the deterministic surrogate model
7: Store the lower and upper bounds of the interval settlement fields
8: Provide the interval settlement data of several monitoring points for RNN training and testing
9: Provide the interval settlement data of the complete settlement field for POD-RBF training and testing
Online stage
1: Input: an interval of the geotechnical parameters, the recorded history from time steps 1 to N of the steering parameters and chosen values of steering parameters in the next time step $N+1$
2: Approximate the bounds of the complete displacement field from time step 1 to N (by POD-RBF)
3: Predict the bounds of the interval settlements at selected points for next time step $N+1$ (by RNN)
4: Predict the interval settlement field of next time step $N+1$ (by GPOD)
5: Update the interval bounds of the complete settlement field from time step 1 to $N+1$
6: Repeat steps 3 and 4 with updated values

In the offline stage, i.e. in the design stage of a tunnel project, deterministic input-output data sets are collected by varying the input parameters of the numerical model `ekate` used to represent the mechanized tunneling process within a tunnel section. The data sets are utilized to generate a surrogate model with deterministic inputs (geotechnical parameters $\mathbf{X}$, time-variant steering parameters $\mathbf{P}(t)$) and deterministic outputs (time-variant surface settlements $\mathbf{S}(t)$). To capture the uncertainty of geotechnical parameters by means of intervals $\overline{\mathbf{X}}$, the next step is to compute the corresponding system outputs in the context of an interval analysis. This is accomplished by employing the just-built deterministic surrogate model together with an optimization approach (e.g. PSO). The obtained results are patterns of interval $\overline{\mathbf{X}}$ and deterministic $\mathbf{P}(t)$ input data and the corresponding interval output data $\overline{\mathbf{S}}(t)$.

In the online stage, i.e. during the tunnel construction, the interval bounds of expected surface settlements have to be predicted by the surrogate model. For the prediction, the history of the operational parameters is adopted for the time steps 1 to N and the interval settlement field is computed based on chosen values of the steering parameters in time step $N + 1$. The complete settlement field from time step 1 to N is approximated by trained POD-RBF networks for the midpoints and the radiuses, respectively. For the predictions of several monitoring points at time step $N + 1$, trained RNNs are employed for midpoints and radiuses (midpoint-radius representation) or upper and lower bounds (upper-lower-bounds representation). Finally, reconstruction data techniques are applied to approximate the complete interval settlement field based on the outputs of the two previous methods. For midpoint-radius representation, the GPOD and NNMF approaches are adopted for the midpoints and the radiuses respectively. Meanwhile, upper bounds and lower bounds of the surface settlement field are reconstructed to satisfy the constraint of generating valid interval data by a constrained GPOD method. Finally, the predicted results are included into the available data set and the procedure is repeated for the subsequent steps.

5. Processing Interval Data with the Hybrid Surrogate Model

This section briefly describes the computational approaches of each component of the hybrid surrogate model for interval data: process prediction (prediction the settlements of selected monitoring points for the next time steps), field approximation by interpolating with complete data (approximation of the settlement fields from starting time step up to current time step) and reconstruction missing data (prediction of complete settlement field for the next time step).

5.1. Process prediction with recurrent neural networks for interval data

For the approximation and prediction of dependencies between structural processes, recurrent neural networks (RNNs) are beneficial. RNNs are able to learn dependencies between data series without considering time as additional input parameter. This enables to capture time-dependent phenomena in data series and predict (extrapolate) further structural responses. The layered network structure of the RNNs is similar to the architecture of feed forward neural networks, see e.g. (Freitag, 2015). In addition to the hidden neurons, so-called context neurons are used to consider the structural history. For each hidden and each output neuron, a context neuron is assigned. These context neurons send time delayed context signals to the hidden and output neurons.

In order to process interval data with RNNs, optimization approaches or interval analysis can be applied, see e.g. (Freitag et al., 2011) to directly compute the lower and upper bounds by interval arithmetic operations, see also (Freitag, 2010). An alternative to these approaches is the midpoint-radius representation of interval data, where two separate RNNs for the midpoints and the radiuses are generated, see (Freitag et al., 2016).

Table II. POD procedure to find the basis vectors capture a desired accuracy.

Input: Given matrix $\mathbf{S}$, desired accuracy E
Output: Truncated POD basis vectors $\hat{\mathbf{\Phi}}$
1: Compute covariance matrix $\mathbf{C} = \mathbf{S}^{\mathrm{T}} \cdot \mathbf{S}$
2: Compute eigenvalue decomposition $[\mathbf{\Psi}, \mathbf{\Lambda}] = eig(\mathbf{C})$
3: Set $\mathbf{\Phi}_i = \mathbf{S} \cdot \mathbf{\Psi}_{-,i}/\sqrt{\lambda_i}$, where $\mathbf{\Psi}_{-,i}$ is the ith column of matrix $\mathbf{\Psi}$
4: Set $\lambda_i = \mathbf{\Lambda}_{ii}$ for $i = 1, ..., M$
5: Define K based on desired accuracy E as following $\sum_{i=1}^{K} \lambda_i / \sum_{i=1}^{M} \lambda_i \geqslant E$
6: **return** truncated POD basis $\hat{\mathbf{\Phi}}$ by taking the first K columns of $\mathbf{\Phi}$

5.2. Field approximation with complete interval data

In general, interval data can be split using midpoint-radius or lower-upper-bounds representations. If the latter is adopted, constraints are required to ensure that the prediction results for lower bound are always smaller than the results for upper bounds. Meanwhile, the first representation requires that the prediction for the radius component must be non-negative. In the paper, two separate POD-RBF surrogate models for the midpoints and the radiuses are created to produce quick predictions of the system response (i.e. the interval settlement field) corresponding to an arbitrary set of input parameters (realisations of geotechnical interval parameters and deterministic steering parameters) by interpolation between the sample data points. The basis idea of the POD approach and how to combine the method with RBF to form a surrogate model are described in detail in (Freitag et al., 2015). The below sections explain this procedure briefly.

5.2.1. *Proper Orthogonal Decomposition*

POD can be seen as a model reduction technique or as a widely used method in exploratory data analysis. This approach aims to extract a compact representation of high-dimensional data by projecting the data into a lower-dimensional space. The full orthonormal basis of the subspace can be used to approximate the given set of data in an optimal least-squares sense. By truncating the basis, cheap reduced order models or surrogate models are formed. POD approach has been known under various name depending on the area of application such as: Karhunen-Loeve Decomposition (KLD) (Karhunen., 1946; Loeve., 1978) in stochastics, Principal Component Analysis (PCA) in data analysis (Hotelling., 1933) or empirical orthogonal function in oceanography and meteorology (Lorenz, 1956). The procedure is explained in the algorithm in Table II.

A high-dimensional matrix $\mathbf{S}$ and a single column of $\mathbf{S}$ can be approximated as a linear combination of the truncated basis vectors $\hat{\mathbf{\Phi}}$ as $\mathbf{S} \approx \hat{\mathbf{\Phi}} \cdot \hat{\mathbf{A}}$ and $\mathbf{S}_i \approx \hat{\mathbf{\Phi}} \cdot \hat{\mathbf{A}}_i$. At this step, *truncated* "amplitude" matrix and vector, $\hat{\mathbf{A}}$ and $\hat{\mathbf{A}}_i$, contain constant values associated with the given matrix $\mathbf{S}$. Hence, only an approximation for snapshots that were generated in the original high-dimensional snapshots matrix $\mathbf{S}$ is available.

Table III. POD-RBF procedure to predict output system response from an arbitrary set of input parameters.

Input: Snapshots output matrix $\mathbf{S}$, snapshots input matrix $\mathbf{z}$, arbitrary input vector $\mathbf{z}^*$, desired accuracy E
Output: System response vector $\mathbf{S}^*$
1: Compute truncated POD basis $\hat{\mathbf{\Phi}}$ based on E (see algorithm in Table II)
2: Compute $f_j(\mathbf{z}^i)$ with $\mathbf{z}^i = \mathbf{z}^*$ and $i, j = 1, ..., M$
3: Form matrix $\mathbf{F}$ from previous step
4: Compute $\hat{\mathbf{A}} = \hat{\mathbf{\Phi}}^{\mathrm{T}} \cdot \mathbf{S}$
5: Compute $\mathbf{B}$ based on $\mathbf{F}$, $\hat{\mathbf{A}}$
6: Compute $f_j(\mathbf{z}^*)$ with $j = 1, ..., M$
7: Form vector $\mathbf{F}^*$ from previous step
8: **return** System response vector $\mathbf{S}^* = \hat{\mathbf{\Phi}} \cdot \mathbf{B} \cdot \mathbf{F}^*$

5.2.2. *POD-RBF*

To pass from discrete type of a response to a rather continuous one, each amplitude vector is modified as a nonlinear function of input parameters on which the system depends. The amplitude matrix $\hat{\mathbf{A}}$ can be related to interpolation functions by an unknown matrix of constant coefficients $\mathbf{B}$.

$$\hat{\mathbf{A}} = \mathbf{B} \cdot \mathbf{F}, \tag{4}$$

$\mathbf{F}$, being a set of predefined interpolation functions $f_j(\mathbf{z})$ of input parameters $\mathbf{z}$, is given in the following form $\mathbf{F}_i = [f_1(\mathbf{z}^i)...f_j(\mathbf{z}^i)...f_M(\mathbf{z}^i)]^T$. The choice of $f_j(\mathbf{z})$ can be arbitrary and in this study inverse multiquadric radial function, a type of RBF (see (Hardy, 1990) for a description), is chosen as interpolation functions. An approximation of the output system response corresponding to an arbitrary set of input parameters is obtained following the algorithm in Table III.

5.3. Reconstruction interval missing data

5.3.1. *Midpoint-radius representation*

For midpoint-radius representation, the missing midpoints are reconstructed by the unconstrained GPOD and the NNMF approach is employed for the missing radiuses.

5.3.1.1. *Unconstrained GPOD* Another extension of POD based on a combination of basic POD method with linear regression is called Gappy POD (GPOD). The method has been developed in (Everson and Sirovich, 1995) to resconstruct human face images from incomplete data sets. The complete vector for the entire grid is reconstructed by combining POD basis together with gappy data (which is data given at very few of the grid points). Since there is no requirements for the outputs of the method, it is refered to "unconstrained GPOD" method in this paper. In (Bui-Thanh et al., 2004), this methodology was successfully employed for data reconstruction in the field of aerodynamic. The paper shows a very effective way to reconstruct the flowfields from incomplete aerodynamic data set by using GPOD. The gappy POD procedure is described below.

Without any missing data, an arbitrary snapshot $\mathbf{S}_j$, which belongs to a set of snapshots, can be approximated as a linear combination of the first K POD basis vectors $\mathbf{\Phi}$ and an amplitude vector $\mathbf{A}_j$ as described in subsection "Proper Orthogonal Decomposition". The amplitude vector is calculated by minimising the error norm

$$min. \parallel \mathbf{S}_j - \hat{\mathbf{\Phi}} \cdot \hat{\mathbf{A}}_j \parallel_{L^2}^2 \tag{5}$$

The same least square approach can be effectively used to restore missing data of an incomplete data snapshot $\mathbf{S}^*$ by

$$min. \parallel \mathbf{S}^* - \hat{\mathbf{\Phi}} \cdot \hat{\mathbf{A}}^* \parallel_{L^2}^2 \tag{6}$$

However, due to missing elements, the L^2 norm in Eq. (6) cannot be evaluated correctly. As a remedy, the Gappy POD procedure employs the concept of a gappy norm based on available data. Firstly, the locations of missing data must be identified by a vector $\mathbf{m}$ as following

$$\begin{aligned} \mathbf{m}_i &= 0, \quad \text{for locations of unknown or missing data} \\ \mathbf{m}_i &= 1, \quad \text{for locations of known data} \end{aligned} \tag{7}$$

The gappy norm is defined with a gappy inner product $(\cdot, \cdot)_n$, such that

$$\parallel \mathbf{S}_j \parallel_n^2 = (\mathbf{S}_j, \mathbf{S}_j)_n = (m \circ \mathbf{S}^*, m \circ \mathbf{S}^*)_{L^2} = \parallel m \circ \mathbf{S}^* \parallel_{L^2}^2, \tag{8}$$

where $\circ$ denotes point-wise multiplication. The complete (repaired) vector from $\mathbf{S}^*$ can be reproduced using the assumption that $\mathbf{S}^*$ can be characterized with the existing snapshots set $\mathbf{S}$. The intermediate repaired vector $\widetilde{\mathbf{S}}^*$ can be expressed in terms of *truncated* POD basis vectors $\hat{\mathbf{\Phi}}$ as follows

$$\widetilde{\mathbf{S}}^* \approx \hat{\mathbf{\Phi}} \cdot \hat{\mathbf{A}}^*. \tag{9}$$

The vector $\hat{\mathbf{A}}^*$ can be computed by minimizing the error $E = \parallel \mathbf{S}^* - \widetilde{\mathbf{S}}^* \parallel_n^2$. A solution to this so-called *least squares* or *linear regression* problem is given by a linear system of equations

$$\mathbf{M} \cdot \hat{\mathbf{A}}^* = \mathbf{R} \tag{10}$$

with

$$\begin{aligned} \mathbf{M} &= (\hat{\mathbf{\Phi}}^{\mathrm{T}}, \hat{\mathbf{\Phi}}) \\ \mathbf{R} &= (\hat{\mathbf{\Phi}}^{\mathrm{T}}, \mathbf{S}^*) \end{aligned} \tag{11}$$

Solving Eq. (9) with $\hat{\mathbf{A}}^*$ computed from Eqs. (10) and (11), the intermediate repaired vector $\widetilde{\mathbf{S}}^*$ is obtained. Finally, by replacing the missing elements in $\mathbf{S}^*$ by these in $\widetilde{\mathbf{S}}^*$ the complete vector of output system responses is reconstructed. The step by step of GPOD procedure is shown in the algorithm in Table IV.

5.3.1.2. *Non-Negative Matrix Factorization* For midpoint-radius representation of interval data, the midpoint component is handled well with the unconstrained GPOD method described in previous section. Alternatively, the Non-Negative Matrix Factorization (NNMF) is utilized to ensure the

Table IV. GPOD procedure to reconstruct the complete solution vector from incomplete solution vector.

Input: Snapshots output matrix $\mathbf{S}$, mask vector $\mathbf{m}$, incomplete solution vector $\mathbf{S}^*$, desired accuracy E
Output: Complete solution vector $\mathbf{S}^*$
1: Compute truncated POD basis $\hat{\mathbf{\Phi}}$ based on E (see algorithm in Tabel II)
2: Compute $\mathbf{M} = (\hat{\mathbf{\Phi}}^{\mathrm{T}}, \hat{\mathbf{\Phi}})$
3: Compute $\mathbf{R} = (\hat{\mathbf{\Phi}}^{\mathrm{T}}, \mathbf{S}^*)$
4: Compute $\hat{\mathbf{A}}^*$ from $\mathbf{M}$ and $\mathbf{R}$
5: Compute $\widetilde{\mathbf{S}}^* = \hat{\mathbf{\Phi}} \cdot \hat{\mathbf{A}}^*$
6: **return** Complete solution vector $\mathbf{S}^*$ by replacing missing elements from corresponding elements of $\widetilde{\mathbf{S}}^*$

positive sign of the reconstructed results for the radiuses. The NNMF was first suggested by Paatero and Tapper (Paatero and Tapper, 1994) as a concept of Positive Matrix Factorisation concentrating on a specific application concerned with Byzantine algorithms. Modern NNMF algorithms can be divided into four categories: Standard NNMF, Constrained NNMF, Structured NNMF and Generalised NNMF. In this paper, the Standard NNMF is utilized for radius predictions as described below.

Given a $(N \times M)$ non-negative matrix ${}_r\mathbf{S}$ and a reduced rank k, the NNMF algorithm is searching for two non-negative matrices $\mathbf{W}_{n\times k}$ and $\mathbf{H}_{k\times m}$ that satisfies the following optimization problem

$$min. \frac{1}{2} \parallel {}_r\mathbf{S} - \mathbf{W} \cdot \mathbf{H} \parallel_F^2 \text{ subject to}, \mathbf{W}, \mathbf{H} \geq 0. \tag{12}$$

Similar to the POD approach, $\mathbf{W}$ and $\mathbf{H}$ are denoted as the *basis matrix* and *coefficient matrix*, respectively. The alternating non-negative least squares (NNLS) algorithm proposed in (Kim and Park., 2008), which ensures the convergence of the minimization problem in Eq. (12), is implemented in this paper.

The reconstruction procedure for a non-negative vector containing the radiuses $\mathbf{S}^+$ now can follow the steps listed in the GPOD method with some minor modifications. The corresponding objective function $\mathbf{E} = \parallel \mathbf{S}^+ - \mathbf{W} \cdot \mathbf{H}^+ \parallel_n^2$ to be minimised contains the distances between the available incomplete data vector and the predicted vector. The non-negative *basis matrix* $\mathbf{W}$ is assumed to be known from the available non-negative data matrix ${}_r\mathbf{S}$. The coefficient vector $\mathbf{H}^+$ is obtained considering the non-negativity constraint by solving the *non-negative least squares* problem

$${}_r\mathbf{M} \cdot \mathbf{H}^+ = {}_r\mathbf{R}, \tag{13}$$

with

$$\begin{aligned} {}_r\mathbf{M} &= (\mathbf{W}^{\mathrm{T}}, \mathbf{W}) \\ {}_r\mathbf{R} &= (\mathbf{W}^{\mathrm{T}}, \mathbf{S}^+) \end{aligned} \tag{14}$$

The non-negative constrained least squares problem in Eq. (13) is solved by an algorithm introduced in (VanBenthem and Keenan, 2004). Finally, replacing the missing elements in the incomplete vector of radiuses, the complete or repaired radiuses vector of the system response is reconstructed.

5.3.2. *Upper-lower-bounds representation*
For the upper-lower-bounds representation, the unconstrained GPOD and a constrained GPOD techniques are utilized to predict the upper and lower bounds respectively. The unconstrained GPOD described in the previous section can be applied for the prediction of either the upper bound or the lower bound of the interval surface settlement field. In this paper, the upper bound ${}_u\mathbf{S}$ is chosen to predict first and the lower bound ${}_l\mathbf{S}$ is approximated considering the predicted result of upper bound as a constraint in the reconstruction procedure.

5.3.3. *Constrained GPOD*
In particular, the intermediate solution ${}_l\hat{\mathbf{A}}$ of the *least squares* problem in Eq. (10) needs to satisfy a constraint as following

$$ {}_l\widetilde{\mathbf{S}} \approx \hat{\mathbf{\Phi}} \cdot {}_l\hat{\mathbf{A}} \leq {}_u\mathbf{S}. \tag{15}$$

This is done by implementing a quadratic programming algorithm, which uses an active set method similar to that introduced in (Gill et al., 1981).

6. Examples

6.1. Verification Example

The proposed method for interval data is firstly illustrated with a benchmark from structural analysis. Figure 1 shows the chosen example, which is a cantilever beam with a moving single load. In this example, the interval bounds of the deflection $\overline{\mathbf{S}}$ and the modulus elasticity of the beam

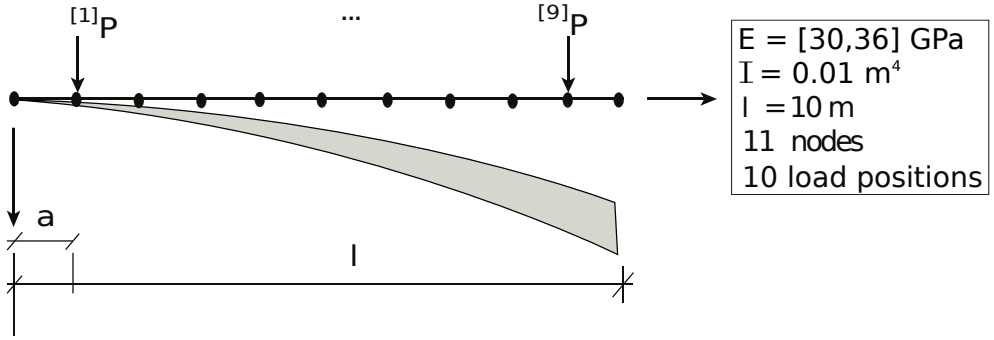

Figure 1. Verification example.

material $\overline{E} = [30, 36]$ GPa are the outputs and inputs of the investigations. The single load ${}^{[n]}P$ is considered as a time-variant parameter moving along the beam from node 2 to node 11. The scenarios of changing ${}^{[n]}P$ in each time step can be arbitrary but the value of ${}^{[n]}P$ is assumed to be restricted in a range from 10kN to 100kN. Given a scenario for stepwise moving load ${}^{[n]}P$ from $\mathbf{a}$=1,2,..,9 m, see Figure 2, the objective of this investigation is to predict the interval deflection of the complete beam when $\mathbf{P}_t$ moves to the final position node 11, i.e. $\mathbf{a}$=10 m. This is done with the assumption such that only the interval deflection at nodes 2,6 and 10 (i.e. $\mathbf{x}$=1,5 and 9 m) can be

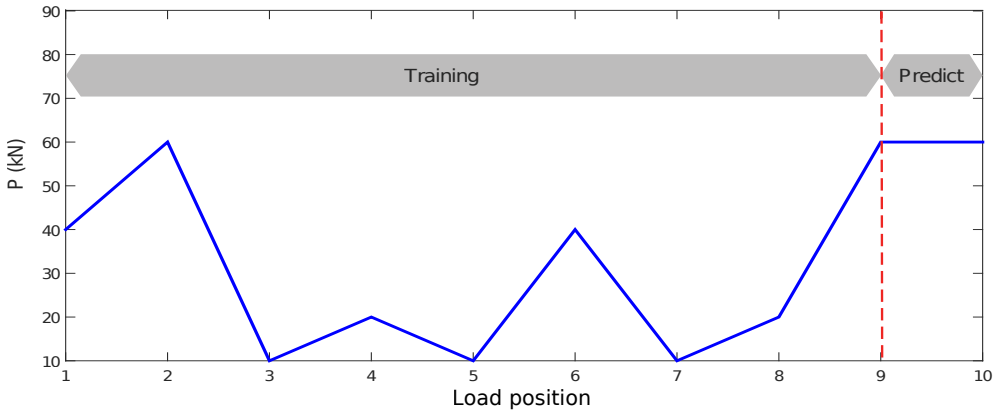

Figure 2. An arbitrary scenario of changing and moving load ${}^{[n]}P$.

observed. The proposed surrogate model predicts the deflections at other nodes of the beam. The predicted results are compared with the analytical solution given as

$$\overline{S} = \frac{Px^2}{6\overline{E}I}(3l - x), \text{ for } 0 < x < a, \tag{16}$$

$$\overline{S} = \frac{Pl^2}{6\overline{E}I}(3x - l), \text{ for } a < x < l. \tag{17}$$

In general, the interval bounds of the deflections for all beam nodes from step 1 to 9 can be calculated using a deterministic surrogate model with an optimization approach. However, in this example, the bounds $\overline{\mathbf{S}}$ can be obtained directly from the above equations using interval arithmetic. The verification procedure is done through the following steps:

1. The surrogate model is created based on results from 1600 snapshots which are obtained from combining 8 different intervals of $\overline{E}$ and 200 scenarios of moving ${}^{[n]}P$. Each snapshot contains the interval displacements of 11 nodes of the beam from step 1 to 9. The snapshots data set is divided into sets for midpoints and radiuses as introduced previously.

2. The interval deflections of complete beam nodes from step 1 to 9 corresponding to the given interval of $\overline{E} = [30, 36]GPa$ and the scenario of changing ${}^{[n]}P$ from step 1 to 9, see Figure 2 are initialized by the POD-RBF approach. These results are represented by two matrices ${}_m\mathbf{S}$ and

${}_r\mathbf{S}$ in the types of midpoints and radiuses respectively.

$$ {}_m\mathbf{S} = \begin{bmatrix} 0.000 & 0.000 & 0.000 & 0.000 & 0.000 & 0.000 & 0.000 & 0.000 & 0.000 \\ 0.017 & 0.162 & 0.037 & 0.108 & 0.066 & 0.365 & 0.090 & 0.239 & 0.855 \\ 0.042 & 0.519 & 0.130 & 0.394 & 0.243 & 1.375 & 0.341 & 0.915 & 3.289 \\ 0.067 & 0.908 & 0.251 & 0.799 & 0.506 & 2.900 & 0.727 & 1.966 & 7.105 \\ 0.092 & 1.297 & 0.377 & 1.262 & 0.824 & 4.811 & 1.221 & 3.329 & 12.104 \\ 0.117 & 1.687 & 0.502 & 1.735 & 1.170 & 6.981 & 1.796 & 4.941 & 18.091 \\ 0.142 & 2.076 & 0.628 & 2.209 & 1.522 & 9.279 & 2.425 & 6.741 & 24.867 \\ 0.167 & 2.465 & 0.753 & 2.682 & 1.873 & 11.599 & 3.080 & 8.665 & 32.235 \\ 0.192 & 2.854 & 0.879 & 3.155 & 2.224 & 13.918 & 3.740 & 10.652 & 39.997 \\ 0.217 & 3.243 & 1.004 & 3.629 & 2.575 & 16.238 & 4.400 & 12.649 & 47.957 \\ 0.242 & 3.632 & 1.130 & 4.102 & 2.926 & 18.558 & 5.060 & 14.646 & 55.950 \end{bmatrix} $$

$$ {}_r\mathbf{S} = \begin{bmatrix} 0.000 & 0.000 & 0.000 & 0.000 & 0.000 & 0.000 & 0.000 & 0.000 & 0.000 \\ 0.003 & 0.015 & 0.008 & 0.015 & 0.015 & 0.039 & 0.020 & 0.035 & 0.082 \\ 0.008 & 0.050 & 0.027 & 0.056 & 0.056 & 0.147 & 0.075 & 0.133 & 0.315 \\ 0.013 & 0.087 & 0.053 & 0.114 & 0.116 & 0.309 & 0.161 & 0.286 & 0.680 \\ 0.018 & 0.124 & 0.079 & 0.180 & 0.189 & 0.513 & 0.270 & 0.485 & 1.159 \\ 0.023 & 0.161 & 0.106 & 0.247 & 0.268 & 0.744 & 0.396 & 0.720 & 1.732 \\ 0.028 & 0.198 & 0.132 & 0.315 & 0.349 & 0.989 & 0.535 & 0.982 & 2.381 \\ 0.033 & 0.235 & 0.158 & 0.382 & 0.429 & 1.237 & 0.680 & 1.262 & 3.086 \\ 0.038 & 0.272 & 0.185 & 0.449 & 0.510 & 1.484 & 0.826 & 1.552 & 3.830 \\ 0.043 & 0.309 & 0.211 & 0.517 & 0.590 & 1.731 & 0.971 & 1.843 & 4.592 \\ 0.048 & 0.347 & 0.238 & 0.584 & 0.671 & 1.979 & 1.117 & 2.133 & 5.357 \end{bmatrix} $$

The upper and lower bounds of the interval deflection field are computed as ${}_u\mathbf{S} = {}_m\mathbf{S} + {}_r\mathbf{S}$ and ${}_l\mathbf{S} = {}_m\mathbf{S}$ - ${}_r\mathbf{S}$. The errors between the predicted bounds and analytical solutions, which are defined as following

$$ error = \sqrt{\frac{\sum_{i=1}^{N}(\mathbf{S}^i_{approx} - \mathbf{S}^i_{analytical})^2}{\sum_{i=1}^{N}(\mathbf{S}^i_{analytical})^2}} \times 100\%, \tag{18} $$

are 5.0% and 5.3% for the upper bound and the lower bound, respectively.

3. Finding the reduced bases of the matrices ${}_m\mathbf{S}$, ${}_r\mathbf{S}$, ${}_u\mathbf{S}$ and ${}_l\mathbf{S}$. The POD procedure are performed to obtain ${}_m\hat{\mathbf{\Phi}}$, ${}_u\hat{\mathbf{\Phi}}$ and ${}_l\hat{\mathbf{\Phi}}$ for the midpoint, upper bound and lower bound matrices, respectively.

Whereas the NNMF approach is used to extract the reduced bases $\mathbf{W}$ for ${}_r\mathbf{S}$.

$$
{}_m\hat{\mathbf{\Phi}} = \begin{bmatrix} 0.000 & 0.000 \\ 0.009 & 0.053 \\ 0.034 & 0.173 \\ 0.073 & 0.302 \\ 0.125 & 0.406 \\ 0.188 & 0.452 \\ 0.258 & 0.411 \\ 0.336 & 0.266 \\ 0.417 & 0.046 \\ 0.500 & -0.209 \\ 0.583 & -0.470 \end{bmatrix} \quad \mathbf{W} = \begin{bmatrix} 0.000 & 0.000 \\ 0.009 & 0.020 \\ 0.034 & 0.079 \\ 0.074 & 0.168 \\ 0.126 & 0.269 \\ 0.188 & 0.360 \\ 0.259 & 0.419 \\ 0.336 & 0.433 \\ 0.417 & 0.410 \\ 0.499 & 0.365 \\ 0.582 & 0.316 \end{bmatrix} \quad {}_u\hat{\mathbf{\Phi}} = \begin{bmatrix} 0.000 & 0.000 \\ 0.009 & 0.052 \\ 0.033 & 0.170 \\ 0.073 & 0.300 \\ 0.125 & 0.405 \\ 0.187 & 0.452 \\ 0.258 & 0.413 \\ 0.335 & 0.267 \\ 0.417 & 0.047 \\ 0.500 & -0.209 \\ 0.583 & -0.471 \end{bmatrix} \quad {}_l\hat{\mathbf{\Phi}} = \begin{bmatrix} 0.000 & 0.000 \\ 0.009 & 0.054 \\ 0.034 & 0.175 \\ 0.073 & 0.305 \\ 0.125 & 0.407 \\ 0.188 & 0.451 \\ 0.259 & 0.410 \\ 0.336 & 0.265 \\ 0.417 & 0.046 \\ 0.500 & -0.209 \\ 0.583 & -0.469 \end{bmatrix}
$$

4. The patterns of input-output data at nodes 2, 6 and 10 of the beam are utilized for constructing two separate RNNs to predict the midpoints and the radiuses for the interval deflections at these selected nodes. With an arbitrary input scenario of changing the load $\mathbf{P}_t$, the outputs, i.e. the deflections at 3 selected nodes, are computed from these RNNs. A network structure with one hidden layer containing 7 hidden neurons was sufficient to predict the midpoint. On the other hand, the radius prediction requires a two hidden layers RNN with 7 neurons per layer. In both networks, a delay of one time step has been selected for the context neurons. From the midpoint-radius prediction results, the upper and lower bounds of the three selected nodes ${}_u\overline{\mathbf{S}}_{RNN}$ and ${}_l\overline{\mathbf{S}}_{RNN}$ are calculated.

$$
{}_u\bar{\mathbf{S}}_{RNN} = \begin{bmatrix} 0.959 \\ 21.013 \\ 57.000 \end{bmatrix} \quad {}_u\bar{\mathbf{S}}_{an} = \begin{bmatrix} 0.967 \\ 20.833 \\ 56.700 \end{bmatrix} \quad {}_l\bar{\mathbf{S}}_{RNN} = \begin{bmatrix} 0.800 \\ 17.607 \\ 47.730 \end{bmatrix} \quad {}_l\bar{\mathbf{S}}_{an} = \begin{bmatrix} 0.806 \\ 17.361 \\ 47.250 \end{bmatrix}
$$

The errors following Eq. (18) for upper and lower bounds approximation are 0.58% and 1.07%, respectively.

5. Finally, the intervals of deflections of all 11 beam nodes in step 10 are predicted. The reduced bases ${}_m\hat{\mathbf{\Phi}}$, $\mathbf{W}$, ${}_u\hat{\mathbf{\Phi}}$ and ${}_l\hat{\mathbf{\Phi}}$ are the inputs of the procedure together with the incomplete vectors ${}_m\mathbf{S}^*$, ${}_r\mathbf{S}^*$, ${}_u\mathbf{S}^*$ and ${}_l\mathbf{S}^*$. The outputs are the complete vectors ${}_{mr}\overline{\mathbf{S}}^*$ and ${}_{ul}\overline{\mathbf{S}}^*$ corresponding to midpoint-radius and upper-lower-bounds approaches. These two vectors are compared with reference analytical solution to verify the accuracy and effectiveness of the two methods.

As introduced previously, the computation of deflection intervals for the cantilever beam is carried out with two approaches: midpoint-radius (mid-rad) and upper-lower-bounds (up-low). The

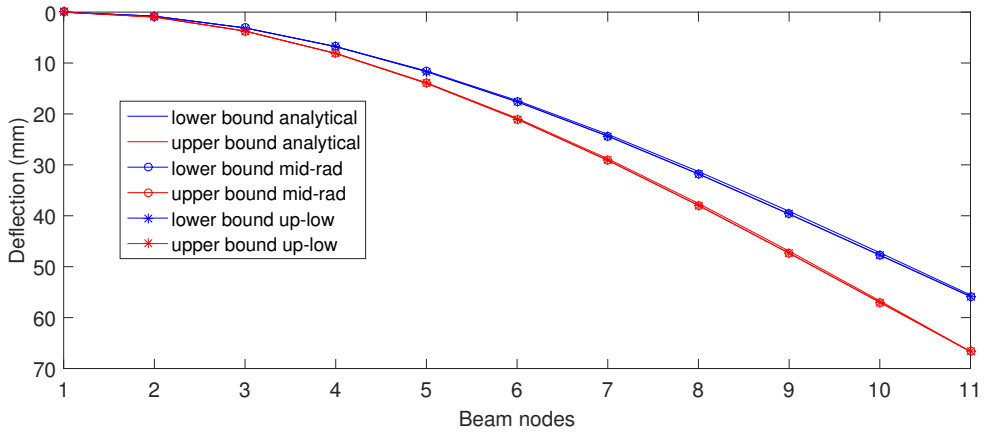

Figure 3. Comparison of predictions from two approaches (mid-rad and up-low) with the analytical solution.

final prediction results of the deflections at step 10 for ${}^{[10]}P = 60$ kN are

$$ {}_{mr}\bar{\mathbf{S}}^* = \begin{bmatrix} [0.000,\ 0.000] \\ \mathbf{[0.800,\ 0.959]} \\ [2.989,\ 3.838] \\ [6.657,\ 8.254] \\ [11.590,\ 14.047] \\ \mathbf{[17.607,\ 21.013]} \\ [24.422,\ 29.043] \\ [31.874,\ 37.882] \\ [39.718,\ 47.289] \\ \mathbf{[47.730,\ 57.000]} \\ [55.804,\ 66.725] \end{bmatrix} \quad {}_{ul}\bar{\mathbf{S}}^* = \begin{bmatrix} [0.000,\ 0.000] \\ \mathbf{[0.800,\ 0.959]} \\ [3.112,\ 3.715] \\ [6.798,\ 8.113] \\ [11.689,\ 13.949] \\ \mathbf{[17.607,\ 21.013]} \\ [24.373,\ 29.093] \\ [31.800,\ 37.960] \\ [39.655,\ 47.352] \\ \mathbf{[47.730,\ 57.000]} \\ [55.840,\ 66.689] \end{bmatrix} \quad \bar{\mathbf{S}}^*_{analytical} = \begin{bmatrix} [0.000,\ 0.000] \\ \mathbf{[0.806,\ 0.967]} \\ [3.111,\ 3.733] \\ [6.750,\ 8.100] \\ [11.556,\ 13.867] \\ \mathbf{[17.361,\ 20.833]} \\ [24.000,\ 28.800] \\ [31.306,\ 37.567] \\ [39.111,\ 46.933] \\ \mathbf{[47.250,\ 56.700]} \\ [55.556,\ 66.667] \end{bmatrix} $$

Figure 3 illustrates the comparison of predictions using two representation approaches together with analytical solution. It is shown, that both methods provide very good predictions for the upper and lower bounds of beam deflection with errors of 0.61%, 1.18% from midpoint-radius representation and 0.34%, 1.09% for upper-lower-bounds representation, respectively. In addition, the prediction accuracy of the surrogate model is further validated by comparing 100 random validation cases with the analytical results. The average error of all validation cases is around 1% or less for both bounds and both methods, which proves the prediction capability of the surrogate model. Therefore the generated surrogate model will be further applied to the analysis considering polymorphic uncertain data, e.g.with in p-box approach. Here, the interval of $\overline{E}$ is fixed in the range from 30 GPa to 36 GPa, meanwhile the moving ${}^{[n]}P$ scenario is treated as a stochastic process. 1000 samples of moving ${}^{[n]}P$ scenarios are randomly generated with the assumption that it follows a Gaussian distributed process with a mean value of ${}^{[n]}P = 50$ kN and the standard deviation of $\sigma = 15$ kN. Figure 4 depicts two curves, which are the minimum and maximum cdfs of the deflection of the beam at node 11 for time step 10, respectively. With the new surrogate model, the results of this analysis are obtained in only half an hour. This is a significant reduction in computation time comparing

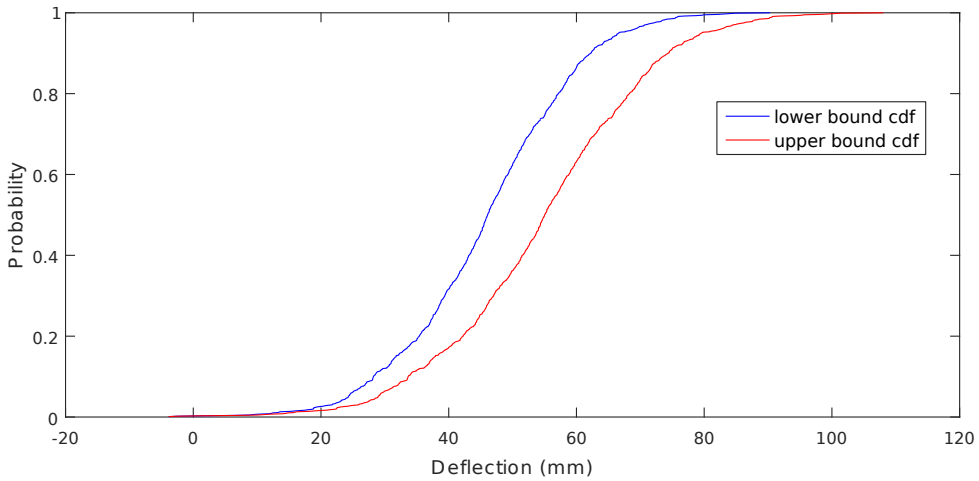

Figure 4. P-box for the deflection of the beam at node 11 for time step 10.

to the optimization approach which normally takes 10 hours to complete the analysis. This enables the application of more advanced and complicated reliability analysis in engineering problems.

6.2. Application Example in Mechanized Tunneling

This section presents an application of the proposed surrogate modeling strategy for interval data based on a synthetic example representing a mechanized tunneling process. The interval results, which are computed from two representation approaches (mid-rad and up-low) are compared with the reference solution obtained from an optimization approach shown in (Freitag et al., 2015) in terms of prediction performance and computation time. The deterministic surrogate model is firstly trained with numerical results from FE simulation model `ekate` described in Section 2. The capability of the deterministic surrogate model is given with more details in (Freitag et al., 2015). Consequently, the interval analyses with the optimization approach are performed to generate data for the training of the proposed hybrid surrogate model with interval data to deliver predictions for the interval bounds of the surface settlements in further time steps of the tunneling process.

The synthetic example simulating the construction by a tunnel boring machine (TBM) of a tunnel section with 8.5m diameter and 8.5m overburden is generated using the `ekate` model. Figure 5 shows the simulation model with dimensions of 48m, 170m and 56m (in x,y,z directions, respectively). The length of each excavation step is 1.5m, i.e the tunnel section consists of 32 steps. The effect of two existing buildings to the surface displacement field is taken into account by applying substitute models with equivalent thickness of 5m and a stiffness of 50 GPa as shown in Figures 5. The tunnel construction process is modeled via a step-by-step procedure consisting of individual phases: soil excavation, applying support pressure, moving shield, applying grouting pressure and lining installation.

The tunnel is completely excavated through soil layer 1 of a ground model comprising of two parallel soil layers with different thicknesses and properties, see Figure 5. The groundwater table

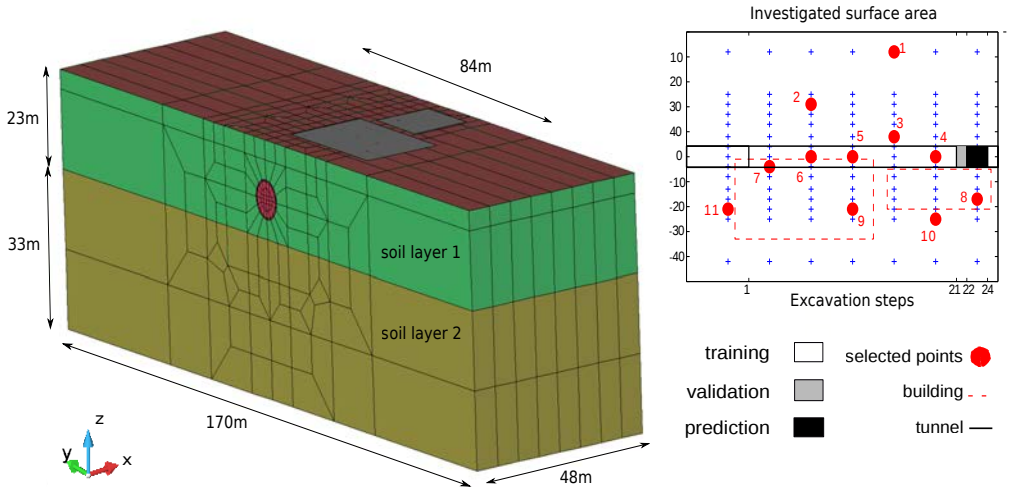

Figure 5. Numerical simulation model of a tunnel section (left) and investigates surface area (right).

is constant along the tunnel and at the ground surface. A time constant support pressure of 180 kPa is applied at the heading face. The grouting pressure ${}^{[n]}P$ in the tail void is considered with a particular value in each excavation step. The soil behavior is described by an elastoplastic model using Drucker-Prager yield criterion with a linear isotropic hardening. Linear elastic behavior is assumed for the shield and tunnel lining.

In this study, the elastic modulus E_1 of the first soil layer is taken as an uncertain parameter defined by an interval as $E_1 = [45{,}52]$ MPa to be comparable with the reference result in (Freitag et al., 2015),. The grouting pressure ${}^{[n]}P$ in each excavation step n is chosen as varying operational parameter. The investigated ranges of these parameters are 20 to 110 MPa for E_1 and 130 to 230 kPa for ${}^{[n]}P$. It is assumed that the current state of the TBM advance corresponds to the 22^{nd} step of the process, i.e. $n = 1, 2.., 22$. The proposed surrogate model is utilized to predict the complete settlement fields in time step 23. Based on the calculated surface displacements, only an effective surface area of 42 m in y-direction from tunnel axis is investigated due to the fact, that the displacements of points located further than this distance are almost zero. Figure 5 (right) shows the investigated surface area with 105 points for which the Z-displacements are considered as outputs of the proposed method. In the example, the interval settlements of 11 selected monitoring points among 105 surface points are predicted by the RNNs with the approach of midpoint-radius representation. Whereas, the complete surface field is reconstructed with both mid-rad and up-low approaches.

Firstly, in the offline stage, 60 numerical simulations are performed to generate data for building the deterministic surrogate model based on a combination of 10 particular values of E_1 with 6 scenarios of changing ${}^{[n]}P$ from time step 1 to n. Then, possible intervals of E_1 are selected and an optimization based interval analysis is performed. The result of this interval analysis are used to generate the proposed surrogate model. Now, in the online stage, the interval surface settlement fields corresponding to the given interval of $E_1 = [45{,}52]$ MPa is computed in real-time.

Table V presents the relative error in percentage for the upper and lower bounds from both methods comparing to the reference solution in (Freitag et al., 2015). The errors are calculated by

$$error = \sqrt{\frac{\sum_{i=1}^{N}(\mathbf{S}_i^{opt} - \mathbf{S}_i^{*})^2}{\sum_{i=1}^{N}(\mathbf{S}_i^{opt})^2}} \times 100\% \,, \tag{19}$$

Table V. Relative prediction error for the two approaches.

	Upper bound		Lower bound	
	mid-rad	up-low	mid-rad	up-low
Error [%]	8.9	8.0	6.2	5.9

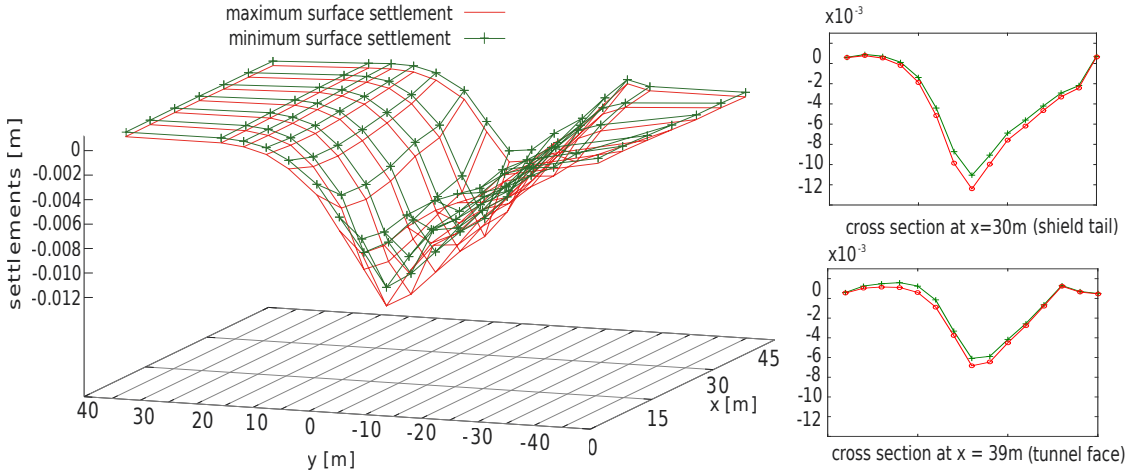

Figure 6. Typical interval field of tunneling induced surface settlements with $\bar{E}_1 = [45, 52]$ MPa.

In Figure 6, the typical computed interval settlement field is represented by its lower and upper bounds. The most important benefit of the proposed approach is, that the computation time is significantly reduced compared to the optimization approach. To obtain the interval bounds from the optimization approach, the required computation time is around 1.5 hours. The proposed approaches needs only 2 seconds to predict the interval settlement field with similar accuracy.

7. Conclusion

In the paper, a hybrid surrogate modeling strategy based on RNN and POD approaches has been developed to predict interval time variant settlement fields induced by mechanized tunneling taking uncertain geotechnical parameters quantified as intervals into account. In order to achieve real-time prediction capabilities, the hybrid RNN-GPOD surrogate model for deterministic data, which has

been previously developed by the authors, has been extended to process interval data by means of the midpoint-radius and upper-lower-bounds representations. Generally, both approaches produced very good prediction in comparison to the optimization approach for interval analysis. However, the computational time is significantly reduced from 1.5 hours by the optimization approach to 2 seconds by the proposed strategy. With such a fast response, it enables to quickly investigate the consequences of certain process parameters on the expected settlements in the subsequent excavation stages. Hence, the proposed strategy can by applied for real-time predictions to support the machine driver in steering the TBM. The upper-lower-bounds approach will be extended for fuzzy data. It is also planned to further develop a p-box approach for real-time applications.

Acknowledgements

Financial support was provided by the German Science Foundation (DFG) in the framework of project C1 of the Collaborative Research Center SFB 837 "Interaction Modeling in Mechanized Tunneling". This support is gratefully acknowledged.

References

Beer, M., Y. Zhang, S. Quek and K. Phoon. Reliability Analysis with Scare Information: Comparing Alternative Approaches in a Geotechnical Engineering Context. *Structural Safety*, 41:1–10, 2013.

Bieniawski, Z. *Engineering Rock Mass Classifications*. Wiley, New York, 1989.

Bui-Thanh, T., K. Damodaran and K. Willcox. Aerodynamic Data Reconstruction and Inverse Design using Proper Orthogonal Decomposition. *The American Institute of Aeronautics and Astronautics (AIAA)*, 42:1505–1516, 2011.

Cao, B. T., S. Freitag and G. Meschke. A hybrid RNN-GPOD Surrogate Model for Real-time Settlement Predictions in Mechanised Tunnelling. *Advanced Modeling and Simulation in Engineering Sciences*, 3:Paper 5, 2016.

Everson, R. and L. Sirovich. Karhunen-Loeve Procedure for Gappy Data. *Journal of the Optical Society of America A: Optics, Image Science and Vision*, 12(8):1657–1664, 1995.

Ferson, S., V. Kreinovich, L. Ginzburg, D. S. Myers and K. Sentz. *Constructing probability boxes and Dempster-Shafer structures*. Tech. Rep. SAND2002-4015, Sandia National Laboratories, 2003.

Fetz, T., M. Oberguggenberger, J. Jäger, D. Köll, G. Krenn, H. Lessmann and R. Stark. Fuzzy Models in Geotechnical Engineering and Construction Management. *Computer-Aided Civil and Infrastructure Eng.*, 14:93–106, 1999.

Freitag, S. *Modellfreie numerische Prognosemethoden zur Tragwerksanalyse*, Dissertation, Veröffentlichungen – Institut für Statik und Dynamik der Tragwerke, Heft 19, TU Dresden, 2010.

Freitag, S. Artificial Neural Networks in Structural Mechanics, in Y. Tsompanakis, J. Kruis, B. Topping (Editors), *Computational Technology Reviews*, Volume 12, pages 1–26. Saxe-Coburg Publications, Stirlingshire, 2015.

Freitag, S., B. T. Cao, J. Ninić and G. Meschke. Hybrid Surrogate Modelling for Mechanised Tunnelling Simulations with Uncertain Data. *International Journal of Reliability and Safety*, 9(2/3):154–173, 2015.

Freitag, S., B. T. Cao, J. Ninić and G. Meschke. Recurrent Neural Networks and Proper Orthogonal Decomposition with Interval Data for Real-Time Predictions of Mechanised Tunnelling Processes, *Computers and Structures*, 2016, submitted.

Freitag, S., W. Graf and M. Kaliske. Recurrent Neural Networks for Fuzzy Data. *Integrated Computer-Aided Engineering*, 18(3):265–280, 2011.

Freitag, S., R. L. Muhanna and W. Graf. Interval Monte Carlo simulation with neural network-based surrogate models. In: G. Deodatis, B. R. Ellingwood, D. M. Frangopol (eds.) *Safety, Reliability, Risk and Life-Cycle Performance of Structures and Infrastructures, Proceedings of 11th International Conference on Structural Safety and Reliability (ICOSSAR 2013)*, New York, Taylor and Francis, London, 431–438, 2013.

Gill, P. E., W. Murray and M. Wright. *Practical Optimization*, Academic Press, London, 1981.

Graf, W., M. Götz and M. Kaliske. Structural design with polymorphic uncertainty models. In: M. Modares (ed.) *Proceedings of the 6th Int. Conference on Reliable Engineering Computing (REC 2014)*, Chicago, 64–76, 2014.

Hanss, M. The transformation method for the simulation and analysis of systems with uncertain parameters. *Fuzzy Sets and Systems*, 130(3):277–289, 2002.

Hardy, R. L. Theory and Applications of the Multiquadric-biharmonic Method: 20 Years of Discovery 1968-1988. *Computers & Mathematics with Applications*, 19(8-9):163–208, 1990.

Hotelling, H. Analysis of a Complex System of Statistical Variables into Principal Components. *Journal of Educational Psychology*, 24:417–441;498–520, 1933.

Karhunen, K. Zur Spektraltheorie stochastischer Prozesse. *Annales Academiae Scientiarum Fennicae. Mathematica*, 34, 1946.

Kasper, T. and G. Meschke. A 3D Finite Element Simulation Model for TBM Tunnelling in Soft Ground. *International Journal for Numerical and Analytical Methods in Geomechanics*, 28:1441–1460, 2004.

Kim, H. and H. Park. Nonnegative Matrix Factorization Based on Alternating Nonnegativity Constrained Least Squares and Active Set Method. *SIAM Journal on Matrix Analysis and Applications*, 30(2):713–730, 2008.

Laursen, T. *Computational Contact and Impact Mechanics*. Springer, Berlin-Heidelberg, 2002.

Loeve, M. *Probability Theory II*, Volume 46 of *Graduate Texts in Mathematics*. Springer Verlag, New York, 1978.

Lorenz, E. N. *Empirical Orthogonal Functions and Statistical Weather Prediction*, Technical Report 1, M.I.T, Department of Meteorology, 1956.

Meschke, G. Consideration of Aging of Shotcrete in the Context of a 3D Viscoplastic Material Model. *International Journal for Numerical Methods in Engineering*, 39:3123–3143, 1996.

Meschke, G., J. Ninic, J. Stascheit and A. Alsahly. Parallelized Computational Modeling of Pile-Soil Interactions in Mechanized Tunneling. *Engineering Structures*, 47:35 – 44, 2013,

Moens, D. and D. Vandepitte. A survey of non-probabilistic uncertainty treatment in finite element analysis. *Computer Methods in Applied Mechanics and Engineering*, 194:1527–1555, 2005.

Moens, D. and M. Hanss. Non-probabilistic finite element analysis for parametric uncertainty treatment in applied mechanics: Recent advances. *Finite Element Analysis and Design*, 47:4–16, 2011.

Möller, B., W. Graf and M. Beer. Fuzzy Structural Analysis Using α-level Optimization. *Computational Mechanics*, 26:547–565, 2000.

Möller, B. and M. Beer. Engineering Computation under Uncertainty – Capabilities of Non-traditional Models. *Computers and Structures*, 86:1024–1041, 2008.

Moore, R. *Methods and Applications of Interval Analysis*, Volume 2. SIAM, Studies in Applied Mathematics, Philadelphia, 1979.

Muhanna, R. L., H. Zhang, and R. L. Mullen. Interval Finite Elements as a Basis for Generalized Models of Uncertainty in Engineering. *Reliable Computing*, 13(2):173–194, 2007.

Nagel, F., J. Stascheit and G. Meschke. Process-oriented Numerical Simulation of Shield Tunneling in Soft Soils. *Geomechanics and Tunnelling*, 3(3):268–282, 2010.

Nagel, F. and G. Meschke. An Elasto-plastic Three Phase Model for Partially Saturated Soil for the Finite Element Simulation of Compressed Air Support in Tunnelling. *International Journal for Numerical and Analytical Methods in Geomechanics*, 34:605–625, 2010.

Ninić, J. *Computational Strategies for Predictions of the Soil-structure Interaction during Mechanized Tunneling*, PhD thesis, Institute for Structural Mechanics, Ruhr University Bochum, 2015.

Paatero, P. and U. Tapper. Positive Matrix Factorization: A Nonnegative Factor Model with Optimal Utilization of Error Estimates of Data Values, *Environmetrics*, 5(2):111–126, 1994.

Rao, M. V. R., R. L. Mullen, and R. L. Muhanna. A new interval finite element formulation with the same accuracy in primary and derived variables. *International Journal for Reliability and Safety*, 5(3/4):336–357, 2011.

Van Benthem, M. and M. Keenan. Fast Algorithm for the Solution of Large-Scale Non-Negativity-Constrained Least Squares Problems, *Journal of Chemometrics*, 18:441–450, 2004.

Zhang, H., R. Mullen and R. Muhanna, Interval Monte Carlo methods for structural reliability, *Structural Safety*, 32:183–190, 2010.

Effect of Statistical Uncertainties on Predicted Extreme Wind Speeds

Á. Rózsás[1] and M. Sýkora[2]
[1]*Department of Structural Engineering, Budapest University of Technology and Economics, Budapest 1111, Hungary, rozsas.arpad@epito.bme.hu*
[2]*Department of Structural Reliability, Klokner Institute, Czech Technical University in Prague, Prague 16608, Czech Republic, miroslav.sykora@cvut.cz*

Abstract: Statistical uncertainties, arising from the uncertainty of parameter estimation and model selection, are often neglected in probabilistic assessment of engineering structures. However, few previous studies indicate that this might cause severe underestimation of extreme loads and lead to insufficient structural reliability. This contribution aims to qualitatively and quantitatively investigate the effect of this simplification on extreme values of wind speed that are commonly associated with design values. The probabilistic modelling of basic wind speeds is thoroughly investigated. Moderately high temporal resolution data – daily 10 min averaged maxima from three distinct one hour long measurement sessions – are obtained from the Carpatclim database, covering a 50-year observation period. Data for Budapest are taken into account as a representative example. Block maxima and peak over threshold approaches are applied to extract maxima and to fit associated distributions. Frequentist and Bayesian statistics are used to assess the effect of statistical uncertainties. The parameter estimation uncertainty is quantified by uncertainty intervals. Statistical model uncertainty is explored using different distribution types and taken into account by Bayesian model averaging. The conducted analyses imply that neglecting statistical uncertainties might yield to considerable underestimation of extreme values. Using the currently widespread annual maxima approach, the parameter estimation uncertainty can lead to underestimation of 1000-year return period values by about 20%. The commonly adopted Gumbel model yields 20% larger values with a return period of 1000 years than those based on the generalized extreme value distribution. The latter fits better to data though unambiguous, fully data-driven recommendation on model selection cannot be made. Bayesian posterior predictive distribution is recommended for accounting parameter estimation uncertainty. Moreover, if viable, smaller than one year block size, multiple maxima in a block, or peak over threshold methods are recommended to increase sample size and reduce statistical uncertainties. This leads to 70% reduction in the range of a 90% confidence interval for 1000-year extremes for the selected location.

Keywords: Bayesian statistics, design value, extreme load, generalized extreme value distribution, model selection, parameter estimation, statistical uncertainty, wind speed

1. Introduction

1.1. Motivation

Probabilistic models of extreme wind speeds are thoroughly studied by researchers from various disciplines, particularly by meteorologists. However, structural reliability requirements often substantially differ from interests of meteorologists, e.g. estimation of large (>1000 year) return period events and focus on prediction

rather than best fit to observations. For instance, extreme events dominating structural reliability may have return periods of thousands years as is a common requirement for structures in nuclear industry. Since observation periods are only small fraction of these return periods, extrapolation to unobserved ranges is inevitable. This can yield to highly uncertain model estimates at the critical tail regions. Nevertheless it appears that this uncertainty is commonly neglected in civil engineering while drafting standards or conducting probabilistic analysis. The aim of this paper is to investigate the effect of this neglect on representative wind speed fractiles and to find out whether the current practice is (reasonably) conservative. Scarcity of observations leads to aforementioned uncertainty for all random variables; hereinafter it is referred to as statistical uncertainty. It is reasonable to make distinction between two classes: parameter estimation uncertainty and model selection uncertainty. The former is concerned with the uncertainty of parameter estimation for a given model, while the latter relaxes this constraint by considering a group of candidate models and quantifying their "goodness".

Previous studies show that the neglect of these uncertainties might cause severe underestimation of extreme loads and lead to insufficient structural reliability. For ground snow load – using the annual maxima for inference – a 1000-year return period value might be underestimated by 20% due to the neglect of parameter estimation uncertainty (Rózsás and Sýkora, 2015a), and the neglect of model selection uncertainty can lead to over an order of magnitude underestimation of failure probability (Rózsás and Sýkora, 2015b). Other studies found similar, often more significant effects in cases of extreme rainfalls (Coles and Pericchi, 2003), extreme hydrological hazards (Sisson et al., 2006), and slope reliability (Li et al., 2015).

In the following we critically review the current practice of extreme wind modelling in civil engineering and propose statistical approaches and a general rationale to quantify and incorporate statistical uncertainties. The applied methods can be utilized for other extreme climatic actions such as flooding and snow loads.

1.2. STATISTICAL MODELLING IN CIVIL ENGINEERING

Table I. reports a brief overview of current civil engineering practice in statistical modelling of extreme wind speeds. Features relevant for the present analysis are highlighted, e.g. applied method to extract extreme values and its parameters of the method, considered distribution type, treatment of statistical uncertainties and sources of information. More details are given in Section 2.

The suite of Eurocodes lacks commentary or references to background documents. However, based on some paragraphs and background documents, it seems that statistical uncertainty has been neglected while drafting EN 1991-1-4 on wind actions on structures. To our knowledge this approach is applied to other actions too, e.g. point estimates are used to derive representative ground snow loads (Sanpaolesi, 1998) and thermal actions as well (Sanpaolesi and Colombini, 2005). Since annual maxima are typically used to infer probabilistic models, and to derive representative fractiles and partial factors in Eurocodes, this neglect might have considerable impact.

The American load code ASCE 7-10 mentions the effect of statistical uncertainty – termed therein as sampling error – on estimating basic wind speed from regional climatic data. However, no general justification is provided and the provision seems to be rather arbitrary.

Table I. Summary of civil engineering practices in statistical modelling of extreme wind speeds.

Reference	Method	Distribution	Variable	Stat. uncertainty
EN 1991-1-4 (4.2)	Block method*	Gumbel	basic wind speed**	neglected
EN 1991-1-4 (E.10)	Block method*	Weibull	wind speed, wind induced cyclic loading	NA
JCSS Part 2.13	Block method*, annual maxima mentioned	Gumbel (Weibull)	wind speed maxima	neglected
(Niemann and Diburg, 2013)	Block method - annual maxima (9-102 observations)	Gumbel, GEV	wind speed annual maxima	neglected
(Kruger, 2010)	Block method with annual maxima and peak over threshold method with various thresholds	GEV, GP, Gumbel, etc.	wind speed maxima	upper bound of 75% confidence interval of parameters
ASCE 7-10 Ch.26.	Block method*	Gumbel	basic wind speed**	guidance for regional data

*Judgement of the authors; **EN 1991-1-4: obtained from 10 minutes mean wind speed at 10 m above ground level in open country terrain, modified to account for the direction of the wind being considered and the season (if required), characteristic value corresponding to 50 years return period; ASCE 7-10: three-second gust speed at 10 m above the ground in open terrain prevailing in the upwind direction (detailed definition in the standard), the value given in the standard corresponding to 300-1700 years return period depending on occupancy category.

Kruger (2010) analyzed extreme wind speeds for South Africa and considered the effect of parameter estimation uncertainty. His approach is to upward adjust the estimated parameters by an appropriate confidence limit: 75% is recommended. This again seems to be unjustified, moreover a snow related study showed that this approach is not appropriate to account for statistical uncertainties and is usually non-conservative (Rózsás and Sýkora, 2015c). This brief review indicates that parameter estimation and model selection uncertainties are commonly neglected or inadequately addressed in probabilistic reliability studies involving wind actions.

1.3. ADOPTED APPROACH AND AVAILABLE DATABASE

Wind speed data from a representative location of the Carpathian Region are initially analyzed by accepting the widespread techniques and assumptions in civil engineering. Then advanced statistical analysis is carried out to quantify and incorporate statistical uncertainties and is considered to provide reference values. To explore the effect of statistical uncertainties, two different statistical paradigms are employed: frequentist and Bayesian statistics. Extreme value theory of mathematical statistics is used to extract extremes from observations and to select theoretically supported distribution functions. All models in this study are fully statistical, e.g. no physical arguments and principles are incorporated.

The wind data under study are obtained from the Carpatclim database (Szalai et al., 2013), covering a 50-year observation period. The climatological grid covers the region between latitudes 44°N and 50°N, and longitudes 17°E and 27°E. The data are gathered at 10 m height above the ground in horizontal direction from 270 stations with relatively homogeneous spatial distribution. These are homogenized and spatially interpolated using meteorological and statistical models; these post-processed data are available in the database and used as inputs in this study. The database has moderately high temporal resolution: for each day maxima of 10 min averaged wind speed from three distinct measurement sessions spanning over one hour,

and about 10 km spatial resolution. Note that the experience from detailed analyses of wind speeds indicates that annual maxima obtained from continuous measurements exceed those inferred from stations with the three measurement sessions per day by about 5 %. Obviously, this difference needs to be taken into account while deriving representative values for structural design, but is neglected in this study focused on comparison of various statistical approaches to modelling of extreme wind speeds.

For the 50-year period more than 18000 observations for a grid point are thus available. The 10 min averaged value "is typically sufficiently long to incorporate most of the shorter period fluctuations in natural wind (turbulence) but is sufficiently short to be normally regarded as representing a period of near-constant background mean wind" (Harper et al., 2010; EN 1991-1-4).

Budapest (E 19.1, N 47.5°) is selected as a representative location to illustrate the effect of parameter estimation and model selection uncertainty. It is characterized by a single type of wind phenomena – strong wind generated by thunderstorms. Thus unimodal distributions (no mixed models) seem to suffice for statistical modelling.

2. Statistical Tools

2.1. CONSIDERED DISTRIBUTIONS

Extreme value theory offers two popular approaches to analyze extremes: block maxima and peak over threshold methods. These are applied to extract maxima from wind speed observations and select asymptotic distribution functions (Coles, 2001; Reiss and Thomas, 2007):

- If observations are divided into blocks and largest values are selected from each, the block maxima distribution asymptotically approaches the generalized extreme value family (GEV) under rather permissive conditions. This method is commonly referred to as block maxima method.
- If values over a selected threshold are considered, the distribution of these values asymptotically approaches the generalized Pareto family (GP) under rather permissive conditions (Coles, 2001; Reiss and Thomas, 2007).

For the block maxima approach with one year block size, two- (LN2) and three-parameter lognormal (LN3), and Gumbel distributions are used in addition to GEV. Gumbel is a special case of the GEV distribution with shape parameter converging to zero, and is commonly used in engineering to model extremes (Table I). Two-parameter lognormal distribution is found to describe well snow extremes, it is mainly applied in the US (ASCE, 2010). The LN3 distribution was successfully applied and propagated in the Czech Republic to model various types of extremes (Holický and Sýkora, 2015 and 2016). For block sizes different from one year, the GEV model is considered only. For multiple maxima in a block analyses, a multivariate generalized extreme value distribution (rGEV) is applied, considering the dependence between maxima in a block (Coles, 2001). In the peak over threshold approach, the GP distribution is used. The applied parametrization of these distributions are given in Table II. The parametrization has no effect on frequentist inference, however marginally affects the Bayesian estimates as priors generally differ for alternative parameterization of the model and flat (uniform) prior on scale and location parameters likely correspond to non-flat priors of moment characteristics.

Table II. Summary of considered distribution types, their application range, and parametrization.

Distribution	Application in this study	Parametrization	Reference
Gumbel	block method; single maxima; 1-year block size	scale and location	(Coles, 2001)
GEV	block method; single maxima; arbitrary block size	shape, scale, and location	(Coles, 2001)
rGEV	block method; multiple maxima; 1-year block size	shape, scale, and location	(Coles, 2001)
LN2	block method; single maxima; 1-year block size	shape and scale	(Singh, 1998)
LN3	block method; single maxima; 1-year block size	shape, scale, and threshold	(Singh, 1998)
GP	peak over threshold, threshold as a study parameter	shape, scale, and threshold	(Coles, 2001)

2.2. STATISTICAL INFERENCE

Frequentist and Bayesian statistical paradigms are selected to fit models and to quantify statistical uncertainties. Bayesian statistics treats parameters as random variables and assigns probability distribution to them. The latter is convenient when the inferred parameters are inputs and the full representation of their uncertainty is needed for instance in probabilistic reliability and risk analyses. Additionally it can handle complex problems with messy data and can combine information from different sources. These advantages distinguish it from the commonly used frequentist statistics that focuses on data variability given a parameter value (Spiegelhalter and Rice, 2009).

The main instrument of Bayesian statistics is Bayes' rule which incorporates the information conveyed by the data and prior knowledge through the likelihood function and prior distribution of parameters, respectively. The distribution of parameters obtained in this why is termed a posterior distribution. When future observations are to be predicted – as is typical in structural reliability studies – the posterior predictive distribution then serves this purpose by averaging over the posterior distribution of parameters (Aitchison and Dunsmore, 1980). Parameter estimation uncertainty can be expressed by providing the whole posterior distribution or its credible intervals (Gelman et al., 2003). Model selection uncertainty can be handled through Bayesian model averaging where weighted average over candidate models is calculated. A weight (b_i) is the probability of the i^{th} model given the data relative to the summed probability of all considered models (Hoeting et al., 1999). The weights favor parsimony (Occam's razor), i.e. penalizes model complexity. Thereby overfitting can be avoided and models with different complexity can be compared. In the Bayesian analyses, flat (uniform) priors are used for all the parameters in Table II with practically infinite range; multiple parameter settings are verified to confirm convergence.

In the frequentist paradigm, the maximum likelihood method is used to obtain point estimates. The uncertainty intervals – termed often as confidence intervals – are obtained by the delta method (Coles, 2001) and bootstrapping (Efron et al., 1994). A resampled empirical distribution function is created using linear interpolation among points within the data range.

In general Bayesian inference requires substantially more computational power than frequentist approaches. Yet these calculations can be carried out on personal computers. The computational burden is even larger for structural reliability applications where uncertain tails of distributions are of crucial importance and their estimation requires much larger simulation numbers. Taking advantage of the small dimension (less or equal to three) of probabilistic models in this study, direct numerical integration is used for Bayesian inference.

3. Results of Analysis

3.1. Block maxima

3.1.1. Annual maxima

Initially representative fractiles for different distributions are calculated and compared. The selected extremes correspond to 50, 100, 500, and 1000-year return period events. The 50-year event is the characteristic value of meteorological actions in Eurocode while the other are intended to indicate the design point coordinate of a structure subject to increasingly dominant wind action or with increasing structural reliability. They are comparable to representative basic wind speeds of ASCE 7-10 that associates 300, 700, and 1700-year return period values with risk categories I, II and III-IV, respectively.

The point estimates of selected extremes with 90% uncertainty intervals are shown in Figure 1. Maximum likelihood point estimates (solid circle) and 90% confidence intervals are obtained by delta method (dashed) and bootstrapping (solid). The bootstrap point estimate is the mean of the sample with symmetrical intervals.

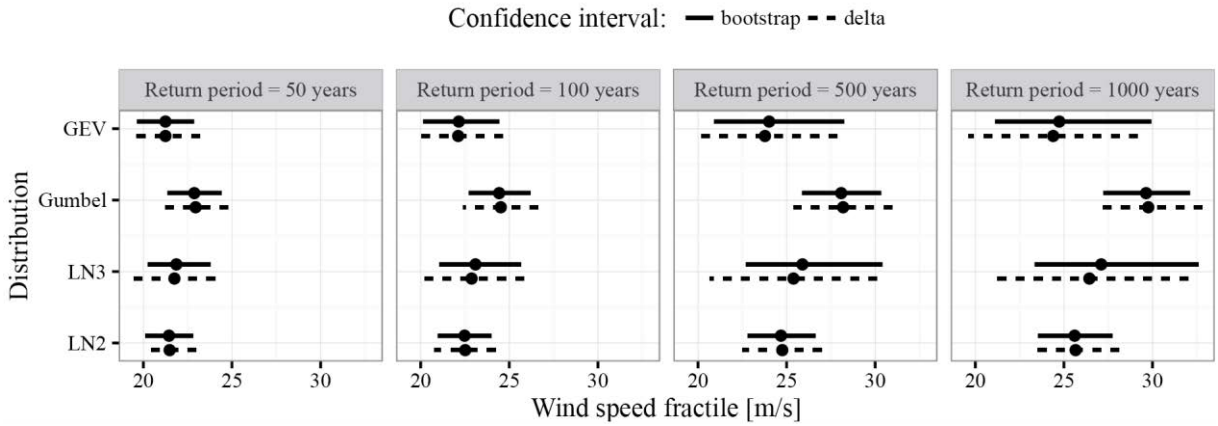

Figure 1. Summary of representative wind extremes with 50, 100, 500, and 1000 years return period for various distributions.

The inference is conducted with one year block size using maximum likelihood method and the confidence intervals are estimated using delta method and bootstrapping. Although the 50-year extremes differ subtly only, the difference is not negligible. For instance the GEV and LN3 distributions yield to 7% lower extreme values than that of Gumbel. The range of 90% confidence intervals is 15% of the associated point estimate.

The bootstrap and delta method confidence intervals match well. However, for larger return periods, their difference progresses particularly in respect of the lower interval endpoints: the delta method tends to provide more conservative estimates. This is partially due to the symmetric nature of delta method based confidence intervals. Confidence intervals are rapidly increasing with an increasing return period. The relative coverage of the 90% confidence intervals to point estimates is 35-40% for the three-parameter distributions; however, they are essentially the same: 15-20% for two-parameter ones even at 1000-year return period level. The difference among distributions in point estimates of 1000-year extremes reaches up to 18%. The results show that both distribution selection and parameter estimation uncertainty have substantial bearing on representative extreme values.

The return period-return level Gumbel plots enable visualization of the effects of distribution selection and parameter estimation uncertainty. Return level plots with confidence intervals are shown in Figure 2. In the figure the maximum likelihood point estimates (white solid line) are accompanied by 90% confidence intervals (gray) obtained by the delta method[1]. The point estimate and confidence interval of the characteristic value v_k along with the number of extreme observations are also displayed on each plot.

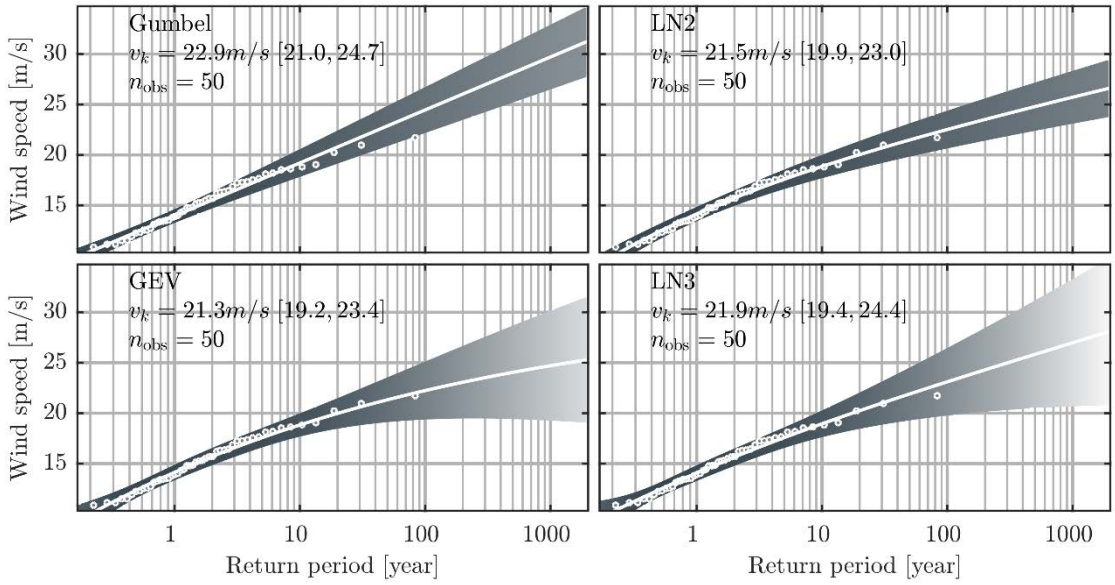

Figure 2. Return level plots of annual wind maxima for the selected distributions.

Although the difference between bootstrap and delta method based confidence intervals can be considerable (Figure 1), the latter is used only in further analysis for simplification. Estimates based on the delta method are deemed to be sufficiently accurate for this investigation. The confidence intervals are substantially widening as the cumulative distribution functions approach the regions with few data and regions of extrapolation. The difference between the models is remarkable, particularly the narrow confidence interval of the Gumbel distribution fails to include the largest observation.

Statistical tests and information theory based goodness-of-fit measures do not clearly support or reject any of the considered distributions even though the tail of the Gumbel model noticeably deviates from the observations. The other distributions – particularly GEV and LN2 – seem to capture the upper tail better. However, this observation needs to be confirmed by analysis of data from more stations.

However for the three-parameter models this is partially attributable to their greater flexibility that is traded-off by increasing parameter estimation uncertainty, i.e. they have wider uncertainty interval than the two-parameter distributions. For two-parameter models, available information allows better model identification.

[1] The interval coloring is 'ink-preserving', i.e. the same 'amount of ink' is used for every vertical section, hence creating a linear transition from the narrowest (dark gray) to the widest interval (white). In a particular 2×2 or 3×2 figure, equal vertical ranges have the same color on each subplot, thus the models are directly comparable based on coloring as well.

The independence of wind speed maxima separated by about four days can be reasonably assumed (Simiu and Heckert, 1996). The focus on annual maxima may thus lead to the loss of information as extreme values generated by less severe storms are discarded, though they can be informative. This additional information can be incorporated by (*i*) reducing block size; (*ii*) considering multiple maxima in a block; and (*iii*) using values above a selected threshold. The first two belongs to the block maxima approach and converge to GEV or GEV-like (rGEV) distributions. The third procedure is commonly referred to as the peak over threshold method and its asymptotic distribution family is the GP distribution (section 3.2). Another approach to reduce sampling variability is to combine wind speed measurements from several stations with similar climatic conditions (Holmes, 1998).

3.1.2. Block maxima with various block sizes

Initially the effect of block size is examined. There is no universal rule to select an optimal block size. Typically the balance between bias and variance is searched. Smaller block increases sample size and thus reduces statistical uncertainties (variance) while non-extreme values might contaminate the sample and introduce bias to the inference.

Figure 3 compares GEV distributions fitted to block maxima with a block size of 1, 1/2, 1/4 and 1/10 of year. The parameters are inferred using the maximum likelihood method. The point estimates (white solid line) are accompanied by 90% confidence intervals (gray) obtained by the delta method. The point estimate and confidence interval of the characteristic value v_k along with the number of extreme observations are also displayed on each plot.

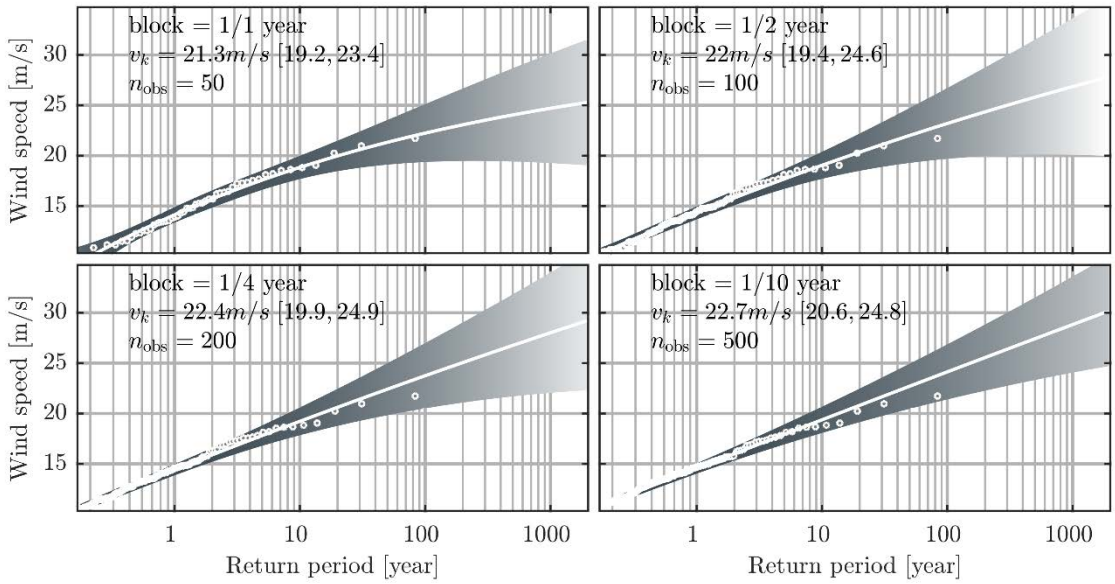

Figure 3. Return level plots of wind maxima with different block sizes (Gumbel plot).

With decreasing block size, smaller observations dominate the fit, yet the 90% confidence intervals still covers all the large observations at the right tail. It is interesting to observe that ten times more observations for the block size of 1/10 of year have no important effect on the confidence intervals of larger upper fractiles.

It seems that the one year blocks capture all the largest values and the enlargement of the sample does not reduce parameter estimation uncertainty in this case. The difference in characteristic value point estimates is subtle, at maximum 6% for 1/10 year block size compared to the one year model. However, the difference between these two models for the extremes with 1000-year return period progresses to 20%. A notable effect of block size reduction is the straightening of the point estimate of the distribution (white solid line), i.e. the shape parameter is approaching zero and the distribution approaches Gumbel distribution.

3.1.3. Multiple maxima in a block

Another technique aimed to increase a sample size considers multiple maxima in a block. This leads to an asymptotic multivariate rGEV distribution. It takes into account the dependence between largest values within the same block, i.e. the second largest must be smaller than the largest. Figure 4 summarizes the results of distribution fitting with number of largest values from 1 to 120 per block. The parameters are inferred using the maximum likelihood method. The point estimates (white solid line) are accompanied by 90% confidence intervals (gray) obtained by the delta method. Also shown in the figure are the point estimates and confidence intervals of the characteristic value v_k along with the number of extreme observations.

Though the number of observations is increased by 120-times, no effect on trends nor on bias in the extreme value-return period plots is observed. However, parameter estimation uncertainty appears to be significantly reduced; the uncertainty intervals for characteristic values reduce by 50% when a number of maxima in a block increases from 1 to 120. The reduction is more pronounced for extremes with longer return periods, e.g. it is 70% for 1000-year return period. The results show that valuable additional information can be extracted from the observations and the uncertainty intervals can be significantly reduced by increasing the number of maxima in a block.

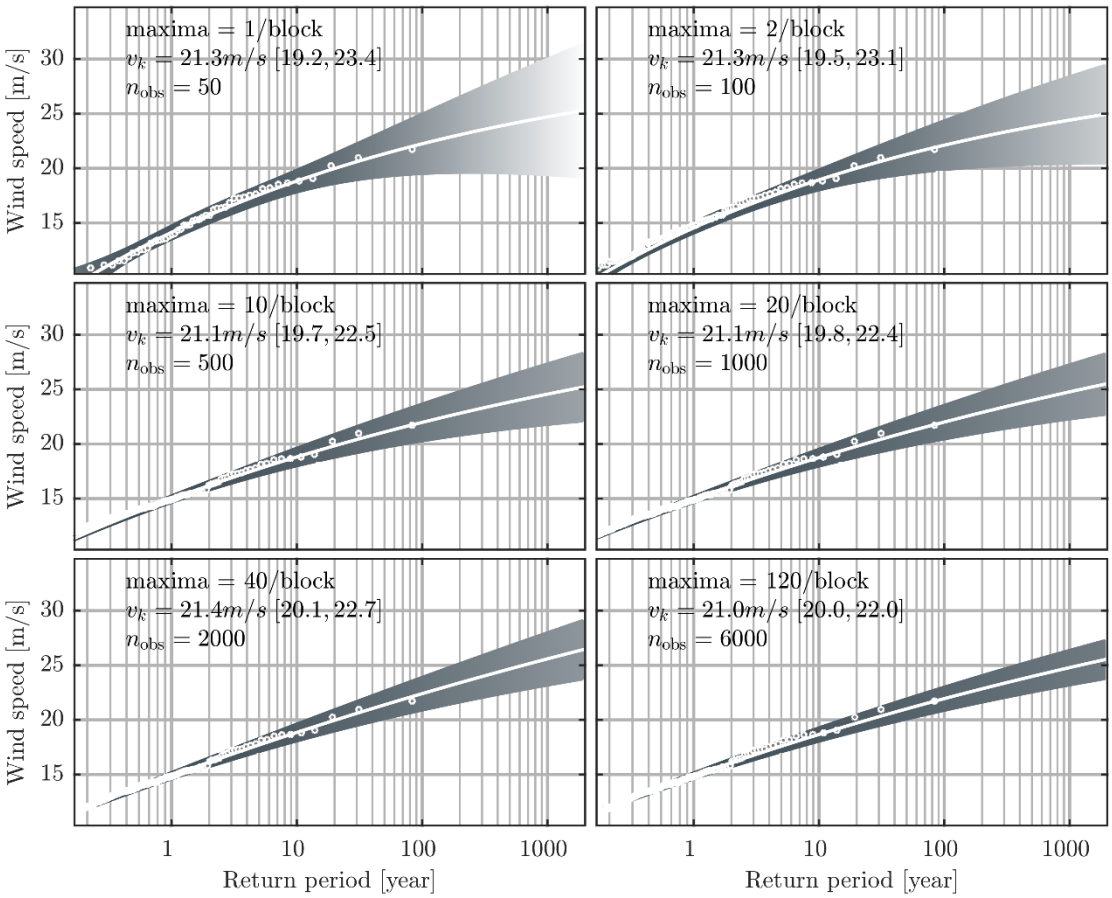

Figure 4. Return level plots wind maxima for various number of maxima in a block; rGEV is used for each plot.

3.2. PEAK OVER THRESHOLD

In this section the peak over threshold method is used to extract extreme wind speeds for Budapest. Since it has different asymptotic distribution than the block maxima, the return value plot transformation is also different, though it has similar characteristics such as logarithmic horizontal scale and linear cumulative distribution if the shape parameter is approaching zero. The threshold selection is complex due to the trade-off between bias and variance as is similar with the block size and multiple largest value selection for block maxima. Again lower threshold allows more observations, however they might not be representative for extremes and can introduce bias.

Mean residual plot and parametric analyses (Coles, 2001) are utilized to assess the stability (variance and bias) of parameter estimates by changing the threshold level. These diagnostic plots suggest an appropriate threshold in the range from 5 to 15 m/s. Return value plots with six different thresholds from this region are presented in Figure 5. The thresholds are chosen to allow comparison with multiple maxima in a block (Figure 4). The GP distribution supported by the extreme value theory is considered for the analyses only. The parameters are inferred using the maximum likelihood method. The point estimates (white solid line) are

accompanied by 90% confidence intervals (gray) obtained by the delta method. The point estimate and confidence interval of the characteristic value v_k along with the number of extreme observations are also displayed on each plot.

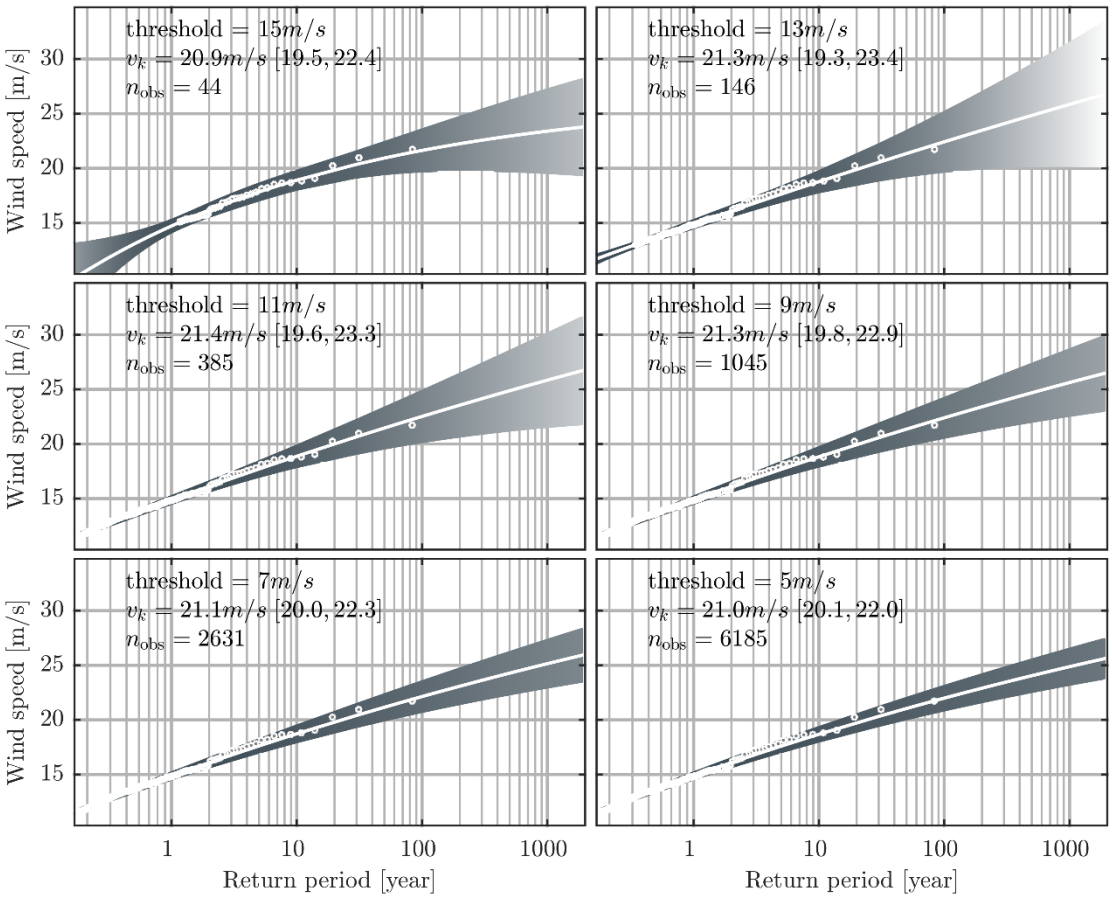

Figure 5. Return level plots wind maxima over various thresholds; GP is used for each plot.

The results show that lower thresholds lead to narrower uncertainty intervals of the fractiles. However, this observation is difficult to generalize as for instance the uncertainty intervals for a threshold of 13 m/s are wider than those for 15 m/s. This discrepancy is attributable to the shift of a shape parameter from negative to positive values. The latter corresponds to a distribution without an upper bound which substantially increases the effect of parameter estimation uncertainty on larger fractiles. For smaller thresholds, this is gradually counterbalanced by the information conveyed by the additional data. Looking at the point estimates of characteristic values, only small differences (up to 2%) are found, thus this representative fractile is sufficiently stable in the investigated range of thresholds. The associated 90% confidence intervals are reduced considerably – by about 50% when the threshold decreases from 15 m/s to 5 m/s. This reduction is the results of a 150-times increased sample size. For larger return periods, the difference of point estimates is larger, it can reach 15% for a 1000-year return period compared to the 15 m/s threshold model. In respect of

bias, the 5 m/s threshold model still seems to be appropriate as all observations are within the confidence interval and the cumulative distribution function is rather stable. Note that these statements apply for the dataset under consideration, other locations might have more consistently varying shape parameter or larger bias at lower thresholds, thus the gain in variance reduction might not be attainable.

Point estimates and confidence intervals obtained for the peak over threshold and multiple maxima block method are in good agreement. The outcomes indicate that parameter estimation uncertainty can be significantly reduced by using the peak over threshold method and incorporation of a great amount of additional data seems not to introduce considerable bias into the model.

3.3. Effect of parameter estimation uncertainty

Uncertainty intervals provide only a visual insight into the effect of parameter estimation uncertainty. This is valuable, but cannot be directly used in probabilistic reliability and risk analyses where all uncertainties need to be taken into account. Therefore, it is more useful to infer the probabilistic distribution of model parameters and capture related uncertainties that can be further propagated and integrated in reliability analysis. This can be readily achieved by Bayesian analysis that treats parameters as random variables. Instead of giving the whole distribution function of uncertain parameters, the parameter estimation uncertainty can be directly incorporated into the distribution of the variable of interest (such as wind speed) by its posterior predictive distribution function. This approach is taken here in conjunction with popular analysis focused on annual maxima. The maximum likelihood, posterior mean, and posterior predictive distributions for Gumbel, LN2, LN3 and GEV are plotted in Figure 6. The posterior predictive is unique for each distribution type.

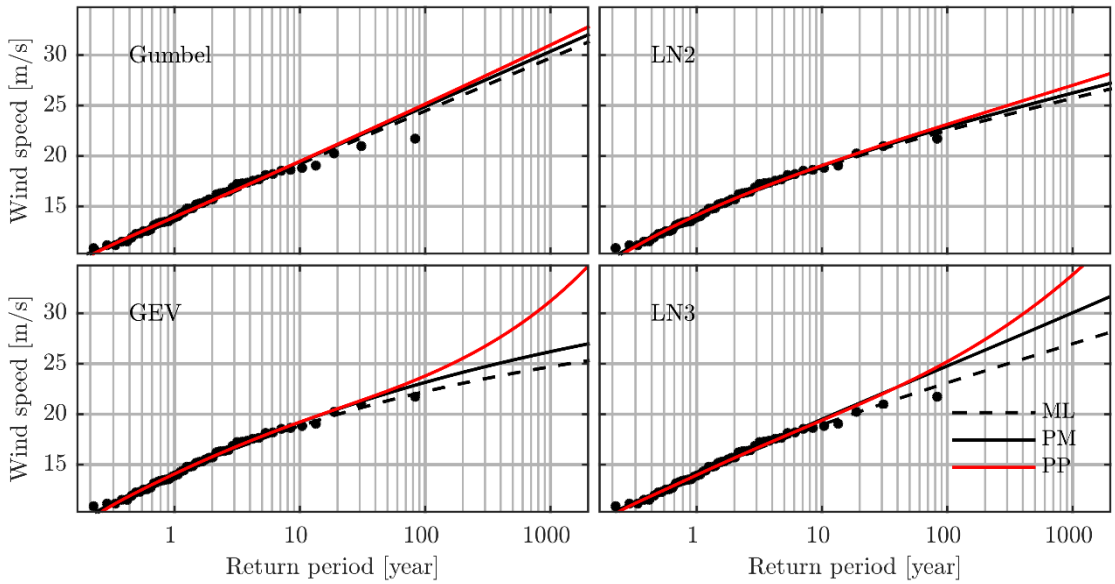

Figure 6. Return level plots of annual maxima with maximum likelihood (dashed black, ML), posterior mean (solid black, PM), and posterior predictive (solid red, PP) distributions.

For the two-parameter models, the effect of parameter estimation uncertainty is negligible even for large return periods (less than 3%). Likewise the effect on characteristic values is negligible for all the models. However, the difference between posterior mean and posterior predictive 1000-year extremes is 12% and 19% for LN3 and GEV, respectively. The results show that parameter estimation uncertainty has significant bearing on larger return period extremes for three-parameter distributions and non-conservative estimates are obtained when its effect is neglected. The plots also show the considerable difference in frequentist and Bayesian point estimates that is a result of the skewed posterior distribution of the fractiles.

3.4. EFFECT OF MODEL SELECTION UNCERTAINTY

Although parameter estimation uncertainty seems to have substantial effect on large return period extremes for three-parameter distributions, this uncertainty might not be of concern when the data can be described by Gumbel or other two-parameter models with sufficient confidence. This section examines this by calculating Bayes weights for each distributions under consideration. The weights express the relative goodness of models; i.e. the relative probability that a distribution is an appropriate underlying model for the observed variable from the considered pool of models.

The calculated weights are 0.22, 0.30, 0.25, and 0.23 for Gumbel, LN2, GEV, and LN3 distributions, respectively. Hence, no distribution is clearly favored. Note that the weights and model averaging is conditional on the pool of candidate models. Figure 7 shows that Gumbel (max. 7%) and LN3 (max. 8%) distributions overestimate the model averaged one while LN2 (max. 8%) and GEV (max. 6%) distributions provide lower estimates. Both types of statistical uncertainty can be incorporated by averaging over the posterior predictive distributions of selected distributions. Note that the model averaged posterior mean is same for each distribution type and associated Bayes weights are indicated in Figure 7.

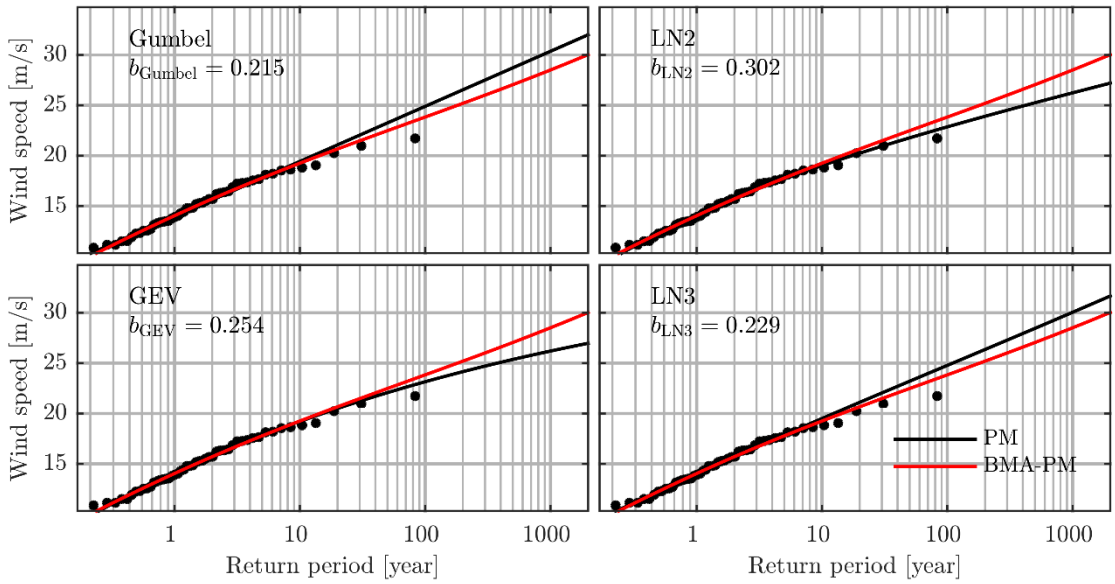

Figure 7. Return level plots of annual wind maxima with Bayesian posterior mean (solid black, PM) and model averaged posterior mean (solid red, BMA-PM) distributions.

4. Conclusions

This contribution compares the current practice of extreme wind speed modelling in civil engineering with more advanced statistical techniques. The former neglects while the latter is capable of quantifying statistical uncertainties. Analysis of extreme wind speeds for the representative location of Budapest reveals that:

- Considering the annual maxima approach, the parameter estimation uncertainty has negligible effect on extremes with long return periods for two-parameter distributions, but it is substantial for three-parameter models. Underestimation can reach up to 20% and the current design practice seems to be non-conservative.
- The popular Gumbel distribution yields about 20% larger 1000-year return period values than those based on the generalized extreme value distribution. The latter fits better to data, though unambiguous recommendation concerning distribution selection cannot be provided due to a limited amount of data.
- Gumbel confidence intervals seem to be deceptively narrow and the largest observation is outside of a 90% uncertainty interval. The generalized extreme value and generalized Pareto distributions imply that the wind maxima have an upper bound, however the 90% confidence intervals overlap with the unbounded region as well.
- If viable, smaller than one year block size, multiple maxima in a block or peak over threshold methods are recommended to increase sample size and reduce statistical uncertainties. This leads to 70% reduction in the range of a 90% confidence interval for 1000-year extremes for the selected location.
- Bayesian posterior predictive distribution is recommended for accounting parameter estimation uncertainty. Furthermore, Bayesian model averaging can be used to account for model selection uncertainty.

The effect of statistical uncertainties on extreme values mainly depends on the available information for probabilistic models. This is particularly important for projecting environmental loads with few observations in a long-term perspective. The recommended procedure can be utilized for other extreme climatic actions such as flooding and snow loads.

Acknowledgements

This work was supported by the Ministry of Education, Youth and Sports of the Czech Republic under Grants LG14012 and LD15037. The numerical analyses are completed using Matlab (Matlab, 2015) and R (R Core Team, 2015), the work and commitment of the developers of these applications are highly appreciated. All codes/ scripts, processed data, and results can be obtained from the authors.

References

ASCE. Minimum Design Loads for Buildings and Other Structures. ASCE/SEI 7-10. Reston, Virginia: American Society of Civil Engineers; 2010.

Aitchison J. and I. R. Dunsmore. *Statistical Prediction Analysis*. New York, USA: Cambridge University Press, 1980.

CEN. Eurocode 1: Actions on structures. Part 1-4: General actions - Wind actions, 2005.

Coles, S. *An Introduction to Statistical Modeling of Extreme Values*. Springer-Verlag, London, 2001.

Coles, S. and L. Pericchi. Anticipating catastrophes through extreme value modelling. *Journal of the Royal Statistical Society. Series C (Applied Statistics)*, 52(4):405–416, 2003.

Efron, B. and R. Tibshirani. *An Introduction to the Bootstrap*. Chapman and Hall/CRC, 1994.

Gelman, A., J. Carlin, H. Stern and D. Rubin. *Bayesian Data Analysis*. CRC Press, USA, 2nd edition, 2003.

Harper B.A., J. D. Kepert and J. D. Ginger. Guidelines for converting between various wind averaging periods in tropical cyclone conditions. World Meteorological Organization. WMO/TD-No. 1555, 2010.

Hoeting, J. A., D. Madigan, A. E. Raftery and C. T. Volinsky. Bayesian model averaging: A tutorial. *Statistical Science*, 14(4):382–417, 1999.

Holický, M. and M. Sýkora. Probabilistic Models for Climatic Actions. In *Proc. 13th International Probabilistic Workshop (IPW 2015)*, pages 281-290, 2015.

Holický, M. and M . Sýkora. Probabilistic Models for Wind Actions. In *Proc. SMRLO'16 The Second International Symposium on Stochastic Models in Reliability Engineering, Life Sciences and Operations Management*, pages 172-175, 2016.

Holmes, J. D. Wind loading of structures: application of probabilistic methods. *Progress in Structural Engineering and Materials*, 1(2):193–199, 1998.

Kruger, A. C. Wind climatology of South Africa relevant to the design of the built environment. (Ph.D.). Stellenbosch University, South Africa, 2010.

Li, D.-Q., X.-S. Tang and K.-K. Phoon. Bootstrap method for characterizing the effect of uncertainty in shear strength parameters on slope reliability. *Reliability Engineering & System Safety*, 140(0):99–106, 2015.

Matlab. version 7.10.0 (R2015a). The MathWorks Inc. Natick, Massachusetts, 2015.

Niemann, H.-J. and S. Diburg. Statistics of extreme climatic actions based on the Gumbel probability distributions with an upper limit. *Computers & Structures*, 126:193–198, 2013.

R Core Team. R: A Language and Environment for Statistical Computing. R Foundation for Statistical Computing, Vienna, Austria, 2015.

Reiss, R.-D. and M. Thomas. *Statistical Analysis of Extreme Values with Applications to Insurance, Finance, Hydrology and Other Fields*. Birkhäuser Basel, 3rd edition, 2007.

Rózsás, Á. and , M. Sýkora. Effect of statistical uncertainties in ground snow load on structural reliability. In *IABSE Conference: Structural Engineering: Providing Solutions to Global Challenges*, pages 220–227, 2015a.

Rózsás, Á. and M. Sýkora. Model comparison and quantification of statistical uncertainties for annual maxima of ground snow loads. In Podofillini, L., Sudret, B., Stojadinovic, B., Enrico, Z., and Kröger, W., editors, *Safety and Reliability of Complex Engineered Systems: ESREL 2015*, p. 2667–2674. CRC Press, 2015b.

Rózsás, Á. and M. Sýkora. Neglect of parameter estimation uncertainty can significantly overestimate structural reliability. Transactions of the VŠB – Technical University of Ostrava, Civil Engineering Series, 15(2):10, 2015c.

Sanpaolesi, L., and S. Colombini. Implementation of Eurocodes. Handbook 3. Action effects for buildings. Chapter IV - Thermal actions on buildings. Aachen, Germany, 2005.

Sanpaolesi, L., D. Currie, P. Sims, C. Sacré, U. Stiefel, S. Lozza, B. Eiselt, R. Peckham, G. Solomos, , I. Holand, R. Sandvik, M. Gränzer, G. König, D. Sukhov, , R. Del Corsoand and P. Formichi. Scientific support activity in the field of structural stability of civil engineering works: Snow loads. Final report phase I. Report, Commission of the European Communities. DGIII-D3, 1998.

Simiu, E. and N. Heckert. Extreme wind distribution tails: A 'peaks over threshold' approach. Journal of Structural Engineering, 122(5):539–547, 1996.

Singh, V. *Entropy-Based Parameter Estimation in Hydrology*. Water Science and Technology Library. Springer Netherlands, 1998.

Sisson, S. A., L. R. Pericchi and S. G. Coles. A case for a reassessment of the risks of extreme hydrological hazards in the Caribbean. *Stochastic Environmental Research and Risk Assessment*, 20(4):296–306, 2006.

Spiegelhalter, D. and K. Rice. Bayesian statistics. *Scholarpedia*, 4(8):5230, 2009.

Szalai, S., I. Auer, J. Hiebl, J. Milkovich, T. Radim, P. Stepanek, P. Zahradnicek, Z. Bihari, M. Lakatos, T. Szentimrey, D. Limanowka, P. Kilar, S. Cheval, G. Deak, D. Mihic, I. Antolovic, V. Mihajlovic, P. Nejedlik, P. Stastny, K. Mikulova, I. Nabyvanets, O. Skyryk, S. Krakovskaya, J. Vogt, T. Antofie and J. Spinoni. Climate of the greater Carpathian Region. Report, 2013.

Probabilistic Modeling of Fatigue Damage in Steel Box-Girder Bridges Subject to Stochastic Vehicle Loads

Yuan Luo [1)], Dong-huang Yan [1)] and Nai-wei Lu [2)]
[1)] *School of Civil Engineering and Architecture, Changsha University of Science and Technology, Changsha 410114, China; y.luo@bauinf.uni-hannover.de*
[2)] *School of Civil Engineering, Southeast University, Nanjing210096, China*

Abstract: Structural failures caused by fatigue damage of several famous steel bridges lead to a wide concern to international bridge industry. A probabilistic fatigue damage modeling method was presented and applied to rib-to-deck details of steel box-girder bridges. In order to solve the time-consuming problems of the bridge finite element analysis under traffic flow loads, a response surface method was used to approximate the function between vehicle axle weight and the equivalent fatigue stresses with a few training data. Finally, the fatigue damage model was applied to the reliability assessment of steel box-girder bridges and the influence of traffic flow parameters on structural fatigue reliability was studied. The numerical results indicate that: the higher occupancy rate of heavy vehicles flow in the slow lane is the main reason for the decrease of the fatigue reliability of corresponding rib-to-deck details compared with the fast lane; the increase of the vehicle axle weight causes a rapid decrease of the fatigue reliability index of the steel box girders. When the annual linear growth factor increases from 0 to 1%, the fatigue reliability index of rib-to-deck detail in the slow lane decreases from 3.42 to 0.72. There is a promising application for stochastic fatigue vehicle flow model and the probabilistic model of fatigue damage.

Keywords: steel box girder, stochastic traffic flow, response surface, fatigue reliability, rib-to-deck

1 Introduction

In recent years, structural failures caused by fatigue damage of several famous steel bridges lead to a wide concern to international bridge engineering (Wolchuk, 2011). However, under the continual growth of vehicle load, several existing steel box-girder bridges in China have suffered from fatigue critical problems (Pan et al., 2011). Since the vehicle load is random in nature, the vehicle induced fatigue damage of actual bridges is a stochastic process. It has been proved to be an urgent issue for probability analysis of fatigue damage of steel box-girder bridges subjected to random vehicle loads**.**

For Long-term structural health monitoring system (SHMS), the sensors are expensive and sensitive to environment factors such as temperature. Besides, finite element method and laboratory fatigue test are common methods to acquire the fatigue stress spectrum. Zhang et al. (2011) indicated the influence of vehicle speed and road surface roughness on fatigue damage. Wang et al. (2013) studied fatigue performance of steel bridge and established probability model utilizing nondestructive detection technology and the fracture mechanics method. The typical fatigue truck load model specified in the native design codes are usually used to obtain structural stress spectrum (Castillo et al., 2014). However, the typical fatigue truck models with deterministic parameters are not suitable to conduct probabilistic fatigue analysis.

In fact, random traffic flow load is appropriate for probabilistic analysis. More effort should been done on the application of traffic flow load model on probabilistic modeling of bridge fatigue damage.

In this paper, a fatigue truck load model is developed for probabilistic modeling of highway bridges. In order to solve the time-consuming problems of the bridge finite element analysis under traffic flow loads, a response surface method is used to approximate the function between vehicle axle weight and the equivalent fatigue stresses. Finally, the fatigue damage model is applied to the reliability assessment of steel box-girder bridges and the influence of traffic flow parameters on structural fatigue reliability is studied.

2 Stochastic Vehicle Flow Model

Due to the different national conditions, guidelines for Design and Maintain of Orthotropic Steel Deck in China recommends a four-axle fatigue vehicle with axle load of 50kN, 100kN, 90kN and 90kN. It is available to obtain fatigue damage values of structures via typical fatigue vehicle with deterministic load mentioned above, but it is not applicable for probability analysis.

In general, the effective stress influence line for the orthotropic steel bridge deck is confined to the region between two diaphragm plats (which is 3.2m in this case study). (Deng et al., 2014). Thus, the parameters in the stochastic vehicle load have different influence on structural fatigue damage. It is acknowledged that vehicle weight, vehicle type, and driving lane have a greater influence on fatigue damage compared with vehicle gap and vehicle speed. Thus, it is appropriate to set the weight, vehicle configuration and driving lane as random variables. Therefore, the randomness of vehicle gap and driving speed are ignored. A framework illustrating the procedures of simulating the traffic flow is shown in Figure 1.

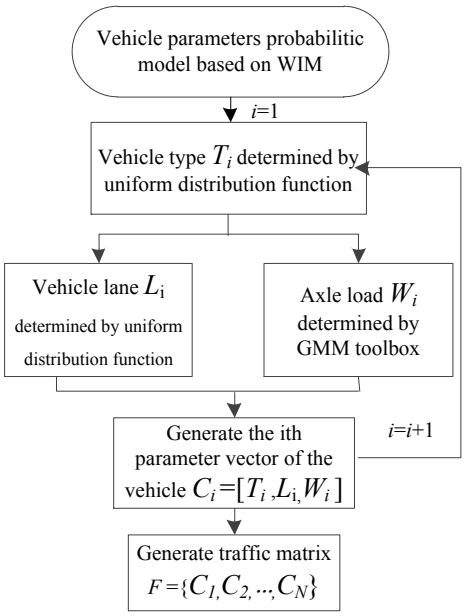

Figure 1. A framework for stochastic traffic flow simulation based on the Monte-Carlo approach (In this article, GMM refers to Gaussian mixture model).

In Figure 1, probability model of vehicle was derived from data obtained by weigh-in-motion (WIM). In Matlab, uniform distribution and GMM functions are used to generate the truck sample. Vehicle matrix C_i was generated by three parameters, including driving lane L_i, vehicle weight W_i, and vehicle configuration T_i. Finally, vehicle matrix F can be obtained in time domain.

The statistic of vehicle of a highway bridge in China is shown in Table I. Note that vehicle with a less vehicle weight than 30 kN were ignored. The axle load of AW_{62} fitted by Gaussian mixture model (GMM) is shown in Figure 2. With these probabilistic models, the stochastic vehicle flow are simulated and shown in Figure 3.

Table I. Statistics of vehicles of a highway based on the WIM system.

Vehicle type	Description	Occupancy rate /%		
		Vehicle type	Slow lane	Fast lane
V_1	Light car	34.64	36.64	63.36
V_2	Truck with 2 axles	26.12	84.58	15.42
V_3	Truck with 3 axles	8.58	91.08	8.92
V_4	Truck with 4 axles	10.24	96.42	3.58
V_5	Truck with 5 axles	4.93	92.60	7.40
V_6	Truck with 6 axles	15.49	98.08	1.92

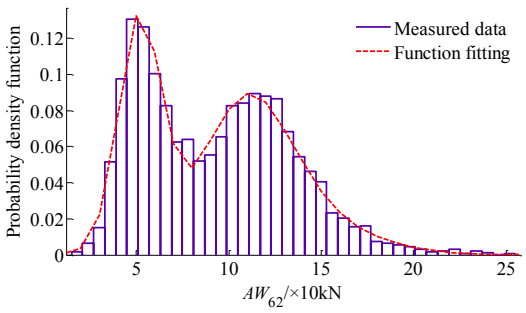

Figure 2. PDF of the axle weight AW62.

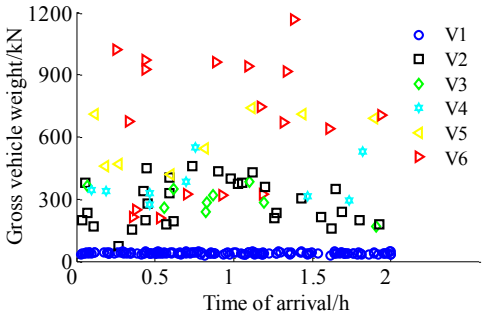

Figure 3. A stochastic fatigue traffic flow sample.

The establishment of stochastic vehicle flow model provides a basis for probability analysis of fatigue damage.

3. Proposed Computational Framework

Response Surface Method (RSM) is proposed to approximate the response function between vehicle parameters and structure fatigue stress. The advantage of the RSM approach is the efficient of computational effort because only small samples are involved in the computation. GMM model with

multiple parameters is used to approximate the PDF of fatigue damage. The computational framework is summarized in Figure 4.

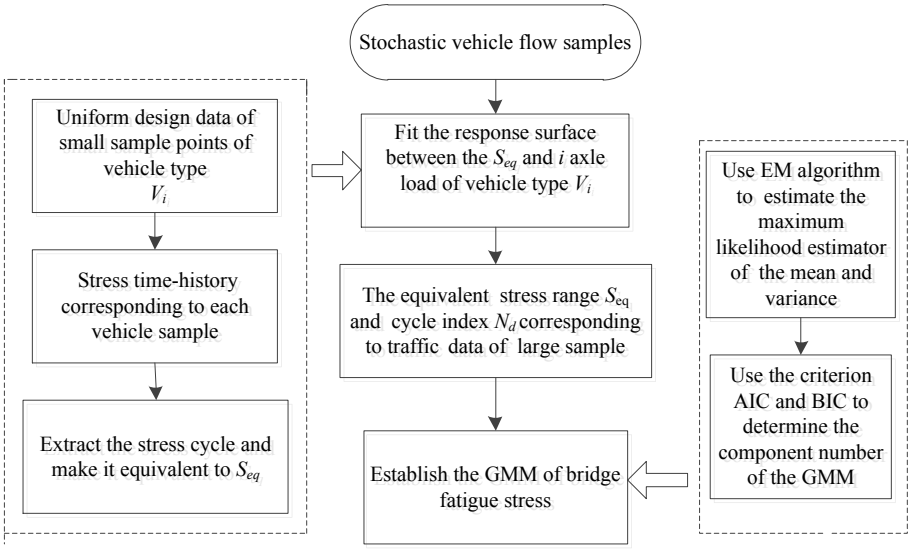

Figure 4. Probability analysis process of fatigue stress.

AW_{in} refers to the nth axle load of the V_ith vehicle type, EM represents the maximum expected value, AIC and BIC are Akaike information criterion and Bayesian criterion in information statistics, respectively. The crucial step in the flow chart is approximating the response surface between axle load and S_{eq}.

Structural response function is the kernel content for the RSM approach (Kang et al., 2010). In general, response surface method is used for approximate nonlinear function associate with small samples. Taking symbol of Vi for example, more than 2i+1 sample points is necessary to determine expression of response surface method. The general formulation of RSM approach is (Kang et al., 2010).

$$Z = G(X) \approx a + \sum_{j=1}^{i} b_j \cdot X_j + \sum_{j=1}^{i} c_j \cdot X_j^2 \tag{1}$$

where, X is a random variable, which is axle load in this paper, a, b, c are undetermined coefficients. It's worth noting that establishment of response surface function is available only with $2i$+1 times of finite element calculation.

Once the time-history of stress ranges are obtained for the FE model, the optimal probability model of GMM for fatigue stress can be established based on Criterion BIC and AIC. The criterion BIC and AIC are available in Deng et al. (2014).

4. Probabilistic Analysis of Fatigue Damage for Steel Box Bridge

Fatigue damage of steel bridge, under vehicle loading, is manifested in the location of rib-to-deck(Chen et al., 2014). The rib-to-deck details is specified as number 71 in Eurocode3, the corresponding strength

coefficient proves respectively to be K_C=7.16×10^{11}, K_D=1.90×10^{15}. The following formulas are available on the basis of linear damage rule and *S-N* curve, with the introduction of equivalent stress-range S_{eq} (Guo and Chen, 2011).

$$D_{eq} = \frac{N_d S_{eq}^5}{K_D} = \sum_{S_i \geq \sigma_D} \frac{n_i S_i^3}{K_C} + \sum_{S_j < \sigma_D} \frac{n_j S_j^5}{K_D} \tag{2a}$$

$$S_{eq} = \left[\frac{\sum_{S_i \geq \Delta\sigma_D} \frac{n_i S_i^3}{K_C} + \sum_{S_i < \Delta\sigma_D} \frac{n_j S_j^5}{K_D}}{N / K_D} \right]^{1/5} \tag{2b}$$

$$N = \sum_{S_i \geq \Delta\sigma_D} n_i + \sum_{S_i < \Delta\sigma_D} n_j \tag{2c}$$

where n_i is the number of stress cycles, for $S_i \geq \Delta\sigma_D$. Otherwise it turns into n_j. D_{eq} is equivalent cumulative damage. Fatigue failure of the steel decks, mainly includes weld toe cracks and welding cracks. The finite element model of a standard girder is shown in Figure 5.

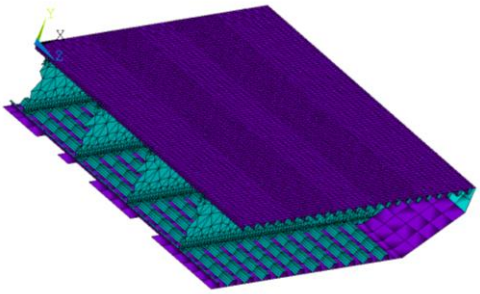

Figure 5. Finite element model of a steel box girder.

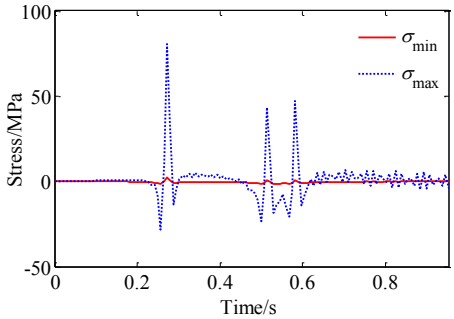

Figure 6. Stress-time curves of roof U-rib of the steel box girder.

In fact, the road surface has a certain effect on the fatigue stress. The loading area for the tires is revised as 3.4cm×33.4cm for the front wheels, and 73.4cm×33.4cm for the rear wheels. Stress-time history for the rib-to-deck details is calculated in FE model and shown in Figure 6. The vehicle driving speed is 20m/s. In Figure 6, σ_{min} and σ_{max} are the minimum and maximum stress time-histories. This stress time-history in Figure 6 obviously contains three peak values. They are corresponding to the location crossed by three vehicle axles. S_{eq} could be obtained through disposing of aforementioned time-histories in accordance with rainflow counting method and Eq.(4). The response surface was approximated with S_{eq} and AW_{31}, AW_{32} with Eq.(1). The simulated response function is shown in Figure 7.

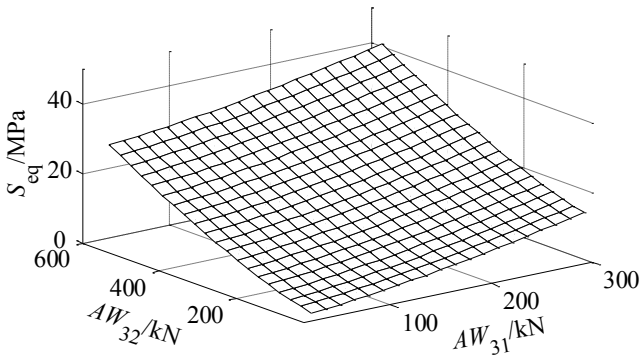

Figure 7. Response surface of Seq and axle weigh of V3.

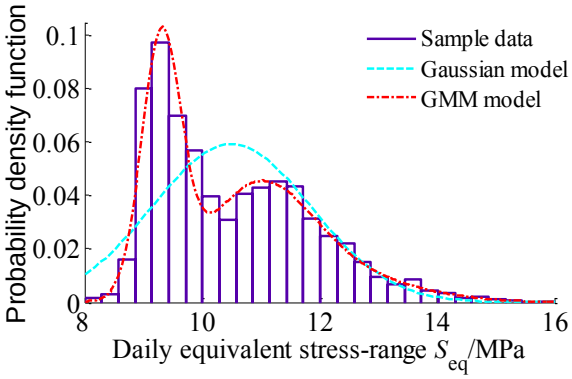

Figure 8. Fatigue stress probability density of the rib-to-deck detail of driveway under the random traffic flow samples.

Equivalent stress-range S_{eq} of rib-to-deck for steel box girder, under the action of traffic samples, can be obtained with vehicle type corresponding to each response surface function. According to response surface algorithm, vehicles with three axles corresponds to seven sample points, while vehicles with six axles corresponds to thirteen sample points. Thus, the whole vehicle types correspond to fifty sample points. Using vehicle type V3 as an example, in the case, calculation time of the condition of one hundred thousand truck flow within 100 days requires 49 days, compared with 36 minutes with application of response surface method mentioned above. It can be verified that the introduction of response surface method can solve the time-consuming problem in fatigue stress analysis.

In accordance with model establishment method of GMM shown in Figure 2, probability density curve of equivalent stress-range can be available shown in Figure 8. GMM parameters are illustrated in Table II, where a_i refers to the weight of Gaussian mixture distribution, μ_i refers to the mean value of the ith Gaussian distribution function, σ_i is the standard deviation of the ith Gaussian distribution function.

Table II. Parameters of GMM of S_{eq}.

a_1	0.38
a_2	0.62
μ_1	9.43
μ_2	3.74
σ_1	3.44
σ_2	2.31

In Figure 8, the probability density function of equivalent stress-range has approximately two peaks, The two peaks are corresponding to probability density function of axle load in Figure 2. They are associated with empty and full loading condition. With the probability density functions of S_{eq}, GMM is better to approximate the PDF of fatigue stress compared with a single Normal distribution. In Table II, the two mean parameters of GMM, is associated with the two peak values of probability density in Figure 8.

The probability model of the fatigue damage indicated the feasibility to analyze fatigue stress of steel box girder bridges under stochastic vehicle load.

5. Application of the Probabilistic Model: Reliability Assessment

One of application for fatigue damage model under the action of stochastic vehicle flow is fatigue reliability assessment. Limit state function with vehicle flow parameters taken into consideration could be developed as follows, on the base of linear damage rule.

$$g_n(\boldsymbol{X}) = \Delta - D_n(\mathrm{X}) = \Delta - 365 S_{\mathrm{eq}}^5 \cdot N_{\mathrm{d}} \cdot w \cdot \sum_{i=1}^{n} \left[1 + (i-1)a\right]^5 / K_{\mathrm{D}} \tag{3a}$$

$$N_{\mathrm{d}} = ADTT_{\mathrm{sl}} \cdot \sum_{i=1}^{n} p_i \cdot n_i \tag{3b}$$

where n (unit in year) denotes the service time. w is transverse distribution coefficient of wheelmark. a is annual increase rate of axil weight. Δ stands for critical parameters for fatigue damage. p_i and n_i represent respectively occupancy rate and numbers of axletree of vehicle type i. $ADTT_{\mathrm{sl}}$ is daily traffic volume. The statistical data of random variable X, associated with four parameters, is illustrated in Table III.

Table III. Stochastic of random variables.

Variable/Unit	Distribution type	The mean	The standard deviation
S_{deq}/MPa	GMM	As shown in Table II	
N_{d}	Normal distribution	Eq(2)	Eq(2) ×0.1
Δ	Lognormal distribution	1	0.3
K_{D}	Lognormal distribution	3.47×10^{14}	1.56×10^{14}
w	Normal distribution	0.78	0.078

In allusion to explicit functions shown in Eq.(3), reliability index, calculated by traditional first order second moment method, will encounter bigger errors, due to higher nonlinear frequency and various distribution types of random variables. In this paper, random samples obeying normal distribution, lognormal distribution and Gaussian mixture distribution functions were generated with the integration of Monte Carlo sampling method and MATLAB software.

Firstly, variation tendency concerning fatigue reliability index and failure probability of rib-to-deck, at the location of slow and fast lane, has been analyzed in Figure 9, without the consideration of increase in axle load.

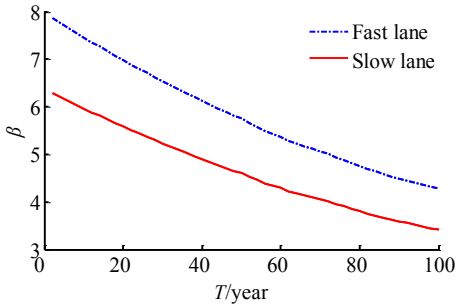

Figure 9. Fatigue reliability index of the rib-to-deck detail during the operation period.

As the Figure 9 illustrated, fatigue reliability index at rib-to-deck on slow lane drops from 6.29 to 3.42. With the growth of service time, although a downward trend of fatigue reliability index occurs both at rib-to-deck on slow and fast lane, reliability index of slow lane is relatively lower than that of fast lane. This occurs because more than 90% of trucks with at least 3 axis act generally on slow lane shown in Table 1.

Due to the exponential relationship between axle load and fatigue damage, growth of the axle load will have great influence on fatigue reliability. With the annual growth factor of axle load—a set from 0 to 1%，the variation tendency at rib-to-deck on slow lane is shown in Figure 10.

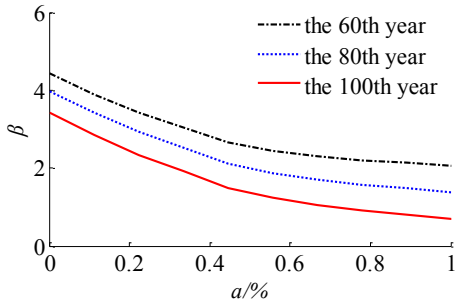

Figure 10. Influence of increase of vehicle weight on fatigue reliability index.

As shown in Figure 10, fatigue reliability index at rib-to-deck of steel box girder drops rapidly under the consideration of growth of vehicle weight. With the annual growth coefficient of vehicle weight increasing from 0 to 1%, the corresponding fatigue reliability indexes in the 60th, 80th, 100th year are found to change from 4.43 to 2.01, 3.98 to 1.30 and 3.42 to 0.72 in the meantime. It can be found that fatigue reliability index drops along with the growth of the bridge service time in this regard. In conclusion, the service time and increase of axle load have significant influences on fatigue reliability of welded details.

In the operation management of the bridges, particular attentions should be given to statistical analysis about operating vehicles. It is available to take certain measures to controlled traffic, based on the reliability assessment method described in this paper, when statistical parameters of vehicle grow excessively fast.

6. Conclusion

Fatigue truck models with deterministic parameters were developed to be a stochastic vehicle flow model. In order to solve the time-consuming problems of the bridge finite element analysis under traffic flow loads, a response surface method has been used to approximate the function between vehicle axle weight and the equivalent fatigue stresses with a few training data. A probabilistic fatigue damage modeling method was presented and applied to rib-to-deck details of steel box-girder bridges. Finally, the fatigue damage model was applied to the reliability assessment of steel box-girder bridges. Research results provide theoretical foundation for operation management and traffic restrictions of bridges. Main conclusions are summarized as follows.

(1) Stochastic vehicle flow model involving statistical characteristics of vehicles has a certain application prospect in probability analysis of fatigue damage for steel bridge and reliability assessment.

(2) Higher occupancy of heavy vehicle on slow lane has been proved to be significant cause, which leads to fatigue reliability index of slow lane much lower than that of fast lane.

(3) The growth of axle load results in rapid decline in fatigue reliability index of steel box girder. As the annual growth factor of vehicle weight increase from 0 to 1%, fatigue reliability index of the 100th year drops from 3.42 to 0.72.

Still at issue is influence which vehicle speed and road surface roughness, in stochastic vehicle flow model, make on fatigue damage. Growth factors of traffic volume and vehicle weight remain to be integrated by long-term monitoring data.

References

Castillo E., J. M. Menéndez and S. Sánchez-Cambronero. A hierarchical Optimization Problem: Estimating Traffic Flow Using Gamma Random Variables in a Bayesian Context *Computers & Operations Research*, 41: 240-251, 2014.

Chen, Y. X., P. M. Lv and C. J. Guo. Study on Fatigue Performance of Orthotropic Steel Bridge Deck U-rib and Cover Weld Structure.*Journal of Chang'an University(Natural Science Edition)*, 34(1): 49-55, 2014.

Deng, Y., A. Q. Li and Y. Liu. Probabilistic Modeling of Fatigue Loading Effects and Fatigue Reliability Evaluation for Steel Bridges Based on Monitored Data. *China Civil Engineering Journal*, 47(7): 79-87, 2014.

Deng, Y., Y. Liu and D. Feng. Monitoring Damage Evolution of Steel Strand Using Acoustic Emission Technique and Rate Process Theory. *Journal of Central South University*, 21(9): 3692-3697, 2014.

Guo, T. and Y. Chen. Field Stress/Displacement Monitoring and Fatigue Reliability Assessment of Retrofitted Steel Bridge Details. *Engineering Failure Analysis*, 18(1): 354-363, 2011.

Kang, S., H. Koh and J. Choo. An Efficient Response Surface Method Using Moving Least Squares Approximation for Structural Reliability Analysis. *Probabilistic Engineering Mechanics*, 25(4), 365-371, 2011.

Wang, C. S., B. N. Fu and Q. Z. Fatigue Test on Full-scale Orthotropic Steel Bridge Deck. *China Journal of Highway and Transport*, 26(2): 69-76, 2013.

Wolchuk, R. Discussion of "I-35W Bridge Collapse" by S. Hao. *Journal of Bridge Engineering*, 16(4): 570-571, 2011.2011, 16(4): 570-571.

Zhang, W. and C. S. Cai. Fatigue Reliability Assessment for Existing Bridges Considering Vehicle Speed and Road Surface Conditions. *Journal of Bridge Engineering*, 17(3): 443-453, 2011.

Dynamic Reliability Assessment for Long-Span Bridges under Heavy Stochastic Traffic Flows

Naiwei Lu[1)], Mohammad Noori[1)] and Michael Beer[2)]
[1)] *School of Civil Engineering, Southeast University, Nanjing 210096, China, n.lu@bauinf.uni-hannover.de*
[2)] *Institute of Computer Science in Civil Engineering, Leibniz University Hannover, Hannover 30167, Germany, beer@bauinf.uni- hannover.de*

Abstract: Long-span highway bridges simultaneously suffer from a large number of vehicle loads. With the ever-increase of the traffic loads, the safety problem of the in-service bridges is particularly serious. A framework for analysis the dynamic reliability of long-span bridges under stochastic traffic flows was proposed. The framework integrates the monitored traffic data, vehicle-bridge interaction theory, and dynamic reliability theory. A suspension bridge with main-span of 820m was chosen as an engineering prototype for the purpose of illustrating the feasibility of the proposed framework. The numerical results indicate that: the stochastic traffic flow model is appropriate to be applied in reliability analysis of bridges, because the probabilistic information was included in the stochastic traffic flow. The corresponding probabilistic model of dynamic response of bridges can be obtained by the numerical simulation of vehicle-bridge interaction. The busy traffic flow was demonstrated to be the main reason for the displacement first passage failure of the suspension bridges. Furthermore, the failure probability increases with the growth of the occupancy rate of the busy traffic flow in the daily traffic flow.

Keywords: dynamic reliability, stochastic traffic flow, suspension bridge, first-passage, root-mean-square

1. Introduction

In recent years, a steady increase in the vehicle volume and cross vehicle weight, which has been caused by the rapid growth and expansion of urban developments and subsequent increase in inter-city and interstate transportation, have caused a threat to the safety of bridges (Chen and Wu, 2010). The overloading traffic due to this vehicle volume increase has become the main factor resulting in shortening the service life and even causing collapse of bridges in most countries (Deng et al., 2015). With the widespread increase of vehicle volume and cross vehicle weight, several in-service bridges built decades ago, utilizing the old design codes, are damaged or even collapsed. Therefore, the structural safety of existing bridges caused by sustainable growth of traffic volume and assessing the load-carrying capability are serious issues that should be carefully studied.

The commonly used method for the evaluation of the vehicle load in bridge design and safety assessment are specifications in the national design codes developed in the individual countries. The practical application of these codes have proved to be successful as they allowed for keeping in operation many bridges that no longer met the design criteria but were otherwise able to safely carry the applied loads. Because of the success of these national codes and more recent research findings the possibility of developing a new Eurocode for bridge safety assessment is under consideration. In the design specifications, the vehicle loads were calculated based on the statistical data of collected from large volume of vehicles in multiple regions. Due to changes that have occurred in the traffic flow and volume in recent

years, these data may no longer be suitable or relevant for all existing bridges. Some the shortcomings are for instance the design loads considered in these codes which do not take into consideration the random nature of the actual vehicle flow and vehicle loads (Bu et al., 2006). There are additional shortcomings in the existing codes. For instance, the design load considered in these codes are based on an overall estimation of the number of vehicles. Thus, although slender long-span bridges may carry a large number of heavy trucks simultaneously, this factor has not been considered in these code. Traffic flow is a more realistic model to simulated vehicles passing over lender long-span bridges instead of vehicle load that is based on estimating the number of vehicles (Han et al., 2015). Subsequently, a more realistic vehicle model with a focus on estimating traffic flow should be developed and incorporated. Stochastic traffic flow is the most effective and realistic model that needs to be considered especially for long-span bridges since the random loading caused due to traffic flow results in direct and severe vibration of bridges, compared with, and in contrast to, the transient vibration of a single vehicle. There are uncertainties associated with the vehicle physical parameters as well as its dynamic characteristics. Xiang et al. (2007) evaluated the bridge structural reliability considering the vehicle-bridge dynamic interaction, however, the reliability evaluation method that they utilized is a traditional static reliability method which does not take into account the random vibration of the bridge caused by the road surface roughness and the bridge-vehicle interaction.

This paper aims at developing a general framework to evaluate the reliability of long-span bridges subjected to stochastic traffic flows utilizing the first-passage approach formulated on the basis of Rice's formula. As the first step, three types of stochastic traffic flow, including free flow, moderate flow, and busy flow, are simulated adopting the cellular automation approach and weigh-in-motion data. Under the long-time effect of simulated traffic flows, the stochastic characters of the dynamic behavior of bridges are simulated and computed utilizing a simplified traffic-bridge interaction theory. Finally, a suspension bridge with a mid-span of 820m is selected to conduct a numerical study, which includes incorporating a large number of traffic parametric studies, such as traffic density and service time.

2. Theoretical basics

2.1 VEHICLE-BRIDGE INTERACTION

The vehicle model and bridge model are established separately and combined with their coupling equations. For the vehicle models, the transitional method is adopting several mass blocks, springs, and damping dashpots. The full vehicle model, half vehicle model, and quarter vehicle model were defined by many researchers (e.g. Yin et al., 2012). In order to simplify the illustration in the present paper, a half vehicle model is shown in Figure 1.

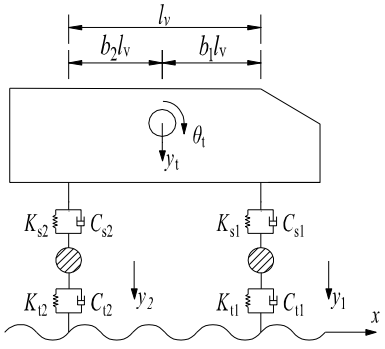

Figure 1. A half vehicle model in the study.

More details for the half vehicle model as well as the relevant information can be founded by Yin et al. (2012). The general coupled equations of the vehicle-bridge system can be constructed through a relatively lengthy derivation as

$$\begin{bmatrix} M_{\mathrm{v}} & 0 \\ 0 & M_{\mathrm{b}} \end{bmatrix} \begin{Bmatrix} \ddot{u}_{\mathrm{v}} \\ \ddot{u}_{\mathrm{b}} \end{Bmatrix} + \begin{bmatrix} C_{\mathrm{v}} & 0 \\ 0 & C_{\mathrm{b}} \end{bmatrix} \begin{Bmatrix} \dot{u}_{\mathrm{v}} \\ \dot{u}_{\mathrm{b}} \end{Bmatrix} + \begin{bmatrix} K_{\mathrm{v}} & 0 \\ 0 & K_{\mathrm{b}} \end{bmatrix} \begin{Bmatrix} u_{\mathrm{v}} \\ u_{\mathrm{b}} \end{Bmatrix} = \begin{Bmatrix} F_{\mathrm{vg}} + F_{\mathrm{vb}} \\ F_{\mathrm{bg}} + F_{\mathrm{bv}} \end{Bmatrix} \tag{1}$$

where, M_v, C_v, and K_v are the mass, damping, and stiffness matrices of the vehicle, respectively; M_b, C_b, and K_b are the mass, damping, and stiffness matrices of the bridge, respectively; u_v and u_b are the displacement of the vehicle and the bridge, respectively; F_{vg} and F_{bg} are the self-weight of the vehicle and the bridge, respectively; F_{vb} and F_{bv} are the vehicle-bridge interaction forces.

Currently, many studies on the multiple-vehicle effects on bridges suggest that the interaction effects between different vehicles on the same long-span bridges, such as cable-stayed bridges and suspension bridges, are insignificant. Furthermore, the dynamic interactions between different vehicles may become negligible. Therefore, individual vehicle may be approximated as a directly applied force on the bridge, independent of other vehicles. An equivalent dynamic wheel loading (EDWL) approach was presented by Chen and Wu (2007). Replacing the physical moving vehicles on the bridge by EDWL, the fully coupled equations in Eq. (1) can be simplified to

$$M_b\ddot{u}_b + C_b\dot{u}_b + K_b u_b = F_{bg} + F_{eq}^{wheel} \tag{2}$$

$$\{F(\mathrm{t})\}_{eq}^{wheel} = \sum_{j=1}^{n_v} \left\{ \left[1 - R_j(t)\right] \mathrm{G}_j \cdot \sum_{k=1}^{n_a} \left\{ h_k[x_j(t) + \alpha_{\mathrm{k}}[x_j(t) d_j(t)]] \right\} \right\} \tag{3}$$

where, R_j, G_j, x_j, and d_j are the dynamic wheel ratio, self-weight of the jth vehicle, longitudinal location, and transverse location of the gravity center of the jth vehicle on the bridge, respectively; h_{k} and a_{k} are the kth vertical and the torsional mode shapes of the bridge. The total number of vehicles n_v changes with time depending on the simulation results of the stochastic traffic flow. The feasibility analysis has been conducted by Chen and Cai (2007) by comparing the bridge response estimations using fully coupled interaction analysis and the EDWL approach.

Due to the random nature of the traffic loads, the bridge responses under stochastic traffic flow are random processes (Wu and Law, 2011). Consequently, a convergence analysis is required for the purpose of obtaining rational estimations of the probabilistic dynamic behavior of the bridge response. In addition, the displacement of long-span bridges highly depend on the vehicle density (Chen and Wu, 2010). Even through the vehicle density is time variant in one day, the interval vehicle density exhibits stationarity in a time domain. On this basis, the traffic model can be divided into several models in the time domain according to the statistics of the traffic density. Once the traffic model is determined, the sample of the responses will exhibit ergodicity on the premise of a long analytical time.

2.3 FIRST-PASSAGE FORMULATIONS

The first-passage probability, which describes the probability that a scalar process exceeds a prescribed threshold during an interval of time, is of great engineering interest. The probability is essential for estimating the serviceability reliability of bridges. The first-passage probability of a zero-mean stochastic process $X(t)$ over a prescribed double-sided threshold $|x|$=a during an interval time $t \in (0, \tau)$ can be written as

$$p(a,\tau) = P(a \le \max\nolimits_{0 \le t \le \tau} |X(t)|) \tag{4}$$

In general, there is no exact solution for the probability. Rice (1945) adopted Poisson assumption to approximate the probability of Eq. (4) and presented the well-known Rice's formula. For the random vibration of bridges under traffic loads, the mean value of responses of bridge beams are greater than zero in theory, while they are far less than threshold *a* for a safety design. In this case, the crossing rate under the threshold *–a* can then be written as

$$v^{-}(-a)=\frac{\sigma_{\dot{X}}}{2\pi\sigma_{X}}\exp(-\frac{(a-E_{X})^{2}}{2\sigma_{X}^{2}}) \tag{5}$$

where, E_x is the mean value of random process X, $\dot{X}$ is the derivation of X, σ_X and $\sigma_{\dot{X}}$ are the root mean square of X and $\dot{X}$, respectively. Note that the Rice formula adopts two assumptions including the over-crossing theory and the Poisson distribution. Thus, the validity for applying to this study should be further investigated by comparing to the Monte Carlo simulation. In the present study, the results calculated by the Rice formula can be considered as references.

Considering the density of stochastic traffic flow, the first-passage probability of bridge girders under multiple types of traffic flows can be written as

$$p(a,T)\cong 1-\sum_{i=1}^{n}\exp\left[-v_{i}^{-}(-a)\cdot\rho_{i}\cdot T\right] \tag{6}$$

$$\rho_{i}=\frac{t_{i}}{T}=\frac{t_{i}}{\sum_{i=1}^{n}t_{i}} \tag{7}$$

$$v^{-}(-a,t_{i})=\frac{\sigma_{\dot{X}(i)}}{2\pi\sigma_{X(i)}}\exp(-\frac{(a-E_{x(i)})^{2}}{2\sigma_{X(i)}^{2}}) \tag{8}$$

where, the entire time T is divided into n intervals indicated as t_i according to the density of stochastic traffic flow, such as free traffic flow, moderate traffic flow, and busy traffic flow; v_i and ρ_i correspond to the crossing rate and occupancy of the ith traffic term, respectively; $X(i)$ and $\dot{X}(i)$ denote the structural response and the corresponding time derivative under the ith traffic term, respectively; and $\sigma_{x(i)}$ and $\sigma_{\dot{X}(i)}$ denote the RMS of the $X(i)$ and $\dot{X}(i)$, respectively.

3. Case study

3.1 WEIGH-IN-MOTION SYSTEM

A weigh-in-motion (WIM) system utilizes scales or pressure sensors embedded into the road pavement to measure parameters of crossing vehicles such as axle weight and speed. These systems are widely used in highways for the purpose of controlling heavy traffic load such as overloaded trucks. Statistical approaches are adopted to establish the probability model of the axle weight, speed, vehicle type, and/or other relevant information with these vehicle data. In general, both the vehicle type and vehicle speed fit normal distribution, the axle weight fits a bimodal distribution, and the vehicle gap, i.e., the gap between two vehicles in a lane, fits a Gamma or Weibull distribution depending on the vehicle density. The bridge loadings models are closely related to vehicle gross weights, axle weight and axle spacing (Miao and Chen, 2002). Although thousands of vehicles cross a the bridge every day and the vehicle types, gross vehicle weights and axle weights are quite different, statistical characteristic can be obtained via the big data of these parameters. If the mathematical distributions of these parameters can be obtained accurately,

bridge live load models can then be easily formulated. A WIM system used in this paper is shown in Figure 2. A diagram illustrating the relationship between the vehicle and the WIM is shown in Figure 3.

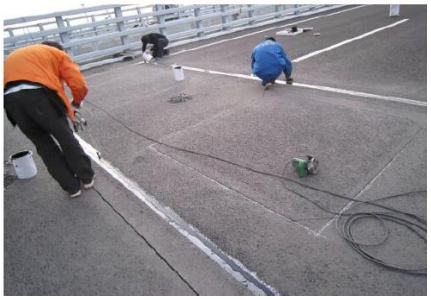

Figure 2. A WIM system.

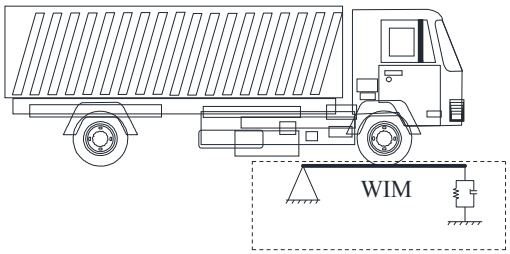

Figure 3. A truck passing on a WIM system.

This system has been working about 5 years and more than ten million vehicle data has been collected. According to the axle configurations, all vehicles collected from the WIM data can be classified into 6 categories. Taking vehicle type 6 (with 6 axles) as an example, its corresponding probability models for axle weight are show in Figure 4, where the axle weight of the vehicle type 6 AW_{64} follows a Gaussian mixture distribution. The simulated stochastic traffic flow is shown in Figure 5.

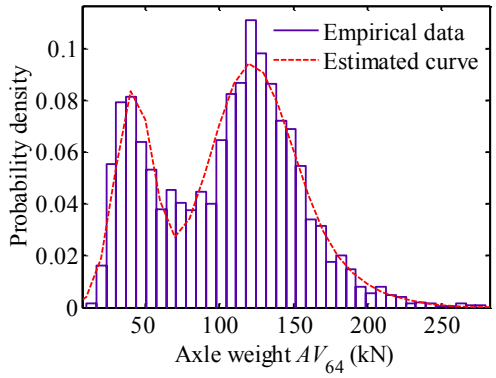

Figure 4. Probability density of parameters in V6.

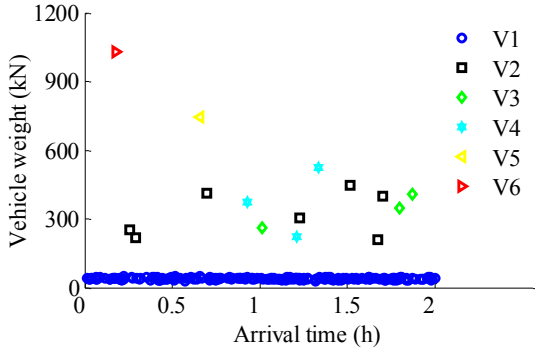

Figure 5. Simulated stochastic traffic flows.

The vehicle density strongly depends on vehicle gaps that changes greatly during the day and night, but it follow the peoples' daily life style, which means people usually go out in the morning and return in the evening. Thus, in order to establish the probability model of the vehicle gaps, the traffic flow is divided into three parts: free traffic, moderate traffic, and busy traffic, according to the vehicle volume per hour. With the WIM data of three typical dates, the boundary line between busy traffic, moderate traffic, and free traffic is determined as 400 vehicles per hour and 200 vehicles per hour in a driving direction. It can be found that the time of busy traffic flow is about 4 hours (occupancy rate ρ_1=17%), the time of moderate traffic flow is about 6 hours (occupancy rate ρ_2=25%), the time of free traffic flow is about 14 hours (occupancy rate, ρ_3= 58%).

3.2 A SUSPENSION BRIDGE

A long-span highway bridge in Sichuan province of China named Nanxi Yangzi River Bridge is shown in Figure 6. A WIM system was installed on the suspension bridge.

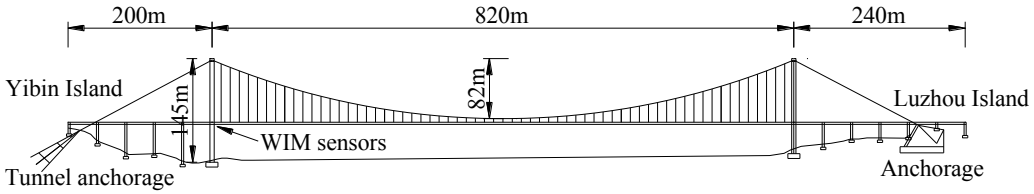

Figure 6. Elevation layout of the prototype bridge.

In order to perform the dynamic response analysis of the prototype bridge under traffic flow, a finite element model was established using ANSYS software. The model is shown in Figure 9, where the Beam44 element was used to simulate the steel box girders and towers, and the Link10 element was used to simulate the cables and the hangers. The roughness displacement was derived after the adoption of roughness factor of $20\times10^{-6}m^3$/cycle for good road condition as shown in Figure 7.

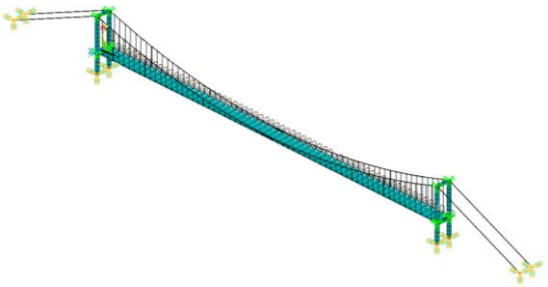

Figure 7. Finite Element Model of Nanxi Yangtze River Bridge.

3.3 RESULTS AND DISCUSSIONS

With the combined use of EDWL approach and the transient analysis function of ANSYS software, the time-history of the suspension bridge girders were obtained and shown in Figure 8. From Figure 8 it can be found that the *L*/4 girders vibrate seriously compared with *L*/2 girders. Furthermore, the displacement of a certain girder under busy flow is larger than that under free flow, which means that the vehicle density has significant impact on the displacement of the girders. The mean value of the displacement under busy flow is larger than that of the moderate flow and free flow.

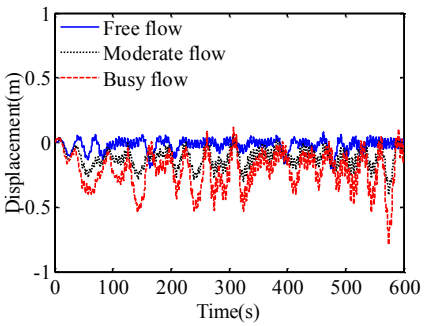

Figure 8. Vertical displacement of the girder in quarter-span under stochastic traffic flow.

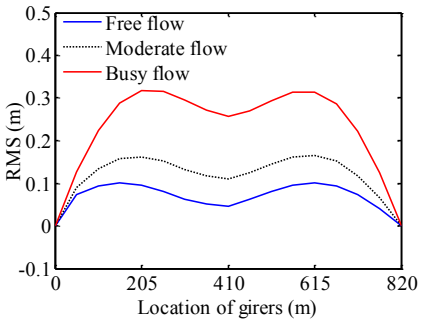

Figure 9. Statistics of displacement of girders under simulated traffic flows.

By the same way, the RMS of all girders can be calculated and the results versus the location of the girders are shown in Figure 9. As can be seen from Figure 9, the following results can be obtained: (1) the RMS of all girders are symmetric and increase rapidly when the free traffic flow changes to be busy traffic flow; (2) the shape of the two type of values are obviously different, where the mean value fits a V-type distribution, while the RMS fits a M-type distribution; and (3) the peak-value of mean value of all girders is located at the mid-span location, while the peak-value of RMS is located at the quarter-span location. A physical interpretation of these results can be explained by the structural modal shape. It is observed that the shape of the RMS is similar to the 1st vertical modal shape, while the shape of the mean value is similar to the 2st vertical modal shape. It was also observed from the animation of the transient analysis that the girder in the quarter-span had a sever vibration compared with the girder in mid-span.

Once the statistical information are obtained from the traffic-bridge dynamic analysis, the first-passage reliability can be calculated by employing the Rice formula. According to the design code in China (MOCAT 2004), the threshold in Eq. (6) a is equal to $L/400$=2.05m, where L is the length of mid-span of the bridge. The first-passage reliability indexes of the quarter-span of the suspension bridge girders subjected to free traffic, moderate flow, and heavy flow are shown in Figure 10.

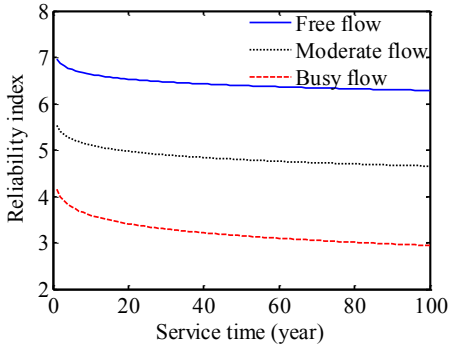

Figure 10. Frist-passage reliability of the suspension bridge girders subjected to three types of traffic flow.

It can be found that there is an obvious demarcation line between them, where the reliability index for the case of busy traffic flow is the smallest and that of the heavy traffic flow is the greatest. When the service time of the bridge increase from 1a to 100a, the corresponding first-passage reliability index of the

bridge decrease from 4.15 to 2.94. For the same service time, 100a, the reliability of the square-span girder under free flow, moderate flow, and busy flow are 6.28, 4.65, and 2.94, respectively. It can be found that the type of traffic flow, rather than the service time, has a significant influence on the first-passage reliability index of the bridge.

4. Conclusions

A general framework was developed for evaluating the serviceability reliability of long-span bridges subjected to stochastic traffic flow considering the actual stochastic traffic information. Three types of stochastic traffic flows, including busy flow, moderate flow, and free flow, was simulated by the cellular automation approach using the weigh-in-motion data. The traffic flow was transformed into time-variant vertical forces using an equivalent dynamic wheel load approach for the purpose of simulating time-history responses of a bridge girder in the finite element model. Statistical information of the bridge responses, such as mean value and root-mean-square, was then calculated. Then, the first-passage reliability of a case study bridge was calculated based on the established first-passage model utilizing the basis of Rice's formula.

In the case study, three types of traffic flow as well as the corresponding responses of the suspension bridge girders were simulated and subsequently the statistical analysis of first-passage problem was conducted. Numerical results indicated that: (1) under stochastic traffic flow, the shape of distribution for the mean value and RMS of all girders are different, where the mean value fits a V-type distribution; (2) the peak-value of mean value of all girders is located at the mid-span location, while the peak-value of RMS is located at the quarter-span location; (3) considering the design service life (1a to 100a) and the assumed occupancy of statistical busy flow, the first-passage reliability index of the above locations dropped from 4.72 to 3.68. Consideration of busy traffic flow is obvious important for assessing safety of long-span bridges. These numerical results are valuable contributions to the literature.

The result can be checked by the rough Monte Carlo simulation in theory. However, it's an extremely time-consuming problem for carrying out a long-time simulation with a normal personal computer.

Acknowledgements

The research was supported by the National Basic Research Program (973 program) of China (Grant No. 2015CB057705), the National Science Foundation of China (Grant No. 51378081), and the China Postdoctoral Science Foundation (Grant No. 2015M580383).

References

Bu, J., S. Law and X. Zhu. Innovative bridge condition assessment from dynamic response of a passing vehicle. Journal of Engineering Mechanics, 10.1061/(ASCE)0733-9399(2006)132:12(1372), 1372-1379, 2006.

Chen, S. and C. Cai. Equivalent wheel load approach for slender cable-stayed bridge fatigue assessment under traffic and wind: Feasibility study. Journal of Bridge Engineering, 10.1061/(ASCE)1084-0702(2007)12:6(755), 755-764, 2007.

Chen, S. and J. Wu. Dynamic performance simulation of long-span bridge under combined loads of stochastic traffic and wind. Journal of Bridge Engineering, 10.1061/(ASCE)BE.1943-5592.0000078, 219-230, 2010

Deng, L., W. Wang and Y. Yu. State-of-the-Art Review on the Causes and Mechanisms of Bridge Collapse." Journal of Performance of Constructed Facilities, 10.1061/(ASCE)CF. 1943-5509. 0000731, 04015005, 2015

Han, W., J. Wu, C. Cai, et al. (2015). "Characteristics and dynamic impact of overloaded extra heavy trucks on typical highway bridges." Journal of Bridge Engineering, 10.1061/(ASCE)BE.1943-5592.0000666, 05014011, 2015

Miao, T. and T. Chen. Bridge live load models from WIM data. Engineering Structure, 24(8), 1071-1084, 2002

Ministry of Communications and Transportation (MOCAT). General code for design of highway bridges and culverts. JTG D60-2004, Beijing, China., 2004

Rice, S. "Mathematical analysis of random noise." The Bell System Technical Journal, 24(1): 46-156, 1945

Wu, S. and S. Law. Evaluating the response statistics of an uncertain bridge–vehicle system." Mechanical System Signal Process, 27(1), 576-589, 2012.

Xiang, T., R. Zhao and T. Xu. "Reliability evaluation of vehicle–bridge dynamic interaction". Journal of Structural Engineering, 10.1061/(ASCE)0733-9445(2007)133:8(1092), 1092-1099, 2007

Yin, X., C. Cai, Y. Liu and Z. Fang. Experimental and numerical studies of nonstationary random vibrations for a high-pier bridge under vehicular loads." J. of Bridge Eng., 10.1061/(ASCE)BE.1943-5592.0000435, 1005-1020, 2013.

Reliability Assessment of Long-Span Cable-Stayed Bridges Based on Hybrid Algorithm

Yang Liu, Qinyong Wang and Naiwei Lu
School of Civil Engineering and Architecture, Changsha University of Science and Technology, Changsha 410114, China

Abstract: In order to evaluate the reliability of long-span cable-stayed bridges, a computational framework utilizing a hybrid algorithm is developed. The framework integrates the advantages of finite element analysis, radial basis function neural networks, genetic algorithms, and Monte-Carlo importance sampling method (MCIS) together. These approaches are combined intelligently with consideration of a platform. The feasibility of this framework is verified through a case study, where a prestressed concrete cable-stayed bridge is presented. The parametric study indicates that: a) the failure probability caused by displacement limit of mid-span is greater than that caused by the cable strength failure. b) the mean value and standard deviation of vehicle loads have a higher influence on reliability of the cable-stayed bridge.

Keywords: cable-stayed bridge, reliability, neural network, genetic algorithm, Monte Carlo simulation

1. Introduction

Cable-stayed bridges were widely used for long-span bridges because of their superior mechanical characteristics and reasonable economy. With consideration of increase of traffic flows and resistance deterioration, more attention should be taken more attention for the structural safety of these bridges. It is necessary to evaluate the reliability of these bridges using a high efficient algorithm.

The common used reliability evaluation method is the First-order Second-moment Method (FOSM), Monte Carlo sampling method (MCS), response surface method (RSM), random finite element method (RFEA). The RSM together with artificial neural network (ANN) was proposed to calculate structural failure probability and the method was proved to have a higher efficiency and precision compared with traditional FOSM method (Cheng et al., 2008). The FOSM method was utilized to evaluate reliability of RunYang Yangtze River Bridge and parameters were also carried out (Wang et al., 2010). A joint algorithm which combined RFEA and RSM, FEM, MCS methods was proposed to analysis the dynamic features of JiangYin Yangzte River Bridge where the joint algorithm was proved to be accurate and efficient (Cheng and Xiao, 2005).

There are three major problems in reliability assessment of long–span prestressed concrete (PC) cable-stayed bridge. First, structural nonlinearity during construction is getting more important with increase of the length of cable-stayed bridges. Second, there are many parameters for construction analysis and many random variables in the reliability analysis model. Finally, the structural response functions are implicit without a specific expression. With consideration of these reasons, the common reliability methods have some limits in evaluating reliability of cable-stayed bridges Thus, it is urgent to develop an effective and precise approach for reliability assessment of cable-stayed bridges.

In this paper, a hybrid approach will be developed for reliability assessment of long-span cable-stayed bridges. The hybrid approach will be verified through several numerical studies. Finally, the hybrid approach will be used for reliability assessment of a long-span suspension bridge. Parametric studies of the bridge will be discussed.

2. Mathematical Model

The structural system of cable-stayed bridges are highly statically indeterminate and geometric nonlinear. Therefore, the limit states functions of long-span cable-stayed bridge are complex and implicit with lots of random variables. It is important to establish an appropriate mathematical model for the cable-stayed bridge.

In actual, the reliability index of bridge under serviceability limit states is lower than the index under ultimate limit states (Wu and Zhao, 2006), so bridge reliability assessment is commonly analyzed to meet requirements under serviceability limit states instead of under ultimate limit states. In order to control stress, cracks and deformation under a certain limiting value under serviceability states and guarantee bridge structure in service, assessment of service performance for bridge is critically analyzed under serviceability limit states. Strength failure of a stay-cable and displacement transfinite failure of mid-span for main girder are taken into consideration in this paper. The limit state functions of cable-stayed bridges caused by strength failure of cables and displacement failure of girders can be written as

$$Z_1 = T_{\mathrm{u}}^{\,i} - T_{\mathrm{cab}}^{\,i}(x_1,...,x_n) \tag{1}$$

$$Z_2 = u_{\max} - u_{\mathrm{mid}}(x_1,...,x_n) \tag{2}$$

Where x is random variables, $T_{\mathrm{u}}^{\,i}$ is yield strength of the i th stay-cable, n is the number of strands in a stay-cable , A is cross-sectional area of single strands, σ_{b} is yield strength of single strands,

$T_{\text{cab}}{}^{i}(x_1,...,x_n)$ is of the cable force of the *i*th cable. The maximum of vertical deflection $u_{\max}$ for concrete cable-stayed bridge is less than $L/500$（L is mid-span of main girder） under vehicle load according to the chinese national standard (JTJ027-96, 1996), $u_{\text{mid}}(x_1,\ldots,x_n)$ is vertical displacement value of mid-span node for main girder under vehicle load. $T_{\text{cab}}{}^{i}(x_1,\ldots,x_n)$ and $u_{\text{mid}}(x_1,\ldots,x_n)$ both are high-order nonlinearity implicit performance function. All of the structural response functions can be calculated with the hybrid approach which will be illustrated below.

3. Proposed Hybrid Approach

The procedure of hybrid algorithm for structural reliability assessment is shown in Figure 1. As shown in Figure 1, the hybrid algorithm integrates the FEA, Neural networks, GA, and MCS together to computate the reliability index of cable-stayed bridges.

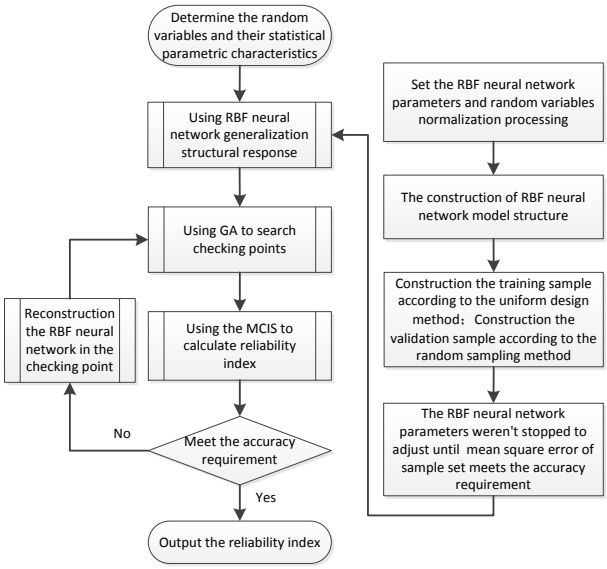

Figure 1. Flowchart of the Hybrid approach for Structural Reliability Analysis.

RBF neural networks in the hybrid algorithm is used to approximate the structural response function. RBF neural network is a feedforward neural network which is composed of input layer, hidden layer and output layer. The hidden layer of radial basis function is Gaussion function, while the out layer is linear

functions. The kernel Gaussion is

$$G_i(x) = \exp\left[-\frac{(x-c_i)^T(x-c_i)}{2\sigma_i^2}\right] \tag{3}$$

Where x is m-dimensional vector of input data, c_i and σ_i are the mean and standard deviation of RBF neural network respectively, respectively. T is a transposed matrix.

For finite element analysis of the Long-span PC cable-stayed bridge, the high-order indetermination, strong nonlinearity, implicit performance function should be paid special attention. The RBF neural network is used to approximate the structural response instead of the FEA model. The advantage of RBF method is the computational efficiency and precision compared with the traditional BP neural networks. The RBF neural networks are especially efficient for structural high-order multivariate nonlinear functions. A RBF neural network is shown in Figure 2, where x and y are input data and output data of structural response, respectively.

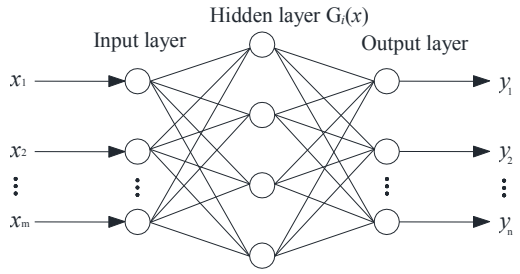

Figure 2. The Structural Diagram of RBF Neural Network.

Sample points are chosen according to the sample value range using a sample point formation method. In order to ensure design sample points are in an effective range, numerical value distributes betweenμ-3σ and μ+3σ) were used in this paper with consideration of the 3σ principle (Zhang et al., 2008). Uniform design (UD) method is used to simulate the experimental data, because the UD method has a supper performance in making the samples have a uniform distribution compared with the orthogonal design method. A data processing system (DPS) (Tang and Zhang, 2012) is used in this paper to simulate the uniform distribution samples, because of its multi-factors and multi-lever-figures by multi-iterations feature. After that the RBF neural network will be selected to conduct the response function approximation.

Genetic algorithm is used to search checking point in structural reliability index calculation. The search problem can be concluded in a constrained optimization models as follows.

$$\begin{cases} \min \quad \beta^2 = \sum_{i=1}^{n} \left[\dfrac{\left(x_i^* - \mu_{x_i}' \right)}{\sigma_{x_i}'} \right]^2 \\ \text{s.t.} \quad Z = Z_i(x_1, ..., x_n) = 0 \end{cases} \tag{4}$$

Where $x_1,\ldots,x_n$ are structural independent random variances, respectively. The structural limit state equation can be written as $Z_i(x_1,\ldots,x_n)=0$. Rosenblatt transformation or orthogonal transformation (Li and Hu, 2000) can be used to transform the relative random variables into linear independent standard normal distribution random variables. Afterwards, the equivalent normal distribution characteristic values, such as mean value μ_{x_i}' and standard deviation σ_{x_i}', can be obtained. Reliability index β is defined as the shortest distance from origin to limit state plane in the standard normal coordinate system, where x_i^* is the most probability failure point.

On account of only existing one equality constraint in constraint optimization problem of calculating structural reliability, genetic algorithm is not suitable for the optimal solution. In addition, the constraint optimization should be transformed to unconstraint optimization, when using the genetic algorithm. In order to solve constraint optimization problem in Eq. (4), =a penalty function is used in this paper.

Failure probability P_f is usually quite small in actual engineering structures. When P_f is less than 10^{-3}, the sample number should be greater than 10^5 for the purpose of ensuring the computational accuracy. When the estimation P_f error of failure probability P_f is less than 20%, the probability is greater than 95%, where the relative error ε of P_f is 0.2 and significance level $u_{\alpha/2}$ is 1.96 (Gong et al, 2012). The sampling number N should satisfy the inequality.

$$N \geq \frac{100\left[\Phi(-2\beta)\exp(\beta^2) - \Phi^2(-\beta) \right]}{\Phi^2(-\beta) - \Phi^3(-\beta)} \tag{5}$$

Where β is an predicted reliability index, $\Phi()$ is an standard normal cumulative probability distribution function.

Importance sampling approach also known as variance reduction technique is adopted to reduce the sample size, the technique improves computational efficiency in conditions of guarantee of the same precision. Importance sampling method increases sample points in failure region appropriately to reduce variance through altering the sample center. This method is often applied in many areas because of its feasibility and efficiency.

According to the above mentioned computational framework of the hybrid algorithm, DPS uniform

experimental design of data processing system, MATLAB neural network, genetic algorithm toolbox and APDL language platform are applied comprehensively. The calculation flowchart of these computer programs is shown in Figure 3.

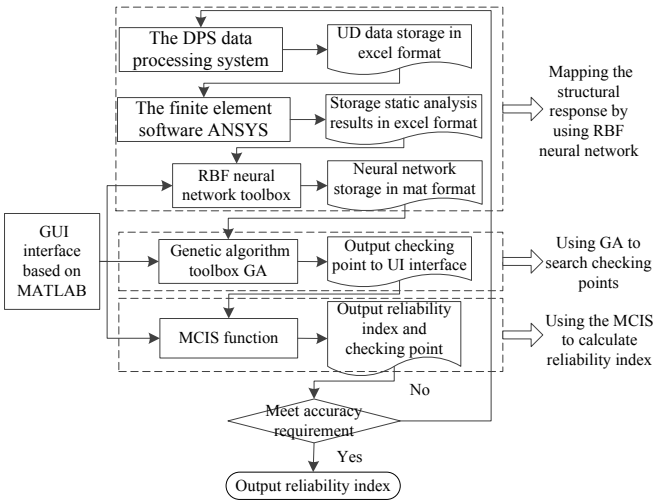

Figure 3. Framework of a software for Structural Reliability Assessment.

Firstly, uniform experimental data is obtained by DPS data processing system, and sample parameters are stored in this system. Secondly, ANSYS finite element analysis software is used to conduct structural static analysis. The results and sample parameters are imported in structural response of RBF neural network toolbox in order to get limit state equations. Thirdly, the GA genetic algorithm toolbox is used to search the design points. UD data is utilized to transform location of sample center. Finally, structural reliability index β gets in design point location by MCIS, while the precision requirement is satisfied. Otherwise, the above steps are repetition over and over again until meet precision requirement.

4. Validation Examples

Computational precision and reliability analysis of the hybrid algorithm will be verified systematically in this section. Two validation examples will be discussed. The first one is reliability analysis of performance function which has explicit analytic expression and higher nonlinearity degree. The other is reliability analysis of simplified bridge structure. In addition, compared with computational result of other methods is included.

4.1. NUMERICAL EXAMPLE ANALYSIS

Expression of performance function in case 1 is Z=18.46-7.48X_1/X_2^3, where X_1 and X_2 both are random variables, X_1~N(10,2)，X_2~N(2.5,0.375).

Expression of performance function in case 2 is $Z=X_1 \cdot X_2-X_3$, where X_1 and X_2 are random variables, X_1~N(0.5472,0.0274)，X_2~N(3.8,0.304)，X_3~N(1.3,0.91).

Table 1. Reliability calculation results of Case 1 and Case 2.

Case	Computational program	MC	FOSM	Reference(Gui J S, Kang H G, 2004)		Hybrid algorithm
				Partial RBF	Modified whole RBF	
Case 1	Reliability index	2.338	2.330	2.350	2.330	2.332
	Iterations	-	6	4	6	4
Case 2	Reliability index	3.806	3.795	3.799	3.798	3.801
	Iterations	-	6	5	9	4

As shown in Table 1, iterations of the hybrid algorithm is the least compared with other response surface methods mentioned in Table 1 and hybrid algorithm achieves the goal of improvement of computational efficiency. Hybrid algorithm can meet precision requirement as the same as other response surface methods, furthermore, its iterations reduce 20% and precision improves 25%.

4.2. RELIABILITY ANALYSIS OF BROTONNE CABLE-STAYED BRIDGE

A cable-stayed bridge named Brotonne bridge is selected herein as an additional verification example. More details regarding the limit state functions, description of the random variables and the statistical information can be found (Shen and Wang, 1996). As shown in Table 2, sampling times of MCS is 10^6 so that it is a precise value. Reliability index of hybrid algorithm has higher precision than reliability index of FOSM or RSM methods, and calculation result of hybrid algorithm is similar to the value that calculated by MCS method (Zhang et al., 2008; Zhang and Liu, 2001). Hence, hybrid algorithm proposed by this paper has better precision and can get corresponding checking point which is not list in Table 2 in reliability calculation of explicit performance function.

Table 2. Results of Static Reliability Analysis for Brotonne Cable-stayed Bridge.

Failure mode		Details	Methods					
			MCS	FOSM	RSM	Reference (Zhang J R, Liu Y, 2001)	Reference (Zhang Q H, Bu Y Z, Li Q, 2008)	Hybrid algorithm
Girders	static bending	Reliability index	3.6104	3.5658	3.5740	3.6193	3.6102	3.6153
	static torsion		-	6.0027	6.0027	6.6027	6.6027	6.0027
Cables and towers	Bulking along transverse bridge	Reliability index	-	9.7007	9.7397	9.7032	9.7042	9.7126
	Strength along longitudinal bridge		3.5128	3.4946	3.4973	3.5063	3.5146	3.5117

5. Case Study

5.1. BRIDGE DESCRIPTION

Kangbo bridge is located in Luyu highways in Sichuang province. It is a prestress concrete cable-stayed bridge with midspan of 420m as shown in Figure 4. The material of main girders is C60 concrete, that of towers is C50 concrete. Every tower contains 34 pairs of stay cables. The width of bridge deck is 30m, which is arranged in six-lanes.

5.2. RANDOM VARIABLES

As the random variables is associated with materials, external load, and so on. Structural random variables in this paper are elasticity modulus E_i of main girder, towers and stay cables, cross-sectional area A_i,

bending inertia moment I_i , material density γ_i, secondary dead load q_s and vehicle load q_k, statistical parameters of these basic random variables need the results of actual bridge detection.

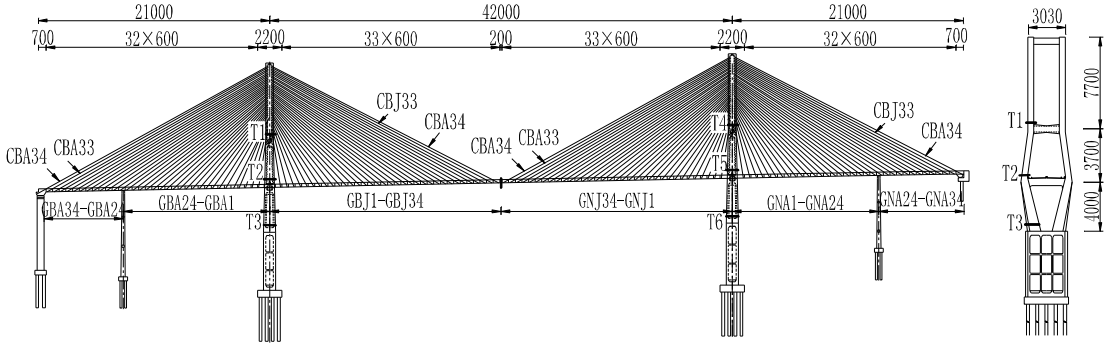

Figure 4. The General Arrangement Diagram of the Kangbo Bridge (unit: cm).

Bridge structure suffers many kinds of loads. In addition, the loading positions are complex under normal circumstance. As a result, structural reliability analysis mainly associates with dead load and live load for simplification. Live load on the deck regards as the shape of uniform distribution for calculating easily. Structural static reliability is lower only under consideration of uniform live load of mid-span for main girder of cable-stayed bridge when bridge has different distribution form of live load (Biondini et al., 2008). Therefore, vehicle load is simplified as uniform load of mid-span for main girder in the below static reliability analysis of cable-stayed bridge. Dead load and live load uniform distributed in mid-span of main girder is considered in this paper. Statistical parameters characteristics of random variables in this paper are shown in Table 3.

5.3. FINITE ELEMENT MODEL

Structure of long-span cable-stayed bridge is complex and its geometric nonlinear effects are important. Thus, structural reliability analysis should include their effects. Secondary sequence response surface method calculates reliability of main girder for Nanjing second bridge considering geometric nonlinear effect of cable-stayed bridge (Chen et al., 2000). It indicates that the reliability index of linear calculation is greater than that of nonlinear solution. RSM, FEM, FOSM and importance sampling method are used to analyze static reliability of main girder for Nanjing second bridge, the result shows that sag effect of stay cables cannot neglect in the field of geometric nonlinear effect and the beam-column effect and large displacement effect can neglect when static reliability of cable-stayed bridge is analyzed (Cheng and Xiao, 2004).

Table 3. Statistical Parameters of Random Variables of the Kangbo Bridge.

Type	Locations	Symbol	Distribution shape	Mean value	Standard variance
Elasticity modulus /(kN·m^{-2})	Main girder	E_1	Normal	3.64E7	3.64E6
	Towers	E_2	Normal	3.52E7	3.52E6
	Stay cables	E_3	Normal	1.95E8	1.95E7
Cross-sectional area /m^2	Main girder (standard beam section)	A_1	Lognormal	20.846	1.042
	Main girder (auxiliary pier)	A_2	Lognormal	24.694	1.235
	The body of towers	A_3	Lognormal	26.868	1.343
	The root of towers	A_4	Lognormal	22.280	1.114
	Single strand in stay cables	A_5	Lognormal	1.4E-4	7.0E-6
Density /(kN·m^{-3})	Main girder	γ_1	Normal	26.56	1.33
	Towers	γ_2	Normal	26.24	1.31
	Stay cables	γ_3	Normal	78.5	3.93
Second moment of area /m^4	Main girder (standard beam section)	I_1	Lognormal	18.598	0.930
	Main girder (auxiliary pier)	I_2	Lognormal	23.015	1.151
	The body of towers	I_3	Lognormal	120.864	6.043
	The root of towers	I_4	Lognormal	275.517	13.776
Secondary dead load /(kN·m^{-1})	Main girder	q_s	Normal	132	6.6
Vehicle load /(kN·m^{-1})	Main girder of the whole bridge	q_k	Extremum Type I	63.5	6.35

This paper is proposed parametric plane finite element model of the Kangbo bridge based on ANSYS, geometric nonlinear factors of sag effect for stay cables are considered by equivalent elastic modulus method. Main girder and towers are simulated by BEAM 44 units and the sum of units is 470, stay cables are simulated by LINK 10. Initial cable force is the measured force, the prestressed effect and the concrete shrinkage and creep effect are not considered in calculation.

5.4. LIMIT STATE FUNCTION

Long-span cable-stayed bridges are statically indeterminate. Since they consists lots of complicate elements, such as main girders, towers, stay cables, auxiliary piers, and so on. Nonlinear degree is higher so that the structural limit state functions are complex. As a result, the progress of searching the major failure mode is extremely complicated. In general, structural reliability analysis is associated with failure components,

where serviceability is important under actual operation state.

The serviceability limit state is defined as the event that structural stress or crack exceeds a threshold. Hence, in this paper, two failure modes are considered as serviceability limit states including strength failure of a single stay-cable and vertical displacement failure of the girders.

The limit state function is shown in Eq.(1) and Eq.(2). The potential failure elements are shown in Figure 4. The serious number of stay-cables are CBA1~CBA34、CBJ1~CBJ34、CNJ1~CNJ34、CNA1~CNA34. The strength failure event is caused by four longest stay cables named as CBA34, CBJ34, CNJ34 and CNA34 on the north tower. The yield strength σ_b of cables is 1860MPa. The threshold of vertical deflection u_{max} for the main girders of cable-stayed concrete bridge is 0.84m under vehicle load without consideration of impact factor (JTJ027-96, 1996).

5.5. Network Parameters Selection and Reliability Analysis Result

For reliability analysis, several random variables are selected in this paper referred from calculation results about sensitivity factors of structural static reliability (Cheng and Xiao, 2004). A RBF neural network is designed and the network has 17 nodes of input layer. They are random variables considered in structural analysis progress primarily and 5 nodes of output layer which are displacement of mid-span for structural main girder, cable force of CBA34, CBJ34, CNJ34 and CNA34. Parameters in RBF neural network are shown in Table 4.

Table 4. Parameters of RBF Neural Network.

Items	Numerical value	Introductions
Nodes of the input layer	17	Random variables in Tab.3
Nodes of the output layer	5	u_{mid} 和 T_{cab}^{i}(i=CBA34, CBJ34, CNJ34,CNA34)
The class number of training data	200	Uniform design chart is ($U_{200}(200^{17})$)
The class number of test data	30	random drawing
Network control precision	1e-6	Precision of network training after data normalization
Precision testing requirements	1%	The error rate of mid-span displacement and #CNA34 cable force

Static reliability of cable-stayed bridge is calculated utilizing the hybrid approach. Under serviceability limit state, vehicle loads are distributed uniformly in mid-span of main girder. The corresponding static reliability β of displacement limit failure in mid-span for main girder is 7.394. The reliability indices of strength failure for #CBA34、#CBJ34、#CNJ34 and #CNA34 cables are β_{CBA34}=4.973, β_{CBJ34}=5.236, β_{CNJ34}=5.112 and β_{CNA34}=4.867. The five reliability indices are shown in Figure 5.

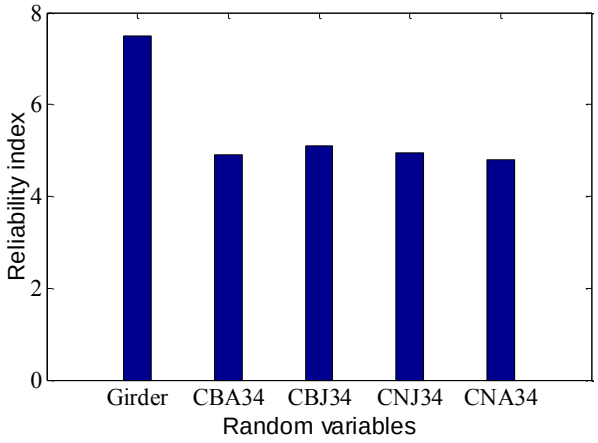

Figure 5. The Reliability Indices of the Critical Failure Location.

Structural reliability index β is calculated by mean value, standard deviation, of random variables. It is necessary to do research about influence on reliability index β by mean value, standard deviation, of random variables. It is sensitivity study of random variables (Cheng and Li, 2009). Reliability index β sensitivity on mean value μ_i, standard deviation σ_i of random variables is obtained by approximate formulae as follows (Hohenbichler and Rackwitz, 1986).

$$\begin{cases} \dfrac{\partial \beta}{\partial \mu_i} \approx -\alpha_i \\ \dfrac{\partial \beta}{\partial \sigma_i} = -\beta \alpha_i^{\,2} \end{cases} \tag{6}$$

Where α_i is direction of the ith random variable in standard normal distribution space, β is reliability index, μ_i and σ_i are mean value and standard deviation of the ith random variable. Sensitivity of reliability index on different mean value and standard deviation of random variable is observed under vehicle load distributed in whole main span in the point of mid-span of main span, as shown in Figure 6, reliability index is the most sensitive to mean value and standard deviation of vehicle load $q_{k.}$

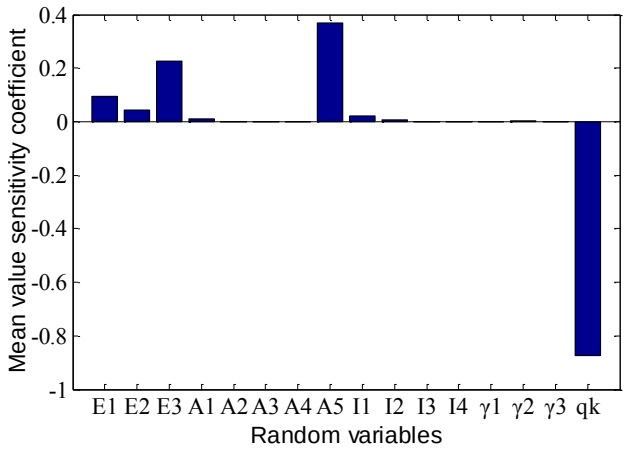

(a) The mean of random variable.

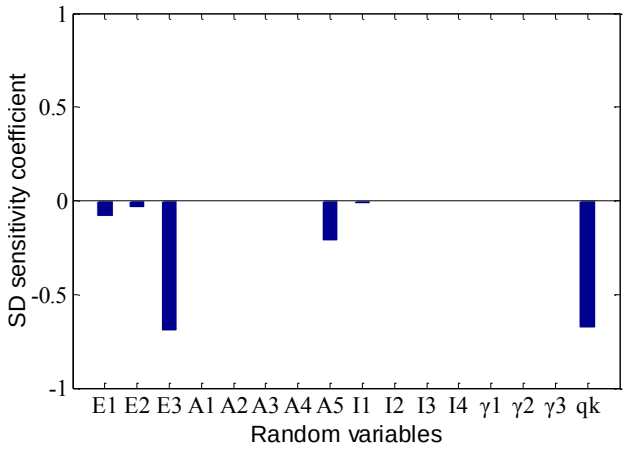

(b) The standard deviation of random variable.

Figure 6. Sensitivity of the Reliability Index for the Random Variables of Mean, Standard Deviation.

The influence of vehicle load on reliability index is studied under different mean coefficient (Kong et al, 2012). The variation tendencies of reliability index β under displacement ultra-limit failure state in mid-span of main girder and strength failure state of the four longest stay cables are shown in Figure 7, where intervals of mean coefficient for vertical load q_k is 1~2.

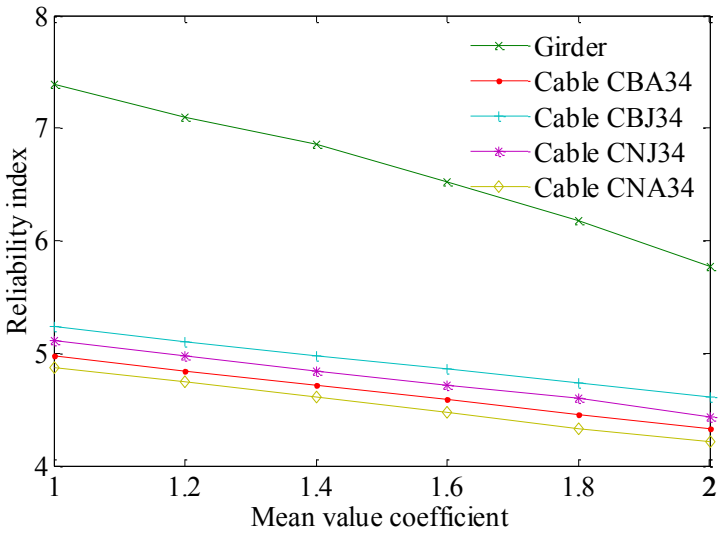

Figure 7. Reliability Index of Critical Failure Locations under Different Mean Coefficient of Vehicle Loads.

It can be found from Figure 7 that reliability indices β of displacement failure of mid-span for main girder and strength failure of that four longest stay cables are decrease with the increase of mean coefficient of vehicle load. When mean coefficient increase to 2.0, the displacement ultra-limit failure declines 30.786% and the strength failure declines 16.558%~18.923%. With gradually development of mean coefficient, downward trend of the displacement ultra-limit failure is more obvious. The reliability index of displacement ultra-limit failure for mid-span is greater than strength failure of four long stay cables.

6. Conclusions

This paper presented a hybrid algorithm method for reliability analysis of long-span PC cable-stayed bridge based on reliability theory. The hybrid algorithm method was used to analyze reliability index of a long-span PC cable-stayed bridge under vehicle load. Influence of random variables on structural reliability index has been conducted with a sensitivity analysis. The following conclusions can be obtained:

a) The hybrid approach integrates the advantage of RBF neural network, GA and Monte Carlo importance sampling method. Two numerical studies are utilized to verify the feasibility of the hybrid approach applied to reliability calculation of large complicated structures. The analysis results indicate that the hybrid approach has satisfactory accuracy and calculation efficiency.

b) In the case study, the reliability index for displacement failure of griders in mid-span is greater than reliability index for strength failure of the stay-cable.

c) Parametric sensitivity analysis indicates that reliability index of cable-stayed bridge is sensitive to mean and standard deviation of vehicle load. The other sensitive factors are cross section area of stay cable, mean and standard deviation of elasticity modulus.

d) Reliability indices of displacement failure of mid-span for main girder and strength failure of the four longest stay cables are decrease with the increase of mean coefficient of vehicle load. Besides, downward trend of the displacement ultra-limit failure is more obvious with gradually development of mean coefficient.

References

Biondini, F., D. M. Frangopol and P.G. Malerba. Uncertainty Effects on Lifetime Structural Performance of Cable-stayed Bridges[J]. Probabilistic Engineering Mechanics, 23(4):509−522, 2008.

Chen, T. B., S. Q. Wang and Z. Y. Shi. Reliability Analysis of Cable-stayed Bridges Considering Geometrical Non-linearity[J]. Journal of Tongji University (Natural Science), 28(4):407−412, 2000.

Cheng, J., Q. S. Li and R. C. Xiao. A New Artificial Neural Network-based Response Surface Method for Structural Reliability Analysis [J]. Probabilistic Engineering Mechanics, 23(1):51−63, 2008.

Cheng, J. and R. C. Xiao. Probabilistic Free Vibration and Flutter Analyses of Suspension Bridges[J]. Engineering structures, 27(10):1509−1518, 2005.

Cheng, J. and R. C. Xiao. Static Reliability Analysis of Cable-stayed Bridge[J]. Journal of Tongji University (Natural Science), 32(12):1593−1598, 2004.

Cheng, J. and Q. S. Li. Reliability Analysis of a Long Span Ateel Arch Bridge Against Wind-induced Stability Failure During Construction[J]. Journal of Constructional Steel Research, 65(3):552−558, 2009.

Gong, Q., J. Zhang, C. Tan, et al. Neural Networks Combined with Importance Sampling Techniques for Reliability Evaluation of Explosive Initiating Device[J]. Chinese Journal of Aeronautics, 25(2):208−215, 2012.

Gui, J. S. and H. G. Kang. The Study of the Whole Response Surface Method for Structural Realibility Analysis[J]. Journal of Building Structures, 25(4):100−105, 2004.

Hohenbichler, M. and R. Rackwitz. Sensitivity and Importance Measures in Structural Reliability[J]. Civil Engineering Systems, 3(4):203−209, 1986.

JTJ027-96, Chinese Design Specification of Highway Cable-stayed Bridge[S].

Kong, X., D. J. Wu, C. S. Cai, et al. New Strategy of Substructure Method to Model Long-span Hybrid Cable-stayed Bridges under Vehicle-induced Vibration[J]. Engineering Structures, 34:421−435, 2012.

Li, X. J. and Y. C. Hu. Study on the Approximate Structural Reliability Analysis Method Based on GA-NN Combined Technology[J]. China Civil Engineering Journal, 33(5):40−45, 2000.

Shen, H. S. and X. Y. Wang. Static and Dynamic Analysis of Girders of Cable-stayed Bridges[J]. China Journal of Highway and Transport, 9(1):59−65, 1996.

Tang, Q. Y. and C. X. Zhang. Data Processing System (DPS) Software with Experimental Design, Statistical Analysis and Data Mining Developed for Use in Entomological Research [J]. Insect Science. 20(2):254−260, 2012.

Wang, Y., Z. X. Li and A. Q. Li. Combined Use of SHMS and Finite Element Strain Data for Assessing the Fatigue Reliability Index of Girder Components in Long-span Cable-stayed Bridge[J]. Theoretical and Applied Fracture Mechanics, 54(2):127−136, 2010.

Wu, F. W. and L. Zhao. Static Reliability Analysis of the Main Girder of Concrete Cable-stayed Bridge[J]. Journal of the China Railway Society, 28(3):88−91, 2006.

Zhang, Q. H., Y. Z. Bu and Q. Li. Hybrid Chaos Algorithm of Structural Reliability Analysis of Cable-stayed Bridge[J]. China Journal of Highway and Transport, 21(3):48−52, 2008.

Zhang, J. R. and Y. Liu. Realibility Analysis of Cable-stayed Bridge Using GAS and ANN[J]. China Civil Engineering Journal, 34 (1):7−13, 2001.

Damage Identification and Uncertainties in Coupled Non-Linear Thermo-Hydro-Mechanical Problems Applied to Masonry Dams

Long Nguyen-Tuan[1)], Tom Lahmer[1)], Carsten Könke[1)] and Volker Bettzieche[2)]
[1)] *Institute of Structural Mechanics – Bauhaus-Universität Weimar,*
Marienstrasse 15, 99423 Weimar, Germany,
{*long.nguyen.tuan, tom.lahmer and carsten.koenke*}*@uni-weimar.de*
[2)] *Department of Dam Maintenance and Geotechnics, Ruhrverband, Germany,*
vbe@ruhrverband.de

Abstract: In this paper, we introduce a method to identify a damage zone and the material properties at the damage zone by means of inverse analysis based on a series of measurement data such as transient displacements, temperatures and water pressures. The inverse problem is solved iteratively by the Particle Swarm Optimization method. The uncertainty of the measurement data may propagate to the uncertainty in the identification of the damage zone. This paper considers the uncertainty of the measurements by assuming different noise levels of the measurements. The uncertainty of the damage zone can be quantified by its probability distribution.

Keywords: damage identification, masonry dam, optimization, uncertainty quantification

1. Introduction

After more than one hundred years in use, material properties of the masonry dam bodies are changed. The deterioration of the material properties is supposed because of ageing, weathering and chemical effects. Consequently, there could appear some zones or cracks, where the properties of the material (e.g. stiffness, permeability and thermal conductivity) have a big change. It is useful and economic that the damage zone can be identified based on the present measurement data, which are obtained via the devices which are permanently installed in the dam.

Ordinarily, masonry dams have to bear two major loads: water pressure and self-weight load. Besides that the temperature inside the dam structure varies according to the water levels and air temperatures. This causes stresses within the structure and deformation of the dam. These behaviours have been monitored in terms of temporal displacement, water pressure, and temperature. According to the measurement in (Bettzieche, 2004), the effect of temperature on the deformation of the masonry dam is significant. Therefore, thermal conduction, water transport and force - deformation relations have to be considered when performing numerical simulations of the dam (Nguyen-Tuan et al., 2015).

The damage can be identified based on statistics and optimization against the experimental data such as reduction of natural frequencies (Wang and He, 2007) or monitoring of displacements with radar (Ardito and Cocchetti, 2006). The damage zone of the dam has been also identified using the inverse problem based on a hydro-mechanical model (Lahmer, 2010). It is to note that the

reliability of the solution of the inverse problem depends on the accuracy of the measurements, the variety of the measurements and the variety of loading conditions. The variety of the measurements is determined by the distribution of the measurement points and the type of measurements (e.g. displacement, water pressure, seepage of water and temperature). In this paper, we introduce a method to identify the damage zone by means of inverse analysis based on a series of measurement data such as transient displacements, temperatures and water pressures. The inverse problem is solved iteratively by the Particle Swarm Optimization (PSO) (Kennedy and Eberhart, 1995). The uncertainties of the measurement data may propagate to the uncertainty in the identification of the damage zone. This paper considers the uncertainties of the measurements by assuming different noise realizations in the data and the uncertainties of the damage zone can be quantified by its probability distribution.

2. Methodology

2.1. Formulation of inverse analysis

The forward operator (F), which maps the input model parameters of the damage zone to the responses at the finite sub-domains or boundaries (i.e displacement u, water pressure P_l and temperature T), is

$$\begin{aligned} F : X &\to Y \\ \boldsymbol{p} &\mapsto (u, P_l, T), \end{aligned} \tag{1}$$

where X denotes the parameter space, Y denotes the space of responses. The responses at the sub-domains Γ is denoted by a set of responses e.g. $\boldsymbol{y}(t) = y(u(t), P_l(t), T(t))$, where t is the time, u is the displacement, P_l is the liquid pressure and T is the temperature. The measurements of the responses are generally distorted by a certain amount of noise. These measurements with noise are denoted by $\boldsymbol{y}^{\varepsilon}$. The $\boldsymbol{\varepsilon}$ is introduced as a set of random noise in the measurements, i.e.

$$\boldsymbol{y}^{\varepsilon}(t) = \boldsymbol{y}(t) + \boldsymbol{\varepsilon}(t). \tag{2}$$

Assuming that a finite element model is used as forward operator, which maps a model with damage zone to the model responses accurately, the inverse problem with given measured data is defined by

$$F(\boldsymbol{p}) = \boldsymbol{y}^{\varepsilon}(t). \tag{3}$$

In the indirect method of inverse analysis, the parameters $\boldsymbol{p}$ are estimated by minimising a norm of the difference between the measured responses ($\boldsymbol{y}^{\varepsilon}$) and the model responses ($F(\boldsymbol{p})$). The norm is known as 'objective function'. The optimization algorithms drive an objective function in a way to find the minimum value of the objective function by changing the input parameters systematically. The questions of the inverse problem are to define the parameters as variables for the forward model, to define the objective function and to establish a suitable iterative algorithm for optimizing the objective function.

2.2. Objective function

Let $\boldsymbol{y}^{\varepsilon}$ be a set of measured data from an experiment and $\boldsymbol{y}^{c}$ be a set of obtained data by numerical simulation depending on a vector of model parameters $\boldsymbol{p} = \{p_1, p_2, ..., p_J\}$. The difference between the calculated and measured values defines the residual

$$f_{tmd}(\boldsymbol{p}) = y^{\varepsilon}_{tmd} - y^{c}_{tmd}. \tag{4}$$

It is defined that $t = 1, 2, ..., T_t$, where T_t is the number of measured data according to time, $m = 1, 2, ..., M$, where M is the number of selected points for observation, $d = 1, 2, ..., D$ is the number of serial measurements, for instance temperature, degree of saturation, or stress in one location and ω_{tmd} is the weighting factor for each measurement, a function of the model parameters is expressed as a normalized weighted sum of the squared errors

$$f_d^{MAE}(\boldsymbol{p}) = \sqrt{\sum_{t=1}^{T_t}\sum_{m=1}^{M} \frac{[f_{tmd}(\boldsymbol{p})]^2 \omega_{tmd}}{\sum_{t=1}^{T_t}\sum_{m=1}^{M}[y^{\varepsilon}_{tmd}]^2}}\ , \tag{5}$$

where values of ω_{tmd} depend on the importance and reliability of the analysed data. In Eq. (5), it is assumed that $\sum_{t=1}^{T_t}\sum_{m=1}^{M}[y^{\varepsilon}_{tmd}]^2$ is larger than zero.
Finally, considering the multi-field data, such as D different serial measurements, the objective function is defined as

$$f(\boldsymbol{p}) = \frac{1}{D}\sum_{d=1}^{D} f_d^{MAE}(\boldsymbol{p})\omega_d\ , \tag{6}$$

where ω_d is the weighting factor for each serial measurement.

In special cases, when the y^{ε} cannot be measured at each point, i.e. the flux of water out of the dam, the common method to do so is to collect the amount of water on finite areas. Figure 2 illustrates the water collection along the downstream side. The water fluxes at the areas $a-b$, $b-c$, $c-d$, $d-e$ and $e-f$ are collected at the collecting point a, b, c, d and e respectively. Therefore, in the numerical simulation we have to integrate the water in each domain ($a-b$, $b-c$, $c-d$, $d-e$ and $e-f$) in order to compare with the measurement data. For instance, water collected Q_o at a collecting point is

$$Q_o = \int_a^b q_o \mathrm{d}l = \int_a^b \left[q_x \cos(\theta) + q_y \sin(\theta)\right] \mathrm{d}l, \tag{7}$$

where q_o is the flux of water out of line a-b at position l. The direction of the flow is perpendicular with the boundary plain, therefore, q_o is converted from flux flowing x axis and flux following y axis, see Fig 1. Here, θ denotes the angle between boundary line and vertical axis.

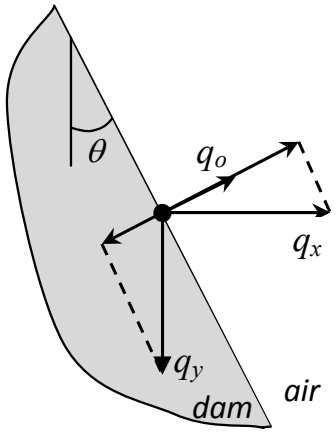

Figure 1. Axis translation of the out flow of water.

2.3. Parameterization of the forward problem

The parameters of the forward problem include a set of parameters for the initial materials (structures and subsoils), a set of parameters for the damage material, a set of parameters defining the geometry of the initial forward problem and a set of parameters defining the geometry of the damage zone. In this paper, we define the sets of parameters for the initial materials and the set of parameters defining the geometry of the initial forward problem as the constants. The set of parameters defining the geometry of the damage zone is considered the unknowns in the inverse problem. The geometry of damage zone is diverse. The complex geometry could lead to the complex function with many parameters, which could slow down the convergence of the objective function. It is acceptable if the damage zone can be quantified approximately by less number of parameters. In this paper, the geometry of the damage geometry is defined by a moving elliptic shape. The material parameters of the damage zone are also considered the unknowns. Therefore, the damage zone can be defined as follows,

$$g(\boldsymbol{p}) = g(\boldsymbol{p}_g, \boldsymbol{p}_m) \tag{8}$$

where $\boldsymbol{p}_g$ is the vector defining the geometry of the damage, $\boldsymbol{p}_g = (a, b, x_c, y_c, \alpha)$, in which a is the major radius, b is the minor radius, $(x_c,\ y_c)$ are the center coordinates in the x, y plain, α the rotation angle of the major diameter. The elements inside this ellipse are defined as damage material. The example of the damage zone in the dam body is presented in Figure 2, the white elements represent the damage zone, which are bounded by the function $g(\boldsymbol{p}_g)$.

The vector $\boldsymbol{p}_m$ includes model parameters defining the behaviour of the material at the damage zone, $\boldsymbol{p}_m = (E, k_o, \lambda)$, in which E is the elastic modulus, k_o is the intrinsic permeability, λ is the thermal conductivity. The deterioration of the material properties at the damage zone has close correlation with the porosity. The change of porosity effects explicitly the elastic modulus, the permeability and the thermal conductivity. Therefore, the relations between E, k_o and λ are described in the constitutive models. With the change of porosity, these parameters will change, accordingly. Consequently, the number of unknown parameters reduces.

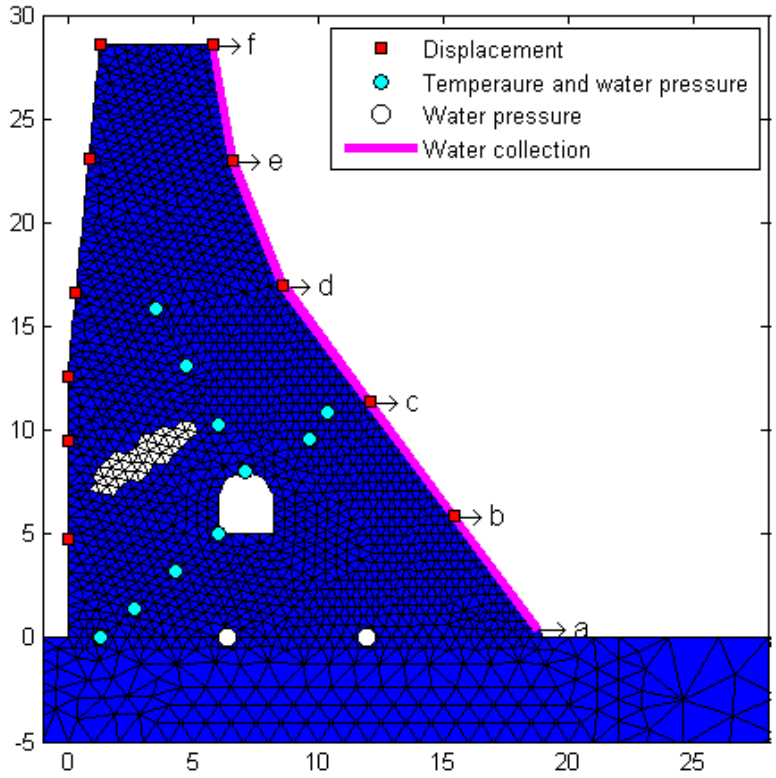

Figure 2. Geometry, assumed damage zone and measurement locations.

2.4. Optimization method

Particle swarm optimisation works basically by considering a population (called a "swarm") of candidate solutions of the optimisation problem (called particles). These particles are moved around in the search space according to several simple laws. The movements of the particles are guided by their own best known position in the search space as well as the entire swarm's best known position. Translating this to parameter identification problems, we consider a collection (swarm) of parameter vectors. Now, the entries in the vectors are repeatedly updated by combining local and global information about the values of the objective functions for the different parameter vectors. When better vectors are discovered, they will determine the further updates of the parameters. This process is repeated iteratively and by doing so, it is expected that a satisfactory solution of the calibration problem will eventually be discovered with high probability.

2.5. Uncertainties in damage identification

The sources of uncertainties in identification of the damage are of different types, for instance, the inhomogeneous material, the accuracy of the model, the accuracy of the measurements and the uncertainty of the optimization algorithm. This paper firstly intends to quantify the uncertainties caused by the accuracy of the measurements and the uncertainty of the optimization algorithm. By changing the amount of noise $\boldsymbol{\varepsilon}$ ($\varepsilon = \delta R_n y^{\varepsilon}$), where ε is an entry of $\boldsymbol{\varepsilon}$, R_n is a random number following the standard normal distribution, δ is the noise level, the accuracy of the re-constructed shapes will be considered.

Secondly, the uncertainty of the optimization algorithm can be quantified by the distribution of the solution, when the optimization is repeated n times with the random initial guess in the search space (Nguyen-Tuan et al., 2016), it is called sampling process. The samples of the optimizations are accessed by statistical methods accordingly.

2.6. Forward model: balance equations

The THM problems are formulated by a system of coupled balance equations. Equations for mass balance were established by following the compositional approach (Olivella et al., 1996). Constitutive equations are used to connect between the primary unknowns (i.e. displacements, liquid pressure, gas pressure and temperature) to the parameters and the dependent variables e.g. water saturation, energy flux and so on. In the sequel, we describe briefly the forward model by giving the most essential balance equations.

Mass balance of water: Water is present in the liquid phase. The total mass balance of water is expressed as follows:

$$\frac{\partial}{\partial t}\left(\theta_w\right) + \nabla \cdot \left(\boldsymbol{q}_w\right) = f^w. \tag{9}$$

where f^w is an external supply of water, θ_w is the volumetric mass of water, $\boldsymbol{q}_w$ is the advective fluxes.

Momentum balance for the medium: The momentum balance reduces to the equilibrium of stresses if the inertial terms are neglected as:

$$\nabla \cdot \boldsymbol{\sigma} + \boldsymbol{b} = \boldsymbol{0}, \tag{10}$$

where, $\boldsymbol{\sigma}$ is the stress tensor and $\boldsymbol{b}$ is the vector of body forces.

Internal energy balance for the medium: Heat transfer is modelled considering heat conduction of material and heat transport by means of mass motion. The equation for the internal energy balance for the porous medium is established taking into account the internal energy in each phase (E_s, E_l) as:

$$\begin{aligned} &\frac{\partial}{\partial t}\left(E_s \rho_s \left(1-\phi\right) + E_w \rho_w \phi\right) + \\ &\quad \nabla \cdot \left(\boldsymbol{i}_c + \boldsymbol{j}_{Es} + \boldsymbol{j}_{Ew}\right) = f^Q, \end{aligned} \tag{11}$$

where, $\boldsymbol{i}_c$ is the energy flux due to the conduction through the porous medium, the fluxes $\boldsymbol{j}_{Es}$, $\boldsymbol{j}_{Ew}$ are advective fluxes of energy caused by mass motions and f^Q is an internal/external energy supply, ρ_s is the density of solid, ρ_w is the density of the liquid i.e. 1000 [kg.m^{-3}].

The final objective is to find the unknowns from the balance equations. Therefore, the dependent variables have to be related to the unknowns in the following constitutive relations. The constitutive relations of the coupled THM model includes thermo-elastic model for stress-strain relation, constitutive model for water transport (Darcy's law) and constitutive model for heat conduction (Fourier's law). The validation of the model in the non-damage case is reported in Nguyen-Tuan et al..

3. Application to Masonry Dams

3.1. Geometry and discretization

The cross section of the Fürwigge dam is used for forward and inverse simulations. The data are generated synthetically by solving the forward problem. To avoid inverse crimes (Colton and Kress, 2013), the generation of the synthetic measurements is performed on a different mesh from the inverse process. The geometry and discretization mesh, which can be seen in Figure 2, are used for synthesizing measurement data. This mesh has 2520 elements. In the inverse process, the geometry mesh has 3357 elements. It is assumed that the white elements is a damage zone where its material properties ($\boldsymbol{p}_m$) are defined by its porosity.

3.2. Damage indentification

The assumed damage zone is pure artificial and not related to the current working conditions of the Füwigge dam. The search space is illustrated in Figure 3. The noise level is $\delta = \pm 1$ and $\pm 5\%$. We chose a swarm size of 24 particles. The reason is that the convergence of the big swarm is faster than the convergence of the small swarm, and the big swarm will decrease the probability of the local minimum trap.

The measurement data, which are used to formulate the objective function, are established by the displacement, temperature, water pressure and the collection of the water outflow. Displacement are measured by 2 radar devices at the downstream side and pendulum for the upstream side, herein 11 measurement points are the selected (red rectangular points). Water pressures and temperatures are measured at the cyan circular points (10 points), the water pressures are additional measured at two more white points as it was designed in Fürwigge dam, see Figure 2. Thermocouples are used to measure temperature. Water pressures are measured by piezometers or tensiometers. The volume of water outflow at downstream side (magenta line) are measured at the collecting points (a, b, c, d and e). In numerical simulation, the water outflow is computed as in Eq. (8). The porosity is the unknown quantity and it varies in the bounds from 0.30 to 0.65.

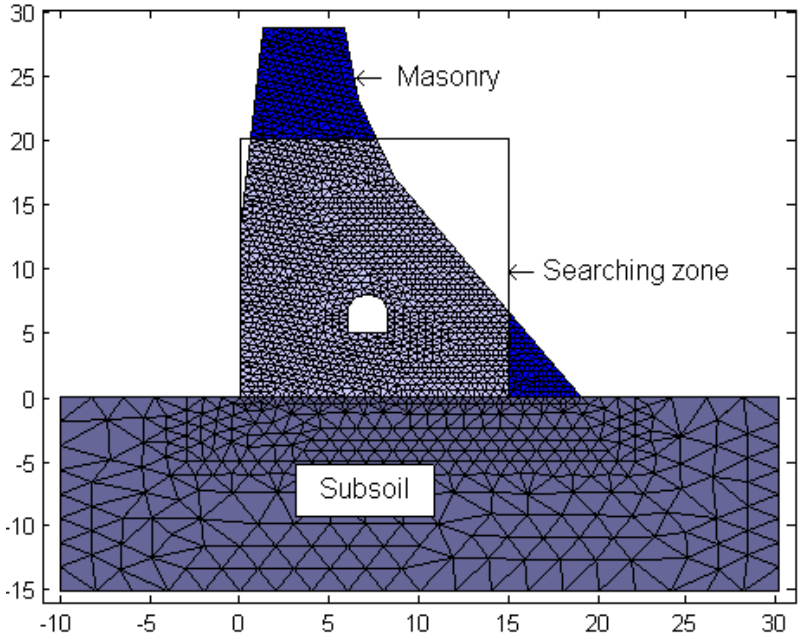

Figure 3. Materials and searching zone.

4. Results

Figure 4 presents the re-construction (inverse) solutions considering several noise levels. When the level of noise increases from ±1% to ±5% the uncertainty of the solutions increase, accordingly. The best objective functions presented in the figure is of the solution with ±1% noise level. The deterioration of the material properties is defined by the material porosity (ϕ). The solution in terms of porosity shows that the inverse solutions are close to the exact solution. The figure shows that the PSO method can be a good method for damage identification.

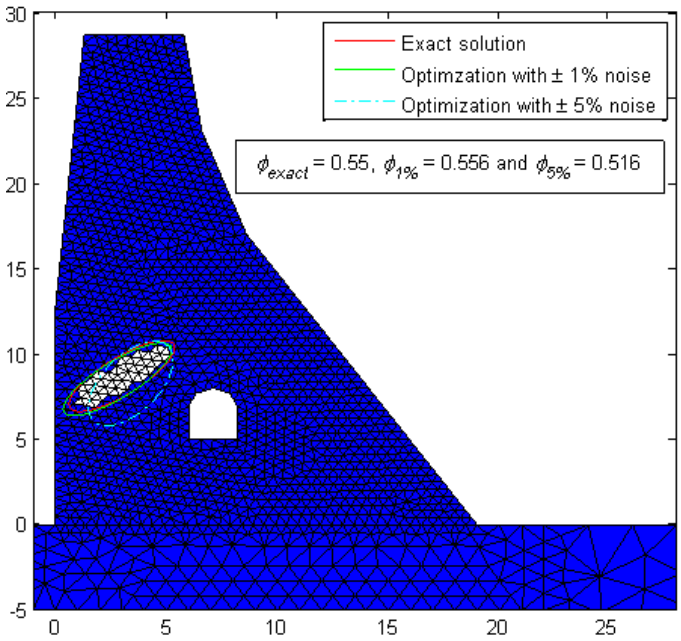

Figure 4. Results of optimization for different noise levels.

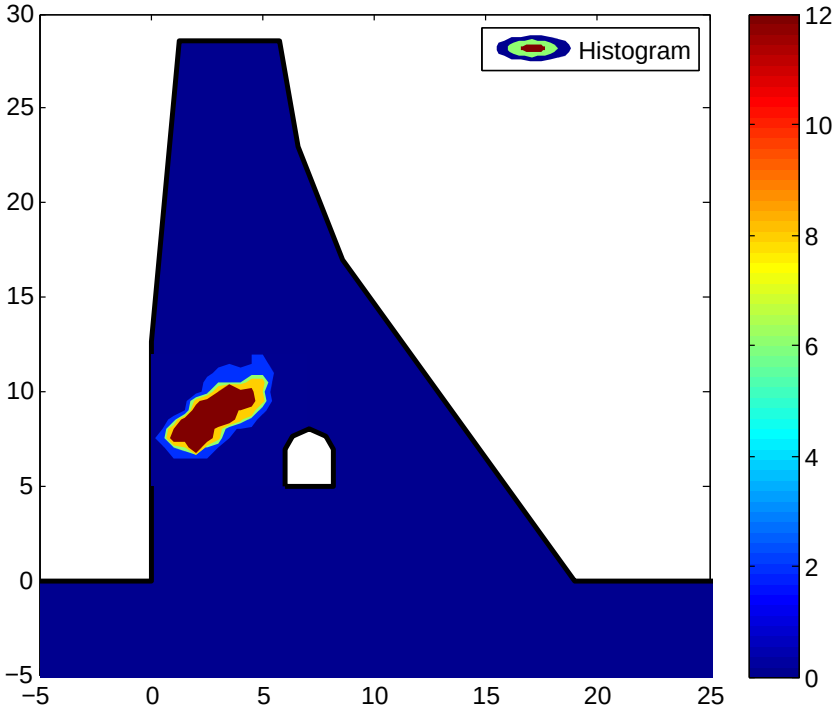

Figure 5. Histogram of the solutions ($\delta = 0\%$).

The inverse problem is solved repeatedly 15 times by PSO method. In order to avoid the dependence of the initial guess, the initial guesses of the particles are randomly uniform distributed in their search space. The histogram of the solution is presented in Figure 5. The color bar illustrates the frequency of the solutions which describe the damage zone. Certainly, the solution can not fit totally with the exact solution, because we used different meshes in the inverse and forward problems. It shows that the method can identify the damage zone with small uncertainty, when the noise level is zero. However, the uncertainty can also increase when the noise level increases. It can be recognized that the solutions are not identical with different initial guesses, however, the convergence of the solution is close to the exact solution.

5. Conclusion

In this paper, we introduce the method to not only detect the damage zone but also identify the severity of the damage. The severity of the damage is described by its material parameters in the coupled THM model. The PSO shows that it is a robust method in searching the minimum of the non-linear objective functions. The accuracy of the measurement data effects significantly the uncertainty of the results of the inverse problems. The uncertainty of the inverse problem can be quantified by the the probability distribution of the solutions obtained from the sampling process.

References

Ardito, R. and G. Cocchetti. Statistical approach to damage diagnosis of concrete dams by radar monitoring: Formulation and a pseudo-experimental test. *Engineering Structures*, 28(14):2036–2045, 2006.

Bettzieche, V. Mathematisch-statistische Analyse von Messwerten der Talsperrenueberwachung. *Wasserwirtschaft*, 94(01–02):1–5, 2004.

David Colton and Rainer Kress. *Inverse Acoustic and Electromagnetic Scattering Theory* (3 ed.). Applied Mathematical Sciences 93. Springer-Verlag New York, 2013.

Huyer, W. and A. Neumaier. Global optimization by multilevel coordinate search. *J. Global Optimization*, 14:331–355, 1999.

Kennedy, J. and R. Eberhart. Particle swarm optimization. In *Proceedings of IEEE International Conference on Neural Networks. IV*, pages 1942–1948, 1995.

Lahmer, T. Crack identification in hydro-mechanical systems with applications to gravity water dams. *Journal of Inverse Problems in Science and Engineering*, 18(8):1083–1101, 2010.

Nguyen-Tuan, L., T. Lahmer, V. Bettzieche, and K. Koenke. Simulation models for 3D coupled thermo-hydro-mechanical problems in masonry dams. In *Proc. of The 6-th Int. Conf. Approx. Methods and Numerical Modelling in Environment and Natural Resources*, June 2015.

Nguyen-Tuan, L., T. Lahmer, M. Datcheva, E. Stoimenova, and T. Schanz. A novel parameter identification approach for buffer elements involving complex coupled thermo-hydro-mechanical analyses. *Computers and Geotechnics*, 76:23–32, 2016.

Olivella, S., J. Carrera, A. Gens, and E. E. Alonso. Numerical formulation for a simulator (CODE_BRIGHT) for the coupled analysis of saline media. *Engineering Computations*, 13:87–112, 1996.

Wang, B. S. and Z. C. He. Crack detection of arch dam using statistical neural network based on the reductions of natural frequencies. *Journal of Sound Vibration*, 302:1037–1047, 2007.

AUTHOR INDEX